12-11-2017 10:30 AM

Studying Metal-Organic Frameworks via Solid-State NMR: Gas Dynamics, Structure Determination, and Phase Transition

Yue Zhang
The University of Western Ontario

Supervisor
Huang, Yining
The University of Western Ontario

Graduate Program in Chemistry
A thesis submitted in partial fulfillment of the requirements for the degree in Doctor of Philosophy

Recommended Citation

Zhang, Yue, "Studying Metal-Organic Frameworks via Solid-State NMR: Gas Dynamics, Structure Determination, and Phase Transition" (2017). *Electronic Thesis and Dissertation Repository*. 5162.
https://ir.lib.uwo.ca/etd/5162

Abstract

Metal-organic frameworks (MOFs) are a class of microporous materials constructed from virtually endless combinations of metal centres and organic linkers. MOFs have attracted intense research interest in recent decades due to their outstanding properties such as extremely high surface areas, tuneable pore topologies, good stabilities, and many others. These materials are also promising candidates for gas storage. In this work, solid-state NMR (SSNMR) spectroscopy has been employed to study MOFs and adsorbed guest molecules. SSNMR spectroscopy can provide information on the short-range environment about target nuclei and can also reveal the dynamics of guest molecules.

This thesis begins with a general outline of MOFs, along with a physical and experimental background on SSNMR. Following this, variable temperature (VT) static ^{13}C and ^{2}H SSNMR experiments are described, which employed isotopically-labeled $^{13}CO_2$, $^{2}H_2$ and deuterated-methane to study the dynamics of carbon dioxide, hydrogen and methane within different MOFs. The CO_2 adsorption sites within MIL-53 and metal-fumarate MOFs have been experimentally confirmed using ^{1}H-^{13}C cross polarization (CP) SSNMR experiments. Along with dynamic information, the binding strength of various gases within MOFs was also investigated using SSNMR experiments. ^{2}H SSNMR and powerful complementary techniques, including single crystal X-ray diffraction (SCXRD) and DFT calculations, was used to reveal the methane adsorption sites, methane adsorption behaviour, and the presence of the nuclear independent chemical shift (NICS) effect within several MOFs. The successful synthesis of new Ga- and In-fumarate MOFs is also included in this thesis. Synchrotron powder X-ray diffraction (pXRD) refinement and $^{69/71}$Ga SSNMR experiments at 21.1 T have been employed to determine the crystal structure of Ga-fumarate. CO_2 adsorption within fumarate MOFs has also been comprehensively studied using SSNMR experiments. This thesis also includes a comprehensive SSNMR study of different phases of the flexible Ga-MIL-53 MOF. It is shown that $^{69/71}$Ga SSNMR spectra are very sensitive to distortions in the octahedral GaO_6 secondary building units within Ga-MIL-53; by extension, $^{69/71}$Ga NMR parameters are indicative of the particular crystallographic phase of Ga-MIL-53.

This thesis demonstrates SSNMR is an advanced technique to study gas dynamics within MOFs and also a powerful tool that can assist in probing MOF structures. Based on the study, novel MOFs, which have excellent guest capacity can be designed in the future.

Keywords

Metal-organic frameworks, solid-state NMR, guest dynamics, CO_2, H_2, CH_4, quadrupolar nuclei, ultrahigh field

Co-Authorship Statement

This thesis is a result of joint research. All materials in this thesis are presented in manuscript format, which contain previously published manuscripts and submitted manuscripts. Prof. Yining Huang, as my advisor and supervisor, made key contributions to the thesis and was the corresponding author on all the presented papers. I acknowledge Dr. Bryan E. G. Lucier, who assisted with the writing and editing of all manuscripts.

Chapter 2 has been previously published in *Phys. Chem. Chem. Phys.*, **2016**, 18, 8327-8341, and was co-authored by Yue Zhang, Bryan E. G. Lucier, and Yining Huang. The samples were prepared by Yue Zhang. Yue Zhang and Bryan E. G. Lucier performed the experiments and prepared the manuscript. Yining Huang revised the manuscript

The majority of *Chapter 3* has been published as a communication (*Chem. Commun.*, **2016**, 52, 7541-7544) co-authored by Bryan E. G. Lucier,* Yue Zhang,* Kelly J. Lee, Yuanjun Lu, and Yining Huang. Bryan E. G. Lucier and Yue Zhang contributed equally to this paper. The manuscript was written by Bryan E. G. Lucier. Yue Zhang prepared most of the samples and performed the experiments. Kelly J. Lee and Yuanjun Lu provided the formate MOFs used in this paper. Yining Huang revised the manuscript. Part of *Chapter 3* (D_2 adsorption within Mg-formate) has been submitted to *Concepts Magn. Reson. Part A* and is co-authored by Bryan E. G. Lucier, Yue Zhang, and Yining Huang. Bryan E. G. Lucier prepared the manuscript. Yue Zhang preformed the SSNMR experiments on D_2 adsorption within Mg-formate MOFs, and Yining Huang revised the manuscript.

Chapter 4 is a manuscript under preparation and planned for publication. Yue Zhang prepared the samples, performed SSNMR experiments, and wrote the manuscript. The manuscript was edited by Bryan E. G. Lucier. Michael Fischer performed DFT calculations. Paul D. Boyle is credited for the SCXRD experiments. Zhehong Gan and Yining Huang revised the manuscript.

Chapter 5 is also a manuscript under preparation that will eventually be published. Yue Zhang synthesised most of the samples and prepared the manuscript. Bryan E. G. Lucier edited the manuscript. Sarah M. Mckenzie and Karanpreet Gill are credited for the preparation of In-fumarate. The pXRD refinement was done by Mihails Argangelskis and Tomislav Friščić (McGill University). Joel Reid acquired the pXRD patterns at the Canadian Light Source. Victor V. Terskikh acquired $^{69/71}$Ga and ^{115}In SSNMR spectra at 21.1 T (National Ultra-Highfield Facility for Solids, Ottawa). Yining Huang revised the manuscript.

Chapter 6 is from the published article co-authored by Yue Zhang, Bryan E. G. Lucier, Victor V. Terskikh, Renlong Zheng, and Yining Huang (*Solid State Nucl. Magn. Reson.*, **2017**, 84, 118-131). Yue Zhang synthesised most of the samples and performed all the experiments at 9.4 T. The manuscript was prepared by Yue Zhang and Bryan E. G. Lucier. Victor V. Terskikh undertook all SSNMR experiments at 21.1 T. Renlong Zheng was responsible for preparing samples of Ga-MIL-53 loaded with organic guests at high loading levels. Yining Huang revised the manuscript.

Acknowledgments

Four years ago, I decided to come to Canada, seeking a Ph.D. degree under the supervision by Prof. Yining Huang at Western University. Looking back now, I can recognize that it was one of the best decisions I have made. During these four years, I have worked with so many talented individuals, who were always available to help and support me to go this far.

First and foremost, I would like to express my heartfelt thanks to my supervisor, Prof. Yining Huang, for giving me this opportunity to work in this program and for all his kind supervision and encouragement throughout my entire project. Without him, I would not have started such an amazing journey.

Second, I would like to give my gratitude to our outstanding postdoctoral fellow, Dr. Bryan E. G. Lucier, for teaching me the techniques of SSNMR, giving me helpful advice on my project, editing my manuscript, and drinking beer with me. We have shared a wonderful time during these four years.

A big thanks is due to my old mentor Prof. Stuart L. James and past colleague Dr. Jose Casaban at *Queen's University Belfast*. The knowledge and habits I gained from them made my life much easier during my Ph.D. study.

I gratefully acknowledge the faculty and staff in the Department of Chemistry at Western University. I would like to thank Dr. Mathew Willans for his great help with the NMR spectrometer, and Dr. Paul Boyle for single crystal XRD experiments. Thanks are also given to Ms. Darlene McDonald and Ms. Anna Vandendries-Barr for their help during my program. I would like to thank Ms. Janice Mathers, Ms. Sandy Holtslag and Ms. Sue England for helping me to finish my teaching assistant duties. I would like to thank Mr. Yves Rambour in the glassblowing shop for providing us with many sample tubes over the past four years.

I would also like to thank our collaborators. I would like to thank Dr. Victor V. Terskikh at the *National Ultrahigh-field NMR Facility for Solids* for acquiring NMR spectra at 21.1 T and performing CASTEP calculations. I would like to thank Dr. Michael Fischer at the *University of Bremen* for performing DFT calculations on deuterated methane. I would like to thank Dr. Zhehong Gan at the *National High Magnetic Field Laboratory* for assisting with the analysis and explanation of ^{2}H SSNMR spectra. I would like to thank Dr. Joel Reid at the *Canadian Light Source* and Dr. Mihails Arhangelskis and Dr. Tomislav Friščić at *McGill University* for their kind help with pXRD refinement and DFT calculations.

I would like to thank the undergraduate students who I have worked with for their for their hard work and contributions to material included in my thesis: Sarah McKenzie, Kelly Lee, Grace Wang, Cici Yang, Yawen Wang, Renlong Zheng, and Karanpreet Gill.

Moreover, I would like to extend my gratitude to my friends and colleagues. Thanks to Yuanjun Lu and Shan Jiang for providing me with innumerable snacks. Thanks to Ray Hu and Riva Ye for their delicious BBQ. Thanks to Eric Wang for providing endless happiness. Thanks to Xuzhao Zhao's positive energy, and thanks to Nancy Liu for taking care of my dog. Thanks to Vince Guo and Zhiqiang Wang for teaching me how to play badminton. I thank Jun Li, Hanqing Zhao and Ni Zhou for their delicious cakes and Chinese food. Thanks to my buddies Qingliang Yang, Guobang Huang, Kai Gao, and Jiang Wang, you are great basketball teammates and drinking buddies. Thanks to Oliver Wang and Eve Chen for helping me keep a young mindset. Thanks to Shoushun Chen for being a good roommate. I would also like to thank Dr. Mansheng Chen, Dr. Jun Xu, Dr. Wei Wang, Dr. Haiyan Mao, Dr. Farhana Gil-E-Noor, Pan Wang, Mengnan Guo, Yingying Jiang, Bowei Wu, Dr. Tetyana Levchenko, Maxwell Goldman, Michelle Li, Fraser Filice, Dr. Renjie Hou, Dr. Shan Gao, Xiutian Cui, Biqiong Wang, Donghan Chen, and all my friends in China and the U.K. for their great support.

Finally and most importantly, I would like to express my deepest gratitude to my wife, my family, and my dog. Without their unconditional and everlasting support through the past years, this would not be possible.

Table of Contents

List of Tables

List of Figures

List of Abbreviations

as	as-made
ANG	adsorbed natural gas
BDC	1, 4 - benzenedicarboxylate
bdp	1, 4 - benzenedipyrazolate
BET	Brunauer-Emmett-Teller
bipy	2, 2’ – bipyridyl
BTC	1, 3, 5 - benzenetricarboxylate
BTT	1, 3, 5 – benzenetristetrazolate
CASTEP	Cambridge serial total energy package
CNG	compressed natural gas
COF	covalent organic framework
CP	cross-polarization
CPMG	Carr-Purcell Meiboom-Gill
CPO	coordination polymer of Oslo
CS	chemical shift
CSA	chemical shift anisotropy
CT	central transition
DAC	diamond anvil cell
DEF	*N*, *N* - diethylformamide
DMF	*N*, *N* - dimethylformamide
dobdc	2, 5 – dioxide – 1, 4 - benzenedicarboxylate
DOE	Department of Energy
DFT	density functional theory
EA	elemental analysis

EB	ethylbenzene
EFG	electric field gradient
enp	empty narrow pore
EXPRESS	exchange program for relaxing spin systems
FID	free induction decay
FT	Fourier transformation
FTIR	Fourier transform infrared spectroscopy
FWHH	full-width at half-height
GGA	generalized gradient approximation
GIPAW	gauge-including projector-augmented wave
HB	Herzfeld-Berger
HKUST	Hong Kong University of Science and Technology
ht	high temperature
LNG	liquid natural gas
int	intermediate
IR	infrared spectroscopy
IRMOF	isoreticular metal-organic framework
lt	low temperature
MAS	magic angle spinning
MCT	mercury cadmium telluride
MIL	Materials of the Institute Lavoisier
MOF	metal-organic framework
MX	*meta*-xylene
NG	natural gas
NMR	nuclear magnetic resonance
o. d.	outer diameter

OMS	open metal site
OX	*ortho*-xylene
PAS	principal axis system
PBE	Perdew-Burke-Ernzerhof
phen	*o*-phenantroline
ppm	parts per million
PX	*para*-xylene
pXRD	powder X-ray diffraction
pyz	pyrazine
QI	quadrupolar interaction
rf	radio frequency
SBU	secondary building unit
SCXRD	single crystal X-ray diffraction
SNU	Seoul National University
SSNMR	solid-state nuclear magnetic resonance
ST	satellite transition
TGA	thermogravimetric analysis
THF	tetrahydrofuran
TMS	tetramethysilane
WURST	wideband uniform-rate smooth truncation
S/N	signal-to-noise ratio
SEM	scanning electron microscopy
VOCS	variable-offset cumulative spectrum
VT	variable-temperature
XRD	X-ray diffraction

List of Symbols

B_0	static external magnetic field
B_1	applied radio frequency field
B_{eff}	effected magnetic field
C_2	two-fold rotation axis
C_6	six-fold rotation axis
C_{Q}	nuclear quadrupolar coupling constant
d	dipolar coupling constant
$\mathbf{D}$	dipolar coupling tensor
e	elementary electron charge (1.602×10^{-19} C)
h	Planck constant (6.626×10^{-34} J·s)
I	nuclear spin quantum number
$\mathbf{I}$	nuclear spin angular momentum vector
k	Boltzmann constant
mb	millibarn (10^{-31} m^2)
m_{I}	magnetic nuclear spin quantum number
$\mathbf{M}$	magnetization vector
N_α	Boltzmann population of lower energy levels
N_β	Boltzmann population of higher energy levels
Q	nuclear electric quadrupole moment
r	internuclear distance
S	spin quantum number
$\mathbf{S}$	spin angular momentum vector
T	temperature
T_1	spin-lattice or longitudinal relaxation time

T_2	spin-spin or transverse relaxation time
V_{XX}, V_{YY}, V_{ZZ}	principal components of the EFG tensor
α, β, γ	Euler angles
$\hbar$	Planck constant/2π
γ	gyromagnetic ratio
δ	chemical shift
δ_{11}, δ_{22}, δ_{33}	principal components of the chemical shift tensor
δ_{iso}	isotropic chemical shift
η_Q	EFG tensor asymmetry parameter
θ, ϕ	polar angles
κ	skew of the chemical shift tensor
μ	nuclear spin magnetic moment
μ_0	vacuum permeability constant
ω_0	Larmor frequency
ω_1	oscillation frequency of applied field
ω_{rf}	oscillation frequency of rf pulse
ω_Q	quadrupole frequency
ω_R	spinning rate
σ	chemical shielding
σ_{11}, σ_{22}, σ_{33}	principal components of the chemical shielding tensor
τ	interpulse delay
Ω	span of the chemical shift tensor

Chapter 1

1 General Introduction

1.1 Metal-organic frameworks (MOFs)

1.1.1 Composition and properties of MOFs

In the past twenty years, a novel class of materials known as metal-organic frameworks (MOFs)[1-4] has become one of the fastest-growing fields in chemistry. MOFs are porous crystalline materials constructed from two major components: metal ions/metal clusters (secondary building units (SBUs)) and organic linkers (Figure 1-1).[1-5] The combination of these two elements often leads to a structure with permanent porosity.

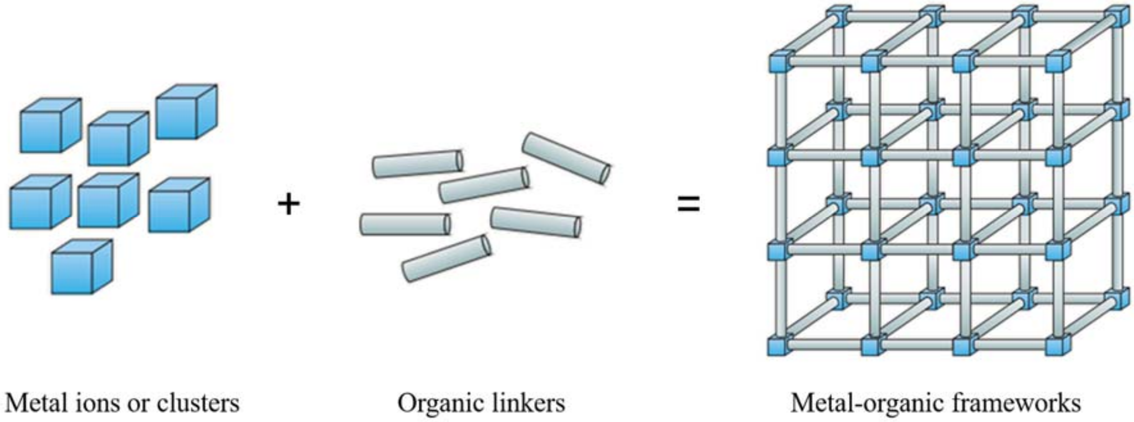

Figure 1-1: Schematic diagram of the composition of MOFs. (Reproduced from Ref. 5)

The surface areas of MOFs typically range from hundreds to thousands of m^2/g, which surpasses those of other traditional porous materials such as activated carbons and zeolites. Despite the ultra-high surface areas, MOFs are also regarded as advanced porous materials due to their particular composition, which leads to many possible structures and applications, listed (i-v) as follows.[6] (i) The porosity of MOFs can be modified by incorporating different inorganic and organic units. Preparing MOFs with high porosity, usually requires long organic linkers, while short organic linkers usually lead to a lower porosity (Figure 1-2).[7] (ii) The topology of a MOF can be maintained while modifying porosity (Figure 1-2). (iii) A specfic geometrical shape of MOF channels can be achieved using specific SBUs and organic linkers of the appropriate shape. (iv) The reactivity of the pores, including the presence of catalytic sites, can be achieved by introducing metal-organic complexes into the framework.[8] (v) MOFs can be functionalized by many different functional groups (Figure 1-2), thus, MOF properties can be modified. For example, gas selectivity in MOF-5 can be achieved by functionalizing the framework with different functionalized groups.[9]

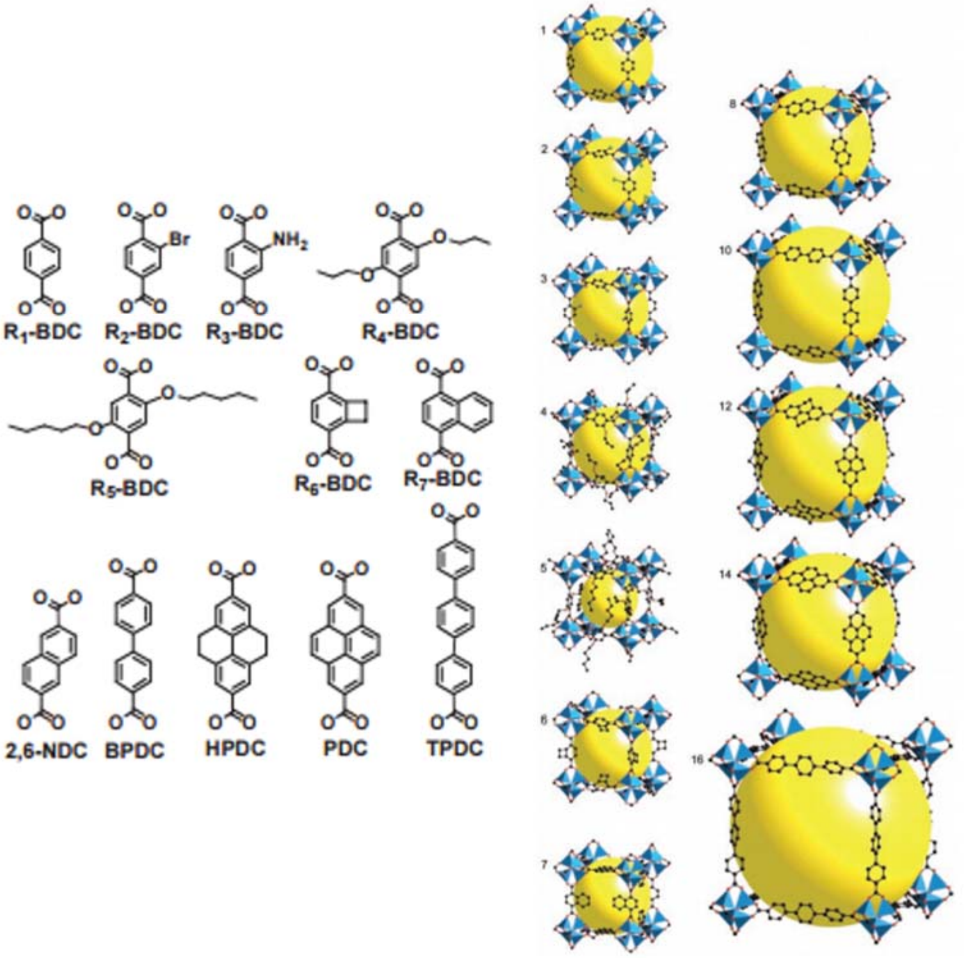

Figure 1-2: The ligand derivatives of IRMOFs. The central yellow spheres represent accessible and open pore spaces. The pore size can be enlarged by using longer organic linkers. The frameworks also can be functionalized by different functional groups. (Reproduced from Ref. 7)

MOFs also have relative high thermal, chemical, and mechanical stabilities due to the presence of multiple strong chemical bonds, including C-C, C-N, C-O, metal-O, etc.[5-6].

1.1.2 Applications of MOFs

Gas storage[10-12] is the most common application of MOFs one due to the instinsic properties of MOFs: i) the high porosity of MOFs means these materials have rather large gas adsorption capacities;[13] ii) the gas loading capacities of MOFs can be enhanced by introducing various functional sites into frameworks;[9] iii) characterization of gas adsorption in MOFs is possible, in which the gas adsorption sites can be revealed using single crystal X-ray diffraction,[14] neutron diffraction,[14] computational calculation,[15] and NMR experiments,[16] With this in mind, the rational design of MOFs with better gas capacity is possible. CO_2, CH_4, and H_2 have been the most comprehensively studied gases in MOFs.

1.1.2.1 Carbon dioxide capture and storage.

Global warming has become a critical environmental issue in our time due to the current and historical emission of greenhouse gases.[17] CO_2 is the main component of greenhouse gases, therefore, capturing CO_2 from waste flue gas or the atmosphere using adsorbents has become an promising route for reducing atmospheric CO_2 levels. One of the most crucial performance parameters for CO_2 capture materials is their CO_2 selectivity. A high CO_2 selectivity is preferred, since the CO_2 component of the flue gas can be completely removed by highly selective adsorbents. Another important consideration for CO_2 capture is the affinity of the adsorbent toward CO_2. A suitable interaction strength is required for reversible CO_2 adsorption: if the interaction is too strong, a high energy is required for CO_2 desorption, however, if the reaction is too weak, the CO_2 selectivity is greatly reduced. CO_2 capture target set by US Department of Energy (DOE) is to reduce the cost of CO_2 capture to less than $40/tonne by 2025 and less than $10/tonne beyond 2035.[18]

To date, many materials have been explored as potential CO_2 adsorbents, including aqueous alkanolamine solutions, zeolites, activated carbons, and MOFs. Aqueous alkanolamine solutions for CO_2 capture has been studied for many decades and are still considered the performance standard or benchmark. Alkanolamines interact with CO_2 to form carbamate or bicarbonate species (Scheme 1-1). This chemical adsorption process leads to a high CO_2 affinity. However, aqueous alkanolamine solutions have some significant limitations. First, the high CO_2 affinity requires a high energy input for releasing captured CO_2 gas. Aqueous alkanolamine solutions are also relatively unstable at high temperatures.[19] Zeolites are another candidates for CO_2 adsorption. Zeolites are robust porous materials, which have well-studied structures, and an inexpensive synthetic process. However, zeolites rapidly adsorb water vapour from the flue gas stream, which limits their CO_2 adsorption capacities.[19] Activated carbons have also attracted a lot of attentions as a CO_2 adsorbent. The relatively higher surface area leads to higher CO_2 capacities at high pressures, however, the lower enthalpy of adsorption for CO_2 leads to lower CO_2 capacities at ambient pressure, which is not suitable for flue gas CO_2 capture.[19]

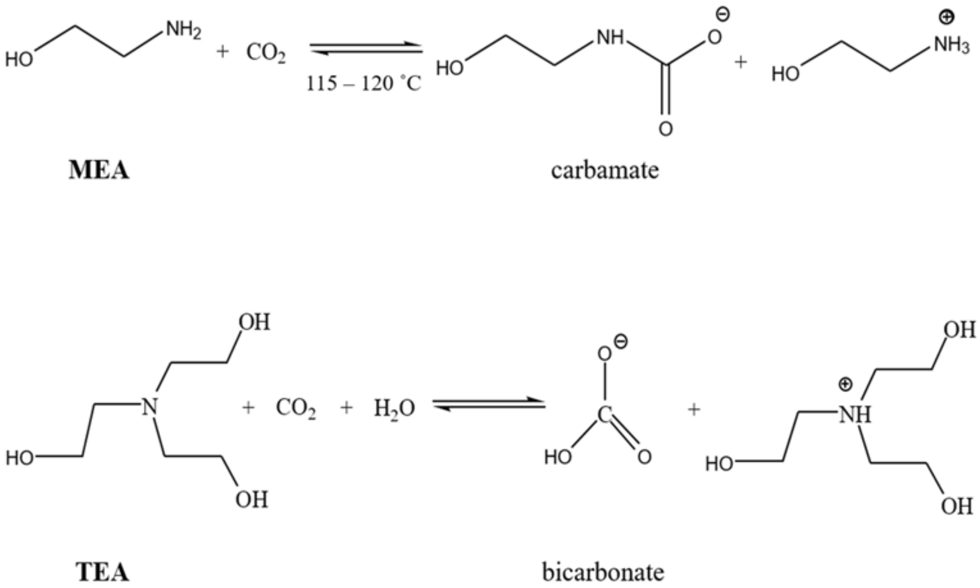

Scheme 1-1: The reaction of CO_2 with two alkanolamine solutions is illustrated. The reaction of CO_2 with monoethanolamine (MEA) resulting in a carbamate product is shown at top, while the reaction of CO_2 with triethanolamine (TEA) giving a bicarbonate product is shown on the bottom. (Reproduced from Ref. 19)

Among all of these CO_2 adsorbents, MOFs have been considered next-generation materials due to their extremely high porosity and functionlizable channels.[19-21] Numerous studies of CO_2 adsorption using MOFs have been reported, and various approaches for enhancing the CO_2 adsorption capacity in MOFs have been established. Functionalizing pores by nitrogen bases is one of the efficient ways to increase the CO_2 capacities of MOFs. In some cases, acid-base interactions between nitrogen base functional groups and CO_2 molecules have been observed. For example, IRMOF-1 ($Zn_4O(BDC)_3$) (BDC = 1,4-benzenedicarboxylate) adsorbs 4.6 wt.% CO_2 at 298 K and 1.1 bar, however, amine-functionalized IRMOF-3 ($Zn_4O(NH_2\text{-}BDC)_3$) adsorbs 5.0 wt.% CO_2 under these conditions. The enhanced CO_2 capacity is caused by the interactions between amino groups and CO_2 molecules.[22] In some other cases, the amine groups do not directly interact with CO_2 molecules. For example, in amine-functionalized MIL-53 ($Al(OH)(NH_2\text{-}BDC)$), the presence of amine groups increases the acidity of bridging -OH moieties, which act as CO_2 adsorption sites, thus increasing the interaction strength and enhancing the CO_2 capacity.[23] The functionalization of MOFs by other strong polarizing organic functional groups can also enhance CO_2 capacities. For example, the CO_2 capacity of nitro-functionalized MIL-53 ($Al(OH)(NO_2\text{-}BDC)$) is 10.8 wt.% at 298 K and 1 bar, which is even higher than that of amine-functionalized MIL-53 (7.8 wt.%).[24] The increased CO_2 capacity in nitro-functionalized MIL-53 is due to the stronger interaction between CO_2 and functional groups. Creating open metal sites (OMSs) significantly enhances CO_2 adsorption capacities. $Cu_3(BTC)_2$, also known as HKUST-1, is one of the first reported MOFs with unsaturated OMSs. The CO_2 capacity of $Cu_3(BTC)_2$ can reach 18.4 wt.% at 1 bar and 298 K,[25] which is significantly higher than most of MOFs without OMSs. Experimental[26] and computational[27] studies both indicate CO_2 adsorbed within $Cu_3(BTC)_2$ strongly interacts with OMSs due to the high charge density on Cu^{2+} cations.

The most straightforward method to enhance the CO_2 capacities of MOFs is by increasing the surface areas of MOFs. Previously, Furukawa[13] *et al.* prepared a series of MOFs generated from $Zn_4O(CO_2)_6$ unit with large organic linkers and featuring ultra-high porosity. Among them, MOF-200 and MOF-210 exhibit very high Brunauer-Emmett-Teller (BET) surface area of 4530 m^2/g and 6240 m^2/g, respectively, and a record CO_2 capacity of *ca.* 71 wt.% at 50 bar. The CO_2 capacity of MOFs at low pressure or ambient pressure is more important for flue gas CO_2 capture, and the capacity mainly depends on the CO_2-adsorbent interactions that are present. Mg-MOF-74, which has Mg^{2+} OMSs exhibits an excellent CO_2 capacity at ambient pressure. The CO_2 capacity of Mg-MOF-74 is 37.8 wt.% at 298 K and 1 bar,[28] which also indicates that OMSs are instrumental for achieving a high CO_2 capacity in MOFs.

1.1.2.2 Methane storage.

Methane (CH_4) is considered a cleaner energy source that has the highest possible hydrogen to carbon ratio and relatively lower carbon emissions. However, one significant challenge for CH_4 storage is its extremely low energy density at ambient conditions; it is only 0.04 MJ/L versus 32.4 MJ/L for gasoline.[29] Therefore, the storage of CH_4 is extremely challenging. The current CH_4 storage methods for vehicles include compressed natural gas (CNG), liquefied natural gas (LNG), and adsorbed natural gas (ANG).[30] CNG is natural gas that is usually compressed to 20 MPa. The high-pressure storage condition requires a costly compression process and a heavy, large, mechanically strong tank. The energy density of CNG increases to 8.8 MJ/L at 20 MPa and 293 K,[30] which is still much lower than that of gasoline. LNG is natural gas that is condensed to a liquid by cooling it below 111 K.[30] The volume of LNG is much smaller than CNG, which makes LNG more convenient for transportation, and the energy density is increased to 22.2 MJ/L in LNG.[31] However, a double-wall vacuum-insulated pressurized tank and low temperatures are needed to keep the natural gas in a liquid form.[30] ANG is natural gas that is adsorbed within adsorbent materials. ANG technology has the potential to replace CNG and LNG technologies because ANG permits lower operating pressures at room temperature. The tank involved with ANG technology is also much lighter, which reduces the cost and safety concerns in comparison to CNG and LNG. Therefore, ANG has been chosen to study in recent years.

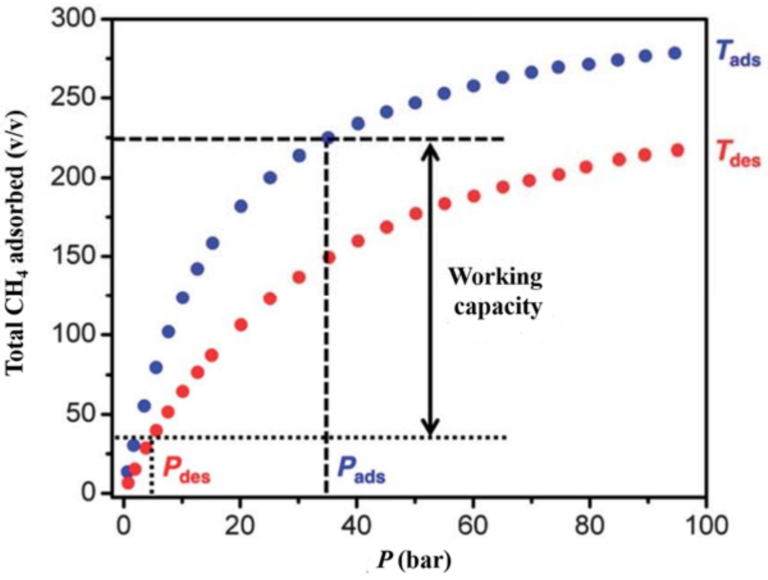

Figure 1-3: The working capacity calculated from a particular adsorption temperature (T_{ads}) and pressure (P_{ads}) and a specific desorption temperature (T_{des}) and pressure (P_{des}). (Reproduced from Ref. 32)

Many porous materials including zeolites, carbonaceous materials, covalent organic frameworks (COFs), and MOFs are currently considered promising materials for CH_4 storage.[31] A good CH_4 adsorbent should not only have a high maximum adsorption capacity, but also should have a high usable capacity or working capacity, which is defined as the amount of CH_4 released from a adsorption pressure (35 to 65 bar) to a specific desorption pressure (generally 5.8 bar due to typical engine inlet pressures) (Figure 1-3).[32]

Recently, the U.S. Department of Energy (DOE) updated their methane storage target for ANG applications to a total volumetric storage capacity of 350 cm^3 (STP)/cm^3 (STP = standard temperature and pressure), a total gravimetric storage capacity of 50 wt.% , and a volumetric working capacity of 315 cm^3 (STP)/cm^3 at room temperature.[33] Although no porous adsorbent has yet reached the DOE target, MOFs still have a higher working capacity versus other porous adsorbents.[34] Therefore, MOFs are considered as the most promising porous candidates for CH_4 adorption.[34-37]

Methods to increase the CH_4 capacity of MOFs have been established: (i) Creating OMSs in MOFs is one of the most efficient ways to enhance methane adsorption in

MOFs.[38] The MOF-74 series of MOFs have a high concentration of OMSs and are one of the most studied. The MOF-74 series of MOFs have excellent methane capacities; the total CH_4 adsorption capacities at 298 K and 35 bar range from 150 to 190 cm^3/cm^3.[39] Neutron diffraction experiments have indicated that CH_4 molecules are adsorbed within MOF-74 through Coulombic interactions with OMSs.[40]

(ii) Controlling the pore size is another useful method to enhance the methane capacities of MOFs. For example, MOF-5 ($Zn_4O(BDC)_3$), which has a pore size of 9.2 × 9.2 $Å^2$ has a total methane capacity of 109 cm^3/cm^3. $Zn_2(BDC)(dabco)$ (dabco = 1, 4 – diazabicyclo[2. 2. 2]octane) framework, which has the same topology as MOF-5 can be generated by incorporating some dabco linkers into MOF-5. The pore size of $Zn_2(BDC)(dabco)$ is 4.0 × 7.5 $Å^2$, which is smaller than that of MOF-5. However, the total CH_4 capacity of $Zn_2(BDC)(dabco)$ is 137 cm^3/cm^3, which is higher than that of MOF-5.[38] Snurr and co-workers performed computational simulations, which yielded over 137953 hypothetical MOF structures and their methane uptakes at 35 bar and 298 K. From all these simulated topologies, the best hypothetical MOFs for methane uptake were found to be those with pore sizes ranging from 4 to 8 Å.[41] Our SSNMR and DFT calculation studies in Chapter 4 also demonstrate that MOFs with smaller pore size exhibit stronger methane binding strengths.

(iii) Very recently, Mason and co-workers[42] showed that flexible MOFs enhance the methane working capacity through thermal management. This is because methane adsorption is an exothermic process and methane desorption is an endothermic process. During methane adsorption, the pore size of a flexible MOF will be expanded. The expansion of the framework is an endothermic process since energy is needed to overcome the thermodynamic stability of the small pore or collapsed phase. Therefore, the heat released during methane adsorption (exothermic) would help to expand the pore of the flexible MOF. Similarly, the transition from the expanded phase to collapsed phase of the flexible MOF is an exothermic process, the heat released from the framework assists in methane desorption (endothermic). In Mason's work, two MOFs named Co(bdp) and Fe(bdp) (bdp = 1, 4 - benzenedipyrazolate) were used to study methane adsorption. S-shaped methane adsorption isotherms have been observed in their studies, which means methane adsorption is reduced at low desorption pressures, and thus this MOF has a large working capacity (Figure 1-4). Also, Co(bdp) has the highest reported working capacity of 155 cm^3/cm^3 for a MOF at 298 K between 35 and 5 bar.[42] MOF-519 has the highest reported working capacity of 210 cm^3/cm^3 at 298 K between 65 and 5 bar.[43]

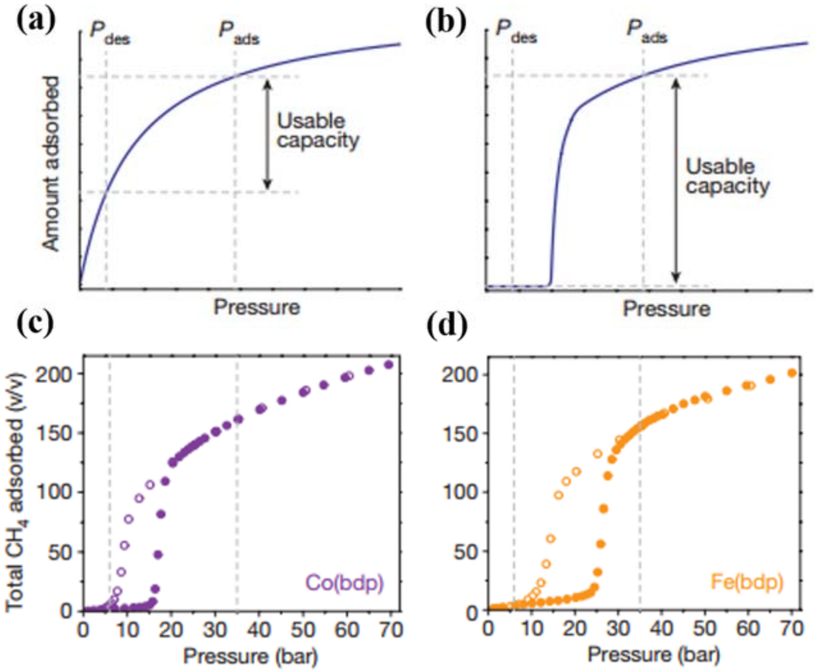

Figure 1-4: The usable capacity or working capacity for adsorbent with a classical Langmuir-type adsorption isotherm and an S-shaped adsorption isotherm are shown in (a) and (b), respectively. Total CH_4 adsorption isotherms for Co(bdp) and Fe(bdp) are shown in (c) and (d). Filled circles denote adsorption and open circles denote desorption. (Reproduced from Ref. 42)

1.1.2.3 Hydrogen storage.

H_2 is considered an ideal clean energy carrier. It is carbon free and only gives off water as a byproduct. H_2 has a higher gravimetric energy density than that of gasoline (120 MJ/kg *vs*. 44.5 MJ/kg),[44] however, similar to CH_4, the volumetric energy density of H_2 is much smaller than that of gasoline (0.0108 MJ/L *vs*. 32.4 MJ/L).[45] The low volumetric energy density makes H_2 storage a great challenge, especially considering the main applications are found in automobiles,[46] where size and weight restrictions complicate issues. The U.S. DOE has set the 2020 H_2 storage target as 5.5 wt.% in gravimetric capacity and 40 g/L in volumetric capacity at temperatures ranging from -40 to 60 °C under 100 atm. Unfortunately, none of the H_2 storage technologies has reached this target yet.[47]

To date, three H_2 storage technologies have been studied in depth: mechanical storage, storage using chemical hydrides, and storage using adsorbents.[46, 48] Mechanical H_2 storage methods are currently the most widely used, but usually require the compression and cryogenic cooling of H_2. The energy density of compressed liquid H_2 can only reach 10 MJ/L (87g/L at 21 K and 234 bar), which is still lower than that of gasoline. Storing compressed gaseous or liquid H_2 in a vehicle requires a large storage tank, and the tank must be reinforced to prevent explosion during a crash or accident. The unique requirements of the tank limit the development of H_2 storage in vehicles. Chemical hydrides contain chemically bound hydrogen and can store significant amounts of hydrogen. However, releasing H_2 from chemical hydrides usually requires high temperatures. Moreover, chemical hydrides are not rechargeable on board a fuel cell vehicle, therefore, chemical hydrides are not considered ideal storage media. The third H_2 storage method is H_2 adsorption into solid adsorbents, which include zeolites, carbon materials, COFs, and MOFs. This method is a compromise to reach a relative high H_2 energy density with good H_2 accessibility (Figure 1-5) so far.

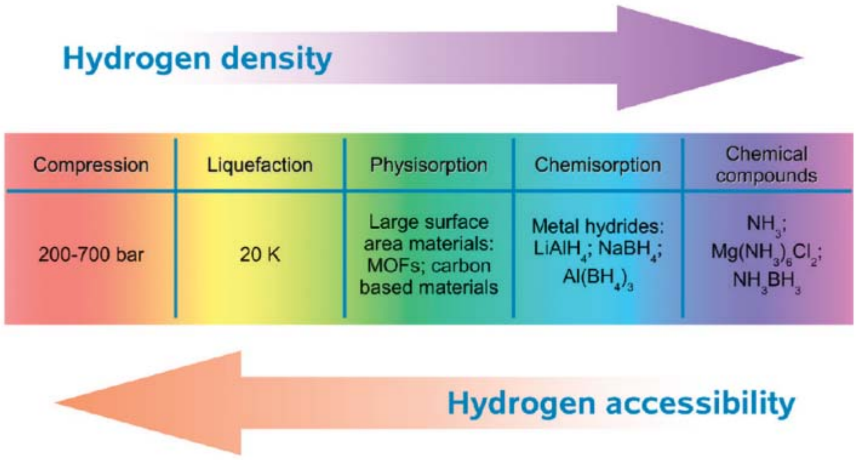

Figure 1-5: The H_2 accessibility and H_2 energy density of different storage technologies (Reproduced from Ref. 48)

Among all porous materials, MOFs have exhibited the best performance and are considered the most promising materials for H_2 storage due to their high surface areas, excellent porosities, and tuneable nature.[45, 47, 49-50] The documented strategies for improving hydrogen storage capacities in MOFs are very similar to those for improving CH_4 storage in MOFs. Increasing surface area is the most straightforward method to improve H_2 capacities, especially for high-pressure H_2 storage (Figure 1-6).[47] The current benchmark MOF for hydrogen storage at 77 K and 80 bar is MOF-210, which has a BET surface area of 6240 m^2/g with a hydrogen capacity of 15.0 wt. %.[13] However, at low adsorption pressures (1 bar), reduced H_2 adsorption capacities have been observed (Figure 1-6) when the surface area is over 2000 m^2/g. This is likely because the surface cannot be saturated with H_2 molecules under the condition of very high surface area, since low-pressure H_2 adsorption may be influenced by either pore size or the binding strength of adsorption sites.[47] For example, the H_2 capacity of SUN-77 (1.80 wt.%, 10.5 g/L) (SNU = Seoul National University) is higher than that of MOF-177 (1.24 wt. %, 8.6 g/L), however, the BET surface area of SNU-77 (3670 m^2/g) is smaller than that of MOF-177 (4750 m^2/g).[47]

Creating OMSs is also an efficient way to increase hydrogen binding strength, thus improving H_2 capacities.[47, 49] Neutron diffraction experiments confirm that H_2 adsorbed in MOFs with OMSs prefers to interact with OMSs first. The H_2 adsorption energy can reach *ca*. 12 kJ/mol in MOFs with OMSs, which is higher than most MOFs without OMSs. The Mn-BTT (BTT = 1, 3, 5 - benzenetristetrazolate) MOF, which has Mn^{2+} OMSs, has by far the highest reported H_2 capacity at 298 K and 90 bar of 12 g/L.[51]

A small pore size is also necessary to achieve high H_2 capacities at room temperature. This is because the small pore usually leads to relative higher interaction energies. The highest reported H_2 adsorption energy so far is within SNU-15 at 15.1 kJ/mol.[52] The high H_2 adsorption energy of SNU-15 is mainly due to its small pore size. However, the limitations of small pore size are also apparent, the small pore size leads to a low BET surface area and a low total H_2 capacity of the MOF.

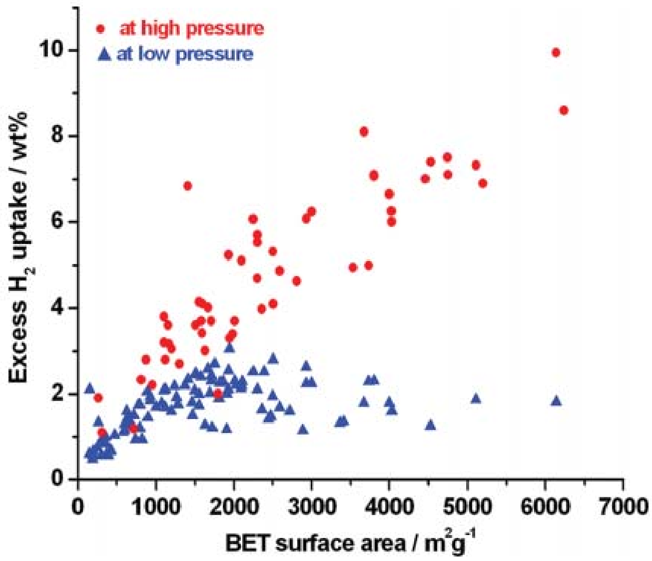

Figure 1-6: The relationship between H_2 adsorption capacities at 77 K and BET surface areas of MOFs. The "low pressure" labels represents 1 bar and the "high pressure" label includes pressures ranging from 10 to 90 bar. (Reproduced from Ref. [47])

Even though MOFs have relatively better performance as H_2 adsorbents versus other porous materials, it must be noted that the adsorption temperature to achieve high capacity is still very low. For example, MOF-5, which is the most widely studied MOF for H_2 storage, has an excellent capacity of 66 g/L (10 wt.%) at 77 K and 100 bar,[53] however, this capacity is dramatically reduced to 8.9 g/L at 298 K due to the weak interaction between H_2 and MOF-5 framework (adsorption enthalpy is only -6.9 kJ/mol).[54] With this in mind, although the development of MOFs still has a long way to go to achieve practical applications in H_2 storage, the future is certainly bright.

1.1.2.4 Other applications.

Many potential applications of MOFs exist beyond gas storage. MOFs have been shown as promising materials for liquid separation,[55] drug delivery,[56] catalysis,[57] proton conductor,[58] sensing,[59] and many other applications. Challenges in large scale synthesis and commercialization still exist, however, by using alternative processing techniques to reduce their costs, MOFs will have a future in industrial applications.

1.1.3 MOFs studied in the thesis

MIL-53. MIL-53 (MIL= Materials of the Institute Lavoisier)[60] is a class of well-studied flexible MOFs, whose framework contains octahedral $MO_4(OH)_2$ SBUs (M = Al,[61] Ga,[62] In,[63] Cr,[60] Fe,[64] Sc[65]) and 1,4-benzenedicarboxylate (BDC) linkers. Each octahedral SBU consists of a metal centre connected to four oxygen atoms from four different benzenedicarboxylate (BDC) ligands and two bridging hydroxyl oxygen atoms (Figure 1-7(a)). These hydroxyl oxygen atoms link the SBUs *via* corner-sharing to form an infinite chain (Figure 1-7(b)) and the chains are interconnected by BDC linkers to create one-dimensional rhombic channels (Figure 1-7(c)). MIL-53 exhibits the ability to reversibly change phase and pore size in response to stimuli in a process known as the “breathing effect.” Within as-made MIL-53 (MIL-53(*as*)), the rhombic pores measure *ca*. 12 x 17 Å^2 and are occupied by excess BDC linkers from the MOF synthesis. At elevated temperatures, the surplus BDC ligands are purged from the MOF channels to generate the high-temperature phase MIL-53(*ht*), which has empty *ca.* 13 x 16 Å^2 pores. MIL-53(*ht*) readily adsorbs water from air at room temperature to form the low-temperature phase MIL-53(*lt*), which features narrow *ca.* 7 x 19 Å^2 pores.

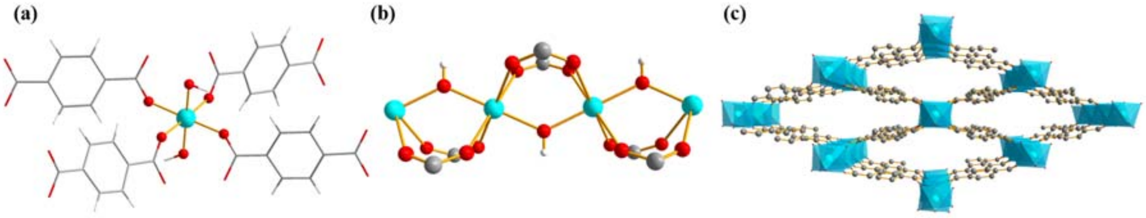

Figure 1-7: The octahedral $MO_4(OH)_2$ SBU of MIL-53 is shown in (a). The metal centre is bound to four oxygen atoms from four BDC linkers and two oxygen atoms from two bridging -OH groups. In (b), the one-dimensional chain formed by SBUs is illustrated. The expanded framework of MIL-53 is shown in (c). The colors red, grey, white and light blue correspond to oxygen, carbon, hydrogen and the metal centre, respectively.

A520. The A520[66] MOFs are structural analogues of MIL-53. In the A520 MOFs, each metal centre is coordinated to four oxygen atoms from four different fumarate ligands, as well as two oxygen atoms from two separate bridging hydroxyl groups to form an octahedral $MO_4(OH)_2$ (M = Al, Ga, In) SBU (Figure 1-8(a)). A one-dimensional chain is formed by SBUs connected via corner sharing (Figure 1-8(b)); in turn, the chains are cross-linked by fumarate linkers to form rhombic shaped channels (Figure 1-8(c)). Compared to MIL-53, the A520 MOFs are more rigid, due to the rigid character of the fumarate linker compared to the BDC one. The pore dimensions of A520 are *ca*. 12 x 12 $Å^2$.

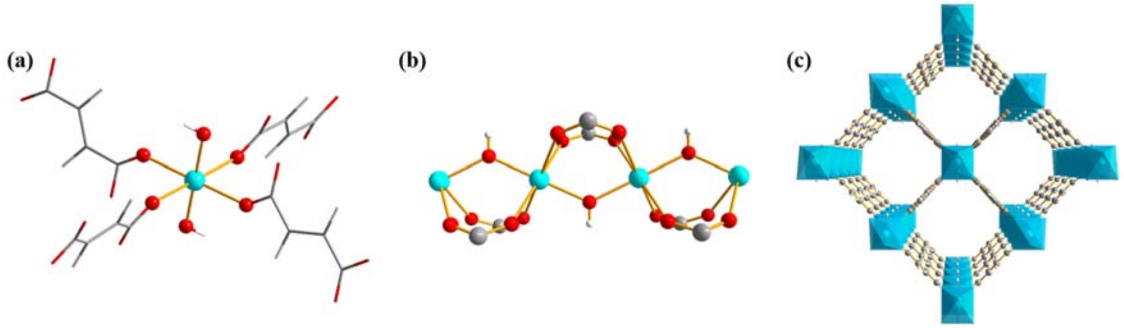

Figure 1-8: The octahedral $MO_4(OH)_2$ SBU of MIL-53 is shown in (a). The metal centre connects with four oxygen atoms from four fumarate linkers and two oxygen atoms from two bridging -OH groups. In (b), the one-dimensional chain formed by SBUs is illustrated. The expanded framework of MIL-53 is shown in (c). The colors red, grey, white and light blue correspond to oxygen, carbon, hydrogen and the metal centre, respectively.

MOF-74. MOF-74[67] is a class of well-studied MOFs with open metal sites (OMSs), consisting of infinite $M_3O_3(CO_2)_3$ (M = Co,[68] Fe,[69] Ni,[70] Mn,[71] Zn,[67] Mg,[72] Cu,[73] Cd[74]) rods and 2,5-dioxide-1,4-benzenedicarboxylate (dobdc) linkers to generate honeycomb-shaped channels (Figure 1-9(b)) that have metal centres at each vertex with a metal-metal distance of *ca*. 9 Å. In MOF-74, each metal centre is coordinated to three carboxyls and two hydroxyl groups from four dobdc linkers, along with a coordinating solvent (*e.g.* tetrahydrofuran (THF), *N, N*-dimethylformamide (DMF), or water) (Figure 1-9(a)). The coordinated solvent molecules can be removed *via* activation and the resulting unsaturated open metal sites (OMSs) encourage gas adsorption.

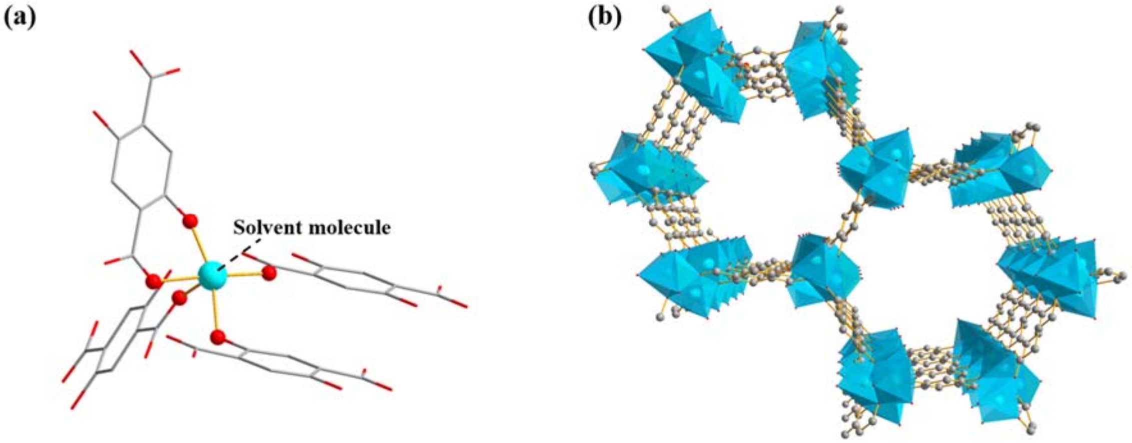

Figure 1-9: The coordination environment of the metal centre in MOF-74 is shown in (a). The metal centre coordinates to three carboxyls groups and two hydroxyl groups from four dobdc linkers. The honeycomb-shaped channels of MOF-74 is shown in (b). The colors red, grey, and light blue correspond to oxygen, carbon, and the metal centre, respectively.

α-$Mg_3(HCO_2)_6$ and α-$Zn_3(HCO_2)_6$. α-$Mg_3(HCO_2)_6$[75] and α-$Zn_3(HCO_2)_6$[76] are ultramicroporous MOFs and structural analogues, which are relatively easy and inexpensive to synthesise. In the structure of these two formate MOFs, each metal centre is coordinated to six oxygen atoms from different formate linkers, which generates MO_6 (M = Mg, Zn) octahedral SBU (Figure 1-10(a)). There are four crystallographically independent metal sites in these metal formate MOFs (Figure 1-10(a)), arising from different distributions of Mg/Zn-O bond lengths and O-Mg/Zn-O bond angles. The octahedral SBUs connect through edge-sharing to form SBU chains, and the chains are interconnected by vertex-sharing SBUs, forming one-dimensional zigzag channels with measured pore dimension of *ca*. 4.5 x 5.5 Å^2 (Figure 1-10(b)). The small pore size of formate MOFs encourages dispersive and non-dispersive interactions between the guest gas molecules and frameworks, increasing the gas adsorption capacity.

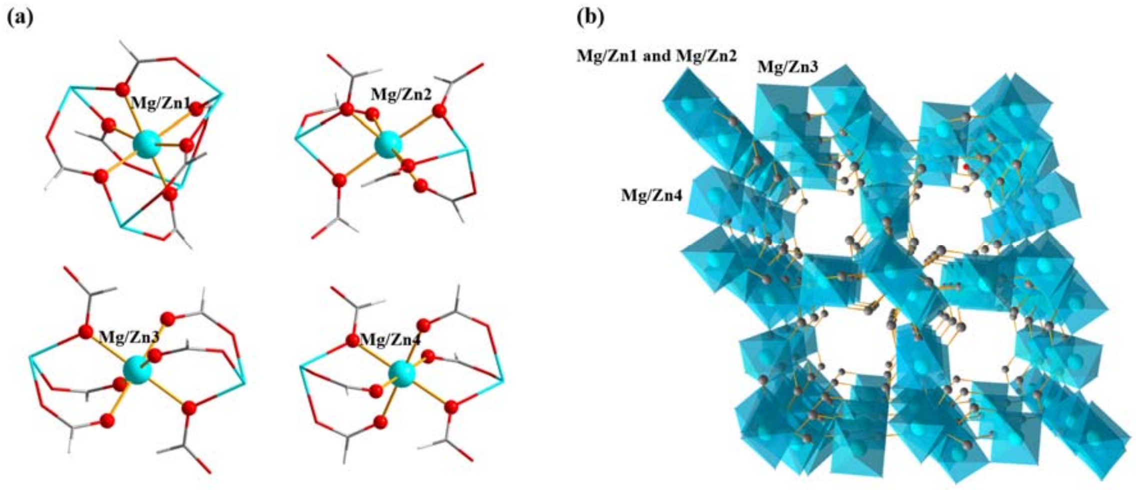

Figure 1-10: The four crystallographically independent metal sites in the metal-formate MOFs are shown in (a). Each metal centre coordinates to six oxygen atoms from formate linkers to form octahedral SBU. The expanded structure of the formate MOFs is illustrated in (b). The colors red, grey, white and light blue correspond to oxygen, carbon, hydrogen and the metal centre, respectively.

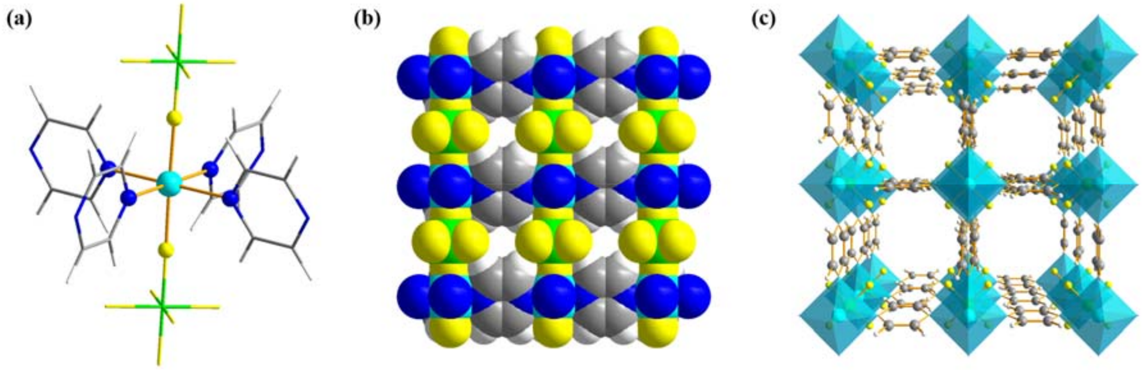

Figure 1-11: The octahedral ZnN_4F_2 SBU in SIFSIX-3-Zn is shown in (a). The metal centre is connected to four nitrogen atoms from four pyz linkers and two fluorine atoms from two axial SiF_6^{2-} linkers. In (b), a space-filling view of the *ac* plane is illustrated, with all pyz planes parallel to the *c*-axis. A view of the *ab* plane is shown in (c), where one-dimensional square channels surrounded by pyz panels can be observed. Carbon is colored grey, nitrogen is dark blue, hydrogen is white, fluorine is yellow, and metal centre is light blue.

SIFSIX-3-Zn. SIFSIX-3-Zn[77] is an ultramicroporous MOF with a pore diameter of *ca.* 3.8 Å, which is even smaller than those of α-$Mg_3(HCO_2)_6$ and α-$Zn_3(HCO_2)_6$. In SIFSIX-3-Zn, the Zn metal centre is coordinated to pyrazine (pyz) linkers, forming a two-dimensional square grid network. The networks are pillared by SiF_6^{2-}, producing a primitive-cubic net. The ZnN_4F_2 SBUs of SIFSIX-3-Zn have an octahedral topology. (Figure 1-11(a)). All pyz planes in the structure are parallel to the crystallographic *c* axis (Figure 1-11(b)), creating one-dimensional squared channels surrounded by pyz panels (Figure 1-11(c)). The extremely small pore size greatly enhances the interactions between gas molecules and SIFSIX-3-Zn frameworks due to the stronger dispersive and non-dispersive interaction.

1.2 Introduction to solid-state nuclear magnetic resonance (SSNMR)

1.2.1 Physical Background

In general, most of the elements in the periodic table have at least one NMR-active isotope, which have a non-zero angular momentum (**I**) quantity which is also known as spin. The nuclear spin angular momentum is an intrinsic property of the nucleus and is associated with a nuclear spin quantum number *I*.[78] An NMR-active isotope must have a non-zero nuclear spin quantum number *I*, which requires an odd number in either the neutrons or protons of the nucleus. The guideline to predict nuclear spin quantum number *I* is illustrated in Table 1-1.

Table 1-1: The guideline to predict spin quantum number *I*.

Number of protons	Number of neutrons	Spin
Even	Even	Zero
Odd	Odd	Integer (i.e., 1)
Odd	Even	Half-integer (i.e., 1/2, 3/2)
Even	Odd	Half-integer (i.e., 1/2, 3/2)

The nuclear spin **I** has a linear relationship with the nuclear magnetic moment (μ):[79]

$$\mu = \gamma \mathbf{I} \qquad \textbf{Equation 1-1}$$

where γ is the gyromagnetic ratio, which is a constant for any given type of nucleus and is usually specified in units of rad s^{-1} T^{-1}. The gyromagnetic ratio determines the size of μ, which is related to the charge (e) and mass (m) of a proton:

$$\gamma = \frac{e}{2m} g \qquad \textbf{Equation 1-2}$$

where g is the nuclear g-factor, which is unique for each nuclear isotope. The γ value can be either positive or negative. For nuclei with $\gamma > 0$, μ points in the same direction to **I**, while, for nuclei with $\gamma < 0$, μ points in the opposite direction to **I**.[78]

The nuclear spin not only interacts with external magnetic fields such as a strong static external applied magnetic field B_0 and a small radio frequency (rf) field B_1, but also participates in other internal interactions. These interactions can be written in the Hamiltonian format of NMR interactions:[79-80]

$$\hat{H}_{\mathrm{NMR}} = \hat{H}_{\mathrm{Z}} + \hat{H}_{\mathrm{rf}} + \hat{H}_{\mathrm{CS}} + \hat{H}_{\mathrm{D}} + \hat{H}_{\mathrm{J}} + \hat{H}_{\mathrm{Q}} \qquad \textbf{Equation 1-3}$$

Where the subscripts Z, rf, CS, D, J, and Q denote Zeeman, radio frequency, chemical shielding, dipolar coupling, *J*-coupling, and quadrupolar interactions, respectively. In most experiments, the Zeeman interaction dominates the appearance of a SSNMR spectrum due to the magnitude of the strong external magnetic field B_0, and all other interactions are considered as perturbations upon the Zeeman interaction.[79-80] The magnitudes of nuclear spin interactions are listed in Table 1-2.

Table 1-2: Magnitudes of nuclear spin interactions (reproduced from Ref. 80)

Interaction	Typical magnitude (Hz)	Comments
Zeeman	10^7-10^9	Interaction with external magnetic field B_0
Radio frequency	10^3-10^5	Interaction with external rf field B_1
Chemical shielding	10^2-10^5	Perturbations of the magnetic field by the electrons (local magnetic environment)
Dipolar	10^3-10^4	Through space spin-spin interaction
J-coupling	1-10^3	Spin-spin interaction mediated via the chemical bonds (local chemical environment)
Quadrupolar	10^3-10^7	Interaction of nuclear quadrupolar moment with the electric field gradient (EFG, local electronic environment)

1.2.1.1 Zeeman interaction

The Zeeman interaction is typically larger than other interactions (Table 1-2) and describes the interaction between an NMR-active nucleus and a strong static externally applied magnetic field denoted B_0.[79-80] Based on quantum mechanics, an NMR-active nucleus with a spin quantum number I has $2I + 1$ energy levels, which correspond to all possible quantum numbers m. The spin quantum number m can take $2I + 1$ values: I, $I - 1$, $I - 2$, $I - 3$, …, $-I$. In the absence of the external magnetic field B_0, these energy levels are degenerate, however, when the nucleus is introduced into B_0, the energy levels become non-equivalent and split to the $2I + 1$ energy levels (Figure 1-12). These energy levels are separated by a difference which is related to the external magnetic field B_0 and the nuclear gyromagnetic ratio γ, and is directly proportional to the Larmor frequency ω_0:[79-80]

$$\Delta E = \gamma \hbar B_0 = \hbar \omega_0 \qquad \textbf{Equation 1-4}$$

where $\hbar$ is Plank's constant (h) divided by 2π. Thus, the Larmor frequency in units of rad s^{-1} can be calculated as: [80-81]

$$\omega_0 = \gamma B_0 \qquad \textbf{Equation 1-5}$$

In an external magnetic field B_0, nuclear spins precess about the direction of B_0. The precession of magnetic spins occurs at a rate of ω_0, which is known as Larmor precession. From Equation 1-5, the Larmor frequency depends upon both the gyromagnetic ratio γ and the magnitude of B_0. The Larmor frequency generally ranges from 1-1000 MHz on NMR spectrometers.[80] Nuclei that have larger Larmor frequencies are better suited for NMR experiments. This is because larger Larmor frequencies means bigger energy difference between spin states, therefore, the transition between different states is more easily detectable.

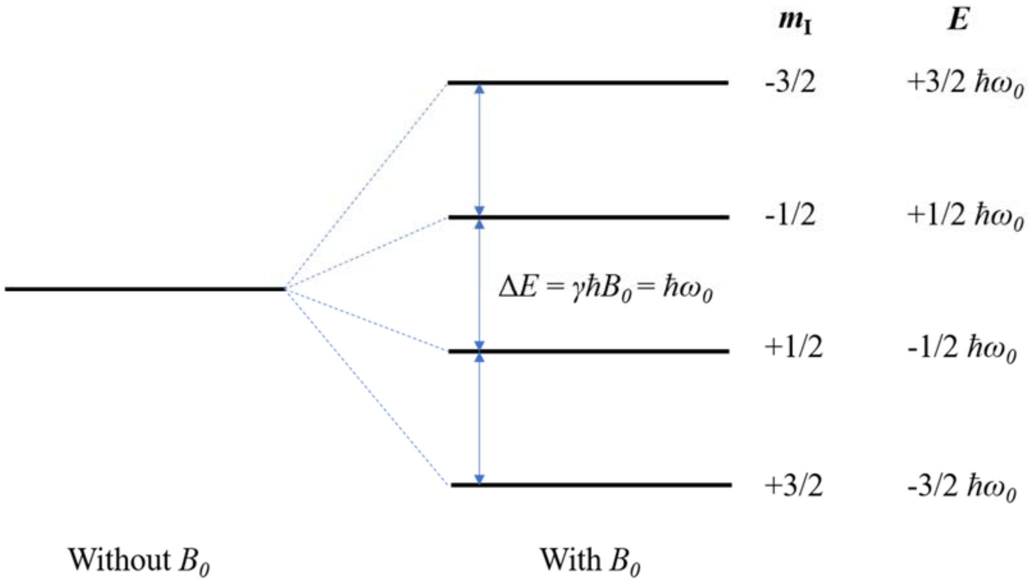

Figure 1-12: Illustration of Zeeman splitting of a spin-3/2 nucleus in an external magnetic field B_0.

It must be noted that, the NMR signal is induced by the transition between different energy levels, therefore, the difference of population between different energy levels plays an important role in the magnitude of NMR signal. In an external magnetic field B_0, the sample is in thermal equilibrium, and the population of different energy levels is dictated by a Boltzmann distribution:[82]

$$\frac{N_\beta}{N_\alpha} = e^{-\Delta E/kT} = e^{-\hbar\omega_0/kT}$$ **Equation 1-6**

where N_β is the number of spins in higher energy state β, N_α is the number of spins in lower energy state α, k is the Boltzmann constant (1.38×10^{-23} JK^{-1}), and T is the temperature in Kelvin (K). The Boltzmann distribution indicates $N_\alpha > N_\beta$, and a net adsorption of energy will occur during the transition from α state to β state to induce NMR signal. It must be noted that the population difference is usually tiny between the α state and β state, which is the underlying reason for the low sensitivity of NMR spectroscopy.

The Hamiltonian of Zeeman interaction can be described as:[79]

$$\hat{H}_Z = -\gamma\hbar\hat{I}_z B_0$$ **Equation 1-7**

where $\hat{I}_z$ is the operator for the z component of nuclear spin, which is in either in the same or opposite direction of the applied external magnetic field B_0.

1.2.1.2 Radio frequency (rf) interaction

An electromagnetic radio frequency (rf) wave, which has an oscillating magnetic field B_1 along a direction perpendicular to the external magnetic field B_0, is arranged in the NMR experiment to interact with the nucleus in addition to B_0.[79] When the frequency of the rf pulse (ω_{rf}) is set at or near the Larmor frequency of the NMR-active nucleus, it can induce nuclear spin state transitions.

In the laboratory frame, the B_1 field can be written as two components (B_1^+ and B_1^-) rotating about B_0 in opposite directions, and only the component that rotates in the same direction as the precession of the nuclear spin has a significant effect on the net magnetization vector **M**.[81] By introducing a rotating frame of reference, which rotates about the B_0 or z-axis at a rate of ω_{rf}, the B_1 field appears static and now has a significant influence on the net magnetization. In the rotating frame, the effect of the external magnetic field B_0 is reduced by a factor of ω_{rf}/ω_0 when the B_1 field is applied. The reduced B_0 field and B_1 field add vectorially to give a net effective magnetic field B_{eff} as shown in Figure 1-13(a).[81] When the rf pulse is on resonance, where $\omega_{rf} = \omega_0$, the B_0 field is removed in rotating frame and now $B_{eff} = B_1$. As a result, the magnetization vector **M** precesses about the B_1 field at a rate of γB_1 or ω_1. Figure 1-13(a) can be relabelled with frequencies as shown in Figure 1-13(b).[81]

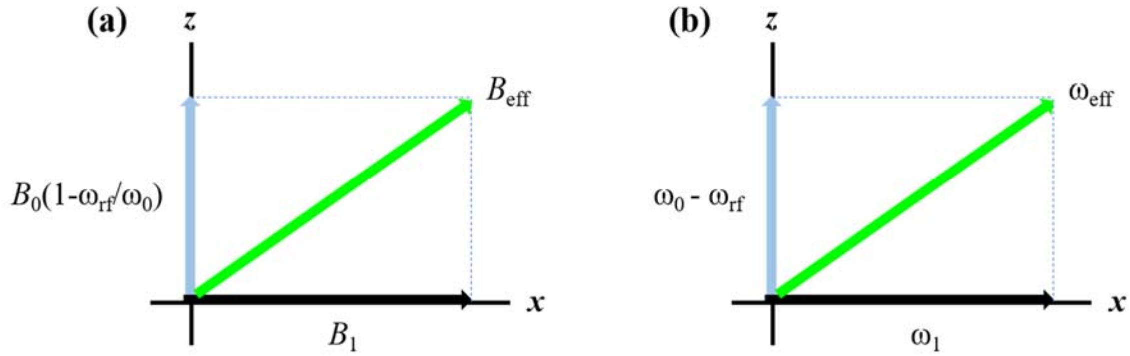

Figure 1-13: The magnetic fields present in the rotating frame are shown in (a). The magnetic fields can be relabelled with frequencies and illustrated in (b).

In the rotating frame, an rf pulse rotates the spin magnetization through flip angle θ_{rf}, which is the angle that B_1 manipulates the magnetization through the time τ_{rf} (Figure 1-14). The flip angle is described as:

$$\theta_{rf} = \omega_1\tau_{rf} = \gamma B_1\tau_{rf}$$ **Equation 1-8**

In NMR experiments, a $\theta_{rf} = \pi/2$ radian or 90 ° pulse rotates the magnetization from the +*z* direction to the transverse *xy* plane and results in a net adsorption of energy, inducing spin population transitions from the low spin state (*e.g.* +1/2) to the high spin state (*e.g.* -1/2). When the rf pulse is turned off, only B_0 is present, and **M** begins to precess about B_0 at the Larmor frequency, and induces a weak oscillating electric current in the NMR coil, which is detected as the NMR signal.

The rf interaction Hamiltonian can be written as:[79-80]

$$\hat{H}_{\mathrm{rf}} = 2\hbar\omega_1\hat{I}_x \cos(\omega_{\mathrm{rf}}t + \alpha) \qquad \textbf{Equation 1-9}$$

where $\hat{I}_x$ is the x-component of the spin operator and α is the phase of the applied rf field.

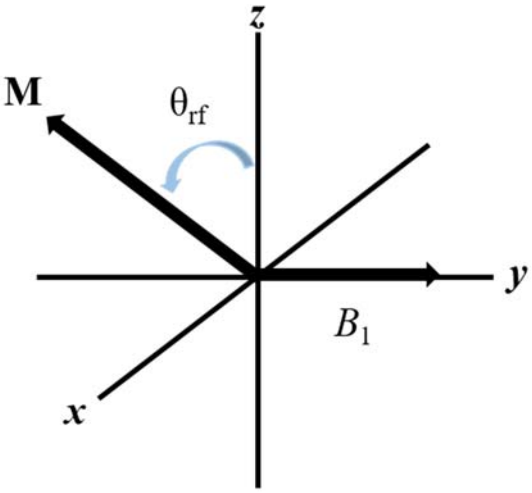

Figure 1-14: The effect of an rf pulse (B_1) on magnetization (**M**) in the rotating frame.

1.2.1.3 Chemical shielding interaction

In an external magnetic field B_0, the electrons in molecular or atomic orbitals that surround nuclei circulate about B_0. The circulated electrons induce a weak additional secondary magnetic field. Therefore, the total effective magnetic field experienced at the nucleus arises from both the induced secondary field and the external field B_0, giving rise to small deviations in the frequency in which nuclei precess about B_0. This is known as the chemical shielding interaction, and the NMR frequency change caused by the shielding interaction in an NMR spectrum is known as chemical shielding. The chemical shielding is anisotropic or directionally dependent; the exact frequency shift of the CS depends on the specific orientation of the crystallite with respect to the magnetic field, and within any given powdered SSNMR sample, all orientations of the crystallites with respect to the magnetic field exist.

The chemical shielding Hamiltonian for a given nuclear spin can be described as:[79]

$$\hat{H}_{\mathrm{CS}} = -\gamma\hbar\hat{\mathbf{I}}\boldsymbol{\sigma}B_0 \qquad \textbf{Equation 1-10}$$

where $\hat{\mathbf{I}}$ is the spin operator, and $\boldsymbol{\sigma}$ is a second-rank chemical shielding tensor. The orientation dependence or anisotropy of the chemical shielding tensor can be described by a 3 × 3 matrix:[79]

$$\boldsymbol{\sigma} = \begin{pmatrix} \sigma_{xx} & \sigma_{xy} & \sigma_{xz} \\ \sigma_{yx} & \sigma_{yy} & \sigma_{yz} \\ \sigma_{zx} & \sigma_{zy} & \sigma_{zz} \end{pmatrix} \qquad \textbf{Equation 1-11}$$

In NMR experiments, only the symmetric chemical shielding tensor components contribute to the appearance of NMR spectra. The symmetrized chemical shielding tensor can be diagonalized to yield three principal components, which correspond to the principal axis system (PAS):[80]

$$\boldsymbol{\sigma}^{\mathbf{PAS}} = \begin{pmatrix} \sigma_{11} & 0 & 0 \\ 0 & \sigma_{22} & 0 \\ 0 & 0 & \sigma_{33} \end{pmatrix} \qquad \textbf{Equation 1-12}$$

These three components describe the degree of chemical shielding in all three dimensions and are ordered such that $\sigma_{11} \leq \sigma_{22} \leq \sigma_{33}$, where σ_{11} corresponds to the least shielded component and σ_{33} is the most shielded component. In the PAS, the three principal components represent chemical shielding along three orthogonal directions as shown in Figure 1-15(a).

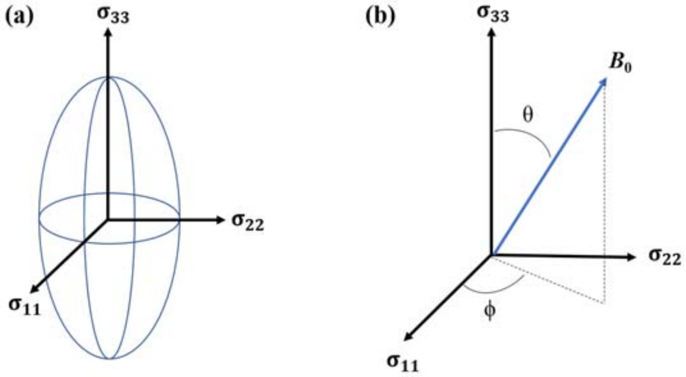

Figure 1-15: An ellipsoid representation of the shielding tensor is shown in (a). In (b), the polar angles θ and ϕ, which define the orientation of the B_0 in the principal axis frame of the shielding tensor, are illustrated.

In the PAS of the shielding tensor, if the direction of B_0 is described by the polar angles θ and ϕ (Figure 1-15(b)), the chemical shielding frequency shift can be defined as:[79]

$$\omega_{CS}(\theta,\phi) = -\omega_0(\sigma_{11}\sin^2\theta\cos^2\phi + \sigma_{22}\sin^2\theta\sin^2\phi + \sigma_{33}\cos^2\theta) \quad \textbf{Equation 1-13}$$

For a shielding tensor with axial symmetry ($\sigma_{11} = \sigma_{22}$), Equation 1-13 can be simplified to:[79]

$$\omega_{CS}(\theta) = -\omega_0\sigma_{33}\frac{1}{2}(3\cos^2\theta - 1) \quad \textbf{Equation 1-14}$$

Based on Equation 1-13 and Equation 1-14, the magnitude of chemical shielding depends on the orientation of a molecule in the external magnetic field B_0. In a powdered sample, the molecules are orientated in all possible orientations with respect to B_0, therefore, any possible combination of polar angles θ and ϕ exists, and the observed chemical shielding for each particle is distinct, which gives rise to a manifold of possible resonances that trace out a broad powder pattern. However, in a solution or gaseous sample, molecules undergo fast isotropic tumbling on the NMR timescale, resulting in a sharp isotropic and directionally-averaged NMR resonance.

Chemical shielding describes the difference between the sample frequency (ω_{sample}) and the Larmor frequency (ω_0), however, when performing NMR experiments, the chemical shift (δ) is a more convenient comparison, where the sample frequency is referenced to a standard reference sample (ω_{ref}) and the difference in resonant frequency between the standard and experimental sample is relatively small and measured in parts per million (ppm):[80]

$$\delta = \frac{\omega_{sample} - \omega_{ref}}{\omega_{ref}} \times 10^6 \quad \textbf{Equation 1-15}$$

The conversion between chemical shift (CS) and chemical shielding is:[80]

$$\delta = \frac{\sigma_{ref} - \sigma_{sample}}{1 - \sigma_{ref}} \approx \sigma_{ref} - \sigma_{sample}\ (1 \gg \sigma_{ref}) \quad \textbf{Equation 1-16}$$

In a chemical shift anisotropy (CSA) dominated powder pattern, the shape of the powder pattern is determined by the three principal components of the CS tensor, δ_{11}, δ_{22}, and δ_{33}. The CS principal components are ordered such that $\delta_{11} \geq \delta_{22} \geq \delta_{33}$, with δ_{11} corresponding to the highest frequency and δ_{33} the lowest. In this thesis, CSA is described using the Herzfeld-Berger (HB) convention. The relationship is expressed below:[80]

$$\delta_{iso} = (\delta_{11}+\delta_{22}+\delta_{33})/3 \qquad \textbf{Equation 1-17}$$

$$\Omega = \delta_{11}-\delta_{33} \qquad \textbf{Equation 1-18}$$

$$\kappa = 3(\delta_{22}-\delta_{iso})/\Omega \qquad \textbf{Equation 1-19}$$

where Ω is the span or width of the powder pattern; κ is the skew, which describes the axial symmetry of the CS tensor and ranges from -1 to 1; and δ_{iso} is the isotropic chemical shift, where positive and negative value are associated with the nucleus being deshielded and shielded in comparison to the reference compound, respectively. Simulated ^{13}C CSA powder patterns with different CS tensor parameters are shown in Figure 1-16.

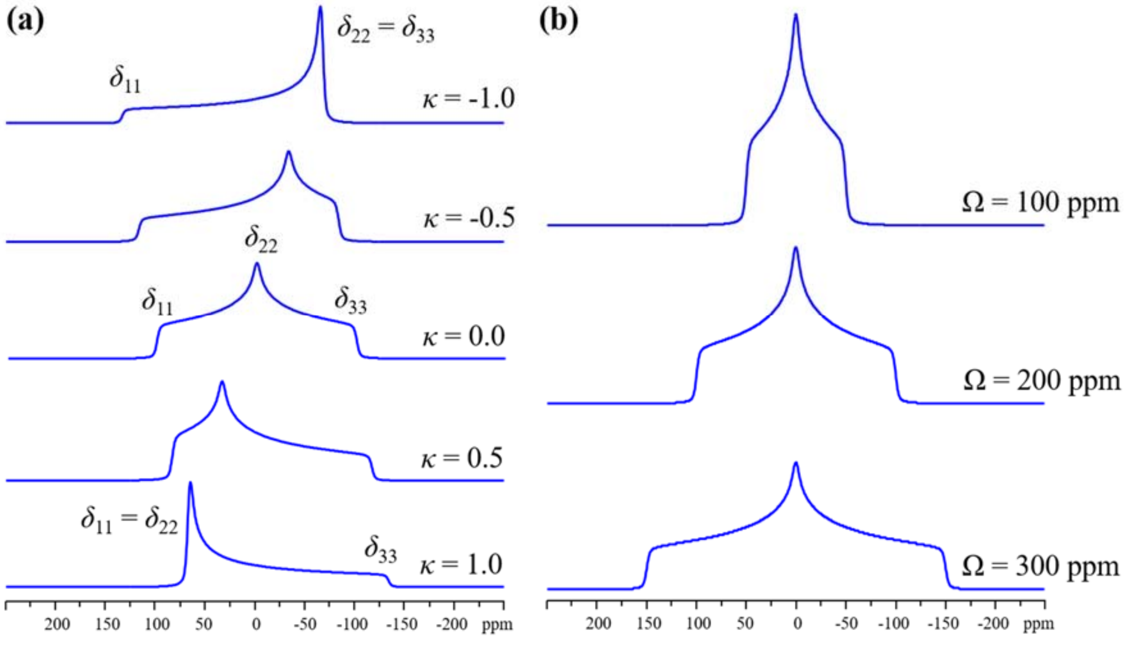

Figure 1-16: Simulated ^{13}C SSNMR CSA-dominated powder patterns using different κ values with Ω = 200 ppm and δ_{iso} = 0 ppm are shown in (a). In (b), the shape of simulated ^{13}C powder patterns generated from different Ω values with κ = 0 and δ_{iso} = 0 ppm are illustrated.

1.2.1.4 Dipolar coupling interaction

The direct dipolar coupling interaction, also known as dipole-dipole coupling, arises from coupling between two magnetic dipoles, and is dependent upon through-space nuclear proximity. The dipolar coupling interaction of two spins (denoted as *I* and *S*) can be classified as either the homonuclear or heteronuclear dipolar interaction, with the interaction Hamiltonian in angular frequency units (rad s^{-1}) described as:[79]

$$\hat{H}_{\mathrm{D}} = -2\,\hat{\mathbf{I}}\cdot\mathbf{D}\cdot\hat{\mathbf{S}} \qquad \textbf{Equation 1-20}$$

$$\hat{H}_{\mathrm{D}} = -\frac{\mu_0}{4\pi}\,\gamma_{\mathrm{I}}\gamma_{\mathrm{S}}\hbar\left(\frac{\mathbf{I}\cdot\mathbf{S}}{r^3} - 3\frac{(\mathbf{I}\cdot\mathbf{r})(\mathbf{S}\cdot\mathbf{r})}{r^5}\right) \qquad \textbf{Equation 1-21}$$

where **D** is the dipolar coupling tensor, which describes how the spin *S* is influenced by the spin *I* in the applied external field B_0 with a given orientation of the *I*-*S* internuclear vector; $\hat{\mathbf{I}}$ and $\hat{\mathbf{S}}$ are the nuclear spin operators; μ_0 is the vacuum permeability constant; **r** is the internuclear vector; and *r* is the internuclear distance. The strength of the dipolar coupling interaction is described by the dipolar coupling constant *d*:[79]

$$d = \hbar\left(\frac{\mu_0}{4\pi}\right)\frac{1}{r^3}\gamma_{\mathrm{I}}\gamma_{\mathrm{S}} \qquad \textbf{Equation 1-22}$$

1.2.1.5 J-coupling interaction

The J-coupling interaction is also known as the indirect or scalar coupling, which rises from the indirect interaction of nuclear magnetic moments mediated by electrons through the chemical bonds between nuclei.[80] The J-coupling is a through-bond interaction, where the first spin *I* perturbs surrounding electrons, which then produce an additional magnetic field at the second spin *S*. The J-coupling leads to splitting of the resonance in the NMR spectrum. The J-coupling is mainly observed in solution NMR and less frequently observed in SSNMR, since J-coupling is relatively weak in magnitude (i.e., 1-10000 Hz) and the line broadening involved in SSNMR, along with other interactions such as chemical shielding and quadrupolar interactions, can easily obscure the spectral effects of J-coupling.

1.2.1.6 Quadrupolar coupling interaction

For a nucleus with a spin number $I > 1/2$, the charge distribution is non-spherical, giving rise to an electric quadrupole moment. A quadrupolar nucleus not only interacts with external and internal magnetic fields but also with any electric field gradients (EFGs) present about the nucleus. The quadrupolar interaction between the quadrupole moment and EFG affects the nuclear spin energy levels, influencing the appearance of NMR spectra.

The Hamiltonian for the quadrupolar interaction is described as:[79]

$$\hat{H}_{\mathrm{Q}} = \frac{eQ}{6I(2I-1)\hbar}\hat{\mathbf{I}}\cdot e\mathbf{q}\cdot\hat{\mathbf{I}}$$

Equation 1-23

Where $e\mathbf{q}$ is the EFG at the nucleus and $\hat{\mathbf{I}}$ is the nuclear spin operator.

In an external magnetic field, the quadrupolar interaction acts as the largest perturbation of the Zeeman states and can be expanded to higher orders, however, typically corrections up to the second order are sufficient for examining quadrupole interactions which cause splittings less than 1/10 of the Zeeman splitting. The first- and second-order energy corrections to the energies of Zeeman levels from quadrupole coupling interaction are:[79]

$$E_m^{(1)} = \frac{e^2qQ}{4I(2I-1)}(I(I+1) - 3m^2)[\frac{1}{2}(3\cos^2\theta-1) - \eta_{\mathrm{Q}}\cos 2\phi(\cos^2\theta-1)]$$

Equation 1-24

$$E_m^{(2)} = (\frac{e^2qQ}{4I(2I-1)})^2\frac{m}{\omega_0}$$

$$\{-\frac{1}{5}(I(I+1) - 3m^2)(3 + \eta_{\mathrm{Q}}^2)$$

$$+\frac{1}{28}(8I(I+1) - 12m^2 - 3)[(\eta_{\mathrm{Q}}^2 - 3)(3\cos^2\theta - 1) + 6\eta_{\mathrm{Q}}\cos 2\phi\sin^2\theta$$

$$+\frac{1}{8}(18I(I+1) - 34m^2 - 5)[\frac{1}{140}(18 + \eta_{\mathrm{Q}}^2)(35\cos^4\theta - 30\cos^2\theta + 3)$$

$$+\frac{3}{7}\eta_Q\sin^2\theta(7\cos^2\theta-1)\cos2\phi+\frac{1}{4}\eta_Q^2\sin^4\theta\cos4\phi\}$$ **Equation 1-25**

where θ and ϕ are determined by the orientation of the chemical structure containing the nucleus with respect to the applied external magnetic field B_0.

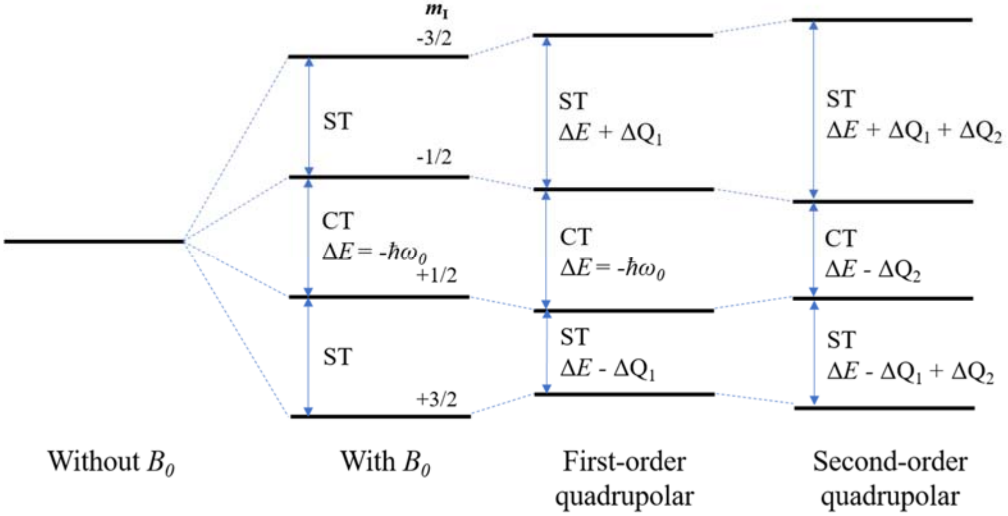

Figure 1-17: An illustration of the splitting of energy levels of a nucleus with $I = 3/2$ due to the Zeeman, first-order quadrupolar and second-order quadrupolar interactions. ΔQ_1 and ΔQ_2 represent the change in transition energy due to the first-order and second-order quadrupolar interactions, respectively.

Figure 1-17 illustrates how the quadrupolar coupling interaction perturbs the Zeeman energy levels of a nucleus with a spin number of half-integer ($I = 3/2$) to the first- and second-order. Although all energy levels are affected by the first-order quadrupolar interaction (FOQI), the energy difference corresponding to the nuclear central transition (CT) from +1/2 to -1/2 remains unchanged. All other transitions (satellite transitions (STs)) are affected by the FOQI and are significantly modified in frequency, leading to spectral broadening. Therefore, detection of the CT is favoured in half-integer quadrupolar SSNMR experiments, since the CT generates a more intense and narrower powder pattern than the STs and is not modified by the FOQI. As shown in Figure 1-17, the CT is influenced by the second-order quadrupolar interaction (SOQI), which has an orientation dependence based on Equation 1-25. The total breadth for the CT in a static sample is described as:[83]

$$\Delta\nu_{CT}=(25+22\eta_Q+\eta_Q^2)A/144 \qquad \textbf{Equation 1-26}$$

where A indicates the second-order quadrupolar broadening of the central transition and is defined as:[83]

$$A=(I(I+1)-\frac{3}{4})\omega_Q^2/\omega_0 \qquad \textbf{Equation 1-27}$$

ω_Q is the quadrupolar frequency and defined as:

$$\omega_Q=\frac{(2\pi)3C_Q}{2I(2I-1)} \qquad \textbf{Equation 1-28}$$

Note that, ω_Q depends on the spin number I. Nuclei with larger nuclear spin I tend to give rise to narrower CT powder patterns.

The quadrupolar coupling interaction can be described by a second-rank EFG tensor. In its PAS, the diagonalized EFG tensor has three non-zero components V_{XX}, V_{YY}, and V_{ZZ}, ordered such that $|V_{XX}| \leq |V_{YY}| \leq |V_{ZZ}|$. Since the EFG tensor is traceless, $V_{XX}+V_{YY}+V_{ZZ}=0$. Two EFG parameters, the quadrupole coupling constant C_Q, and the asymmetry parameter η_Q, are typically used to define the QI and are defined as:[79-80]

$$C_Q=\frac{e^2qQ}{\hbar}=\frac{eV_{ZZ}Q}{\hbar} \qquad \textbf{Equation 1-29}$$

$$\eta_Q=\frac{V_{XX}-V_{YY}}{V_{ZZ}} \qquad \textbf{Equation 1-30}$$

where Q is the nuclear quadrupole moment. The C_Q indicates the magnitude of the quadrupolar interaction and describes the spherical symmetry of the electronic environment about the nucleus. Low C_Q values correspond to a high degree of spherical symmetry, while high C_Q values represent a low degree of spherical symmetry. η_Q is used to describe the axial symmetry of the EFG tensor. The value of η_Q ranges from 0 to 1. An η_Q value of 0 corresponds to an axially symmetry EFG tensor with a C_3 or higher rotational symmetry axis, while higher η_Q values denote a lower degree of axial symmetry. Some examples of typical SOQI dominated CT powder patterns are illustrated in Figure 1-18.

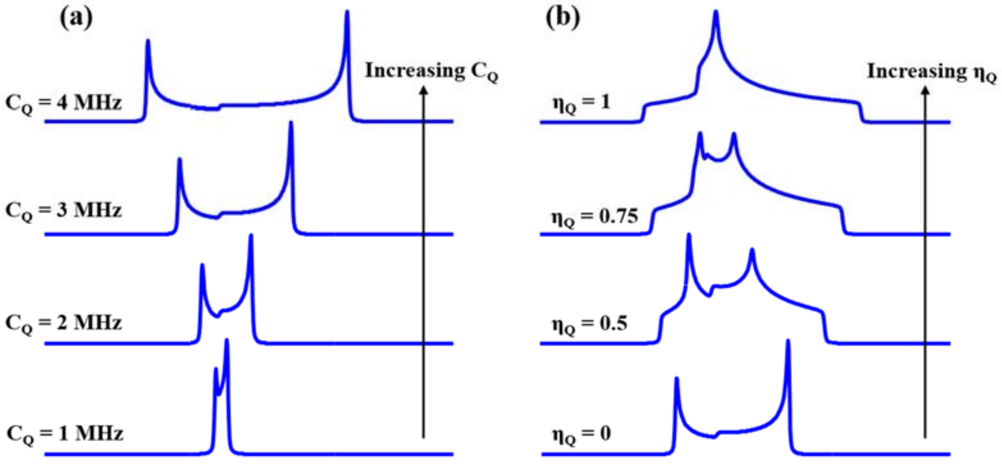

Figure 1-18: An illustration of simulated ^{71}Ga SSNMR spectra (spin-3/2) at a magnetic field of 9.4 T. The effects of changes in C_Q (holding $\eta_Q = 0$) on the CT powder pattern is shown in (a), while the effects of changes in η_Q (holding C_Q = 3 MHz) on a powder pattern are illustrated in (b).

For a quadrupolar nucleus with an integer spin number (*e.g.* $I = 1$), the Zeeman interaction generates two equivalent transitions (Figure 1-19(a)) and only the FOQI significantly influences the SSNMR powder pattern. For the transition from the m to m-1 level, the transition frequency can be calculated from Equation 1-24:

$$\omega_{\mathrm{m}}^{(1)} = [E_{(m-1)}^{(1)} - E_m^{(1)}]/\hbar = \omega_Q(m-\frac{1}{2})\{\frac{1}{2}\left[(3\cos^2\theta-1) - \eta_Q\cos2\phi(\cos^2\theta-1)\right]\}$$

Equation 1-31

For axially symmetric EFG tensors and nuclear environments where $\eta_Q = 0$:

$$\omega_{\mathrm{m}}^{(1)} = \omega_Q/2(m-\frac{1}{2})(3\cos^2\theta-1)$$

Equation 1-32

Therefore, for a spin $I = 1$ nucleus, the m = 1 to m = 0 transition has a $+(3\cos^2\theta-1)$ dependence, and the m = 0 to m = -1 transition has a $-(3\cos^2\theta-1)$ dependence.[84] Figure 1-19(b) shows the spin $I = 1$ powder pattern in an axially symmetric electronic environment.

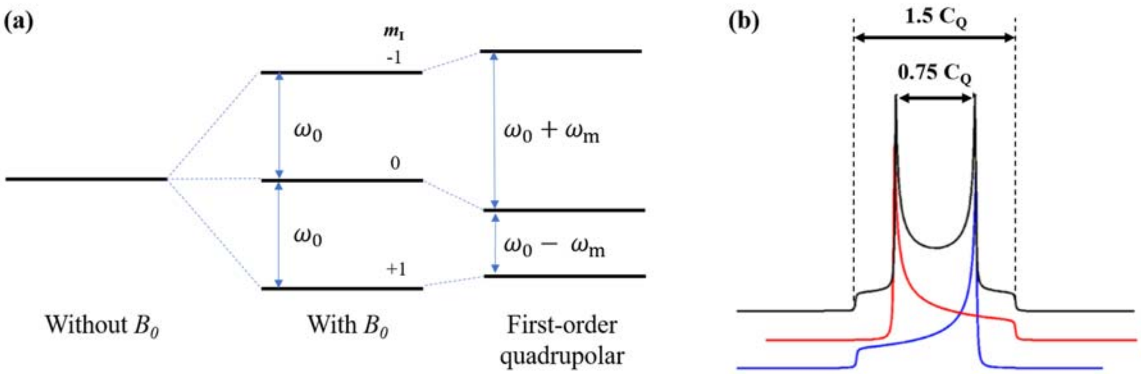

Figure 1-19: In (a), the splitting of energy levels of a nucleus with $I = 1$ due to the Zeeman and FOQI is shown. The quadrupolar SSNMR powder pattern for a spin $I = 1$ nucleus with η_Q value of 0 is shown in (b). Blue and red components represent transitions from m = 1 to m = 0 and m = 0 to m = -1, respectively.

1.2.1.7 Paramagnetic coupling

In NMR experiments, samples with paramagnetic centres have different behaviours versus those with diamagnetic centres. This is because the unpaired electrons on the paramagnetic centres have much large magnetic moment than those of nuclei, generating strong additional magnetic fields that significantly perturb the Zeeman interaction.[85] The interaction between the magnetic moment of unpaired electron and that of the target nucleus is known as paramagnetic coupling, which typically range in magnitude from 10^2-10^6 Hz.[80]

The paramagnetic coupling is treated similar to CSA, and is described by the hyperfine shift δ_{hyp}. The hyperfine shift contains two elements:[86]

$$\delta_{\text{hyp}} = \delta_{\text{con}} + \delta_{\text{dip}} \qquad \textbf{Equation 1-33}$$

where δ_{con} is the Fermi contact shift and δ_{dip} is the dipolar shift.

The Fermi contact shift is a through-bond effect, which is caused by a spin delocalization of the unpaired electron in the paramagnetic centre. The Fermi contact shift can be expressed as:

$$\delta_{\mathrm{con}} = m\frac{S+1}{T}\,\rho_{\alpha\beta} \qquad \textbf{Equation 1-34}$$

where S is the total spin, T is the absolute temperature, m is a collection of constants (23.5 × 10^6 ppm K a.u.$^{-1}$), and $\rho_{\alpha\beta}$ is the Fermi contact spin density. In this thesis, D_2 and deuterated methane adsorbed in MOF-74 with paramagnetic centres have been studied (Chapter 3 and Chapter 4). The unpaired electrons of paramagnetic centres can enter the empty σ^* orbitals of deuterated hydrogen or methane, therefore, the Fermin contact spin density can be found at deuterium nuclei, and Fermi contact shift can be observed.

In contrast, the dipolar shift is a through-space effect, which is proportional to $1/r^3$ (r is the distance from the unpaired electron of paramagnetic centre to the target nucleus). As the temperature drops, the binding energy overcomes thermal energy, therefore, the interactions between gas molecules and paramagnetic metal centres become stronger, reducing the distance between gas molecules and metal centres, and enhancing the dipolar-induced paramagnetic frequency shifts of NMR.

In this thesis, all deuterium spectra acquired within paramagnetic systems are broadened and featureless in appearance (i.e., do not resemble the classic appearance of a Pake doublet) due to the strong influence of paramagnetic coupling, consequently spectral simulation were not straight forward.

1.2.1.8 Euler angles

The NMR powder pattern of a quadrupolar nucleus can be influenced by both the quadrupolar and chemical shift interactions, and the NMR powder pattern is sensitive to the orientations of these NMR tensors. Both the EFG and CS tensor principal axis systems (PASs) can be related to the molecular frame through two distinct sets of eigenvectors. The relationships between these two PASs can be described by three Euler angles, which are illustrated in Figure 1-20.

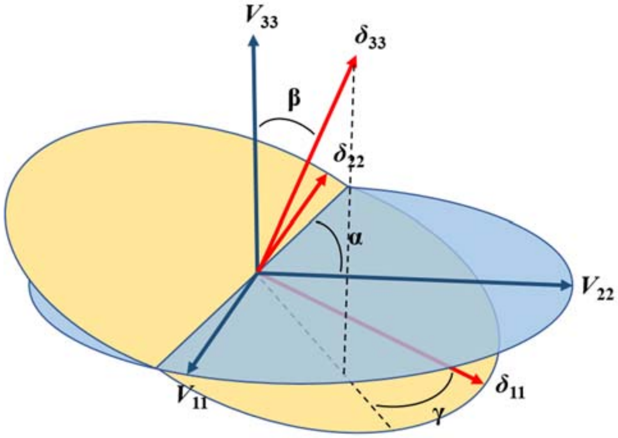

Figure 1-20: A depiction of the Euler angles relating non-coincident EFG and CS tensors.

In this thesis, the Euler angle β, which describes the angle between V_{33} and δ_{33}, has a measurable impact on the ^{2}H SSNMR spectra in Chapter 4. The presence of the CS interactions significantly influences the spectral appearance.

1.2.1.9 Relaxation processes

In NMR experiments, after shutting off the rf pulse, there are several processes that determine how fast the spin population equilibrates between high-energy spin states to low-energy spin states (thermodynamic equilibrium) and how fast the precession of spin states lose coherence, which are known as NMR relaxation. The former is known as T_1 relaxation, or spin-lattice relaxation time, which describes the relaxation of the bulk magnetization back to thermal equilibrium along the direction of B_0 or z-axis (Figure 1-21(a)); the latter is known as T_2 relaxation or spin-spin relaxation, which describes the loss of coherence of magnetization in the transverse xy-plane (Figure 1-21(b)). T_1 values determine the experimental time in NMR experiments (the pulse delay is usually five times longer than T_1). T_2 relaxation can be observed as the exponential decay in the signal of the acquired free induction decay (FID) with time.

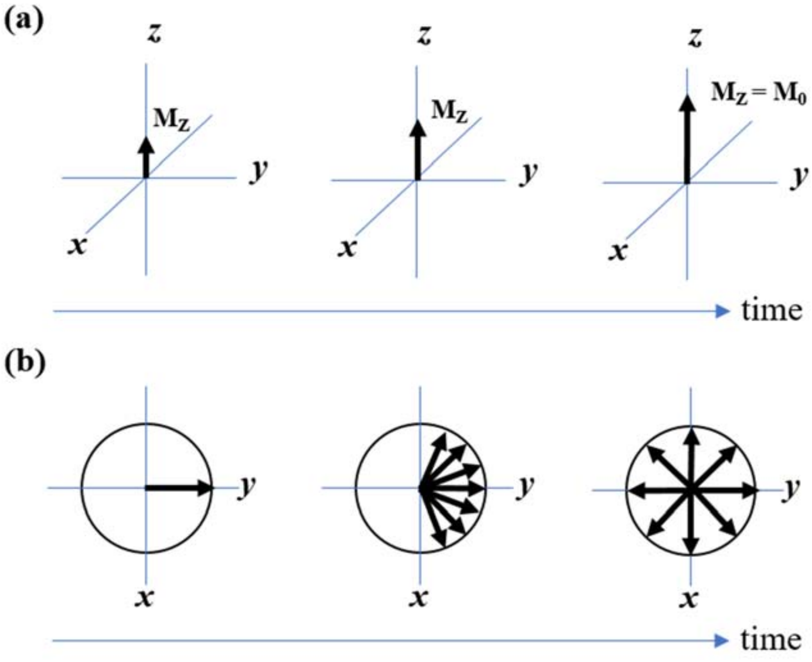

Figure 1-21: T_1 relaxation and T_2 relaxation are shown in (a) and (b), respectively. $\mathbf{M_0}$ in (a) is the net spin magnetization vector, while, $\mathbf{M_Z}$ is the z-component of $\mathbf{M_0}$.

1.2.2 Experimental background

1.2.2.1 Spin-echo and quadrupole-echo pulse sequence

In an NMR experiment, a coil perpendicular to B_0 is used to apply the rf field, which rotates the net spin longitudinal magnetisation to transverse magnetisation. Once the rf field is turned off, the precession of the transverse magnetisation generates a current in the coil, which is NMR FID signal. This current often decays quickly and cannot be measured until after a short "dead time" in the NMR probe after a pulse. For a powder pattern that has a rapidly decaying FID, a significant part of the FID can not be recorded. The missing part of FID means that the resulting NMR lineshape is distorted after Fourier transformation (FT) into the frequency domain. In SSNMR, this problem is resolved by using spin-echo or quadrupole-echo pulse sequences.

The spin-echo pulse sequence is illustrated in Figure 1-22. A 90° pulse along the x-axis is applied first, which rotates the net spin magnetization to the y-axis. A 180° pulse is then applied along the *y*-axis, which rotates the magnetization components 180° about the *y*-axis, followed by a refocusing of the magnetization components after a τ_2 period, which exceeds the dead time of the NMR probe and spectrometer.[79] The spin-echo pulse sequence is typically used for patterns broadened by CSA, while for lines broadened by quadrupolar coupling, a quadrupole-echo pulse sequence is employed by replacing the 180° pulse along the *y*-axis in spin-echo pulse sequence to a 90° pulse.[79]

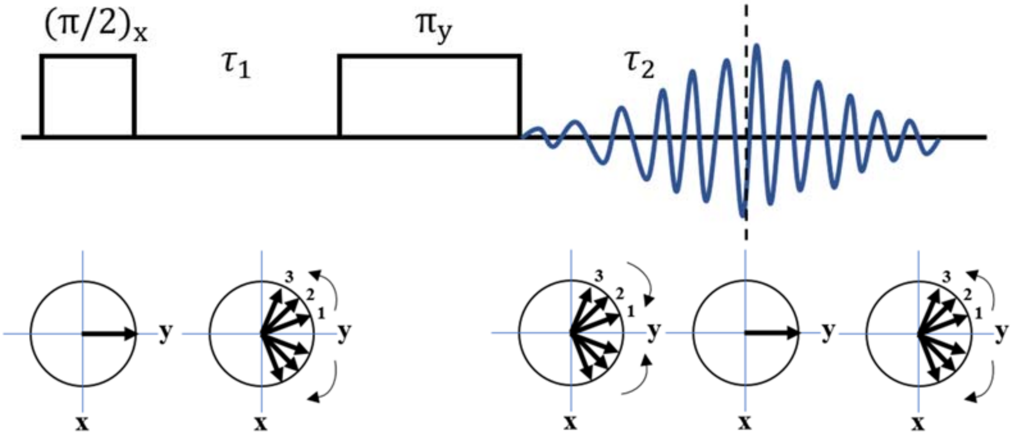

Figure 1-22: The spin-echo pulse sequence, along with the behaviour of the magnetization components in the *xy* plane is shown.

1.2.2.2 DEPTH and DEPTH-echo pulse sequences

An approach to eliminate background signals from the NMR probe involves using the DEPTH pulse sequence. The DEPTH pulse sequence consists of one π/2 pulse applied along the *x*-axis of the rotating frame, generating B_1 in order to tip the magnetization along the *z*-axis into the *xy*-plane. The π/2 pulse is followed by two consecutive π pulses which can eliminate background signals (Figure 1-23(a)).[87-88] In this thesis, all static ^{13}C SSNMR spectra on ^{13}C-enriched $^{13}CO_2$ were acquired using a combined DEPTH and Hahn-Echo sequence (DEPTH-echo pulse sequence),[16] giving rise to ^{13}C powder patterns of CO_2 unaffected by lineshape distortion and background signals. The pulse sequence scheme of DEPTH-echo is illustrated in Figure 1-23(b).

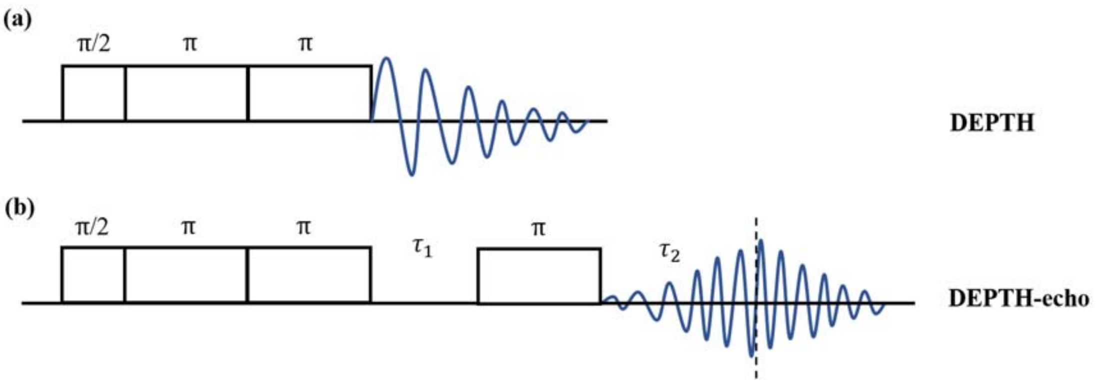

Figure 1-23: A comparison of pulse sequences: (a) the DEPTH pulse sequence versus (b) the DEPTH-echo pulse sequence.

1.2.2.3 Cross-polarization (CP) pulse sequence

The cross-polarization (CP) method is frequently used to enhance NMR signals from dilute spins. This technique is designed to transfer polarization from abundant nuclei I (*i.e.*, ^{1}H and ^{31}P) to dilute nuclei S (*i.e.,* ^{13}C and ^{29}Si). The gain in signal intensity is approximately γ_I/γ_S, where γ_I and γ_S are the gyromagnetic ratios of the abundant and dilute spins. In addition, I spins normally possess shorter T_1 relaxation times than S spins, which leads to shorter experimental times due to a reduction in the pulse delays that need to be employed.[89-90]

The CP pulse sequence is illustrated in Figure 1-24. A π/2 pulse is first applied to the I spins along the x-axis, which rotates the I magnetization to the y-axis in the rotating frame. An on-resonance contact or "mixing" pulse is then applied along the y-axis; the field due to this pulse is known as the spin-lock field and is termed $B_1(I)$. Because the contact pulse is on resonance, the effect of B_0 is eliminated and $B_1(I)$ is the only field acting on the I spins. As a result, $B_1(I)$ acts as the axis of quantization for the I spins in the rotating frame during the spin lock period. At the same time, an rf pulse along the y-axis is applied to the dilute spin S, which generates a spin locking field $B_1(S)$. In order to satisfy the transfer of spin polarization between I and S, the Hartmann-Hahn matching condition must be achieved:[91]

$$\omega_{1I} = \omega_{1S} \qquad \textbf{Equation 1-35}$$

$$\gamma_I B_1(I) = \gamma_S B_1(S)$$ **Equation 1-36**

where equation 1-35 and 1-36 is the Hartmann-Hahn matching conditions under static conditions. The Hartmann-Hahn matching condition under magic angle spinning (MAS) conditions for spin *I* and *S* is:[79]

$$\omega_{1I} = \omega_{1S} \pm \omega_R \text{ or } \pm 2\omega_R$$ **Equation 1-37**

where ω_R is the spinning rate. The time period during polarization transfer is known as contact time (CT).

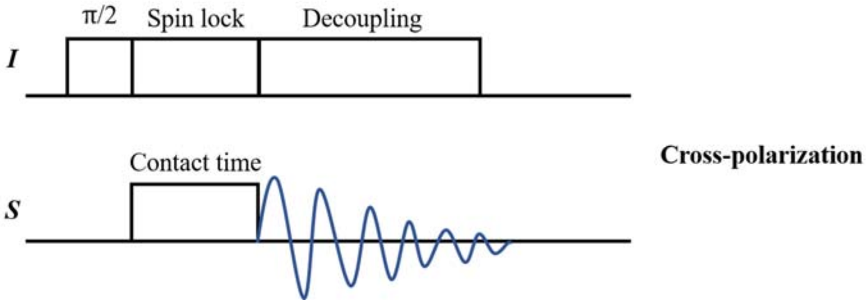

Figure 1-24: The cross-polarization pulse sequence.

The rate of magnetization transfer in a CP experiment relies on the strength of the dipolar coupling between spin *I* and *S*: the stronger the *I-S* dipolar coupling, the faster the rate of. CP transfer to spin *S* initially occurs from the closest spin *I*. With a longer CT, polarization from other *I* spins, which are further away, can be transferred to spin *S*.

1.2.2.4 Magic-angle spinning (MAS)

Magic-angle spinning (MAS) is a widely used SSNMR method to remove the effects of chemical shift anisotropy and dipolar coupling. MAS is also a generally used method to narrow lines from quadrupole interactions. In a MAS experiment, the sample is rotated about an axis oriented at an angle of 54.74 ° (known as the “magic-angle”) with respect to the external magnetic field B_0, since many NMR interactions have an orientation dependence involving the term $(3\cos^2\theta - 1)$. When $\theta = 54.74$ °, the term $(3\cos^2\theta - 1) = 0$, removing the orientation dependence in the NMR interactions mentioned above.

A diagram representing a typical MAS experiment is given in Figure 1-25. If the sample is inclined at an angle θ_R, then θ values vary with time as the molecule rotates with the sample. The time average of $<3\cos^2\theta - 1>$ then can be written as:[79]

$$<3\cos^2\theta - 1> = (3\cos^2\theta_R - 1)\,(3\cos^2\beta - 1)/2 \qquad \textbf{Equation 1-38}$$

where the angle β is between the principal *z*-axis of the NMR tensor and the spinning axis. The value of β is fixed for a given nucleus in a rigid solid. The angle θ_R is the experimentally adjusted angle, and when the θ_R value is set to 54.74 °, the term $(3\cos^2\theta_R - 1) = 0$, therefore, $(3\cos^2\theta - 1) = 0$ based on Equation 1-38, eliminating the first-order effects of anisotropic NMR interactions. For example, MAS experiments are useful for removing the effect of CSA and generating narrower peaks. The second-order quadrupolar interaction is more complicated as described in section 1.2.1.6. MAS cannot fully average the line broadening due to the second-order quadrupolar interaction.

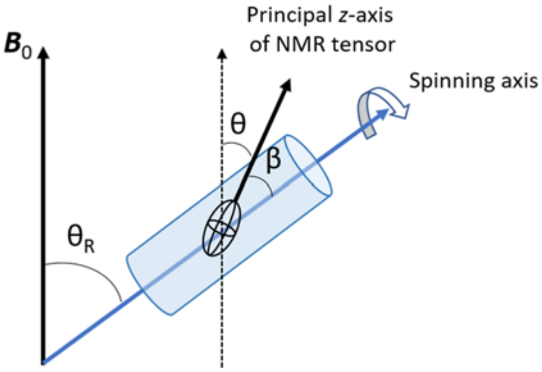

Figure 1-25: A schematic diagram of the magic-angle spinning experiment.

In order to fully eliminate the spectral effects of first-order anisotropic interactions using MAS, the spinning frequency must be greater than the magnitude of the interaction (in Hz). Spinning speeds that do not satisfy this condition produce a series of sharp resonances, known as spinning sidebands, which radiate out from the isotropic resonance. In SSNMR spectra, spinning sidebands are separated in the frequency domain by a frequency equal to the spinning speed in Hz. The isotropic resonance is the only one that does not change its frequency with spinning speed.

1.2.2.5 WURST-CPMG pulse sequence

The WURST-CPMG pulse sequence contains two elements: WURST (wideband uniform-rate smooth truncation) pulses[92-93] and a CPMG (Carr-Purcell Meiboom-Gill) echo train.[94] Unlike rf pulses, which are typically short, rectangular pulses in the time domain with a fixed phase, WURST pulses are of a relatively longer period and are phase modulated. WURST pulses employ a frequency sweep that begins and ends at a large offset from the resonance frequency; the frequency sweep is achieved through phase modulation and satisfying the adiabatic condition. A WURST pulse generates an effective magnetic field (B_{eff}) that moves slowly from the $+z$ axis to $-z$ axis. In order to accomplish adiabatic inversion of the spin magnetization, the change in B_{eff} must be slower than the precession frequency of the nuclear magnetization around B_{eff}. Under this condition, the magnetization vector will along with B_{eff}. WURST pulses have much broader frequency excitation band widths versus the typical square pulses used in NMR.[93]

The CPMG portion of the pulse sequence is used to enhance the signal-to-noise ratio (S/N) and decrease the acquisition times involved in acquiring wideline NMR spectra.[94-96] As shown in Figure 1-26(a), the CPMG pulse sequence consists N-repeated refocusing pulses, resulting in the acquisition of a train of several individual echoes. After Fourier transformation, a spikelet spectrum is generated, in which the shape of the spikelet spectrum traces out the manifold of the powder pattern. The spikelets in a spikelet spectrum are evenly separated by $1/\tau_a$. The number of refocusing loops, N, can be adjusted to exploit longer T_2 values in different samples. Because the entire spectral signal is concentrated into a finite number of spikelets, an increase in the overall S/N is achieved.

The WURST-CPMG pulse sequence is shown in Figure 1-26(b). In the WURST-CPMG pulse sequence, the square or rectangular pulses of the CPMG pulse sequence are replaced by WURST pulses; for this thesis, WURST-80 pulses were used in all circumstances unless specified otherwise. The first WURST-80 pulse rotates the nuclear spin magnetization into the xy-plane, and then the N-repeated WURST-80 pulses are applied to continually refocus the magnetization. WURST-CPMG experiments lower S/N versus conventional CPMG pulse, however, the excitation bandwidth is much larger.

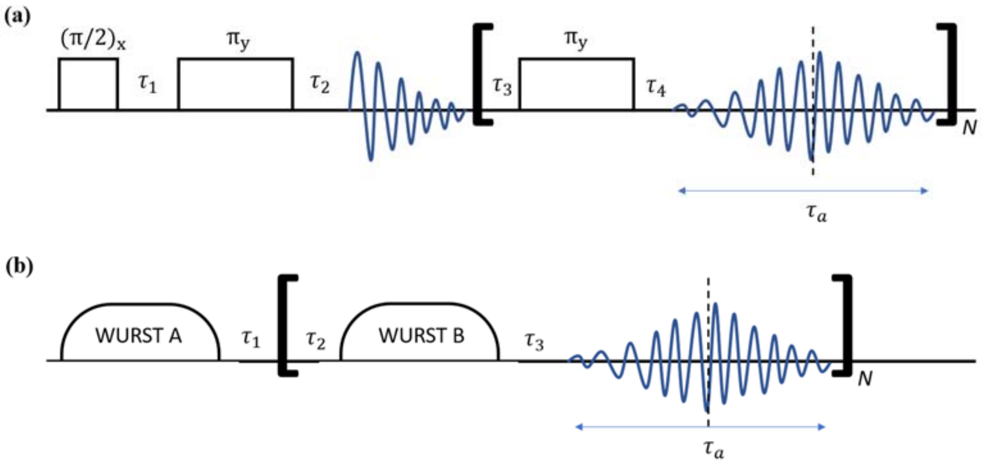

Figure 1-26: (a) The CPMG pulse sequence using ordinary rectangular pulses. (b) The WURST-CPMG pulse sequence (WURST A = WURST B).

1.2.2.6 High Magnetic Field

As shown in Equation 1-4 and Equation 1-6, in an external magnetic field B_0, the population difference between two adjacent spin energy levels increases with B_0, thus the S/N increases with B_0.

The spectral appearance for the same sample at different external magnetic fields is generally distinct, since the chemical shielding and quadrupolar coupling interactions scale in opposite directions with B_0. The spectral impact of the chemical shielding interaction is proportional to the magnetic field, however, for spin half-integer quadrupolar nuclei, the spectra are broadened by the second-order quadrupolar interaction, which is inversely proportional to B_0 (Equation 1-27). For integer spin quadrupolar nuclei, the Zeeman splitting only gives rise to two equivalent spin transitions and the spectra are dominated by the first-order quadrupolar interaction, therefore, high magnetic fields do not change the lineshapes but could improve S/N based on the increased difference in population between spin states. In this thesis, some half-integer nuclei such as ^{71}Ga, ^{69}Ga, and ^{115}In were studied at a high magnetic field of 21.1 T, benefitting from narrower CT powder patterns and high sensitivity.

1.2.3 Theoretical calculations

In this thesis, there are several instances where NMR parameters have been computationally calculated by our collaborators in order to predict the orientations of the NMR interaction tensors and the values of NMR parameters, which can be compared with experimental results. These calculated NMR tensors provide useful information on local short-range structure, symmetry, and the magnetic electronic environment, thus helping us to have a better understanding of the structure.

All calculations were performed using the CASTEP (Cambridge serial total energy package) software package.[97-98] The NMR tensors were calculated using the NMR module[99-100] incorporated in CASTEP, which employs the gauge-including projector-augmented wave (GIPAW) method, pseudopotentials, and plane-wave basis sets.[98] These calculations also employed the generalized gradient approximation (GGA) along with the Perdew− Burke−Ernzerhof (PBE) functional.[101]

1.3 SSNMR for studying molecular motion in solids

1.3.1 Introduction

SSNMR is well-suited for studying molecular dynamics in solid samples. This is because, in solid samples, all nuclear spin interactions are in general anisotropic; the specific magnitude and effect of the NMR interaction depends on the molecular orientation with respect to the applied external magnetic field B_0. Molecular motions will change the orientations of molecular components, and change the local environment of nuclear spins, thus affecting the NMR frequencies and NMR lineshapes. Therefore, based on NMR spectra, molecular motions can be revealed.[79, 102]

In a one-dimensional SSNMR spectrum, the powder pattern lineshape is very sensitive to motions that occur on a time scale less than or about equal to the inverse of the spectral width. It must be noted that the shortest time scale for direct, real-time NMR measurements of transient motions must be longer than 1 μs. This is because rf pulses used in NMR are generally longer than 1 μs, therefore, transient motions occurring on a time scale equal to or less than 1 μs will not have significant effects on NMR spectra. However, for molecules, which have equilibrium dynamics, such as wobbling, the motion occurring on the 1 ps time scale are accessible to NMR measurements.[102]

When calculating the appearance of a SSNMR powder pattern under influenced by molecular motion, a Markov process must be considered for the motion. The Markov process involves the exchange or hopping between N sites. The exchange or hopping time between two sites is infinitesimally negligible compared to the residence time in each site. With this in mind, the time evolution of the transverse magnetization can be modeled. Without molecular motion, the time evolution of the transverse magnetization is described as:[79]

$$\frac{dM^+(\theta, \phi; t)}{dt} = M^+(\theta, \phi; t)(i\omega(\theta, \phi) + T_2) \qquad \textbf{Equation 1-39}$$

And the solution of Equation 1-39 is given by

$$M^+(\theta, \phi; t) = M_0^+(\theta, \phi) \exp(i\omega(\theta, \phi)t + T_2) \qquad \textbf{Equation 1-40}$$

where the molecular orientation in B_0 is described by the polar angles θ and ϕ, as shown in Figure 1-27; T_2 is the spin-spin relaxation time; ω(θ, ϕ) is the resonance frequency of a spin in a molecule with an orientation of θ and ϕ; $M_0^+(\theta, \phi)$ is the initial transverse magnetization with a molecular orientation (θ, ϕ).

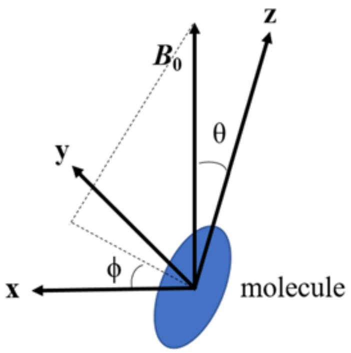

Figure 1-27: Polar angles θ and ϕ, which define the molecular orientation in an external magnetic field B_0.

When considering the molecular motion (reorientations) in a Markov model, Equation 1-39 can be modified to:[79]

$$\frac{\mathrm{d}\mathbf{M}^{+}(\theta, \phi; t)}{\mathrm{d}t} = \mathbf{M}^{+}(\theta, \phi; t)(\mathrm{i}\boldsymbol{\omega}(\theta, \phi) + \mathbf{T_2} + \boldsymbol{\Pi}) \qquad \textbf{Equation 1-41}$$

where $\mathbf{M}^{+}(\theta, \phi; t)$ is an N-dimensional vector whose components originate from the N sites involved in the motional process. $\boldsymbol{\omega}$ is an $N \times N$ diagonal matrix, each element being the resonance frequency to be relevant to the N sites for a molecular orientation (θ, ϕ). $\boldsymbol{\Pi}$ is also a $N \times N$ matrix describing the hopping of magnetization between the N sites. The elements of matrix $\boldsymbol{\Pi}$ are termed as:[79]

$$\Pi_{ij} = \Omega_{ij}\rho_{j} \qquad \textbf{Equation 1-42}$$

where Ω_{ij} describes the inverse of the time for hopping from site j to site i, while, ρ_j describes the population of site j. The solution of Equation 1-41 is given by

$$\mathbf{M}^{+}(\mathrm{t}) = \frac{1}{8\pi^{2}}\int_{0}^{2\pi}\int_{0}^{\pi}\mathbf{M}_{\mathbf{0}}^{+}(\theta, \phi)\exp(\mathrm{i}\boldsymbol{\omega}(\theta, \phi)\mathrm{t} + \mathbf{T_2} + \boldsymbol{\Pi})\sin\theta \mathrm{d}\theta \mathrm{d}\phi \qquad \textbf{Equation 1-43}$$

The FID under conditions of a Markov model is described as:[79]

$$\mathrm{F}(t) = \sum_{\mathrm{i}}^{\mathrm{N}}\mathbf{M}_{\mathbf{i}}^{+}(t) \qquad \textbf{Equation 1-44}$$

therefore, the SSNMR powder patterns under different motional conditions can be calculated.

1.3.2 EXPRESS simulations

EXPRESS (Exchange Program for RElaxing Spin Systems) is a computer program coded in MatLab that simulates NMR lineshapes and relaxation times according to motions in a Markov model.[103] Since EXPRESS simulates the effects of hopping or jumping between different sites, it is essential to define the orientation of NMR tensors in the jump frame.

The orientation of NMR tensors in a given jump frame in the EXPRESS program is specified by the Euler angles (α, β, γ), where α is the rotation angle about the original *z*-

axis in the principle axis frame of NMR tensors and set as 0 ° in EXPRESS program, β is the rotation angle between an NMR tensor and the rotation axis in a new intermediate frame, β describes the wobbling angle or hopping angle in this thesis; γ defines the number of site in EXPRESS program.[103] For example, a C_2 rotation can be defined in EXPRESS by setting γ values in a sequence of 0 ° and 180 °, while a C_6 rotation can be described in EXPRESS by setting γ values in a sequence of 0 °, 60 °, 120 °, 180 °, 240 °, and 300 °.

EXPRESS can solve a broad range of *N* site problems, including hopping in multiple jump frames. For example, for an NMR tensor in two jump frames, the site angles of the first rotation rotate the PAS for the tensor into coincidence with an intermediate frame, while, the second rotation then rotates the axes of the intermediate frame into any orientations with respect to a crystal-fixed frame. However, for the motion that only has one jump frame, the specified angles rotate the PAS axes for a relevant NMR tensor into coincidence with crystal-fixed axes. The schematic of motions in one rotation frame and two rotate frames are shown in Figure 1-28 (a) and (b), respectively.

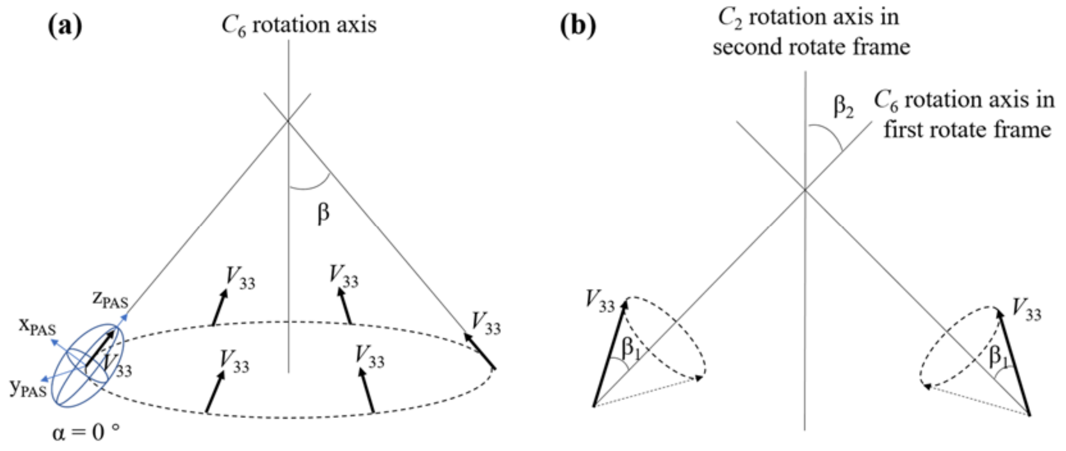

Figure 1-28: Illustrating the orientations of the EFG tensor component V_{33} in different rotation frames. In (a), V_{33} undergoes a six-site jumping (C_6 rotation) through a rotation angle β in one increment, the six jumping sites were defined by setting γ values in a sequence of 0 °, 60 °, 120 °, 180 °, 240 °, and 300 °. In (b), V_{33} undergoes two types of motion. V_{33} first jumps between six sites (accomplished by setting γ_1 as 0 °, 60 °, 120 °, 180 °, 240 °, and 300 °) through a C_6 rotation angle β_1, then jumps between two sites (modeled by setting γ_2 as 0 ° and 180 °) through a C_2 rotation angle β_2.

1.3.3 ^{13}C SSNMR

^{13}C SSNMR spectroscopy is frequently used for studying molecular motions;[16, 104-106] ^{13}C is a spin-1/2 nucleus, and the lineshapes of ^{13}C powder patterns are very sensitive to molecular motions due to the dominance of the anisotropic CS interaction. In this thesis, ^{13}C enriched CO_2 has been used to study the dynamics of CO_2 adsorbed within MOFs (*Chapter 2* and *Chapter 5*).

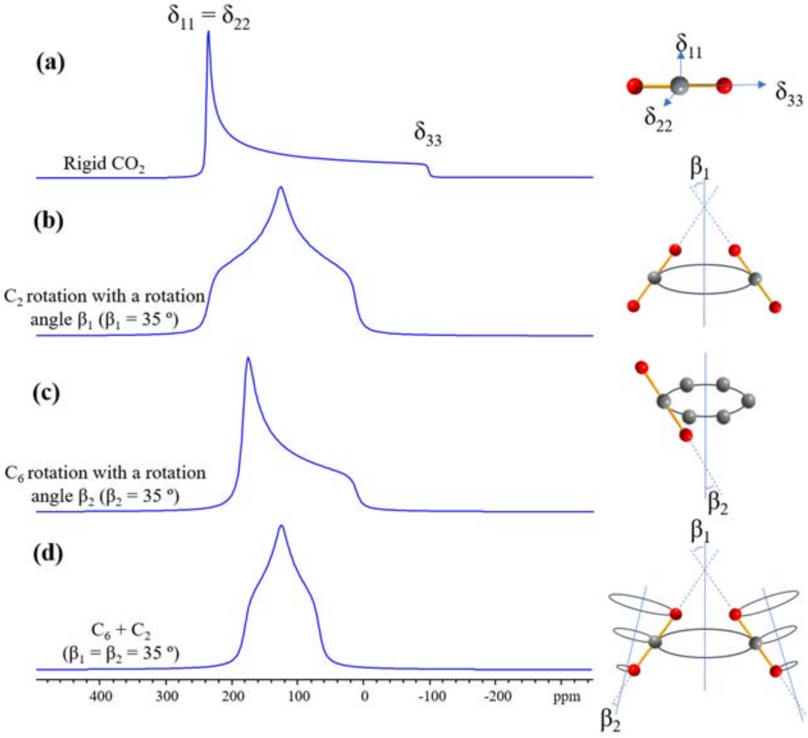

Figure 1-29: Motionally simulated (using δ_{iso} = 125 ppm, Ω = 330 ppm, and κ = 1 with motional rate of 10^7/s) ^{13}C powder patterns of $^{13}CO_2$ for (a) static $^{13}CO_2$, (b) $^{13}CO_2$ undergoing a C_2 rotation through a rotation angle β_1, (c) $^{13}CO_2$ undergoing a C_6 rotation through a rotation angle β_2, and (d) $^{13}CO_2$ undergoing both C_2 and C_6 motions with rotational angles β_1 and β_2.

The powder pattern lineshape of the static $^{13}CO_2$ gives rise to the well known as axially symmetric powder pattern (Figure 1-29(a)). This is because CO_2 is a linear molecule, therefore, $\delta_{11} = \delta_{22}$ (Figure 1-29(a)). In a powder sample, CO_2 molecules are randomly oriented, thus generating a range of chemical shielding frequencies (Equation 1-

14), which give rise to a broad ^{13}C powder pattern. The lineshapes of ^{13}C powder patterns are changed when thermal motion arises as shown in Figure 1-29.

1.3.4 ^{2}H SSNMR

^{2}H SSNMR spectroscopy is frequently used for studying molecular dynamics, since the powder pattern lineshape is very sensitive to the motion and motional rate of the molecule. ^{2}H is a spin $I = 1$ quadrupolar nucleus, therefore, the first-order quadrupolar interaction gives rise to a symmetric doublet powder pattern lineshape. The quadrupole moment (Q) of ^{2}H is 2.860 mb.[107] Other NMR interactions such as chemical shift and the dipolar interaction are usually negligible due to the dominant magnitude of the first-order quadrupolar interaction, however, in this thesis, the chemical shift interaction has indeed been observed in ^{2}H SSNMR spectra when studying deuterated-methane within various MOFs (*Chapter 4*).

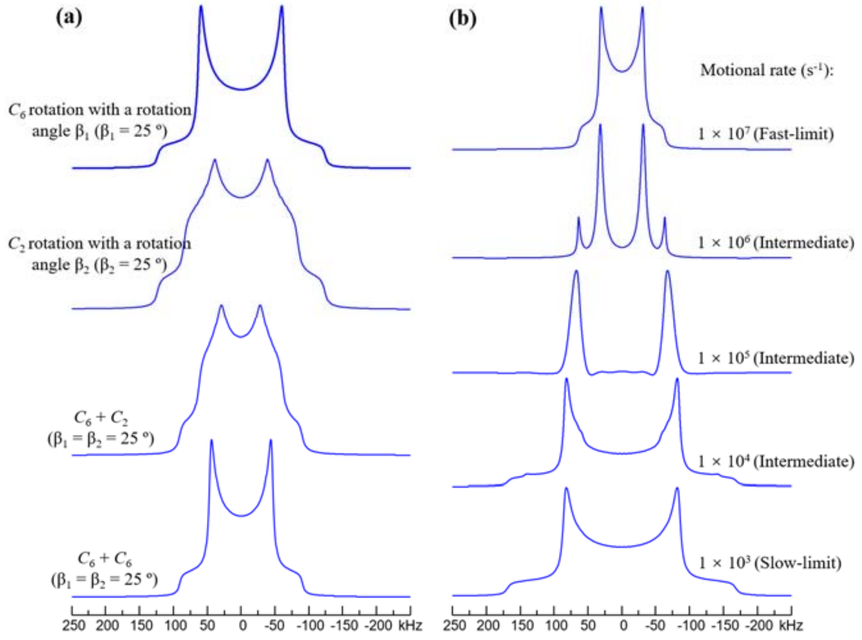

Figure 1-30. A set of motionally simulated ^{2}H powder patterns (using C_Q = 225 kHz and $\eta_Q = 0$ as static ^{2}H NMR parameters) for different types of motions in the fast-limit regime with a motional rate of 1×10^9 s^{-1} are shown in (a). In (b), ^{2}H powder patterns were simulated using a C_6 rotation with a rotation angle of 40 ° at different motional rates.

A static C-D, or D-D, or O-D bond without any intermolecular interactions always gives rise to a Pake doublet powder pattern (as shown in Figure 1-19). V_{33} is usually directed along the bond, while V_{11} and V_{22} are equivalent and perpendicular to the bond (V_{33}), thus giving rise to an axially-symmetric environment ($\eta_Q = 0$). In this thesis, deuterated-methane (*Chapter 4*) and D_2 (*Chapter 3*) adsorbed inside of MOFs have been studied by acquiring static ^{2}H SSNMR experiments. Both static deuterated-methane (CH_3D) and D_2 display Pake doublet powder patterns with $C_Q(^2H)$ values of 192 kHz[108] and 225 kHz,[109] respectively. The lineshapes of ^{2}H powder patterns change when additional motions have been introduced to the studied molecules. As shown in Figure 1-30, both motional types and motional rates can influence the lineshape.

1.4 Objective and Outline of the thesis

The objective of my thesis is threefold: (i) developing an in-depth understanding of gas dynamics, gas binding strengths, and gas binding locations within MOFs; (ii) exploring the power of SSNMR for MOF characterization; and (iii) designing new MOFs, functionalizing their frameworks, and developing their potential applications. SSNMR has been used as a primary characterization method for all three branches, since SSNMR is very sensitive to the motion and the short-range structure of a target nucleus (more detailed information about SSNMR is described in section 1.3 and 1.4).

Seven chapters have been included in this thesis and are organized in the following manner. Chapter 1 introduces the basics of metal-organic frameworks and solid-state NMR. Chapters 2-6 are the results and discussion portion of this thesis. Chapters 2-4 focus on gas adsorption, while Chapter 5 describes the design of new MOFs. In Chapter 2, we tried to determine the CO_2 dynamics, CO_2 binding strength, and CO_2 locations within MIL-53 series MOFs using SSNMR experiments. Chapter 3 describes SSNMR studies about hydrogen dynamics within different MOFs by investigating ^{2}H SSNMR experiments. In Chapter 4, we tried to generate information about methane dynamics, methane binding strengths, and methane binding locations within different MOFs. Different techniques including SSNMR, SCXRD, and DFT calculations have been employed in this chapter. In Chapter 5, a series of new A520 MOFs have been reported. Structures and gas adsorption abilities of these newly reported MOFs have been comprehensively studied by using various techniques. Chapter 6 is focused on the characterization of MOFs using SSNMR. In Chapter 6, we used SSNMR to study the short-range structure of GaO_6 SBUs in guest-loaded Ga-MIL-53 by acquiring static $^{69/71}$Ga SSNMR spectra. Chapter 7 is the last chapter, which contains a summary of this thesis. Future works also have been given in Chapter 7.

1.5 References

1. James, S. L., *Chem. Soc. Rev.* **2003,** *32* (5), 276-288.

2. Rowsell, J. L. C.; Yaghi, O. M., *Microporous Mesoporous Mater.* **2004,** *73* (1-2), 3-14.

3. Zhou, H.-C.; Kitagawa, S., *Chem. Soc. Rev.* **2014,** *43* (16), 5415-5418.

4. Zhou, H.-C.; Long, J. R.; Yaghi, O. M., *Chem. Rev.* **2012,** *112* (2), 673-674.

5. Howarth, A. J.; Liu, Y. Y.; Li, P.; Li, Z. Y.; Wang, T. C.; Hupp, J.; Farha, O. K., *Nat. Rev. Mater.* **2016,** *1* (3), 15018.

6. Furukawa, H.; Cordova, K. E.; O'Keeffe, M.; Yaghi, O. M., *Science* **2013,** *341* (6149), 974.

7. Eddaoudi, M.; Kim, J.; Rosi, N.; Vodak, D.; Wachter, J.; O'Keeffe, M.; Yaghi, O. M., *Science* **2002,** *295* (5554), 469-472.

8. Wang, Z.; Cohen, S. M., *J. Am. Chem. Soc.* **2007,** *129* (41), 12368-12369.

9. Deng, H. X.; Doonan, C. J.; Furukawa, H.; Ferreira, R. B.; Towne, J.; Knobler, C. B.; Wang, B.; Yaghi, O. M., *Science* **2010,** *327* (5967), 846-850.

10. Li, B.; Wen, H.-M.; Zhou, W.; Chen, B., *J. Phys. Chem. Lett.* **2014,** *5* (20), 3468-3479.

11. Li, J.-R.; Kuppler, R. J.; Zhou, H.-C., *Chem. Soc. Rev.* **2009,** *38* (5), 1477-1504.

12. Ma, S.; Zhou, H.-C., *Chem. Commun.* **2010,** *46* (1), 44-53.

13. Furukawa, H.; Ko, N.; Go, Y. B.; Aratani, N.; Choi, S. B.; Choi, E.; Yazaydin, A. O.; Snurr, R. Q.; O'Keeffe, M.; Kim, J.; Yaghi, O. M., *Science* **2010,** *329* (5990), 424-428.

14. Carrington, E. J.; Vitorica-Yrezabal, I. J.; Brammer, L., *Acta Crystallogr. Sect. B-Struct. Sci.Cryst. Eng. Mat.* **2014,** *70*, 404-422.

15. Coudert, F.-X.; Fuchs, A. H., *Coord. Chem. Rev.* **2016,** *307, Part 2*, 211-236.

16. Zhang, Y.; Lucier, B. E. G.; Huang, Y. N., *Phys. Chem. Chem. Phys.* **2016,** *18* (12), 8327-8341.

17. Quadrelli, R.; Peterson, S., *Energy Policy* **2007,** *35* (11), 5938-5952.

18.https://www.netl.doe.gov/File%20Library/Research/Coal/carbon%20capture/Program-Plan-Carbon-Capture-2013.pdf.

19. Sumida, K.; Rogow, D. L.; Mason, J. A.; McDonald, T. M.; Bloch, E. D.; Herm, Z. R.; Bae, T.-H.; Long, J. R., *Chem. Rev.* **2012,** *112* (2), 724-781.

20. Liu, Y. Y.; Wang, Z. Y. U.; Zhou, H. C., *Greenhouse Gas. Sci. Technol.* **2012,** *2* (4), 239-259.

21. Zhang, Z.; Yao, Z.-Z.; Xiang, S.; Chen, B., *Energy Environ. Sci.* **2014,** *7* (9), 2868-2899.

22. Karra, J. R.; Walton, K. S., *J. Phys. Chem. C* **2010,** *114* (37), 15735-15740.

23. Stavitski, E.; Pidko, E. A.; Couck, S.; Remy, T.; Hensen, E. J. M.; Weckhuysen, B. M.; Denayer, J.; Gascon, J.; Kapteijn, F., *Langmuir* **2011,** *27* (7), 3970-3976.

24. Biswas, S.; Ahnfeldt, T.; Stock, N., *Inorg. Chem.* **2011,** *50* (19), 9518-9526.

25. Aprea, P.; Caputo, D.; Gargiulo, N.; Iucolano, F.; Pepe, F., *J. Chem. Eng. Data* **2010,** *55* (9), 3655-3661.

26. Wu, H.; Simmons, J. M.; Srinivas, G.; Zhou, W.; Yildirim, T., *J. Phys. Chem. Lett.* **2010,** *1* (13), 1946-1951.

27. Grajciar, L.; Wiersum, A. D.; Llewellyn, P. L.; Chang, J.-S.; Nachtigall, P., *J. Phys. Chem. C* **2011,** *115* (36), 17925-17933.

28. Bao, Z.; Yu, L.; Ren, Q.; Lu, X.; Deng, S., *J. Colloid. Interface Sci.* **2011,** *353* (2), 549-556.

29. Alternative Fuels Data Center, Fuel Properties Comparison, 2013, http://www.afdc.energy.gov/fuels/fuel_comparison_chart.pdf.

30. Alhasan, S.; Carriveau, R.; Ting, D. S. K., *Int. J. Environ. Stud.* **2016,** *73* (3), 343-356.

31. Makal, T. A.; Li, J.-R.; Lu, W.; Zhou, H.-C., *Chem. Soc. Rev.* **2012,** *41* (23), 7761-7779.

32. Mason, J. A.; Veenstra, M.; Long, J. R., *Chem. Sci.* **2014,** *5* (1), 32-51.

33. He, P.; Lucier, B. E. G.; Terskikh, V. V.; Shi, Q.; Dong, J.; Chu, Y.; Zheng, A.; Sutrisno, A.; Huang, Y., *J. Phys. Chem. C* **2014,** *118* (41), 23728-23744.

34. Li, B.; Wen, H.-M.; Zhou, W.; Xu, Jeff Q.; Chen, B., *Chem* **2016,** *1* (4), 557-580.

35. Peng, Y.; Krungleviciute, V.; Eryazici, I.; Hupp, J. T.; Farha, O. K.; Yildirim, T., *J. Am. Chem. Soc.* **2013,** *135* (32), 11887-11894.

36. He, Y.; Zhou, W.; Qian, G.; Chen, B., *Chem. Soc. Rev.* **2014,** *43* (16), 5657-5678.

37. Fu, J.; Tian, Y.; Wu, J. Z., *Adsorpt.-J. Int. Adsorpt. Soc.* **2015,** *21* (6-7), 499-507.

38. Konstas, K.; Osl, T.; Yang, Y.; Batten, M.; Burke, N.; Hill, A. J.; Hill, M. R., *J. Mater. Chem.* **2012,** *22* (33), 16698-16708.

39. Peng, Y.; Krungleviciute, V.; Eryazici, I.; Hupp, J. T.; Farha, O. K.; Yildirim, T., *J. Am. Chem. Soc.* **2013,** *135* (32), 11887-11894.

40. Wu, H.; Zhou, W.; Yildirim, T., *J. Am. Chem. Soc.* **2009,** *131* (13), 4995-5000.

41. Wilmer, C. E.; Leaf, M.; Lee, C. Y.; Farha, O. K.; Hauser, B. G.; Hupp, J. T.; Snurr, R. Q., *Nat. Chem.* **2012,** *4* (2), 83-89.

42. Mason, J. A.; Oktawiec, J.; Taylor, M. K.; Hudson, M. R.; Rodriguez, J.; Bachman, J. E.; Gonzalez, M. I.; Cervellino, A.; Guagliardi, A.; Brown, C. M.; Llewellyn, P. L.; Masciocchi, N.; Long, J. R., *Nature* **2015,** *527* (7578), 357-361.

43. Gándara, F.; Furukawa, H.; Lee, S.; Yaghi, O. M., *J. Am. Chem. Soc.* **2014,** *136* (14), 5271-5274.

44. van den Berg, A. W. C.; Arean, C. O., *Chem. Commun.* **2008,** (6), 668-681.

45. Sculley, J.; Yuan, D. Q.; Zhou, H. C., *Energy Environ. Sci.* **2011,** *4* (8), 2721-2735.

46. Durbin, D. J.; Malardier-Jugroot, C., *Int. J. Hydrogen Energy* **2013,** *38* (34), 14595-14617.

47. Suh, M. P.; Park, H. J.; Prasad, T. K.; Lim, D. W., *Chem. Rev.* **2012,** *112* (2), 782-835.

48. Jena, P., *J. Phys. Chem. Lett.* **2011,** *2* (3), 206-211.

49. Murray, L. J.; Dinca, M.; Long, J. R., *Chem. Soc. Rev.* **2009,** *38* (5), 1294-1314.

50. Langmi, H. W.; Ren, J.; North, B.; Mathe, M.; Bessarabov, D., *Electrochim. Acta* **2014,** *128*, 368-392.

51. Dinca, M.; Dailly, A.; Liu, Y.; Brown, C. M.; Neumann, D. A.; Long, J. R., *J. Am. Chem. Soc.* **2006,** *128* (51), 16876-16883.

52. Cheon, Y. E.; Suh, M. P., *Chem. Commun.* **2009,** (17), 2296-2298.

53. Kaye, S. S.; Dailly, A.; Yaghi, O. M.; Long, J. R., *J. Am. Chem. Soc.* **2007,** *129* (46), 14176-14177.

54. Gygi, D.; Bloch, E. D.; Mason, J. A.; Hudson, M. R.; Gonzalez, M. I.; Siegelman, R. L.; Darwish, T. A.; Queen, W. L.; Brown, C. M.; Long, J. R., *Chem. Mater.* **2016,** *28* (4), 1128-1138.

55. Van de Voorde, B.; Bueken, B.; Denayer, J.; De Vos, D., *Chem. Soc. Rev.* **2014,** *43* (16), 5766-5788.

56. Horcajada, P.; Chalati, T.; Serre, C.; Gillet, B.; Sebrie, C.; Baati, T.; Eubank, J. F.; Heurtaux, D.; Clayette, P.; Kreuz, C.; Chang, J.-S.; Hwang, Y. K.; Marsaud, V.; Bories, P.-N.; Cynober, L.; Gil, S.; Ferey, G.; Couvreur, P.; Gref, R., *Nat. Mater.* **2010,** *9* (2), 172-178.

57. Liu, J.; Chen, L.; Cui, H.; Zhang, J.; Zhang, L.; Su, C.-Y., *Chem. Soc. Rev.* **2014,** *43* (16), 6011-6061.

58. Ramaswamy, P.; Wong, N. E.; Shimizu, G. K. H., *Chem. Soc. Rev.* **2014,** *43* (16), 5913-5932.

59. Kreno, L. E.; Leong, K.; Farha, O. K.; Allendorf, M.; Van Duyne, R. P.; Hupp, J. T., *Chem. Rev.* **2012,** *112* (2), 1105-1125.

60. Serre, C.; Millange, F.; Thouvenot, C.; Nogues, M.; Marsolier, G.; Louer, D.; Ferey, G., *J. Am. Chem. Soc.* **2002,** *124* (45), 13519-13526.

61. Loiseau, T.; Serre, C.; Huguenard, C.; Fink, G.; Taulelle, F.; Henry, M.; Bataille, T.; Ferey, G., *Chem.-Eur. J.* **2004,** *10* (6), 1373-1382.

62. Vougo-Zanda, M.; Huang, J.; Anokhina, E.; Wang, X. Q.; Jacobson, A. J., *Inorg. Chem.* **2008,** *47* (24), 11535-11542.

63. Anokhina, E. V.; Vougo-Zanda, M.; Wang, X. Q.; Jacobson, A. J., *J. Am. Chem. Soc.* **2005,** *127* (43), 15000-15001.

64. Whitfield, T. R.; Wang, X. Q.; Liu, L. M.; Jacobson, A. J., *Solid State Sci.* **2005,** *7* (9), 1096-1103.

65. Mowat, J. P. S.; Seymour, V. R.; Griffin, J. M.; Thompson, S. P.; Slawin, A. M. Z.; Fairen-Jimenez, D.; Duren, T.; Ashbrook, S. E.; Wright, P. A., *Dalton Trans.* **2012,** *41* (14), 3937-3941.

66. Alvarez, E.; Guillou, N.; Martineau, C.; Bueken, B.; Van de Voorde, B.; Le Guillouzer, C.; Fabry, P.; Nouar, F.; Taulelle, F.; de Vos, D.; Chang, J.-S.; Cho, K. H.; Ramsahye, N.; Devic, T.; Daturi, M.; Maurin, G.; Serre, C., *Angew. Chem. Int. Ed.* **2015,** *54* (12), 3664-3668.

67. Rosi, N. L.; Kim, J.; Eddaoudi, M.; Chen, B.; O'Keeffe, M.; Yaghi, O. M., *J. Am. Chem. Soc.* **2005,** *127* (5), 1504-1518.

68. Dietzel, P. D. C.; Morita, Y.; Blom, R.; Fjellvåg, H., *Angew. Chem. Int. Ed.* **2005,** *44* (39), 6354-6358.

69. Bhattacharjee, S.; Choi, J. S.; Yang, S. T.; Choi, S. B.; Kim, J.; Ahn, W. S., *J. Nanosci. Nanotechnol.* **2010,** *10* (1), 135-141.

70. Dietzel, P. D. C.; Panella, B.; Hirscher, M.; Blom, R.; Fjellvag, H., *Chem. Commun.* **2006,** (9), 959-961.

71. Zhou, W.; Wu, H.; Yildirim, T., *J. Am. Chem. Soc.* **2008,** *130* (46), 15268-15269.

72. Dietzel, P. D. C.; Blom, R.; Fjellvåg, H., *Eur. J. Inorg. Chem.* **2008,** *2008* (23), 3624-3632.

73. Sanz, R.; Martinez, F.; Orcajo, G.; Wojtas, L.; Briones, D., *Dalton Trans.* **2013,** *42* (7), 2392-2398.

74. Díaz-García, M.; Sánchez-Sánchez, M., *Microporous Mesoporous Mater.* **2014,** *190*, 248-254.

75. Rood, J. A.; Noll, B. C.; Henderson, K. W., *Inorg. Chem.* **2006,** *45* (14), 5521-5528.

76. Wang, Z.; Zhang, Y.; Kurmoo, M.; Liu, T.; Vilminot, S.; Zhao, B.; Gao, S., *Aust. J. Chem.* **2006,** *59* (9), 617-628.

77. Nugent, P.; Belmabkhout, Y.; Burd, S. D.; Cairns, A. J.; Luebke, R.; Forrest, K.; Pham, T.; Ma, S.; Space, B.; Wojtas, L.; Eddaoudi, M.; Zaworotko, M. J., *Nature* **2013,** *495* (7439), 80-84.

78. Levitt, M. H., *Spin Dynamics*. Second ed., John Wiley & Sons West Sussex, 2008.

79. Duer, M. J., *Solid-State NMR Spectroscopy: Principles and Applications*. Blackwell Science, Oxford, 2002.

80. K. J. D. Mackenzie, M. E. S., *Multinuclear Solid-State NMR of Inorganic Materials*. Elsevier Science, Oxford, 2002.

81. Keeler, J., *Understanding NMR Spectroscopy*. Second ed., John Wiley & Sons, West Sussex, 2010.

82. Nelson, J. H., *Nuclear Magnetic Resonance Spectroscopy*. Pearson Education, Upper Saddle River, 2003.

83. Cohen, M. H.; Reif, F., *Solid State Phys.* **1957,** *5*, 321-438.

84. Pake, G. E., *J. Chem. Phys.* **1948,** *16* (4), 327-336.

85. Bakhmutov, V. I., *Solid-State NMR in Materials Science Principles and Applications*. Taylor & Francus Group, Boca Raton, 2012.

86. Casabianca, L. B.; Dios, A. C. d., *J. Chem. Phys.* **2008,** *128* (5), 052201.

87. Robin Bendall, M.; Gordon, R. E., *J. Magn. Reson.* **1983,** *53* (3), 365-385.

88. Cory, D. G.; Ritchey, W. M., *J. Magn. Reson.* **1988,** *80* (1), 128-132.

89. Hartmann, S. R.; Hahn, E. L., *Phys. Rev.* **1962,** *128* (5), 2042-2053.

90. Pines, A.; Gibby, M. G.; Waugh, J. S., *J. Chem. Phys.* **1973,** *59* (2), 569-590.

91. Levitt, M. H.; Suter, D.; Ernst, R. R., *J. Chem. Phys.* **1986,** *84* (8), 4243-4255.

92. Kupce, E.; Freeman, R., *J. Magn. Reson., Ser. A* **1995,** *115* (2), 273-276.

93. O'Dell, L. A., *Solid State Nucl. Magn. Reson.* **2013,** *55-56*, 28-41.

94. Larsen, F. H.; Jakobsen, H. J.; Ellis, P. D.; Nielsen, N. C., *J. Phys. Chem. A* **1997,** *101* (46), 8597-8606.

95. Lipton, A. S.; Sears, J. A.; Ellis, P. D., *J. Magn. Reson.* **2001,** *151* (1), 48-59.

96. Siegel, R.; Nakashima, T. T.; Wasylishen, R. E., *J. Phys. Chem. B* **2004,** *108* (7), 2218-2226.

97. Segall, M. D.; Lindan, P. J. D.; Probert, M. J.; Pickard, C. J.; Hasnip, P. J.; Clark, S. J.; Payne, M. C., *J. Phys.:Condens. Matter* **2002,** *14* (11), 2717-2744.

98. Clark, S. J.; Segall, M. D.; Pickard, C. J.; Hasnip, P. J.; Probert, M. J.; Refson, K.; Payne, M. C., *Z. Kristall.* **2005,** *220* (5-6), 567-570.

99. Pickard, C. J.; Mauri, F., *Phys. Rev. B* **2001,** *63* (24).

100. Yates, J. R.; Pickard, C. J.; Mauri, F., *Phys. Rev. B* **2007,** *76* (2).

101. Perdew, J. P.; Burke, K.; Ernzerhof, M., *Phys. Rev. Lett.* **1996,** *77* (18), 3865-3868.

102. Tycko, R., *Nuclear Magnetic Resonance Probes of Molecular Dynamics*. Kluwer Academic, Netherlands, 1994.

103. Vold, R. L.; Hoatson, G. L., *J. Magn. Reson.* **2009,** *198* (1), 57-72.

104. Kong, X.; Scott, E.; Ding, W.; Mason, J. A.; Long, J. R.; Reimer, J. A., *J. Am. Chem. Soc.* **2012,** *134* (35), 14341-14344.

105. Lin, L.; Kim, J.; Kong, X.; Scott, E.; McDonald, T. M.; Long, J. R.; Reimer, J. A.; Smit, B., *Angew. Chem. Int. Ed.* **2013,** *52* (16), 4410-4413.

106. Lu, Y.; Lucier, B. E. G.; Zhang, Y.; Ren, P.; Zheng, A.; Huang, Y., *Phys. Chem. Chem. Phys.* **2017,** *19* (8), 6130-6141.

107. Pyykkö, P., *Mol. Phys.* **2008,** *106* (16-18), 1965-1974.

108. Snyder, L. C., *J. Chem. Phys.* **1978,** *68* (1), 291-294.

109. Code, R. F.; Ramsey, N. F., *Phys. Rev. A* **1971,** *4* (5), 1945-1959.

Chapter 2

2 Deducing CO_2 Motion, Adsorption Locations and Binding Strengths in a Flexible Metal-Organic Framework without Open Metal Sites

Microporous metal-organic frameworks (MOFs) have high surface areas and porosities, and are well-suited for CO_2 capture. MIL-53 features corner-sharing $MO_4(OH)_2$ (M = Al, Ga, Cr, etc.) octahedra interconnected by benzenedicarboxylate linkers that form one-dimensional rhombic tunnels, and exhibits an excellent adsorption ability for guest molecules such as CO_2. Studying the behavior of adsorbed CO_2 in MIL-53 via solid-state NMR (SSNMR) provides rich information on the dynamic motion of guest molecules as well as their binding strengths to the MOF host, and sheds light on the specific guest adsorption mechanisms. Variable-temperature ^{13}C SSNMR spectra of $^{13}CO_2$ adsorbed within various forms of MIL-53 are acquired and analyzed. CO_2 undergoes a combination of two motions within MIL-53; we report the type of motions present, their rates, and rotational angles. ^{1}H-^{13}C CP SSNMR experiments are used to examine the proximity of ^{1}H atoms in the MOF to ^{13}C atoms in CO_2 guests. By replacing ^{1}H for ^{2}H in MIL-53, the location of the CO_2 adsorption site in MIL-53 is experimentally confirmed by ^{1}H-^{13}C CP SSNMR. The binding strength of CO_2 within these MIL-53 MOFs follows the order MIL-53-NH_2 (Al) > MIL-53-NH_2 (Ga) > MIL-53 (Al) > MIL-53 (Ga).

2.1 Introduction

CO_2 emissions have increased dramatically in the past century due to the use of hydrocarbon fuels,[1] and accordingly, global warming has become a critical environmental issue. The development and use of specific materials for CO_2 capture and storage is a promising avenue for slowing or stopping global warming.[2-3] Metal-organic frameworks (MOFs)[4-8] have great potential for CO_2 capture due to their high gas adsorption capacities and ability to selectively adsorb CO_2 from mixtures of different gases.[2, 9-10] CO_2 capture in MOFs with coordinatively unsaturated open metal sites (*e.g.*, Mg-MOF-74/CPO-27-Mg) have been studied extensively using experimental[11-15] and computational[14-17] methods, however, MOFs without open metal sites have also demonstrated high CO_2 affinities when basic nitrogen-containing organic groups (*e.g.* $–NH_2$)[18-22] or polarizing functional organic groups (*e.g.* –F, -Br, -Cl, -OH, -CN, $-NO_2$).[18, 21, 23-25] are incorporated into the linkers.

The MIL-53[26] (MIL= Materials of the Institute Lavoisier) series of MOFs has demonstrated the ability to adsorb CO_2 in significant quantities.[22, 27-30] The framework contains octahedral $MO_4(OH)_2$ (M= Al,[31] Cr,[26] Fe,[32] Ga,[33] In,[34] Sc[35]) secondary building units (SBUs) (Figure 2-1(a)), which are composed of a metal centre connected to four oxygen atoms from four different benzenedicarboxylate (BDC) ligands and two bridging hydroxyl oxygen atoms. These hydroxyl oxygen atoms link the SBUs *via* corner-sharing to form an infinite chain along the crystallographic *c*-axis (Figure 2-1(b)), and the chains are interconnected by BDC linkers to create one-dimensional rhombic channels (Figure 2-1(c)). It should be noted that the expensive nature of Ga, In and Sc metals render these variants of MIL-53 less practical alternatives in the context of using very large quantitiesof MOFs for CO_2 capture.

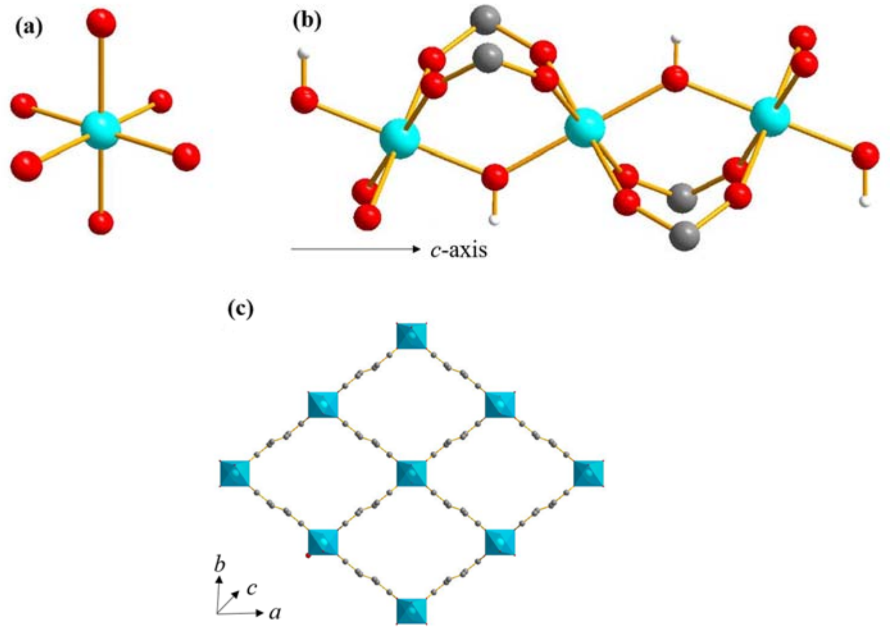

Figure 2-1. The octahedral $MO_4(OH)_2$ secondary building unit (SBU) of the MIL-53 MOF is shown in (a). The chain formed by the SBUs along the crystallographic *c* axis is shown in (b); these chains are interconnected by benzenedicarboxylate (BDC) linkers to create the one-dimensional rhombic channels, as shown in (c). The colors red, grey, white and blue correspond to oxygen, carbon, hydrogen and the metal centre, respectively.

MIL-53 exhibits the ability to reversibly change phase and pore size in response to stimuli in a process known as the "breathing effect."[26] The magnitude of the breathing effect depends on the nature of metal centre, functionalization of bridging ligands, external applied pressure, presence of guest molecules, and temperature.[36-39] Within as-made MIL-53 (MIL-53(*as*)), the rhombic pores measure *ca*. 12 x 17 Å[31] and are occupied by excess BDC linkers from the MOF synthesis. At high temperature, the surplus BDC ligand is purged from the MOF channels to generate the high temperature phase MIL-53(*ht*), which has empty *ca*. 13 x 16 Å pores.[31] MIL-53(*ht*) readily adsorbs water from air at room temperature to form the low temperature phase MIL-53(*lt*), which features narrow *ca*. 7 x

19 Å pores.[31] The *lt-ht* phase transformation leads to an increase in unit cell volume of up to ca. 40%.[39]

MIL-53 exhibits an excellent affinity for CO_2. At 25 bar of pressure and a temperature of 304 K, MIL-53 (Al)(*ht*) can adsorb 30.6 wt% of CO_2, while at 1 bar and 298 K, MIL-53 (Al) can capture 10 wt% of CO_2.[30] Amino functionalized MIL-53 (NH_2-MIL-53(Al)) has also demonstrated significant CO_2 adsorption capacities. At 1 bar and 298 K, NH_2-MIL-53(Al) can capture 12 wt% of CO_2,[29] while at 30 bar, it can adsorb 30 wt% of CO_2.[22] Prior computational studies have indicated the hydroxyl groups participating in the metal-oxygen-metal bond between SBUs are CO_2 adsorption sites in MIL-53.[28] With regards to the $–NH_2$ functional group, computational studies have indicated that there is no direct interaction of CO_2 and amine groups in NH_2-MIL-53,[27] however, the presence of amine groups on the framework linkers may influence the acidity of the bridging OH groups, and thus indirectly improve the adsorption ability.[27]

Solid-state NMR (SSNMR) provides detailed information on the short-range structural, magnetic, and electronic environment about a target nucleus. In the solid state, anisotropic (i.e., directionally-dependent) NMR interactions give rise to broad powder patterns of low signal-to-noise ratio (S/N), rather than the sharp resonances observed in solution NMR. These broad SSNMR spectra are often challenging to acquire, they contain rich information about the local environment and dynamics around the nucleus that may be unavailable from other characterization methods. SSNMR is often used in concert with complementary techniques such as powder X-ray diffraction (pXRD) to explore both the long- and short-range structure within a sample.[40-41]

SSNMR has been employed for a multitude of purposes with respect to MOFs,[42-46] such as probing guest adsorption,[47-49] monitoring phase transformations,[50] determining the number and nature of non-equivalent atomic sites,[51] and examining the local environment of metal centres.[52-53] CO_2 adsorbed in MOFs has recently been investigated via ^{13}C and ^{17}O SSNMR experiments,[45, 54-58] however, the dynamics of CO_2 within MOFs without open metal sites are not well-understood.[45, 58]

In this study, variable-temperature (VT) direct excitation ^{13}C and ^{1}H-^{13}C cross-polarization (CP) SSNMR experiments on $^{13}CO_2$-loaded MIL-53 (Al), MIL-53-NH_2 (Al), MIL-53 (Ga) and MIL-53-NH_2 (Ga) are used to investigate the dynamics of adsorbed CO_2 influenced by the metal centre and functionalized amino groups. Static ^{13}C SSNMR spectra reveal that two distinct CO_2 motional modes are present within these MOFs. ^{1}H-^{13}C CP SSNMR experiments on deuterium exchanged, $^{13}CO_2$-loaded MIL-53 samples are also employed to probe the specific location of CO_2 adsorption sites in this MOF. We now briefly explain our experimental approach and provide the fundamental basis as to why this approach provides unequivocal information about CO_2 dynamics and adsorption sites in MOFs.

The ^{13}C chemical shift is a local molecular property that is primarily dependent on the electron distribution in the CO_2 molecule, and can be modeled by a tensor with three perpendicular components (*vide infra*). The axial symmetry of the CO_2 molecule dictates that the one component of the CS tensor is directed along the O-C-O axis, while the other two components lie in the plane perpendicular to the O-C-O axis and pass through the ^{13}C nucleus. SSNMR experiments yield the magnitudes of each component of the chemical shift tensor and, by extension, richly illustrate the local environment about ^{13}C. In the context of CO_2 adsorption in MOFs, stationary CO_2 corresponds to a quantitatively predictable ^{13}C NMR lineshape with intensities in accordance with the distribution of CO_2 orientations in the polycrystalline sample. Any systematic, non-random dynamic motion of CO_2 about the molecular axis results in a quantitatively predictable averaging of the tensor components; even when two or more types of motions are simultaneously in play, the quantitative nature of the correspondence between the CO_2 motions and the resulting ^{13}C NMR lineshape is preserved.

Calculations to model the effect of dynamic motion on the NMR lineshape are well-known to the NMR community and conveniently performed using the EXPRESS software.[59] In this manner, determination of many specific details regarding the types and rates of CO_2 motion about the adsorption sites in MIL-53 is possible. We can also test the assumption that the CO_2 adsorption site in MIL-53 is specifically located at the bridging -OH group connecting the SBUs, by using a CP NMR experiment that relies on the proximity of ^1H nuclei in the framework and ^{13}C nuclei in adsorbed CO_2. This test involves replacing the ^1H nuclei of the bridging –OH groups with ^2H nuclei through deuteration in the MOF synthesis; the presence or lack of signal in ^1H-^{13}C CP NMR spectra will prove if the adsorption site for CO_2 is indeed close to the ^1H position on the bridging –OH groups.

2.2 Experimental Section

2.2.1 MOF synthesis

All chemicals were obtained from Sigma-Aldrich, and were used without further purification. MIL-53 (Al), NH_2-MIL-53 (Al), and MIL-53 (Ga) were synthesized using methods described in prior works (see Appendix A),[22, 31, 39] however, to the best of our knowledge, we are reporting the first hydrothermal synthesis of NH_2-MIL-53 (Ga).

NH_2-MIL-53 (Ga): $Ga(NO_3)_3 \cdot xH_2O$ (1.35 g, 5.30 mmol), 2-aminobenzene-1,4-dicarboxylic acid (1.50 g, 8.30 mmol) and 20 mL deionized H_2O were mixed into a 23 mL Teflon-lined stainless steel autoclave and heated at 150 °C for 3 days. The yellow powdered product was washed three times with deionized water and dried using vacuum filtration.

2.2.2 Sample activation

The activation process of MIL-53(*as*) consisted of first exchanging the trapped BDC organic linker with *N,N*-dimethylformamide (DMF) at high temperature in an autoclave overnight (*i.e.*, ≥ 12 h). For activation of MIL-53 (Al) and NH_2-MIL-53 (Al), 0.5 g of the as-made product and 10 mL of DMF were placed into a 23 mL Teflon-lined stainless steel autoclave and heated at 423 K. The DMF exchange of MIL-53 (Ga) and NH_2-MIL-53 (Ga) employed a heating temperature of 473 K. Following exchange of the BDC organic linker for DMF, all MOFs were heated at 473 K under dynamic vacuum (≤ 1 mbar) for 8 h to remove DMF molecules in the channels, yielding MIL-53(*ht*). In ambient conditions, MIL-53(*ht*) rapidly adsorbs water from the air to form MIL-53(*lt*).

2.2.3 Gas adsorption

A Schlenk line was used for gas adsorption experiments. The MIL-53(*lt*) sample was loaded into the bottom of a homemade 5 mm L-shaped glass tube. A thin layer of glass wool was used to secure the sample in place. The glass tube was attached to the Schlenk line and heated at 473 K for 8 h under dynamic vacuum to remove water from the MOF pores before gas loading. A known amount of pressurized $^{13}CO_2$ was then introduced to the vacuum line, and the CO_2 was allowed to occupy both the vacuum line and the glass tube containing the sample (82.7 cm^3). The bottom of the CO_2-filled glass tube was immersed in liquid nitrogen to freeze CO_2 within the sample, and the glass tube was then flame-sealed from the Schlenk line. The overall CO_2 loading amount is expressed by the molar ratio between CO_2 and the metal. In this study, 0.2 CO_2/metal samples were prepared and characterized by SSNMR. Previous studies have shown that the maximum CO_2 loading amount in narrow-pore MIL-53 (Al) and NH_2-MIL-53 (Al, Ga) is ca. 0.5 CO_2/metal at 273 K,[30, 60] while our measured CO_2 adsorption isotherm (Appendix, Figure 2-A3) indicates that the maximum amount of CO_2 that can be loaded in the narrow pore phase of MIL-53 (Ga) at 273 K is approximately 0.39 CO_2/metal. In that sense, this study employs a CO_2 loading level that is 40 % of the maximum loading possible in narrow-pore MIL-53(Al) and NH_2-MIL-53 (Al, Ga), and ca. 50 % of the maximum CO_2 capacity in narrow-pore MIL-53(Ga).

In the conditions employed in this study, all MIL-53 variants are expected to reside in the narrow-pore phase, as has been observed for both MIL-53-Al[30] and MIL-53-Sc[61] at the loading level of 0.2 CO_2/M. The study on MIL-53-Sc further explored changes in pore size associated with CO_2 loading, and found only a slight increase in pore size from 7.95 Å to 8.14 Å as the CO_2 loading level increased from 0.45 CO_2/M to 0.67 CO_2/M;[61] this ca. 2% difference in pore size with a ca. 50 % increase in CO_2 loading means that any pore distortions or expansion associated with our loading level of 0.20 CO_2/M are undoubtedly minor and should have a negligible effect on CO_2 dynamics in MIL-53 (Al, Ga). Our CO_2 adsorption isotherm of narrow-pore Ga-MIL-53 (Figure 2-A3) also does not exhibit any evidence that a phase change from the narrow-pore phase or significant pore expansion has occurred when the pressure is lower than 1 bar.

2.2.4 Deuterium exchange in MIL-53

0.1g MIL-53(*lt*) was immersed in 2 mL D_2O within a homemade 5 mm L-shaped glass tube for two days. During the exchange process, the glass tube was sealed with parafilm. The D_2O was extracted and replaced three times per day to ensure thorough deuteration of the sample. After D_2O exchange, the sample was activated and loaded with CO_2.

2.2.5 Powder X-ray diffraction

All pXRD patterns were acquired using an Inel CPS Powder Diffractometer operating with Cu Kα radiation. Reflections were collected at 2θ values between 5 and 120 degrees. All pXRD patterns are depicted in Figure 2-A1 of the Appendix.

2.2.6 Solid-state NMR and DEPTH-echo pulse sequence.

SSNMR experiments were carried out on a Varian Infinity Plus spectrometer operating at a magnetic field of 9.4 T ($\nu_0(^{13}C)$ = 100.6 MHz) using a Varian/Chemagnetics 5 mm HX static probe. A Varian VT temperature control unit was used to adjust the temperature from 153 K to 393 K. Temperatures were measured to ± 2 K and calibrated using the ^{207}Pb chemical shift of $Pb(NO_3)_2$ (s) across the experimental temperature range.[62] All SSNMR spectra were acquired using the DEPTH-echo pulse sequence, which is the combination of both the DEPTH[63] and Hahn-echo pulse sequences. We have found that combining both the DEPTH and Hahn-echo features results in enhanced background signal suppression versus either individual pulse sequence in identical experimental times, especially when broad ^{13}C resonances are involved (Figure 2-A2 of the Appendix).

A ^{13}C 90 $^{\circ}$ pulse length of 3.1 μs was employed for DEPTH-echo SSNMR experiments. The optimized ^{13}C pulse delays between scans were 7.5 s for MIL-53 (Al) and NH_2-MIL-53 (Al), and were 7 s for MIL-53 (Ga) and NH_2-MIL-53 (Ga). When the temperature was below 193 K, the optimized ^{13}C pulse delays of all sampless increased to 15 s. All spectra were acquired using a ^{1}H decoupling field of 81 kHz. For ^{1}H-^{13}C CP experiments, spectra with moderate (5 ms) and short (0.5 ms) contact times (CT) were acquired at temperatures of 173 K and 293 K. In the case of deuterium exchanged samples, only a CT of 5 ms was employed, since this allowed for observation of all resonances in ^{13}C powder patterns of all samples prior to deuterium exchange (*vide infra*, Results and Discussion). For deuterium exchanged MIL-53 (Al) and MIL-53 (Ga), the ^{1}H-^{13}C CP spectra were only collected at 173 K, because the ^{13}C SSNMR resonance corresponding to CO_2 component can only be observed at 173 K in the non-exchanged samples (*vide infra*), For deuterium exchanged NH_2-MIL-53 (Al) and NH_2-MIL-53 (Ga), the ^{1}H-^{13}C CP spectra were collected at both 173 K and 293 K, since the ^{13}C resonance corresponding to CO_2 can be observed at these two temperatures. ^{13}C SSNMR spectra were referenced to the resonance of methylene carbon in ethanol, which is located at ca. 58.05 ppm from TMS (tetramethylsilane).[64] The WSolids[65] computer software was used to obtain observed (i.e., apparent) NMR parameters, while the EXPRESS[59] software was used to simulate the effects of CO_2 dynamics on ^{13}C SSNMR powder patterns and extract motional information.

The chemical shift (CS) interaction can be modeled by a tensor defined by three orthogonal components, δ_{11}, δ_{22}, and δ_{33}, which are ordered such that $\delta_{11} \geq \delta_{22} \geq \delta_{33}$. The isotropic chemical shift, δ_{iso}, is defined as $\delta_{iso} = (\delta_{11} + \delta_{22} + \delta_{33})/3$. The span of the CS tensor, Ω, describes the breadth of the powder pattern, and is the difference between the largest and smallest components of the CS tensor, $\Omega = \delta_{11} - \delta_{33}$. The skew of the CS tensor, κ, is defined as $\kappa = 3(\delta_{22} - \delta_{iso})/\Omega$. Values for κ range from -1 to $+1$, with either limit representing an axially symmetric CS tensor.

2.3 Results and Discussion

In this section, we present NMR results for CO_2 adsorbed in various MOFs, and analyze the ^{13}C SSNMR spectra in order to identify and understand the motional modes of CO_2. For readers who are not familiar with NMR and uninterested in specific details, a brief summary of our findings in plain language is listed at the beginning of this section.

2.3.1 Non-technical summary

The motion of CO_2 guests adsorbed within the MIL-53 (Al, Ga) and MIL-53-NH_2

(Al, Ga) series of MOFs has been investigated. In MIL-53, CO_2 simultaneously undergoes both a localized wobbling about the adsorption site, as well as a non-localized twofold hopping between the two equivalent adsorption sites. The wobbling and hopping motions occur through specific angles that depend on the metal centre and functional groups incorporated in MIL-53. The wobbling and hopping angles in MIL-53-NH_2 are relatively small, indicating that –NH_2 functionalization of the linkers is associated with tighter, stronger binding of guest CO_2 molecules. The presence of Ga in MIL-53 is associated with larger CO_2 wobbling and hopping motional angles versus Al-based MIL-53, clearly demonstrating that the metal centre has a strong influence on binding ability. The CO_2 binding strength in this series of MOFs is summarized as follows: MIL-53-NH_2 (Al) > MIL-53-NH_2 (Ga) > MIL-53 (Al) > MIL-53 (Ga). The wobbling and hopping angles of CO_2 fall as temperature decreases. From the trend illustrated in Figure 2-8, the wobbling and hopping angles will approach zero as the temperature drops to absolute zero (0 K). This is in good agreement with expectations from the crystal structure: when hopping is halted or frozen out, the occupancies of the two equivalent CO_2 adsorption sites would be 0.5. Our experiments unambiguously confirm that the CO_2 adsorption sites in MIL-53 are located on the bridging –OH groups linking MO_6 (M = Al, Ga) octahedra, in good agreement with predictions from previous computational studies.

2.3.2 Examining the dynamics of CO_2 within MIL-53 MOFs

The static ^{13}C SSNMR spectra of CO_2 adsorbed in MIL-53 (Al) at temperatures ranging from 153 K to 373 K (Figure 2-2(a)) feature a broad powder pattern corresponding to adsorbed CO_2, which exhibits a temperature-dependent lineshape. The strong adsorption interaction between CO_2 and MIL-53 (Al) is reflected in the breadth of these chemical shift anisotropy (CSA) dominated powder patterns. Temperature-induced changes in the width and shape of the ^{13}C resonance are linked to the motion of adsorbed CO_2 within the MOF (*vide infra*).[55, 57] At high temperatures (*i.e.*, 313 to 353 K), a sharp resonance at ca. 125 ppm is also apparent; this signal is associated with unadsorbed CO_2, which has fast dynamics or has fast exchange with CO_2 inside the pore,[57] and is the only observed resonance at temperature at temperatures above 353 K.

The observed CS parameters of CO_2 in MIL-53 (Al) are summarized in Table 2-1. The apparent span (Ω) gradually decreases from 296(4) ppm to 223(1) ppm as the temperature increases from 153 K to 353 K. The observed skew (κ) also decreases from 0.99(1) to 0.60(1) as the temperature rises from 153 K to 353 K. With respect to the CS parameters of rigid CO_2 ($\Omega = 335$ ppm, $\kappa = 1$),[66] the observation of smaller ^{13}C Ω values indicates that CO_2 within MIL-53 (Al) has increased motion at high temperatures, while the temperature-dependent κ values also confirm the presence of dynamic motion on the NMR timescale. Motionally-averaged NMR spectra may be simulated by the EXPRESS software,[59] which models the effect of dynamic motion on NMR interactions and corresponding spectra. The EXPRESS-simulated ^{13}C SSNMR powder patterns of CO_2 within MIL-53 (Al) are shown in Figure 2-2(b), and were obtained under the fast motion limit (*i.e.*, motional rates of $\geq 10^9$ Hz). The simulated powder patterns reveal that two types of dynamic CO_2 motions occur in this system: a six-fold (C_6) rotation and a two-fold (C_2) rotation. The C_6 rotation angle (α) varies from 12 ° at 153 K to 21 ° at 353 K, while the C_2 rotation angle (β) varies from 12 ° to 24 ° across the same temperature range. We propose that the C_6 rotation describes the localized wobbling of CO_2 molecules about the bridging hydroxyl group in MIL-53 (Figure 2-3(a)), while the C_2 rotation describes the non-localized hopping of CO_2 between two separate bridging hydroxyl sites (Figure 2-3(b) and (c)).

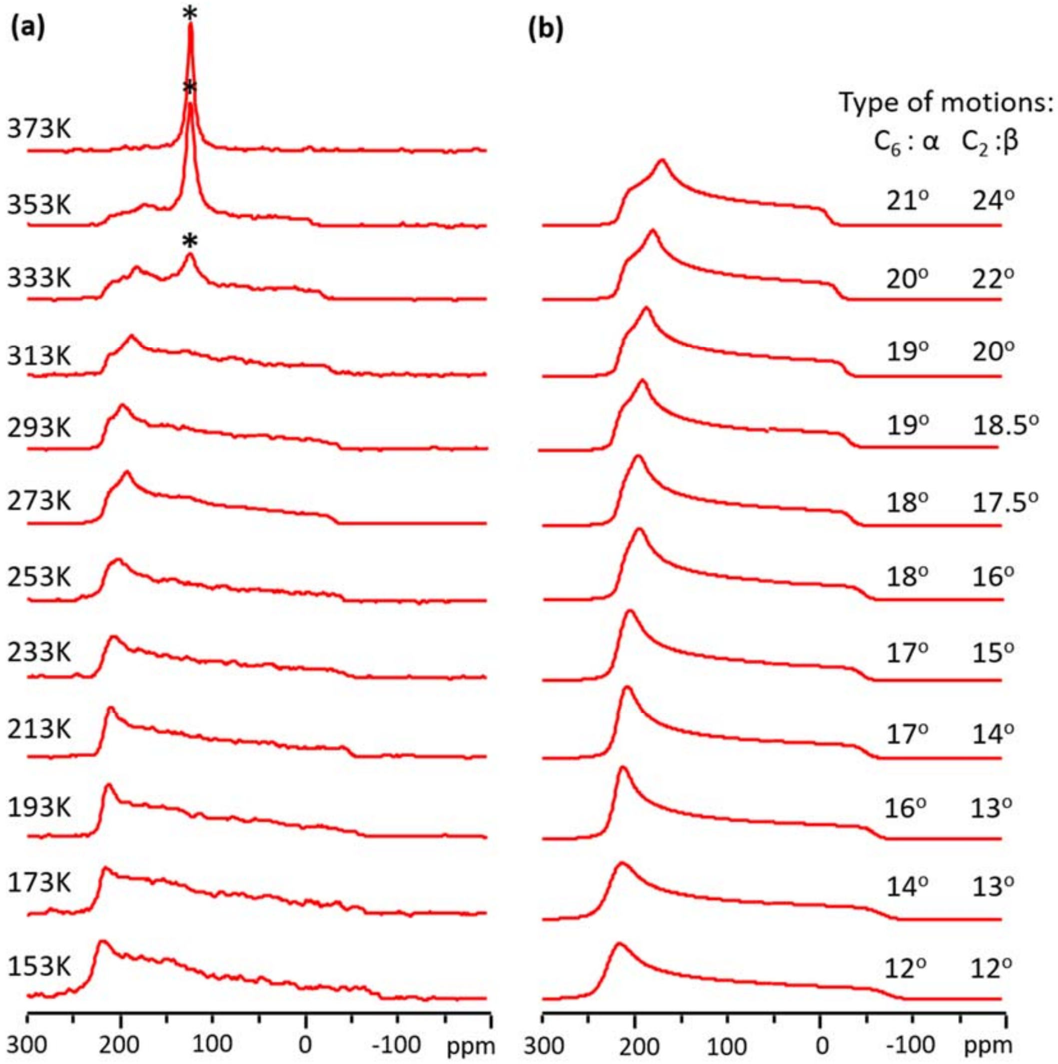

Figure 2-2. The experimental and simulated static ^{13}C SSNMR spectra of adsorbed CO_2 within MIL-53 (Al) are shown in (a) and (b) respectively. The simulated powder patterns were generated using the EXPRESS software and a fast rate of motion (10^9 Hz) for both dynamic modes. The C_6 motion (six-fold rotation) and accompanying angle α describe the localized wobbling of CO_2 about the adsorption site (see Figure 2-3(a)), while the C_2 motion and β refer to a non-localized two-fold hopping between two adsorption sites (see Figure 2-3(b) and (c)). The asterisk (*) denotes a sharp resonance at high temperature that corresponds to gaseous, unbound CO_2.

Table 2-1. The observed, or apparent, ^{13}C CS parameters of CO_2 adsorbed within MIL-53, as obtained from analytical simulations of static ^{13}C DEPTH-echo variable temperature SSNMR spectra.[a]

T	MIL-53 (Al)			MIL-53 (Ga)			NH_2-MIL-53 (Al)			NH_2-MIL-53 (Ga)		
	δ_{iso} (ppm)[b]	Ω (ppm)[c]	κ[d]	δ_{iso} (ppm)	Ω (ppm)	κ	δ_{iso} (ppm)	Ω (ppm)	κ	δ_{iso} (ppm)	Ω (ppm)	κ
393 K				124(1)	191(1)	0.34(1)	124(1)	238(1)	0.76(1)	122(1)	230(1)	0.70(1)
373 K				125(1)	191(1)	0.35(1)	125(1)	251(1)	0.79(1)	123(1)	230(1)	0.72(1)
353 K	125(1)	223(1)	0.60(1)	125(1)	194(1)	0.39(1)	125(1)	250(1)	0.80(1)	127(1)	236(1)	0.74(1)
333 K	125(1)	234(2)	0.70(1)	124(1)	198(2)	0.41(1)	124(1)	257(2)	0.84(1)	126(1)	239(1)	0.75(1)
313 K	125(1)	243(2)	0.76(1)	124(1)	201(2)	0.46(1)	124(2)	259(2)	0.87(1)	125(1)	239(2)	0.77(1)
293 K	126(1)	246(2)	0.78(1)	123(1)	204(2)	0.51(1)	123(2)	266(2)	0.90(1)	123(1)	247(2)	0.80(1)
273 K	126(1)	250(2)	0.83(1)	124(2)	208(2)	0.57(1)	123(2)	268(3)	0.92(1)	127(1)	248(2)	0.82(1)
253 K	126(1)	258(2)	0.86(1)	125(2)	218(2)	0.61(1)	122(2)	275(3)	0.94(1)	126(1)	254(2)	0.84(1)
233 K	126(1)	263(3)	0.90(1)	125(2)	228(3)	0.66(1)	122(2)	277(3)	0.97(1)	126(2)	261(2)	0.87(1)
213 K	126(2)	266(3)	0.94(1)	125(2)	236(3)	0.73(1)	123(3)	277(3)	0.99(1)	127(1)	264(3)	0.90(1)
193 K	126(2)	278(3)	0.96(1)	125(2)	247(3)	0.79(1)	120(3)	297(4)	1.00(1)	124(2)	274(3)	0.92(2)
173 K	126(2)	287(4)	0.98(1)	125(2)	256(3)	0.86(2)	122(3)	299(4)	1.00(1)	125(2)	282(3)	0.94(2)
153 K	125(2)	296(4)	0.99(1)	125(2)	267(4)	0.90(2)	124(3)	309(4)	1.00(1)	125(2)	289(3)	0.97(2)

[a]The uncertainties in δ_{iso}, Ω, and κ were measured from experimental spectra and corresponding simulations. [b]Isotropic chemical shift: $\delta_{iso} = (\delta_{11} + \delta_{22} + \delta_{33})/3$. [c]Span: $\Omega = \delta_{11} - \delta_{33}$. [d]Skew: $\kappa = 3(\delta_{22} - \delta_{iso})/\Omega$

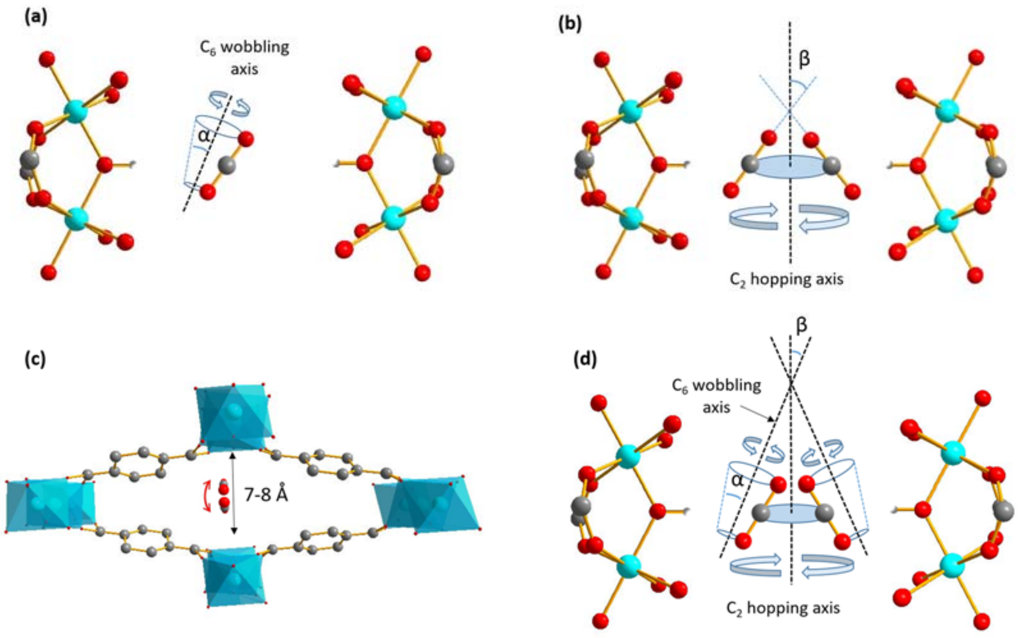

Figure 2-3. The localized C_6 rotation, or wobbling, of CO_2 with a rotation angle α is shown in (a). An illustration of how CO_2 hops between the closest two adsorption sites with the hopping angle β between the longitudinal axis of CO_2 and the C_2 rotation axis is provided in (b). A schematic of how illustrates how CO_2 hops between the closest two adsorption sites in the *xy* plane in MIL-53 is shown in (c). The combination of wobbling (C_6 rotation, α) and two-site hopping (C_2 rotation, β) is depicted in (d). The colors red, grey, white and blue correspond to oxygen, carbon, hydrogen and the metal centre.

CO_2 wobbles through an angle α between the longitudinal axis of CO_2 and the wobbling axis (Figure 2-3(a)). CO_2 hops along both the circumference of the channel in the *xy* plane (Figure 2-3(c)) and along the length of the channel in the *z* direction. Previous computational studies have postulated that CO_2 molecules within MIL-53 and NH_2-MIL-53 interact with the bridging -OH groups of the SBUs at opposite sides of the channel.[27-28] Our data experimentally confirms that CO_2 hops across the channel, alternating between two opposite CO_2 adsorption sites about an angle β between the longitudinal axis of CO_2 and the C_2 rotation axis (Figure 2-3(b)). This type of hopping in the *xy* plane causes a reorientation of the ^{13}C CS tensor with respect to the molecule, influencing ^{13}C NMR powder patterns. In contrast, CO_2 hopping along the *z* direction is a translational motion that does not change the orientation of the ^{13}C CS tensors with respect to the molecule, therefore, CO_2 hops in the longitudinal direction (i.e., *z* direction) of the channel do not influence these ^{13}C SSNMR spectra. The combination of wobbling and hopping is shown in Figure 2-3(d). Both the wobbling and hopping angles increase with temperature, indicating reduced CO_2 binding ability at high temperatures.

To explore the effect of a different metal centre on CO_2 adsorption in MIL-53, the gallium analogue was investigated. The static ^{13}C SSNMR spectra of CO_2 adsorbed in MIL-53 (Ga) were acquired from 153 K to 393 K and are shown in Figure 2-4(a). In this instance, a resonance corresponding to unadsorbed mobile CO_2 was observed at temperatures above 313 K. Unlike MIL-53 (Al), the broad underlying ^{13}C powder pattern corresponding to adsorbed CO_2 in MIL-53 (Ga) is evident at temperatures above 353 K. These unique ^{13}C SSNMR observations arise because the magnitude of the breathing effect in MIL-53 depends on the metal centre incorporated.[39] In MIL-53 (Al), the *lt* phase changes to the *ht* phase at 373 K, increasing the unit cell volume and pore size.[31] The larger pores and void space available in the *ht* phase discourages interactions between CO_2 and the adsorption site,[28] leading to the observation of unbound CO_2 in ^{13}C SSNMR experiments. In contrast, MIL-53 (Ga) only transitions to the *ht* phase when the temperature exceeds 493 K.[39] At 373 K and 393 K, narrow-pore MIL-53 (Ga) provides less mobility for CO_2, encouraging interaction with the adsorption sites within the MOF, and giving rise to a broad powder pattern.

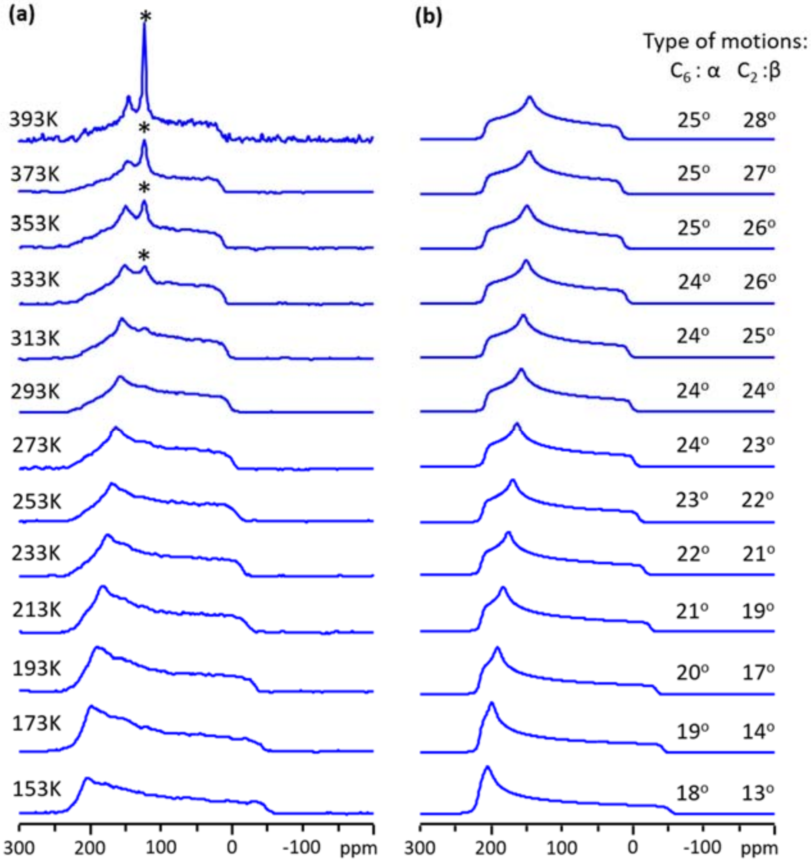

Figure 2-4. The experimental and simulated static ^{13}C SSNMR spectra of CO_2 adsorbed within MIL-53 (Ga) are illustrated in (a) and (b), respectively. The asterisk (*) denotes a sharp resonance at high temperature that corresponds to gaseous, unbound CO_2. The simulated powder patterns were generated using the EXPRESS software and a fast rate of motion (10^9 Hz) for both dynamic modes. CO_2 adsorbed in MIL-53 (Ga) has same motions as CO_2 within MIL-53 (Al), which is a localized wobbling (C_6 with rotation angle α) and a non-localized two-site hopping (C_2 with rotation angle β) between two adsorption sites.

The observed CS parameters of CO_2 within MIL-53 (Ga) exhibit a similar trend as CO_2 in MIL-53 (Al) (Table 2-1). As the temperature increases from 153 K to 393 K, Ω gradually decreases from 267(4) ppm to 191(1) ppm, and κ changes from 0.90(2) to 0.34(1). EXPRESS simulations of experimental ^{13}C powder patterns (Figure 2-4(b)) reveal that CO_2 molecules are also dynamic in this system, undergoing localized wobbling and non-localized two-site hopping at a motional rate $\geq 10^9$ Hz in MIL-53 (Ga), which are strikingly similar to the CO_2 dynamics present in MIL-53 (Al) (Figure 2-3(d)). The wobbling angle (α) increases from 18 ° to 25 ° and the hopping angle (β) climbs from 13 ° to 28 ° for CO_2 molecules in MIL-53 (Ga) as the temperature rises from 153 K to 393 K. At all temperatures, CO_2 adsorbed within MIL-53 (Ga) displays reduced apparent CS parameters and larger rotation angles versus CO_2 in MIL-53 (Al), indicating that CO_2 within MIL-53 (Ga) is more dynamic and is bound less tightly to the MOF. The difference in CO_2 binding ability between these two metal centres may be due to the different atomic radii. Larger atomic sizes can affect the metal-oxygen bond lengths and angles, which may influence the CO_2 binding strength associated with the bridging hydroxyl adsorption site.

Previous research has indicated that the presence of -NH_2 functional groups on the BDC linkers within MIL-53 may enhance CO_2 capture ability.[22, 29] To study the effect of this amine functional group on CO_2 dynamics, static VT ^{13}C SSNMR spectra of CO_2 adsorbed within NH_2-MIL-53 (Al) were recorded at temperatures ranging from 153 K to 393 K (Figure 2-5(a), Table 2-1). The broad CS powder patterns in the low temperature spectra of NH_2-MIL-53 (Al) are similar to those of MIL-53 (Al, Ga). A sharp resonance in the NH_2-MIL-53 (Al) spectrum corresponding to free CO_2 first emerges at 333 K, however, the intensity of this resonance at high temperatures is reduced compared to the resonance observed in MIL-53 (Al) and MIL-53 (Ga). The observed Ω values decrease from 309(4) ppm to 238(1) ppm as temperature increases from 153 K to 393 K. κ values also decrease as temperature increases, and κ is equal to 1 from 153 K to 193 K, corresponding to an axially symmetric CS tensor. In comparison with MIL-53 (Al), CO_2 adsorbed within NH_2-MIL-53 (Al) displays larger ^{13}C Ω and κ values, revealing that the presence of the –NH_2 functional group results in less dynamic CO_2 and stronger MOF-CO_2 binding.[27]

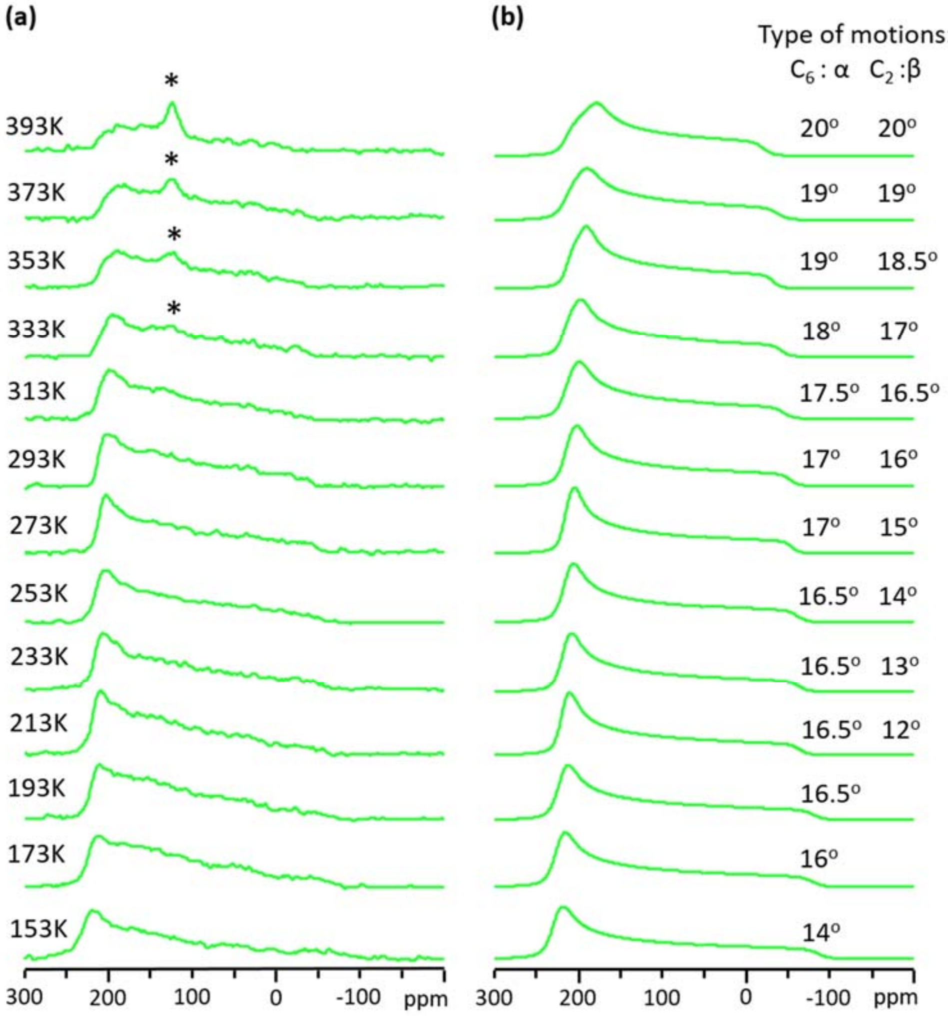

Figure 2-5. The experimental static ^{13}C SSNMR spectra of adsorbed CO_2 within NH_2-MIL-53 (Al) are shown in (a) and simulated static ^{13}C SSNMR spectra are shown in (b). The simulated powder patterns were generated using the EXPRESS software and a fast rate of motion (10^9 Hz) for both dynamic modes. The C_6 motion (six-fold rotation) and α describe localized wobbling of CO_2 about the adsorption site, while the C_2 motion and β refer to a non-localized two-fold hopping between two adsorption sites. The asterisk (*) denotes a sharp resonance at high temperature that corresponds to gaseous, unbound CO_2.

Simulations indicate that a C_6 wobbling and a C_2 hopping of CO_2 occur in NH_2-MIL-53 (Al) when the temperature is higher than 213 K (Figure 2-5(b)). Since CO_2 is adsorbed at the same molecular sites in NH_2-MIL-53 (Al) and MIL-53 (Ga, Al),[27-28] we propose that CO_2 within NH_2-MIL-53 (Al) undergoes the same type of motions: a localized wobbling on an individual adsorption site through a rotation angle of α, and a non-localized two-site (C_2) hopping through a rotation angle of β between adsorption sites (Figure 2-3(d)). When the temperature is below 213 K, the C_2 hopping of CO_2 molecules is no longer apparent in ^{13}C SSNMR spectra of NH_2-MIL-53 (Al), leaving only the localized wobbling that is modeled by a C_6 rotation. The C_6 rotation angle (α), or wobbling angle, increases from 14 ° to 20 ° as the temperature rises from 153 K to 393 K, while the C_2 jumping angle (β) increases from 12 ° to 20 ° as the temperature increases from 213 K to 393 K. The presence of relatively small rotation angles across all temperatures, paired with the lack of C_2 hopping at low temperatures, reflect a much stronger CO_2 binding ability in NH_2-MIL-53 (Al) versus MIL-53 (Al, Ga).

In order to have a better understanding of the influence of metal centre and functional group on gas adsorption, NH_2-MIL-53 (Ga) was also studied. Static ^{13}C SSNMR spectra of adsorbed CO_2 within NH_2-MIL-53 (Ga) were acquired in the temperature range from 153 K to 393 K (Figure 2-6(a)). A narrow central ^{13}C resonance corresponding to free CO_2 is apparent at room temperature and dominates the spectrum at high temperatures, indicating that the MOF has a relatively low CO_2 adsorption capacity and binding strength in the context of this study. This decreased CO_2 adsorption capacity may be due to the reduction of available surface area: the BET surface area of NH_2-MIL-53 (Ga) is only 210 m^2/g,[67] which is far below the BET surface area of MIL-53 (Ga) (1230 m^2/g).[67] The decreased binding strength associated with CO_2 adsorption may be due to the Ga metal centre used in this variant of NH_2-MIL-53: a larger atomic size can also affect the metal-oxygen bond lengths and angles, which may influence the CO_2 binding strength associated with the bridging hydroxyl adsorption site in NH_2-MIL-53.

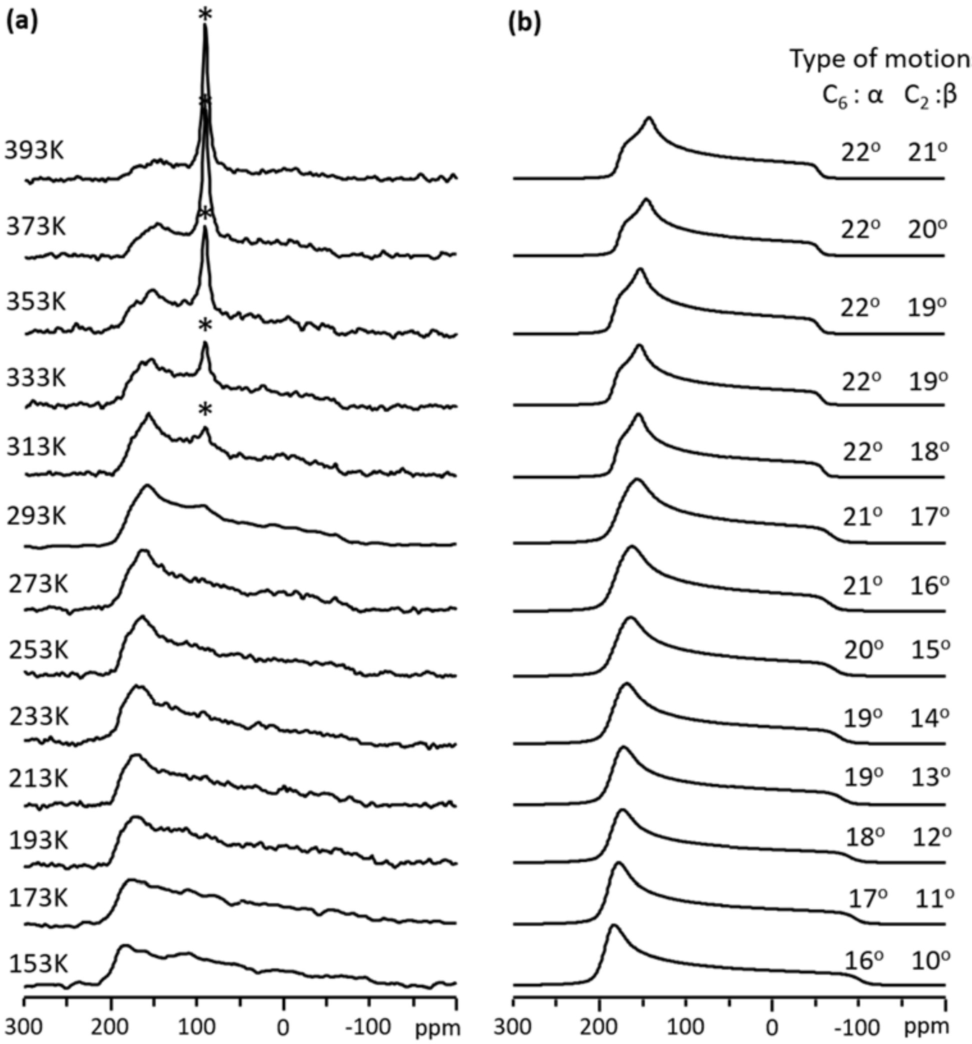

Figure 2-6. The experimental and simulated static ^{13}C SSNMR spectra of adsorbed CO_2 within NH_2-MIL-53 (Ga) are shown in (a) and (b) respectively. The simulated powder patterns were generated using the EXPRESS software and a fast rate of motion (10^9 Hz) for both dynamic modes. The C_6 motion (six-fold rotation) and α describe localized wobbling of CO_2 about the adsorption site, while the C_2 motion and β refer to a non-localized two-fold hopping between two adsorption sites. The asterisk (*) denotes a sharp resonance at high temperature that corresponds to gaseous, unbound CO_2.

The observed ^{13}C CS parameters of adsorbed CO_2 in NH_2-MIL-53 (Ga) decrease as temperature increases (Table 2-1). Ω values decrease from 289(3) to 230(1) ppm as the temperature rises from 153 K to 393 K, while κ diminishes from 0.97(2) at 153 K to 0.70(1) at 393 K. The observed Ω and κ values in NH_2-MIL-53 (Ga) are larger than those in MIL-53 (Ga), but smaller than those in NH_2-MIL-53 (Al), indicating that CO_2 dynamics and MOF-CO_2 binding strength in NH_2-MIL-53 (Ga) lie between those observed in MIL-53 (Ga) and NH_2-MIL-53 (Al).

EXPRESS simulations (Figure 2-6(b)) again show that two type of CO_2 motions (Figure 2-3(d)) are present: a localized C_6 wobbling and a non-localized C_2 jumping. The C_6 wobbling angle, α, varies from 16 ° at 153 K to 22 ° at 393 K, while the C_2 hopping angle β increases from 10 ° at 153 K to 21 ° at 393 K. CO_2 adsorbed within NH_2-MIL-53 (Ga) exhibits both wobbling and hopping even at low temperatures. The increased dynamics of CO_2 versus within NH_2-MIL-53 (Al) indicates that the nature of the metal centre plays a role in guest adsorption, likely due to the influence of the specific metal centre on the binding ability of the bridging OH groups between SBUs.

The graphs in Figure 2-7 and Figure 2-8 provide a comparison of ^{13}C CS parameters and rotation angles within all four MIL-53 variants. The ^{13}C CS parameters are related to the motion of CO_2 within MOFs; CO_2 molecules moving through larger wobbling angles are generally linked to reduced Ω values,[57] and in this case, the κ value is intimately related to the hopping angle. In the MIL-53 and NH_2-MIL-53 MOFs, larger CO_2 hopping angles correspond to smaller κ values. CO_2 adsorbed within NH_2-MIL-53 (Al) exhibits the largest Ω and κ values observed under any acquired temperature, while CO_2 in MIL-53 (Ga) is linked to the smallest Ω and κ values (Figure 2-7). The interpretation of these findings is that CO_2 within MIL-53-NH_2 (Al) is bound tightest and undergoes a relatively small amount of dynamic motion, while CO_2 within MIL-53 (Ga) is bound weakest and undergoes increased dynamics. Amine functionalization of the linkers in MIL-53 (Al, Ga) leads to the observation of smaller α and β CO_2 motional angles in comparison to ordinary MIL-53 (Figure 2-8), indicating that CO_2 is adsorbed more strongly and exhibits reduced dynamics when the MIL-53 linker is functionalized with the NH_2 group. It is important to again note that the metal centre has a clear influence on CO_2 binding ability in all variations of MIL-53. CO_2 adsorbed in MIL-53 (Ga) is more dynamic than CO_2 adsorbed in MIL-53 (Al), and CO_2 adsorbed in NH_2-MIL-53 (Ga) exhibits enhanced dynamics versus CO_2 adsorbed in NH_2-MIL-53 (Al).

The results in Figure 2-8 display a trend that agrees well with rational expectations. The compromise between increasing kinetic energy at higher temperatures versus the net attractive adsorption energy results in an increasing C_6 rotation angle with temperature. Although the NMR parameters were acquired across a 250 ° range, the trend is to approach ca. 0 degrees in both hopping and wobbling angles at absolute zero, as it should. There are two symmetrically equivalent adsorption sites within one MIL-53 cavity; at the limit of 0 K, Figure 2-8 suggests the hopping motion would be frozen out and the occupancies of the two equivalent sites would be 0.5.

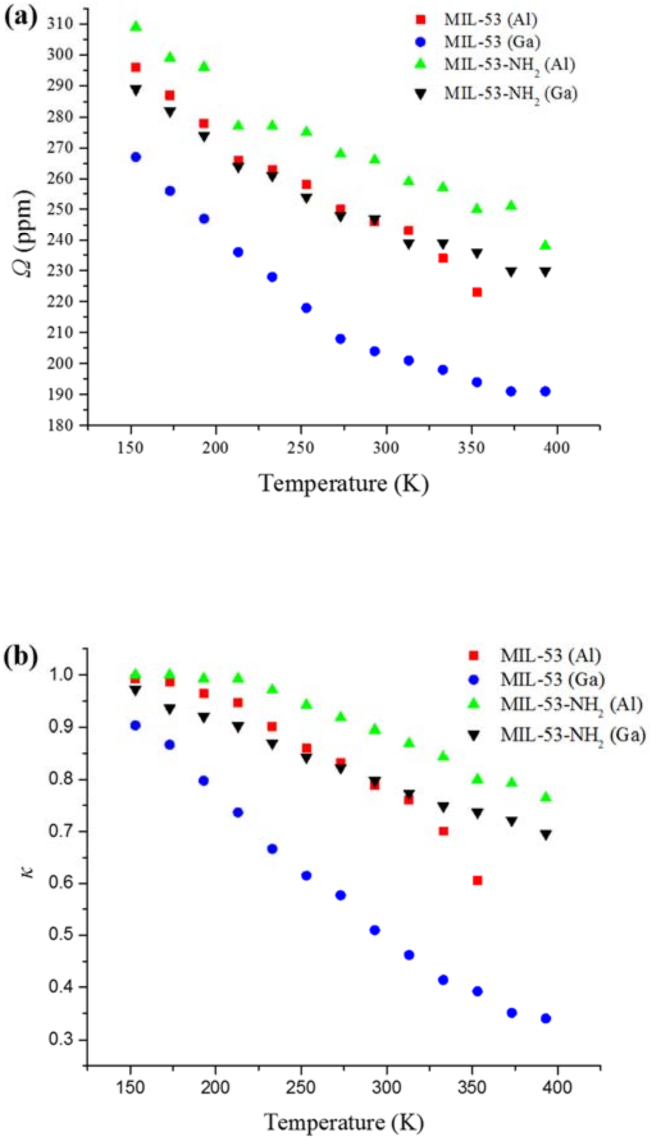

Figure 2-7. A comparison of ^{13}C span (Ω) and skew (κ) NMR parameters corresponding to of CO_2 adsorbed in different MIL-53 MOFs across temperature from 153 K to 393 K are shown in (a) and (b), respectively.

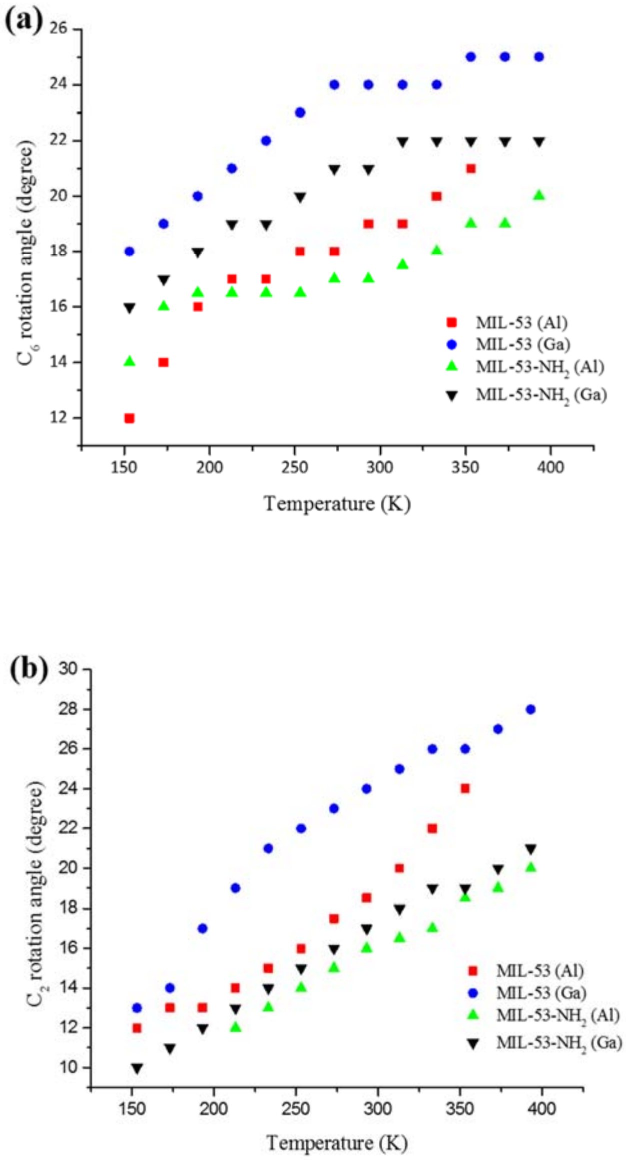

Figure 2-8. A comparison of C_6 rotation angle (α) describing local wobbling in MIL-53 across temperatures from 153 K to 393 K is shown in (a) and a graph of the C_2 rotation angle (β) corresponding to non-localized hopping of CO_2 versus temperature is depicted in (b).

2.3.3 Studying the interaction of CO_2 with adsorption sites

SSNMR experiments employing cross polarization (CP) from ^1H to ^{13}C were employed to study the adsorption strength between CO_2 guests and the MIL-53 host. CP experiments are mediated by dipolar coupling and, by extension, internuclear distance;[68] this dependence can be exploited to obtain detailed information on the spatial proximity between nuclei. The contact time (CT) in CP experiments describes the period of time that CP is allowed to occur. With longer CTs, polarization across longer internuclear distances can typically be transferred, and when shorter CTs are employed, only ^{13}C nuclei that are relatively proximate to ^1H will be detected. In this instance, ^1H-^{13}C CP experiments have been employed to explore the location of the CO_2 adsorption sites in MIL-53, which have been postulated to be proximate to the hydroxyl group joining SBUs.[27-28]

In MIL-53 (Al), ^1H-^{13}C CP SSNMR experiments were employed on both the empty framework and CO_2-loaded samples (Figure 2-9(a)). The ^{13}C resonances observed in the empty framework arise from carbon atoms in the BDC linkers. Hydrogen is directly bound to carbon in BDC, therefore, ^1H polarization is efficiently transferred to ^{13}C, resulting in a very strong resonance. The use of long and short CTs in ^1H-^{13}C CP SSNMR experiments on the CO_2-loaded sample at room temperature results in similar spectra, which both resemble those of the empty framework. The absence of a ^{13}C resonance corresponding to adsorbed CO_2 at 293 K in ^1H-^{13}C CP SSNMR spectra of MIL-53 (Al) is due to the long hydroxyl ^1H-$^{13}CO_2$ distance and the highly dynamic motion of CO_2 molecules, which rapidly modulate and average the weak dipolar couplings. At 173 K, the intensity of the highest frequency peak in the CP NMR spectra (denoted * in Figure 2-9(a)) is enhanced versus room temperature NMR spectra when both long and short CTs are employed. This high frequency resonance approximately corresponds to the δ_{11} component of the ^{13}C CS tensor from adsorbed CO_2 detected *via* ^{13}C DEPTH-echo SSNMR spectra at the same temperature (Figure 2-2), and indeed represents adsorbed CO_2. At low temperatures, the

CO_2 molecule is less dynamic, preserving the dipolar coupling between the adsorption site and CO_2, and permitting the detection of adsorbed CO_2 by ^1H-^{13}C CP experiments.

^1H-^{13}C CP SSNMR experiments were also performed on empty MIL-53 (Ga) and CO_2-loaded MIL-53 (Ga) samples (Figure 2-9(b)). The room temperature ^1H-^{13}C CP SSNMR spectra of CO_2-loaded MIL-53 (Ga) resemble the CP spectra of the empty framework when both long and short CTs are used, indicating that the CO_2 molecule undergoes very fast dynamic motion, and that there may be a relatively long ^1H-$^{13}CO_2$ distance at this temperature. The CO_2 resonance is only apparent at 173 K when a long CT is employed, indicating a weaker ^1H-^{13}C dipolar interaction between CO_2 molecule and the adsorption site in MIL-53 (Ga) compared with MIL-53 (Al) at this temperature, this data supports the interpretation that CO_2 is bound weaker in MIL-53 (Ga) than in MIL-53 (Al).

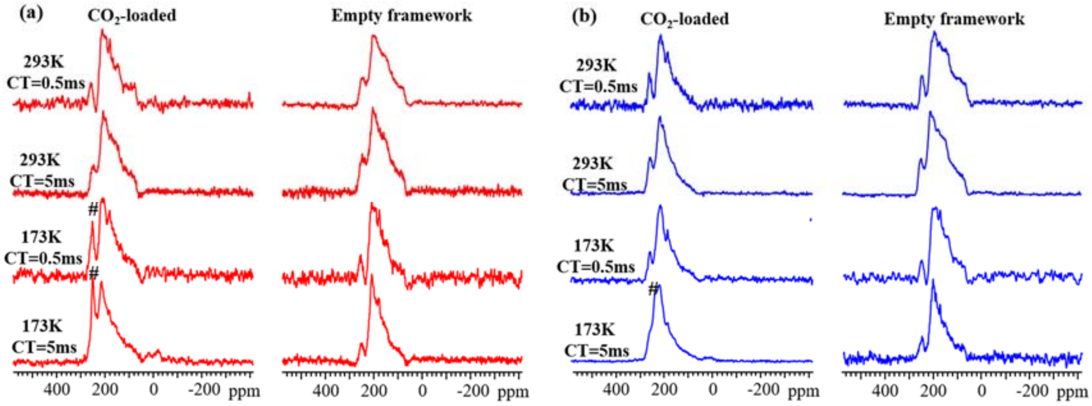

Figure 2-9. Static ^1H-^{13}C CP SSNMR spectra of MIL-53 (Al) and MIL-53 (Ga) are shown in (a) and (b), respectively. Spectra of both CO_2 adsorbed samples and empty frameworks using different CP contact times (CTs) were acquired at 293 K and 173 K. The pound sign (#) denotes the resonance corresponding to adsorbed CO_2.

The ^1H-^{13}C CP SSNMR spectra of NH_2-MIL-53 (Al, Ga) feature ^{13}C resonances corresponding to both the framework and adsorbed CO_2 at room temperature, even when short CTs are employed (Figure 2-10). These findings confirm that a strong dipolar interaction exists between CO_2 guests and the adsorption site within the amine-functionalized versions of MIL-53. CO_2 molecules are bound more strongly and exhibit reduced dynamics versus non-functionalized MIL-53 (Al, Ga). At low temperatures, the intensity of the resonance corresponding to adsorbed CO_2 is enhanced, in agreement with the enhanced binding indicated by low temperature ^{13}C DEPTH-echo SSNMR experiments. Previous research has shown that there is no direct interaction of CO_2 and the amine functional groups in these systems,[27] therefore, the enhancement of the resonance linked to adsorbed CO_2 must be due to an increase in the dipolar coupling strength between hydrogen atoms from the adsorption site and carbon from adsorbed CO_2. These ^1H-^{13}C CP SSNMR experimental results clearly show that the presence of an amino group enhances the binding strength between CO_2 guests and the MIL-53 host.

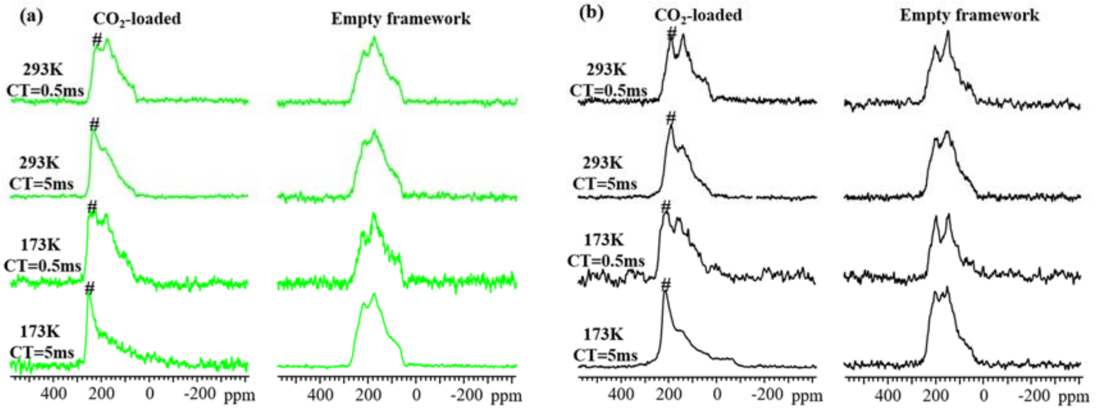

Figure 2-10. ^1H-^{13}C static CP SSNMR spectra of NH_2-MIL-53 (Al) and NH_2-MIL-53 (Ga) are shown in (a) and (b), respectively. NMR Spectra of both CO_2 adsorbed samples and empty frameworks with different contact time (CT) were acquired at 293 K and 173 K. The pound sign (#) denotes the resonance of adsorbed CO_2.

To probe the specific location of CO_2 adsorption sites within MIL-53, ^1H-^{13}C SSNMR CP experiments were performed on deuterium-exchanged MIL-53 samples. Since

^{2}H cannot participate in ^{1}H-^{13}C CP experiments, ^{13}C nuclei proximate to ^{2}H are not detected. It has been observed that the H atom in –OH groups can be easily exchanged by ^{2}H in ^2H_2O.[69-70] Previous studies have indicated that the bridging –OH group which connects SBUs in MIL-53 is the CO_2 adsorption site.[27-28] In a deuterium exchanged MIL-53 sample, only the ^{1}H atoms on the bridging –OH group are replaced by ^{2}H, forming a –O^{2}H hydroxyl group. In this manner, the CO_2 adsorption site may be inferred from the success or failure of ^{1}H-^{13}C CP experiments on deuterium-exchanged MIL-53.

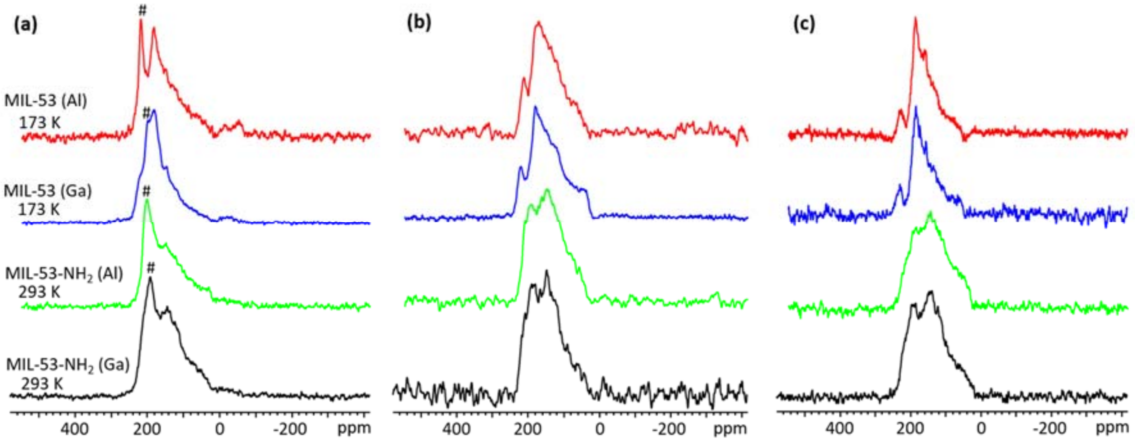

Figure 2-11. Static ^{1}H-^{13}C CP SSNMR spectra of CO_2-loaded non-deuterated samples, CO_2-loaded deuterium exchanged samples and empty frameworks are shown in (a), (b) and (c), respectively. For MIL-53 (Al) and MIL-53 (Ga), the spectra were obtained at 173 K with CT = 5 ms, For MIL-53-NH_2 (Al) and MIL-53-NH_2 (Ga), the spectra were obtained at 293 K with CT = 5 ms. The pound sign (#) denotes the resonance of adsorbed CO_2.

Since the ^{13}C powder pattern corresponding to adsorbed CO_2 within MIL-53 (Al) and MIL-53 (Ga) could only be detected in ^{1}H-^{13}C CP SSNMR spectra at 173 K in non-deuterated samples, ^{1}H-^{13}C SSNMR CP experiments on deuterium exchanged MIL-53 (Al, Ga) were only performed at 173 K (Figure 2-11). The only ^{13}C resonances present in the ^{1}H-^{13}C CP SSNMR spectra of the deuterium exchanged MIL-53 samples correspond to the

BDC linker of the MOF; the resonance corresponding to adsorbed CO_2 is not present. The ^{1}H-^{13}C dipolar interaction between the framework adsorption sites and adsorbed CO_2 in deuterium exchanged MIL-53 samples is absent due to the deuteration of the –OH group connecting the SBUs. These ^{1}H-^{13}C CP SSNMR spectra provide strong proof that the bridging –OH group between SBUs is the CO_2 adsorption site within MIL-53.

The ^{1}H-^{13}C CP SSNMR spectra of deuterium exchanged NH_2-MIL-53 (Al, Ga) samples at 293 K (Figure 2-11) are very similar to those of the empty frameworks, suggesting that ^{1}H-^{13}C dipolar coupling between CO_2 and the adsorption site within the MOF is absent. Interestingly, at 173 K, ^{1}H-^{13}C CP SSNMR spectra of deuterated NH_2-MIL-53 (Al, Ga) feature a resonance corresponding to adsorbed CO_2 (denoted # in Figure 2-12), however, the intensity of this CO_2-linked resonance is low, while the intensity of framework ^{13}C resonances is relatively high. These spectra indicate that weak ^{1}H-^{13}C dipolar couplings between CO_2 carbon atoms and hydrogen are present at low temperature in deuterium exchanged NH_2-MIL-53 (Al) and NH_2-MIL-53 (Ga). Unfortunately, in MIL-53-NH_2, the hydrogen atoms associated with the –NH_2 amino group may also participate in fast deuterium exchange,[71-72] hence, ^{1}H-^{13}C CP SSNMR experiments alone cannot distinguish whether the CO_2 adsorption site in deuterated NH_2-MIL-53 lies on the linker amino group or the SBU –OH moiety.[27] The weak ^{1}H-^{13}C dipolar interactions at this temperature could also involve the carbon atom of CO_2 molecule and ^{1}H atoms located on the BDC linker. Since the NH_2-MIL-53 is associated with a narrower pore size than MIL-53,[27, 73] short distances between CO_2 and the benzene ring of the BDC linker may be possible, permitting a weak ^{1}H-^{13}C dipolar interaction.

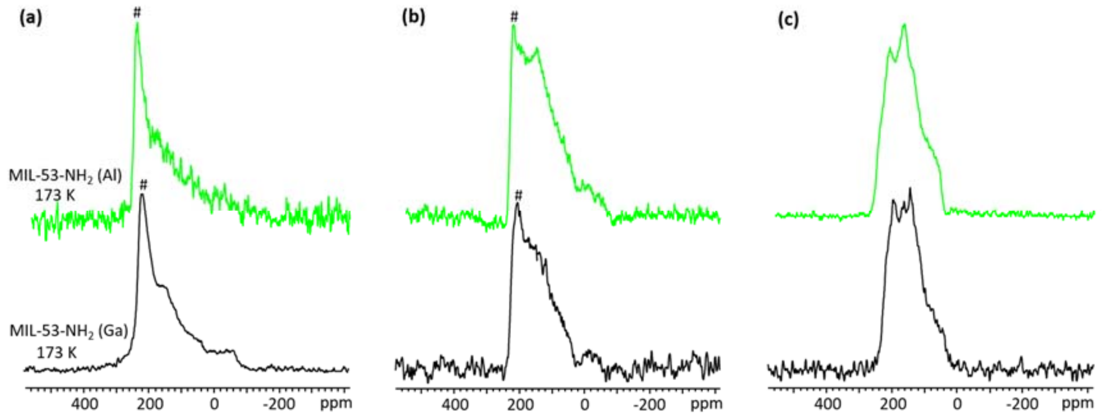

Figure 2-12. ^{1}H-^{13}C CP SSNMR spectra of CO$_2$-loaded non-deuterated samples, CO$_2$-loaded deuterium exchanged samples and empty frameworks are shown in (a), (b) and (c), respectively. All the spectra were obtained at 173 K with CT = 5 ms. The pound sign (#) denotes the resonance of adsorbed CO$_2$.

2.4 Conclusions

^{13}C SSNMR experiments have been used to probe the CO$_2$ dynamics and binding strength within a MOF without open metal sites. CO$_2$ guests in MIL-53 (Al, Ga) and NH$_2$-MIL-53 (Al, Ga) undergo both a localized wobbling and a non-localized hopping between two separate adsorption sites. Simulations of experimental SSNMR data provide the rates and angles associated with each type of motion. All of the motional angles increase with temperature from 153 K to 393 K. These ^{13}C SSNMR spectra reveal that differences in CO$_2$ binding strength among the various MIL-53 MOFs are linked to (i) the nature of the metal centre and (ii) the presence of functional groups on the BDC linkers. The relatively weaker CO$_2$ binding interaction in non-functionalized MIL-53 results in increased CO$_2$ mobility. ^{1}H-^{13}C CP SSNMR experiments indicate that CO$_2$ binding strength in MIL-53 is influenced by the nature of the metal centre and the presence of functional groups. ^{1}H-^{13}C CP SSNMR spectra of deuterated MIL-53 suggests that the bridging hydroxyl groups between metal centres serve as the CO_2 adsorption sites within MOFs.

Our work provides a clear picture of CO_2 dynamics in MIL-53, and advances the understanding of gas adsorption in MOFs without open metal sites. Detailed knowledge and understanding of the dynamics in this series of MOFs should unlock avenues for modifications to existing and future MOFs in order to improve the CO_2 wt % uptake at a given temperature, working towards the goal of long-term CO_2 capture and sequestration in MOFs. More detailed SSNMR studies are currently being performed to probe the fine details underpinning CO_2 adsorption within the MIL-53 series of MOFs. *Ab initio* calculations are another complementary avenue that can accurately predict NMR parameters associated with gases adsorbed in MOFs;[74] this route should allow detailed analysis of individual contributions to NMR parameters and assist in fully characterizing CO_2 adsorption and dynamics in the MIL-53 system.

2.5 References

1. Quadrelli, R.; Peterson, S., *Energy Policy* **2007,** *35* (11), 5938-5952.

2. Sumida, K.; Rogow, D. L.; Mason, J. A.; McDonald, T. M.; Bloch, E. D.; Herm, Z. R.; Bae, T. H.; Long, J. R., *Chem. Rev.* **2012,** *112* (2), 724-781.

3. D'Alessandro, D. M.; Smit, B.; Long, J. R., *Angew. Chem. Int. Ed.* **2010,** *49* (35), 6058-6082.

4. Zhou, H.-C.; Kitagawa, S., *Chem. Soc. Rev.* **2014,** *43* (16), 5415-5418.

5. Furukawa, H.; Cordova, K. E.; O'Keeffe, M.; Yaghi, O. M., *Science* **2013,** *341* (6149), 974.

6. Zhou, H.-C.; Long, J. R.; Yaghi, O. M., *Chem. Rev.* **2012,** *112* (2), 673-674.

7. Rowsell, J. L. C.; Yaghi, O. M., *Microporous Mesoporous Mater.* **2004,** *73* (1-2), 3-14.

8. James, S. L., *Chem. Soc. Rev.* **2003,** *32* (5), 276-288.

9. Zhang, Z.; Zhao, Y.; Gong, Q.; Li, Z.; Li, J., *Chem. Commun.* **2013,** *49* (7), 653-661.

10. Li, J.; Ma, Y.; McCarthy, M. C.; Sculley, J.; Yu, J.; Jeong, H.-K.; Balbuena, P. B.; Zhou, H., *Coord. Chem. Rev.* **2011,** *255* (15–16), 1791-1823.

11. Montoro, C.; Garcia, E.; Calero, S.; Perez-Fernandez, M. A.; Lopez, A. L.; Barea, E.; Navarro, J. A. R., *J. Mater. Chem.* **2012,** *22* (20), 10155-10158.

12. Mason, J. A.; Sumida, K.; Herm, Z. R.; Krishna, R.; Long, J. R., *Energy Environ. Sci.* **2011,** *4* (8), 3030-3040.

13. Lee, Y. G.; Moon, H. R.; Cheon, Y. E.; Suh, M. P., *Angew. Chem. Int. Ed.* **2008,** *47* (40), 7741-7745.

14. Canepa, P.; Nijem, N.; Chabal, Y. J.; Thonhauser, T., *Phys. Rev. Lett.* **2013,** *110* (2), 026102.

15. Valenzano, L.; Civalleri, B.; Chavan, S.; Palomino, G. T.; Areán, C. O.; Bordiga, S., *J. Phys. Chem. C* **2010,** *114* (25), 11185-11191.

16. Canepa, P.; Arter, C. A.; Conwill, E. M.; Johnson, D. H.; Shoemaker, B. A.; Soliman, K. Z.; Thonhauser, T., *J. Mater. Chem. A* **2013,** *1* (43), 13597-13604.

17. Valenzano, L.; Civalleri, B.; Sillar, K.; Sauer, J., *J. Phys. Chem. C* **2011,** *115* (44), 21777-21784.

18. Cmarik, G. E.; Kim, M.; Cohen, S. M.; Walton, K. S., *Langmuir* **2012,** *28* (44), 15606-15613.

19. Choi, S.; Watanabe, T.; Bae, T. H.; Sholl, D. S.; Jones, C. W., *J. Phys. Chem. Lett.* **2012,** *3* (9), 1136-1141.

20. Vaidhyanathan, R.; Iremonger, S. S.; Shimizu, G. K. H.; Boyd, P. G.; Alavi, S.; Woo, T. K., *Science* **2010,** *330* (6004), 650-653.

21. Torrisi, A.; Bell, R. G.; Mellot-Draznieks, C., *Cryst. Growth Des.* **2010,** *10* (7), 2839-2841.

22. Couck, S.; Denayer, J. F. M.; Baron, G. V.; Remy, T.; Gascon, J.; Kapteijn, F., *J. Am. Chem. Soc.* **2009,** *131* (18), 6326-6327.

23. Huang, Y.; Qin, W.; Li, Z.; Li, Y., *Dalton Trans.* **2012,** *41* (31), 9283-9285.

24. Devic, T.; Salles, F.; Bourrelly, S.; Moulin, B.; Maurin, G.; Horcajada, P.; Serre, C.; Vimont, A.; Lavalley, J. C.; Leclerc, H.; Clet, G.; Daturi, M.; Llewellyn, P. L.; Filinchuk, Y.; Ferey, G., *J. Mater. Chem.* **2012,** *22* (20), 10266-10273.

25. Yang, Q.; Wiersum, A. D.; Llewellyn, P. L.; Guillerm, V.; Serred, C.; Maurin, G., *Chem. Commun.* **2011,** *47* (34), 9603-9605.

26. Serre, C.; Millange, F.; Thouvenot, C.; Nogues, M.; Marsolier, G.; Louer, D.; Ferey, G., *J. Am. Chem. Soc.* **2002,** *124* (45), 13519-13526.

27. Stavitski, E.; Pidko, E. A.; Couck, S.; Remy, T.; Hensen, E. J. M.; Weckhuysen, B. M.; Denayer, J.; Gascon, J.; Kapteijn, F., *Langmuir* **2011,** *27* (7), 3970-3976.

28. Ramsahye, N. A.; Maurin, G.; Bourrelly, S.; Llewellyn, P. L.; Serre, C.; Loiseau, T.; Devic, T.; Ferey, G., *J. Phys. Chem. C* **2008,** *112* (2), 514-520.

29. Arstad, B.; Fjellvag, H.; Kongshaug, K. O.; Swang, O.; Blom, R., *Adsorpt.-J. Int. Adsorpt. Soc.* **2008,** *14* (6), 755-762.

30. Bourrelly, S.; Llewellyn, P. L.; Serre, C.; Millange, F.; Loiseau, T.; Ferey, G., *J. Am. Chem. Soc.* **2005,** *127* (39), 13519-13521.

31. Loiseau, T.; Serre, C.; Huguenard, C.; Fink, G.; Taulelle, F.; Henry, M.; Bataille, T.; Ferey, G., *Chem.-Eur. J.* **2004,** *10* (6), 1373-1382.

32. Whitfield, T. R.; Wang, X. Q.; Liu, L. M.; Jacobson, A. J., *Solid State Sci.* **2005,** *7* (9), 1096-1103.

33. Vougo-Zanda, M.; Huang, J.; Anokhina, E.; Wang, X. Q.; Jacobson, A. J., *Inorg. Chem.* **2008,** *47* (24), 11535-11542.

34. Anokhina, E. V.; Vougo-Zanda, M.; Wang, X. Q.; Jacobson, A. J., *J. Am. Chem. Soc.* **2005,** *127* (43), 15000-15001.

35. Mowat, J. P. S.; Seymour, V. R.; Griffin, J. M.; Thompson, S. P.; Slawin, A. M. Z.; Fairen-Jimenez, D.; Duren, T.; Ashbrook, S. E.; Wright, P. A., *Dalton Trans.* **2012,** *41* (14), 3937-3941.

36. Serra-Crespo, P.; Dikhtiarenko, A.; Stavitski, E.; Juan-Alcaniz, J.; Kapteijn, F.; Coudert, F. X.; Gascon, J., *CrystEngComm* **2015,** *17* (2), 276-280.

37. Biswas, S.; Ahnfeldt, T.; Stock, N., *Inorg. Chem.* **2011,** *50* (19), 9518-9526.

38. Devic, T.; Horcajada, P.; Serre, C.; Salles, F.; Maurin, G.; Moulin, B.; Heurtaux, D.; Clet, G.; Vimont, A.; Greneche, J. M.; Le Ouay, B.; Moreau, F.; Magnier, E.; Filinchuk, Y.; Marrot, J.; Lavalley, J. C.; Daturi, M.; Ferey, G., *J. Am. Chem. Soc.* **2010,** *132* (3), 1127-1136.

39. Volkringer, C.; Loiseau, T.; Guillou, N.; Ferey, G.; Elkaim, E.; Vimont, A., *Dalton Trans.* **2009,** (12), 2241-2249.

40. Martineau, C., *Solid State Nucl. Magn. Reson.* **2014,** *63-64*, 1-12.

41. R. K. Harris; R. E. Wasylishen; Duer, M. J., *NMR Crystallography*. John Wiley & Sons Ltd., U.K., 2009.

42. Huang, Y., Xu, J., Gul-E-Noor, F., He, P., *Encyclopedia of Inorganic and Bioinorganic Chemistry, Vol. 1*. John Wiley & Sons, Ltd., Chichester, UK 2014.

43. Ashbrook, S. E.; Dawson, D. M.; Seymour, V. R., *Phys. Chem. Chem. Phys.* **2014,** *16* (18), 8223-8242.

44. Sutrisno, A.; Huang, Y., *Solid State Nucl. Magn. Reson.* **2013,** *49-50*, 1-11.

45. Hoffmann, H. C.; Debowski, M.; Muller, P.; Paasch, S.; Senkovska, I.; Kaskel, S.; Brunner, E., *Materials* **2012,** *5* (12), 2537-2572.

46. Xu , J.; Lucier , B. E. G.; Sinelnikov, R.; Terskikh, V. V.; Staroverov, V. N.; Huang, Y., *Chem.-Eur. J.* **2015,** *21*, 14348-14361.

47. Kolokolov, D. I.; Jobic, H.; Rives, S.; Yot, P. G.; Ollivier, J.; Trens, P.; Stepanov, A. G.; Maurin, G., *J. Phys. Chem. C* **2015,** *119* (15), 8217-8225.

48. Lieder, C.; Opelt, S.; Dyballa, M.; Henning, H.; Klemm, E.; Hunger, M., *J. Phys. Chem. C* **2010,** *114* (39), 16596-16602.

49. Ibrahim, B.; Lucier, B. E. G.; Xu, J.; He, P.; Huang, Y., *Can. J. Chem.* **2015,** *93* (9), 960-969.

50. Springuel-Huet, M.-A.; Nossov, A.; Adem, Z.; Guenneau, F.; Volkringer, C.; Loiseau, T.; Férey, G.; Gédéon, A., *J. Am. Chem. Soc.* **2010,** *132* (33), 11599-11607.

51. Xu, J.; Terskikh, V. V.; Huang, Y., *Chem.-Eur. J.* **2013,** *19* (14), 4432-4436.

52. He, P.; Xu, J.; Terskikh, V. V.; Sutrisno, A.; Nie, H. Y.; Huang, Y., *J. Phys. Chem. C* **2013,** *117* (33), 16953-16960.

53. Sutrisno, A.; Terskikh, V. V.; Shi, Q.; Song, Z.; Dong, J.; Ding, S.; Wang, W.; Provost, B. R.; Daff, T. D.; Woo, T. K.; Huang, Y., *Chem.-Eur. J.* **2012,** *18* (39), 12251-12259.

54. Wang, W. D.; Lucier, B. E. G.; Terskikh, V. V.; Wang, W.; Huang, Y., *J. Phys. Chem. Lett.* **2014,** *5* (19), 3360-3365.

55. Lin, L.-C.; Kim, J.; Kong, X.; Scott, E.; McDonald, T. M.; Long, J. R.; Reimer, J. A.; Smit, B., *Angew. Chem. Int. Ed.* **2013,** *52* (16), 4410-4413.

56. Gul-E-Noor, F.; Mendt, M.; Michel, D.; Poppl, A.; Krautscheid, H.; Haase, J.; Bertmer, M., *J. Phys. Chem. C* **2013,** *117* (15), 7703-7712.

57. Kong, X.; Scott, E.; Ding, W.; Mason, J. A.; Long, J. R.; Reimer, J. A., *J. Am. Chem. Soc.* **2012,** *134* (35), 14341-14344.

58. Peksa, M.; Burrekaew, S.; Schmid, R.; Lang, J.; Stallmach, F., *Microporous Mesoporous Mater.* **2015,** *216*, 75-81.

59. Vold, R. L.; Hoatson, G. L., *J. Magn. Reson.* **2009,** *198* (1), 57-72.

60. Serra-Crespo, P.; Gobechiya, E.; Ramos-Fernandez, E. V.; Juan-Alcañiz, J.; Martinez-Joaristi, A.; Stavitski, E.; Kirschhock, C. E. A.; Martens, J. A.; Kapteijn, F.; Gascon, J., *Langmuir* **2012,** *28* (35), 12916-12922.

61. Chen, L.; Mowat, J. P. S.; Fairen-Jimenez, D.; Morrison, C. A.; Thompson, S. P.; Wright, P. A.; Düren, T., *J. Am. Chem. Soc.* **2013,** *135* (42), 15763-15773.

62. Dybowski, C.; Neue, G., *Prog. Nucl. Mag. Res. Sp.* **2002,** *41* (3–4), 153-170.

63. Cory, D. G.; Ritchey, W. M., *J. Magn. Reson* **1988,** *80* (1), 128-132.

64. Gottlieb, H. E.; Kotlyar, V.; Nudelman, A., *J. Org. Chem.* **1997,** *62* (21), 7512-7515.

65. Eichele K.; Wasylishen R. E., *WSolids1* University of Tübingen, Tübingen, Germany, **2009**.

66. Beeler, A. J.; Orendt, A. M.; Grant, D. M.; Cutts, P. W.; Michl, J.; Zilm, K. W.; Downing, J. W.; Facelli, J. C.; Schindler, M. S.; Kutzelnigg, W., *J. Am. Chem. Soc.* **1984,** *106* (25), 7672-7676.

67. Canivet, J.; Bonnefoy, J.; Daniel, C.; Legrand, A.; Coasne, B.; Farrusseng, D., *New J. Chem.* **2014,** *38* (7), 3102-3111.

68. Duer, M. J., *Solid-State NMR Spectroscopy Principles and Applications*. Blackwell Science, Oxford, 2002.

69. Stewart, J. H.; Shapiro, R. H.; Depuy, C. H.; Bierbaum, V. M., *J. Am. Chem. Soc.* **1977,** *99* (23), 7650-7653.

70. Jackman, L. M.; Sternhell, S., *Applications of Nuclear Magnetic Resonance Spectroscopy in Organic Chemistry (Second Edition)*. Pergamon Press Ltd., Oxford U. K., 1969.

71. Hanson, J. R., *The Organic Chemistry of Isotopic Labelling*. Royal Society of Chemistry, Cambridge, UK, 2011.

72. Pavia, D. L.; Lampman, G. M.; Kriz, G. S.; Vyvyan, J. A., *Introduction to Spectroscopy, Fourth Edition*. Brooks Cole, Belmont, USA, 2008.

73. Serra-Crespo, P.; van der Veen, M. A.; Gobechiya, E.; Houthoofd, K.; Filinchuk, Y.; Kirschhock, C. E. A.; Martens, J. A.; Sels, B. F.; De Vos, D. E.; Kapteijn, F.; Gascon, J., *J. Am. Chem. Soc.* **2012,** *134* (20), 8314-8317.

74. Lopez, M. G.; Canepa, P.; Thonhauser, T., *J. Chem. Phys.* **2013,** *138* (15), 154704.

2.6 Appendix

Table 2-A1. The number of scans acquired during static ^{13}C and ^{1}H-^{13}C cross-polarized (CP) variable temperature (VT) SSNMR experiments on the MIL-53 system.

	NMR Experiment		
Compound	**^{13}C VT**	**^{1}H-^{13}C CP (293 K)**	**^{1}H-^{13}C CP (173 K)**
MIL-53 (Al)[a]	896	734	1152
MIL-53 (Ga)[a]	704	610	360
NH_2-MIL-53 (Al)[a]	640	1800	512
NH_2-MIL-53 (Ga)[a]	576	2000	371
MIL-53 (Al)[b]			960
MIL-53 (Ga)[b]			1000
NH_2-MIL-53 (Al)[b]		2000	320
NH_2-MIL-53 (Ga)[b]		2000	640

[a]: The CO_2 loading level is 0.2 CO_2/metal by molar ratio, please see the Experimental section in main text for additional details; [b]: These are deuterium exchanged samples loaded with CO_2 at a loading level 0.2 CO_2/metal.

Synthesis of the different forms of MIL-53

MIL-53 (Al): $Al(NO_3)_3 \cdot 9H_2O$ (1.30 g, 3.46 mmol), benzene-1,4-dicarboxylic acid (BDC, 0.29 g, 1.73 mmol) and 10 mL deionized H_2O were mixed into a 23 mL Teflon-lined stainless steel autoclave and heated at 220 ºC for 3 days. The white product was obtained as a powder, which was washed three times with deionized water and dried using vacuum filtration.

NH_2-MIL-53 (Al): $AlCl_3\cdot 6H_2O$ (1.28 g, 5.30 mmol), 2-aminobenzene-1,4-dicarboxylic acid (1.50 g, 8.30 mmol) and 20 mL deionized H_2O were mixed into a 23 mL Teflon-lined stainless steel autoclave and heated at 150 °C for 3 days. The yellow powdered product was washed three times with deionized water and dried using vacuum filtration.

MIL-53 (Ga): $Ga(NO_3)_3\cdot xH_2O$ (0.26 g, 1 mmol), benzene-1,4-dicarboxylic acid (0.33 g, 2 mmol) and 10 mL deionized H_2O were mixed into a 23 mL Teflon-lined stainless steel autoclave and heated at 200 °C for 3 days. The product was obtained as colorless needle shaped crystals, which were washed three times with deionized water and dried using vacuum filtration.

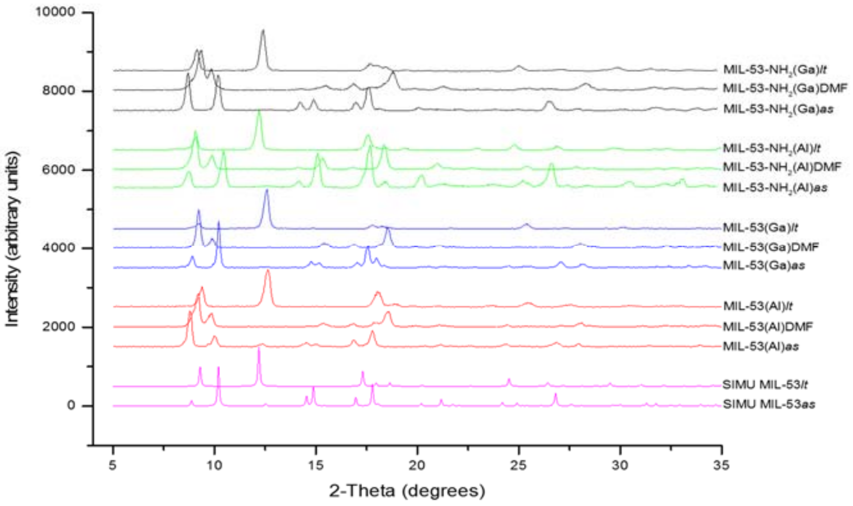

Figure 2-A1. The experimental and simulated powder X-ray diffraction of MIL-53 series MOFs are shown. The "SIMU" label denotes the simulated powder patterns, MIL-53*as* corresponds to the experimental pXRD pattern of as-made MIL-53, MIL-53*lt* corresponds to the experimental low temperature phase pXRD pattern of MIL-53, and MIL-53DMF represents the experimental pXRD pattern of MIL-53 MOF after DMF exchange.

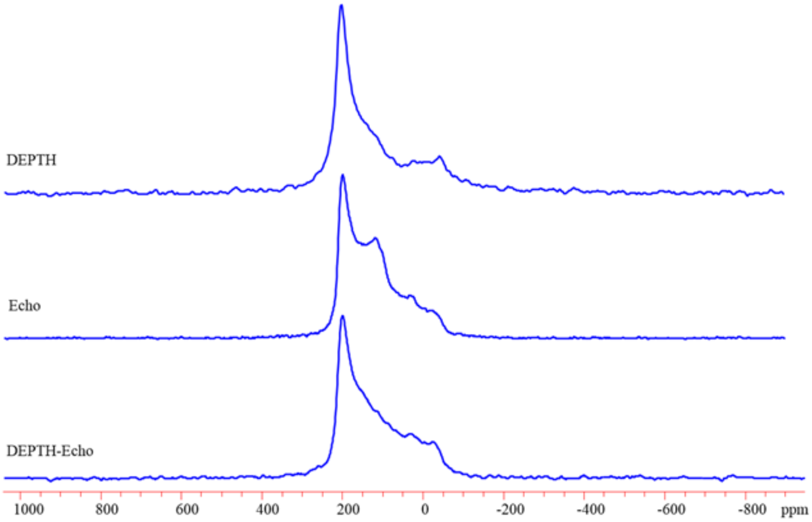

Figure 2-A2. The static ^{13}C SSNMR spectra of $^{13}CO_2$ adsorbed within MIL-53 (Al) at 293 K is shown, as acquired by using three different pulse sequences at 293 K are shown. Note the relatively small amount of spectral distortion associated with the combined DEPTH-echo pulse sequence, which was used for all direct-excitation ^{13}C experiments in this study.

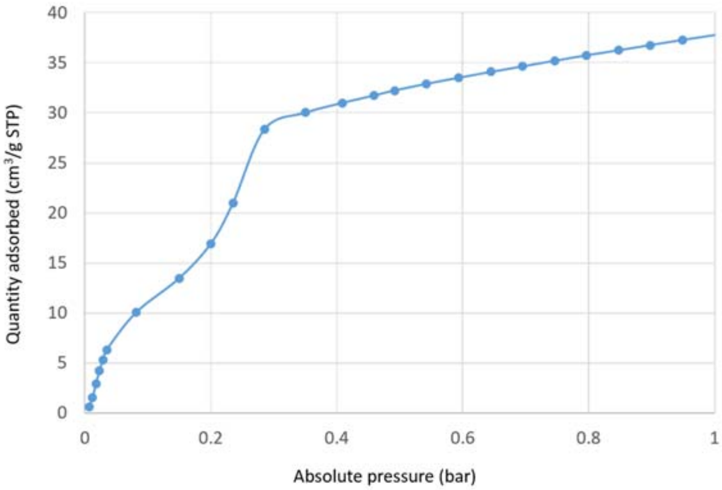

Figure 2-A3. CO_2 adsorption isotherm of MIL-53 (Ga) at 273 K. The stepwise adsorption is due to the phase transfer from very narrow pore to narrow pore

Chapter 3

3 Grasping Hydrogen Adsorption and Dynamics in Metal-Organic Frameworks using ^{2}H Solid-State NMR

Record greenhouse gas emissions have spurred the search for clean energy sources such as hydrogen (H_2) fuel cells. Metal-organic frameworks (MOFs) are promising H_2 adsorption and storage media, but knowledge of H_2 dynamics and adsorption strength in these materials is lacking. Variable-temperature (VT) ^{2}H solid-state NMR (SSNMR) experiments targeting $^{2}H_2$ gas (*i.e.*, D_2) shed light on D_2 adsorption and dynamics within six representative MOFs: UiO-66, M-MOF-74 (M = Zn, Mg, Ni), and α-$M_3(COOH)_6$ (M = Mg, Zn). D_2 binding is relatively stronger in Mg-MOF-74, Ni-MOF-74, α-$Mg_3(COOH)_6$, and α-$Zn_3(COOH)_6$, giving rise to broad ^{2}H SSNMR powder patterns. In contrast, D_2 adsorption is weaker in UiO-66 and Zn-MOF-74, as evidenced by the narrow ^{2}H resonances that correspond to rapid reorientation of the D_2 molecules. Employing ^{2}H SSNMR experiments in this fashion holds great promise for the correlation of MOF structural features and functional groups/metal centres to H_2 dynamics and host-guest interactions.

3.1 Introduction

Carbon dioxide (CO_2) is associated with the greenhouse effect and global warming. H_2 fuel cells and other "greener" solutions are the future energy sources for automobiles, however, many proposals for H_2 storage involve tanks of compressed H_2,[1] which is flammable and a safety liability. Safer alternatives for H_2 storage, such as crystalline materials,[1-2] are desired. Metal-organic frameworks (MOFs) are ordered three-dimensional structures consisting of metal centres or metal-inorganic units joined by organic linkers. By varying the MOF topology, metal centre, and linkers,[3] tailored large surface areas and guest binding strengths are possible. Several MOFs have shown H_2 adsorption and storage capabilities,[4] including UiO-66,[5-6] MOF-74,[7] α-$Mg_3(COOH)_6$.[8]

X-ray diffraction is widely used to investigate gas adsorption in MOFs but cannot reliably locate H_2. Neutron diffraction can find H_2 but little motional details can be obtained. Adsorption isotherms provide H_2 capacity yet yield little positional or dynamic data. IR spectroscopy may indicate H_2 adsorption and binding sites, but H_2 motion remains unknown. Computational methods can estimate H_2 location and dynamics, yet demand experimental verification. In order to (i) move MOFs toward practical incorporation as H_2 storage media, and (ii) enhance H_2 capacity in future MOFs, knowledge of the dynamic behavior of H_2 in today's MOFs is critical. SSNMR is a sensitive probe of the local nuclear electronic and magnetic environment, and provides rich information on MOFs from the perspective of the metals,[9] organic linkers,[10] guest molecules,[11] and dynamic components.[12-13] NMR interactions are generally anisotropic (directionally-dependent) with respect to the magnetic field and are influenced by dynamics in a predictable manner; rich motional information can be extracted from spectral simulations.[14]

When dynamics are of interest in NMR, the ^{2}H isotope is preferred over ^{1}H. ^{2}H has a spin of 1 and is subject to the anisotropic quadrupolar interaction (QI) between the nuclear quadrupole moment and surrounding electric field gradients (EFGs). Any motion that reorients the ^{2}H EFG tensor influences the QI; since the ^{2}H SSNMR spectrum is dominated by the QI, ^{2}H SSNMR is a powerful probe of guest dynamics. ^{1}H is a spin-1/2 nucleus that suffers from very strong ^{1}H-^{1}H homonuclear dipolar coupling in solids, resulting in broad ^{1}H SSNMR spectra that rarely yield useful information. ^{2}H SSNMR has proven to be an effective tool for studying the binding in metal-dihydrogen complexes,[15-17] and has been successfully used to probe D_2 mobility within a Ru-modified MOF.[18] Wright et al. have shown that ^{2}H SSNMR provides rich information on the dynamics of deuterated linkers and guests in MOFs and microporous materials.[19-23] Herein, we use VT ^{2}H SSNMR to probe H_2 adsorption in a series of different MOFs, studying the significant differences in D_2 adsorption behavior and dynamics within UiO-66, M-MOF-74 (M = Zn, Mg, Ni), and α-$M_3(COOH)_6$ (M = Mg, Zn).

3.2 Experimental Section

3.2.1 MOF synthesis

All chemicals were obtained from Sigma-Aldrich and were used without further purification. Mg-MOF-74, Ni-MOF-74, Zn-MOF-74, UiO-66, and α-$Mg_3(COOH)_6$ were synthesized using previously described methods, which are detailed below.[24-29]

Mg-MOF-74. 0.75 mmol (0.1486 g) of 2,5-dihydroxyterephthalic acid (H_4DOBDC) was dissolved in 10 mL tetrahydrofuran (THF) in a 23 mL Teflon-lined stainless steel autoclave. 3 mL of 1.0 M aqueous sodium hydroxide solution was then added to the reagent mixture. 1.5 mmol (0.3846 g) $Mg(NO_3)_2·6H_2O$ was dissolved in 5 mL deionized water, and then added to the reagent mixture in the Teflon inlet while stirring. The reagent mixture was heated in the autoclave at 110 ºC for 3 days. The powdered yellow product was washed three times with THF and dried using vacuum filtration.

Ni-MOF-74. 0.75 mmol (0.1486 g) of H_4DOBDC was first dissolved in 10 mL THF within a 23 mL Teflon-lined stainless steel autoclave. 1.5 mmol (0.3733 g) of $Ni(CH_3COO)_2·4H_2O$ was dissolved in 5 mL deionized water and then added to the reagent mixture in the Teflon inlet. After 1 hour of stirring in ambient conditions, the autoclave was sealed, and the mixture was planed in a 110 °C oven for 3 days. The ochre (i.e., yellow-orange-brown) product was obtained as a powder, which was washed three times with THF and dried using vacuum filtration.

Zn-MOF-74. Both 10 mL of THF and 0.75 mmol (0.1486 g) of H_4DOBDC were added to a 23 mL Teflon-lined stainless steel autoclave. Once the H_4DOBDC was dissolved, 3 mL aqueous sodium hydroxide solution (1 M) was added to the reagent solution. 1.5 mmol (0.4462 g) $Zn(NO_3)_2·6H_2O$ was first dissolved in 5 mL deionized water, and the resulting solution was added to the reagent mixture in the Teflon inlet while stirring. The reactants in the autoclave were heated at 110 ºC for 3 days, yielding a powdered yellow-green product that was washed three times with THF and dried using vacuum filtration.

UiO-66. A mixture of 0.54 mmol (0.125 g) $ZrCl_4$, 5 mL *N*,*N*-dimethylformamide (DMF), and 1 mL concentrated HCl (ca. 12.1 M) were mixed together and sonicated for 20 minutes until fully dissolved. This mixture was then transferred to a 23 mL Teflon-lined stainless steel autoclave, along with 0.75 mmol (0.123 g) terephthalic acid (H_2BDC) and 10 mL DMF. The resulting reagent mixture was sonicated for another 20 minutes. The autoclave was then heated for 24 hours at 80 ºC. The white product was obtained as a powder, which was washed three times with DMF, followed by another three times with ethanol. The product was dried using vacuum filtration.

α-$Mg_3(COOH)_6$. 3 mmol (0.7692 g) $Mg(NO_3)_2 \cdot 6H_2O$, 6 mmol (0.2762 g) formic acid (HCOOH), and 10 mL DMF were first mixed in a 23 mL Teflon-lined stainless steel autoclave and then heated at 110 ºC for 2 days. The white crystalline product was washed with DMF and dried using vacuum filtration.

3.2.2 Sample activation

In order to prepare activated (dehydrated) samples, the as-made Ni-MOF-74, Zn-MOF-74, UIO-66, α-$Mg_3(COOH)_6$, and α-$Zn_3(COOH)_6$ samples were heated at 150 ºC under dynamic vacuum (*i.e.*, < 1 mbar) for 8 hours. For Mg-MOF-74, an additional solvent-exchange step was required to isolate a pure, activated MOF. 0.25 g of the as-made sample was solvent-exchanged by exposure to 10 mL of methanol in an autoclave at 200 ºC for 7 days. Each day, the autoclave was removed from the oven, and the methanol stock was replaced. In the final step, the methanol exchanged Mg-MOF-74 sample was heated at 250 ºC under dynamic vacuum for 8 hours.

3.2.3 Gas adsorption

All solid-state NMR experiments were performed on a wide-bore Varian/Chemagnetics InfinityPlus NMR spectrometer operating at 9.4 T ($\upsilon_0(^2H) = 61.32$ MHz) and equipped with a 5 mm static HX probe. A sample of D_2O (l) was used as a secondary chemical shift reference at $\delta_{iso} = 4.8$ ppm with respect to neat $(CD_3)_4Si$.[30] The experimental temperature was controlled by a Varian VT control unit, and all temperatures were calibrated to ± 3 ° K using the ^{207}Pb chemical shift of a solid sample of lead nitrate across the experimental temperature range.[31] A quadrupolar echo pulse sequence of the format ($\pi/2 - \tau_1 - \pi/2 - \tau_2$) with exorcycle phase cycling was used to acquire undistorted ^{2}H NMR spectra,[32] employing a $\pi/2$ pulse width of 1.8 μs, an interpulse τ_1 time of 30 μs, and a τ_2 period of 25 μs. A ^{1}H decoupling field of ca. 90 kHz was applied during all NMR experiments.

All spectra were acquired using calibrated ^{2}H pulse delays ranging from 1 to 3 s, depending on the experimental temperature. A spectral width of 200 kHz and acquisition time of 20.5 ms was employed for all ^{2}H NMR experiments, except those on Ni-MOF-74 at temperatures of 213 K and below, which used a spectral width of 400 kHz and an acquisition time of 10.25 ms. In addition, during NMR experiments on D_2 gas adsorbed in Ni-MOF-74, the transmitter position was also gradually moved from 61.325 MHz at room temperature to 61.396 MHz at 133 K in order to ensure complete excitation and detection of the broad ^{2}H powder pattern.

3.2.4 NMR parameters

The ^{2}H nucleus has a spin of 1, which means that ^{2}H has an electric quadrupole moment (Q) and is subject to the quadrupolar interaction (QI). The QI arises from the coupling between the electric quadrupole moment of ^{2}H and surrounding local electric field gradients (EFGs). The EFG may be modeled by a traceless tensor with three orthogonal components V_{11}, V_{22}, and V_{33}, where $|V_{11}| \leq |V_{22}| \leq |V_{33}|$. ^{2}H SSNMR spectra are dominated by the first-order quadrupolar interaction, which is described using two quantities. The quadrupolar coupling constant (C_Q) describes the local spherical symmetry about ^{2}H, and is defined such that $C_Q = (eQV_{33}/h) \times 9.7177 \times 10^{21}$; e is the fundamental electric charge, h is Planck's constant, V_{33} is the component of the EFG tensor that is largest in magnitude, and 9.7177×10^{21} is a conversion factor from atomic units to Hz. A large C_Q value is indicative of relatively low local symmetry, while low C_Q values are associated with ^{2}H environments of high symmetry and/or significant molecular dynamics. The asymmetry parameter, η_Q, corresponds to the degree of axial symmetry about ^{2}H, where $\eta_Q = (V_{11} - V_{22})/V_{33}$. A high η_Q value translates to low local axial symmetry, while a low η_Q value indicates that axial symmetry is largely preserved about ^{2}H. When ^{2}H resides in an environment of high local rotational symmetry (i.e., on a ≥ C_3 rotational axis), η_Q is necessarily equal to zero.

3.2.5 Spectra simulations

The WSolids software program[33] was used to perform analytical simulations of experimental data and determine the observed, or apparent, NMR parameters. The error or uncertainty in NMR parameters was ascertained via bidirectional variation of each individual NMR parameter until noticeable discrepancies between the simulated and experimental spectra were apparent. The EXPRESS software[14] was used to simulate the effects of dynamic motion on the ^{2}H quadrupolar parameters and corresponding powder patterns, yielding the types and rates of motions present, along with their respective motional angles at all experimental temperatures.

3.2.6 Powder X-ray diffraction

The identity of all MOF products was confirmed through the use of powder XRD experiments, which were performed on an Inel CPS powder diffractometer operating with Cu Kα radiation. Reflections were collected at 2θ values ranging from 5 to 120 °. All pXRD patterns are depicted in Figure 3-A1.

3.3 Results and Discussion

3.3.1 SSNMR study of D_2 adsorbed within UIO-66

UiO-66[6] is a three-dimensional MOF composed of $Zr_6O_4(OH)_4$ units and 1,4-benzenedicarboxylate (BDC) linkers, with large octahedral and tetrahedral cages of pore sizes ca. 11 Å and 8 Å, respectively (Figure 3-1(a)). VT ^{2}H SSNMR spectra of D_2 in UiO-66 (Figure 3-1(b)) feature a narrow resonance from 293 K to 133 K with a full width at half height (FWHH) of 45 Hz throughout. Although D_2 is adsorbed in UiO-66, the large pores permit rapid diffusion of D_2 guests through the MOF void space,[5] eliminating the spectral broadening effects of the QI and giving rise to a sharp, motionally-averaged ^{2}H resonance. The narrow lineshape indicates that any localized MOF-D_2 interactions are relatively weak and easily overcome by diffusion. The tetrahedral and octahedral pore geometry may also contribute to the observed narrow resonance.

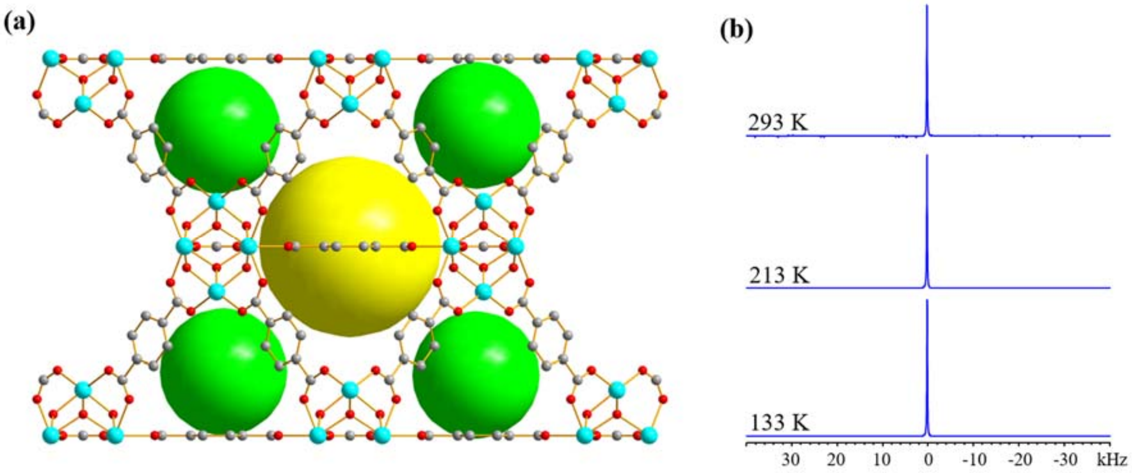

Figure 3-1. The structure of UiO-66 is shown in (a), featuring octahedral cages highlighted by the larger yellow sphere. The face of each octahedral cage is shared with 8 smaller tetrahedral cages, denoted by relatively smaller green spheres. The colors red, grey and cyan correspond to oxygen, carbon and the zirconium metal centre, respectively. Hydrogen atoms are omitted for clarity. The experimental static variable-temperature ^2H SSNMR spectra of D_2 adsorbed within UiO-66 are shown in (b). D_2 is highly mobile within the large cavities of UiO-66, giving rise to a sharp resonance at all experimental temperatures.

3.3.2 SSNMR study of D_2 adsorbed within MOF-74

M-MOF-74 (M = metal) is composed of metal centres connected by 2,5-dioxido-1,4-benzenedicarboxylate (dobdc) linkers that form honeycomb-shaped channels ca. 9 Å wide with metal centres at each vertex (Figure 3-2). Each metal centre is connected to five oxygen atoms from four linkers in the as-made MOF, along with a sixth oxygen from a water molecule that can be removed via activation. The resulting coordinatively-unsaturated open metal site (OMS) strongly encourages adsorption of H_2.[7, 34] The nature of the metal centre influences H_2 binding affinity, which increases in the order Zn < Mg < Ni.[7] The ^2H SSNMR spectrum of

D_2 in Zn-MOF-74 features a narrow resonance of 80 Hz FWHH at 293 K (Figure 3-3(a)), implying D_2 undergoes rapid isotropic reorientation in the MOF. The FWHH increases to 120 Hz at 213 K and 1920 Hz at 133 K. At lower temperatures, D_2 motion is reduced, leading to a large increase in FWHH. The ^{2}H resonance widths in Zn-MOF-74 are much larger than in UiO-66 at all temperatures, indicating that D_2 is considerably less mobile in Zn-MOF-74 due to metal-H_2 interactions; however, the lack of spectral features at 133 K confirms that D_2 dynamics remain rapid, and efficient H_2 diffusion pathways in the MOF-74 family are known to exist.[35]

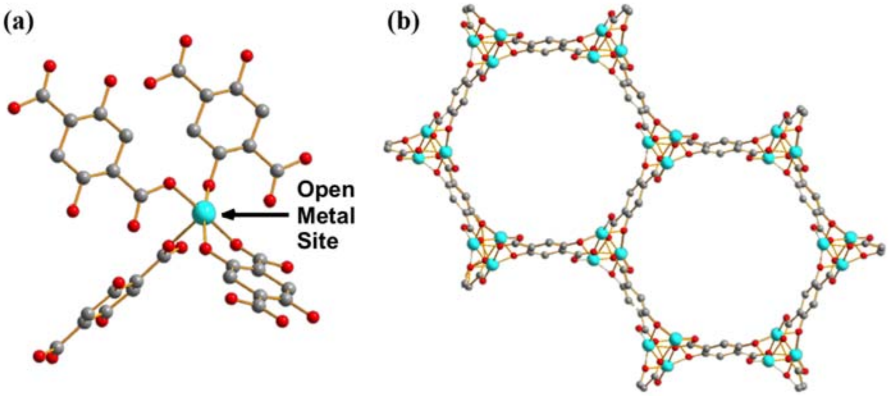

Figure 3-2. The local environment of the Mg centre in activated MOF-74 is shown in (a), showing the coordinatively-unsaturated open metal site (OMS) accessible from the interior of the MOF channel. In (b), the one-dimensional honeycomb-shaped channels of MOF-74 are shown. The colors red, grey and cyan correspond to oxygen, carbon and the metal centre, respectively. Hydrogen atoms are omitted for clarity.

Mg-MOF-74 has a higher affinity for H_2/D_2 and yields the VT SSNMR spectra in Figure 3-3(b). The narrow resonance at 293 K corresponds to highly mobile D_2 gas, while emerging broad spectral features at 173 K indicate the onset of significant D_2 adsorption. At 153 K, adsorbed D_2 gives rise to two broad ^{2}H powder patterns along with a narrow central resonance from free D_2 in the centre of the pores. The wide ^{2}H lineshapes at 133 K are intense, well-defined, and associated with most of the D_2 in Mg-MOF-74 (Figure 3-3(c)). By comparing the ^{2}H quadrupolar coupling constant (C_Q) of gaseous D_2 (225 kHz[36]) to the apparent C_Qs of D_2 in Mg-MOF-74 (Table 3-1), D_2 dynamic information can be extracted.[17] Observed $C_Q(^2H)$ values in Mg-MOF-74 are far less than 225 kHz, and are also smaller than the $C_Q(^2H)$ range of ca. 30 – 120 kHz associated with η^2 bonding between a metal and D_2 in metal-dihydrogen complexes,[17, 37-39] implying fast D_2 motion exists here and that the metal-D_2 interactions in Mg-MOF-74 are weaker than the bonding in metal-dihydrogen complexes. It should be noted that at the experimental temperatures and magnitudes of quadrupolar coupling in this study, any spectral effects arising from D_2 rotational tunneling are expected to be negligible.[40-41]

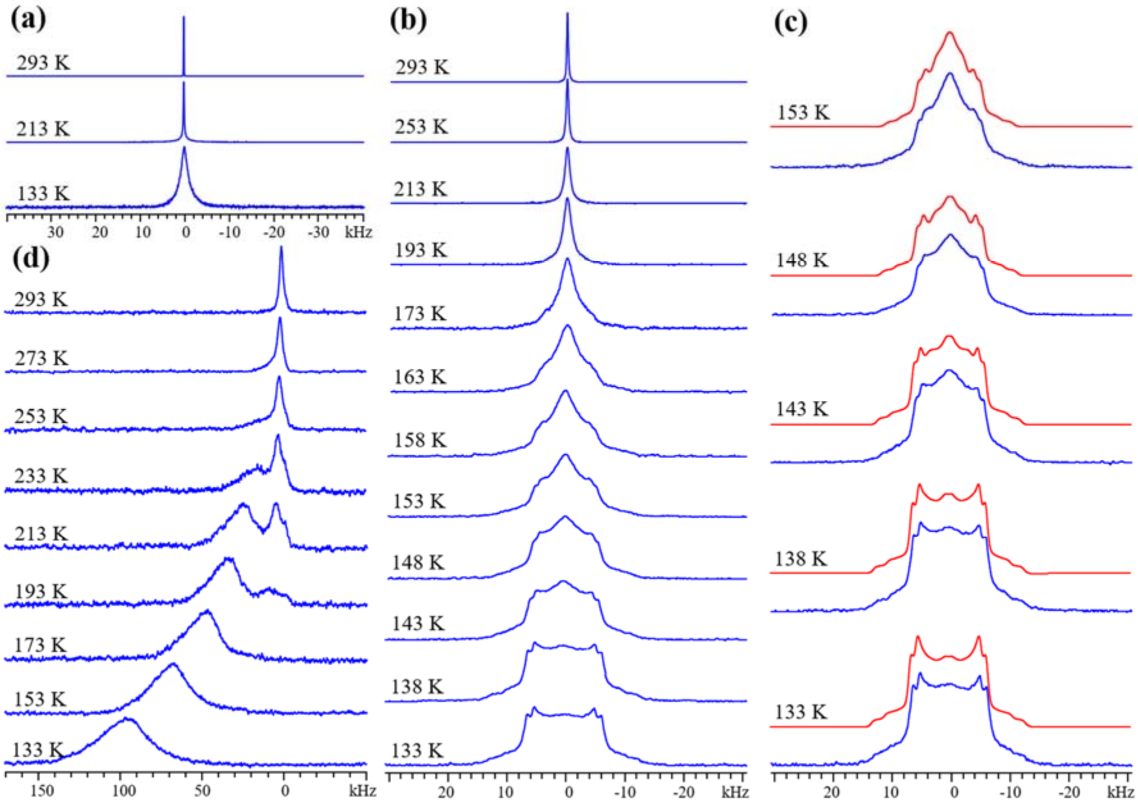

Figure 3-3. The experimental static VT ^2H SSNMR spectra of adsorbed D_2 within (a) Zn-MOF-74, (b,c) Mg-MOF-74, and (d) Ni-MOF-74 are depicted. Experimental (blue) and simulated (red) ^2H SSNMR spectra in Mg-MOF-74 at low temperatures are shown in (c). The sharp resonance at ca. 0 kHz in all spectra at high temperatures corresponds to mobile or very weakly adsorbed D_2; this resonance is broadened in (d) due to the influence of the paramagnetic Ni metal centre.

Table 3-1. The observed ^{2}H quadrupolar parameters in D_2-loaded Mg-MOF-74 at a loading level of 0.2 D_2/metal.[a,b,c]

Temperature (K)	Site	Relative intensity	C_Q (kHz)	η_Q
153	1	1	14.3(1)	0
	2	0.7	11.2(1)	0
148	1	1	15.3(1)	0
	2	0.7	12.4(1)	0
143	1	1	16.2(1)	0
	2	0.7	13.3(1)	0
138	1	1	17.0(2)	0
	2	0.7	13.9(1)	0
133	1	1	17.3(2)	0
	2	0.7	14.3(1)	0

[a] The loading level of D_2 : Mg was 0.2 in this sample of Mg-MOF-74, see Experimental details in Appendix (Section 3.6). See Table 3-A1 for NMR parameters of a 0.1 D_2:Mg sample. [b] The numbers in the parentheses correspond to the uncertainties in experimental parameters. [c] In these simulations, a sharp isotropic resonance at ca. 0 ppm was used to simulate the narrow, intense signal corresponding to mobile D_2, which lacks any quadrupolar parameters.

The same two powder patterns and NMR parameters persist, along with the sharp component, when the loading level is halved to 0.1 D_2/Mg (Figures 3-A2, Figure 3-A3 Table 3-A1). The two broad ^{2}H powder patterns of D_2 in Mg-MOF-74 reveal that there are two similar, but nonequivalent D_2 molecules (D_2(1) and D_2(2)) adsorbed on two different OMSs, as indicated by their QI parameters and D_2 motions (see Appendix), while the narrow third resonance indicates that highly mobile D_2 is also present. Previous studies have suggested that there may be two very similar H_2 adsorption sites of nearly identical adsorption enthalpy localized on the OMS near our experimental loading levels with slightly different interaction geometries.[42-43] There are 6 OMSs located near the same cross-sectional plane per channel (Figure 3-2(b)). At the low loading level of 0.1 D_2/metal, on average, there is less than one D_2 guest per channel cross-section. Thus, it is reasonable to assume that no two D_2 molecules are adsorbed simultaneously on the same OMS at any given time. It is likely that each channel cross-section contains only 1 D_2 molecule that is in rapid exchange among the 6 sites (*vide infra*). Based on the intensity ratios in Table 3-A1, ca. 59% of the channel cross-sections are populated by D_2(1) and 41% of the channel cross-sections are occupied by D_2(2).

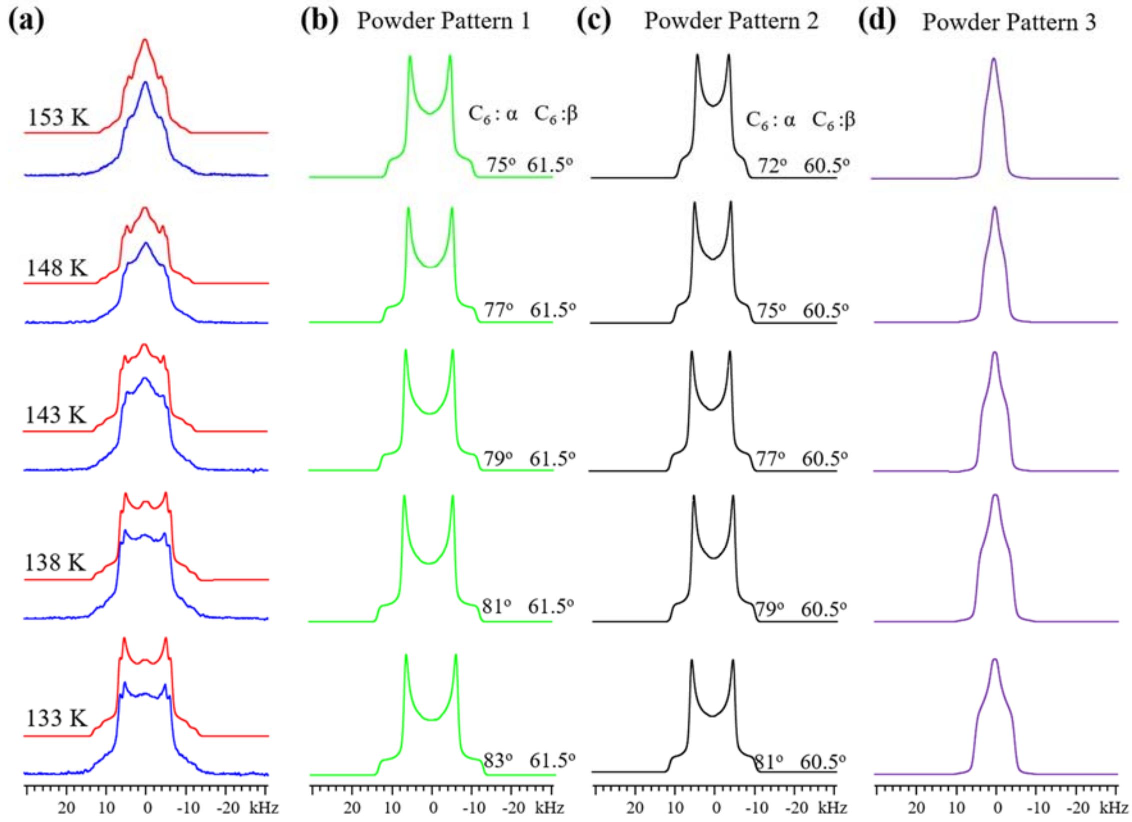

Figure 3-4. ^{2}H SSNMR spectra of D_2 adsorbed in Mg-MOF-74 at a loading level of 0.2 D_2 : Mg are illustrated. In (a), a comparison of experimental (blue) and simulated (red) static ^{2}H SSNMR spectra at low temperatures is shown. The individual simulated spectra for each powder pattern are shown in (b), (c), and (d). All simulations were performed using a fast rate of motion (10^9 Hz). The C_6 six-fold rotation and accompanying angle α describe the localized wobbling of D_2 at the adsorption sites on the open metal site, while the other C_6 motion and the angle β refer to a non-localized six-fold hopping about the circumference of the MOF channel between open metal sites. Powder patterns 1 and 2 are assigned to D_2 adsorbed on the open metal site, while powder pattern 3 corresponds to mobile D_2 not locally adsorbed to the MOF.

Using the known ^{2}H QI parameters of D_2 gas ($C_Q(^2H)$ = 225 kHz, $\eta_Q = 0$),[36] simulations[14] of motionally-averaged ^{2}H spectra (Figure 3-4) reveal common D_2 dynamics exist at the two similar adsorption sites on the OMS in Mg-MOF-74 (Figure 3-2(a)). D_2 undergoes a local rotation or "wobbling" modeled by a sixfold rotation about the minimum energy configuration with respect to the OMS (Figure 3-5(a)), as well as a non-localized six-site hopping along the pore edge (Figure 3-5(b)). The combined motional model is shown in Figure 3-5(c). The wobbling describes a rotation of the D-D bond about the axis passing through the OMS (Figure 3-5(a)), as defined by the angle α. It is likely that the wobbling rotation represents a model for some kind of rotational diffusion on the OMS. The hopping occurs between six nearly coplanar OMSs, where three reside in one plane, and the other three OMSs are in a very proximate plane slightly offset along the longitudinal direction of the channel. It should be noted that since the wobbling and hopping motional rates are in the fast exchange limit, there are an infinite number of C_n ($n \geq 3$) jumping motions that could lead to the observed powder patterns. The dynamic behavior of D_2 at both adsorption sites is strikingly similar, supporting the notion of two H_2 adsorption sites of nearly identical interaction geometry and enthalpy on the OMS: each has D_2 wobbling angles increasing from ca. 74 ° at 293 K to 82 ° at 133 K, along with constant hopping angles of ca. 60 ° (Figure 3-4). The larger wobbling angle at low temperatures enhances the interaction of D_2 with the Mg site. It should also be noted that simulation of fast-exchange SSNMR spectra can sometimes lead to more than one motional model. However, we were unable to simulate the split "horns" or characteristic "shoulders" of the low-temperature spectra using a single adsorption site with any type of possible motions. These results also suggest that there does not seem to be significant exchange of D_2 between the two adsorption sites; raising the possibility that the sites are somehow segregated or correspond to slightly different types of OMSs in separate MOF channels. The calculated H_2 position in Co-MOF-74[44] strongly agrees with the orientations in our motional model, while the types of D_2 dynamics resemble those of CO_2 and CO in MOF-74.[45-47] To confirm at low temperatures the D_2 motional rate remains in the fast (i.e., $\geq 10^7$ Hz) and not the intermediate regime, quadrupolar echo experiments with different inter-pulse delays were performed, resulting in unchanged spectra (Figures 3-A4 and A5, Table 3-A2).

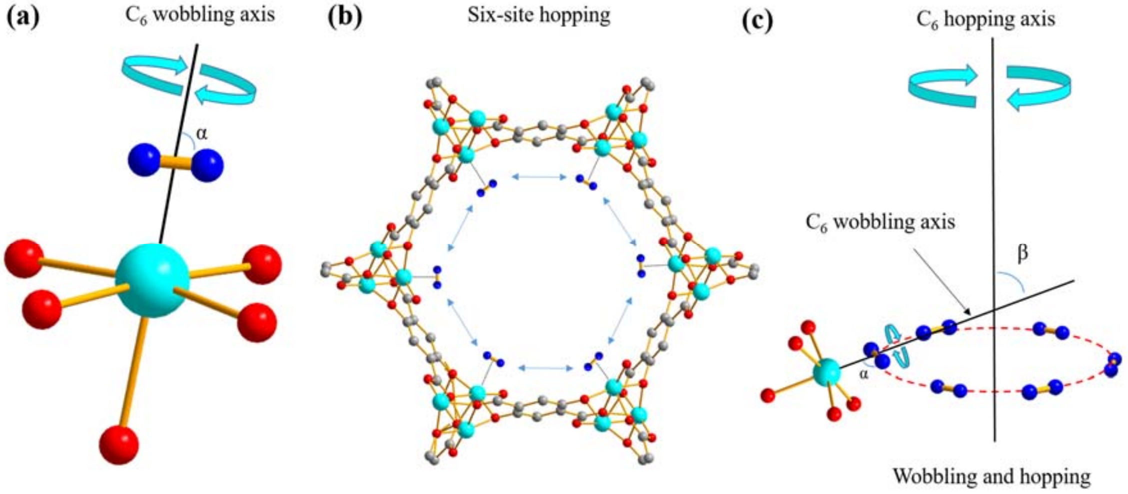

Figure 3-5. The localized C_6 rotation, or wobbling, of D_2 molecules adsorbed on the OMS is shown in (a). The black dashed line represents the metal-D_2 vector; the cone of D_2 wobbling movement traces out an angle α about the wobbling axis. A schematic of D_2 hopping in MOF-74 is shown in (b). The combination of wobbling (C_6 rotation, α) and six-site hopping (C_6 rotation, β) of D_2 molecules in MOF-74 is shown in (c), where the wobbling axis makes an angle β with respect to the hopping axis. The colors red, grey, blue and cyan correspond to oxygen, carbon, deuterium and the metal centre, respectively. Our data indicates that there are two very similar D_2 adsorption sites on the OMS, giving rise to two separate ^{2}H SSNMR powder patterns.

Ni-MOF-74 has a stronger H_2/D_2 binding affinity.[7] Unlike diamagnetic Zn^{2+} and Mg^{2+}, Ni^{2+} is paramagnetic in this MOF. The ^{2}H magnetic dipole couples with those of proximate unpaired electrons, resulting in spectral broadening and unusual chemical shifts when D_2 is near Ni^{2+}. VT ^{2}H SSNMR spectra of D_2 in Ni-MOF-74 (Figure 3-3(d)) at room temperature reveal that D_2 is mobile and/or rapidly exchanging with adsorbed D_2. The broad 1.2 kHz FWHH confirms D_2 and Ni^{2+} proximity. At 273 K, a second, broader resonance emerges at 140 ppm, corresponding to D_2 adsorbed on the OMS. At 213 K, the broad resonance is at 375 ppm and is the dominant feature. The broad resonance increases in frequency, width, and relative intensity as temperature is reduced; the narrower resonance at lower frequency vanishes at 173 K, implying most D_2 is adsorbed. At 133 K a broad, featureless ^2H resonance of FWHH 30 kHz centered about 1550 ppm is evident, confirming a majority of D_2 is adsorbed at the OMS. The featureless nature of these resonances prohibits detailed analysis.[48]

3.3.3 SSNMR study of D_2 adsorbed within α-$Mg_3(COOH)_6$

α-$Mg_3(COOH)_6$ is porous MOF[8, 29, 49] with one-dimensional zig-zag channels of small ca. 4-5 Å diameter (Figure 3-6). It is possible to load H_2 within α-$Mg_3(COOH)_6$, and the corresponding NMR parameters and motional data may be extracted from ^2H SSNMR spectra of deuterated H_2 gas (i.e, $^2H_2$ or D_2). In this work, we have successfully obtained and simulated ^2H SSNMR spectra at temperatures ranging from 293 to 123 K (Figure 3-7(a)) to extract both the apparent ^2H NMR parameters as well as the motional parameters[14] (Table 3-2), which can be interpreted given the known ^2H QI parameters of D_2 gas ($C_Q(^2H)$ = 225 kHz, $\eta_Q = 0$).[36]

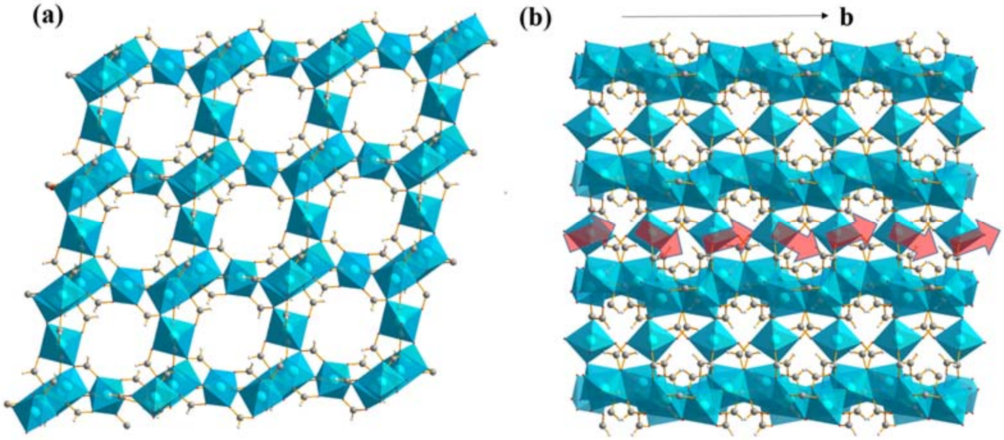

Figure 3-6. The structure of the α-$Mg_3(COOH)_6$ is shown, with views chosen to feature (a) the one-dimensional channels along the (0 1 0) direction, and (b) the zig-zag longitudinal shape of the channels along the crystallographic *b* axis.

Table 3-2. The apparent NMR parameters (relative intensity, C_Q, η_Q) and dynamic (C_6, C_2) parameters of D_2 guests in α-$Mg_3(COOH)_6$. In all instances, $\delta_{iso} = 0$ ppm. Site 3 corresponds to the sharp central resonance arising from free, non-adsorbed D_2; SSNMR indicates that there are only two unique adsorption sites for D_2 at these temperatures and loading levels. All motions occur at a rate ≥ 10^7 Hz.

Temperature (K)	**Site**	**Relative intensity**	**C_Q (kHz)**	**η_Q**	**C_6 wobbling (α, °)**	**C_2 hopping (β, °)**
163	1	1.00(5)	19.2(1)	0.59(1)	46.0(1)	50.7(2)
	2	1.00(5)	22.7(1)	0.72(1)	44.2(1)	51.9(2)
	3	0.42(2)	0.7(1)	1.00(10)		
153	1	1.00(5)	20.3(1)	0.59(1)	45.4(1)	50.7(2)
	2	1.00(5)	24.2(1)	0.72(1)	43.4(1)	51.9(2)
	3	0.31(2)	0.7(1)	1.00(10)		
143	1	1.00(5)	22.0(1)	0.59(1)	44.5(1)	50.7(2)
	2	1.00(5)	25.5(1)	0.72(1)	42.8(1)	51.9(2)
	3	0.21(2)	0.7(1)	1.00(10)		
133	1	1.00(5)	23.5(1)	0.58(1)	43.8(1)	50.6(2)
	2	1.00(5)	27.2(2)	0.71(1)	41.9(1)	51.8(2)
	3	0.16(1)	0.8(1)	1.00(10)		
128	1	1.00(5)	24.0(1)	0.58(1)	43.5(1)	50.6(2)
	2	1.00(5)	28.0(2)	0.71(1)	41.5(1)	51.8(2)
	3	0.13(1)	0.9(1)	1.00(10)		
123	1	1.00(5)	24.8(1)	0.57(1)	43.1(1)	50.5(2)
	2	1.00(5)	29.0(2)	0.70(1)	41.0(1)	51.7(2)
	3	0.11(1)	0.9(1)	1.00(10)		

The presence of two similar ^{2}H SSNMR powder patterns of equal relative intensity (Figure 3-7(b,c)) indicates that two unique D_2 adsorption sites are equally populated throughout the temperature range of our VT SSNMR experiments along with a sharp resonance attributed to free isotropically tumbling D_2, although there is additional subtle "shouldering" evident on the very outside edges of the ^{2}H SSNMR powder pattern at 123 K that hints at the existence of an additional third unique D_2 adsorption site at lower temperatures (Figure 3-7(b,c)). In agreement, theoretical calculations have indicated that there should be three H_2 adsorption sites present in α-$Mg_3(COOH)_6$ at a loading level of

1.6 hydrogen molecules per unit cell;[50] which is slightly higher than our loading level of ca. 1.2 D_2 molecules per unit cell. It is likely that, at our relatively lower H_2 loading level, the third H_2 adsorption site only becomes significantly populated at very low temperatures (*i.e.*, < 123 K).

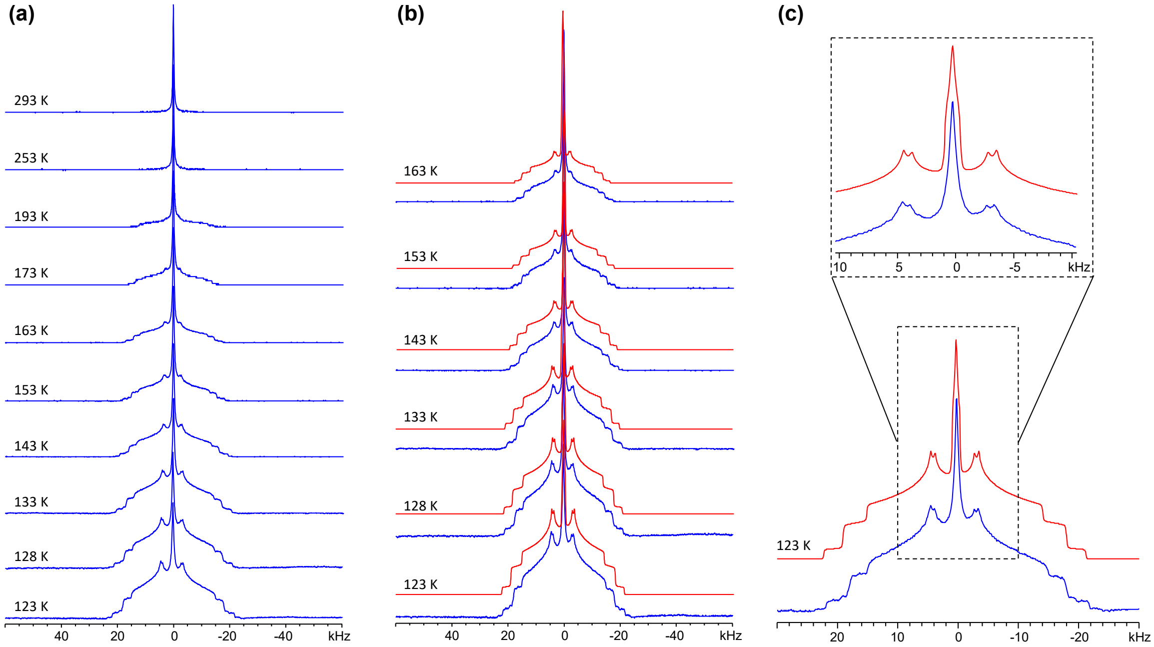

Figure 3-7. The experimental static VT ^{2}H SSNMR spectra of D_2 adsorbed in α-$Mg_3(COOH)_6$ are shown as blue traces in (a), with the corresponding low-temperature analytical simulations shown as red traces in (b). In (c), an enlargement of the experimental and simulated ^{2}H powder patterns at 123 K are shown at bottom, with the splitting of the interior "horns" indicative of the presence of two individual powder patterns shown inset at top.

Judging from the very similar ^{2}H SSNMR powder patterns (Figure 3-8), the two D_2 adsorption sites within α-$Mg_3(COOH)_6$ seem to be nearly identical in relative population and local environment at all experimental temperatures, implying that both adsorption sites are located in nearly identical environments. In this case, one of the most interesting observations is that η_Q strays from 0 in α-$Mg_3(COOH)_6$, indicating there is a significant bonding interaction between the MOF and D_2 that is influencing the orientation and magnitude of the ^{2}H EFG tensor components. Dynamic simulations of ^{2}H SSNMR spectra indicate that D_2 adsorbed within α-$Mg_3(COOH)_6$ undergoes both localized rotational wobbling as well as non-localized twofold (C_2) hopping between adsorption sites (Table 3-2). As the temperature decreases, the ^{2}H powder pattern width (*i.e.*, $C_Q(^2H)$) increases, and the wobbling angle (α) of D_2 in α-$Mg_3(COOH)_6$ decreases (Table 3-2), reflecting decreased D_2 mobility at lower temperatures. At this point, the nature of the adsorption sites is unclear from SSNMR experiments. We are currently performing more detailed studies in order to extract detailed D_2 motional and adsorption information from α-$Mg_3(COOH)_6$.

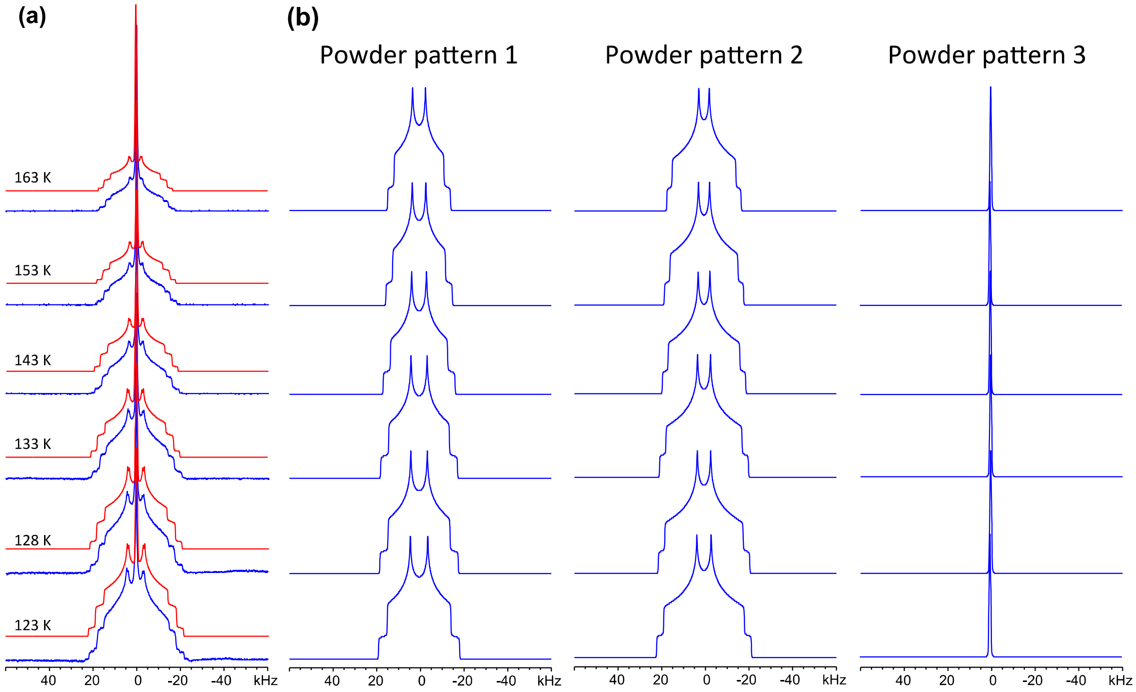

Figure 3-8. The experimental (blue) and motionally-simulated (red) static VT ^{2}H SSNMR spectra of D_2 in α-$Mg_3(COOH)_6$ are shown in (a), with all three powder patterns that contribute to the overall simulation shown side-by-side in (b) for clarity. Note that the resonance illustrated on the right is a very narrow resonance originating from free, non-adsorbed, isotropically tumbling D_2 molecules.

3.4 Conclusions

^{2}H SSNMR spectroscopy has revealed unique insights into H_2 dynamics and adsorption locations within these six MOFs; this information is unavailable or very difficult to obtain using traditional MOF characterization methods such as adsorption isotherms and X-ray diffraction. Complementary methods such as neutron diffraction, inelastic neutron scattering, and VT infrared spectroscopy are necessary to locate adsorption locations, but yield limited motional data. Variation of the MOF topology, metal centre, and linker gives rise to very different D_2 dynamic behaviors and adsorption strengths. Further studies employing lower temperatures (i.e., < 100 K) are necessary to reduce H_2 mobility and obtain richer dynamic knowledge in these systems, however, these experiments are not yet possible with the equipment available to us. We have used relatively low levels of D_2 loading to simplify these systems for spectral simulations; the next step is to explore higher D_2 loading levels in order to understand the implications for H_2 motion in a practical hydrogen storage setting. The comprehensive molecular-level knowledge of H_2 dynamics and adsorption in MOFs available from ^2H SSNMR spectroscopy will undoubtedly assist in establishing clear links between H_2 dynamics and high-capacity H_2 storage in porous materials, with clear applications in green energy solutions.

3.5 References

1. Durbin, D. J.; Malardier-Jugroot, C., *Int. J. Hydrogen Energy* **2013,** *38* (34), 14595-14617.

2. Yang, J.; Sudik, A.; Wolverton, C.; Siegel, D. J., *Chem. Soc. Rev.* **2010,** *39* (2), 656-675.

3. Allendorf, M. D.; Stavila, V., *CrystEngComm* **2015,** *17* (2), 229-246.

4. Suh, M. P.; Park, H. J.; Prasad, T. K.; Lim, D.-W., *Chem. Rev.* **2012,** *112* (2), 782-835.

5. Chavan, S.; Vitillo, J. G.; Gianolio, D.; Zavorotynska, O.; Civalleri, B.; Jakobsen, S.; Nilsen, M. H.; Valenzano, L.; Lamberti, C.; Lillerud, K. P.; Bordiga, S., *Phys. Chem. Chem. Phys.* **2012,** *14* (5), 1614-1626.

6. Cavka, J. H.; Jakobsen, S.; Olsbye, U.; Guillou, N.; Lamberti, C.; Bordiga, S.; Lillerud, K. P., *J. Am. Chem. Soc.* **2008,** *130* (42), 13850-13851.

7. Zhou, W.; Wu, H.; Yildirim, T., *J. Am. Chem. Soc.* **2008,** *130* (46), 15268-15269.

8. Schmitz, B.; Krkljus, I.; Leung, E.; Höffken, H. W.; Müller, U.; Hirscher, M., *ChemSusChem* **2010,** *3* (6), 758-761.

9. He, P.; Lucier, B. E. G.; Terskikh, V. V.; Shi, Q.; Dong, J.; Chu, Y.; Zheng, A.; Sutrisno, A.; Huang, Y., *J. Phys. Chem. C* **2014,** *118* (41), 23728-23744.

10. Kolokolov, D. I.; Stepanov, A. G.; Guillerm, V.; Serre, C.; Frick, B.; Jobic, H., *J. Phys. Chem. C* **2012,** *116* (22), 12131-12136.

11. Kolokolov, D. I.; Jobic, H.; Rives, S.; Yot, P. G.; Ollivier, J.; Trens, P.; Stepanov, A. G.; Maurin, G., *J. Phys. Chem. C* **2015,** *119* (15), 8217-8225.

12. Zhu, K.; O'Keefe, C. A.; Vukotic, V. N.; Schurko, R. W.; Loeb, S. J., *Nat. Chem.* **2015,** *7* (6), 514-519.

13. Vukotic, V. N.; O'Keefe, C. A.; Zhu, K.; Harris, K. J.; To, C.; Schurko, R. W.; Loeb, S. J., *J. Am. Chem. Soc.* **2015,** *137* (30), 9643-9651.

14. Vold, R. L.; Hoatson, G. L., *J. Magn. Reson.* **2009,** *198* (1), 57-72.

15. Gutmann, T.; del Rosal, I.; Chaudret, B.; Poteau, R.; Limbach, H. H.; Buntkowsky, G., *ChemPhysChem* **2013,** *14* (13), 3026-3033.

16. Morris, R. H., *Coord. Chem. Rev.* **2008,** *252* (21-22), 2381-2394.

17. Facey, G. A.; Fong, T. P.; Gusev, D.; Macdonald, P. M.; Morris, R. H.; Schlaf, M.; Xu, W., *Can. J. Chem.* **1999,** *77* (11), 1899-1910.

18. Schröder, F.; Esken, D.; Cokoja, M.; van den Berg, M. W. E.; Lebedev, O. I.; Van Tendeloo, G.; Walaszek, B.; Buntkowsky, G.; Limbach, H.-H.; Chaudret, B.; Fischer, R. A., *J. Am. Chem. Soc.* **2008,** *130* (19), 6119-6130.

19. Mowat, J. P. S.; Miller, S. R.; Griffin, J. M.; Seymour, V. R.; Ashbrook, S. E.; Thompson, S. P.; Fairen-Jimenez, D.; Banu, A.-M.; Düren, T.; Wright, P. A., *Inorg. Chem.* **2011,** *50* (21), 10844-10858.

20. Gonzalez, J.; Devi, R. N.; Wright, P. A.; Tunstall, D. P.; Cox, P. A., *J. Phys. Chem. B* **2005,** *109* (46), 21700-21709.

21. Gonzalez, J.; Devi, R. N.; Tunstall, D. P.; Cox, P. A.; Wright, P. A., *Microporous Mesoporous Mater.* **2005,** *84* (1-3), 97-104.

22. Devi, R. N.; Edgar, M.; Gonzalez, J.; Slawin, A. M. Z.; Tunstall, D. P.; Grewal, P.; Cox, P. A.; Wright, P. A., *J. Phys. Chem. B* **2004,** *108* (2), 535-543.

23. Carter, V. J.; Kujanpää, J. P.; Riddell, F. G.; Wright, P. A.; Turner, J. F. C.; Catlow, C. R. A.; Knight, K. S., *Chem. Phys. Lett.* **1999,** *313* (3–4), 505-513.

24. Dietzel, P. D.; Johnsen, R. E.; Blom, R.; Fjellvag, H., *Chem. -Eur. J.* **2008,** *14* (8), 2389-2397.

25. Dietzel, P. D. C.; Blom, R.; Fjellvag, H., *Eur. J. Inorg. Chem.* **2008,** (23), 3624-3632.

26. Dietzel, P. D. C.; Panella, B.; Hirscher, M.; Blom, R.; Fjellvag, H., *Chem. Commun.* **2006,** (9), 959-961.

27. Katz, M. J.; Brown, Z. J.; Colon, Y. J.; Siu, P. W.; Scheidt, K. A.; Snurr, R. Q.; Hupp, J. T.; Farha, O. K., *Chem. Commun.* **2013,** *49* (82), 9449-9451.

28. Rood, J. A.; Noll, B. C.; Henderson, K. W., *Inorg. Chem.* **2006,** *45* (14), 5521-5528.

29. Wang, Z.; Zhang, Y.; Kurmoo, M.; Liu, T.; Vilminot, S.; Zhao, B.; Gao, S., *Aust. J. Chem.* **2006,** *59* (9), 617-628.

30. Gottlieb, H. E.; Kotlyar, V.; Nudelman, A., *J. Org. Chem.* **1997,** *62* (21), 7512-7515.

31. Dybowski, C.; Neue, G., *Prog. Nucl. Magn. Reson. Spectrosc.* **2002,** *41* (3–4), 153-170.

32. Antonijevic, S.; Wimperis, S., *J. Magn. Reson.* **2003,** *164* (2), 343-350.

33. Eichele K.; Wasylishen R. E., *WSolids1* University of Tübingen, Tübingen, Germany, **2009**.

34. Sumida, K.; Brown, C. M.; Herm, Z. R.; Chavan, S.; Bordiga, S.; Long, J. R., *Chem. Commun.* **2011,** *47* (4), 1157-1159.

35. Canepa, P.; Nijem, N.; Chabal, Y. J.; Thonhauser, T., *Phys. Rev. Lett.* **2013,** *110* (2), 026102.

36. Code, R. F.; Ramsey, N. F., *Phys. Rev. A* **1971,** *4* (5), 1945-1959.

37. Walaszek, B.; Adamczyk, A.; Pery, T.; Xu, Y. P.; Gutmann, T.; Amadeu, N. D.; Ulrich, S.; Breitzke, H.; Vieth, H. M.; Sabo-Etienne, S.; Chaudret, B.; Limbach, H. H.; Buntkowsky, G., *J. Am. Chem. Soc.* **2008,** *130* (51), 17502-17508.

38. Bakhmutov, V. I., *Magn. Reson. Chem.* **2004,** *42* (1), 66-70.

39. Macholl, S.; Matthes, J.; Limbach, H. H.; Sabo-Etienne, S.; Chaudret, B.; Buntkowsky, G., *Solid State Nucl. Magn. Reson.* **2009,** *36* (3), 137-143.

40. Wehrmann, F.; Albrecht, J.; Gedat, E.; Kubas, G. J.; Eckert, J.; Limbach, H. H.; Buntkowsky, G., *J. Phys. Chem. A* **2002,** *106* (12), 2855-2861.

41. Wehrmann, F.; P. Fong, T.; H. Morris, R.; Limbach, H.-H.; Buntkowsky, G., *Phys. Chem. Chem. Phys.* **1999,** *1* (17), 4033-4041.

42. Vitillo, J. G.; Regli, L.; Chavan, S.; Ricchiardi, G.; Spoto, G.; Dietzel, P. D. C.; Bordiga, S.; Zecchina, A., *J. Am. Chem. Soc.* **2008,** *130* (26), 8386-8396.

43. Dietzel, P. D. C.; Georgiev, P. A.; Eckert, J.; Blom, R.; Strassle, T.; Unruh, T., *Chem. Commun.* **2010,** *46* (27), 4962-4964.

44. Kapelewski, M. T.; Geier, S. J.; Hudson, M. R.; Stück, D.; Mason, J. A.; Nelson, J. N.; Xiao, D. J.; Hulvey, Z.; Gilmour, E.; FitzGerald, S. A.; Head-Gordon, M.; Brown, C. M.; Long, J. R., *J. Am. Chem. Soc.* **2014,** *136* (34), 12119-12129.

45. Lin, L. C.; Kim, J.; Kong, X. Q.; Scott, E.; McDonald, T. M.; Long, J. R.; Reimer, J. A.; Smit, B., *Angew. Chem. Int. Ed.* **2013,** *52* (16), 4410-4413.

46. Wang, W. D.; Lucier, B. E. G.; Terskikh, V. V.; Wang, W.; Huang, Y., *J. Phys. Chem. Lett.* **2014,** *5*, 3360-3365.

47. Lucier, B. E. G.; Chan, H.; Zhang, Y.; Huang, Y., *Eur. J. Inorg. Chem.* **2016**, *13-14,* 2017-2024.

48. Lee, H.; Polenova, T.; Beer, R. H.; McDermott, A. E., *J. Am. Chem. Soc.* **1999,** *121* (29), 6884-6894.

49. Rood, J. A.; Noll, B. C.; Henderson, K. W., *Inorg. Chem.* **2006,** *45* (14), 5521-5528.

50. Pham, T.; Forrest, K. A.; Falcao, E. H. L.; Eckert, J.; Space, B., *Phys. Chem. Chem. Phys.* **2016,** *18* (3), 1786-1796.

3.6 Appendix

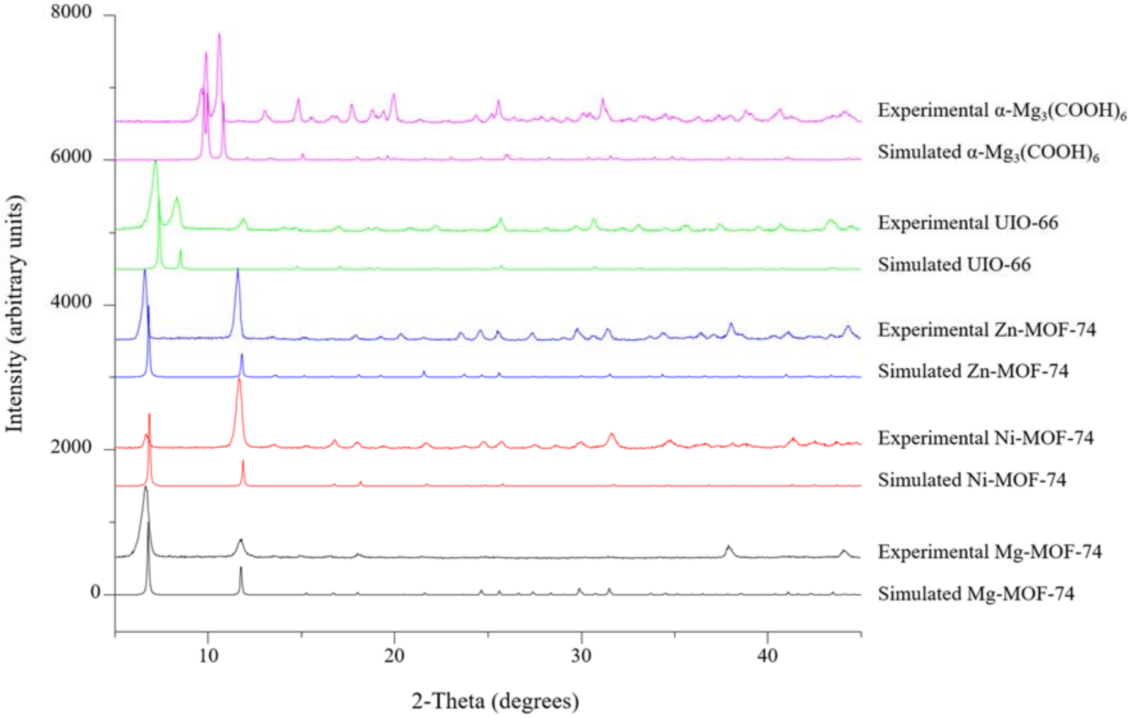

Figure 3-A1. The experimental and simulated powder X-ray diffraction patterns of the MOFs included in this study.

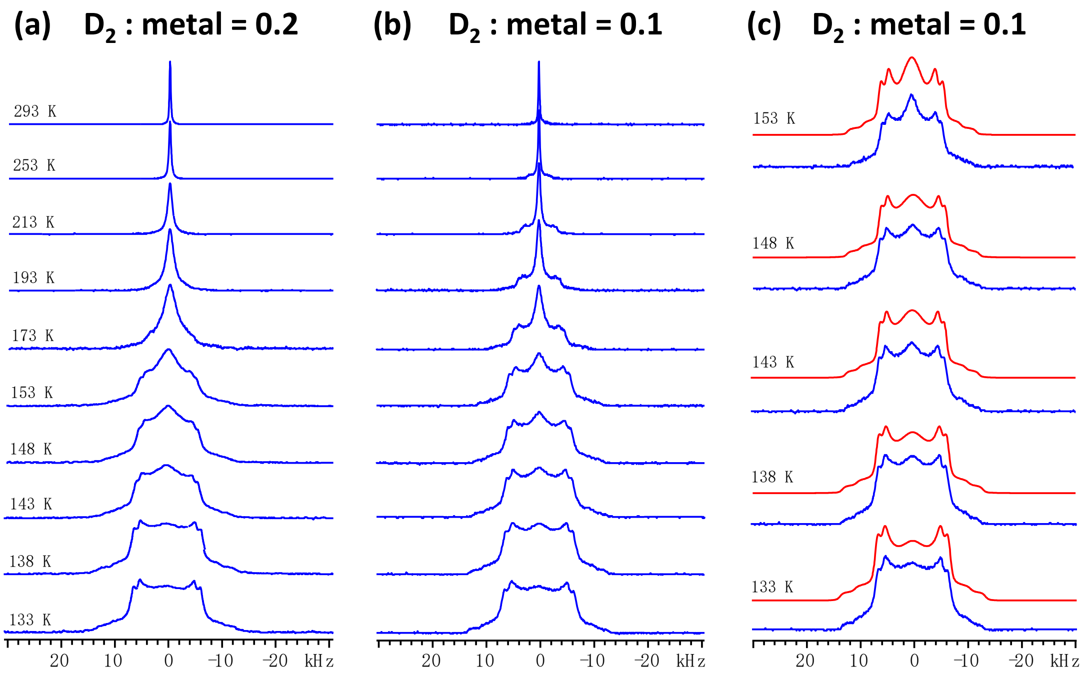

Figure 3-A2. The experimental ^{2}H SSNMR spectra of D_2 loaded in Mg-MOF-74 at the loading levels of 0.2 and 0.1 D_2:Mg are shown in (a) and (b), respectively. In (c), simulated spectra for the 0.1 loading level are shown, with corresponding parameters summarized in Table 3-A1. See Figure 3-A3 for a deconvolution of the 0.1 loading level simulations.

Table 3-A1. The observed ^{2}H quadrupolar parameters in D_2-loaded Mg-MOF-74 at a loading level of 0.1 D_2/metal.[a,b,c]

Temperature (K)	Site	Relative intensity	C_Q (kHz)	η_Q
153	1	1	15.6(1)	0
	2	0.7	12.3(1)	0
148	1	1	16.2(1)	0
	2	0.7	12.9(1)	0
143	1	1	16.7(1)	0
	2	0.7	13.4(1)	0
138	1	1	17.5(2)	0
	2	0.7	13.9(1)	0
133	1	1	18.9(2)	0
	2	0.7	14.3(1)	0

[a] The loading level of D_2:Mg was 0.1 in this sample of Mg-MOF-74. [b] The numbers in the parentheses correspond to the uncertainties in experimental parameters. [c] In these simulations, a sharp isotropic resonance at ca. 0 ppm was used to simulate the narrow, intense signal corresponding to mobile D_2, which lacks any quadrupolar parameters.

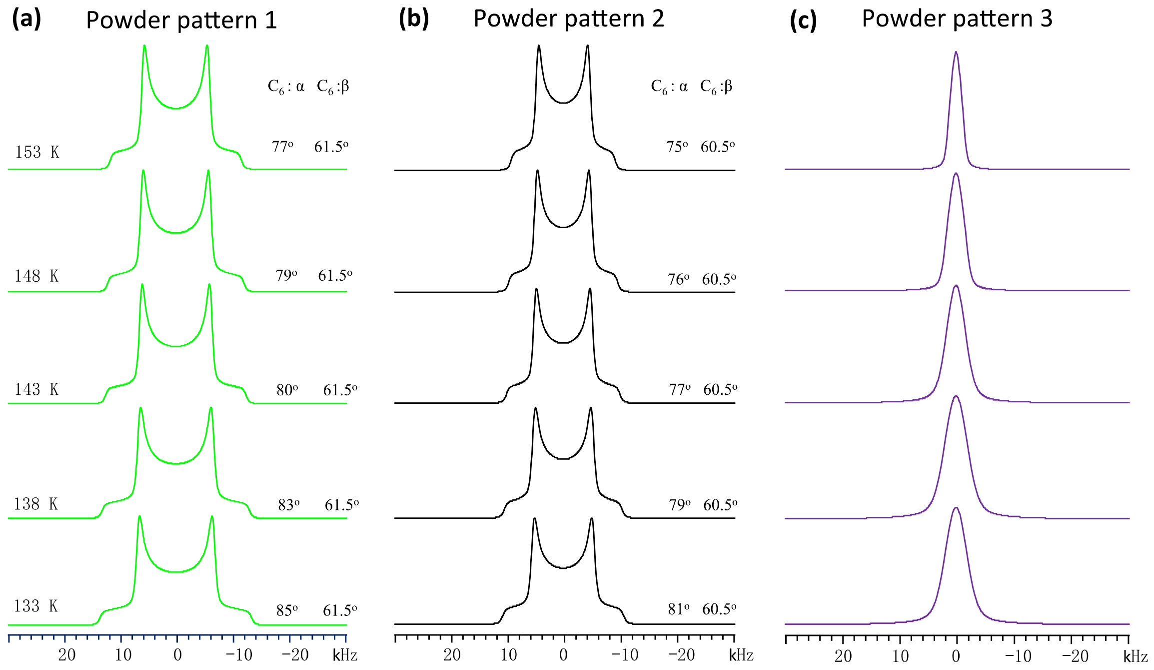

Figure 3-A3. A deconvolution of the powder patterns that compose the ^{2}H SSNMR spectrum of 0.1 D_2/Mg loaded in Mg-MOF-74. The individual simulated spectra for each powder pattern are shown in (a), (b), and (c). All simulations were performed using the EXPRESS software and a fast rate of motion (10^9 Hz). The C_6 sixfold rotation and accompanying angle α describe the localized wobbling of D_2 about the adsorption site (*i.e.*, open metal site), while the other C_6 motion and the angle β refer to a non-localized six-fold hopping of D_2 about the circumference of the MOF channel between open metal sites. The intensity ratio between powder patterns 1 and 2 is 1: 0.7 in this temperature range. Powder patterns 1 and 2 are assigned to D_2 adsorbed on the open metal site in slightly different geometries, orientations, and/or locations. The third powder pattern corresponds to free, mobile D_2 and is modeled by a narrow distribution.

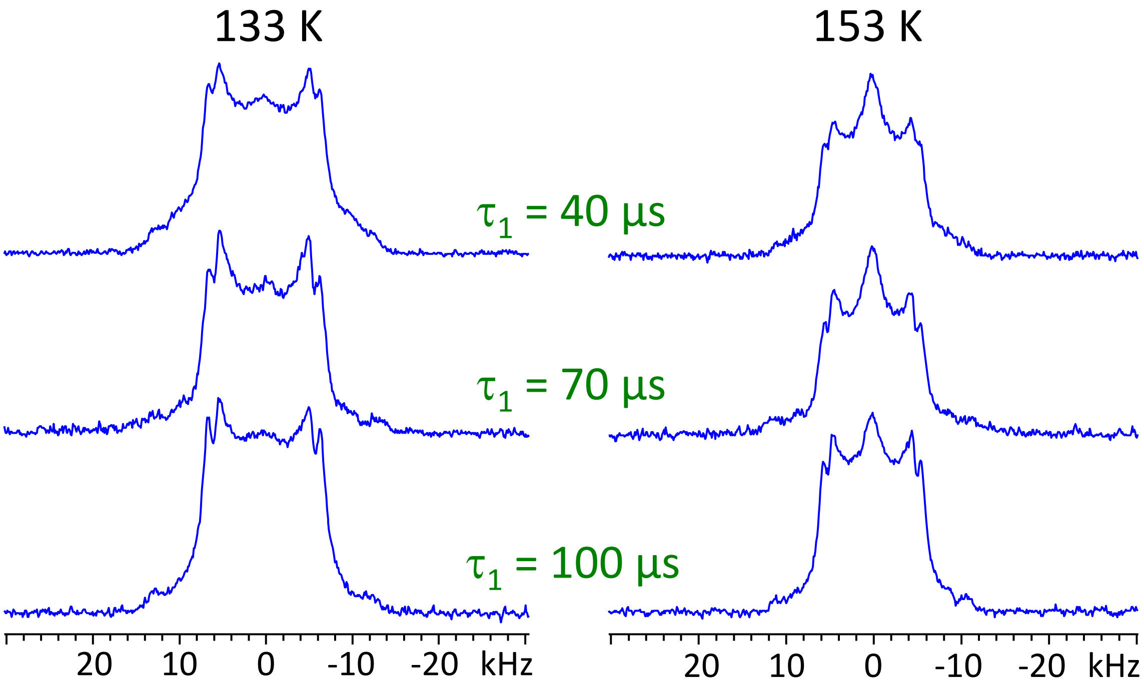

Figure 3-A4. The ^{2}H SSNMR powder patterns of D_2 adsorbed in Mg-MOF-74 at 133 K (left column) and 153 K (right column), as obtained using different interpulse delays. The interpulse delay refers to the time period τ_1 between the two $\pi/2$ pulses in the solid-echo pulse sequence of the form [$(\pi/2)$ - τ_1 - $(\pi/2)$ - τ_2 – acquisition]. For both sets of experiments, a τ_2 value of 25 μs and a receiver delay of 20 μs were used. The lack of powder pattern variation at each temperature when the interpulse delay is varied confirms that both types of adsorbed D_2 molecules participate in dynamics at a rate located in the fast motion regime ($\geq 10^7$ Hz).

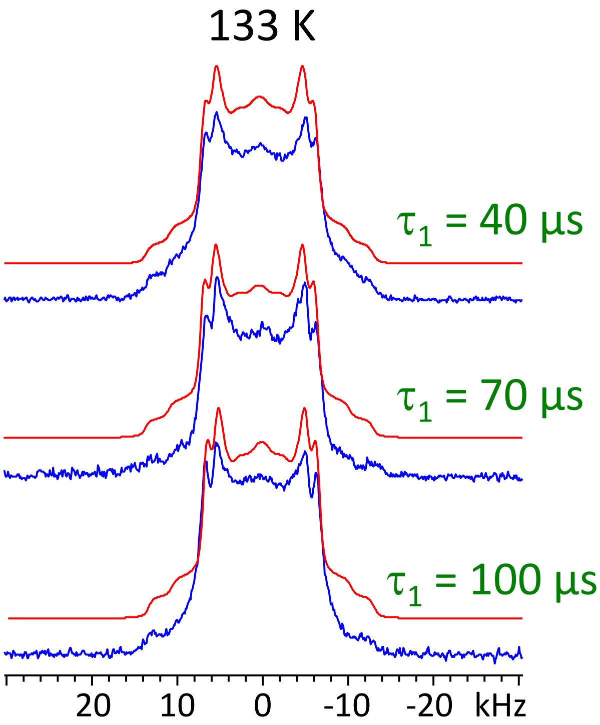

Figure 3-A5. The simulated and experimental ^{2}H SSNMR spectra of D_2 adsorbed in Mg-MOF-74 at 133 K, as obtained using different interpulse delays. The interpulse delay refers to the time period τ_1 between the two $\pi/2$ pulses in the solid-echo pulse sequence of the form $[(\pi/2) - \tau_1 - (\pi/2) - \tau_2 -$ acquisition]. A τ_2 value of 25 µs and a receiver delay of 20 µs were employed for the acquisition of all three spectra. The lack of powder pattern variation at each temperature when the interpulse delay is varied confirms that both types of adsorbed D_2 molecules are undergoing dynamics at a rate in the fast motion regime ($\geq 10^{7}$ Hz).

Table 3-A2. The observed ^{2}H quadrupolar parameters in D_2-loaded Mg-MOF-74 at a temperature of 133 K and a loading level of 0.1 D_2/metal, as a function of changes in the interpulse delay.[a,b,c]

Interpulse delay (μs)	**Site**	**Relative intensity**	**C_Q (kHz)**	**η_Q**
40	1	1	18.9(2)	0
	2	0.70(3)	14.3(1)	0
70	1	1	18.9(2)	0
	2	0.72(3)	14.3(1)	0
100	1	1	18.9(2)	0
	2	0.65(4)	14.3(1)	0

[a] The interpulse delay refers to the time period τ_1 between the two $\pi/2$ pulses in the solid-echo pulse sequence of the form $[(\pi/2) - \tau_1 - (\pi/2) - \tau_2 -$ acquisition] . [b] The numbers in the parentheses correspond to the uncertainties in experimental parameters. [c] In these simulations, a sharp isotropic resonance at ca. 0 ppm was used to simulate the narrow, intense signal corresponding to mobile D_2, which lacks any quadrupolar parameters.

Chapter 4

4 Exploring Methane Adsorption and Dynamics in Metal-Organic Frameworks

Methane is a promising clean and inexpensive energy alternative to traditional fossil fuels, however, its low volumetric energy density at ambient conditions has made devising viable, efficient methane storage systems very challenging. Metal-organic frameworks (MOFs) are promising candidates for methane storage. In order to improve the methane storage capacity of MOFs, a better understanding of methane adsorption, mobility, and host-guest interactions within MOFs must be realized. In this study, methane adsorption within α-$Mg_3(HCO_2)_6$, α-$Zn_3(HCO_2)_6$, SIFSIX-3-Zn, and M-MOF-74 (M = Mg, Zn, Ni, Co) has been comprehensively examined. Single crystal X-ray diffraction (SCXRD) experiments and DFT calculations of methane adsorption locations were performed for α-$Mg_3(HCO_2)_6$, α-$Zn_3(HCO_2)_6$, and SIFSIX-3-Zn. The SCXRD thermal ellipsoids indicate methane possesses significant mobility at the adsorption sites in each system. ^{2}H solid-state NMR (SSNMR) of deuterated CH_3D, CH_2D_2, and CD_4 guests yields a surprising finding: the ^{2}H SSNMR spectra are influenced by chemical shielding anisotropy in addition to the quadrupolar interaction. To the best of our knowledge, the ^{2}H SSNMR spectra document the first observation of the nuclear independent chemical shift (NICS) effect in MOFs. In addition, ^{2}H SSNMR and DFT calculations strongly indicate that the methane adsorption strength is inversely proportional to MOF pore size and dispersive forces are responsible for methane adsorption in these systems. This work lays a very promising foundation for future studies of methane adsorption locations and dynamics within adsorbent MOF materials.

4.1 Introduction

With the rapid population growth and technological advances occurring in our modern world, the demand for energy is constantly increasing. The most commonly used energy sources are based on fossil fuels, which produce carbon dioxide emissions when combusted and are a main contributor to climate change phenomena including global warming. With this in mind, the development of alternative cleaner energy sources is of great interest in order to stem the flow of CO_2 into the Earth's atmosphere.

Natural gas (NG), which mainly consists of methane, is an attractive substitute energy source due to its significant natural abundance, higher energy per unit mass versus all other hydrocarbons, and relatively lower carbon emissions as compared to typical fossil fuels.[1-2] Despite the advantages of NG, its volumetric energy density at ambient temperature and pressure is much lower than that of gasoline, demanding the use of relatively large storage vessels and rendering CH_4 storage very challenging in applications where space is limited, such as automobiles.[3-4] In addition, CH_4 gas is flammable and a safety hazard when stored in its pure form.

With the considerable storage and safety challenges associated with NG, attractive alternative strategies such as the adsorption and storage of CH_4 within porous and microporous materials have emerged in recent years.[5-6] When using a porous adsorbent to store and release CH_4, the guest adsorption ability of the material is typically defined by the volumetric usable CH_4 capacity, which is the difference between CH_4 capacity at the storage pressure (generally 35-65 bar) and the amount of CH_4 that remains within the adsorbent at the desorption pressure (generally 5.8 bar).[1, 7-8] In this context, the development of adsorbents for NG storage with high volumetric usable CH_4 capacity is critical for implementing NG as a practical alternative energy source in many applications.

Metal-organic frameworks (MOFs) are a class of crystalline porous materials that are composed of metal ions or metal-inorganic clusters connected by organic bridging ligands.[9-11] MOFs have many potential applications, including in the adsorption and storage of various gases[12-13] such as methane.[1, 14-15] By varying the topology and composition, the resulting MOF can be tailored to exhibit new or enhanced properties, including increased methane adsorption capacity.[12] Many MOFs have exhibited promising CH_4 adsorption and storage capabilities.[6, 15] The highest documented usable CH_4 capacity (*vide supra*) in these materials is 155 v/v and 197 v/v for adsorption at 35 bar and 65 bar, respectively, which was achieved using a Co(bdp) (bdp = 1,4-benzenedipyrazolate) MOF as the adsorbent.[16] Other MOFs, such as Basolite A520 (aluminum fumarate), have also shown promise as NG sorbents in automotive applications.[17]

There are several experimental avenues for characterizing CH_4-loaded MOFs, investigating their CH_4 adsorption locations, and measuring adsorption capacities. The most commonly employed method is to determine the CH_4 adsorption isotherms of the adsorbent MOF.[18] The measured CH_4 adsorption isotherms provide useful information regarding adsorption capacity and the isosteric heat of CH_4 adsorption, but cannot locate the number and location of CH_4 adsorption sites within the MOF. Crystallographic and diffraction methods have been quite useful for investigating CH_4 adsorption in MOFs.[19] In particular, neutron diffraction has been used to accurately locate methane adsorption sites,[20-22] however, obtaining detailed motional information is not possible. Single crystal X-ray diffraction (SCXRD) is an also a very useful characterization route, however, *in situ* SCXRD studies of guest adsorption in MOFs are uncommon,[23-25] owing to (i) the considerable difficulties in growing single crystals of many MOFs, and (ii) the lack of information availability regarding hydrogen atom positions. In addition, SCXRD studies of guest gases in MOFs are further complicated when relatively small and mobile gases of low electron density (*i.e.*, methane) are involved, owing to the considerable difficulties in locating the guests. Powder X-ray diffraction (pXRD) studies are useful in the many instances where growing MOF single crystals is very challenging or impossible, but extracting detailed structural information and/or crystal structures demands high-quality acquisitions and involves navigating a relatively complicated Rietveld refinement process. Nonetheless, pXRD has been used in several instances, such as for studying phase transitions in flexible MOFs during CH_4 adsorption.[16, 26-27] Computational methods can also be used to identify probable CH_4 adsorption locations in MOFs.[28-29]

In order to move MOFs toward practical incorporation as CH_4 storage media and enhance usable CH_4 capacity in future MOFs, more detailed knowledge of the adsorption of CH_4 within different kinds of MOFs is critical. However, adsorption isotherms and X-ray diffraction techniques alone cannot provide clear and definitive information regarding the host-guest interactions and mobility of CH_4 inside the MOF channels, while computational studies demand experimental verification. Solid-state NMR (SSNMR) spectroscopy is a sensitive probe of short-range structure[30-35] and can provide detailed information on guest adsorption, structure, mobility, and host-guest interactions in MOFs.[25, 32-33, 35-43] NMR interactions are generally directionally-dependent (*i.e.*, anisotropic) and are affected by dynamics in a predictable manner, therefore, information regarding guest mobility and adsorption can be extracted from SSNMR spectra of gases within MOFs.[44] ^{2}H is an attractive target due to its nuclear properties. ^{2}H has a spin of 1 and is subject to the anisotropic quadrupolar interaction (QI) between the nuclear quadrupole moment and surrounding electric field gradients (EFGs). Any motion that reorients the ^{2}H EFG tensor influences the QI, and thus has an effect on the ^{2}H SSNMR spectral lineshape. Previous studies have proven that ^{2}H SSNMR can provide rich information on the local structure, host-guest interactions, and dynamics of deuterated linkers[45-50] and guests[40-41, 51-53] such as

D_2[40] in MOFs and microporous materials.

Herein, we describe a detailed SCXRD, computational, and SSNMR study of methane adsorption locations and dynamics in four MOFs: α-$Mg_3(HCO_2)_6$, α-$Zn_3(HCO_2)_6$, SIFSIX-3-Zn, and M-MOF-74 (M: Mg, Zn, Ni, Co). This selection of MOFs allows for multiple comparisons, such as between MOFs which have same topology but different metal centres (α-$Zn_2(HCO_2)_6$, α-$Mg_2(HCO_2)_6$), MOFs with very small channels (SIFSIX-3-Zn) versus those with relatively larger channels (MOF-74), and MOFs that have fully saturated metal centres (α-$Mg_3(HCO_2)_6$, α-$Zn_3(HCO_2)_6$, SIFSIX-3-Zn) versus MOFs which have coordinatively-unsaturated open metal sites (MOF-74). Plane-wave DFT calculations were also employed calculate ^{2}H NMR parameters, as well as to confirm the number and location of adsorption sites within α-$Mg_3(HCO_2)_6$, α-$Zn_3(HCO_2)_6$, and SIFSIX-3-Zn. The knowledge gained in this work regarding adsorbed methane has clear practical implications for adapting and tailoring MOFs for the purposes of enhanced CH_4 adsorption and storage.

4.2 Experimental Section.

MOF synthesis. All chemicals were obtained from Sigma-Aldrich and were used without further purification. The α-$Mg_3(HCO_2)_6$, α-$Zn_3(HCO_2)_6$, SIFSIX-3-Zn, and Mg-MOF-74 MOFs were synthesized using previously described methods[54-57] with some slight modifications, and all details are included in the Section 4.6.

MOF activation. The sample activation procedure involves the use of heat and vacuum to purge residual solvent molecules from the pores of the as-made MOF. In order to prepare activated MOF samples, the as-made α-$Mg_3(HCO_2)_6$, α-$Zn_3(HCO_2)_6$ and SIFSIX-3-Zn samples were heated at 100 °C, 150 °C and 80 °C, respectively, under dynamic vacuum (*i.e.*, < 1 mbar) for at least 12 hours.

For Mg-MOF-74, an additional solvent-exchange step on the as-made sample was required before the activation process, which is briefly described here. 0.25 g of the as-made Mg-MOF-74 sample incorporating THF was solvent-exchanged by exposure to 10 mL of methanol in an autoclave at 200 °C for 7 days. Each day, the autoclave was removed from the oven, brought to room temperature, and the methanol stock was replaced. After 7 days, the THF solvent was fully replaced by methanol solvent within Mg-MOF-74. In the final step, the methanol exchanged Mg-MOF-74 sample was heated at 250 °C under dynamic vacuum for 8 hours, purging all methanol solvent and generating the activated Mg-MOF-74 sample.

Gas adsorption and loading within MOFs. A Schlenk line was used for all gas adsorption and loading procedures. The MOF sample was first loaded into the bottom of a homemade 5 mm L-shaped glass tube. A thin layer of glass wool was then inserted above the sample in the tube in order to secure the sample in place. The glass tube was then attached to the Schlenk line and sample activation was performed. After activation, a known amount of pressurized CH_3D was introduced to the vacuum line, and the CH_3D gas was allowed to occupy both the vacuum line and the glass tube containing the sample, which has a measured volume of ca. 82.7 cm^3. The bottom of the CH_3D-filled glass tube was then immersed in liquid nitrogen to freeze CH_3D within the sample, and the glass tube end (now containing both CH_3D and the MOF sample) was then flame-sealed off from the Schlenk line. The overall CH_3D loading amount is expressed by the molar ratio between CH_3D and the metal. For the ^2H SSNMR experiments in this study, 0.1 CH_3D/metal samples were prepared for the α-$Mg_3(HCO_2)_6$ and α-$Zn_3(HCO_2)_6$ MOFs, while 0.2 CH_3D/metal samples were prepared for the SIFSIX-3-Zn and Mg-MOF-74 MOFs.

Powder X-ray diffraction. The identity of all MOF products was confirmed through the use of powder XRD experiments, which were performed on an Inel CPS powder diffractometer operating with Cu Kα radiation ($\lambda = 1.5406$ Å). Reflections were collected at 2θ values ranging from 5 to 120 ° with a total acquisition time of ca. 3 minutes for each pXRD pattern. All pXRD patterns are illustrated in Figure 4-A1.

Single crystal X-ray diffraction (SCXRD). The CH_3D-loaded MOF single crystal samples were prepared using a Schlenk line and the same gas adsorption procedure described above for SSNMR samples, however, the gas loading level for SCXRD samples was set to saturation rather than a defined loading ratio or amount. After gas loading and flame sealing, the glass tubes were broken, and the methane-saturated samples were immediately coated with paratone oil in order to retain as much methane gas as possible within the MOFs. An optical microscope was then used to select high-quality single-crystals for structural analysis.

All SCXRD measurements were performed on a Bruker Kappa Axis Apex2 diffractometer at a temperature of 110 K. The frame integration was performed using SAINT.[58] The resulting raw data were scaled and absorption corrected using a multi-scan averaging of symmetry equivalent data with SADABS.[59] The methane-loaded MOF structures were solved using a dual space methodology incorporated in the SHELXT program.[60] All non-hydrogen framework atoms were obtained from the initial structural solution. The hydrogen atoms were then introduced at idealized positions and were allowed to ride on the parent atom. The carbon atomic positions for the methane molecules were obtained from a difference Fourier map. The structural model was fit to the data using a full matrix least-squares method based on F^2. The calculated structure factors included corrections for anomalous dispersion from the usual tabulation. The structure was refined using the SHELXL-2014 program from the SHELX suite of crystallographic software.[61] Graphic plots were produced using the NRCVAX program suite.[62] A detailed summary of the crystallographic data of methane-loaded α-$Mg_3(HCO_2)_6$, α-$Zn_3(HCO_2)_6$ and SIFSIX-3-

Zn are given in the Section 4.6.

Density-functional theory calculations. DFT calculations for methane-loaded MOFs were performed using the CASTEP code.[63] The calculations used the PBE exchange-correlation functional[64] in conjunction with the D2 dispersion correction devised by Grimme.[65] All NMR parameters were calculated employing the gauge-including projector augmented waves (GIPAW) formalism.[66-67] Further details on the calculations are included in the Section 4.6.

^{2}H solid-state NMR experiments. All SSNMR experiments were performed on a wide-bore Varian/Chemagnetics InfinityPlus NMR spectrometer operating at 9.4 T (υ_0(^{2}H) = 61.32 MHz) with a 5 mm static HX probe. A sample of D_2O (l) was used as a secondary chemical shift reference at δ_{iso} = 4.8 ppm with respect to neat $(CD_3)_4Si$.[68] The experimental temperature was controlled by a Varian VT control unit, and all temperatures were calibrated to ± 3 K using the ^{207}Pb chemical shift of a solid sample of lead nitrate across the experimental temperature range.[69] A quadrupolar echo pulse sequence of the format ($\pi/2 - \tau_1 - \pi/2 - \tau_2$) was used to acquire ^{2}H NMR spectra, employing a $\pi/2$ pulse width of 4.5 μs, an interpulse τ_1 time of 45 μs, and a τ_2 duration of 25 μs. A ^{1}H decoupling field of ca. 63 kHz was applied during all ^{2}H SSNMR experiments. All spectra were acquired using calibrated ^{2}H pulse delays ranging from 1 to 3 s, depending on the sample and experimental temperature. A spectral width of 20 kHz was employed for ^{2}H SSNMR experiments involving CH_3D and CH_2D_2 adsorbed in α-$Mg_3(HCO_2)_6$, α-$Zn_3(HCO_2)_6$, and Mg-MOF-74; however, a spectral width of 30 kHz was required for ^{2}H SSNMR experiments on CH_3D and CH_2D_2 adsorbed within SIFSIX-3-Zn.

Spectral simulation software. The WSolids[70] computer software was used to perform analytical simulations of experimental SSNMR spectra in order to obtain the apparent or observed ^{2}H NMR parameters.

4.3 Results and Discussion

4.3.1 Methane adsorption within α-$Mg_3(HCO_2)_6$

MOFs with small pores tend to have stronger interactions with guests.[1, 14-15] α-$Mg_3(HCO_2)_6$ is an ultra-microporous MOF with relatively small one-dimensional zigzag-shaped channels that measure *ca*. 4.8 Å in diameter.[54] CH_4 adsorption isotherms[71-72] and DFT calculations[73] have indicated that α-$Mg_3(HCO_2)_6$ is a promising methane adsorbent and possesses a good selectivity of CH_4 over N_2 gas.[72-73] However, there has not been a comprehensive physical investigation of α-$Mg_3(HCO_2)_6$ to determine the specific methane adsorption site locations and host-guest interactions involved. We have performed an intertwined SCXRD, computational, and SSNMR investigation of methane adsorption within α-$Mg_3(HCO_2)_6$.

SCXRD and DFT investigations of methane-loaded α-$Mg_3(HCO_2)_6$. Many details concerning methane adsorption within the α-$Mg_3(HCO_2)_6$ MOF are unknown or have not been experimentally established. SCXRD is an attractive route for investigating the location of guest adsorption sites in MOFs,[19, 25, 74] and has been used to unambiguously determine the number and location of methane adsorption sites in α-$Mg_3(HCO_2)_6$.

The carbon atomic positions of CH_3D guests within α-$Mg_3(HCO_2)_6$ have been successfully obtained from SCXRD experiments at 110 K. For ease of comparison with ^{2}H SSNMR experiments, singly-deuterated CH_3D guests were used rather than CH_4; see the ^{2}H SSNMR section for more details (*vide infra*). The methane carbon positions established from SCXRD are shown from two different perspectives in Figures 4-1(a) and (b). Although a MOF sample saturated with CH_3D was used, the SCXRD results indicate that the CH_3D occupancy is actually 0.25 (*i.e.*, 1.0 CH_3D/unit cell) under these experimental conditions. There are two separate, symmetry equivalent methane adsorption sites in each channel, and two symmetry equivalent channels are present in each unit cell, yielding four methane adsorption sites but only one crystallographically unique methane molecule per unit cell (*i.e.*, there is one unique methane adsorption site). The two symmetry-related methane adsorption sites in each channel are located 5.423 Å apart, on the opposite sides of the zigzag-shaped MOF channels that run along the crystallographic *b* axis (Figure 4-1(b)). The CH_3D carbon atom lies 3.799 Å away from the carbon atom of the formate linker and 3.814 Å from the oxygen atom on the same formate linker (Figure 4-1(c)). The position of the CH_3D carbon atom suggests that the hydrogen and oxygen atoms of the formate linker play a role in methane adsorption within α-$Mg_3(HCO_2)_6$ *via* weak and distant electrostatic interactions. The thermal ellipsoid of the methane carbon atom was also obtained from SCXRD measurements (Figure 4-A2) and is relatively large, particularly along the direction of the zigzag-shaped channels in α-$Mg_3(HCO_2)_6$ and toward the adjacent symmetry-equivalent methane carbon atom, implying that methane rapidly moves between adjacent adsorption sites located along the channels.

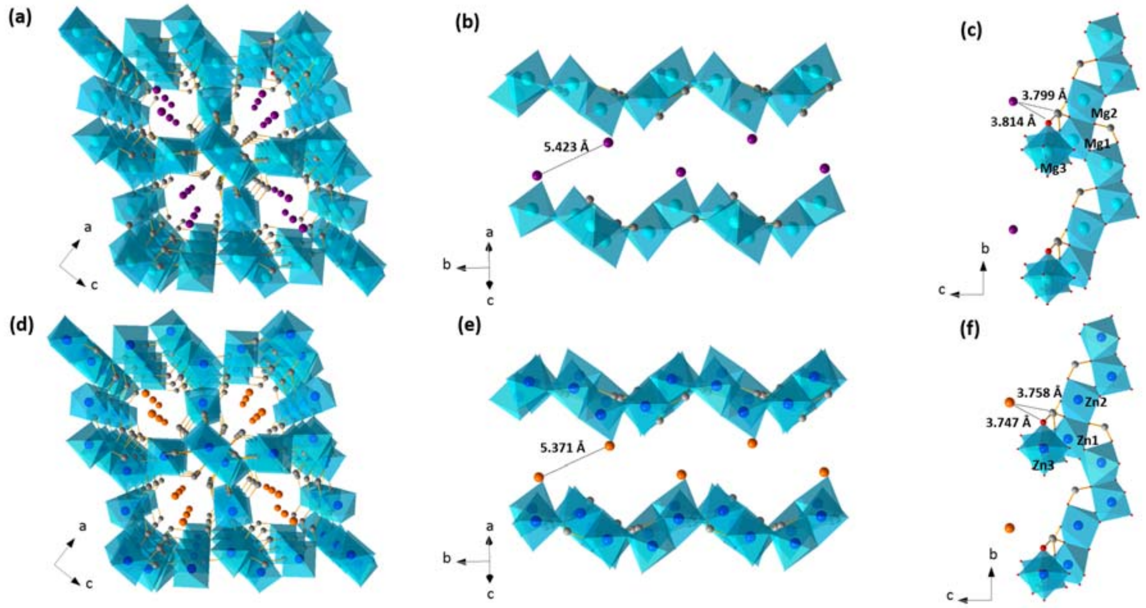

Figure 4-1. The extended framework structure of the CH_3D-loaded α-$Mg_3(HCO_2)_6$ MOF, as viewed along the crystallographic *b* axis, is shown in (a). The locations of CH_3D carbon atoms (colored purple) along one of the zigzag-shaped channels of α-$Mg_3(HCO_2)_6$ are shown in (b), while in (c), the shortest distances between the adsorbed CH_3D carbon atom and the framework atoms of α-$Mg_3(HCO_2)_6$ are depicted. The extended long-range structure of the CH_3D-loaded α-$Zn_3(HCO_2)_6$ MOF, as viewed along the crystallographic *b* axis, is illustrated in (d), along with the local positions of adsorbed CH_3D carbon atoms (colored orange) within its zigzag-shaped channels in (e). The shortest distances between the carbon atom of CH_3D and the atoms of the α-$Zn_3(HCO_2)_6$ framework are shown in (f). Carbon is colored gray, oxygen is red, blue is zinc, light blue is magnesium, purple denotes the carbon atoms of CH_3D within α-$Mg_3(HCO_2)_6$, and orange spheres represent carbon atoms of CH_3D molecules within α-$Zn_3(HCO_2)_6$. Detailed information on DFT optimized methane-loaded α-$Mg_3(HCO_2)_6$ and α-$Zn_3(HCO_2)_6$ structures can be found in Figure 4-A3 and Figure 4-A5, respectively.

A previous computational study suggested that methane can reside in two crystallographically distinct adsorption sites in α-$Mg_3(HCO_2)_6$ which have very similar adsorption energies,[73] however, this contradicts our SCXRD findings, and neither of the predicted adsorption sites are coincident with the single crystallographic site obtained from SCXRD. In order to resolve the differences between prior computational results and the SCXRD data, we have performed a detailed DFT study involving (i) geometry optimizations to understand adsorption site locations, (ii) calculations of adsorption site energies, and (iii) calculations of ^{2}H NMR parameters (*vide infra*). Our DFT calculations involved geometry optimizations of methane guests at different initial locations within α-$Mg_3(HCO_2)_6$ at a loading level identical to that of the SCXRD experiments (1.0 methane molecules per unit cell), followed by a comparison of the final methane guest location versus the methane carbon position and associated thermal ellipsoid obtained from SCXRD experiments. DFT calculations using a loading level of 4.0 methane/unit cell produced generally similar results and are described further in the Appendix (Section 4.6).

The guest methane molecule locations were optimized along with the positions of all atoms in the MOF, which was accomplished by relaxing all atomic coordinates but fixing the lattice parameters to the experimental values obtained from SCXRD (see Appendix in Section 4.6). The results of DFT geometry optimizations are shown from a long-range (Figure 4-A3) and a short-range Figure 4-2 perspective. The experimental SCXRD methane carbon position is also included in Figure 4-2, along with its carbon displacement ellipsoid. The DFT-optimized methane site is quite proximate to the SCXRD methane carbon position and lies well inside the carbon displacement ellipsoid. These geometry optimizations support and can subtly refine the single methane position in α-$Mg_3(HCO_2)_6$ obtained using SCXRD.

The specific methane adsorption isosteric enthalpy at the DFT-optimized single methane adsorption site within α-$Mg_3(HCO_2)_6$ at the SCXRD methane loading level of 1.0

molecules/unit cell was determined to -25.1 kJ/mol. The dispersive contribution was calculated as -20.3 kJ/mol (Table 4-A1), implying that van der Waals forces drive methane adsorption in this system, while electrostatics play a minor role. The methane adsorption isosteric enthalpy is not strongly influenced by the methane loading level; a value of -25.1 kJ/mol was calculated at the DFT-optimized adsorption site with a loading level of 1.0 methane/unit cell, and this calculated value only changes slightly to -25.7 kJ/mol when the loading level is quadrupled to 4.0 methane/unit cell. A more detailed discussion of the DFT results at higher methane loading levels can be found in the Appendix (Section 4.6). It should be noted that the large methane carbon displacement ellipsoid from SCXRD suggests there is a large region near the methane adsorption site where adsorption energies are quite similar.

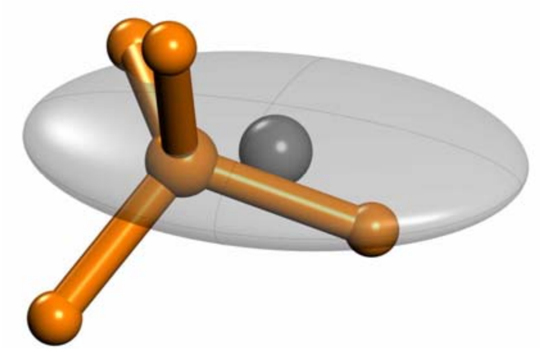

Figure 4-2. The DFT results using a loading level of 1.0 methane molecule/unit cell of Mg-formate are shown. A visualization of the CH_4 carbon atom and its thermal ellipsoid, as determined from SCXRD analysis of methane-loaded Mg-formate, are shown in grey along with the methane adsorption site obtained from DFT calculations. The orange methane molecule is the resulting methane position after DFT optimization of our SCXRD structure; the methane hydrogen atoms were added computationally and their position was also optimized.

There is strong agreement between SCXRD experiments and DFT calculations, which both indicate that a single unique methane adsorption site is located on a "smeared out" equipotential energy surface present within α-$Mg_3(HCO_2)_6$. To verify the presence of a single unique methane adsorption site, and to probe the local environment and dynamics of adsorbed methane guests, ^{2}H SSNMR experiments were performed.

Investigating methane within α-$Mg_3(HCO_2)_6$ *via* ^{2}H SSNMR. Static VT ^{2}H SSNMR experiments on singly-deuterated methane (CH_3D) adsorbed in α-$Mg_3(HCO_2)_6$ were performed at temperatures ranging from 123 K to 293 K. The experimental static ^{2}H VT SSNMR spectra of CH_3D adsorbed within α-$Mg_3(HCO_2)_6$ at a loading level of 0.1 CH_3D/Mg (1.2 CH_3D molecules/unit cell) are shown in Figure 4-3(a). At 293 K, a sharp resonance is present, which corresponds to rapidly and isotropically tumbling CH_3D. The anisotropic quadrupolar interaction (QI) is typically the primary origin of ^{2}H spectral broadening, and when CH_3D is rapidly isotropically tumbling, the ^{2}H EFG tensor is reoriented through all possible directions, removing the anisotropy of the QI and eliminating the broadening effects of the QI on the ^{2}H SSNMR spectrum. Although the ^{2}H SSNMR spectral appearance is typically dominated by the QI, it should be noted that the chemical shift (CS) interaction may also influence and broaden ^{2}H SSNMR spectra; however, much like the case of the QI, rapid isotropic tumbling removes the CS anisotropy (CSA) and eliminates its spectral effects.

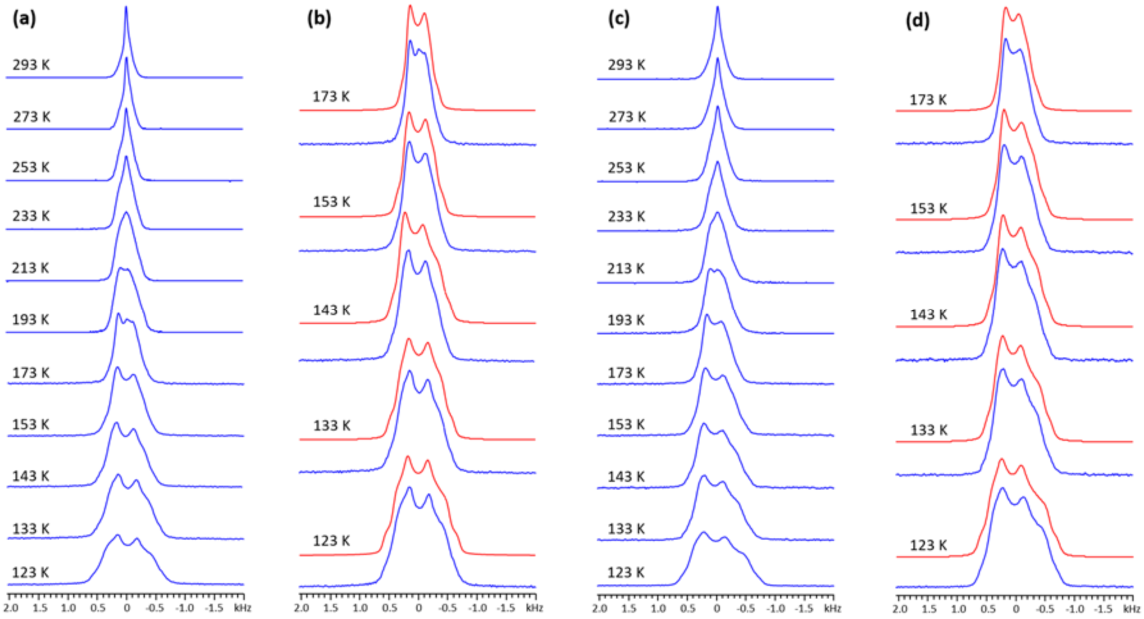

Figure 4-3. The experimental static VT ^{2}H SSNMR spectra of CH_3D adsorbed within α-$Mg_3(HCO_2)_6$ acquired at 9.4 T are depicted in (a), along with a comparison of the experimental (blue) and analytical simulated (red) low temperature ^{2}H SSNMR spectra in (b). In (c), the experimental static VT ^{2}H SSNMR spectra of CH_3D adsorbed within α-$Zn_3(HCO_2)_6$ acquired at 9.4 T are shown. A comparison of experimental (blue) and analytical simulated (red) ^{2}H SSNMR spectra of CH_3D in α-$Zn_3(HCO_2)_6$ at low temperatures is given in (d).

Table 4-1. The observed ^{2}H NMR parameters of CH_3D adsorbed in four different MOFs, as obtained at different experimental temperatures.

MOF	Temperature (K)	C_Q (Hz)	η_Q	Ω (ppm)	κ	δ_{iso} (ppm)	β[a]
α-$Mg_3(HCO_2)_6$	123	860 (10)	0.47 (3)	0.8 (5)	-1.0 (5)	-0.7 (1)	0 (30)
	133	760 (10)	0.42 (3)	0.8 (5)	-1.0 (5)	-0.6 (1)	0 (30)
	143	660 (10)	0.38 (2)	0.8 (5)	-1.0 (5)	-0.5 (1)	0 (30)
	153	570 (10)	0.33 (2)	0.8 (5)	-1.0 (5)	-0.4 (1)	0 (30)
	173	460 (10)	0.23 (2)	0.8 (5)	-1.0 (5)	-0.3 (1)	0 (30)
α-$Zn_3(HCO_2)_6$	123	920 (10)	0.50 (3)	2.0 (5)	-1.0 (5)	-0.4 (1)	0 (30)
	133	770 (10)	0.45 (3)	2.0 (5)	-1.0 (5)	-0.4 (1)	0 (30)
	143	710 (10)	0.40 (3)	2.0 (5)	-1.0 (5)	-0.3 (1)	0 (30)
	153	640 (10)	0.30 (2)	2.0 (5)	-1.0 (5)	-0.2 (1)	0 (30)
	173	500 (10)	0.20 (2)	2.0 (5)	-1.0 (5)	-0.2 (1)	0 (30)
SIFSIX-3-Zn	123	3700 (80)	0.35 (3)	2.5 (5)	-1.0 (5)	-2.0 (2)	80 (10)
	133	3400 (80)	0.33 (3)	2.5 (5)	-1.0 (5)	-2.0 (2)	80 (10)
	143	3000 (50)	0.31 (3)	2.5 (5)	-1.0 (5)	-2.0 (2)	80 (10)
	153	2700 (50)	0.30 (3)	2.5 (5)	-1.0 (5)	-2.0 (2)	80 (10)
	173	2200 (20)	0.30 (3)	2.5 (5)	-1.0 (5)	-2.0 (2)	80 (10)
	193	1800 (20)	0.27 (3)	2.5 (5)	-1.0 (5)	-2.0 (2)	80 (10)
	213	1520 (20)	0.25 (3)	2.5 (5)	-1.0 (5)	-2.0 (2)	80 (10)
Mg-MOF-74	123	620 (5)	0.00 (5)	2.0 (5)	-1.0 (5)	-0.8 (1)	80 (10)
	128	570 (5)	0.00 (5)	2.0 (5)	-1.0 (5)	-0.8 (1)	80 (10)
	133	520 (5)	0.00 (5)	2.0 (5)	-1.0 (5)	-0.8 (1)	80 (10)
	138	480 (5)	0.00 (5)	2.0 (5)	-1.0 (5)	-0.8 (1)	80 (10)
	143	420 (5)	0.00 (5)	2.0 (5)	-1.0 (5)	-0.8 (1)	80 (10)

[a] The angle β refers to the Euler angle between the V_{33} component of the EFG tensor and the δ_{33} component of the CS tensor. The other Euler angles were not found to significantly impact spectral appearance.

As the temperature is reduced, the ^{2}H spectra of CH_3D adsorbed within α-$Mg_3(HCO_2)_6$ gradually grow broader. Experimental ^{2}H powder patterns at and below 173 K exhibit characteristic features and lineshapes that can be simulated to extract the apparent

NMR parameters. Each ^{2}H SSNMR spectrum between 173 and 123 K features one ^{2}H powder pattern, which indicates that CH_3D resides at a single crystallographically unique adsorption site, or multiple symmetry-equivalent adsorption sites, within α-$Mg_3(HCO_2)_6$ at this loading level. The observation of a single powder pattern is in excellent agreement with the one crystallographically unique methane molecule adsorption site evident from SCXRD experiments and DFT calculations. The observed $C_Q(^2H)$ values of CH_3D adsorbed within α-$Mg_3(HCO_2)_6$ increase from 460 Hz at 173 K to 860 Hz at 123 K, while η_Q values also rise from 0.23 at 173 K to 0.47 at 123 K (Table 4-1). It is particularly noteworthy that the observed $C_Q(^2H)$ values are less than 0.5 % the magnitude of the reported[75] and DFT-calculated $C_Q(^2H)$ values (Table 4-A2) of a single static CH_3D molecule, which are both 192 kHz. The vastly smaller observed experimental $C_Q(^2H)$ values and diminished apparent QI are a clear sign that we are observing a time-averaged ^{2}H SSNMR spectrum involving fast-exchanging (i) free CH_3D isotropically tumbling in the pores, and (ii) CH_3D interacting with the α-$Mg_3(HCO_2)_6$ MOF and undergoing anisotropic motion.

Curiously, the ^{2}H powder patterns exhibit distorted lineshapes that significantly stray from that of a typical QI-dominated ^{2}H Pake doublet.[76] The only method to simulate this peculiar ^{2}H lineshape is by introducing the effects of CSA, which has been known to contribute to ^{2}H NMR lineshapes.[77-79] The observed ^{2}H span value of 0.8 ppm is smaller than the plane-wave DFT calculated span value of 9.0 ppm (Table 4-A2), which can be attributed to nearly isotropic tumbling of CH_3D that diminishes the CSA and reduces the apparent span to a significantly smaller value. The ^{2}H CS and QI of CH_3D are subject to very different magnitudes of time-averaged motional scaling in this MOF: the observed span values are ca. 9 % of the calculated span value, while observed $C_Q(^2H)$ values are less than 0.5 % of the calculated and reported $C_Q(^2H)$ values.

A possible explanation for the different magnitudes of EFG and CS motional averaging is the nucleus-independent chemical shift (NICS) effect, which is now discussed.[80-82] The presence of an external magnetic field influences the MOF electrons to circulate and produce an induced magnetic field within the MOF, particularly near the MOF surfaces. As guest methane molecules become adsorbed to the MOF, the induced magnetic field generated by the MOF electrons influences the local magnetic environment about the ^{2}H nuclei within methane guests, increasing the apparent ^{2}H CSA and also making a contribution to the ^{2}H isotropic chemical shift (Table 4-1). Previous studies have indicated that the magnitude of the NICS is closely linked to the adsorbent-adsorbate distance,[83-84] or in this case, the MOF-methane distance. As guest methane molecules approach the MOF surface and become adsorbed, the magnitudes of the NICSs increase, resulting in more significant contributions to the ^{2}H CSA and isotropic chemical shift (Figure 4-4).

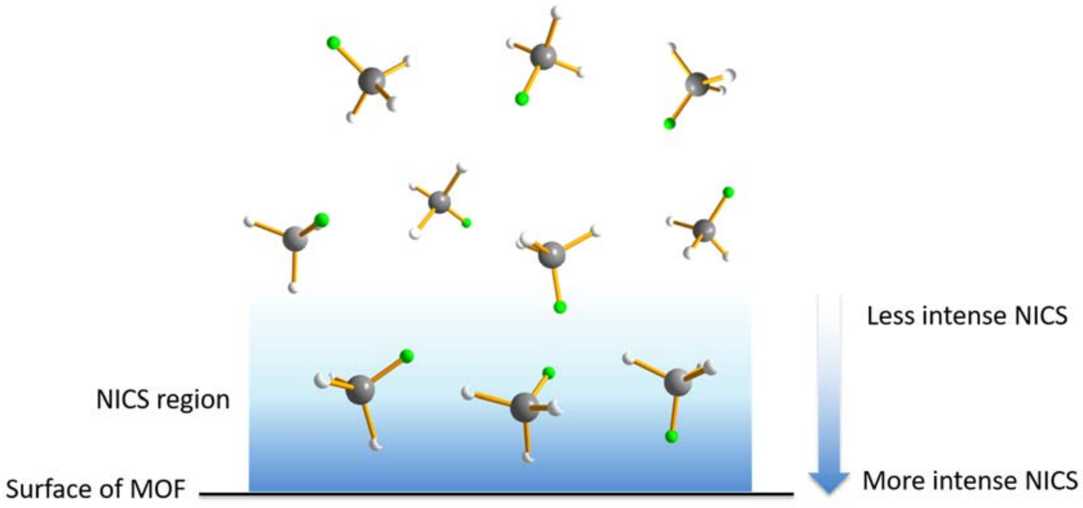

Figure 4-4. An illustration of NICS effect. As CH_3D molecules approach the MOF surface, the magnitudes of the NICSs increase, resulting in more significant contributions to the ^{2}H CSA and isotropic chemical shift.

In α-$Mg_3(HCO_2)_6$, the free CH_3D methane molecules undergoing isotropic or nearly isotropic tumbling are in fast exchange with adsorbed CH_3D methane guests proximate to the MOF surface that are undergoing slightly non-isotropic motion; ^2H SSNMR spectra of CH_3D reflect a time-averaged picture of both CH_3D methane species. The time-averaged motional scaling factor of the QI and CSA determines the ^2H NMR linewidth and lineshape. The motional scaling factor is the same for the QI and CSA, however, the NICS effect introduces additional CSA in adsorbed methane molecules located near the MOF surface. As the temperature is lowered, more methane guests are adsorbed, and methane spends a relatively longer time at the MOF surfaces. The time-averaged population of adsorbed versus free methane guests is altered, which in turn influences the time-averaged motional scaling factor of the CSA, since more methane molecules are now adsorbed and subject to the NICS effect. The net effect on ^2H SSNMR spectra of methane is a larger apparent CSA due to the NICS contribution, which explains the unexpectedly significant influence of CS on these ^2H lineshapes. This is especially significant because to the best of our knowledge, NICS effects have not yet been reported for guest molecules in MOFs. It should also be noted that ^2H δ_{iso} values decrease for methane adsorbed within α-$Mg_3(HCO_2)_6$ as the temperature is reduced (Table 4-1), reflecting increased contributions from the NICS as the time-averaged methane populations evolve.

The calculated ^2H NMR parameters for methane at the geometry-optimized SCXRD adsorption site are nearly identical to the parameters for a single static CH_3D molecule (Table 4-A2). The main divergence in calculated NMR parameters for CH_3D occurs for the CS skew (κ) values, which is likely due to very distant methane-framework interactions that slightly influence the CS tensor.

4.3.2 Methane adsorption within α-$Zn_3(HCO_2)_6$

The α-$Zn_3(HCO_2)_6$ MOF is analogous to α-$Mg_3(HCO_2)_6$, featuring zinc metal centres and formate linkers that form a similar 3D crystalline structure,[55] with a slightly smaller channel diameter of 4.44 Å in the Zn analogue versus 4.58 Å in the Mg variant.[73] Although CH_4 adsorption in α-$Zn_3(HCO_2)_6$ has not been extensively studied, a recent computational study has indicated that α-$Zn_3(HCO_2)_6$ exhibits a stronger interaction with methane than α-$Mg_3(HCO_2)_6$; the reported calculated isosteric adsorption enthalpy of methane within α-$Zn_3(HCO_2)_6$ is -27.6 kJ/mol versus -25.7 kJ/mol in α-$Mg_3(HCO_2)_6$.[73] In order to establish the methane adsorption site locations in α-$Zn_3(HCO_2)_6$ and understand the reasons for the subtle difference in methane adsorption energies between the two formate MOFs, SCXRD, DFT, and ^{2}H SSNMR experiments have been performed on α-$Zn_3(HCO_2)_6$.

SCXRD and DFT calculations of methane-loaded α-$Zn_3(HCO_2)_6$. The CH_3D adsorption sites within α-$Zn_3(HCO_2)_6$ have been successfully located using SCXRD. The occupancy of CH_3D within CH_3D-saturated α-$Zn_3(HCO_2)_6$ at our experimental loading level was determined to be 0.33 (1.32 molecules/unit cell), which is slightly higher than that of α-$Mg_3(HCO_2)_6$ (1.0 molecules/unit cell). The CH_3D adsorption sites in the crystal structure of CH_3D-saturated α-$Zn_3(HCO_2)_6$ are shown in Figure 4-1(d), and are located in a similar position as those within α-$Mg_3(HCO_2)_6$. There are two symmetry-equivalent CH_3D adsorption sites, yet only one crystallographically unique adsorption site in α-$Zn_3(HCO_2)_6$. The two symmetry-equivalent methane adsorption sites are located 5.371 Å apart and can be found on opposite sides of the zigzag-shaped channels that run along the crystallographic *b* axis (Figure 4-1(e)). The ORTEP drawing of the α-$Zn_3(HCO_2)_6$ structure about the methane adsorption site (Figure 4-A4) highlights the relatively large thermal ellipsoid associated with the methane carbon atom. The large thermal ellipsoid indicates that despite the observation of a single unique methane adsorption site in this system, there is a rather large area of similar methane adsorption enthalpies (*i.e.*, a large equipotential energy surface) present about the adsorption site. In an interesting note, the SCXRD thermal ellipsoid is actually spherical in α-$Zn_3(HCO_2)_6$, as opposed to the flatter oblong ellipse observed in α-$Mg_3(HCO_2)_6$.

The closest framework atom to the position of the adsorbed CH_3D carbon atom is an oxygen atom of the formate linker located 3.747 Å away, which is part of the ZnO_6 octahedron with Zn3 located at the centre (Figure 4-1(f)). The CH_3D carbon atom is also found 3.758 Å from the carbon atom on the formate linker, hinting that one or both of the formate hydrogen and oxygen atoms acts as the partner for attractive interactions with methane. The aforementioned interatomic distances in α-$Zn_3(HCO_2)_6$ are relatively shorter the 3.814 Å methane carbon - framework oxygen and 3.799 Å methane carbon – framework carbon distances within α-$Mg_3(HCO_2)_6$, in good agreement with a prior DFT computational study that indicated α-$Zn_3(HCO_2)_6$ possesses a higher methane binding strength versus α-$Mg_3(HCO_2)_6$.[73] The Mg- and Zn-formate MOFs feature fully saturated metal centres and have the same topology as well as organic linker, thus, any changes in adsorption strength cannot be due to unique host-guest interactions specific to one MOF.

DFT geometry optimizations and calculations based on our SCXRD structure were performed to investigate the methane adsorption energy. The calculated isosteric adsorption enthalpy of methane within α-$Zn_3(HCO_2)_6$ at a loading level of 1.0 methane/unit cell is -27.9 kJ/mol (Table 4-A1), which is quite similar to the -27.6 kJ/mol value produced by previous DFT calculations.[73] It is very interesting to note that the non-dispersive contribution in α-$Zn_3(HCO_2)_6$ is -5.3 kJ/mol (Table 4-A1), which is only 0.5 kJ/mol stronger than that of α-$Mg_3(HCO_2)_6$ (-4.8 kJ/mol), however, the dispersive contribution in α-$Zn_3(HCO_2)_6$ is -22.6 kJ/mol, which is 2.3 kJ/mol stronger than that of α-$Mg_3(HCO_2)_6$ (Table 4-A1). These values reveal that the stronger methane binding strength in α-$Zn_3(HCO_2)_6$ are likely due to increased van der Waals interactions arising from the smaller pore size. The DFT geometry optimizations are shown from a long-range perspective in Figure 4-A5. Our SCXRD and DFT findings strongly support the notion that pore size is the main determinant of methane adsorption strength in this formate MOF family. These findings are supported by previous calculations that linked the host-methane interaction energy for methane to the pore diameter in these metal formate MOFs, with smaller pore diameters leading to stronger interactions.[73] To probe the effects of reduced pore size on methane binding strength, as well as to verify the presence of a single unique methane adsorption site, ^{2}H SSNMR experiments were performed on α-$Zn_3(HCO_2)_6$.

^{2}H SSNMR examination of methane within α-$Zn_3(HCO_2)_6$. Static ^{2}H VT SSNMR experiments on singly-deuterated methane within α-$Zn_3(HCO_2)_6$ at a loading level of 0.1 CH_3D/Zn (1.2 CH_3D molecules/unit cell) were performed at temperatures ranging from 123 K to 293 K (Figure 4-3(c)). At 293 K, CH_3D is highly mobile within α-$Zn_3(HCO_2)_6$ and gives rise to a sharp resonance, and the ^{2}H SSNMR spectra become steadily broader as the temperature decreases. At and below 173 K, the spectrum exhibits well-defined features, indicating that the anisotropy of the QI and CS interaction is not completely removed, and therefore not all methane molecules are undergoing completely isotropic tumbling. The methane ^{2}H SSNMR lineshape between 123 and 173 K is composed of a single ^{2}H powder pattern, reflecting the presence of a single crystallographically unique methane adsorption site in α-$Zn_3(HCO_2)_6$, in excellent agreement with SCXRD and DFT results.

The observed $C_Q(^2H)$ values of CH_3D adsorbed within α-$Zn_3(HCO_2)_6$ increase from 500 Hz at 173 K to 920 Hz at 123 K (Table 4-1), yet these values are far less than the $C_Q(^2H)$ of 192 kHz associated with static CH_3D. We are again observing a time-averaged ^{2}H SSNMR spectrum between fast-exchanging free CH_3D isotropically tumbling in the pores and adsorbed CH_3D undergoing non-isotropic motions while interacting with the α-

$Zn_3(HCO_2)_6$ surfaces. The calculated $C_Q(^2H)$ for methane at the geometry-optimized SCXRD adsorption site is also nearly identical to the parameters for a single static CH_3D molecule (Table 4-A2), clearly indicating that time-averaged motional scaling of the QI must be responsible for the very small observed $C_Q(^2H)$ values. The increase in observed $C_Q(^2H)$ as temperature is reduced reflects a decrease in time-averaged methane mobility, since the anisotropy of the QI is removed to a lesser degree and the apparent $C_Q(^2H)$ values correspondingly increase. The observed η_Q values increase from 0.20 to 0.50 as temperatures decrease from 173 K to 123 K.

Much like the case of α-$Mg_3(HCO_2)_6$, the ^2H powder patterns of adsorbed CH_3D in α-$Zn_3(HCO_2)_6$ are clearly influenced by CSA that is not completely removed by methane motion (Table 4-1); this is reflected in the apparent span values of 2.0 ppm across the experimental temperature range. While the anisotropy of the QI is largely removed by nearly isotropic time-averaged CH_3D motion at low temperatures, a significant CSA contribution remains due to the NICS effect arising from the nearby MOF surface (*vide supra*). As the temperature is reduced, methane molecules remain in fast exchange but spend less time as isotropically tumbling free guests, and a larger fraction of time as adsorbed species undergoing slightly non-isotropic motions near the MOF surface and experiencing NICS effects. The net result is less time-averaged motional scaling of the CSA, making CSA effects more apparent in the ^2H SSNMR spectra of fast-exchange guest methane molecules in α-$Zn_3(HCO_2)_6$.

The VT ^2H SSNMR spectral lineshapes of CH_3D in both α-$Zn_3(HCO_2)_6$ and α-$Mg_3(HCO_2)_6$ are similar, hinting that CH_3D has comparable mobility and adsorption energies in both systems. However, the ^2H SSNMR spectra of CH_3D in α-$Zn_3(HCO_2)_6$ are broader than those of CH_3D in α-$Mg_3(HCO_2)_6$ at any given temperature, indicating that less of the CSA and QI anisotropy is removed, and thus methane is relatively less mobile and more strongly adsorbed in α-$Zn_3(HCO_2)_6$. This hypothesis is supported by the observed NMR parameters in Table 4-1: methane $C_Q(^2H)$ values are 1-12 % higher and the ^2H span value is 250 % higher in α-$Zn_3(HCO_2)_6$ versus α-$Mg_3(HCO_2)_6$ across the experimental temperature range. The ^2H SSNMR findings of stronger methane binding in α-$Zn_3(HCO_2)_6$ as compared to α-$Mg_3(HCO_2)_6$ are in agreement with the relatively shorter methane-framework distances in α-$Zn_3(HCO_2)_6$ indicated from our SCXRD and DFT computational results. The relatively larger magnitude of apparent ^2H CSA in α-$Zn_3(HCO_2)_6$ is likely related to pore size, since the pores are slightly smaller in this MOF and thus more methane guests are proximate to the MOF surfaces and experiencing some degree of the NICS effect at any given time. It should also be noted that the ^2H δ_{iso} values decrease for deuterated methane adsorbed within α-$Zn_3(HCO_2)_6$ as the temperature is reduced (Table 4-1), which is again due to increased NICS effects: the time-averaged population of methane molecules adsorbed and located near the MOF surface increases at lower temperatures. To further investigate the relationship between pore size and methane adsorption in MOFs, along with the influence of the NICS effect on ^2H SSNMR spectra of methane guests, the ultramicroporous SIFSIX-3-Zn MOF was examined.

4.3.3 Methane adsorption and dynamics within SIFSIX-3-Zn

SIFSIX-3-Zn is an ultramicroporous MOF well-suited for the selective adsorption of small gases;[57, 85] for example, SIFSIX-3-Zn exhibits a selective CO_2 capture in the presence of water.[57] SIFSIX-3-Zn also has good methane capacity at low pressure (12.6 mg/g at 1 bar) due to the small pore size.[57] The "SIFSIX" name originates from the presence of pillared SiF_6^{2-} units within the MOF. In SIFSIX-3-Zn, the Zn(II) centre is saturated and octahedrally coordinated to four different N atoms from four different pyrazine ligands, as well as two F atoms from two SiF_6^{2-} ions (Figure 4-5). The fluorine atoms are axially coordinated to Zn and the corresponding Zn-Zn axial distance is 7.6 Å, while the four pyrazine linkers are equatorially coordinated to Zn, and the Zn-Zn equatorial distance is 7.1 Å.[86] The planes of the pyrazine linkers in SIFSIX-3-Zn are oriented parallel to the crystallographic *c* axis, producing square-shaped MOF channels measuring 3.8 Å[57, 86] from corner to corner, which are significantly smaller than the calculated 4.58 Å and 4.44 Å[73] pore sizes in α-$Mg_3(HCO_2)_6$ and α-$Zn_3(HCO_2)_6$, respectively. The very small pore size of SIFSIX-3-Zn is promising for methane storage applications: since the interactions between methane molecules and MOFs are typically van der Waals (*i.e.*, dispersive) interactions, the methane binding strength of a MOF should be enhanced as the pore size is reduced,[12, 87-88] as was observed in the case of α-$Zn_3(HCO_2)_6$ versus α-$Mg_3(HCO_2)_6$ (*vide supra*). Despite the promising features that exist within ultramicroporous SIFSIX-3-Zn for methane adsorption, a detailed study of the corresponding methane adsorption sites has not yet been performed. Using SCXRD, DFT calculations, and VT ^{2}H SSNMR experiments, we now examine methane adsorption sites and host-guest interactions in SIFSIX-3-Zn.

SCXRD and DFT calculations of SIFSIX-3-Zn loaded with methane. In order to locate the methane adsorption sites inside the channels of SIFSIX-3-Zn, SCXRD of SIFSIX-3-Zn saturated with CH_3D was performed at 110 K, yielding the crystal structure shown in Figure 4-5. The CH_3D carbon atom positions in the long-range crystal structure of CH_3D-saturated SIFSIX-3-Zn as viewed along the crystallographic *c* axis are shown in Figure 4-5(a). When viewing the crystal structure along the *c* axis, the carbon atoms of CH_3D are located exactly in the middle of the MOF channels at a distance of 3.504 Å from the closest framework atoms, which are the fluorine atoms of the SiF_6^{2-} linkers (Figure 4-5(b)). This suggests that the fluorine atoms play an important role in methane adsorption, which is reasonable in light of a previous study that concluded the non-dispersive CO_2 adsorption mechanisms in SIFSIX-3-Zn involve the fluorine atoms of SiF_6^{2-} anions.[57] In a similar manner, the non-dispersive mechanisms underpinning methane adsorption in

SIFSIX-3-Zn should involve interactions between the partially positive hydrogen atoms of methane molecules and the negatively charged fluorine atoms of the SiF_6^{2-} linkers. The coordinatively-saturated Zn centres are unable to directly interact with CH_3D.

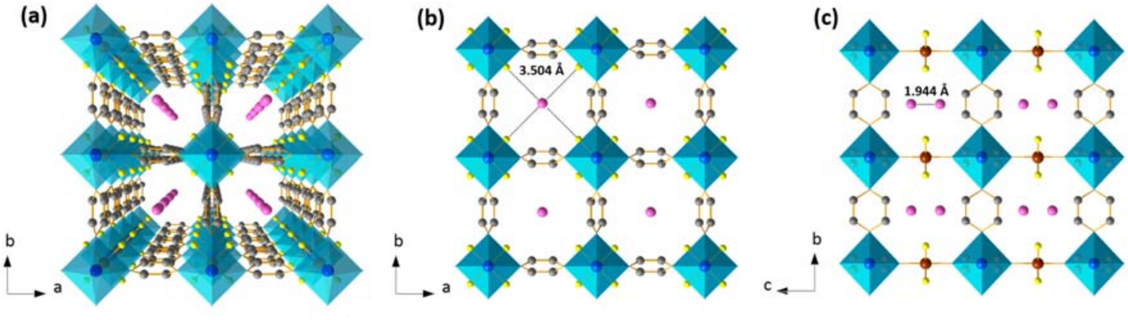

Figure 4-5. The long-range structure of SIFSIX-3-Zn as determined from our SCXRD experiments is illustrated in (a) as viewed along the crystallographic *c* axis, along with the purple carbon atom positions of adsorbed CH_3D within the pores. In (b), the purple CH_3D carbon atom locations in one cross-section of the SIFSIX-3-Zn crystal structure are shown as viewed along the *c* axis, where the shortest distance between CH_3D carbon atoms and the framework (*i.e.*, the fluorine atoms of SiF_6) was measured as 3.504 Å. The locations of the magenta carbon atoms of CH_3D in SIFSIX-3-Zn, as viewed along the *a* axis, are depicted in (c), with the distance between the carbon atoms of adjacent adsorbed CH_3D molecules indicated as 1.944 Å. In this illustration, carbon is colored gray, zinc is blue, silicon is brown, fluorine is yellow, nitrogen is light pink, and the carbon atoms of adsorbed CH_3D within SIFSIX-3-Zn are magenta. Detailed information on DFT optimized methane-loaded SIFSIX-3-Zn structure can be found in Figure 4-A7.

The methane carbon positions in SIFSIX-3-Zn are easier to visualize along the crystallographic *a* axis, as shown in Figure 4-5(c). This perspective clearly illustrates the two symmetry-equivalent adsorption sites per unit cell, however, there is only one crystallographically unique methane adsorption site. The distance between the two symmetry-equivalent CH_3D adsorption sites is only 1.944 Å, which is much shorter than the *ca.* 5.4 Å distance between adjacent methane adsorption sites in the α-$Mg_3(HCO_2)_6$ and α-$Zn_3(HCO_2)_6$ MOFs. The short distance between adjacent CH_3D adsorption sites in SIFSIX-3-Zn means they cannot be simultaneously populated in the same unit cell, which is supported by the 0.38 molecule/unit cell occupancy of the methane carbon atom. The ORTEP diagram of methane in the asymmetric unit of SIFSIX-3-Zn highlights the very large thermal ellipsoid of the CH_3D carbon atom, along with its anisotropic elongation along the crystallographic *c* axis (Figure 4-A6). The large ellipsoid confirms that methane is remarkably mobile at 110 K, while the ellipsoid extension towards adjacent symmetry-equivalent carbon positions indicates that methane tends to move between the two equivalent adsorption sites.

The DFT optimized adsorption site (Figure 4-A7) and the adsorption site determined *via* SCXRD are located only 0.98 Å apart. Nonetheless, the DFT optimized methane adsorption site is located very close to the methane carbon ellipsoid determined *via* XRD, and these two complementary techniques are still in generally good agreement. The calculated adsorption isosteric enthalpy is -33.3 kJ/mol (Table 4-A1), which indicates SIFSIX-3-Zn has a significantly stronger methane binding strength versus both the Mg- and α-$Zn_3(HCO_2)_6$ MOFs. Based on DFT optimizations, the methane H atoms make distant 2.5 – 3.4 Å contacts with the framework fluorine atoms, these non-dispersive contributions are calculated to contribute only -0.6 kJ/mol to guest adsorption (Table 4-A1), which indicates that the H-F electrostatic interaction is quite weak. In contrast, the dispersive adsorption contribution was found to be -32.7 kJ/mol (Table 4-A1), which is a clear indication that the relatively stronger methane binding strength in SIFSIX-3-Zn chiefly arises from its remarkably small pore size. In order to understand the effect of these narrower pores and stronger host-guest interactions on the local electronic and magnetic structure of adsorbed methane, static ^{2}H VT SSNMR experiments were performed.

^{2}H SSNMR examination of methane within SIFSIX-3-Zn. Static ^{2}H VT SSNMR spectra obtained at temperatures ranging from 123 K to 293 K are shown in Figure 4-6(a). At 293 K, the spectrum consists of a sharp resonance along with a relatively broader powder pattern that exhibits some spectral features (Figure 4-6(a)). The sharp narrow resonance corresponds to CH_3D that is rapidly isotropically tumbling within SIFSIX-3-Zn, and it decreases in intensity with temperature until the sharp line is not visible at or below 213 K. Similar to the case of methane in the Mg- and Zn-formate MOFs, the broader underlying time-averaged ^{2}H powder pattern arises from free CH_3D methane tumbling in the pore undergoing fast exchange with adsorbed CH_3D methane that is interacting with the surface and undergoing non-isotropic motion. The observation of a single ^{2}H SSNMR powder pattern indicates there is only one crystallographically unique methane adsorption site in SIFSIX-3-Zn, in good agreement with our SCXRD experiments and DFT optimizations.

The observed $C_Q(^2H)$ value of CH_3D adsorbed within SIFSIX-3-Zn is 1520 Hz at 213 K, and this value increases as temperature decreases, reaching 3700 Hz at 123 K (Table 4-1). The observed $C_Q(^2H)$ values associated with CH_3D in SIFSIX-3-Zn remain far less than either the 192 kHz[75] value for static methane or the calculated $C_Q(^2H)$ value of ca. 190 kHz for methane at the geometry-optimized SCXRD adsorption site (Table 4-A2), indicating that time-averaged CH_3D motion must be removing much of the QI anisotropy. However, the observed time-averaged motionally-scaled $C_Q(^2H)$ values of methane within SIFSIX-3-Zn are significantly larger than those of methane within the Mg- and Zn-formate MOFs at any given temperature, indicating that there is a larger degree of methane molecules undergoing non-isotropic motion, and thus stronger host-guest interactions within SIFSIX-3-Zn. This SSNMR-based conclusion is strongly supported by the relatively larger calculated adsorption isosteric enthalpy of methane in SIFSIX-3-Zn versus the Mg- and Zn-formate MOFs (*vide supra*, Table 4-A1).

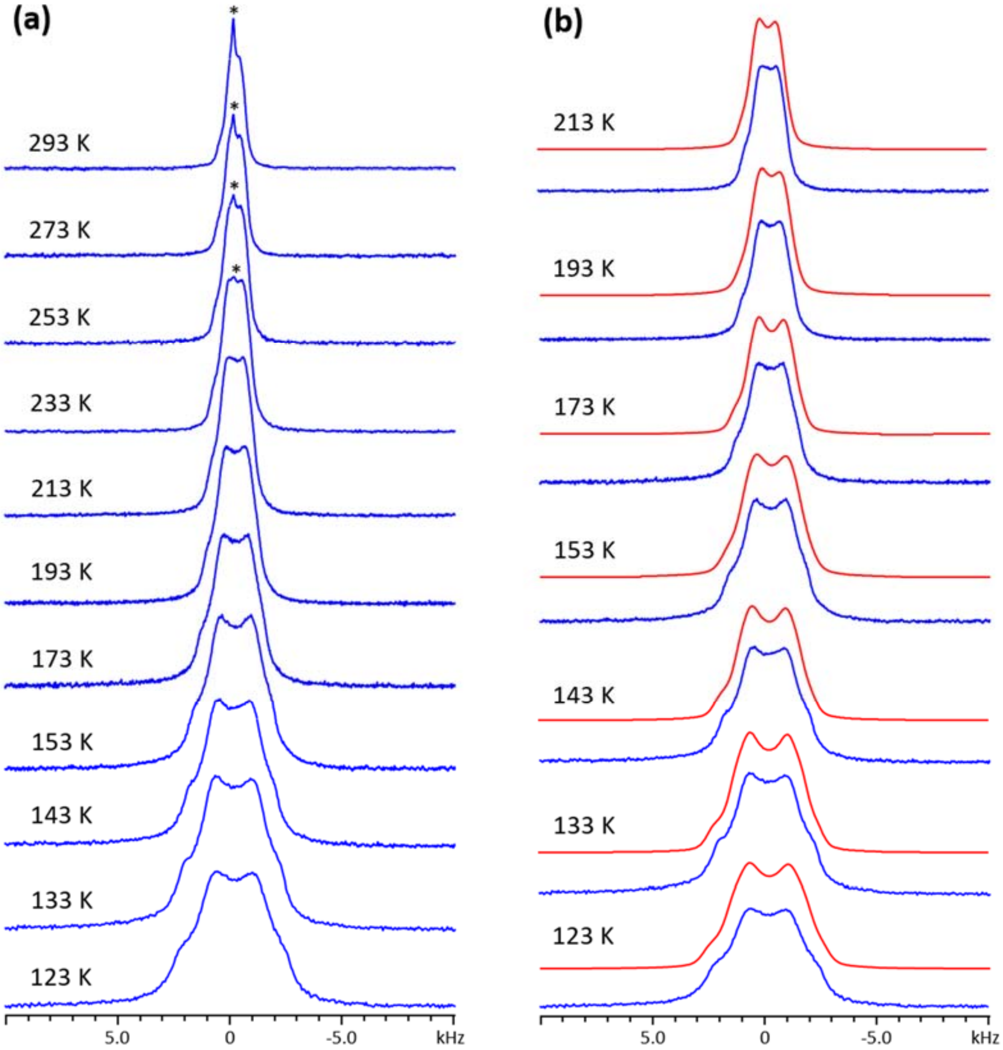

Figure 4-6. In (a), the experimental static VT ^{2}H SSNMR spectra of CH_3D adsorbed within SIFSIX-3-Zn are illustrated. A comparison of the experimental (blue) and analytical simulated (red) low temperature ^{2}H SSNMR spectra of CH_3D in SIFSIX-3-Zn is shown in (b). The asterisk (*) in (a) denotes the sharp central ^{2}H resonance arising from non-adsorbed CH_3D undergoing rapid isotropic tumbling.

Even with the increased QI and relatively broader time-averaged ^{2}H SSNMR powder patterns of CH_3D in SIFSIX-3-Zn, the spectral lineshape is significantly influenced by CSA. The observed Ω value is 2.5 ppm at all temperatures, which is larger than the 2.0 and 0.8 ppm values in Zn- and Mg-formate, respectively. Much like the case of $C_Q(^2H)$, it appears that larger Ω values are linked to smaller pore sizes and stronger methane binding in these three MOFs. We propose that this elevated span value arises from a relatively larger NICS effect; stronger host-guest interactions cause a significantly larger fraction of methane molecules to be adsorbed near the SIFSIX-3-Zn surface and thus subject to the NICS at any given time. In SIFSIX-3-Zn, a CH_3D ^2H δ_{iso} value of -2.0 ppm was observed at temperatures ranging from 213 K to 123 K (Table 4-1), which is much larger in magnitude than the -0.2 to -0.7 ppm values observed for CH_3D in Zn- and Mg-formate. The larger magnitude of the observed δ_{iso} value again indicates that the NICS effect on methane guests is significantly stronger in SIFSIX-3-Zn.

The β parameter denotes the angle between the V_{33} component of the ^2H EFG tensor and the δ_{33} component of the ^2H CS tensor. Interestingly, the observed β value for adsorbed CH_3D is 80 ° in SIFSIX-3-Zn, but is 0 ° in Mg- and Zn-formate. DFT calculations for all four ^2H positions on adsorbed methane in Mg- and Zn- formate, along with three of four ^2H positions for adsorbed methane in SIFSIX-3-Zn, predict β values close to 0 ° (Table 4-A2). Thus, it appears that one of both of the ^2H V_{33} or δ_{33} tensor components have been reoriented for CH_3D adsorbed in SIFSIX-3-Zn. In terminally bound ^2H atoms, it is well-known that the V_{33} component of the EFG tensor is almost always located along the direction of the single chemical bond, and there are no indications from SCXRD or DFT that significant hydrogen bonding interactions or additional chemical bonds involving methane H/D atoms that may reorient the V_{33} component are present with the SIFSIX-3-Zn framework. Thus, the most likely scenario is that the δ_{33} component of the CS tensor has been reoriented by some phenomenon to produce the observed β value of 80 °. Based on the relatively strong NICS influence on ^{2}H CSA parameters in SIFSIX-3-Zn, we hypothesize that the NICS is also responsible for the change in β: the NICS significantly alters the CS tensor orientation of adsorbed methane molecules located close to the internal surfaces of SIFSIX-3-Zn, rendering the CH_3D ^{2}H CS and EFG tensors nearly perpendicular rather than coincident.

SIFSIX-3-Zn, α-$Mg_3(HCO_2)_6$, and α-$Zn_3(HCO_2)_6$ all feature saturated metal centres that cannot directly interact with methane guests. However, in many MOFs, the presence of a coordiatively-unsaturated open metal site (OMS) facilitates guest gas adsorption and can boost total adsorption capacity. In order to investigate the influence of OMSs on methane adsorption and ^{2}H SSNMR spectra, the M-MOF-74 material was examined.

4.3.4 ^{2}H SSNMR of methane adsorbed within M-MOF-74

M-MOF-74 (M = metal) is a well-known MOF consisting of metal centres joined by 2,5-dioxido-1,4-benzenedicarboxylate (dobdc) linkers, forming a framework that features hexagonal or honeycomb-shaped channels that have metal centres at each vertex with a metal-metal distance of *ca*. 9 Å.[56, 89] In the as-made version of MOF-74, each metal centre is connected to five oxygen atoms from four dobdc linkers and a sixth oxygen atom from a solvent molecule originating from the synthesis, such as tetrahydrofuran. The coordinated solvent molecules can then be removed *via* activation (*i.e.*, heating and vacuum) to create coordinatively-unsaturated OMSs, which are accessible to guests within the pores and thus act as the adsorption sites for guest gases such as methane.[21] The nature of the metal centre influences the methane binding strength, which has been found to follow the order Ni > Co > Mg > Zn.[1, 21, 90] In M-MOF-74, the adsorbed methane molecule is located adjacent to the square plane of the MO_5 pyramid of the OMS in order to maximize host-guest interactions.[21] Although the locations of adsorbed methane in these systems are known,[21] the host-guest interactions between methane and M-MOF-74 have not yet been explored *via* SSNMR methods.

The VT ^{2}H SSNMR spectra of CH_3D within the diamagnetic Mg-MOF-74 are shown in Figure 4-7. At 293 K, only a single sharp, narrow resonance corresponding to highly mobile, isotropically tumbling CH_3D is observed. The ^{2}H SSNMR resonance grows gradually broader as the temperature decreases, reflecting a gradual reduction in time-averaged CH_3D dynamics. A well-defined and relatively broader ^{2}H powder pattern corresponding to the presence of adsorbed methane is only observed at and below 143 K, which is a lower temperature than powder patterns were observed in the other MOFs within this study; this finding suggests that Mg-MOF-74 has a weaker methane binding strength than α-$Mg_3(HCO_2)_6$, α-$Zn_3(HCO_2)_6$, and SIFSIX-3-Zn. This observation is in good agreement with a previous study that indicated Mg-MOF-74 has a isosteric enthalpy of methane adsorption of -18.5 kJ/mol,[21] which is lower than that of α-$Mg_3(HCO_2)_6$, α-$Zn_3(HCO_2)_6$, and SIFSIX-3-Zn calculated in this work.

The observed ^{2}H NMR parameters for methane adsorbed in Mg-MOF-74 at and below 143 K are listed in Table 4-1. The observed $C_Q(^2H)$ values are relatively small, and increase from 420 Hz at 143 K to 620 Hz at 123 K. Since these $C_Q(^2H)$ values are much less than the known static value of 192 kHz, the vast majority of methane molecules are undergoing rapid isotropic tumbling in M-MOF-74, it is again apparent that we are observing a time-averaged ^{2}H SSNMR spectrum arising from free CH_3D tumbling in the pore undergoing fast-exchange with CH_3D interacting with the surface in M-MOF-74. The observed $C_Q(^2H)$ values are the lower than those of α-$Mg_3(HCO_2)_6$, α-$Zn_3(HCO_2)_6$, and SIFSIX-3-Zn at any given temperature, strongly suggesting that Mg-MOF-74 has the weakest methane binding strength of the four. It is again apparent that the ^{2}H powder patterns are distorted from purely QI-dominated lineshapes due to the presence of CSA that is not wholly removed by rapid guest motion (Table 4-1). Much like the previously discussed α-$Mg_3(HCO_2)_6$, α-$Zn_3(HCO_2)_6$, and SIFSIX-3-Zn, there is a significant NICS contribution to the ^{2}H CSA of methane in Mg-MOF-74, as evidenced by the negative ^{2}H δ_{iso} value of -0.8 ppm and ^{2}H span value of 2.0 ppm throughout the experimental temperature range. The ^{2}H β angle is 80 ° in this system, indicating that despite the relatively weak methane binding strength in Mg-MOF-74, a significant population of methane guests are adsorbed and located close enough to the MOF surface to experience a sizable NICS effect, reorienting the δ_{33} component of the ^{2}H CS tensor away from the D-C bond vector in methane.

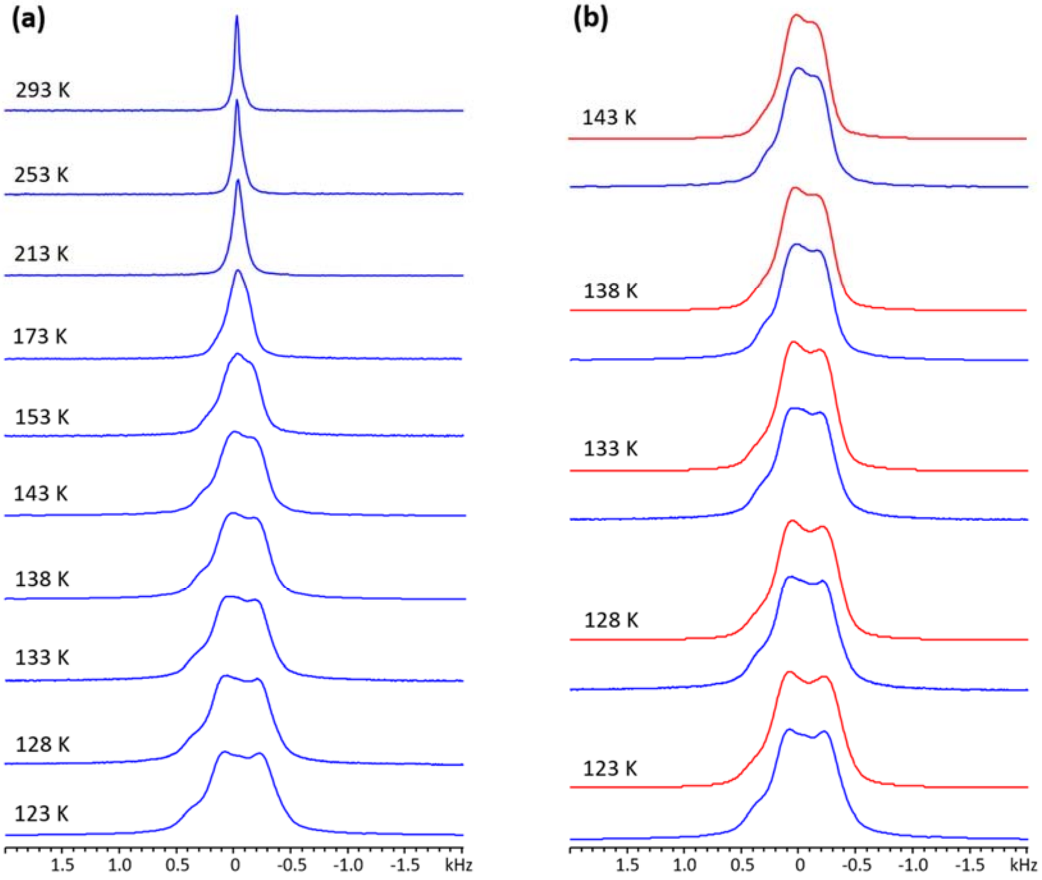

Figure 4-7. The experimental static VT ^{2}H SSNMR spectra of CH_3D adsorbed in Mg-MOF-74 are shown in (a), along with a comparison of the experimental (blue) and analytical simulated (red) low temperature ^{2}H SSNMR spectra in (b).

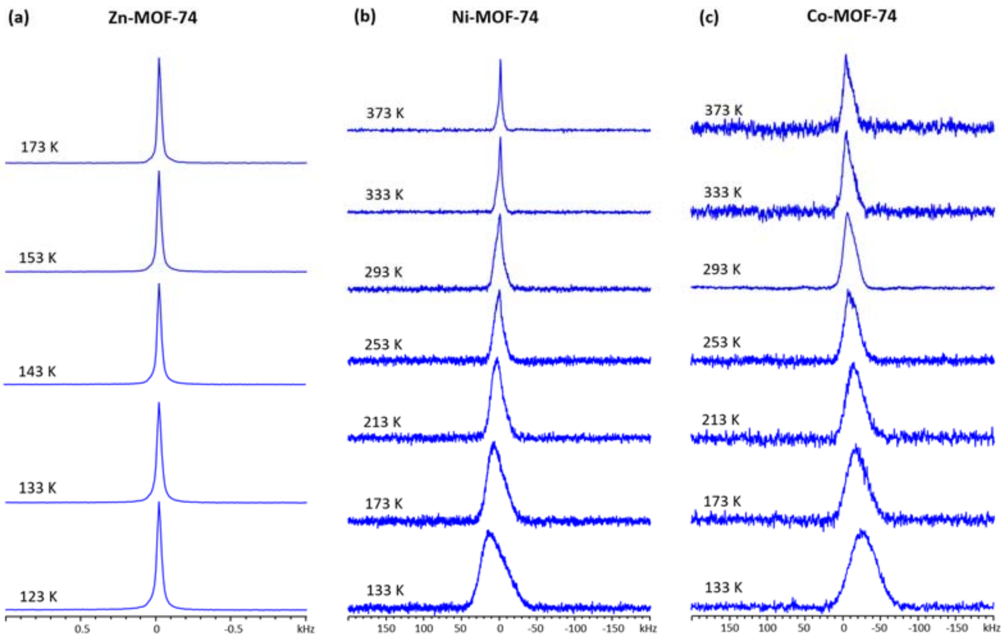

Figure 4-8. The experimental static VT ^{2}H SSNMR spectra of CH_3D adsorbed within Zn-MOF-74, Ni-MOF-74, and Co-MOF-74 at a loading level of 0.2 CH_3D/metal are depicted in (a), (b), and (c), respectively. Note the difference in x-axis scale between (a), (b), and (c). The spectral broadening and apparent change in isotropic chemical shifts observed in Ni-MOF-74 and Co-MOF-74 are due to the presence of paramagnetic metal centres and the corresponding coupling between the paramagnetic metal centre and the deuterium nucleus in CH_3D. In Ni-MOF-74, the position of the uppermost point of the ^{2}H resonance shifts from -1.4 kHz at 373 K to 12.0 kHz at 133 K, for a total frequency shift of ca. 13.5 kHz. In Co-MOF-74, the position of the uppermost point of the ^{2}H resonance shifts from -4.7 kHz at 373 K to -26.3 kHz at 133 K, for a total frequency shift of ca. 22 kHz.

The VT ^{2}H SSNMR spectra of CH_3D adsorbed within the diamagnetic Zn-MOF-74 were also obtained, and the low temperature spectra are shown in Figure 4-8(a). Throughout the experimental temperature range, the ^{2}H SSNMR spectrum features only a single sharp resonance, corresponding to highly mobile and isotropically tumbling CH_3D molecules. This observation is somewhat surprising, given that the methane binding strength in Zn-MOF-74 (isosteric enthalpy of adsorption: -18.3 kJ/mol) is very similar to that of Mg-MOF-74 (isosteric enthalpy of adsorption: -18.5 kJ/mol).[21] A possible explanation comes from the calculated 29.7 kJ/mol binding energy of methane on the Zn^{2+} OMSs at 0 K, which is 4.1 kJ/mol lower than that on Mg^{2+} OMSs;[21] this difference may lead to increased methane mobility and explain why a featureless ^2H resonance was observed in CH_3D-loaded Zn-MOF-74. Another possible reason for the differences in binding strength between Mg- and Zn-MOF-74 could be the repulsion interaction, which is stronger between methane and framework in Zn-MOF-74. The featureless nature of these Zn-MOF-74 spectra prevents any simulations to extract apparent ^2H NMR parameters.

Ni-MOF-74 (isosteric enthalpy of adsorption: -20.2 kJ/mol) and Co-MOF-74 (isosteric enthalpy of adsorption: -19.6 kJ/mol) exhibit stronger methane binding strengths versus Mg-MOF-74 and Zn-MOF-74,[21] however, the paramagnetic Ni^{2+} and Co^{2+} centres in MOF-74 present a unique challenge for ^2H SSNMR experiments. When a CH_3D guest is proximate to these paramagnetic metal centres, the large magnetic moment of the unpaired electrons in Ni^{2+} and Co^{2+} couples with the ^2H nucleus in CH_3D, resulting in spectral broadening and unusual chemical shifts. The VT ^2H SSNMR spectra of CH_3D adsorbed within Ni- and Co-MOF-74 are shown in Figures 4-8(b) and (c). At 373 K, the ^2H SSNMR spectra of adsorbed-CH_3D within Ni-MOF-74 and Co-MOF-74 exhibit a single resonance with a full width at half height (FWHH) of 3.3 kHz and 12.2 kHz, respectively. This pronounced spectral broadening confirms that CH_3D is located close to the paramagnetic open metal sites (*i.e.*, CH_3D is proximate to or physically adsorbed on the OMS). The broad ^2H resonances in Ni- and Co-MOF-74 increase in width as temperature is reduced, and the resonances are gradually shifted to higher and lower frequencies, respectively. The increases in resonance width and magnitude of frequency shifts are indicative of increasingly stronger interactions between CH_3D guests and the paramagnetic OMSs as temperature is reduced; this agrees with the common observation of increased methane localization on the adsorption site as temperature is reduced for all other MOFs within this study. It is very interesting to note that even Ni-MOF-74 has stronger methane binding strength than that of Co-MOF-74, the ^{2}H resonance width of CH_3D within Ni-MOF-74 is narrower than that of Co-MOF-74 at any acquiring temperatures (Figures 4-8(b) and (c)). Therefore, we concluded that the paramagnetic interaction has a more pronounced impact on the ^{2}H SSNMR spectrum of CH_3D in Co-MOF-74 versus that of Ni-MOF-74, which can be rationalized by the higher number of unpaired electrons in Co^{2+}: there are 3 unpaired electrons in Co^{2+} and 2 unpaired electrons in Ni^{2+}.

4.3.5 Comparison of the ^{2}H SSNMR spectra of CH_3D, CH_2D_2, and CD_4

The VT ^{2}H SSNMR spectra of CH_2D_2 and CD_4 adsorbed in α-$Mg_3(HCO_2)_6$ (Figure 4-A8(a) and (b)), α-$Zn_3(HCO_2)_6$ (Figure 4-A8(c) and (d)), and Mg-MOF-74 (Figure 4-A10), along with CH_2D_2 adsorbed in SIFSIX-3-Zn (Figure 4-A9) were also acquired to investigate the effect of different deuteration patterns on the host-guest interactions, ^{2}H SSNMR spectra, and associated ^{2}H NMR parameters within these MOFs. A stacked illustration of CH_3D, CH_2D_2, and CD_4 ^{2}H SSNMR spectra is provided in Figure 4-A11.

In almost all instances, CH_2D_2 yielded a relatively narrower ^{2}H powder pattern with significantly less features versus those of CH_3D. Furthermore, in SIFSIX-3-Zn, no ^{2}H NMR parameters could be extracted from the relatively featureless ^{2}H SSNMR spectra of CH_2D_2. The differences between the ^{2}H SSNMR spectra of CH_3D and CH_2D_2 guests are likely due to their number of deuterons. When these deuterated methane guests are adsorbed within the four MOFs, the methane motions are no longer completely isotropic due to the host-guest interactions between methane and the MOF surface. Since the degree of deuteration slightly changes the shape of methane due to the different C-H and C-D bond lengths, the magnitude of the interaction between deuterated-methane molecules and MOF surfaces is also altered.

$C_Q(^2H)$ values are significantly reduced for the CH_2D_2 isomer (Table 4-A3) versus those of the CH_3D isomer, presumably reflecting a decrease in binding strength or a difference in the local methane structure with increased deuteration. It should be noted that a minor reduction in $C_Q(^2H)$ values is expected when comparing the CH_3D to CH_2D_2, [91] but not to such a large degree as observed here: the reported $C_Q(^2H)$ value for static CH_2D_2 is 160 kHz,[92] or ca. 83 % that of the 192 kHz for CH_3D, however, the observed CH_2D_2 $C_Q(^2H)$ values in these MOFs are significantly less than 83 % those of their CH_3D counterparts at any given temperature.

The CD_4 isotope is much more difficult to compare: the fully deuterated methane isomer, CD_4, yielded a single narrow and featureless resonance in all MOFs (Figure 4-A11), and could not be simulated to extract any ^2H NMR parameters. A previous study[93] indicated static CD_4 gives rise to a single featureless ^2H resonance line due to the tetrahedral symmetry of the CD_4 molecule, hence, it is impossible to say if the very narrow lineshapes here arise from the nature of CD_4 or some deuteration-dependent alteration of methane adsorption strength in these MOFs.

The ^2H CSA span values are also influenced by the degree of deuteration of methane guests. ^2H span values are reduced when moving from the CH_3D to the CH_2D_2 isomer in α-$Mg_3(HCO_2)_6$ and Mg-MOF-74, but are increased in α-$Zn_3(HCO_2)_6$ (Tables 1 and Table 4-A3). ^2H CSA makes an even smaller contribution in the CD_4 isomer. Although no ^2H NMR parameters can be obtained from the single ^2H resonance arising from CD_4 within these MOFs, the resonance is actually asymmetric, with more intensity concentrated on the low-frequency portion and less intensity within the tailing high-frequency (Figures 4-A11). This asymmetry indicates that a very small ^{2}H CSA contribution to adsorbed methane guests is also present in ^{2}H SSNMR spectra of the CD_4 isomer. From these findings, it is apparent that ^{2}H SSNMR is an extremely sensitive probe of methane adsorption in MOFs.

4.4 Conclusions

The combination of SCXRD, DFT calculations, and 2H SSNMR experiments has revealed rich insights regarding methane adsorption and mobility in the α-$Mg_3(HCO_2)_6$, α-$Zn_3(HCO_2)_6$, SIFSIX-3-Zn, and MOF-74 metal-organic frameworks.

SCXRD experiments were able to unambiguously locate the single crystallographically unique methane adsorption site within α-$Mg_3(HCO_2)_6$, α-$Zn_3(HCO_2)_6$, and SIFSIX-3-Zn at these guest loading levels. In α-$Mg_3(HCO_2)_6$ and α-$Zn_3(HCO_2)_6$, the adsorption site is located proximate to a carbon and an oxygen atom of the formate linkers, while in SIFSIX-3-Zn, the adsorbed methane molecules are positioned in the centre of the channel. In all MOFs, the thermal ellipsoid of the methane carbon is quite large, reflecting a high degree of methane mobility. DFT calculations produced the geometry-optimized position of methane in these MOF structures, which were found to be in good agreement with SCXRD experimental results. Notably, DFT calculations also revealed the presence of a large area of similar methane adsorption enthalpies and equipotential energy surface about the SCXRD-determined single methane adsorption site in α-$Mg_3(HCO_2)_6$. Calculations indicate methane adsorption is driven mainly by dispersive forces within these MOFs, which were found to be inversely proportional to pore size. The calculated total isoteric heats of adsorption follow the order: SIFSIX-3-Zn (33.3 kJ/mol) > α-$Zn_3(HCO_2)_6$ (27.9 kJ/mol) > α-$Mg_3(HCO_2)_6$ (25.1 kJ/mol).

Static VT ^{2}H SSNMR experiments of singly-deuterated CH_3D guests confirmed that only one crystallographically unique methane adsorption site exists in each MOF at the experimental guest loading levels. The appearance of ^{2}H SSNMR spectra was largely determined by the ^{2}H QI, which is significantly reduced by the nearly isotropic motion of methane. Increases in the observed $C_Q(^{2}H)$ values are strongly correlated to increases in methane binding strength within all four MOFs studied. Interestingly, the apparent ^{2}H CSA should be completely eliminated by motional averaging, but CSA also makes a contribution to the ^{2}H spectral appearance; this phenomenon is the first observation of the NICS effect in MOFs, which re-introduces a significant amount of ^{2}H CSA to adsorbed methane molecules located near the MOF surface. The methane binding strength is strongly linked to the magnitude of the NICS effect, and the magnitude of the NICS effect is readily indicated by the observed ^{2}H span values, isotropic chemical shifts, and orientation of the CS tensor with respect to the EFG tensor. ^{2}H SSNMR experiments of CH_3D adsorbed at the OMSs in Mg- and Zn-MOF-74 confirm that Mg-MOF-74 has a stronger methane binding ability than Zn-MOF-74. For CH_3D adsorbed in Co- and Ni-MOF-74, the ^{2}H SSNMR spectra are broadened by interactions between the paramagnetic metal centres and methane deuterium nuclei, with NMR parameters unavailable from the broad, featureless spectra.

This work is an excellent illustration of how much high-quality data regarding methane adsorption sites, host-guest interactions, guest mobility, and guest deuteration can be obtained when using a combination of SCXRD, DFT, and SSNMR methods. To the best of our knowledge, this is also an exciting first report of the NICS effect in MOFs, which should be quite useful for the future SSNMR study of many different MOF guest species. Using the combination of SSNMR, SCXRD, and DFT calculations, methane adsorption may now be extensively investigated within other MOFs and porous materials, and the knowledge obtained from this investigative approach should prove very helpful for the development of novel MOFs and porous materials for methane adsorption.

4.5 References

1. Mason, J. A.; Veenstra, M.; Long, J. R., *Chem. Sci.* **2014,** *5* (1), 32-51.

2. Service, R. F., *Science* **2014,** *346* (6209), 538-541.

3. Zhou, H.-C.; Kitagawa, S., *Chem. Soc. Rev.* **2014,** *43* (16), 5415-5418.

4. Howarth, A. J.; Liu, Y. Y.; Li, P.; Li, Z. Y.; Wang, T. C.; Hupp, J.; Farha, O. K., *Nat. Rev. Mater.* **2016,** *1* (3), 15018.

5. Makal, T. A.; Li, J.-R.; Lu, W.; Zhou, H.-C., *Chem. Soc. Rev.* **2012,** *41* (23), 7761-7779.

6. Kumar, K. V.; Preuss, K.; Titirici, M.-M.; Rodríguez-Reinoso, F., *Chem. Rev.* **2017,** *117* (3), 1796-1825.

7. Rowsell, J. L. C.; Yaghi, O. M., *Microporous Mesoporous Mater.* **2004,** *73* (1-2), 3-14.

8. Simon, C. M.; Kim, J.; Gomez-Gualdron, D. A.; Camp, J. S.; Chung, Y. G.; Martin, R. L.; Mercado, R.; Deem, M. W.; Gunter, D.; Haranczyk, M.; Sholl, D. S.; Snurr, R. Q.; Smit, B., *Energ. Environ. Sci.* **2015,** *8* (4), 1190-1199.

9. James, S. L., *Chem. Soc. Rev.* **2003,** *32* (5), 276-288.

10. Zhou, H.-C.; Kitagawa, S., *Chem. Soc. Rev.* **2014,** *43* (16), 5415-5418.

11. Zhou, H.-C.; Long, J. R.; Yaghi, O. M., *Chem. Rev.* **2012,** *112* (2), 673-674.

12. Li, B.; Wen, H.-M.; Zhou, W.; Chen, B., *J. Phys. Chem. Lett.* **2014,** *5* (20), 3468-3479.

13. Ma, S.; Zhou, H.-C., *Chem. Commun.* **2010,** *46* (1), 44-53.

14. He, Y.; Zhou, W.; Qian, G.; Chen, B., *Chem. Soc. Rev.* **2014,** *43* (16), 5657-5678.

15. Konstas, K.; Osl, T.; Yang, Y.; Batten, M.; Burke, N.; Hill, A. J.; Hill, M. R., *J. Mater. Chem.* **2012,** *22* (33), 16698-16708.

16. Mason, J. A.; Oktawiec, J.; Taylor, M. K.; Hudson, M. R.; Rodriguez, J.; Bachman, J. E.; Gonzalez, M. I.; Cervellino, A.; Guagliardi, A.; Brown, C. M.; Llewellyn, P. L.; Masciocchi, N.; Long, J. R., *Nature* **2015,** *527* (7578), 357-361.

17. Gaab, M.; Trukhan, N.; Maurer, S.; Gummaraju, R.; Müller, U., *Microporous Mesoporous Mater.* **2012,** *157*, 131-136.

18. Peng, Y.; Krungleviciute, V.; Eryazici, I.; Hupp, J. T.; Farha, O. K.; Yildirim, T., *J. Am. Chem. Soc.* **2013,** *135* (32), 11887-11894.

19. Carrington, E. J.; Vitorica-Yrezabal, I. J.; Brammer, L., *Acta Crystallogr. Sect. B* **2014,** *70*, 404-422.

20. Getzschmann, J.; Senkovska, I.; Wallacher, D.; Tovar, M.; Fairen-Jimenez, D.; Düren, T.; van Baten, J. M.; Krishna, R.; Kaskel, S., *Microporous Mesoporous Mater.* **2010,** *136* (1–3), 50-58.

21. Wu, H.; Zhou, W.; Yildirim, T., *J. Am. Chem. Soc.* **2009,** *131* (13), 4995-5000.

22. Wu, H.; Zhou, W.; Yildirim, T., *J. Phys. Chem. C* **2009,** *113* (7), 3029-3035.

23. Kim, H.; Samsonenko, D. G.; Das, S.; Kim, G.-H.; Lee, H.-S.; Dybtsev, D. N.; Berdonosova, E. A.; Kim, K., *Chem. Asian J.* **2009,** *4* (6), 886-891.

24. Miller, S. R.; Wright, P. A.; Devic, T.; Serre, C.; Férey, G.; Llewellyn, P. L.; Denoyel, R.; Gaberova, L.; Filinchuk, Y., *Langmuir* **2009,** *25* (6), 3618-3626.

25. Chen, S.; Lucier, B. E. G.; Boyle, P. D.; Huang, Y., *Chem. Mater.* **2016,** *28* (16), 5829-5846.

26. Llewellyn, P. L.; Horcajada, P.; Maurin, G.; Devic, T.; Rosenbach, N.; Bourrelly, S.; Serre, C.; Vincent, D.; Loera-Serna, S.; Filinchuk, Y.; Férey, G., *J. Am. Chem. Soc.* **2009,** *131* (36), 13002-13008.

27. Ramsahye, N. A.; Trung, T. K.; Bourrelly, S.; Yang, Q.; Devic, T.; Maurin, G.; Horcajada, P.; Llewellyn, P. L.; Yot, P.; Serre, C.; Filinchuk, Y.; Fajula, F.; Férey, G.; Trens, P., *J. Phys. Chem. C* **2011,** *115* (38), 18683-18695.

28. Getman, R. B.; Bae, Y.-S.; Wilmer, C. E.; Snurr, R. Q., *Chem. Rev.* **2012,** *112* (2), 703-723.

29. Gomez-Gualdron, D. A.; Gutov, O. V.; Krungleviciute, V.; Borah, B.; Mondloch, J. E.; Hupp, J. T.; Yildirim, T.; Farha, O. K.; Snurr, R. Q., *Chem. Mater.* **2014,** *26* (19), 5632-5639.

30. Huang, Y.; Xu, J.; Gul-E-Noor, F.; He, P., Metal-organic frameworks: NMR studies of quadrupolar nuclei. In *Encyclopedia of Inorganic and Bioinorganic Chemistry*, John Wiley & Sons, Ltd: 2011.

31. Hoffmann, H. C.; Debowski, M.; Muller, P.; Paasch, S.; Senkovska, I.; Kaskel, S.; Brunner, E., *Materials* **2012,** *5* (12), 2537-2572.

32. Sutrisno, A.; Huang, Y., *Solid State Nucl. Magn. Reson.* **2013,** *49–50*, 1-11.

33. Ashbrook, S. E.; Dawson, D. M.; Seymour, V. R., *Phys. Chem. Chem. Phys.* **2014,** *16* (18), 8223-8242.

34. He, P.; Lucier, B. E. G.; Terskikh, V. V.; Shi, Q.; Dong, J.; Chu, Y.; Zheng, A.; Sutrisno, A.; Huang, Y., *J. Phys. Chem. C* **2014,** *118* (41), 23728-23744.

35. Mali, G., Looking into metal-organic frameworks with solidstate NMR spectroscopy. In *Metal-Organic Frameworks*, InTech: 2016.

36. Kong, X. Q.; Scott, E.; Ding, W.; Mason, J. A.; Long, J. R.; Reimer, J. A., *J. Am. Chem. Soc.* **2012,** *134* (35), 14341-14344.

37. Lin, L.-C.; Kim, J.; Kong, X.; Scott, E.; McDonald, T. M.; Long, J. R.; Reimer, J. A.; Smit, B., *Angew. Chem. Int. Ed.* **2013,** *52* (16), 4410-4413.

38. Wang, W. D.; Lucier, B. E. G.; Terskikh, V. V.; Wang, W.; Huang, Y., *J. Phys. Chem. Lett.* **2014,** *5* (19), 3360-3365.

39. Lucier, B. E. G.; Chan, H.; Zhang, Y.; Huang, Y., *Eur. J. Inorg. Chem.* **2016,** *2016* (13-14), 2017-2024.

40. Lucier, B. E. G.; Zhang, Y.; Lee, K. J.; Lu, Y.; Huang, Y., *Chem. Commun.* **2016,** *52* (48), 7541-7544.

41. Xu, J.; Sinelnikov, R.; Huang, Y., *Langmuir* **2016,** *32* (22), 5468-5479.

42. Zhang, Y.; Lucier, B. E. G.; Huang, Y., *Phys. Chem. Chem. Phys.* **2016,** *18* (12), 8327-8341.

43. Lu, Y.; Lucier, B. E. G.; Zhang, Y.; Ren, P.; Zheng, A.; Huang, Y., *Phys. Chem. Chem. Phys.* **2017,** *19* (8), 6130-6141.

44. Vold, R. L.; Hoatson, G. L., *J. Magn. Reson.* **2009,** *198* (1), 57-72.

45. Gonzalez, J.; Nandini Devi, R.; Tunstall, D. P.; Cox, P. A.; Wright, P. A., *Microporous Mesoporous Mater.* **2005,** *84* (1–3), 97-104.

46. Gould, S. L.; Tranchemontagne, D.; Yaghi, O. M.; Garcia-Garibay, M. A., *J. Am. Chem. Soc.* **2008,** *130* (11), 3246-3247.

47. Kolokolov, D. I.; Jobic, H.; Stepanov, A. G.; Guillerm, V.; Devic, T.; Serre, C.; Férey, G., *Angew. Chem. Int. Ed.* **2010,** *49* (28), 4791-4794.

48. Mowat, J. P. S.; Miller, S. R.; Griffin, J. M.; Seymour, V. R.; Ashbrook, S. E.; Thompson, S. P.; Fairen-Jimenez, D.; Banu, A.-M.; Düren, T.; Wright, P. A., *Inorg. Chem.* **2011,** *50* (21), 10844-10858.

49. Vukotic, V. N.; Harris, K. J.; Zhu, K.; Schurko, R. W.; Loeb, S. J., *Nat. Chem.* **2012,** *4* (6), 456-460.

50. Kolokolov, D. I.; Stepanov, A. G.; Jobic, H., *J. Phys. Chem. C* **2014,** *118* (29), 15978-15984.

51. Ueda, T.; Kurokawa, K.; Omichi, H.; Miyakubo, K.; Eguchi, T., *Chem. Phys. Lett.* **2007,** *443* (4–6), 293-297.

52. Bureekaew, S.; Horike, S.; Higuchi, M.; Mizuno, M.; Kawamura, T.; Tanaka, D.; Yanai, N.; Kitagawa, S., *Nat. Mater.* **2009,** *8* (10), 831-836.

53. Kolokolov, D. I.; Jobic, H.; Rives, S.; Yot, P. G.; Ollivier, J.; Trens, P.; Stepanov, A. G.; Maurin, G., *J. Phys. Chem. C* **2015,** *119* (15), 8217-8225.

54. Rood, J. A.; Noll, B. C.; Henderson, K. W., *Inorg. Chem.* **2006,** *45* (14), 5521-5528.

55. Wang, Z.; Zhang, Y.; Kurmoo, M.; Liu, T.; Vilminot, S.; Zhao, B.; Gao, S., *Aust. J. Chem.* **2006,** *59* (9), 617-628.

56. Dietzel, P. D. C.; Blom, R.; Fjellvåg, H., *Eur. J. Inorg. Chem.* **2008,** *2008* (23), 3624-3632.

57. Nugent, P.; Belmabkhout, Y.; Burd, S. D.; Cairns, A. J.; Luebke, R.; Forrest, K.; Pham, T.; Ma, S.; Space, B.; Wojtas, L.; Eddaoudi, M.; Zaworotko, M. J., *Nature* **2013,** *495* (7439), 80-84.

58. Bruker-AXS, S., *version 2013.8,* **2013**, Bruker-AXS, Madison, WI 53711, USA.

59. Bruker-AXS, S., *version 2012.1,* **2012**, Bruker-AXS, Madison, WI 53711, USA.

60. Sheldrick, G., *Acta Crystallogr. Sect. A* **2015,** *71* (1), 3-8.

61. Sheldrick, G., *Acta Crystallogr. Sect. C* **2015,** *71* (1), 3-8.

62. Gabe, E. J.; Le Page, Y.; Charland, J.-P.; Lee, F. L.; White, P. S., *J. Appl. Cryst.* **1989,** *22* (4), 384-387.

63. Clark, S. J.; Segall, M. D.; Pickard, C. J.; Hasnip, P. J.; Probert, M. J.; Refson, K.; Payne, M. C., *Z. Kristall.* **2005,** *220* (5-6), 567-570.

64. Perdew, J. P.; Burke, K.; Ernzerhof, M., *Phys. Rev. Lett.* **1996,** *77* (18), 3865-3868.

65. Grimme, S., *J. Comput. Chem.* **2006,** *27* (15), 1787-1799.

66. Pickard, C. J.; Mauri, F., *Phys. Rev. B* **2001,** *63*, 245101.

67. Yates, J. R.; Pickard, C. J.; Mauri, F., *Phys. Rev. B* **2007,** *76*, 024401.

68. Gottlieb, H. E.; Kotlyar, V.; Nudelman, A., *J. Org. Chem.* **1997,** *62* (21), 7512-7515.

69. Dybowski, C.; Neue, G., *Prog. Nucl. Magn. Reson. Spectrosc.* **2002,** *41* (3–4), 153-170.

70. Eichele K.; Wasylishen R. E., *WSolids1* University of Tübingen, Tübingen, Germany, **2009**.

71. Hu, J.; Sun, T.; Ren, X.; Wang, S., *Microporous Mesoporous Mater.* **2015,** *204*, 73-80.

72. Spanopoulos, I.; Bratsos, I.; Tampaxis, C.; Kourtellaris, A.; Tasiopoulos, A.; Charalambopoulou, G.; Steriotis, T. A.; Trikalitis, P. N., *CrystEngComm* **2015,** *17* (3), 532-539.

73. Fischer, M., *Microporous Mesoporous Mater.* **2016,** *219*, 249-257.

74. Gonzalez, M. I.; Mason, J. A.; Bloch, E. D.; Teat, S. J.; Gagnon, K. J.; Morrison, G. Y.; Queen, W. L.; Long, J. R., *Chem. Sci.* **2017,** *8* (6), 4387-4398.

75. Snyder, L. C., *J. Chem. Phys.* **1978,** *68* (1), 291-294.

76. Duer, M. J., NMR Techniques for Studing Molecular Motion in Solids. In *solid-state NMR spectroscopy principles and applications*, Blackwell Science: 2002.

77. Poupko, R.; Luz, Z.; Vega, A. J.; Zimmermann, H., *J. Chem. Phys.* **1987,** *86* (10), 5358-5364.

78. Hauch, A.; Bildsøe, H.; Jakobsen, H. J.; Skibsted, J., *J. Magn. Reson.* **2003,** *165* (2), 282-292.

79. Antonijevic, S.; Wimperis, S., *J. Chem. Phys.* **2005,** *122* (4), 044312.

80. Chen, Z.; Wannere, C. S.; Corminboeuf, C.; Puchta, R.; Schleyer, P. v. R., *Chem. Rev.* **2005,** *105* (10), 3842-3888.

81. Sebastiani, D., *ChemPhysChem* **2006,** *7* (1), 164-175.

82. Stanger, A., *J. Org. Chem.* **2006,** *71* (3), 883-893.

83. Forse, A. C.; Griffin, J. M.; Presser, V.; Gogotsi, Y.; Grey, C. P., *J. Phys. Chem. C* **2014,** *118* (14), 7508-7514.

84. Li, K.; Bo, Z.; Yan, J.; Cen, K., *Sci. Rep.* **2016,** *6*, 39689.

85. Elsaidi, S. K.; Mohamed, M. H.; Schaef, H. T.; Kumar, A.; Lusi, M.; Pham, T.; Forrest, K. A.; Space, B.; Xu, W. Q.; Halder, G. J.; Liu, J.; Zaworotko, M. J.; Thallapally, P. K., *Chem. Commun.* **2015,** *51* (85), 15530-15533.

86. Uemura, K.; Maeda, A.; Maji, T. K.; Kanoo, P.; Kita, H., *Eur. J. Inorg. Chem.* **2009,** *2009* (16), 2329-2337.

87. Wilmer, C. E.; Leaf, M.; Lee, C. Y.; Farha, O. K.; Hauser, B. G.; Hupp, J. T.; Snurr, R. Q., *Nat. Chem.* **2012,** *4* (2), 83-89.

88. Schoedel, A.; Ji, Z.; Yaghi, O. M., *Nat. Energy* **2016,** *1*, 13.

89. Rosi, N. L.; Kim, J.; Eddaoudi, M.; Chen, B.; O'Keeffe, M.; Yaghi, O. M., *J. Am. Chem. Soc.* **2005,** *127* (5), 1504-1518.

90. Mercado, R.; Vlaisavljevich, B.; Lin, L.-C.; Lee, K.; Lee, Y.; Mason, J. A.; Xiao, D. J.; Gonzalez, M. I.; Kapelewski, M. T.; Neaton, J. B.; Smit, B., *J. Phys. Chem. C* **2016,** *120* (23), 12590-12604.

91. Burnell, E. E.; Lange, C. A. d., *J. Chem. Phys.* **1982,** *76* (7), 3474-3479.

92. Buchman, S.; Candela, D.; Vetterling, W. T.; Pound, R. V., *Phys. Rev. B* **1983,** *28* (1), 8-14.

93. Anderson, C. H.; Ramsey, N. F., *Phys. Rev.* **1966,** *149* (1), 14-24.

4.6 Appendix

Experimental details

MOF synthesis. All chemicals were obtained from Sigma-Aldrich and were used without further purification.

α-$Mg_3(HCO_2)_6$, Mg-formate. 3 mmol (0.7692 g) of $Mg(NO_3)_2 \cdot 6H_2O$, 6 mmol (0.2762 g) of formic acid (HCOOH), and 10 mL of dimethylformamide (DMF) were mixed together within a 23 mL Teflon-lined stainless steel autoclave, which was then sealed and heated in an oven at 110 °C for 2 days. The white crystalline product was washed three times with DMF and dried using vacuum filtration at room temperature.

α-$Zn_3(HCO_2)_6$, Zn-formate. 10 mmol (3.0 g) of $Zn(NO_3)_2 \cdot 6H_2O$ was first dissolved in 25 mL methanol in a small beaker. In a separate container, 43 mmol (2.0 g) of formic acid and 30 mmol (3.0 g) of triethylamine (TEA) were also dissolved in 25 mL of methanol. These two methanol-reagent solutions were then mixed gently with each other in a clean glass vial. The vial was then covered by parafilm, and a series of pinholes were poked through the parafilm to aid in product crystallization. After leaving the solution undisturbed for three days, colorless single crystals of product were apparent and could be collected. The single crystals were then washed three times with methanol and dried using vacuum filtration at room temperature.

SIFSIX-3-Zn. A solution was first made by adding 1.3 mmol (0.10 g) of pyrazine to 2.0 mL of methanol. In a glass vial, the pyrazine solution was then gently mixed with a separate solution of 0.6 mmol (0.13 g) $ZnSiF_6 \cdot xH_2O$ in 2.0 mL of methanol. The product was obtained as yellow crystals after three days, and was then washed three times with methanol and dried using vacuum filtration at room temperature.

Mg-MOF-74. To begin, 0.75 mmol (0.1486 g) of 2,5-dihydroxyterephthalic acid (H_4DOBDC) was dissolved in 10 mL tetrahydrofuran (THF) within a 23 mL Teflon-lined stainless steel autoclave. To this reagent mixture, 3 mL of a 1.0 M aqueous NaOH solution was then added. The third component, 1.5 mmol (0.3846 g) $Mg(NO_3)_2 \cdot 6H_2O$, was dissolved in 5 mL of deionized water and then added to the reagent mixture in the Teflon inlet while stirring. The resulting reagent mixture was then sealed within the autoclave, which was placed into an oven and heated at 110 °C for 3 days. The product was obtained as a yellow powder, which was washed three times with THF and then dried using vacuum filtration at room temperature.

Zn-MOF-74. 10 mL of THF and 0.75 mmol (0.1486 g) of H_4DOBDC were mixed within a 23 mL Teflon-lined stainless steel autoclave. Once the solid H_4DOBDC was dissolved in the THF, 3 mL of 1.0 M aqueous sodium hydroxide solution was added to the reagent mixture. In a separate container, 1.5 mmol (0.4462 g) of $Zn(NO_3)_2 \cdot 6H_2O$ was dissolved in 5 mL deionized water; this solution was then added to the reagent mixture in the Teflon inlet while stirring. The mixture was sealed within the autoclave, which was then placed in an oven and heated at 110 °C for 3 days. The product was obtained as a yellow-green powder, which was first washed three times with THF and then washed with methanol three more times. The washed product was then dried using vacuum filtration at room temperature.

Ni-MOF-74. 0.75 mmol (0.1486 g) of H_4DOBDC was first dissolved in 10 mL THF within a 23 mL Teflon-lined stainless steel autoclave. In a separate container, 1.5 mmol (0.3733 g) of $Ni(CH_3COO)_2 \cdot 4H_2O$ was dissolved in 5 mL deionized water, and the resulting solution was then added to the reagent mixture in the Teflon inlet. After 1 hour of stirring the resulting reagent mixture in ambient conditions, the autoclave was sealed and placed in a 110 °C oven for 3 days. The ochre (*i.e.*, yellow-orange-brown) product was obtained as a powder, which was washed three times with THF followed by three more washes using methanol. The washed product was then dried using vacuum filtration at room temperature.

Co-MOF-74. 0.75 mmol (0.1486 g) of H_4DOBDC was first dissolved in 10 mL THF within a 23 mL Teflon-lined stainless steel autoclave. A solution of 1.5 mmol (0.3736 g) of $Co(CH_3COO)_2 \cdot 4H_2O$ in 5 mL H_2O was then added to the reagent mixture. The autoclave containing the reagents was then sealed and placed in a 110 °C oven for 3 days. The off-purple product was obtained as a powder, which was washed three times with THF, washed another three times with methanol, and then dried using vacuum filtration at room temperature.

CASTEP calculations. DFT calculations for methane-loaded Mg-formate, Zn-formate, and SIFSIX-3-Zn were performed using version 7 of the CASTEP code, which employs a combination of a plane wave basis and pseudopotentials. Ultrasoft pseudopotentials were generated on the fly. The plane wave cutoff energy was set to 650 eV, and the first Brillouin zone was sampled using a 2 × 2 × 2 Monkhorst-Pack grid of *k*-points. The calculations used the PBE exchange-correlation functional in conjunction with the D2 dispersion correction devised by Grimme. For Mg-formate, two different methane-loaded structures were investigated, with one incorporating 1 CH_4 guest/unit cell and the other using 4 CH_4 guests/unit cell. The methane loading levels of Zn-formate and SIFSIX-3-Zn are 1 CH_4 guest/unit cell and 0.25 CH_4 guest/unit cell, respectively.

Additional results and discussion: DFT calculations of methane within Mg-formate. Our DFT calculations involved geometry optimizations of methane guests at different initial locations within α-$Mg_3(HCO_2)_6$ at loading levels of 1.0 and 4.0 methane molecules per unit cell, followed by a comparison of the final methane guest location versus the methane carbon position and associated thermal ellipsoid obtained from SCXRD experiments. Three different initial guest methane positions were explored and then geometry-optimized within Mg-formate: site EXP, site A, and site B. Site EXP refers to the methane adsorption site obtained from our SCXRD experiments, while site A and site B denote the two methane adsorption sites obtained from a previous DFT study. It should be noted that the guest methane molecule positions were optimized along with the positions of all atoms in the MOF, which was accomplished by relaxing all atomic coordinates but fixing the lattice parameters to the experimental values from the SCXRD investigation listed in Appendix A. The DFT calculations were performed at loading levels of both 1.0 methane molecules/unit cell and 4.0 methane molecules/unit cell.

The results of DFT geometry optimizations are shown in Figure 4-A12, where Figure 4-A12(a) shows results at a loading level of 1.0 methane molecules/unit cell and Figure 4-A12(b) was constructed from the results at 4.0 methane molecules/unit cell. For clarity, site EXP1 refers to the 1.0 methane/unit cell results, while site EXP2 denotes the 4.0 methane/unit cell calculations. In Figure 4-A12, the experimental SCXRD methane carbon position is included, along with its carbon displacement ellipsoid. Figures 4-A12(a) and (b) are strikingly similar, indicating that the methane loading level does not have a very strong influence on the methane adsorption site location. The DFT-optimized Site EXP1 and Site EXP2 are quite proximate to the SCXRD methane carbon position and lie well inside the carbon displacement ellipsoid. Sites EXP1 and EXP2 are approximately 0.3 Å apart, and site EXP1 is closer to the experimental SCXRD site; this is because since site EXP1 was obtained using approximately the same methane loading level as SCXRD experiments.

The proximity of potential adsorption sites obtained from geometry optimizations, along with the large carbon displacement ellipsoid obtained from SCXRD experiments, suggest that there is a large region near the experimentally-determined methane adsorption site where adsorption energies are relatively similar. The methane adsorption energies within Mg-formate at loading levels of 1.0 and 4.0 methane molecules/unit cell were obtained from DFT calculations and are listed in Table 4-A4 and Table 4-A5. The first notable observation is that the calculated energies for all sites falls within a ca. 1 kJ/mol range despite their differences in location, confirming that there indeed is a large area of similar adsorption enthalpies (*i.e.*, a "smeared out" equipotential energy surface) within Mg-formate; in fact, we cannot rule out that additional local minima could be found if additional DFT calculations using different starting locations and orientations of the methane molecule were performed. Methane molecules at site A are associated with slightly lower adsorption energies than site B at both methane loading levels, which is in line with the location of site A within the SCXRD carbon displacement ellipsoid and the location of site B just outside the displacement ellipsoid. The methane adsorption energies are not strongly influenced by the methane loading level, as evidenced by the similar adsorption isosteric enthalpy of -25.1 kJ/mol for site EXP1 (1.0 methane/unit cell) and -25.7 kJ/mol for site EXP2 (4.0 methane/unit cell). The relatively larger magnitude of adsorption enthalpy of Site EXP2 is likely due to the increased presence of $CH_4 – CH_4$ intermolecular interactions.

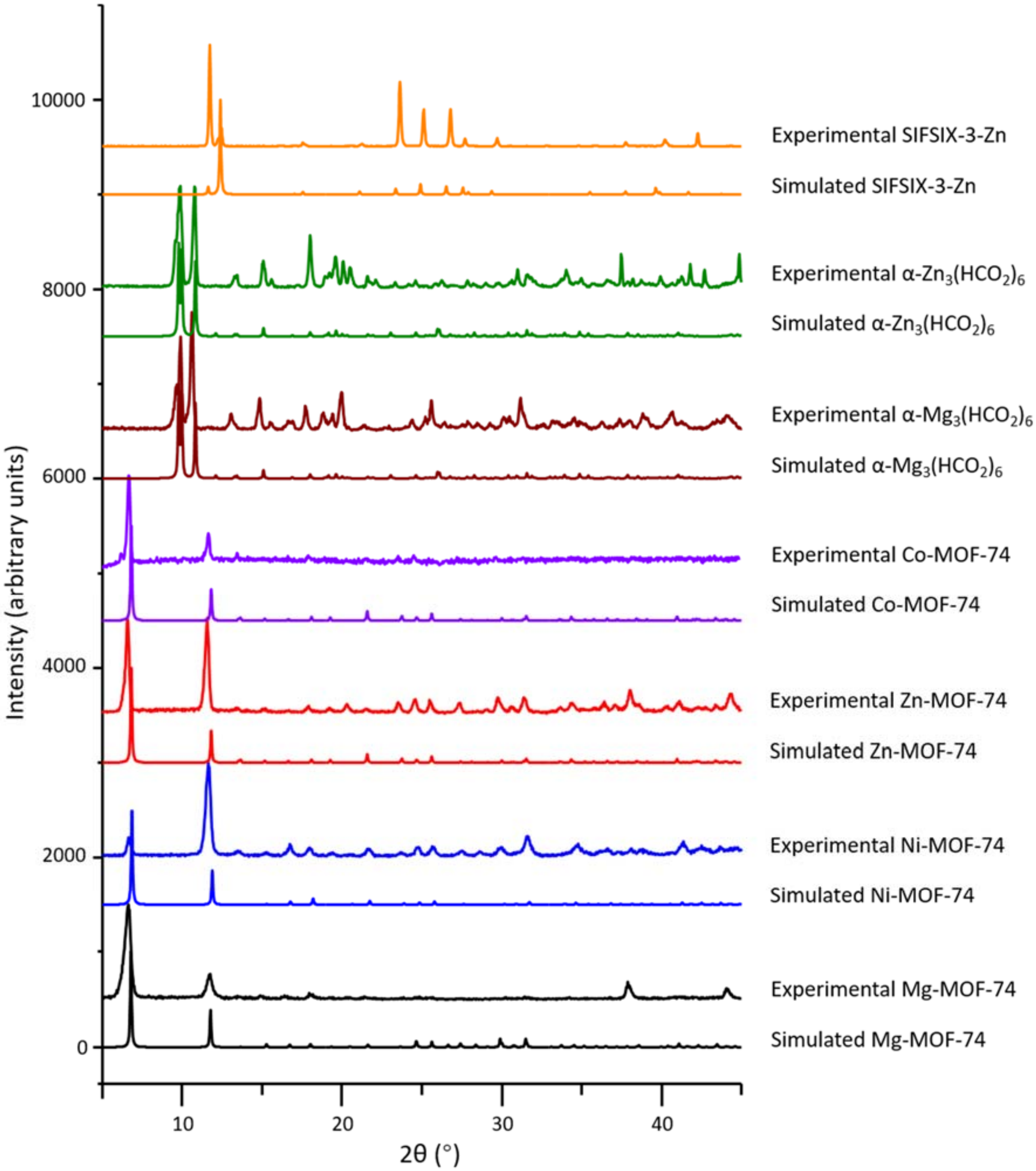

Figure 4-A1. The experimental and simulated powder X-ray diffraction patterns of the MOFs included in this study. All simulations were calculated from reported crystal structures.

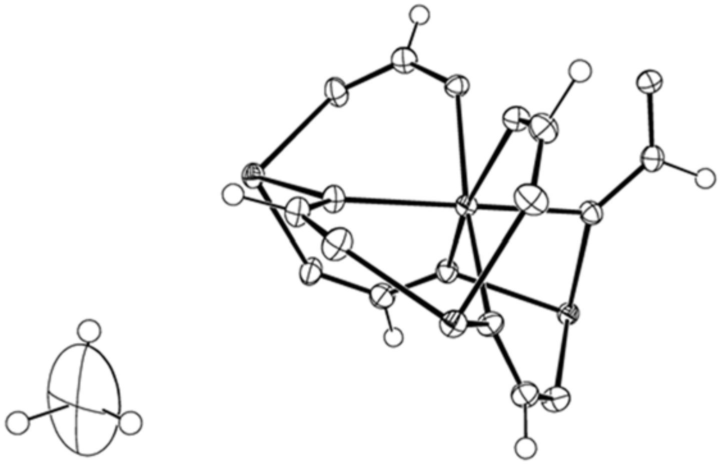

Figure 4-A2. An ORTEP drawing of the asymmetric unit showing CH_3D adsorbed within α-$Mg_3(HCO_2)_6$. Note the very large thermal ellipsoid for the carbon atom of CH_3D, which reflects a high degree of guest methane mobility. The ellipsoids are drawn at the 50% probability level and all hydrogen atoms were drawn with arbitrary radii for clarity.

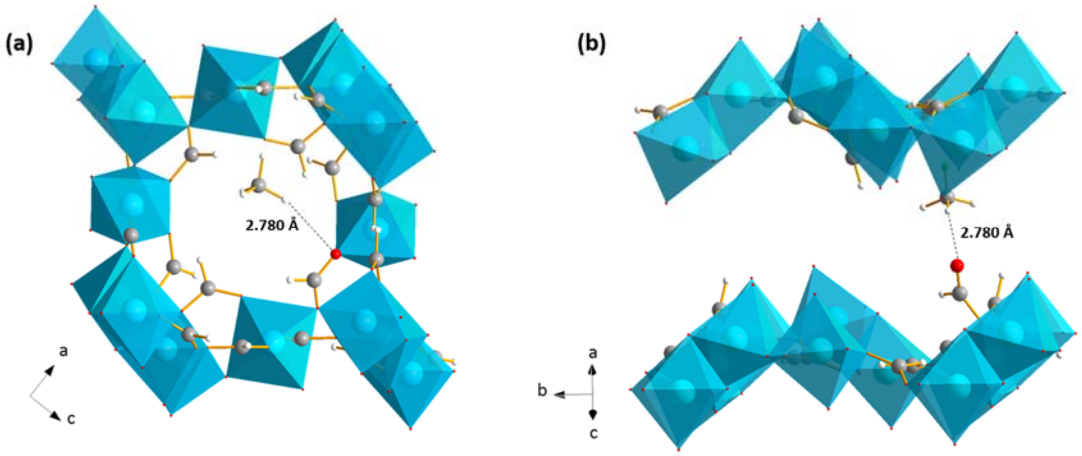

Figure 4-A3. The DFT optimized methane-loaded Mg-formate structure at a loading level of 1.0 methane/unit cell are shown from various perspectives. The shortest distances between the adsorbed methane hydrogen atom and the framework atoms of α-$Mg_3(HCO_2)_6$ are depicted in (a) and (b) from two different projections. The colors blue, grey, white and green correspond to the magnesium metal centre, carbon, hydrogen, and deuterium, respectively.

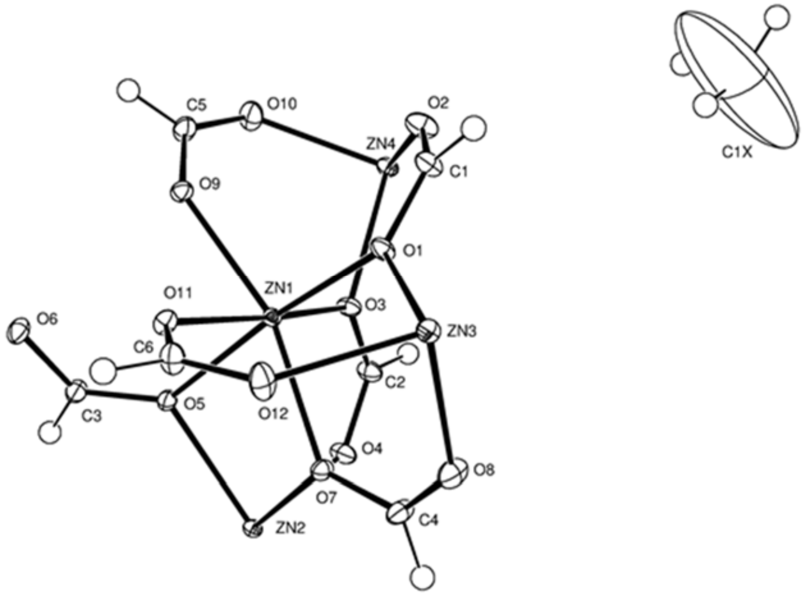

Figure 4-A4. An ORTEP drawing of the asymmetric unit of CH_3D adsorbed in α-$Zn_3(HCO_2)_6$. Note the large thermal ellipsoid of the CH_3D carbon atom in the bottom right, which reflects the high mobility of methane guests. All ellipsoids are drawn at the 50% probability level except for hydrogen atoms, which were drawn with arbitrary radii for clarity.

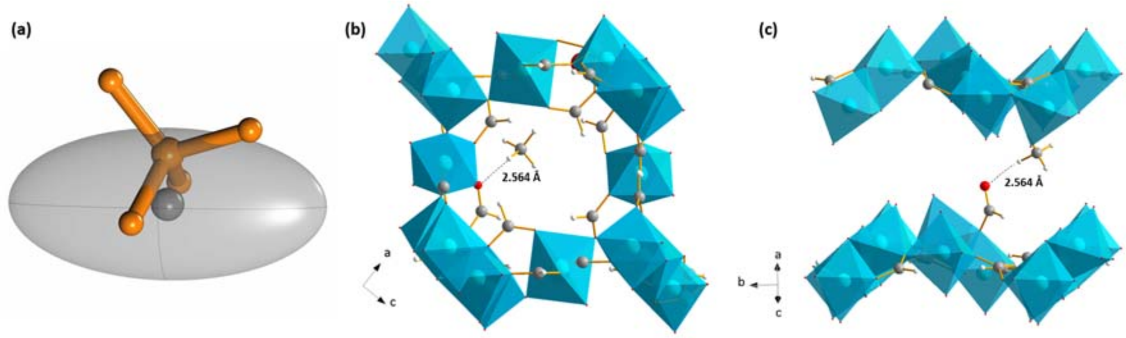

Figure 4-A5. The results of DFT geometry optimizations are shown from a short-range ((a)) and a long-range ((b) and (c)) perspective using a loading level of 1.0 methane molecule/unit cell. (a) illustrates a visualization of the CH_4 carbon atom and its thermal ellipsoid, as determined from SCXRD analysis of methane-loaded α-$Zn_3(HCO_2)_6$ are shown in grey along with the methane adsorption site (orange) obtained from DFT calculations. The shortest distances between the adsorbed methane hydrogen atom and the framework atoms of α-$Zn_3(HCO_2)_6$ are depicted in (b) and (c) in two different projections. The colors blue, grey, white and green correspond to the zinc metal center, carbon, hydrogen, and deuterium, respectively.

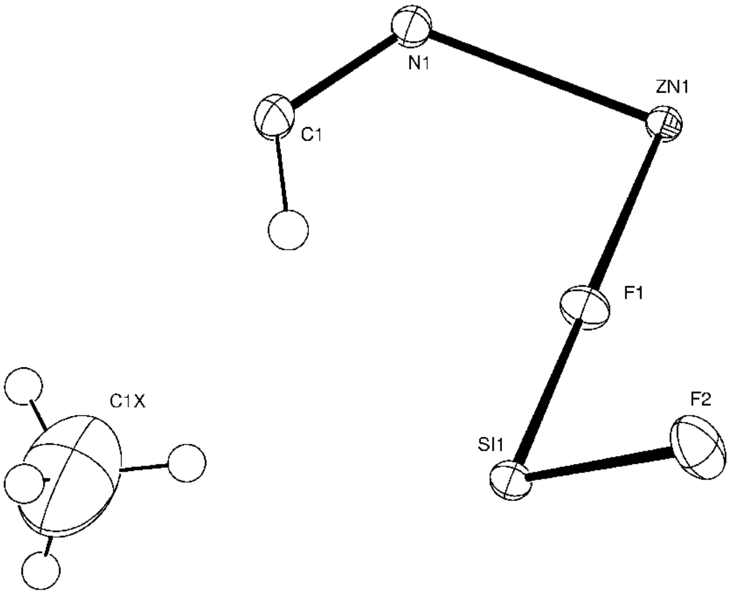

Figure 4-A6. An ORTEP drawing of CH_3D adsorbed within the asymmetric unit of SIFSIX-3-Zn is depicted. The ellipsoids are drawn at the 50% probability level for all atoms except hydrogen; the hydrogen atoms were drawn with arbitrary radii for clarity. Note the very large thermal ellipsoid associated with the CH_3D carbon atom, C1X, which reflects the mobility of methane guests in this MOF.

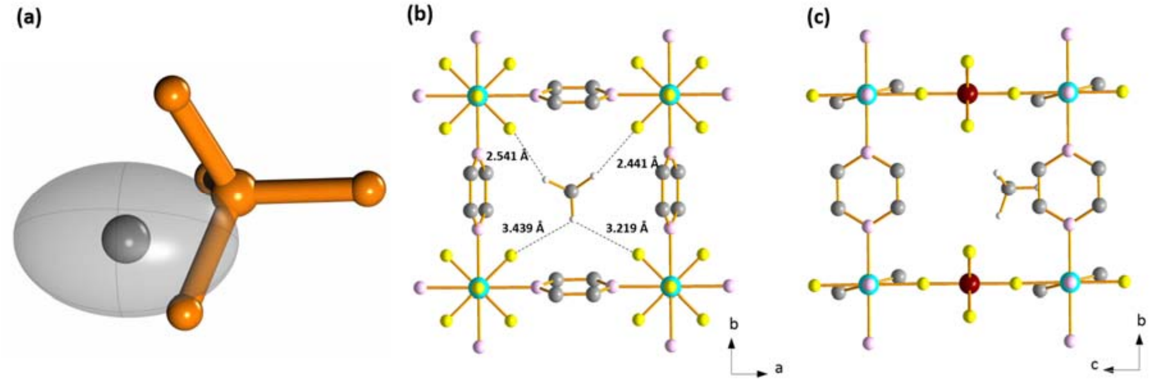

Figure 4-A7. The results of DFT geometry optimizations are shown from a short-range ((a)) and a long-range ((b) and (c)) perspective using a loading level of 0.25 methane molecule/unit cell. (a) illustrates a visualization of the CH_4 carbon atom and its thermal ellipsoid, as determined from SCXRD analysis of methane-loaded SIFSIX-3-Zn, are shown in grey along with the methane adsorption site (orange) obtained from DFT calculations. The shortest distances between the adsorbed methane hydrogen atom and the framework atoms of SIFSIX-3-Zn are depicted in (b), while (c) illustrates the methane position when viewed along the *a*-axis. In this illustration, carbon is colored gray, zinc is blue, silicon is brown, fluorine is yellow, nitrogen is light pink, hydrogen is white.

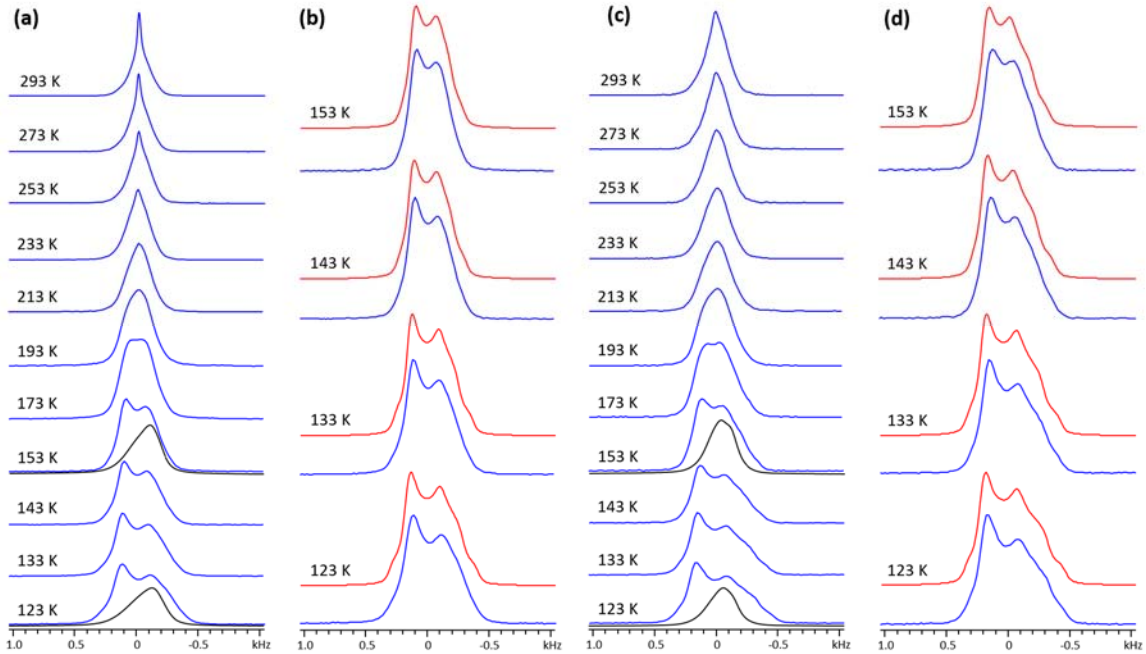

Figure 4-A8. The experimental static VT ^{2}H SSNMR spectra of CH_2D_2 adsorbed within α-$Mg_3(HCO_2)_6$ are depicted in (a), along with a comparison of experimental (blue) and analytical simulated (red) ^{2}H SSNMR spectra at low temperatures in (b). In (c), the experimental static VT ^{2}H SSNMR spectra of CH_2D_2 adsorbed within α-$Zn_3(HCO_2)_6$ are shown. A comparison of experimental (blue) and analytical simulated (red) ^{2}H SSNMR spectra of CH_2D_2 in α-$Zn_3(HCO_2)_6$ at low temperatures is shown in (d). The experimental static VT ^{2}H SSNMR spectra of CD_4 adsorbed within α-$Mg_3(HCO_2)_6$ and α-$Zn_3(HCO_2)_6$ are shown as black traces in (a) and (c), respectively, at temperatures of 153 and 123 K.

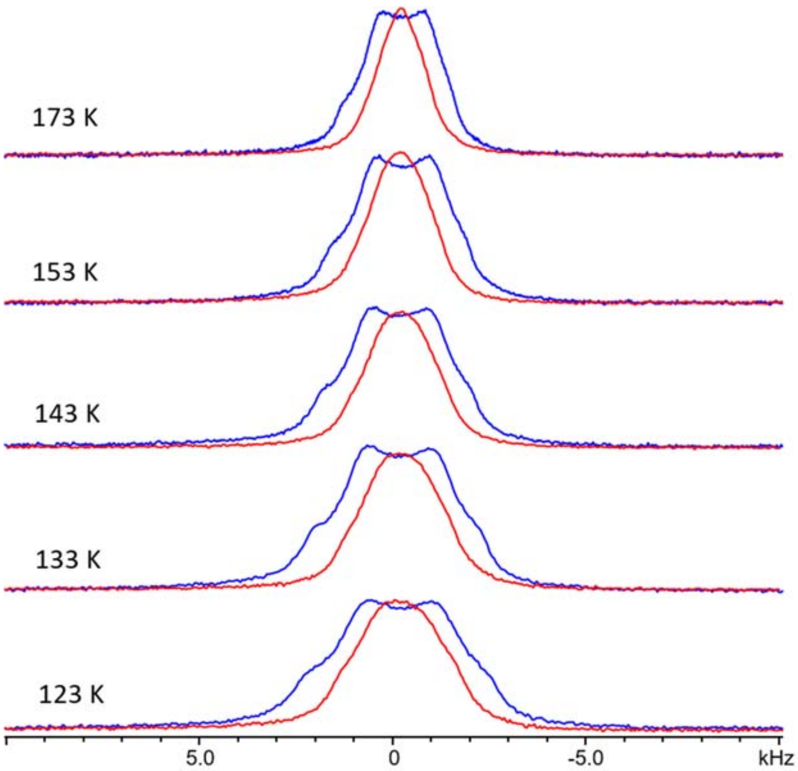

Figure 4-A9. A comparison of the experimental static VT ^{2}H SSNMR spectra of CH_3D (blue traces) and CH_2D_2 (red traces) adsorbed within SIFSIX-3-Zn, as obtained using a guest loading level of 0.2 CH_2D_2/Zn and 0.2 CH_3D/Zn. The ^{2}H SSNMR powder patterns of CH_2D_2 guests are narrower than those of CH_3D at all experimental temperatures due to the smaller $C_Q(^2H)$ value of CH_2D_2.

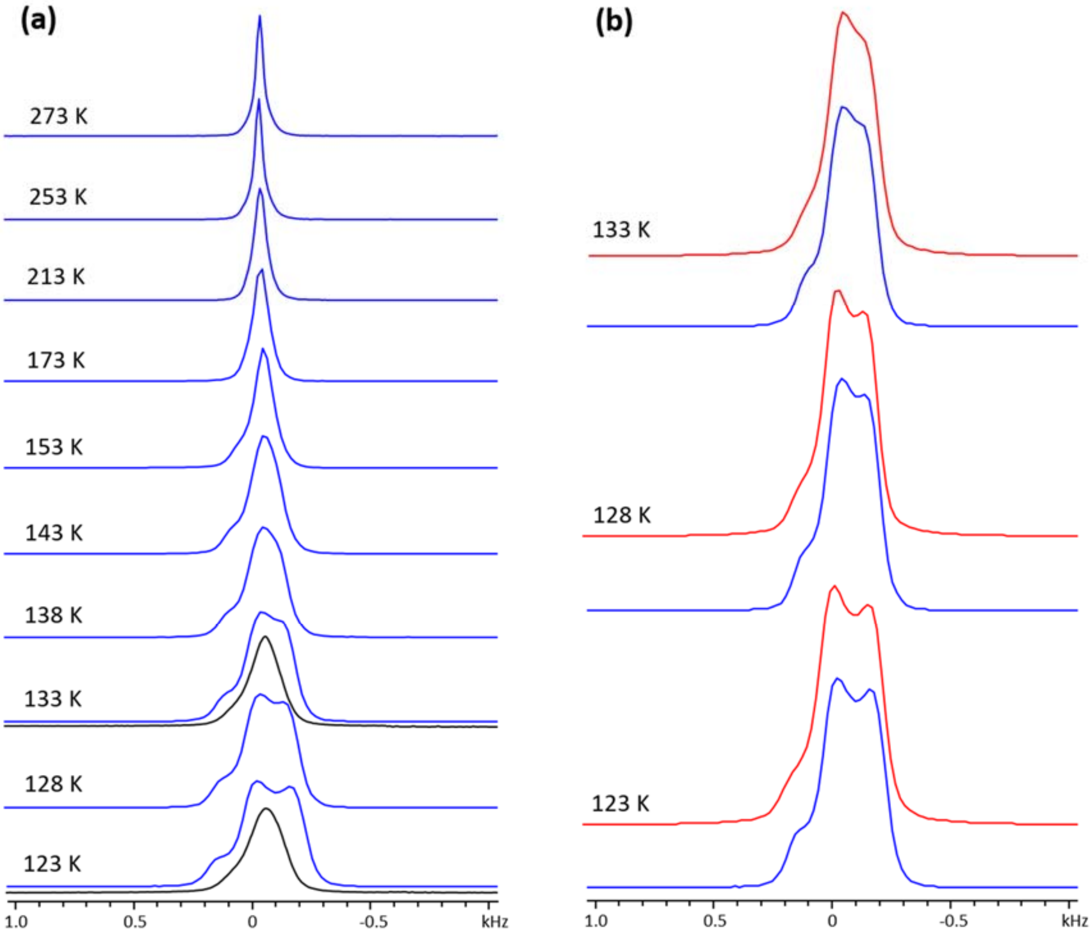

Figure 4-A10. The experimental static VT ^{2}H SSNMR spectra of CH_2D_2 adsorbed in Mg-MOF-74 at a loading level of 0.2 CH_2D_2/Mg are shown in (a), alongside a comparison of the experimental (blue) and analytical simulated (red) ^{2}H SSNMR spectra at low temperatures in (b). The VT ^{2}H SSNMR spectra of adsorbed CH_2D_2 are narrower than those of CH_3D, and these spectra of CH_2D_2 only exhibit well-defined features at relatively lower temperatures versus the spectra of CH_3D. The experimental static VT ^{2}H SSNMR spectra of CD_4 adsorbed within Mg-MOF-74 are shown in (a) as black traces.

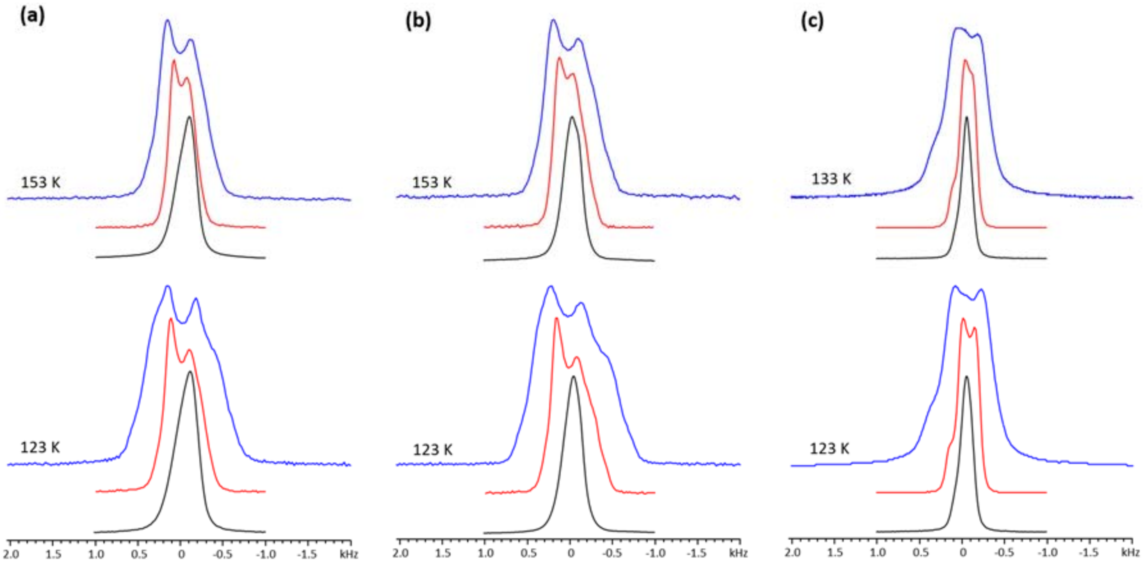

Figure 4-A11. Comparisons of ^{2}H SSNMR spectra of CH_3D (blue spectra), CH_2D_2 (red spectra), and CD_4 (black spectra) adsorbed within (a) α-$Mg_3(HCO_2)_6$, (b) α-$Zn_3(HCO_2)_6$, and (c) Mg-MOF-74.

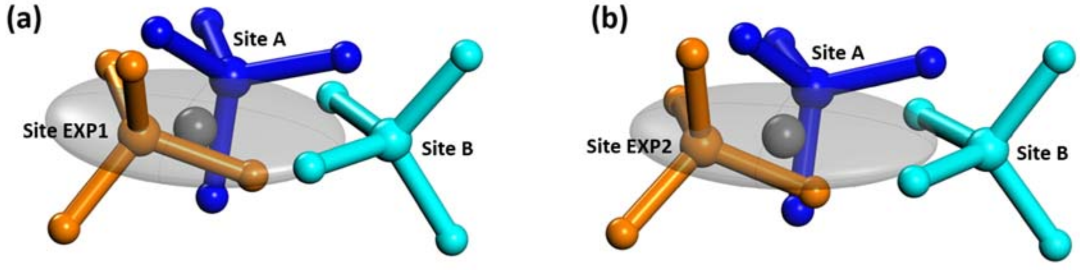

Figure 4-A12. A visualization of the CH_4 carbon atom and its thermal ellipsoid, as determined from SCXRD analysis of methane-loaded Mg-formate, are shown in grey along with the three methane adsorption sites obtained from DFT calculations. The orange methane molecule labeled "Site EXP" is the resulting methane position after DFT optimization of our SCXRD structure; the methane hydrogen atoms were added computationally and their position was also optimized. The blue methane corresponds to the optimized position of adsorption site A and the cyan methane represents the optimized position of adsorption site B. Sites A and B refer to the final positions resulting from DFT optimizations where the reported methane adsorption sites from a previous DFT study[1] were used as starting positions for the optimization after being placed within the XRD-derived crystal structure obtained in this study, see details in the main text and Appendix. The DFT results using a loading level of 1.0 methane molecule/unit cell of Mg-formate are shown in (a), while the corresponding results using a loading level of 4.0 methane molecules/unit cell of Mg-formate are shown in (b). The size of the SCXRD carbon thermal ellipsoid corresponds to a probability of 90% for the carbon atom to lie within the ellipsoid. Note that sites EXP and A lie within the SCXRD carbon ellipsoid, and Site B is nearby. The colors blue, grey, white and green correspond to the metal centre, carbon, hydrogen, and deuterium, respectively

Table 4-A1. Isoteric adsorption enthalpies (in kJ mol^{-1}) obtained from DFT calculations of α-$Mg_3(HCO_2)_6$ containing 1.00 and 4.00 CH_4/unit cell, α-$Zn_3(HCO_2)_6$ containing 1.00 CH_4/unit cell, and SIFSIX-3-Zn containing 0.25 CH_4/unit cell. Along with the total adsorption energy E_{ads}, the dispersive contribution E_{disp} and non-dispersive contribution $E_{non\text{-}disp}$ are also given.

MOF (loading level)	E_{ads} / kJ mol^{-1}	E_{disp} / kJ mol^{-1}	$E_{non\text{-}disp}$ / kJ mol^{-1}
α-$Mg_3(HCO_2)_6$ (1.00 CH_4/unit cell)	-25.1	-20.3	-4.8
α-$Mg_3(HCO_2)_6$ (4.00 CH_4/unit cell)	-25.7	-21.1	-4.6
α-$Zn_3(HCO_2)_6$ (1.00 CH_4/unit cell)	-27.9	-22.9	-5.3
SIFSIX-3-Zn (0.25 CH_4/unit cell)	-33.3	-32.7	-0.6

Table 4-A2. Plane-wave DFT calculated ^{2}H NMR parameters for CH_3D guests positioned at the DFT-optimized SCXRD experimental locations within α-$Mg_3(HCO_2)_6$ at two different methane loading levels, α-$Zn_3(HCO_2)_6$ at a methane loading level of 1.0 methane molecules/unit cell, and SIFSIX-3-Zn at a methane loading level of 0.25 methane molecules/unit cell.

Site		**C_Q (kHz)**	**η_Q**	**Ω (ppm)**	**κ**	**β (°)**
Single static CH_3D molecule		192	0.000	9.024	-1.000	0.000
Site EXP1 in DFT optimized XRD structure of α-$Mg_3(HCO_2)_6$ at a loading level of 1.0 methane molecule/unit cell	^{2}H atom #1[a]	189	0.002	9.894	-0.525	11.015
	^{2}H atom #2[a]	191	0.009	9.969	-0.407	5.812
	^{2}H atom #3[a]	188	0.004	12.779	-0.515	6.318
	^{2}H atom #4[a]	192	0.006	7.660	-0.853	8.990
Site EXP2 in DFT optimized XRD structure of α-$Mg_3(HCO_2)_6$ at a loading level of 4.0 methane molecules/unit cell	^{2}H atom #1[a]	189	0.002	10.664	-0.524	7.599
	^{2}H atom #2[a]	190	0.008	10.663	-0.566	6.427
	^{2}H atom #3[a]	188	0.004	12.121	-0.555	8.920
	^{2}H atom #4[a]	192	0.006	7.624	-0.838	7.288
Site EXP in DFT optimized XRD structure of α-$Zn_3(HCO_2)_6$ at a loading level of 1.0 methane molecules/unit cell	^{2}H atom #1[a]	189	0.004	13.138	-0.364	4.304
	^{2}H atom #2[a]	185	0.005	12.283	-0.443	7.837
	^{2}H atom #3[a]	191	0.009	11.889	-0.334	1.582
	^{2}H atom #4[a]	189	0.006	8.240	-0.765	8.303
Site EXP in DFT optimized XRD structure of SIFSIX-3-Zn at a loading level of 0.25 methane molecules/unit cell[b]	^{2}H atom #1[a]	186	0.007	11.757	-0.625	3.664
	^{2}H atom #2[a]	191	0.004	2.845	-0.212	47.077
	^{2}H atom #3[a]	192	0.009	13.018	-0.248	7.021
	^{2}H atom #4[a]	186	0.005	11.940	-0.529	7.184
	^{2}H atom #5[a]	186	0.007	11.750	-0.625	3.655
	^{2}H atom #6[a]	191	0.004	2.851	-0.211	47.071
	^{2}H atom #7[a]	192	0.009	13.016	-0.248	7.014
	^{2}H atom #8[a]	186	0.006	11.932	-0.530	7.185

Table 4-A3. The observed ^{2}H NMR parameters of adsorbed CH_2D_2 in Mg-MOF-74, α-$Zn_2(HCO_2)_6$ and α-$Mg_2(HCO_2)_6$ at different temperatures, as obtained using analytical and motional simulations of experimental data.

MOF	Temperature (K)	C_Q (Hz)	η_Q	Ω (ppm)	κ	δ_{iso} (ppm)	β[a]
α-$Mg_3(HCO_2)_6$	123	490 (10)	0.31 (1)	1.2 (5)	-1.0 (5)	-0.80 (5)	0 (20)
	133	440 (10)	0.27 (1)	1.2 (5)	-1.0 (5)	-0.75 (5)	0 (20)
	143	380 (5)	0.24 (1)	1.2 (5)	-1.0 (5)	-0.65 (5)	0 (20)
	153	350 (5)	0.22 (1)	1.2 (5)	-1.0 (5)	-0.65 (5)	0 (20)
α-$Zn_3(HCO_2)_6$	123	540 (10)	0.35 (1)	1.9 (5)	-1.0 (5)	-0.40 (5)	0 (20)
	133	500 (10)	0.32 (1)	1.9 (5)	-1.0 (5)	-0.40 (5)	0 (20)
	143	440 (5)	0.28 (1)	1.9 (5)	-1.0 (5)	-0.25 (5)	0 (20)
	153	390 (5)	0.27 (1)	1.9 (5)	-1.0 (5)	-0.10 (5)	0 (20)
Mg-MOF-74	123	290 (5)	0.00 (5)	1.3 (2)	-1.0 (2)	-1.10 (5)	80 (10)
	128	240 (5)	0.00 (5)	1.3 (2)	-1.0 (2)	-1.10 (5)	80 (10)
	133	220 (5)	0.00 (5)	1.3 (2)	-1.0 (2)	-1.10 (5)	80 (10)

[a] The angle β refers to the Euler angle between the V_{33} component of the EFG tensor and the δ_{33} component of the CS tensor. The other Euler angles were not found to significantly impact spectral appearance.

Table 4-A4. The methane adsorption energies (in kJ mol^{-1}) obtained from DFT calculations of α-$Mg_3(HCO_2)_6$ containing 1.0 methane molecule/unit cell, considering three different adsorption sites.

	E_{ads} / kJ mol^{-1}
Site EXP1	-25.1
Site A	-26.1
Site B	-25.6

Table 4-A5. The methane adsorption energies (in kJ mol^{-1}) obtained from DFT calculations of α-$Mg_3(HCO_2)_6$ containing 4.0 methane molecules/unit cell, considering three different adsorption sites

	E_{ads} / kJ mol^{-1}
Site EXP2	-25.7
Site A	-26.3
Site B	-25.9

SCXRD details

SCXRD of CH_3D-saturated α-$Zn_3(HCO_2)_6$

Data Collection and Processing. The sample was mounted on a Mitegen polyimide micromount with a small amount of Paratone N oil. All X-ray measurements were made on a Bruker Kappa Axis Apex2 diffractometer at a temperature of 110 K. The unit cell dimensions were determined from a symmetry constrained fit of 9057 reflections with $5.02° < 2\theta < 103.34°$. The data collection strategy was a number of ⍰ and ⍰ scans which collected data up to 107.998° (2θ). The frame integration was performed using SAINT.[2] The resulting raw data was scaled and absorption corrected using a multi-scan averaging of symmetry equivalent data using SADABS.[3]

Structure Solution and Refinement. The structure was solved by using a dual space methodology using the SHELXT program.[4] All non-hydrogen atoms were obtained from the initial solution. The framework hydrogen atoms were introduced at idealized positions and were allowed to ride on the parent atom. From a difference Fourier map, a peak of 0.98 $e^-/Å^3$ found in the channel. This was presumed to be the carbon from the CH_3D molecule. The occupancy was set to 0.333 based on information provided by the sample originator. All non-hydrogen atoms except for the methane carbon were refined anisotropically while the methane carbon was refined isotropically. The hydrogen atoms bound to the methane carbon were placed at calculated positions and were allowed to ride on the parent carbon. The structural model was fit to the data using full matrix least-squares based on F^2. The calculated structure factors included corrections for anomalous dispersion from the usual tabulation. The structure was refined using the SHELXL-2014 program from the SHELX suite of crystallographic software.[5] Graphic plots were produced using the NRCVAX program suite.[6]

Table 4-A6. Summary of crystal data for CH_3D-saturated α-$Zn_3(HCO_2)_6$

Formula	$C_{6.33}H_{7.33}O_{12}Zn_3$
Formula Weight (*g/mol*)	471.55
Crystal Dimensions (*mm*)	0.438 × 0.275 × 0.244
Crystal Color and Habit	colourless prism
Crystal System	monoclinic
Space Group	$P\ 2_1/n$
Temperature, K	110
a, Å	11.3206(17)
b, Å	9.8247(17)
c, Å	14.453(3)
a,°	90
b,°	91.266(12)
g,°	90
V, $Å^3$	1607.1(5)
Number of reflections to determine final unit cell	9057
Min and Max 2q for cell determination, °	5.02, 103.34
Z	4
F(000)	925
r (*g/cm*)	1.949
l, Å, (MoKa)	0.71073
m, (cm^{-1})	4.492
Diffractometer Type	Bruker Kappa Axis Apex2
Scan Type(s)	phi and omega scans
Max 2q for data collection, °	107.998
Measured fraction of data	0.998
Number of reflections measured	187927
Unique reflections measured	19644
R_{merge}	0.0308
Number of reflections included in refinement	19644
Cut off Threshold Expression	I > 2sigma(I)
Structure refined using	full matrix least-squares using F^2
Weighting Scheme	w=1/[sigma^2(Fo^2)+(0.0186P)^2+0.3615P] where P=(Fo^2+2Fc^2)/3

Number of parameters in least-squares	197
R_1	0.0236
wR_2	0.0467
R_1 (all data)	0.0377
wR_2 (all data)	0.0494
GOF	1.029
Maximum shift/error	0.002
Min & Max peak heights on final DF Map (e^-/Å)	-0.697, 0.609

Where:

$R_1 = S(|F_o| - |F_c|) / S F_o$

$wR_2 = [S(w(F_o^2 - F_c^2)^2) / S(w F_o^4)]^{½}$

$GOF = [S(w(F_o^2 - F_c^2)^2) / (\text{No. of reflns. - No. of params.})]^{½}$

Table 4-A7. Atomic coordinates for CH_3D-saturated α-$Zn_3(HCO_2)_6$

Atom	x	y	z	$U_{iso/equiv}$
Zn1	0.24327(2)	0.07719(2)	0.36816(2)	0.00624(1)
Zn2	0.24084(2)	0.39086(2)	0.31281(2)	0.00709(1)
Zn3	0.5000	0.0000	0.5000	0.00820(1)
Zn4	0.0000	0.0000	0.5000	0.00856(1)
O1	0.31553(3)	-0.02716(4)	0.47701(3)	0.00933(6)
C1	0.25761(5)	-0.10573(6)	0.53054(4)	0.01086(8)
O2	0.14916(4)	-0.11482(5)	0.53364(4)	0.01342(7)
O3	0.10240(4)	0.15490(4)	0.43937(3)	0.00942(6)
C2	0.07049(5)	0.27880(6)	0.44880(4)	0.01084(8)
O4	0.11239(4)	0.37896(4)	0.40888(3)	0.01205(7)
O5	0.19205(4)	0.19921(4)	0.25434(3)	0.00894(5)
C3	0.16974(5)	0.17216(6)	0.16973(4)	0.01032(7)
O6	0.18274(4)	0.05990(4)	0.13121(3)	0.01189(6)
O7	0.34702(4)	0.25515(4)	0.39032(3)	0.00899(6)
C4	0.42268(5)	0.28841(6)	0.45312(4)	0.01186(8)
O8	0.48141(4)	0.20966(5)	0.50239(3)	0.01371(7)
O9	0.14902(4)	-0.08354(4)	0.30489(3)	0.00915(6)
C5	0.04486(5)	-0.12973(7)	0.31361(4)	0.01243(8)
O10	-0.02365(4)	-0.10441(5)	0.37663(3)	0.01472(8)

O11	0.36975(3)	-0.00748(4)	0.28050(3)	0.00894(6)
C6	0.48170(5)	-0.01489(6)	0.28817(4)	0.01136(8)
O12	0.54104(4)	0.00406(6)	0.35984(3)	0.01437(7)
C1X	0.2033(12)	-0.1312(13)	0.8148(9)	0.174(5)
H1	0.3024	-0.1621	0.5716	0.013
H2	0.0085	0.2959	0.4905	0.013
H3	0.1403	0.2446	0.1323	0.012
H4	0.4350	0.3830	0.4629	0.014
H5	0.0169	-0.1901	0.2667	0.015
H6	0.5235	-0.0370	0.2339	0.014
H1XA	0.2697	-0.1340	0.7747	0.262
H1XB	0.2085	-0.2097	0.8542	0.262
H1XC	0.1328	-0.1396	0.7771	0.262
H1XD	0.2027	-0.0487	0.8504	0.262

Table 4-A8. Anisotropic displacement parameters for CH_3D-saturated α-$Zn_3(HCO_2)_6$

Atom	u^{11}	u^{22}	u^{33}	u^{12}	u^{13}	u^{23}
Zn1	0.00654(2)	0.00598(2)	0.00620(2)	0.00015(2)	0.00015(2)	0.00037(2)
Zn2	0.00827(2)	0.00594(2)	0.00705(2)	-0.00005(2)	-0.00005(2)	0.00101(2)
Zn3	0.00600(3)	0.00968(3)	0.00884(3)	-0.00041(2)	-0.00140(2)	0.00123(3)
Zn4	0.00719(3)	0.00922(3)	0.00935(3)	-0.00109(2)	0.00224(2)	0.00162(3)
O1	0.00706(12)	0.01162(15)	0.00928(13)	-0.00117(11)	-0.00062(10)	0.00343(11)
C1	0.00819(16)	0.01276(19)	0.01159(19)	-0.00090(14)	-0.00043(14)	0.00461(15)
O2	0.00761(13)	0.01489(17)	0.01783(18)	-0.00056(12)	0.00158(13)	0.00536(15)
O3	0.00911(13)	0.00780(13)	0.01150(14)	0.00015(11)	0.00335(11)	0.00111(11)
C2	0.01085(17)	0.00930(18)	0.01258(19)	0.00057(14)	0.00469(15)	0.00080(15)
O4	0.01428(16)	0.00848(14)	0.01360(16)	0.00036(12)	0.00525(13)	0.00177(12)
O5	0.01226(14)	0.00704(13)	0.00743(13)	-0.00013(11)	-0.00160(11)	-0.00003(10)
C3	0.01467(19)	0.00752(17)	0.00866(17)	0.00139(15)	-0.00250(15)	0.00025(13)
O6	0.01792(17)	0.00812(14)	0.00950(14)	0.00252(13)	-0.00280(13)	-0.00143(11)
O7	0.00911(13)	0.00809(13)	0.00964(14)	-0.00100(11)	-0.00269(11)	0.00080(11)
C4	0.01295(19)	0.00814(17)	0.0142(2)	-0.00079(15)	-0.00519(16)	-0.00056(15)
O8	0.01404(16)	0.01077(16)	0.01598(18)	0.00103(13)	-0.00724(14)	0.00023(13)
O9	0.00842(12)	0.00901(13)	0.01010(14)	-0.00174(11)	0.00158(11)	-0.00127(11)

C5	0.01101(18)	0.0152(2)	0.01114(19)	-0.00523(16)	0.00196(15)	-0.00283(16)
O10	0.01110(15)	0.0213(2)	0.01195(16)	-0.00521(14)	0.00389(13)	-0.00288(15)
O11	0.00690(12)	0.01007(14)	0.00984(14)	0.00017(10)	-0.00004(10)	-0.00200(11)
C6	0.00784(16)	0.0167(2)	0.00952(18)	0.00018(15)	0.00083(14)	-0.00113(16)
O12	0.00879(14)	0.0244(2)	0.00983(15)	-0.00056(14)	-0.00141(12)	0.00008(15)

Table 4-A9. Bond lengths for CH_3D-saturated α-$Zn_3(HCO_2)_6$

Zn1-O1	2.0343(5)	C1-O2	1.2328(7)
Zn1-O3	2.0635(5)	C1-H1	0.9500
Zn1-O9	2.1036(5)	O3-C2	1.2779(7)
Zn1-O11	2.1041(5)	C2-O4	1.2403(7)
Zn1-O5	2.1064(5)	C2-H2	0.9500
Zn1-O7	2.1266(5)	O5-C3	1.2714(7)
Zn2-O6[1]	2.0323(5)	C3-O6	1.2456(7)
Zn2-O4	2.0361(5)	C3-H3	0.9500
Zn2-O11[1]	2.0759(5)	O6-Zn2[4]	2.0323(5)
Zn2-O7	2.1019(5)	O7-C4	1.2766(7)
Zn2-O5	2.1316(5)	C4-O8	1.2356(7)
Zn2-O9[1]	2.1460(5)	C4-H4	0.9500
Zn3-O8[2]	2.0710(6)	O9-C5	1.2722(7)
Zn3-O8	2.0710(6)	O9-Zn2[4]	2.1460(5)
Zn3-O12[2]	2.0887(6)	C5-O10	1.2346(7)
Zn3-O12	2.0887(6)	C5-H5	0.9500
Zn3-O1[2]	2.1242(5)	O11-C6	1.2718(7)
Zn3-O1	2.1242(5)	O11-Zn2[4]	2.0759(5)
Zn4-O10[3]	2.0693(6)	C6-O12	1.2362(8)
Zn4-O10	2.0694(6)	C6-H6	0.9500
Zn4-O2[3]	2.0794(5)	C1X-H1XA	0.9599
Zn4-O2	2.0794(5)	C1X-H1XB	0.9600
Zn4-O3[3]	2.1149(5)	C1X-H1XC	0.9599
Zn4-O3	2.1149(5)	C1X-H1XD	0.9600
O1-C1	1.2832(7)		

1. -x+1/2, y+1/2, -z+1/2
2. 1-x, -y,1+ -z

3. -x, -y,1+ -z
4. -x+1/2,-1+ y+1/2, -z+1/2

Table 4-A10. Bond angles for CH$_3$D-saturated α-Zn$_3$(HCO$_2$)$_6$

O1-Zn1-O3	95.90(2)	O2-Zn4-O3^{3}	87.85(2)
O1-Zn1-O9	98.59(2)	O10^{3}-Zn4-O3	86.48(2)
O3-Zn1-O9	95.992(19)	O10-Zn4-O3	93.52(2)
O1-Zn1-O11	89.95(2)	O2^{3}-Zn4-O3	87.85(2)
O3-Zn1-O11	172.009(17)	O2-Zn4-O3	92.15(2)
O9-Zn1-O11	77.696(19)	O3^{3}-Zn4-O3	179.999(15)
O1-Zn1-O5	171.804(16)	C1-O1-Zn1	124.57(4)
O3-Zn1-O5	88.65(2)	C1-O1-Zn3	119.66(4)
O9-Zn1-O5	87.68(2)	Zn1-O1-Zn3	115.77(2)
O11-Zn1-O5	86.22(2)	O2-C1-O1	126.02(5)
O1-Zn1-O7	94.96(2)	O2-C1-H1	117.0
O3-Zn1-O7	92.921(19)	O1-C1-H1	117.0
O9-Zn1-O7	162.904(17)	C1-O2-Zn4	139.15(4)
O11-Zn1-O7	91.996(19)	C2-O3-Zn1	128.99(4)
O5-Zn1-O7	77.96(2)	C2-O3-Zn4	118.84(4)
O6^{1}-Zn2-O4	94.56(2)	Zn1-O3-Zn4	112.16(2)
O6^{1}-Zn2-O11^{1}	96.36(2)	O4-C2-O3	126.45(5)
O4-Zn2-O11^{1}	92.36(2)	O4-C2-H2	116.8
O6^{1}-Zn2-O7	94.17(2)	O3-C2-H2	116.8
O4-Zn2-O7	90.50(2)	C2-O4-Zn2	130.47(4)
O11^{1}-Zn2-O7	168.830(17)	C3-O5-Zn1	132.66(4)
O6^{1}-Zn2-O5	169.720(19)	C3-O5-Zn2	127.61(4)
O4-Zn2-O5	92.117(19)	Zn1-O5-Zn2	97.39(2)
O11^{1}-Zn2-O5	91.16(2)	O6-C3-O5	126.30(5)
O7-Zn2-O5	77.94(2)	O6-C3-H3	116.8
O6^{1}-Zn2-O9^{1}	88.29(2)	O5-C3-H3	116.8
O4-Zn2-O9^{1}	169.590(18)	C3-O6-Zn2^{4}	126.81(4)
O11^{1}-Zn2-O9^{1}	77.364(19)	C4-O7-Zn2	125.69(4)
O7-Zn2-O9^{1}	99.287(19)	C4-O7-Zn1	132.62(4)
O5-Zn2-O9^{1}	86.518(18)	Zn2-O7-Zn1	97.69(2)

O8^2-Zn3-O8	180.0	O8-C4-O7	126.40(6)
O8^2-Zn3-O12^2	91.26(2)	O8-C4-H4	116.8
O8-Zn3-O12^2	88.74(2)	O7-C4-H4	116.8
O8^2-Zn3-O12	88.74(2)	C4-O8-Zn3	131.82(4)
O8-Zn3-O12	91.26(2)	C5-O9-Zn1	133.39(4)
O12^2-Zn3-O12	180.0	C5-O9-Zn2^4	126.35(4)
O8^2-Zn3-O1^2	91.587(18)	Zn1-O9-Zn2^4	97.733(18)
O8-Zn3-O1^2	88.413(18)	O10-C5-O9	126.87(6)
O12^2-Zn3-O1^2	95.14(2)	O10-C5-H5	116.6
O12-Zn3-O1^2	84.86(2)	O9-C5-H5	116.6
O8^2-Zn3-O1	88.414(18)	C5-O10-Zn4	131.61(4)
O8-Zn3-O1	91.586(18)	C6-O11-Zn2^4	127.92(4)
O12^2-Zn3-O1	84.86(2)	C6-O11-Zn1	131.32(4)
O12-Zn3-O1	95.14(2)	Zn2^4-O11-Zn1	99.95(2)
O1^2-Zn3-O1	180.0	O12-C6-O11	125.90(5)
O10^3-Zn4-O10	180.00(3)	O12-C6-H6	117.1
O10^3-Zn4-O2^3	91.23(2)	O11-C6-H6	117.1
O10-Zn4-O2^3	88.77(2)	C6-O12-Zn3	132.95(4)
O10^3-Zn4-O2	88.77(2)	H1XA-C1X-H1XB	107.2
O10-Zn4-O2	91.23(2)	H1XA-C1X-H1XC	107.9
O2^3-Zn4-O2	180.0	H1XB-C1X-H1XC	107.9
O10^3-Zn4-O3^3	93.52(2)	H1XA-C1X-H1XD	111.2
O10-Zn4-O3^3	86.48(2)	H1XB-C1X-H1XD	111.2
O2^3-Zn4-O3^3	92.15(2)	H1XC-C1X-H1XD	111.2

1. -x+1/2, y+1/2, -z+1/2
2. 1-x, -y,1+ -z
3. -x, -y,1+ -z
4. -x+1/2,-1+ y+1/2, -z+1/2

Table 4-A11. Torsion angles for CH_3D-saturated α-$Zn_3(HCO_2)_6$

Zn1-O1-C1-O2	-11.48(9)	Zn2-O7-C4-O8	176.13(5)
Zn3-O1-C1-O2	168.55(5)	Zn1-O7-C4-O8	23.90(10)
O1-C1-O2-Zn4	-22.43(11)	O7-C4-O8-Zn3	7.04(11)
Zn1-O3-C2-O4	7.41(10)	Zn1-O9-C5-O10	-14.37(11)

Zn4-O3-C2-O4	-170.97(5)	Zn2^1-O9-C5-O10	-172.12(5)
O3-C2-O4-Zn2	1.81(10)	O9-C5-O10-Zn4	-7.93(11)
Zn1-O5-C3-O6	-6.11(10)	Zn2^1-O11-C6-O12	-152.20(5)
Zn2-O5-C3-O6	152.41(5)	Zn1-O11-C6-O12	15.31(10)
O5-C3-O6-Zn2^1	-6.90(9)	O11-C6-O12-Zn3	20.16(11)

1. -x+1/2,-1+ y+1/2, -z+1/2

SCXRD of CH_3D-saturated α-$Mg_3(HCO_2)_6$

Data Collection and Processing. The sample was mounted on a Mitegen polyimide micromount with a small amount of Paratone N oil. All X-ray measurements were made on a Bruker Kappa Axis Apex2 diffractometer at a temperature of 110 K. The unit cell dimensions were determined from a symmetry constrained fit of 6014 reflections with 9.78° < 2θ < 132.58°. The data collection strategy was a number of ⍰ and ⍰ scans which collected data up to 132.58° (2θ). The frame integration was performed using SAINT.[2] The resulting raw data was scaled and absorption corrected using a multi-scan averaging of symmetry equivalent data using SADABS.[3]

Structure Solution and Refinement. The initial phases were obtained by using an isomorphous structure. All non-hydrogen framework atoms were included in the initial phasing model. The framework hydrogen atoms were introduced at idealized positions and were allowed to refine isotropically. The highest peak in a difference Fourier map ($0.98e^-/\text{Å}^3$) was located in the void region of the unit cell. The next highest peak was about half as high. This largest peak was assumed to be the carbon atom position (C1X) of the CH_3D molecule. To keep the displacement parameters reasonable, the occupancy of this atom was fixed to 0.25. In a subsequent difference Fourier map the next 4 highest peaks were in the vicinity of C1X and roughly corresponded to possible hydrogen atom positions. These were idealized into an approximately tetrahedral geometry and were constrained to ride on the parent carbon atom. The structural model was fit to the data using full matrix least-squares based on F^2. The calculated structure factors included corrections for anomalous dispersion from the usual tabulation. The structure was refined using the SHELXL-2014 program from the SHELX suite of crystallographic software.[4] Graphic plots were produced using the NRCVAX program suite.[6]

Table 4-A12. Summary of crystal data for CH_3D-saturated α-$Mg_3(HCO_2)_6$

Formula	$C_{6.25}H_7Mg_3O_{12}$
Formula Weight (*g/mol*)	347.05
Crystal Dimensions (*mm*)	0.133 × 0.113 × 0.102
Crystal Color and Habit	colourless prism
Crystal System	monoclinic
Space Group	$P\ 2_1/n$
Temperature, K	110
a, Å	11.3348(11)
b, Å	9.8430(13)
c, Å	14.5348(18)
a,°	90
b,°	91.430(6)
g,°	90
V, $Å^3$	1621.1(3)
Number of reflections to determine final unit cell	6014
Min and Max 2q for cell determination, °	9.78, 132.58
Z	4
F(000)	706
r (*g/cm*)	1.422
l, Å, (CuKa)	1.54178
m, (cm^{-1})	2.232
Diffractometer Type	Bruker-Nonius KappaCCD Apex2
Scan Type(s)	phi and omega scans
Max 2q for data collection, °	132.58
Measured fraction of data	0.976
Number of reflections measured	17161
Unique reflections measured	2775
R_{merge}	0.0357
Number of reflections included in refinement	2775
Cut off Threshold Expression	I > 2sigma(I)
Structure refined using	full matrix least-squares using F^2
Weighting Scheme	$w=1/[sigma^2(Fo^2)+(0.0510P)^2+1.4251 P]$ where $P=(Fo^2+2Fc^2)/3$

Number of parameters in least-squares	226
R_1	0.0321
wR_2	0.0951
R_1 (all data)	0.0371
wR_2 (all data)	0.0986
GOF	1.104
Maximum shift/error	0.000
Min & Max peak heights on final DF Map (e^-/Å)	-0.257, 0.494

Where:

$R_1 = S(|F_o| - |F_c|) / S\, F_o$

$wR_2 = [\, S(w(F_o^2 - F_c^2)^2) / S(w\, F_o^4)\,]^{\frac{1}{2}}$

$GOF = [\, S(w(F_o^2 - F_c^2)^2) / (\text{No. of reflns. - No. of params.})\,]^{\frac{1}{2}}$

Table 4-A13. Atomic coordinates for CH_3D-saturated α-$Mg_3(HCO_2)_6$

Atom	x	y	z	$U_{iso/equiv}$
Mg1	0.24366(6)	0.07890(7)	0.36526(5)	0.01150(18)
Mg2	0.23950(6)	0.38888(7)	0.31011(5)	0.01238(19)
Mg3	0.5000	0.0000	0.5000	0.0136(2)
Mg4	0.0000	0.0000	0.5000	0.0135(2)
O1	0.31695(13)	-0.02613(15)	0.47486(10)	0.0137(3)
C1	0.2579(2)	-0.1011(2)	0.52912(16)	0.0161(5)
O2	0.14968(13)	-0.10646(16)	0.53257(11)	0.0182(4)
O3	0.10173(13)	0.15226(15)	0.43744(10)	0.0144(3)
C2	0.06947(19)	0.2763(2)	0.44507(16)	0.0164(5)
O4	0.11140(13)	0.37418(15)	0.40399(11)	0.0164(3)
O5	0.19186(13)	0.20074(15)	0.25346(10)	0.0137(3)
C3	0.16929(19)	0.1702(2)	0.16944(15)	0.0149(5)
O6	0.18497(13)	0.05785(15)	0.13344(10)	0.0160(3)
O7	0.34328(13)	0.25613(15)	0.38887(10)	0.0137(3)
C4	0.4218(2)	0.2874(2)	0.44980(16)	0.0172(5)
O8	0.48039(13)	0.20752(16)	0.49711(11)	0.0177(4)
O9	0.15055(13)	-0.08152(15)	0.30355(10)	0.0138(3)
C5	0.0482(2)	-0.1315(2)	0.31537(16)	0.0172(5)
O10	-0.01779(14)	-0.10651(17)	0.37889(11)	0.0187(4)
O11	0.36922(13)	-0.00588(15)	0.27989(10)	0.0135(3)

C6	0.4802(2)	-0.0160(2)	0.28971(16)	0.0165(5)
O12	0.53755(13)	-0.00022(16)	0.36206(11)	0.0182(4)
C1X	0.199(2)	-0.123(3)	0.8164(17)	0.157(15)
H1	0.302(2)	-0.160(3)	0.5701(18)	0.019(6)
H2	0.004(2)	0.289(3)	0.4877(18)	0.018(6)
H3	0.136(2)	0.240(3)	0.1316(18)	0.016(6)
H4	0.433(2)	0.384(3)	0.4577(18)	0.020(7)
H5	0.024(2)	-0.196(3)	0.264(2)	0.026(7)
H6	0.522(2)	-0.035(3)	0.238(2)	0.024(7)
H1XA	0.2267	-0.1890	0.7738	0.236
H1XB	0.1164	-0.1151	0.8002	0.236
H1XC	0.2385	-0.0372	0.8090	0.236
H1XD	0.2100	-0.1528	0.8788	0.236

Table 4-A14. Anisotropic displacement parameters for CH_3D-saturated α-$Mg_3(HCO_2)_6$

Atom	u^{11}	u^{22}	u^{33}	u^{12}	u^{13}	u^{23}
Mg1	0.0110(4)	0.0117(4)	0.0119(4)	-0.0001(3)	0.0006(3)	0.0004(3)
Mg2	0.0124(4)	0.0120(4)	0.0127(4)	0.0000(3)	0.0004(3)	0.0009(3)
Mg3	0.0110(5)	0.0158(5)	0.0140(5)	-0.0001(4)	-0.0008(4)	0.0010(4)
Mg4	0.0113(5)	0.0148(5)	0.0144(5)	-0.0009(4)	0.0027(4)	0.0016(4)
O1	0.0110(7)	0.0161(8)	0.0140(8)	-0.0011(6)	0.0001(6)	0.0027(6)
C1	0.0148(12)	0.0170(12)	0.0162(11)	0.0001(9)	-0.0006(9)	0.0030(9)
O2	0.0128(8)	0.0197(9)	0.0223(9)	-0.0005(6)	0.0029(6)	0.0036(7)
O3	0.0134(7)	0.0138(8)	0.0163(8)	0.0006(6)	0.0023(6)	0.0005(6)
C2	0.0138(11)	0.0187(13)	0.0168(11)	0.0004(9)	0.0021(9)	-0.0004(9)
O4	0.0174(8)	0.0139(8)	0.0181(8)	0.0001(6)	0.0044(6)	0.0016(7)
O5	0.0154(8)	0.0133(8)	0.0124(8)	-0.0009(6)	0.0001(6)	0.0003(6)
C3	0.0152(11)	0.0153(12)	0.0142(12)	-0.0002(9)	-0.0004(9)	0.0026(9)
O6	0.0195(8)	0.0128(8)	0.0158(8)	0.0020(6)	-0.0009(6)	-0.0008(6)
O7	0.0131(7)	0.0137(8)	0.0143(8)	-0.0009(6)	-0.0014(6)	-0.0001(6)
C4	0.0171(11)	0.0156(12)	0.0188(12)	-0.0012(9)	-0.0023(9)	-0.0021(10)
O8	0.0172(8)	0.0159(8)	0.0197(8)	0.0016(6)	-0.0048(6)	0.0016(7)
O9	0.0122(8)	0.0143(8)	0.0149(8)	-0.0010(6)	0.0020(6)	-0.0008(6)
C5	0.0164(12)	0.0186(12)	0.0167(12)	-0.0029(9)	-0.0003(9)	-0.0010(10)

O10	0.0151(8)	0.0241(9)	0.0170(8)	-0.0044(7)	0.0043(7)	-0.0015(7)
O11	0.0115(8)	0.0140(8)	0.0151(8)	0.0004(6)	0.0010(6)	-0.0012(6)
C6	0.0143(11)	0.0196(12)	0.0158(12)	-0.0003(9)	0.0026(9)	0.0009(9)
O12	0.0139(8)	0.0264(9)	0.0141(8)	-0.0002(6)	-0.0008(6)	0.0010(7)
C1X	0.098(17)	0.26(4)	0.11(2)	-0.01(2)	0.058(16)	0.12(2)

Table 4-A15. Bond lengths for CH$_3$D-saturated α-Mg$_3$(HCO$_2$)$_6$

Mg1-O1	2.0568(16)	Mg4-O3	2.1106(15)
Mg1-O3	2.0723(16)	Mg4-O3^{4}	2.1107(15)
Mg1-O11	2.0856(16)	Mg4-Mg1^{4}	3.5123(8)
Mg1-O9	2.0892(16)	O1-C1	1.280(3)
Mg1-O5	2.0919(16)	C1-O2	1.231(3)
Mg1-O7	2.1015(16)	C1-H1	0.97(3)
Mg1-Mg2	3.1547(11)	O3-C2	1.281(3)
Mg1-Mg2^{1}	3.1713(10)	C2-O4	1.235(3)
Mg1-Mg4	3.5123(8)	C2-H2	0.99(3)
Mg1-Mg3	3.5491(7)	O5-C3	1.277(3)
Mg2-O4	2.0224(17)	C3-O6	1.238(3)
Mg2-O6^{2}	2.0340(17)	C3-H3	0.96(3)
Mg2-O11^{2}	2.0549(16)	O6-Mg2^{1}	2.0340(17)
Mg2-O7	2.0819(16)	O7-C4	1.277(3)
Mg2-O5	2.0921(17)	C4-O8	1.229(3)
Mg2-O9^{2}	2.1142(17)	C4-H4	0.97(3)
Mg2-Mg1^{2}	3.1713(10)	O9-C5	1.275(3)
Mg3-O8^{3}	2.0550(16)	O9-Mg2^{1}	2.1142(17)
Mg3-O8	2.0550(16)	C5-O10	1.228(3)
Mg3-O12	2.0600(16)	C5-H5	1.01(3)
Mg3-O12^{3}	2.0600(16)	O11-C6	1.267(3)
Mg3-O1^{3}	2.1134(14)	O11-Mg2^{1}	2.0550(16)
Mg3-O1	2.1134(14)	C6-O12	1.232(3)
Mg3-Mg1^{3}	3.5492(7)	C6-H6	0.92(3)
Mg4-O2^{4}	2.0397(15)	C1X-H1XA	0.9600
Mg4-O2	2.0397(15)	C1X-H1XB	0.9599
Mg4-O10^{4}	2.0544(16)	C1X-H1XC	0.9600

Mg4-O10	2.0545(16)	C1X-H1XD	0.9600

1. -x+1/2,-1+ y+1/2, -z+1/2
2. -x+1/2, y+1/2, -z+1/2
3. 1-x, -y,1+ -z
4. -x, -y,1+ -z

Table 4-A16. Bond angles for CH_3D-saturated α-$Mg_3(HCO_2)_6$

O1-Mg1-O3	94.97(7)	O8-Mg3-Mg1	71.61(4)
O1-Mg1-O11	89.50(6)	O12-Mg3-Mg1	69.47(4)
O3-Mg1-O11	172.11(7)	O12^{3}-Mg3-Mg1	110.52(4)
O1-Mg1-O9	98.20(6)	O1^{3}-Mg3-Mg1	148.81(4)
O3-Mg1-O9	95.19(6)	O1-Mg3-Mg1	31.19(4)
O11-Mg1-O9	77.70(6)	O8^{3}-Mg3-Mg1^{3}	71.61(4)
O1-Mg1-O5	171.85(7)	O8-Mg3-Mg1^{3}	108.39(4)
O3-Mg1-O5	89.26(6)	O12-Mg3-Mg1^{3}	110.53(4)
O11-Mg1-O5	87.12(6)	O12^{3}-Mg3-Mg1^{3}	69.48(4)
O9-Mg1-O5	88.32(6)	O1^{3}-Mg3-Mg1^{3}	31.19(4)
O1-Mg1-O7	94.92(6)	O1-Mg3-Mg1^{3}	148.81(4)
O3-Mg1-O7	92.80(6)	Mg1-Mg3-Mg1^{3}	180.0
O11-Mg1-O7	93.29(6)	O2^{4}-Mg4-O2	180.00(9)
O9-Mg1-O7	163.96(7)	O2^{4}-Mg4-O10^{4}	90.00(6)
O5-Mg1-O7	77.89(6)	O2-Mg4-O10^{4}	90.00(6)
O1-Mg1-Mg2	133.32(5)	O2^{4}-Mg4-O10	90.00(6)
O3-Mg1-Mg2	77.57(5)	O2-Mg4-O10	90.00(6)
O11-Mg1-Mg2	104.00(5)	O10^{4}-Mg4-O10	180.0
O9-Mg1-Mg2	128.15(5)	O2^{4}-Mg4-O3	89.74(6)
O5-Mg1-Mg2	41.06(4)	O2-Mg4-O3	90.26(6)
O7-Mg1-Mg2	40.82(4)	O10^{4}-Mg4-O3	87.92(6)
O1-Mg1-Mg2^{1}	107.15(5)	O10-Mg4-O3	92.07(6)
O3-Mg1-Mg2^{1}	132.49(5)	O2^{4}-Mg4-O3^{4}	90.26(6)
O11-Mg1-Mg2^{1}	39.66(4)	O2-Mg4-O3^{4}	89.74(6)
O9-Mg1-Mg2^{1}	41.32(4)	O10^{4}-Mg4-O3^{4}	92.08(6)
O5-Mg1-Mg2^{1}	74.64(5)	O10-Mg4-O3^{4}	87.93(6)
O7-Mg1-Mg2^{1}	125.30(5)	O3-Mg4-O3^{4}	180.0
Mg2-Mg1-Mg2^{1}	111.53(2)	O2^{4}-Mg4-Mg1^{4}	65.29(5)

O1-Mg1-Mg4	76.41(5)	O2-Mg4-Mg1^4	114.71(5)
O3-Mg1-Mg4	33.24(4)	O10^4-Mg4-Mg1^4	72.35(4)
O11-Mg1-Mg4	143.23(5)	O10-Mg4-Mg1^4	107.65(4)
O9-Mg1-Mg4	71.12(4)	O3-Mg4-Mg1^4	147.45(4)
O5-Mg1-Mg4	110.52(5)	O3^4-Mg4-Mg1^4	32.56(4)
O7-Mg1-Mg4	121.29(5)	O2^4-Mg4-Mg1	114.71(5)
Mg2-Mg1-Mg4	110.40(2)	O2-Mg4-Mg1	65.29(5)
Mg2^1-Mg1-Mg4	112.44(2)	O10^4-Mg4-Mg1	107.65(4)
O1-Mg1-Mg3	32.16(4)	O10-Mg4-Mg1	72.35(4)
O3-Mg1-Mg3	115.60(5)	O3-Mg4-Mg1	32.56(4)
O11-Mg1-Mg3	71.30(4)	O3^4-Mg4-Mg1	147.44(4)
O9-Mg1-Mg3	117.99(5)	Mg1^4-Mg4-Mg1	180.0
O5-Mg1-Mg3	139.83(5)	C1-O1-Mg1	124.01(14)
O7-Mg1-Mg3	70.27(4)	C1-O1-Mg3	119.29(13)
Mg2-Mg1-Mg3	111.02(2)	Mg1-O1-Mg3	116.65(7)
Mg2^1-Mg1-Mg3	104.45(2)	O2-C1-O1	125.9(2)
Mg4-Mg1-Mg3	106.75(2)	O2-C1-H1	116.9(16)
O4-Mg2-O6^2	95.07(7)	O1-C1-H1	117.1(15)
O4-Mg2-O11^2	92.08(7)	C1-O2-Mg4	142.46(15)
O6^2-Mg2-O11^2	94.83(7)	C2-O3-Mg1	127.10(14)
O4-Mg2-O7	89.40(7)	C2-O3-Mg4	118.66(14)
O6^2-Mg2-O7	93.73(7)	Mg1-O3-Mg4	114.21(7)
O11^2-Mg2-O7	171.15(7)	O4-C2-O3	126.0(2)
O4-Mg2-O5	91.13(7)	O4-C2-H2	120.5(16)
O6^2-Mg2-O5	169.89(7)	O3-C2-H2	113.4(16)
O11^2-Mg2-O5	92.92(6)	C2-O4-Mg2	132.35(15)
O7-Mg2-O5	78.32(6)	C3-O5-Mg1	130.81(15)
O4-Mg2-O9^2	169.80(7)	C3-O5-Mg2	128.90(14)
O6^2-Mg2-O9^2	87.25(7)	Mg1-O5-Mg2	97.87(7)
O11^2-Mg2-O9^2	77.82(6)	O6-C3-O5	125.9(2)
O7-Mg2-O9^2	100.38(6)	O6-C3-H3	117.5(15)
O5-Mg2-O9^2	88.04(6)	O5-C3-H3	116.6(15)
O4-Mg2-Mg1	76.46(5)	C3-O6-Mg2^1	128.56(15)
O6^2-Mg2-Mg1	133.23(5)	C4-O7-Mg2	127.16(15)

O11^{2}-Mg2-Mg1	130.87(5)	C4-O7-Mg1	132.50(15)
O7-Mg2-Mg1	41.29(4)	Mg2-O7-Mg1	97.89(7)
O5-Mg2-Mg1	41.06(4)	O8-C4-O7	126.2(2)
O9^{2}-Mg2-Mg1	109.06(5)	O8-C4-H4	119.9(16)
O4-Mg2-Mg1^{2}	130.03(5)	O7-C4-H4	113.9(16)
O6^{2}-Mg2-Mg1^{2}	78.97(5)	C4-O8-Mg3	134.78(15)
O11^{2}-Mg2-Mg1^{2}	40.37(4)	C5-O9-Mg1	133.24(15)
O7-Mg2-Mg1^{2}	140.14(5)	C5-O9-Mg2^{1}	127.43(15)
O5-Mg2-Mg1^{2}	103.05(5)	Mg1-O9-Mg2^{1}	97.95(7)
O9^{2}-Mg2-Mg1^{2}	40.73(4)	O10-C5-O9	126.7(2)
Mg1-Mg2-Mg1^{2}	140.70(3)	O10-C5-H5	121.1(16)
O8^{3}-Mg3-O8	180.0	O9-C5-H5	112.2(16)
O8^{3}-Mg3-O12	89.66(6)	C5-O10-Mg4	134.26(15)
O8-Mg3-O12	90.34(6)	C6-O11-Mg2^{1}	127.60(15)
O8^{3}-Mg3-O12^{3}	90.34(6)	C6-O11-Mg1	130.94(15)
O8-Mg3-O12^{3}	89.66(6)	Mg2^{1}-O11-Mg1	99.97(7)
O12-Mg3-O12^{3}	180.00(9)	O12-C6-O11	126.0(2)
O8^{3}-Mg3-O1^{3}	90.70(6)	O12-C6-H6	116.7(17)
O8-Mg3-O1^{3}	89.30(6)	O11-C6-H6	117.3(17)
O12-Mg3-O1^{3}	86.71(6)	C6-O12-Mg3	135.52(15)
O12^{3}-Mg3-O1^{3}	93.29(6)	H1XA-C1X-H1XB	103.1
O8^{3}-Mg3-O1	89.30(6)	H1XA-C1X-H1XC	111.1
O8-Mg3-O1	90.70(6)	H1XB-C1X-H1XC	111.1
O12-Mg3-O1	93.29(6)	H1XA-C1X-H1XD	111.1
O12^{3}-Mg3-O1	86.71(6)	H1XB-C1X-H1XD	111.1
O1^{3}-Mg3-O1	180.0	H1XC-C1X-H1XD	109.1
O8^{3}-Mg3-Mg1	108.39(4)		

1. -x+1/2,-1+ y+1/2, -z+1/2
2. -x+1/2, y+1/2, -z+1/2
3. 1-x, -y,1+ -z
4. -x, -y,1+ -z

Table 4-A17. Torsion angles for CH_3D-saturated α-$Mg_3(HCO_2)_6$

Mg1-O1-C1-O2	-11.0(3)	Mg2-O7-C4-O8	178.25(17)
Mg3-O1-C1-O2	166.53(18)	Mg1-O7-C4-O8	20.1(4)

O1-C1-O2-Mg4	-21.3(4)	O7-C4-O8-Mg3	6.6(4)
Mg1-O3-C2-O4	6.7(3)	Mg1-O9-C5-O10	-11.4(4)
Mg4-O3-C2-O4	-171.16(17)	Mg2[1]-O9-C5-O10	-174.93(17)
O3-C2-O4-Mg2	1.0(4)	O9-C5-O10-Mg4	-8.2(4)
Mg1-O5-C3-O6	-7.5(3)	Mg2[1]-O11-C6-O12	-148.00(19)
Mg2-O5-C3-O6	150.81(18)	Mg1-O11-C6-O12	15.2(4)
O5-C3-O6-Mg2[1]	-4.6(3)	O11-C6-O12-Mg3	18.4(4)

1. -x+1/2, -1+ y+1/2, -z+1/2

SCXRD of CH_3D-saturated SIFSIX-3-Zn

Data Collection and Processing. The sample was mounted on a Mitegen polyimide micromount with a small amount of Paratone N oil. All X-ray measurements were made on a Bruker Kappa Axis Apex2 diffractometer at a temperature of 110 K. The unit cell dimensions were determined from a symmetry constrained fit of 5072 reflections with $5.4° < 2θ < 65.1°$. The data collection strategy was a number of ⍰ and ⍰ scans which collected data up to 80.584° (2θ). The frame integration was performed using SAINT.[2] The resulting raw data was scaled and absorption corrected using a multi-scan averaging of symmetry equivalent data using SADABS.[3]

Structure Solution and Refinement. The structure was solved by using a dual space methodology using the SHELXT program.[4] All non-hydrogen atoms were obtained from the initial solution. The pyrazine ligand was disordered over two orientations with a crystallographically imposed disorder. The hydrogen atom bound to the pyrazine carbon was introduced at idealized positions and was allowed to ride on the parent atom. There were two peaks in the difference Fourier map near the methane carbon peak. These peaks were set to an idealized distance of 0.96 Å. The remaining two hydrogen atom positions were introduced at idealized position based on the positions of the first two peaks. All hydrogen atom positions associated with the methane molecule also suffer from a crystallographically imposed disorder. The methane hydrogen atoms were allowed to ride on the parent carbon atom. The occupancy of the methane group was allowed to refine until it converged, and then it was fixed for the final cycles of refinement. The structural model was fit to the data using full matrix least-squares based on F^2. The calculated structure factors included corrections for anomalous dispersion from the usual tabulation. The structure was refined using the SHELXL-2014 program from the SHELX suite of crystallographic software.[4] Graphic plots were produced using the NRCVAX program suite.[6]

Table 4-A18. Summary of crystal data for CH_3D-saturated SIFSIX-3-Zn

Formula	$C_{8.38}H_{9.50}F_6N_4SiZn$
Formula Weight (*g/mol*)	373.72
Crystal Dimensions (*mm*)	0.115 × 0.112 × 0.022
Crystal Color and Habit	colourless plate
Crystal System	tetragonal
Space Group	P 4/m m m
Temperature, K	110
a, Å	7.1145(18)
b, Å	7.1145
c, Å	7.536(3)
a,°	90
b,°	90
g,°	90
V, Å^3	381.5(2)
Number of reflections to determine final unit cell	5072
Min and Max 2q for cell determination, °	5.4, 65.1
Z	1
F(000)	186
r (*g/cm*)	1.627
l, Å, (MoKa)	0.71073
m, (*cm*$^{-1}$)	1.746
Diffractometer Type	Bruker Kappa Axis Apex2
Scan Type(s)	phi and omega scans
Max 2q for data collection, °	80.584
Measured fraction of data	0.992
Number of reflections measured	23826
Unique reflections measured	757
R_{merge}	0.0618
Number of reflections included in refinement	757
Cut off Threshold Expression	I > 2sigma(I)
Structure refined using	full matrix least-squares using F^2

Weighting Scheme	$w=1/[sigma^2(Fo^2)+(0.0361P)^2+0.0853 P]$ where $P=(Fo^2+2Fc^2)/3$
Number of parameters in least-squares	28
R_1	0.0308
wR_2	0.0691
R_1 (all data)	0.0415
wR_2 (all data)	0.0721
GOF	1.077
Maximum shift/error	0.000
Min & Max peak heights on final DF Map (e^-/Å)	-1.325, 0.642

Where:

$R_1 = S(|F_o| - |F_c|) / S F_o$

$wR_2 = [S(w(F_o^2 - F_c^2)^2) / S(w F_o^4)]^{½}$

$GOF = [S(w(F_o^2 - F_c^2)^2) / (\text{No. of reflns.} - \text{No. of params.})]^{½}$

Table 4-A19. Atomic coordinates for CH_3D-saturated SIFSIX-3-Zn

Atom	x	y	z	$U_{iso/equiv}$
Zn1	0.5000	0.5000	1.0000	0.00855(10)
Si1	0.5000	0.5000	0.5000	0.00903(16)
F1	0.5000	0.5000	0.73020(18)	0.0130(3)
F2	0.66546(11)	0.66546(11)	0.5000	0.0182(2)
N1	0.5000	0.1960(2)	1.0000	0.0116(2)
C1	0.4471(3)	0.0980(2)	0.8569(2)	0.0158(3)
C1X	0.0000	0.0000	0.629(5)	0.088(13)
H1	0.4086	0.1633	0.7532	0.019
H1XA	0.0000	-0.0989	0.7153	0.132
H1XB	-0.1224	0.0000	0.5750	0.132
H1XC	0.0951	-0.0222	0.5407	0.132
H1XD	0.0245	0.1189	0.6843	0.132

Table 4-A20. Anisotropic displacement parameters for CH_3D-saturated SIFSIX-3-Zn

Atom	u^{11}	u^{22}	u^{33}	u^{12}	u^{13}	u^{23}
Zn1	0.00864(13)	0.00864(13)	0.00836(15)	0.000	0.000	0.000
Si1	0.0100(2)	0.0100(2)	0.0070(3)	0.000	0.000	0.000

F1	0.0156(4)	0.0156(4)	0.0078(6)	0.000	0.000	0.000
F2	0.0201(3)	0.0201(3)	0.0142(5)	-0.0095(4)	0.000	0.000
N1	0.0125(6)	0.0106(6)	0.0116(5)	0.000	0.000	0.000
C1	0.0253(8)	0.0096(6)	0.0124(6)	-0.0005(5)	-0.0043(5)	0.0007(5)
C1X	0.064(14)	0.064(14)	0.14(4)	0.000	0.000	0.000

Table 4-A21. Bond lengths for CH$_3$D-saturated SIFSIX-3-Zn

Zn1-F1	2.0333(16)	N1-C1^{6}	1.3381(18)
Zn1-F1^{1}	2.0333(16)	N1-C1^{7}	1.3381(18)
Zn1-N1^{2}	2.1628(16)	N1-C1	1.3381(18)
Zn1-N1^{3}	2.1628(16)	N1-C1^{8}	1.3381(18)
Zn1-N1^{1}	2.1628(15)	C1-C1^{9}	1.394(3)
Zn1-N1	2.1628(15)	C1-H1	0.9500
Si1-F2^{4}	1.6647(11)	C1X-C1X^{10}	1.94(8)
Si1-F2	1.6647(11)	C1X-H1XA	0.9600
Si1-F2^{5}	1.6648(11)	C1X-H1XB	0.9600
Si1-F2^{3}	1.6648(11)	C1X-H1XC	0.9600
Si1-F1^{4}	1.7348(15)	C1X-H1XD	0.9600
Si1-F1	1.7348(15)		

1. 1-x,1+ -y,2+ -z
2. y,1+ -x,2+ -z
3. 1-y, x, z
4. 1-x,1+ -y,1+ -z
5. y,1+ -x,1+ -z
6. 1-x, y,2+ -z
7. x, y,2+ -z
8. 1-x, y, z
9. x, -y, z
10. -x, -y,1+ -z

Table 4-A22. Bond angles for CH$_3$D-saturated SIFSIX-3-Zn

F1-Zn1-F1^{1}	180.0	F2^{5}-Si1-F1	90.0
F1-Zn1-N1^{2}	90.0	F2^{3}-Si1-F1	90.0
F1^{1}-Zn1-N1^{2}	90.0	F1^{4}-Si1-F1	180.0
F1-Zn1-N1^{3}	90.0	Si1-F1-Zn1	180.0

F1^{1}-Zn1-N1^{3}	90.0	C1^{6}-N1-C1^{7}	32.70(16)
N1^{2}-Zn1-N1^{3}	180.0	C1^{6}-N1-C1	117.17(18)
F1-Zn1-N1^{1}	90.0	C1^{7}-N1-C1	107.35(17)
F1^{1}-Zn1-N1^{1}	90.0	C1^{6}-N1-C1^{8}	107.35(17)
N1^{2}-Zn1-N1^{1}	90.0	C1^{7}-N1-C1^{8}	117.17(18)
N1^{3}-Zn1-N1^{1}	90.0	C1-N1-C1^{8}	32.70(16)
F1-Zn1-N1	90.0	C1^{6}-N1-Zn1	121.41(9)
F1^{1}-Zn1-N1	90.0	C1^{7}-N1-Zn1	121.41(9)
N1^{2}-Zn1-N1	90.0	C1-N1-Zn1	121.41(9)
N1^{3}-Zn1-N1	90.0	C1^{8}-N1-Zn1	121.41(9)
N1^{1}-Zn1-N1	180.0	N1-C1-C1^{9}	121.41(9)
F2^{4}-Si1-F2	180.0	N1-C1-H1	119.3
F2^{4}-Si1-F2^{5}	90.000(15)	C1^{9}-C1-H1	119.3
F2-Si1-F2^{5}	90.000(14)	C1X^{10}-C1X-H1XA	132.8
F2^{4}-Si1-F2^{3}	90.000(14)	C1X^{10}-C1X-H1XB	65.1
F2-Si1-F2^{3}	90.000(14)	H1XA-C1X-H1XB	106.6
F2^{5}-Si1-F2^{3}	180.0	C1X^{10}-C1X-H1XC	46.4
F2^{4}-Si1-F1^{4}	90.0	H1XA-C1X-H1XC	110.4
F2-Si1-F1^{4}	90.0	H1XB-C1X-H1XC	110.4
F2^{5}-Si1-F1^{4}	90.0	C1X^{10}-C1X-H1XD	115.9
F2^{3}-Si1-F1^{4}	90.0	H1XA-C1X-H1XD	110.4
F2^{4}-Si1-F1	90.0	H1XB-C1X-H1XD	110.4
F2-Si1-F1	90.0	H1XC-C1X-H1XD	108.6

1. 1-x,1+ -y,2+ -z
2. y,1+ -x,2+ -z
3. 1-y, x, z
4. 1-x,1+ -y,1+ -z
5. y,1+ -x,1+ -z
6. 1-x, y,2+ -z
7. x, y,2+ -z
8. 1-x, y, z
9. x, -y, z
10. -x, -y,1+ -z

Table 4-A23. Torsion angles for CH$_3$D-saturated SIFSIX-3-Zn

C1^1-N1-C1-C1^2	0.000(1)	C1^4-N1-C1-C1^2	79.68(6)
C1^3-N1-C1-C1^2	-33.84(16)	Zn1-N1-C1-C1^2	180.000(0)

1. 1-x, y,2+ -z
2. x, -y, z
3. x, y,2+ -z
4. 1-x, y, z

Sample input files for DFT calculation

Sample input files for CASTEP calculations

.param file (geometry optimization)

```
comment : Sample geometry optimization

task : GeometryOptimization

xc_functional : PBE

sedc_apply : true

sedc_scheme : G06

spin_polarized : false

opt_strategy : Speed

page_wvfns :        0

cut_off_energy :      650.000000000000000

grid_scale :        2.000000000000000

fine_grid_scale :        2.500000000000000

finite_basis_corr :        2

finite_basis_npoints :        3

elec_energy_tol :   1.000000000000000e-009
```

```
max_scf_cycles :      100
fix_occupancy : true
metals_method : dm
mixing_scheme : Pulay
mix_charge_amp :       0.500000000000000
mix_charge_gmax :       1.500000000000000
mix_history_length :      20
nextra_bands : 0
geom_energy_tol :   1.000000000000000e-006
geom_force_tol :       0.005000000000000
geom_stress_tol :       0.020000000000000
geom_disp_tol :   5.000000000000000e-004
geom_max_iter :      500
geom_method : BFGS
fixed_npw : false
calculate_ELF : false
calculate_stress : false
popn_calculate : true
calculate_hirshfeld : true
calculate_densdiff : false
popn_bond_cutoff :       3.000000000000000
pdos_calculate_weights : false
num_dump_cycles : 0
```

```
write_cif_structure: true

write_cell_structure: true
```

.param file (NMR calculation)

```
task : MagRes

continuation : default

comment : Sample NMR calculation

xc_functional : PBE

sedc_apply : true

sedc_scheme : G06

spin_polarized : false

opt_strategy : Speed

page_wvfns :        0

cut_off_energy :      650.000000000000000

grid_scale :        2.000000000000000

fine_grid_scale :        2.500000000000000

finite_basis_corr :        2

finite_basis_npoints :        3

elec_energy_tol :   1.000000000000000e-009

max_scf_cycles :      100

fix_occupancy : true

metals_method : dm

mixing_scheme : Pulay

mix_charge_amp :        0.500000000000000
```

```
mix_charge_gmax :        1.500000000000000

mix_history_length :       20

nextra_bands : 0

num_dump_cycles : 0

magres_method : crystal

magres_task : NMR

magres_max_cg_steps :      250

bs_max_iter : 250

bs_max_cg_steps : 5

bs_eigenvalue_tol : 1.0e-9

pdos_calculate_weights : false

bs_write_eigenvalues : false
```

Generation strings for on-the-fly pseuodpotentials

(%BLOCK SPECIES_POT in CASTEP .cell file)

```
H  1|0.8|3.675|7.35|11.025|10UU(qc=6.4)[]

C  2|1.4|9.187|11.025|12.862|20UU:21UU(qc=6)[]

N  2|1.5|11.025|12.862|14.7|20UU:21UU(compat7,qc=6)[]

O  2|1.3|16.537|18.375|20.212|20UU:21UU(qc=7.5)[]

F  2|1.4|16.537|18.375|20.212|20UU:21UU(compat7,qc=7.5)[]

Si  2|1.8|3.675|5.512|7.35|30UU:31UU:32LGG(compat7)[]

Mg  2|1.6|2|1.4|6|7|8|30NH:21U:31UU:32LGG(qc=4.5)[]

Zn   3|2|2|1|10.8|11.5|12.5|40UU:41UU:32UU(compat7,qc=6)[]
```

Refernence

1. Fischer, M., DFT-based evaluation of porous metal formates for the storage and separation of small molecules. *Microporous Mesoporous Mater.* **2016**, 219, 249-257.

2. Bruker-AXS, S., version 2013.8, 2013, Bruker-AXS, Madison, WI 53711, USA.

3. Bruker-AXS, S., version 2012.1, 2012, Bruker-AXS, Madison, WI 53711, USA.

4. Sheldrick, G., SHELXT - Integrated space-group and crystal-structure determination. *Acta Crystallogr. Sect. A* **2015**, 71 (1), 3-8.

5. Sheldrick, G., Crystal structure refinement with SHELXL. *Acta Crystallogr. Sect. C* **2015**, 71 (1), 3-8.

6. Gabe, E. J.; Le Page, Y.; Charland, J.-P.; Lee, F. L.; White, P. S., NRCVAX - an interactive program system for structure analysis. *J. Appl. Cryst.* **1989**, 22 (4), 384-387.

Chapter 5

5 Novel Gallium- and Indium-fumarate MOFs: Synthesis, Comprehensive Characterization, Porous Hydrophobicity and CO_2 Dynamics

Metal-organic frameworks (MOFs) are constructed from virtually endless combinations of metal centres and organic linkers, with MOF properties and applications strongly dependent on the nature of building blocks employed and the final crystal structure. Basolite A520 (Al-fumarate) is a reported porous MOF that incorporates aluminum centres along with fumarate linkers, and is a very promising candidate for applications in fields such as gas (*e.g.*, CH_4, CO_2) adsorption; incorporation of an alternate metal centre into this motif may modify these properties and unlock additional desirable features. Furthermore, the adsorption locations, motional rates, and motional angles of guest molecules are critical to increasing adsorption capacity and selectivity, yet remain unknown in this system. In this work, the synthesis and detailed characterization of the gallium and indium fumarate MOFs known as Ga-fumarate and In-fumarate are described. Using a combination of powder X-ray diffraction, Rietveld refinements, solid-state NMR (SSNMR) spectroscopy, infrared spectroscopy, and thermogravimetric analysis, the topologies of Ga-fumarate and In-fumarate are revealed to be analogues of Al-fumarate. Both MOFs exhibit an affinity for CO_2, but Al-fumarate exhibits superior CO_2 adsorption performance versus Ga-fumarate and In-fumarate at 1 bar and 273 K. Ultra-wideline $^{69/71}Ga$ and ^{115}In SSNMR experiments at 21.1 T effectively probe the local structures about Ga and In, and the Ga NMR spectra also provide information to structures determined by pXRD and Rietveld refinements. The role of the metal centre in guest adsorption also has been investigated by $^{69/71}Ga$ and ^{115}In SSNMR experiments. Static ^{13}C and ^{1}H-^{13}C cross-polarization SSNMR experiments yield rich details of CO_2 motion within fumarate MOFs, along with CO_2 adsorption site locations and relative adsorption strengths. The porous hydrophobicity also has been achieved in In-fumarate by replacing bridging –OH groups with $-OCH_3$ groups into the channels.

5.1 Introduction

Metal-organic frameworks (MOFs) have been a topic of exceptional interest over the past twenty years, and continue to be investigated in earnest due to their variety of useful properties and features such as high porosities, large surface areas, exceptional thermal stabilities and catalytic activities.[1-2] The attractive properties of MOFs render these materials promising candidates for a wide range of applications including gas storage,[3-5] gas separation,[4, 6-7] catalysis,[8-9] drug delivery,[10-11] and many others.[12-13] Although the synthesis and characterization of thousands of MOFs has been reported, and despite the increasing commercial availability of MOFs from major vendors, only a minority of MOFs have realized practical commercial applications. For example, there is a zinc glutarate MOF that can be used as an epoxide-polymerization catalyst,[14] and the aluminum-based Basolite A520 (Al-fumarate) MOF can be used as a natural gas sorbent in automotive applications.[15]

Basolite A520 was first reported in a patent authored by BASF scientists,[16] and is associated with a low cost of production, good water stability, a relatively green synthetic route, and the potential for large-scale production. These properties make Basolite A520 a promising candidate for applications in fields such as CH_4 and CO_2 adsorption.[15] The structure of Basolite A520 was not solved initially, owing to the very small size of powdered product crystallites that were associated with the original synthetic route.[16-17] A recent reported synthesis is gentler in nature and has been shown to yield a Basolite A520 product consisting of larger powder crystallites.[17] Using a combination of powder X-ray diffraction (pXRD), solid-state NMR (SSNMR), IR spectroscopy, computational calculations, and thermogravimetric analysis (TGA), it was shown that Basolite A520 is a structural analogue of the well-known MIL-53 MOF (Figure 5-A1).[17]

In Basolite A520, each Al metal centre is coordinated to four oxygen atoms from four different fumarate ligands as well as two oxygen atoms from two separate bridging hydroxyl groups. The resulting AlO_6 building block is the fundamental octahedral secondary building unit (SBU) in Basolite A520. A one-dimensional chain along the crystallographic *a*-axis is formed by SBUs connected via corner sharing; in turn, the chains are cross-linked by fumarate linkers to form rhombic shaped channels.[17] The framework of Basolite A520 is rigid; there is only a small contraction of the unit cell after evacuating guest water molecules from the channels and the pore shape/dimensions are generally preserved.[17] In comparison, although MIL-53 also features one-dimensional chains and rhombic channels formed by corner-sharing AlO_6 SBUs and two bridging hydroxyl groups, the incorporated linker is 1,4-benzenedicarboxylate. This change in linker imparts flexibility to MIL-53 and gives rise to an interesting "breathing effect:"[18-19] the dimensions of the channels can be altered by changing the nature and loading level of guest molecules, in contrast to the rigid Basolite A520.

Many properties and potential applications of Basolite A520 have not been explored, since the crystal structure was only solved last year. This lack of information stands in contrast to the detailed studies and applications for MOFs with known crystal structures. The only gas adsorption isotherm study of Basolite A520 was reported in the patent literature, which indicated that Basolite A520 is a promising CO_2 and H_2 storage material and exhibits good CO_2 selectivity for the separation of CO_2/CH_4 and CO_2/CO

gases.[20] Other very recent reports indicate that Basolite A520 is a good material for fluoride adsorption from water[21] as well as heat transformation,[22] and has great potential for mechanical energy storage.[23] Previous studies have demonstrated that analogue MOFs incorporating different metal centres exhibit different physical or chemical properties, such as an affinity for gas adsorption[3, 5] and catalytic activities.[24-25] It is highly likely that any analogue of Basolite A520 incorporating other metals will exhibit modified or different properties.

With the dual aims of expanding the fumarate MOF family and exploring the intriguing properties and applications of both Basolite A520 and its analogues, the gallium-fumarate and indium-fumarate MOFs have been synthesized and examined. In this study, powder X-ray diffraction (pXRD), Rietveld refinements, infrared spectroscopy (IR), solid-state NMR (SSNMR) spectroscopy, and thermogravimetric analysis (TGA) techniques have been employed to examine Ga-fumarate and In-fumarate from the perspective of both the host MOFs and the guest molecules. The structure of Ga-fumarate has been unambiguously determined from synchrotron pXRD experiments and Rietveld refinement. The hydrated Ga-fumarate (Ga-fumarate-H_2O) structure presents a space group of *I2/a*. The space group of hydrated Ga-fumarate in this work is different to a very recent reported hydrated Ga-fumarate structure, which has a space group of $P2_1/c$.[26] The porous hydrophobicity has been successfully achieved in In-fumarate by replacing part of bridging –OH groups to bridging $–OCH_3$ groups.

$^{69/71}$Ga and ^{115}In SSNMR experiments at a high magnetic field of 21.1 T permit molecular-level investigation of the local structure about Ga and In in various forms of fumarate MOFs, and provide great support to Rietveld refinements. The behavior of CO_2 molecules in Al-, Ga-, and In-fumarate has been probed by ^{13}C SSNMR experiments, which reveal rich details on the types of CO_2 motion present, their motional angles, and the motional rates. ^{1}H-^{13}C CP SSNMR experiments are also used to probe the CO_2 adsorption locations within fumarate MOFs.

This work illustrates how comprehensive combined characterization of the host MOF and guest molecules is possible using a blend of several accessible complementary techniques, and yields a wealth of structural and dynamic information that points toward Al-, Ga-, and In-fumarate applications in water and gas adsorption, among other areas. This work also provides a novel method to design hydrophobic MOF, which is very critical for gas storage and separation, especially considering the industrial applications.

5.2 Experimental Section

All chemicals and solvents were purchased from Sigma Aldrich and were used without further purification.

5.2.1 Sample preparation

Synthesis of Ga-fumarate MOF. In order to optimize the solvothermal synthesis of Ga-fumarate, the use of various Ga sources ($Ga(NO_3)_3 \cdot xH_2O$, $Ga_2(SO_4)_3 \cdot xH_2O$, Ga_2O_3), solvents *(N,N*-dimethylformamide (DMF), H_2O, methanol, ethanol, acetone, acetonitrile, tetrahydrofuran), temperatures (60 °C to 180 °C), and gallium salt/formate ligand ratios (1 : 1 and 1 : 2) was investigated. It became apparent that Ga-fumarate could only be solvothermally synthesized by using $Ga(NO_3)_3 \cdot xH_2O$ as the Ga source and DMF as the solvent, and by utilizing temperatures ranging from 60 °C to 180 °C. The optimal temperature was found to be 80 °C and the ideal ratio of starting materials was determined to be 1:1, on the basis that these conditions yielded a Ga-fumarate product that exhibited the highest measured Brunauer–Emmett–Teller (BET) surface area (851 m^2/g).

$Ga(NO_3)_3·xH_2O$ (1.28 g, 5 mmol), fumaric acid ($C_4H_4O_4$, 0.58 g, 5 mmol), and 10 mL DMF were mixed together in a 23 mL Teflon-lined stainless steel autoclave, which was then sealed and heated at 80 °C for 3 days. After letting the autoclave cool back to room temperature, the white product was obtained as a powder, which was washed three times with DMF and dried using vacuum filtration (elemental analysis (EA): C: 27.51 %, N: 3.67 %, H: 3.43 %). The sample was then activated under dynamic vacuum for 8 h at a temperature of 150 °C in order to evacuate residual linker and solvent from the MOF channels.

Synthesis of In-fumarate MOF. Synthesis of the In-fumarate MOF was achieved through solvothermal techniques and optimized according to the synthetic conditions that resulted in the greatest BET surface area of the product. Similar as Ga-fumarate MOF, Various solvents *(N,N*-dimethylformamide (DMF), H_2O, methanol, ethanol, acetone, acetonitrile, tetrahydrofuran), temperatures (20 °C to 140 °C), and indium salt/formate ligand ratios (1 : 1 and 1 : 2) was investigated. It became apparent that In-fumarate could be solvothermally synthesized by using $In(NO_3)_3·xH_2O$ as the In source and ethanol and methanol as the solvents, and by utilizing temperatures ranging from 20 °C to 120 °C. The hydrophobic In-fumarate MOF has been generated by using methanol as the solvent. The optimal synthesis methods were shown below.

Hydrophilic In-fumarate (In-fumarate-E). $In(NO_3)_3·xH_2O$ (0.15 g, 0.5 mmol), fumaric acid ($C_4H_4O_4$, 0.116 g, 1.0 mmol), and 10 mL ethanol were mixed together in a 20 mL glass vial, which was then sealed and settled at 40 °C for 3 days. The white product was obtained as a powder, which was washed three times with ethanol and dried using vacuum filtration (elemental analysis: C: 20.79 %, H: 1.99 %). The sample was then activated under dynamic vacuum for 8 h at a temperature of 150 °C in order to evacuate residual linker and solvent from the MOF channels. The BET surface area of In-fumarate-

E after activation is 708 m^2/g.

Hydrophobic In-fumarate (In-fumarate-M). $In(NO_3)_3 \cdot xH_2O$ (0.15 g, 0.5 mmol), fumaric acid ($C_4H_4O_4$, 0.058 g, 0.5 mmol), and 10 mL methanol were mixed together in a 20 mL glass vial, which was then sealed and settled at 20 °C for 3 days. The white product was obtained as a powder, which was washed three times with methanol and dried using vacuum filtration (elemental analysis: C: 21.75 %, H: 1.70 %). The sample was then activated under dynamic vacuum for 8 h at a temperature of 150 °C in order to evacuate residual linker and solvent from the MOF channels. The BET surface area of In-fumarate-M after activation is 599 m^2/g.

Preparation of CO_2 loaded samples. A Schlenk line was used for sample activation and loading of CO_2 guests. A known quantity of the fumarate MOF sample was placed into the bottom of a homemade 5 mm L-shaped glass tube. A thin layer of glass wool was used as a permeable cap to secure the sample in place. The glass tube containing the sample was first attached to the Schlenk line and heated at 150 °C for 8 h under dynamic vacuum (*i.e.*, pressure < 1 mbar) to remove any residual solvents or linkers from the MOF channels. A known amount of pressurized $^{13}CO_2$ (herein denoted simply as "CO_2") was then introduced to the vacuum line, and the CO_2 was allowed to occupy both the vacuum line and the glass tube containing the sample; the overall volume of this combined space is known to be 82.7 cm^3. The bottom of the CO_2-filled glass tube containing the fumarate MOF samples was then immersed in liquid nitrogen to freeze and trap CO_2 within the sample, during which the glass tube was flame-sealed off from the Schlenk line. The overall CO_2 loading amount is expressed by the molar ratio between CO_2 and the metal. In this study, 0.2 CO_2/metal samples were prepared and characterized by SSNMR.

Preparation of deuterium-exchanged Al-fumarate and Ga-fumarate samples. The following procedure describes how deuterium-exchanged samples of fumarate MOF were prepared; the aim was to deuterate the bridging hydroxyl groups joining the MO_6 (M = Al, Ga, In) MOF SBUs. 0.10 g of fumarate MOF was immersed in 2 mL of D_2O within a homemade 5 mm L-shaped glass tube for two days. During the exchange process, the glass tube was sealed with parafilm. The D_2O was extracted and replaced three times per day to ensure thorough deuteration of the sample. After D_2O exchange, the sample was activated and loaded with CO_2 according to the previously outlined procedure *(vide supra)*.

5.2.2 Characterization techniques

Powder X-ray diffraction (pXRD). All pXRD patterns for routine characterization were acquired using an Inel CPS Powder Diffractometer operating with Cu Kα radiation (λ = 1.5406 Å). Reflections were collected at 2θ values ranging between 5 and 120 ° using an incremental step size of 0.02 °. The pXRD patterns used for Rietveld refinement of Ga-fumarate were acquired using synchrotron radiation at the Canadian Light Source in Saskatoon, Canada, which employed X-rays with an energy of 18 keV (λ = 0.6883Å).

BET surface areas and CO_2 adsorption isotherms. BET surface areas of each sample were measured at a temperature of 77 K using a Micromeritics ASAP 2020 Surface Area and Porosity Analyzer instrument, operating with nitrogen (N_2) as the probe gas. CO_2 adsorption isotherms were measured at a temperature of 273 K using the same instrument. Prior to measuring the BET surface areas and CO_2 adsorption isotherms, all fumarate MOF samples were degassed under dynamic vacuum (< 1 mbar) at 150 °C for 8 hours using the same instrument.

Fourier Transform Infrared (FTIR) spectroscopy. All Ga-fumarate and In-fumarate samples were packed into a diamond anvil cell (DAC) at room temperature in a glovebox under N_2 atmosphere for FTIR analysis. A customized IR micro-spectroscopy system was used for all IR absorption measurements, along with a commercial Fourier transform infrared (FTIR) Bruker Vertex 80v spectrometer equipped with a Globar mid-IR light source. The micro-IR system was operated under a vacuum of < 5 mbar to ensure H_2O removal from the sample. The IR beam was focused onto the sample in the DAC, and the transmitted IR beam was collected using a wide-band mercury cadmium telluride (MCT) detector equipped with a ZnSe window that permitted measurements in the spectral range between 600 and 12000 cm^{-1}.

Static ^{13}C SSNMR of adsorbed CO_2. All static ^{13}C SSNMR spectra were acquired using the DEPTH-echo pulse sequence[27] at a magnetic field of 9.4 T, employing a ^{13}C 90 ° pulse length of 3.1 μs and a 180 ° pulse length of 6.2 μs. The optimized ^{13}C pulse delays between scans was determined to be 7.5 s for all fumarate MOFs. When the experimental temperature decreased below 193 K, the optimized ^{13}C pulse delays of all samples increased to 15 s. All static spectra were acquired using a ^{1}H decoupling field of 81 kHz. For static ^{1}H-^{13}C CP experiments at 133 K, 10 ms contact times (CT) were employed for the empty frameworks, CO_2 loaded samples, and CO_2 loaded deuterated samples. All static ^{13}C SSNMR spectra were referenced to the high-frequency resonance of carbon in ethanol, which is located at 58.05 ppm with respect to TMS.[28]

$^{69/71}$Ga SSNMR experiments at 21.1 T. All $^{69/71}$Ga SSNMR experiments were performed at a magnetic field of 21.1 T, using a Bruker Avance II NMR spectrometer located at the National Ultrahigh-Field NMR Facility for Solids in Ottawa, ON, Canada. A homemade 5 mm HX static probe was used to acquire all $^{69/71}$Ga spectra (ν_0(^{69}Ga) = 216.0 MHz, ν_0(^{71}Ga) = 274.4 MHz). Both ^{71}Ga and ^{69}Ga NMR shifts were referenced to watersolvated Ga^{3+} using a solution of 1 M $Ga_2(SO_4)_3$ ($\delta_{iso} = 0$).[29] All spectra were acquired using a standard 90 ° - 90 °solid-echo pulse sequence of the form ($\pi/2$ - τ_1 - $\pi/2$ - τ_2 - acq) with a spectral width of 2000 kHz. A 90 ° CT-selective pulse length of 2 μs was used to acquire ^{71}Ga spectra and a 90 ° CT-selective pulse length of 3 μs was used to acquire ^{69}Ga spectra. Pulse delays of 2 s and 0.5 s were employed for the ^{71}Ga and ^{69}Ga spectra of activated Ga-fumarate, respectively. In comparison, the H_2O-adsorbed Ga-fumarate sample required a pulse delay of 1 s for ^{71}Ga experiments but only a pulse delay of 0.5 s for ^{69}Ga spectral acquisition. Due to the relatively large quadrupole moment of ^{69}Ga, the breadth of ^{69}Ga powder patterns was too large to properly excite and acquire in a single experiment. The overall ^{69}Ga powder pattern was constructed by co-adding two or more frequency-stepped individual sub-spectra in technique known as piecewise acquisition or variable-offset cumulative spectrum (VOCS).[30]

^{115}In SSNMR experiments at 21.1 T. All ^{115}In SSNMR experiments were performed at a magnetic field of 21.1 T, using a Bruker Avance II NMR spectrometer located at the National Ultrahigh-Field NMR Facility for Solids in Ottawa, ON, Canada. A homemade 5 mm HX static probe was used to acquire all ^{115}In spectra ($\nu_0(^{115}\text{In}) = 197.2$ MH). The ^{115}In NMR shift was referenced to In^{3+} using 0.1 M $In(NO_3)_3$ in 0.5 M HNO_3 ($\delta_{iso} = 0$).[29] All spectra were acquired using a standard 90 ° - 90 °solid-echo pulse sequence of the form ($\pi/2$ - τ_1 - $\pi/2$ - τ_2 - acq) with a spectral width of 5000 kHz. A 90 ° CT-selective pulse length of 0.5 μs was used to acquire ^{115}In spectra. Pulse delays of 0.25 s was employed for the ^{115}In spectra. Due to the large quadrupole moment of ^{115}In, the breadth of ^{115}In powder patterns was too large to properly excite and acquire in a single experiment. The overall ^{115}In powder pattern was constructed by co-adding two or more frequency-stepped individual sub-spectra in technique known as piecewise acquisition or variable-offset cumulative spectrum (VOCS).

Theoretical Calculations. Plane-wave density functional theory (DFT) calculations are commonly used to complement experimental investigations of NMR parameters in systems incorporating a variety of nuclei and structural motifs.[31] In this study, all calculations were performed using the CASTEP software package[32-33] within Accelrys Materials Studio. The $^{69/71}$Ga and ^{115}In electric field gradient (EFG) and chemical shift (CS) tensor parameters were calculated using the NMR module.[34-35] The gauge-including projector-augmented wave (GIPAW) method was used with pseudopotentials and plane-wave basis sets.[32] All unit cell parameters and atomic coordinates were taken from the refined crystal structures of Ga-fumarate-H_2O. The generalized gradient approximation (GGA) along with the Perdew− Burke−Ernzerhof (PBE) functional[36] was employed. A plane-wave cut off energy of 1000 eV was used, corresponding to the pre-set "fine" basis set accuracy.

Spectral simulation software. The WSolids[37] computer software was used to perform analytical simulations of experimental SSNMR spectra in order obtain all $^{69/71}$Ga NMR parameters as well as the observed or apparent ^{13}C NMR parameters, while the QUEST[38] software was used to simulate ^{115}In spectra. EXPRESS[39] software was used to simulate the effects of CO_2 dynamics on ^{13}C SSNMR powder patterns and to extract CO_2 motional information.

5.3 Results and Discussion

5.3.1 Studying synthesis and structure of Ga-fumarate

Synthesis of Ga-fumarate. The solvothermal method was explored as a possible route to synthesize Ga-fumarate, including the use of methanol, ethanol, H_2O, acetone, acetonitrile, tetrahydrofuran and DMF as potential solvents. Only DMF yielded a crystalline Ga-fumarate product with a pXRD pattern resembling that of Al-fumarate (*vide* *infra*). The use of methanol and ethanol as solvents yielded crystalline powder products that did not exhibit the expected type of pXRD pattern, were not porous, and lost all crystallinity after attempting various activation strategies; these products will not be discussed any further. Amorphous products were obtained using H_2O, acetone, tetrahydrofuran and acetonitrile as solvents. The optimized synthesis of Ga-fumarate involves heating a DMF solution of $Ga(NO_3)_3{\cdot}xH_2O$ and fumaric acid in autoclave at a temperature of 80 °C for 3 days, and then washing the white powdered product three times with DMF (see Experimental section). It must be noted that the recent reported Ga-fumarate has been synthesized using water as synthetic solvent, assisted by NaOH at 403 K.[26] Ga-fumarate synthesized in this work gave rise to the same pXRD powder pattern as reported aqueous synthesis method,[26] indicating Ga-fumarate with the same structure has been generated in our work.

Powder XRD investigation of Ga-fumarate. Preliminary characterization of the Ga-fumarate products were performed using pXRD. The pXRD pattern of as-made Ga-fumarate (Ga-fumarate(*as*)) features relatively broad reflections in the areas where one would expect to find reflections corresponding to water-loaded Al-fumarate (Al-fumarate-H_2O) (Figure 5-1). After activation to purge the MOF pores and exposure to ambient conditions to adsorb H_2O, Ga-fumarate(*as*) becomes Ga-fumarate-H_2O, which yields a pXRD pattern that is strikingly similar to that of Al-fumarate-H_2O and exhibits similar reflection angles and intensities (Figure 5-1). The strong resemblance between the Al-fumarate-H_2O and Ga-fumarate-H_2O pXRD patterns suggests that Ga-fumarate should reside in a similar crystal structure as Al-fumarate. All of the Ga-fumarate-H_2O pXRD reflections are shifted to comparatively lower 2θ angles versus those of Al-fumarate-H_2O; this may reflect an enlarged *d*-spacing in Ga-fumarate-H_2O due to the relatively larger Ga metal centres.

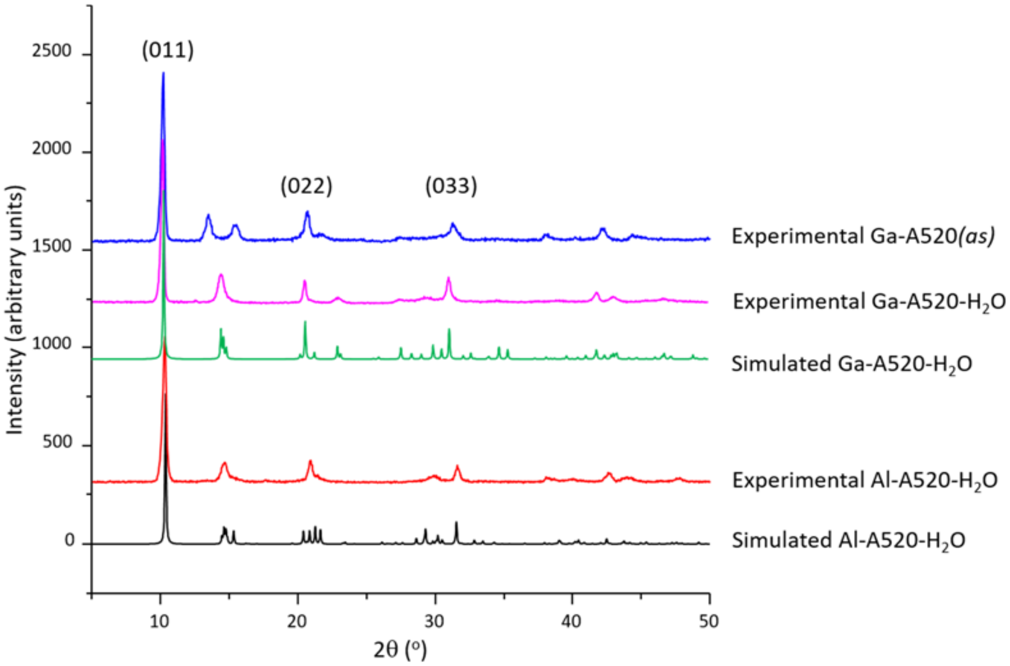

Figure 5-1. A comparison of simulated and experimental pXRD patterns of Al-A520 and Ga-A520. Our TGA studies in this work, along with prior reports,[17] indicate that water is adsorbed into the empty channels of Al-A520 and Ga-A520, after MOF exposure to ambient air. The samples with water inside the channels are termed Al-A520-H$_2$O and Ga-A520-H$_2$O, respectively. The as-made sample of Ga-A520 is referred to Ga-A520(*as*). The 0kk reflections of Ga-A520-H$_2$O are shifted to lower angles versus those of Ga-A520(*as*), which indicates a small contraction of the MOF channel that propagates along the direction of the fumarate linker. Note the x-axis is truncated to exclude angles below 5 °.

Powder XRD experiments were also used to compare rigid Ga-fumarate to its structural analogue, the flexible MIL-53. A prior study has shown that the flexibility of MIL-53 and its guest-dependent variable pore dimensions give rise to distinct pXRD patterns depending on the guest (i.e., DMF versus H$_2$O).[40-41] In contrast, our experimental pXRD patterns of Ga-fumarate(*as*) and Ga-fumarate-H$_2$O are generally similar (Figure 5-1), suggesting Ga-fumarate has rigid framework.

The structural stability of Ga-fumarate was also investigated by using pXRD experiments. An activated Ga-fumarate sample was immersed into a solvent (*e.g.*, water, acetone, methanol, ethanol, etc.) for 7 days, and the sample was then allowed to dry and was examined *via* pXRD. Figure 5-A2(a) shows the resulting pXRD patterns after solvent exposure are quite similar and remain well-defined. This result is a clear indication that the Ga-fumarate is chemically robust, and retain both their structures and their high degree of crystallinity after solvent treatment.

Determining bridging -OH groups *via* SSNMR and IR. The bridging –OH groups between MO_6 (M: metal) SBUs are very important functional groups in MIL-53 that act as CO_2 adsorption sites,[27, 42-43] hence, these –OH groups should be present in the structural analogues Ga-fumarate, and may play an important role in guest adsorption. Therefore, SSNMR and IR experimets have been employed to determine the bridging -OH goups before acquiring Rietveld refinement. ^1H SSNMR experiments reveal the bridging –OH resonance in activated Ga-fumarate has a chemical shift of ca. 2.6 ppm (Figure 5-2(a)), which is similar to the ^1H chemical shift of bridging –OH groups in activated Al-fumarate (1.75 ppm);[17] the slight divergence is due to the nature and influence of the different metal centres. The presence of a bridging –OH group between GaO_6 octahedra can also be observed as an O-H stretching absorption in IR spectra at 3670 cm^{-1} in activated Ga-fumarate (Figure 5-2(b)), which is in the expected region for bridging –OH groups in corner-sharing chains of metal-centreed octahedra.[40]

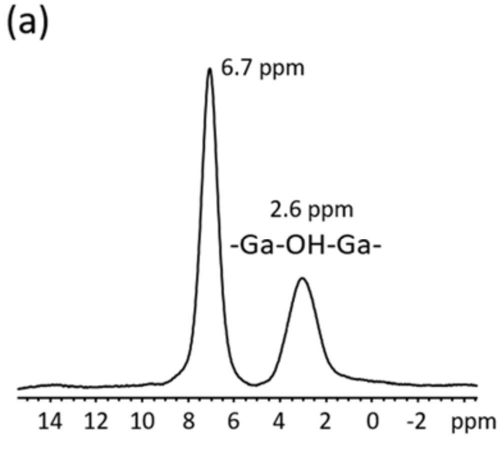

Figure 5-2. The ^{1}H MAS SSNMR spectra of activated Ga-A520 (acquired at a spinning frequency of 14 kHz and a magnetic field of 9.4 T) is shown in (a). The high-frequency resonances located at 6.7 ppm correspond to the hydrogen atom of the fumarate linkers, and the resonances originate from the bridging hydroxyl groups that join the GaO_6 SBUs are observed at 2.6 ppm. The IR spectra of activated Ga-A520 is depicted in (b); the absorption at 3670 cm^{-1} correspond to the O-H vibration of bridging hydroxyl groups

Rietveld refinements of synchrotron X-ray diffraction data of Ga-fumarate. Activated Ga-fumarate readily adsorbs water from the air to become Ga-fumarate-H_2O with a formula of $Ga(OH)(C_4H_2O_4)\cdot 3.5H_2O$, where the 3.5 H_2O/Ga ratio was determined from TGA (Figure 5-A3) and ($C_4H_2O_4$) represents the fumarate linker. The pXRD pattern of Ga-fumarate-H_2O used for refinement was acquired using synchrotron radiation at the Canadian Light Source facility. As a starting point for the refinement, the previously determined structure of Al-fumarate-H_2O was used.[17]

The refinement was successful, yielding the final fit and differences between the calculated and observed patterns shown in Figure 5-3. The goodness-of-fit parameters associated with this Rietveld refinement were $\chi^2 = 1.88$, $R_p = 4.2$ %, and $R_{wp} = 5.8$ %. It was not possible to minimize the χ^2 value any further based on the experimental pXRD pattern, which has anisotropic broadening of the reflections that decrease resolution and could conceal overlapping peaks. The Rietveld refinement of Ga-fumarate-H_2O yielded a monoclinic unit cell in the *I2/a* (no. 15) space group: $a = 6.884(1)$ Å, $b = 12.129\ (2)$ Å, $c = 12.302(2)$ Å, $\alpha = \gamma = 90°$, $\beta = 86.75(2)°$, $V = 1025.47$ Å^3. It must be noted that the structure of Ga-fumarate-H_2O has been reported in a very recent published paper,[26] however, the published structure of Ga-fumarate-H_2O has a space group of $P2_1/c$ with the goodness-of-fit parameters were $\chi^2 = 5.37$, $R_p = 9.22$ %, and $R_{wp} = 13.79$ %. Based on the goodness-of-fit parameters, we have reason to believe that our refined structure is more accurate. Further evidence supporting *I2/a* space group is provided in the $^{69/71}$Ga SSNMR section.

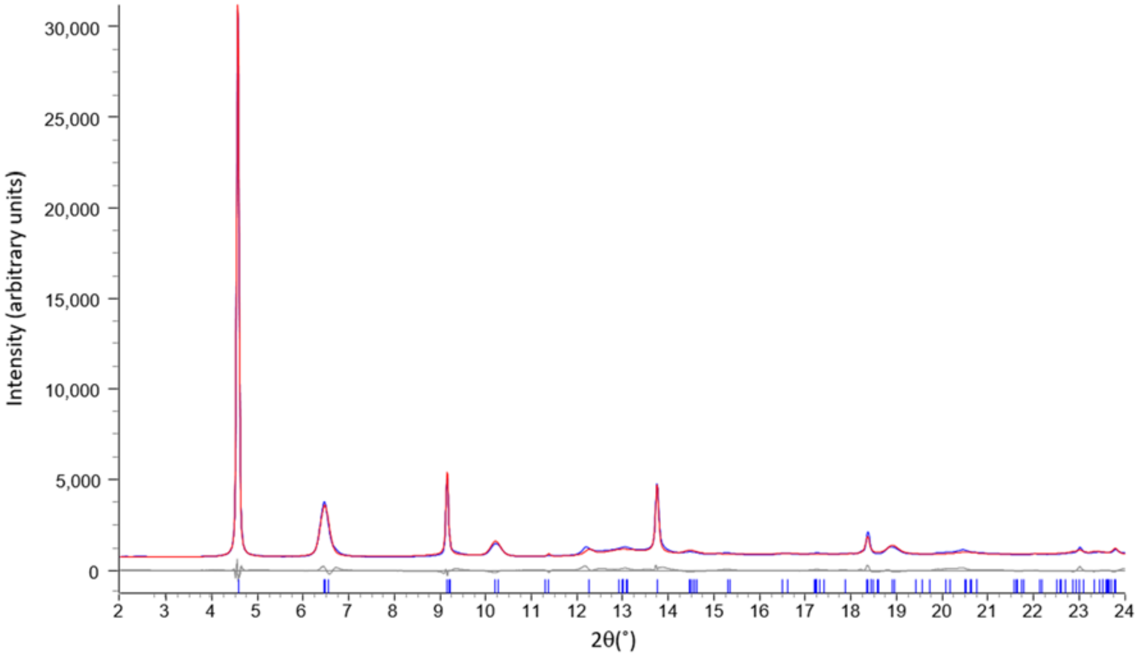

Figure 5-3. The calculated Rietveld plot of Ga-A520-H_2O is shown, along with the experimental synchrotron pXRD pattern and a difference plot. The associated goodness-of-fit parameters are $\chi^2 = 1.88$, $R_p = 4.2$ %, and $R_{wp} = 5.8$ %.

The refined structure of Ga-fumarate-H_2O only has one unique crystallographic Ga site. Each Ga metal centre is connected to six oxygen atoms to form an octahedral secondary building unit (SBU) (Figure 5-4(a)), where four oxygen atoms originate from four different fumarate linkers and the remaining two oxygen atoms belong to bridging hydroxyl groups that join the SBUs. The corner-sharing octahedral GaO_6 SBUs are connected to form a one-dimensional chain (Figure 5-4(b)), which are then interconnected by fumarate linkers to form a MOF that features one-dimensional rhombic-shaped channels (Figure 5-4(c)). The pore size of Ga-fumarate-H_2O measures from corner to corner *ca.* 12 x 12 Å, which is similar to the dimensions of Al-fumarate-H_2O (12 x 12 Å),[17] in line with the numerous structural similarities between the two MOFs. As expected, the refinement revealed that the Ga-fumarate-H_2O channels are occupied by guest H_2O molecules which were adsorbed from the air; only the oxygen positions could be refined. A close view of water oxygen atoms in the channels of Ga-fumarate-H_2O is shown in Figure 5-4(d). The shortest distance between two water oxygen atoms (O_w) in Ga-fumarate-H_2O is 2.49 Å, which is substantially shorter than the 2.71 Å in Al-fumarate-H_2O. The shorter O_w - O_w distance of Ga-fumarate-H_2O is likely due to the smaller free space of the channels. The shortest distance between the oxygen atoms of water molecules (O_w) and the hydrogen atoms of bridging –OH groups in Ga-fumarate-H_2O is 2.488 Å. Such a distance indicates water molecules within the Ga-fumarate channels may interact with the bridging -OH groups. To further probe the local Ga environment, $^{69/71}$Ga SSNMR experiments were performed.

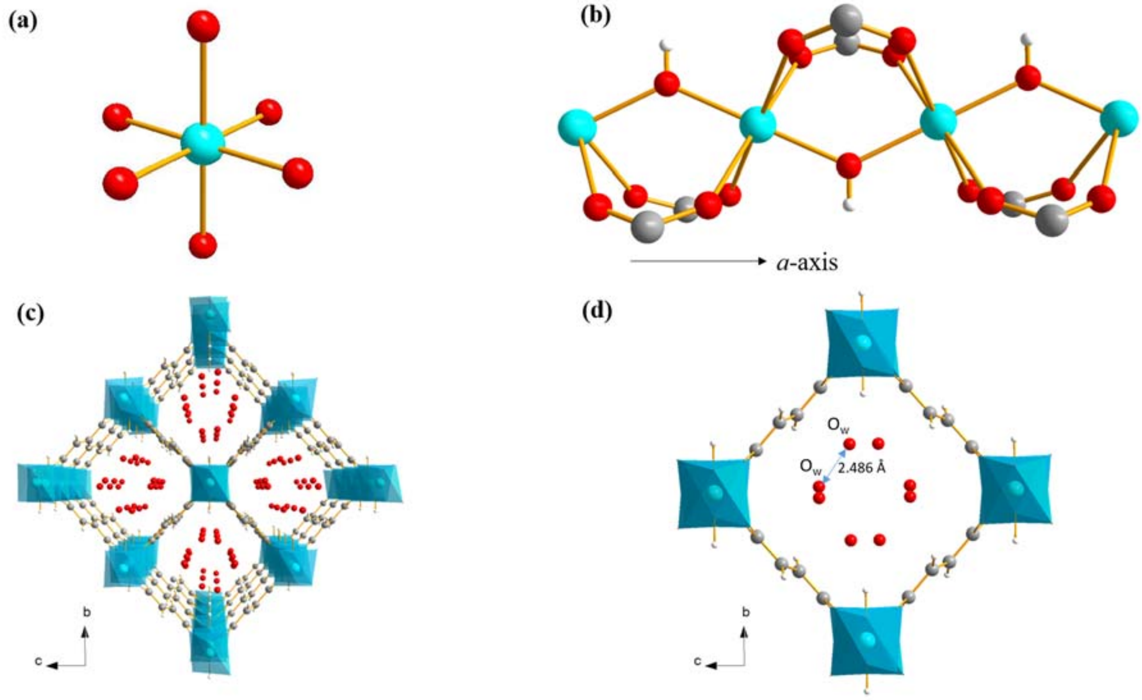

Figure 5-4. The local and long-range structure of Ga-fumarate-H_2O. In (a), the GaO_6 octahedron arising from the $GaO_4(OH)_2$ secondary building unit (SBU) is shown. The SBUs are linked by bridging hydroxyl (OH) groups; the resulting chain of SBUs formed along the crystallographic *b*-axis is shown in (b). The SBU chains are interconnected by fumarate linkers to create the one-dimensional rhombic channels shown in (c). The oxygen atoms associated with water molecules in the channels are depicted more clearly in (d). The colors red, grey, white and blue correspond to oxygen, carbon, hydrogen and the gallium metal centre, respectively.

$^{69/71}$Ga SSNMR experiments at 21.1 T. There is an inherent difficulty with performing ^{69}Ga and ^{71}Ga SSNMR experiments due to the quadrupolar nature of the nuclei (spin 3/2); both ^{69}Ga and ^{71}Ga possess large quadrupole moments of 171 and 107 mb, respectively.[44] These large quadrupole moments couple with surrounding EFGs in a process known as the quadrupolar interaction (QI), which often spreads the $^{69/71}$Ga central transition (i.e., spin -1/2 ↔ +1/2) resonance across large frequency ranges, yielding very broad powder patterns of low signal-to-noise ratio (S/N). NMR parameters relating to the EFG are described in more detail within the Appendix (Section 5.6). The chemical shift (CS) interaction also has a minor influence on $^{69/71}$Ga spectra, however, its effect is limited since the QI is much larger in magnitude.

Acquiring high resolution $^{69/71}$Ga SSNMR spectra of Ga-based MOFs is not a trivial affair. $^{69/71}$Ga magic angle spinning (MAS) SSNMR spectra of MOFs such as MIL-53, MIL-61, MIL-96, MIL-120 and MIL-124 have been reported;[45-46] however, due to the prevalence of large C_Q($^{69/71}$Ga) values and limited MAS frequencies, acquiring high-quality $^{69/71}$Ga MAS NMR spectra of Ga MOFs remains very challenging. Very recently, $^{69/71}$Ga static SSNMR powder patterns of Ga-MIL-53 have been successfully acquired at a magnetic field of 21.1 T.[47] In this study, we have used static quadrupolar echo SSNMR experiments at the same magnetic field of 21.1 T to acquire quality $^{69/71}$Ga NMR spectra of activated Ga-fumarate and Ga-fumarate-H_2O. Acquisition of both ^{69}Ga and ^{71}Ga NMR spectra permits accurate determination of C_Q, η_Q, and the CS parameters, since the same parameters must fit both spectra (except C_Q, which is scaled by the nuclear quadrupole moment).

The $^{69/71}$Ga SSNMR spectra of activated Ga-fumarate and Ga-fumarate-H_2O are shown in Figure 5-5, along with their corresponding simulated spectra; the experimentally determined $^{69/71}$Ga NMR parameters are listed in Table 5-1. As expected, all ^{69}Ga SSNMR spectra (Figure 5-5(a)) are broader than their ^{71}Ga counterparts (Figure 5-5(b)), owing to the relatively larger quadrupole moment of ^{69}Ga. It should be noted that the relatively lower simulated versus experimental intensity of the low-frequency "horn" of all ^{71}Ga spectra and in the ^{69}Ga spectrum of Ga-fumarate-H_2O may be due to anisotropic T_2 relaxation

(Figure 5-A4), which has been observed for spin-1/2 and quadrupolar nuclei in a variety of systems.[48-49]

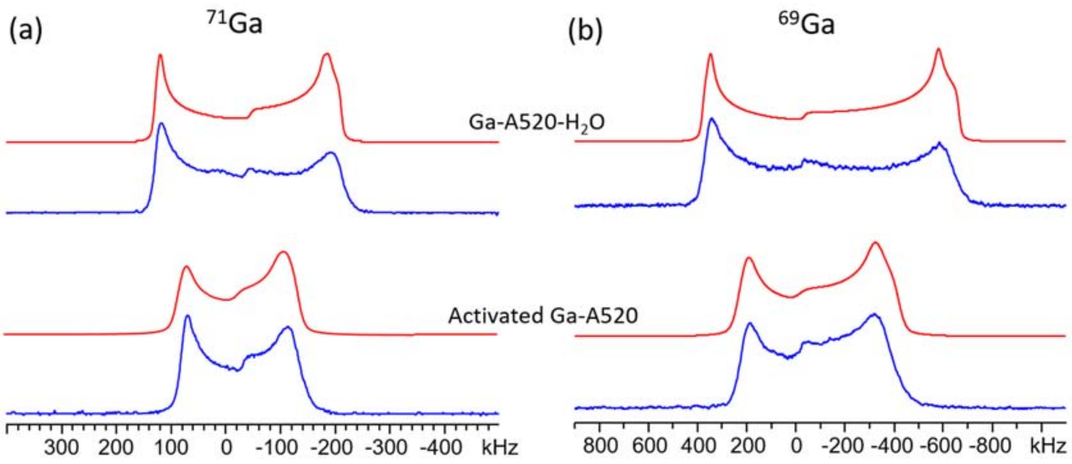

Figure 5-5. Static $^{69/71}$Ga spectra acquired at 21.1 T are depicted. In (a), the experimental ^{71}Ga SSNMR spectra of Ga-fumarate-H$_2$O and activated Ga-fumarate are shown in blue, along with corresponding spectral simulations in red. The ^{69}Ga SSNMR spectra in blue and simulations of the same compounds in red are shown alongside in (b).

$^{69/71}$Ga SSNMR spectra of activated Ga-fumarate and Ga-fumarate-H$_2$O are characteristic of a quadrupolar nucleus residing in a single unique local environment. Observing a single Ga site in $^{69/71}$Ga SSNMR spectra is in good agreement with our Rietveld refined structure, which only has one crystallographic Ga centre. It must be noted that the recent published structure of hydrated Ga-fumarate has four different Ga sites.[26] However, our SSNMR experiments, along with pXRD Rietveld refinement, which has much better fitted parameters (χ^2 = 1.88, R_p = 4.2 %, R_{wp} = 5.8 % *vs* χ^2 = 5.37, R_p = 9.22 %, R_{wp} = 13.79 %[26]), strongly suggest that the hydrated Ga-fumarate has a space group of *I2/a* with only a single Ga site in the structure.

Table 5-1. Experimentally determined and calculated $^{69/71}$Ga SSNMR parameters of activated Ga-fumarate, Ga-fumarate-H_2O and activated (large-pore) MIL-53-Ga. All experimental $^{69/71}$Ga SSNMR spectra were acquired at a magnetic field of 21.1 T.

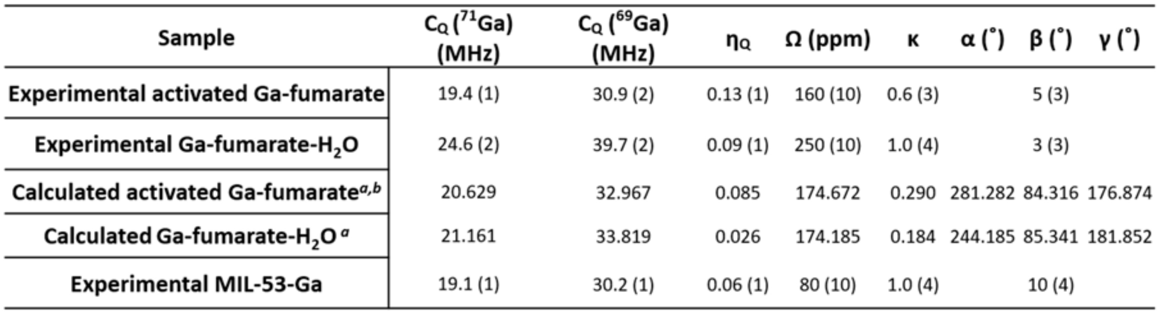

Sample	C_Q (^{71}Ga) (MHz)	C_Q (^{69}Ga) (MHz)	η_Q	Ω (ppm)	κ	α (°)	β (°)	γ (°)
Experimental activated Ga-fumarate	19.4 (1)	30.9 (2)	0.13 (1)	160 (10)	0.6 (3)		5 (3)	
Experimental Ga-fumarate-H_2O	24.6 (2)	39.7 (2)	0.09 (1)	250 (10)	1.0 (4)		3 (3)	
Calculated activated Ga-fumarate[a,b]	20.629	32.967	0.085	174.672	0.290	281.282	84.316	176.874
Calculated Ga-fumarate-H_2O[a]	21.161	33.819	0.026	174.185	0.184	244.185	85.341	181.852
Experimental MIL-53-Ga	19.1 (1)	30.2 (1)	0.06 (1)	80 (10)	1.0 (4)		10 (4)	

[a] The calculated SSNMR parameters of activated Ga-fumarate and Ga-fumarate-H_2O are based on the crystal structure obtained after geometry optimization using the CASTEP software package,[32, 33] which employs plane-wave DFT methods and was also used to calculate all NMR parameters; see Experimental section for further details. [b] The crystal structure of activated Ga-fumarate was obtained by removing water molecules from the channels of the Ga-fumarate-H_2O crystal structure.

The $^{69/71}$Ga powder patterns of Ga-fumarate-H_2O are significantly broader than those of activated Ga-fumarate (Figure 5-5). The different C_Q values (Table 5-1) indicate that some significant reduction of spherical symmetry in the Ga local environment has occurred during the hydration process. The presence of H_2O within the channels of Ga-fumarate-H_2O must be influencing the Ga local environment by either (i) directly influencing the EFG at Ga (*i.e.*, very close proximity or bonding to Ga), or (ii) interacting with the linkers or bridging hydroxyl groups between GaO_6 SBUs, which subsequently distorts the GaO_6 SBUs and modifies the EFG at Ga. The $^{69/71}$Ga asymmetry parameters (η_Q) of both hydrated ($\eta_Q = 0.09$) and dehydrated ($\eta_Q = 0.13$) Ga-fumarate reflect a high degree of axial symmetry that is not significantly altered by hydration. The invariance of

η_Q suggests that there are no H_2O-Ga bonds formed during the hydration of Ga-fumarate, since additional bonding would significantly impact n_Q. In this sense, the changes in $C_Q(^{69/71}Ga)$ with hydration of Ga-fumarate along with stationary n_Q values is likely due to variations in Ga-O bond lengths or ∠O-Ga-O bond angles that originate from relatively strong H_2O interactions with the bridging hydroxyl groups joining GaO_6 octahedra.

Plane-wave DFT calculations of $^{69/71}Ga$ EFG tensor parameters were also performed on the geometry-optimized structures of Ga-fumarate (Table 5-1). The "calculated" crystal structure of activated Ga-fumarate was obtained by removing water molecules from the channels of the Ga-fumarate-H_2O structure we obtained from the Rietveld refinement. All geometry optimization calculations were performed with symmetry constrained to the *I2/a* space group. Both the activated Ga-fumarate and Ga-fumarate-H_2O structures feature a single crystallographically unique Ga site in the structure after geometry optimization (Table 5-1), which is consistent with the Rietveld refinement and $^{69/71}Ga$ SSNMR results. The calculated $C_Q(^{69/71}Ga)$ and η_Q values of activated Ga-fumarate and Ga-fumarate-H_2O are in good agreement with experimental values (Table 5-1). There is a very slight increase in calculated $C_Q(^{69/71}Ga)$ values in Ga-fumarate-H_2O that underestimates the actual observed increase in $C_Q(^{69/71}Ga)$. This underestimation is likely because the DFT calculations assume a static arrangement of water molecules within the channels. In reality, the water molecules are disordered and dynamic, which allows H_2O to sample space proximate to the Ga centre and/or interact with the linkers bound to Ga, thus reducing the spherical symmetry of GaO_6 SBUs within Ga-fumarate-H_2O and increasing experimental $C_Q(^{69/71}Ga)$ values.

The CASTEP calculated NMR parameters based on previous published Ga-fumarate-H_2O structure (space group: $P2_1/c$) gravely deviates from the experimental values (Table 5-A1). The comparison of calculated spectra of these two space groups is shown in

Figure 5-A5. Overall, our SSNMR and computational CASTEP studies support the structure determined here by Rietveld refinement.

5.3.2 Synthesis and characterization of In-fumarate

Solvothermal synthesis of In-fumarate was investigated using various solvents. Different to Ga-fumarate, crystalline In-fumarate MOFs can be yielded by using methanol or ethanol as synthetic solvent. Using other solvents only generated amorphous products or products with different phases. The synthesis of In-fumarate is occurs at lower temperature, with the optimized synthesis temperature of 40 °C and 20 °C by using ethanol and methanol, respectively. It is very interesting to note that the the property of In-fumarate framework can be tuned by using different solvents. Synthesis of In-fumarate using ethanol has generated hydrophilic In-fumarate (In-fumarate-E), which the framework property is similar to Al- and Ga-fumarate, however, synthesis using methanol has generated hydrophobic In-fumarate (In-fumarate-M).

Characterization of In-fumarate-E products were performed using pXRD first, with pXRD patterns shown in Figure 5-6. The experimental pXRD pattern of as-made In-fumarate-E(*as*) has a good agreement with simulated and experimental Ga-fumarate-H_2O pXRD patterns, which indicates In-fumarate-E(*as*) has similar framework structure to Ga-fumarate-H_2O. After evacuating the MOF channels to adsorb H_2O, the pXRD pattern of In-fumarate-E-H_2O is nearly identical to that of In-fumarate-E(*as*), which suggests that In-fumarate-E also has rigid framework. All pXRD reflections in In-fumarate-E samples are shifted to lower 2θ angles versus those of Ga-fumarate, due to the relatively larger In metal centres.

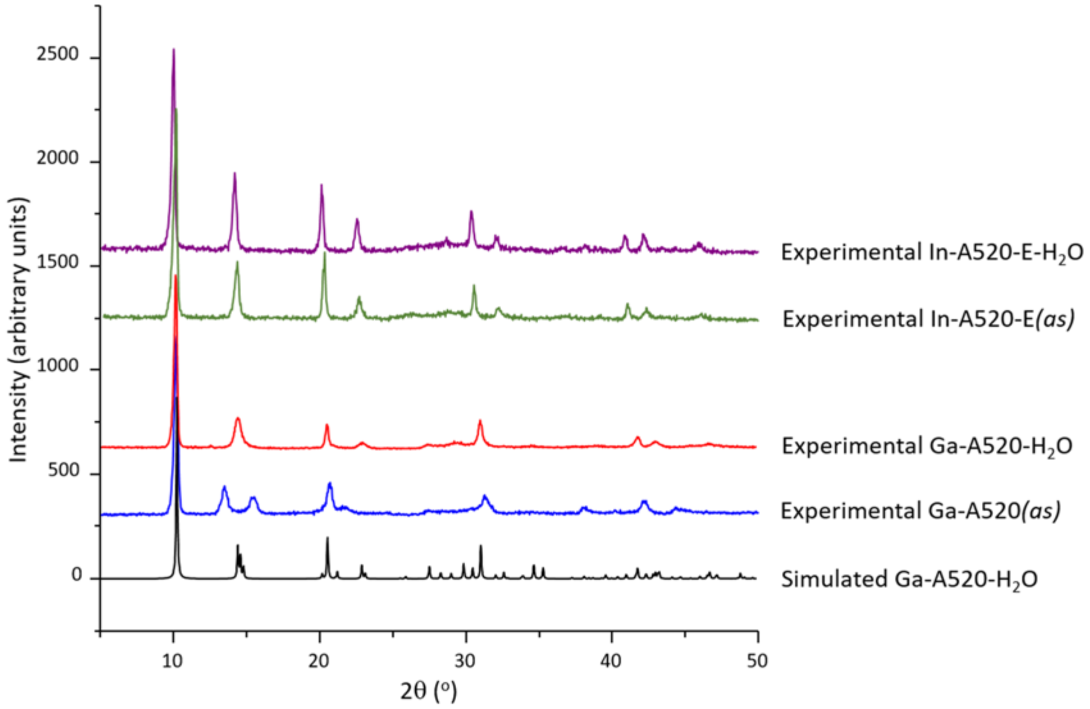

Figure 5-6. A comparison of simulated and experimental pXRD patterns of Ga-fumarate and experimental pXRD patterns of In-fumarate-E. The samples with water inside the channels are termed Ga-fumarate-H_2O and In-fumarate-E-H_2O, respectively. The as-made samples of Ga-fumarate and In-fumarate-E are referred to Ga-fumarate(*as*) and In-fumarate-E*(as)*. The reflections of In-fumarate-E samples are shifted to lower angles versus those of Ga-fumarate samples, due to the relatively larger In metal centres.

The bridging –OH groups in In-fumarate-E have been successfully detected by acquiring ^{1}H MAS SSNMR spectrum and IR spectrum. ^{1}H MAS SSNMR experiment at magnetic field of 21.1 T with a spinning speed of 31.25 kHz reveals that the resonance of bridging –OH groups in activated In-fumarate-E is located at ca. 1.9 ppm (Figure 5-7(a)), which is proximate to the ^{1}H resonance of bridging –OH groups in activated Ga-fumarate (2.6 ppm). The O-H stretching absorption of bridging -OH groups of activated In-fumarate-E in IR spectrum has been observed at 3666 cm^{-1} (Figure 5-7(b)).

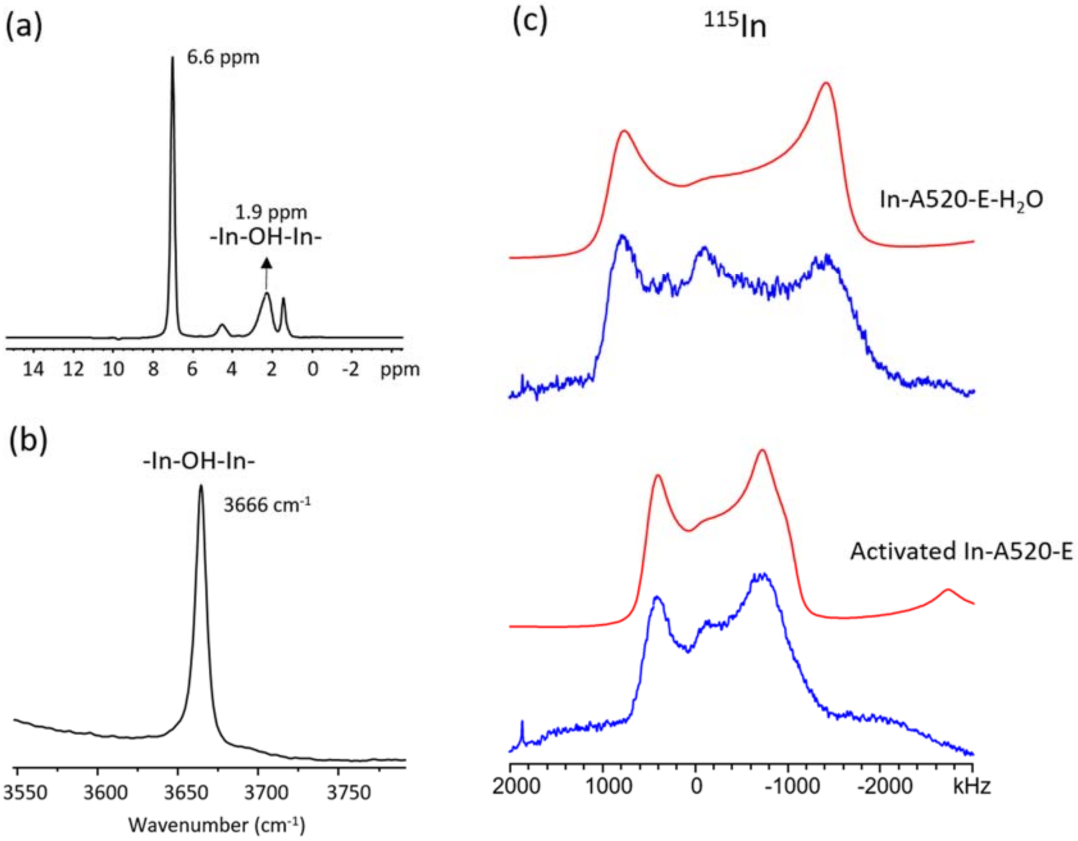

Figure 5-7. The ^{1}H MAS SSNMR spectrum of activated In-fumarate-E acquired with a spinning frequency of 31.25 kHz at magnetic field of 21.1 T is shown in (a). The high-frequency resonances located at 6.6 ppm corresponds to the hydrogen atom of the fumarate linkers, and the resonance originates from the bridging hydroxyl groups that join the InO$_6$ SBUs are observed 1.9 ppm. The detailed assignement of each resonance in (a) can be found in Figure 5-A6. The IR spectrum of activated In-fumarate-E is depicted in (b); the absorption at 3666 cm^{-1} correspond to the O-H vibration of bridging hydroxyl groups. The experimental (blue) and simulated (red) ^{115}In SSNMR spectra of In-fumarate-E-H$_2$O and activated In-fumarate-E are shown in (c).

^{115}In SSNMR experiments at 21.1 T have been performed to study the behavior of In metal centres in In-fumarate-E**.** Compared with $^{69/71}$Ga SSNMR experiments, acquiring a ^{115}In SSNMR spectrum is very challenging and time-consuming due to the much larger quadrupole moment (770 mb), which lead to extremely broad powder patterns with low S/N. The ^{115}In SSNMR spectroscopy has been used to study a variety of materials,[50-53] however, to the best of our knowledge, only two In-based MOFs: In(BDC)$_{1.5}$(bipy), In(BTC)(H_2O)(phen), and MIL-68 have been studied by ^{115}In SSNMR.[54-55] In our study, the ^{115}In SSNMR spectra (Figure 5-7 (c)) of In-fumarate MOFs have been successfully acquired, which provide detailed information on the short-range environment around the In metal centres.

Table 5-2. Experimentally determined and calculated ^{115}In SSNMR parameters of activated In-fumarate-E and In-fumarate-E-H_2O. All experimental ^{115}In SSNMR spectra were acquired at a magnetic field of 21.1 T.

Sample	**C_Q (^{115}In) (MHz)**	**η_Q**
Experimental activated In-fumarate-E	192 (2)	0.21 (2)
Experimental In-fumarate-E-H_2O	260 (3)	0.00 (2)

The ^{115}In SSNMR spectra of activated In-fumarate-E and water adsorbed In-fumarate-E-H_2O are shown in Figure 5-7(c), along with their corresponding simulated spectra; the experimentally determined ^{115}In NMR parameters can be found in Table 5-2. Similar to Ga-fumarate samples, the ^{115}In SSNMR spectra of hydrated In-fumarate-E-H_2O is broader than dehydrated activated In-fumarate-E. Only a single ^{115}In SSNMR powder pattern has been observed in each sample, which suggests that only a single crystallographic In site presents in these two samples. The In metal centre in activated In-fumarate-E corresponds to $C_Q(^{115}In) = 193$ (2) MHz, with $\eta_Q = 0.22$ (2), while the In centre in water adsorbed In-fumarate-E-H_2O corresponds to $C_Q(^{115}In) = 260$ (3) MHz, with $\eta_Q = 0.0$ (2). The increased $C_Q(^{115}In)$ value demonstrates the reduced spherical symmetry of

InO_6 SBUs, which caused by the interaction between water molecules and the framework and gives rise to the non-uniform distribution of In-O bond lengths or ∠O-In-O bond angles. Similar to Ga-fumarate samples, low η_Q values also have been observed in In-fumarate-E samples, which indicate a high degree of axial symmetry of InO_6 SBUs in these two structures. The reduced η_Q value in In-fumarate-E-H_2O should also due to the InO_6 SBUs geometry changing, which caused by the interaction between water molecules and the framework. The ^{115}In SSNMR experiments suggest that In-fumarate-E has similar property as Ga-fumarate in water adsorption.

Hydrophobic In-fumarate-M. One of the most significant limitations of MOFs in industrial applications is their affinity towards water, which may lead to mechanical and chemical instability.[56] For example, in gas capture, MOFs can be degraded or their channels can be occupied by water molecules contained in the gases, significantly changing their adsorption properties,[57] therefore, the development of hydrophobic MOF to eliminate the negative effect of water is becoming critical.

Fortunately, a hydrophobic In-fumarate (In-fumarate-M) has been successfully synthesized using methanol as solvent. Both In-fumarate-E and In-fumarate-M has identical pXRD patterns (Figure 5-A7), indicating the two frameworks have the same topology. However, after activation and exposure to air (with humidity of 20 %) for a week, TGA (Figure 5-8(a)) indicates the absence of water within In-fumarate-M. TGA shows only one weight loss event around 400 °C, which corresponds to the decomposition of the MOF. ^{13}C SSNMR MAS experiment on as-made In-fumarate-M indicates the presence of two different type of $-CH_3$ groups, by observing two distinct ^{13}C resonances at 50.4 ppm and 53.4 ppm (Figure 5-8(b)). After activation, the ^{13}C resonance at 50.4 ppm has been removed due to the evacuation of trapped methanol molecules, however, the other ^{13}C resonance at 53.4 ppm remains in the spectra and has been shifted to 53.0 ppm (Figure 5-

8(c)). The presence of the hydrophobic $–CH_3$ groups explains the hydrophobicity of In-fumarate-M.

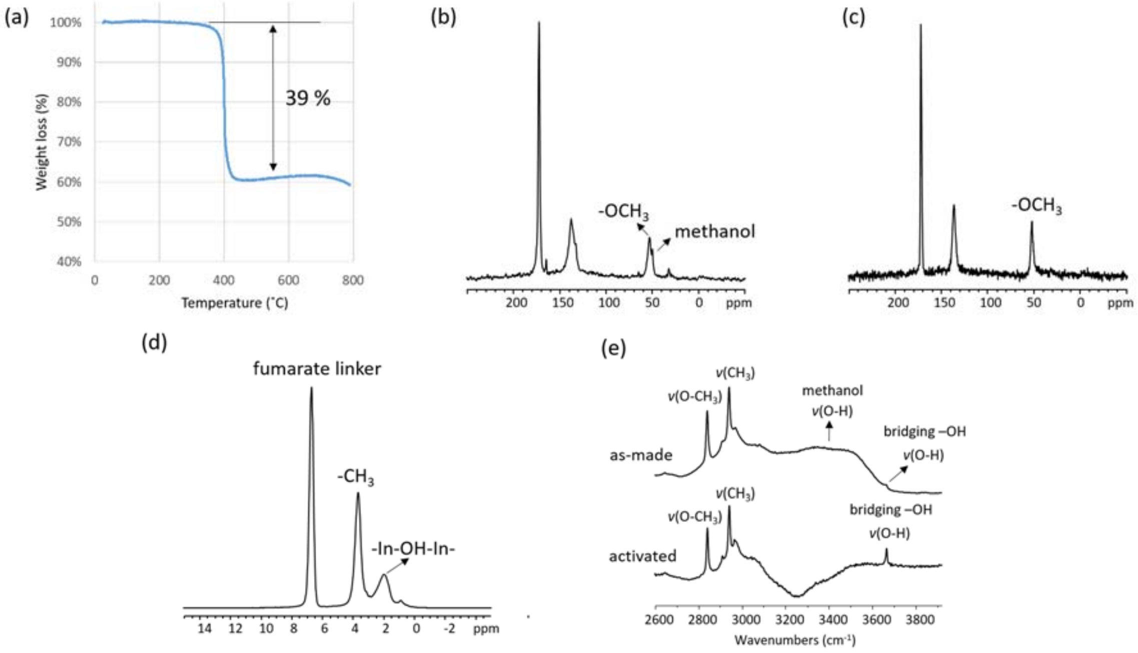

Figure 5-8. The investigation of hydrophobic In-fumarate-M. TGA plot of activated In-fumarate-M followed by exposed in air (20 % r.h.) for 7 days has been illustrated in (a). The ^{13}C MAS spectra of as-made and activated In-fumarate-M are shown in (b) and (c), respectively. The ^{1}H MAS spectrum of activated In-fumarate-M is illustrated in (d). The ^{13}C MAS spectrum is acquired at magnetic field of 9.4 T with a spinning frequency of 14 kHz, while the ^{1}H MAS spectrum is acquired at magnetic field of 21.1 T with a spinning frequency of 31.25 kHz for better resolution. The IR spectrum of as-made and activated In-fumarate-M is depicted in (e).

In order to locate the methyl group, ^{115}In SSNMR experiments, ^{1}H MAS SSNMR and IR experiments have been coordinated. ^{115}In SSNMR experiments were first employed to study the changing of the short-range structure around the In centres. The ^{115}In SSNMR powder pattern of In-fumarate-M activated and exposed in air for 7 days presents a similar lineshape as activated In-fumarate-E (Figure 5-A8) with C_Q and η_Q value slightly decreased to 186(3) MHz and 0.19 (3) (Table 5-A2), respectively. The similar NMR tensor parameters indicate the In metal centres within In-fumarate-M and In-fumarate-E have almost identical local environment, which suggests that the $-CH_3$ group does not interact with the metal centre directly. Based on the ^{1}H MAS SSNMR spectrum acquired at 21.1 T with a spinning speed of 31.25 kHz (Figure 5-8(d)), the ^{1}H resonance on the methyl group has been observed at 3.6 ppm, however, the ^{1}H resonance on the hydroxyl group of methanol cannot be detected. The ^{13}C and ^{1}H MAS SSNMR results suggest that since methanol molecules are removed from the In-fumarate-M channels, the $-OCH_3$ group may incorporate on the framework. IR spectroscopy can provide additional structural details in this case. First, the IR spectrum indicates the absence of methanol in activated In-fumarate-M because the broad O-H stretching adsorption of hydroxyl group on methanol around 3200 to 3600 cm^{-1} is absent (Figure 5-8(e) and Figure 5-A9(e)). Interestingtly, a O-CH_3 stretching adsorption at a wavenumber 2841 cm^{-1} (Figure 5-8(e)) is visible and attributed to an alkoxid ($-OCH_3$) group.[58] Therefore, we suggest that the $-OCH_3$ group may replace –OH group and bridge the InO_6 SBUs. Our hypothesis also has been supported by the intensity of O-H stretching in IR spectra, where the O-H stretching band of bridging –OH in In-fumarate-M at 3666 cm^{-1} has a much lower intensity than that of In-fumarate-E (Figure 5-A9 (d) and (e)). The lower intensity suggests that part of the bridging –OH groups have been replaced by bridging $-OCH_3$ groups. Further TGA studies (Figure 5-A10) on In-fumarate-M demonstrates the water adsorption happened at high humidity (e.g. 80 %). The presence of the bridging $-OCH_3$ in the framework successfully enhanced the hydrophobicity of In-fumarate.

Previous studies on its similar MOF MIL-53 also demonstrated the framework hydrophobicity can be enhanced by replacing the bridging hydroxyl group to oxygen or fluorine.[59-61] However, to the best of our knowledge, this is the first time a hydrophobic channel in MIL-53 like MOFs has been realized by incorporating bridging –OCH_3 groups into the framework. This is the first reported hydrophobic fumarate MOF. Our work provides another possible route to enhance the porous hydrophobicity.

5.3.3 Porosity and gas adsorption of fumarate MOFs

BET surface area measurements. The BET surface areas of Ga-fumarate, In-fumarate-E, and In-fumarate-M were determined by measuring the N_2 adsorption isotherm at 77 K (Figure 5-9(a)). The Ga-fumarate sample synthesized at a temperature of 80 °C exhibited the highest BET surface area of all synthesis temperatures at 851 m^2/g. Other Ga-fumarate synthesis temperatures only generated MOF products with lower BET surface areas (Table 5-A3). The 851 m^2/g BET surface area of Ga-fumarate is lower than the reported BET surface area of Al-fumarate (1080 m^2/g).[17]. The highest BET surface area of In-fumarate-E is 708 m^2/g, which was observed in the sample synthesized at 40 °C (Table 5-A4), while, the highest BET surface area of In-fumarate-M is 599 m^2/g. The reduced In-fumarate-M BET surface area is likely due to the replacement of bridging -OH groups to bridging -OCH_3 groups.

CO_2 adsorption isotherm measurements. The CO_2 adsorption ability of Ga-fumarate, In-fumarate-E, and In-fumarate-M were determined by measuring the CO_2 adsorption isotherm at 273 K and comparing it to that of Al-fumarate (Figure 5-9(b)). At a pressure of 1 bar, Al-fumarate can adsorb 108 cm^3/g STP of CO_2, while Ga-fumarate can adsorb ca. 20 % less (88 cm^3/g STP). The In-fumarate-E and In-fumarate-M have even lower CO_2 capacities, which are 81 cm^3/g STP and 62 cm^3/g STP, respectively. The lower CO_2 adsorption capacity in Ga-fumarate and In-fumarate are likely related to their lower BET surface areas versus Al-fumarate, and may also be indicative of a relatively weaker CO_2 binding strength in Ga- and In-fumarate MOFs. The lowest CO_2 capacity within In-fumarate-M should be related to the presence of bridging –OCH_3 groups, which replaced the promising CO_2 adsorption sites: bridging –OH groups. To further examine the relative adsorption strength, adsorption sites and obtain detailed information on CO_2 dynamic motion in CO_2-loaded fumarate MOFs, $^{69/71}$Ga, ^{115}In and ^{13}C SSNMR experiments were performed.

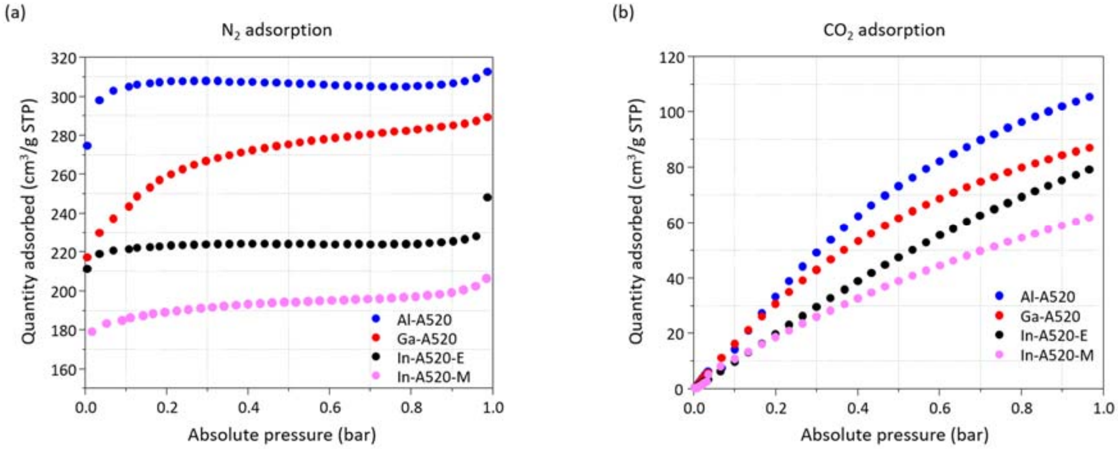

Figure 5-9. The N_2 adsorption isotherms of Al-fumarate, Ga-fumarate, In-fumarate-E, and In-fumarate-M as measured at 77 K, are shown in (a). In (b), the CO_2 adsorption isotherms of Al-fumarate, Ga-fumarate, In-fumarate-E, and In-fumarate-M at 273 K are illustrated.

Static ^{1}H-^{13}C CP SSNMR experiments of CO_2 in deuterated samples. Our prior work on MOFs in the MIL-53 series has proven that static ^{1}H-^{13}C CP SSNMR experiments at low temperatures, in conjunction with deuteration techniques, can be used to confirm if a MOF hydroxyl group serves as a CO_2 adsorption site.[27] In short, if a ^{13}C resonance is observed in ^{1}H-^{13}C CP experiments on a non-deuterated MOF, but the same resonance is not visible in the deuterated MOF, the functional group that has been deuterated must be located at or near the CO_2 adsorption site. This is because ^{1}H-^{13}C CP SSNMR experiments will only detect those ^{13}C nuclei that are proximate to ^{1}H atoms, not those proximate only to ^{2}H atoms. In MIL-53, the bridging hydroxyl groups have been confirmed to be the CO_2

adsorption sites.[42-43] Both fumarate MOFs in this study possess a similar structure to MIL-53, where the MO_6 (M = Al, Ga, In) SBUs are connected through bridging hydroxyl groups; this leads to the preliminary hypothesis that the CO_2 adsorption sites in Al-, Ga-, and In-fumarate are also located near the bridging hydroxyl groups. In order to explore this hypothesis, static ^{1}H-^{13}C CP SSNMR experiments were performed on the empty frameworks, CO_2 loaded but non-deuterated fumarate MOFs featuring –O^{1}H bridging hydroxyl groups, as well as CO_2 loaded and deuterated fumarate MOFs with –O^{2}H groups.

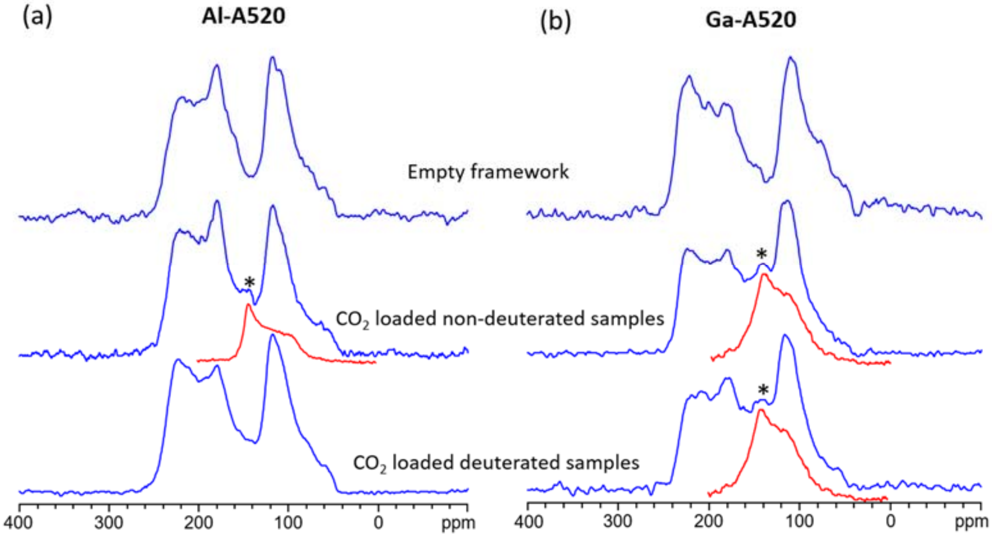

Figure 5-10. Static ^{1}H-^{13}C CP SSNMR spectra acquired using a CP contact time of 10 ms. In the deuterated fumarate samples, the hydrogen atoms of the bridging hydroxyl groups have been replaced by deuterium atoms, which prohibit ^{1}H-^{13}C cross polarization from the bridging hydroxyl hydrogens to adsorbed CO_2 molecules. Therefore, if CO_2 molecules indeed interact with bridging hydroxyl groups, the CO_2 resonance will not be observed in ^{1}H-^{13}C CP experiments of deuterated samples. In this manner, the CO_2 adsorption site location can be investigated. The asterisk sign (*) denotes the resonance corresponding to adsorbed CO_2. Spectra with red colour are the static ^{13}C DEPTH-echo SSNMR spectra of adsorbed $^{13}CO_2$ at the same temperature.

The static ^1H-^{13}C CP SSNMR spectra of Al-fumarate samples acquired at 133 K with a contact time (CT) of 10 ms are shown in Figure 5-10(a). The broad, overlapping ^{13}C powder patterns observed in the empty framework arise solely from the carbon atoms of the fumarate linkers. The spectrum of CO_2 loaded non-deuterated Al-fumarate is similar to that of empty Al-fumarate, however, a small additional resonance at ca. 145 ppm (denoted * in Figure 5-10(a)) is now apparent. This resonance is located at approximately the same frequency as the overlapping δ_{11} and δ_{22} components of the ^{13}C CS tensor from adsorbed CO_2 detected *via* static ^{13}C DEPTH-echo SSNMR spectra at the same temperature (ca. 144 ppm at 133 K, see spectrum with red colour in Figure 5-10(a)), and indeed represents adsorbed CO_2. The assignment of this resonance is unambiguous, since it is not apparent in the ^1H-^{13}C CP SSNMR spectrum of the CO_2 loaded deuterated Al-fumarate sample, which features a $–O^2H$ bridging hydroxyl group rather than a $–O^1H$ one. The static ^1H-^{13}C CP spectra indicate that the CO_2 adsorption site in Al-fumarate is on or near the bridging hydroxyl group.

The case of Ga-fumarate is quite different than that of Al-fumarate. ^1H-^{13}C CP SSNMR experiments on both CO_2 loaded non-deuterated and deuterated Ga-fumarate samples give rise to very similar spectra (Figure 5-10(b)). There is a CO_2 resonance at ca. 143 ppm (denoted * and red spectra in Figure 5-10(b)) that is not present in the empty framework, but is present in CP spectra of both the non-deuterated and deuterated fumarate MOF samples, indicating that ^1H-^{13}C CP is efficient and that CO_2 must be located near one or more ^1H atoms. Since the hydrogen atoms on the bridging hydroxyl groups have been replaced by deuterium atoms in this sample of Ga-fumarate, CO_2 must be interacting or proximate to hydrogen atoms on the organic linkers, which are not replaced by the deuteration process. Hence, despite the structural similarities between Al- and Ga-fumarate MOFs, the adsorption site is located near the bridging hydroxyl groups in Al-fumarate, while CO_2 adsorption must occur relatively closer to the fumarate linkers in Ga-fumarate.

Unfortunately, the CO_2 resonance within CO_2-loaded non-deuterated In-fumarate-E and In-fumarate-M CP spectra (Figure 5-A11) cannot be observed due to the weaker CO_2 binding strength, therefore, the CO_2 adsorption sites within In-fumarate cannot be studied by ^{1}H-^{13}C CP SSNMR experiments.

^{13}C SSNMR targeting adsorbed $^{13}CO_2$. Static ^{13}C SSNMR experiments have been used to investigate CO_2 dynamics and relative binding strengths within MOFs,[27, 62-66] and a recent study has shown that static ^{17}O SSNMR spectra can also yield valuable motional information.[67] Understanding the dynamics of CO_2 within MOFs is a key fundamental step toward establishing links between CO_2 motion, adsorption affinity, and adsorption capacity; this knowledge can be exploited for the future rational design of MOFs with enhanced or "tunable" CO_2 adsorption abilities. In this study, static ^{13}C SSNMR experiments were employed to examine CO_2 dynamics and binding strength within fumarate MOFs using a loading level of 0.2 CO_2 / metal centre in both MOFs.

The static VT ^{13}C SSNMR spectra of CO_2-loaded Al-fumarate were acquired at temperatures ranging from 133 K to 373 K (Figure 5-11(a)), and those of CO_2-loaded Ga-fumarate, In-fumarate-E, and In-fumarate-M were acquired at temperatures between 133 K to 293 K (Figure 5-11(b), (c), (d)); the extracted CS parameters are summarized in Table 5-3. At 293 K, the static ^{13}C SSNMR spectra of $^{13}CO_2$ adsorbed in Al-fumarate features a powder pattern corresponding to a span (Ω) of 27(1) ppm and a skew (κ) value equal to +1. The observation of an anisotropic ^{13}C CS powder pattern, rather than a sharp isotropic resonance, confirms that CO_2 guests are participating in well-defined motions within Al-fumarate instead of rapid isotropic tumbling through the MOF. The apparent ^{13}C Ω value increases from 26(1) ppm at 373 K to 62(1) ppm at 133 K, while the observed κ value remains +1 throughout. The continuous evolution of the ^{13}C powder pattern with temperature (*i.e.*, changes in Ω) is a clear indication that the experimental temperature influences the CO_2 motional angles, which in turn affect the ^{13}C SSNMR spectral appearance and the observed or apparent NMR parameters. At temperatures $\geq$ 313 K, an additional sharp resonance around 125 ppm originates from gaseous, unbound CO_2.[68]

The ^{13}C SSNMR spectra of $^{13}CO_2$ adsorbed in Ga-fumarate at 293 K consist of a single sharp isotropic resonance located at ca. 125 ppm (Figure 5-11(b)) with a full width at half height (FWHH) of 443 Hz. The narrow, featureless resonance indicates that CO_2 guests undergo very fast isotropic tumbling inside Ga-fumarate at 293 K, which removes the anisotropy (*i.e.*, spectral broadening effects) of the CS tensor. In contrast to the relatively broad ^{13}C powder pattern at 293 K in Al-fumarate, the rapid isotropic motion of CO_2 in Ga-fumarate indicates that CO_2 is bound relatively weaker to the Ga analogue, which is in good agreement with the measured CO_2 adsorption isotherms depicted in Figure 5-11(b). As the temperature decreases from 293 to 193 K, the only discernable difference in the ^{13}C SSNMR spectra of CO_2 in Ga-fumarate is a continual broadening of the featureless resonance from a FWHH of 443 Hz to 1384 Hz; the CO_2 does not undergo restricted motion, even at these relatively low temperatures. At 173 K, the observed ^{13}C resonance of CO_2 adsorbed in Ga-fumarate resembles a typical powder pattern, indicating that CO_2 guests now undergo restricted motions, and the spectrum was simulated to extract a Ω value of 40(1) ppm and a κ of 0.50(2) (Table 5-3). The powder pattern continues to broaden and change in appearance as the temperature decreases to 133K, where simulations show Ω is 68(1) ppm and κ is 0.88(2) (Table 5-3). Continued increases in Ω and κ as temperature decreases is a clear sign that adsorbed CO_2 molecules within Ga-fumarate are less dynamic at lower temperatures (*i.e.*, move through smaller motional angles).

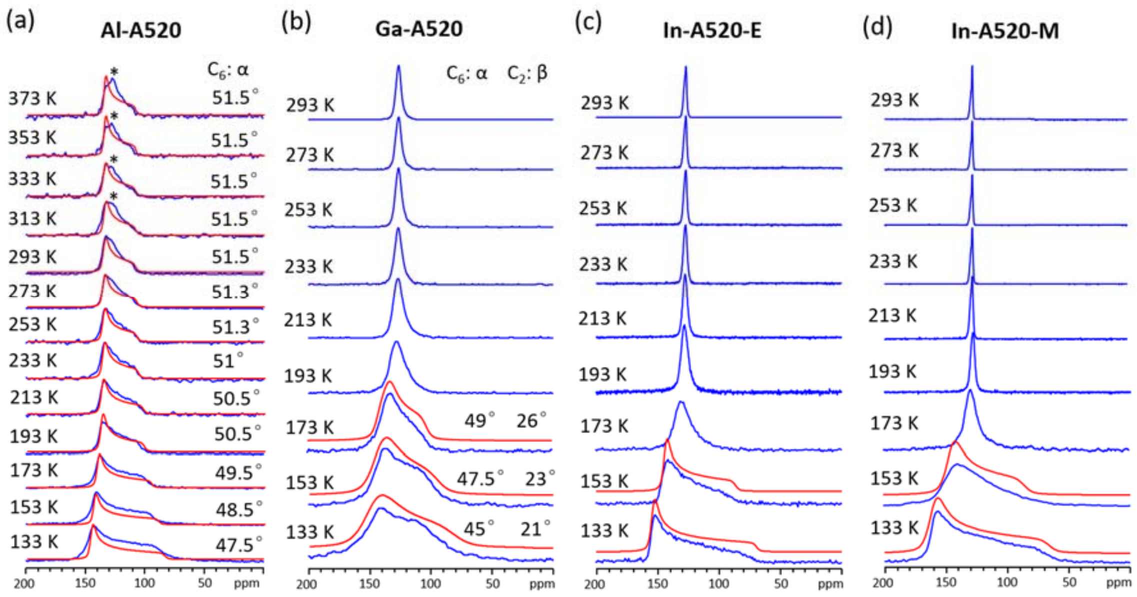

Figure 5-11. The experimental (blue) and simulated (red) static VT ^{13}C SSNMR spectra of CO_2 adsorbed within Al-fumarate, Ga-fumarate, In-fumarate-E and In-fumarate-M are shown in (a), (b), (c), and (d), respectivelt. The simulated powder patterns were generated using the EXPRESS software[40] and a fast rate of CO_2 motion (10^9 Hz). The C_6 motion (six-fold rotation) describes a localized rotational "wobbling" motion of CO_2 upon the adsorption site through the wobbling angle α. The C_2 motion (two-fold rotation) describes the non-localized hopping or jumping of CO_2 through a hopping angle of β between two adsorption sites. The asterisk (*) in (a) at high temperatures marks the sharp resonance at ca. 125 ppm that corresponds to gaseous, unbound CO_2. The uncertainty in α and β is estimated to be ± 0.2°.

Table 5-3. The observed, or apparent, ^{13}C CS parameters of CO_2 adsorbed within Al-fumarate, Ga-fumarate, In-fumarate-E and In-fumarate-M as obtained from analytical simulations of static ^{13}C DEPTH-echo VT SSNMR spectra. The ^{13}C powder pattern of Ga-fumarate with a defined shape can be observed from 173 K to 133 K, while the ^{13}C powder pattern of In-fumarate-E and In-fumarate-M with a defined shape can be observed from 153 K to 133 K.

T	Al-fumarate			Ga-fumarate			In-fumarate-E			In-fumarate-M		
	δ_{iso} (ppm)	Ω (ppm)	κ	δ_{iso} (ppm)	Ω (ppm)	κ	δ_{iso} (ppm)	Ω (ppm)	κ	δ_{iso} (ppm)	Ω (ppm)	κ
373 K	125(1)	26(1)	1.00(2)									
353 K	125(1)	26(1)	1.00(2)									
333 K	125(1)	26(1)	1.00(2)									
313 K	126(1)	27(1)	1.00(2)									
293 K	126(1)	27(1)	1.00(2)									
273 K	126(1)	28(1)	1.00(2)									
253 K	126(1)	28(1)	1.00(2)									
233 K	126(1)	30(1)	1.00(2)									
213 K	125(1)	35(1)	1.00(2)									
193 K	125(1)	36(1)	1.00(2)									
173 K	125(1)	45(1)	1.00(2)	126(1)	40(1)	0.50(2)						
153 K	125(1)	54(1)	1.00(2)	126(1)	56(1)	0.76(2)	126(2)	58(1)	1.00(2)	125(2)	60(1)	1.00(2)
133 K	125(1)	62(1)	1.00(2)	126(1)	68(1)	0.88(2)	127(2)	85(2)	1.00(2)	128(2)	95(2)	1.00(2)

The observed ^{13}C SSNMR spectra of $^{13}CO_2$ adsorbed in In-fumarate-E and In-fumarate-M also show sharp isotropic resonances located at ca. 125 ppm (Figure 5-11(c) and (d)) at 293 K, with narrower FWHH of 283 Hz and 171 Hz, respectively, which indicate CO_2 undergoes fast isotropic tumbling inside In-fumarate-E and In-fumarate-M. The FWHH indicates the CO_2 binding strength within fumarate MOFs follows the order: Al-fumarate > Ga-fumarate > In-fumarate-E > In-fumarate-M, which has a good agreement with the CO_2 adsorption isotherms depicted in Figure 5-9(b). The ^{13}C SSNMR powder patterns of CO_2 within In-fumarate-E and In-fumarate-M start to show up at 153 K, indicating that CO_2 is participating in well-defined motions. The apparent ^{13}C Ω value increases from 58(1) ppm at 153 K to 85(2) ppm at 133 K in In-fumarate-E, while the ^{13}C Ω value increases from 60(1) ppm at 153 K to 95(2) ppm at 133 K in In-fumarate-M (Table 5-3). The observed κ value remains +1 in both In-fumarate-E and In-fumarate-M samples. In order to understand the CO_2 motions within fumarate MOFs, motional simulations have been investigated.

CO_2 dynamic studies. With knowledge of the NMR parameters for static CO_2,[68] the powder patterns of adsorbed $^{13}CO_2$ in Al- and Ga-fumarate MOFs were simulated to obtain accurate information regarding CO_2 motion (Figure 5-11).[39] Simulations indicate that CO_2 molecules within Al-fumarate participate in a localized rotation or "wobbling" through some angle α upon the bridging hydroxyl adsorption site, which was modeled by a six-fold (C_6) rotation at a rate of 10^9 Hz (*i.e.*, in the NMR fast motion regime); a schematic of this motional model is depicted in Figure 5-12(a) and (b). The wobbling angle α decreases from 51.5 ° to 47.5 ° as the temperature decrease from 373 K to 133 K (Figure 5-11(a)), which indicates that the adsorbed CO_2 guests are less dynamic and sample a relatively smaller volume of space at lower temperatures when less thermal energy is available to compete with the adsorptive interaction.

The behavior of CO_2 adsorbed in Al-fumarate contrasts with that of CO_2 adsorbed within Al-MIL-53, which exhibits rotational wobbling but also participates in non-localized two site jumping or "hopping" between symmetry-equivalent adsorption sites located on bridging hydroxyl groups on opposite sides of the rhombic-shaped MOF channels.[27] The lack of CO_2 hopping across the channels of Al-fumarate between two bridging hydroxyl adsorption sites is likely due to the relatively larger pore size of Al-fumarate versus Al-MIL-53 at the same CO_2 loading level. Al-MIL-53 exists in a narrow pore form with dimensions of *ca*. 7 x 19 Å, which closes the distance between CO_2 and bridging hydroxyl groups and makes twofold hopping possible across the relatively shorter space. In contrast, Al-fumarate has a rigid larger pore structure with dimensions of *ca*. 12 x 12 Å, and the relatively longer distance between bridging hydroxyl adsorption sites prevents CO_2 hopping across the channel between these adsorption sites.

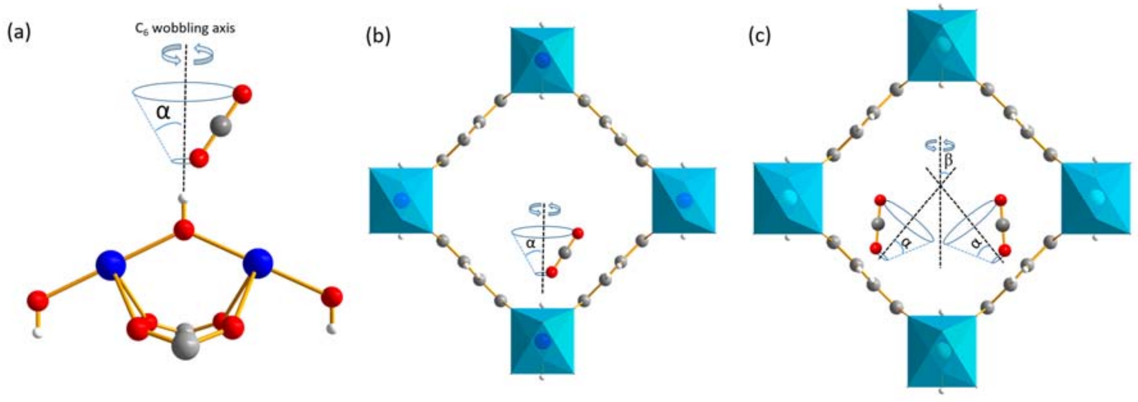

Figure 5-12. In (a), the localized C_6 rotation, or wobbling of CO_2 through a wobbling angle α about the CO_2 adsorption site (*i.e.,* the bridging hydroxyl group between SBUs) within Al-fumarate is shown. A schematic of how a single CO_2 guest wobbles upon adsorption sites in the channels of Al-fumarate is shown in (b). The localized wobbling (C_6 rotation through the angle α) and non-localized two site hopping (C_2 jumping through the angle β) of CO_2 within Ga-fumarate is shown in (c). The colors red, grey, white, dark blue and light blue correspond to oxygen, carbon, hydrogen, aluminum, and the gallium, respectively.

The ^{13}C SSNMR spectrum of CO_2 adsorbed within Ga-fumarate only features a well-defined powder pattern at low temperatures (Figure 5-11(b)), and reliable motional information could still be obtained from these three spectra. Simulations reveal that, in addition to a localized wobbling through some angle α modeled by a C_6 rotation, adsorbed CO_2 guests also undergo a non-localized two-fold (C_2) hopping motion through some angle β between two adsorption sites. As the temperature decreases from 173 K to 133 K, the

CO_2 wobbling angle α falls from 49 ° to 45 °, along with the twofold hopping angle β reduces from 26 ° to 21 °, which strongly hint that CO_2 molecules are significantly less dynamic at lower temperatures, although both types of dynamics remain in the fast motion regime (rate $\geq 10^7$ Hz). Recalling that ^1H-^{13}C CP SSNMR experiments suggested CO_2 adsorption sites in Ga-fumarate are the hydrogen atoms of the organic fumarate linkers (*vide supra*), it follows that the twofold hopping of CO_2 must be between different H atoms of the linkers. We suggest that CO_2 molecules within Ga-fumarate may hop between two spatially proximate H atoms; many of these H atoms are only separated by distances ranging from ca. 5 Å to ca. 7 Å. Our proposed motional model for CO_2 within Ga-fumarate is pictured in Figure 5-12(c).

Powder patterns of CO_2 adsorbed within In-fumarate-E and In-fumarate-M feature similar lineshpes as those of Al-fumarate at temperatures of 153 and 133 K, with larger span values and same skew values. However, powder patterns only can be observed at two temperatures, therefore, accurate motional information cannot be investigated in In-fumarate MOFs.

5.4 Conclusions

The gallium and indium analogues to Basolite A520 (Al-fumarate), Ga-fumarate and In-fumarate have been successfully synthesized using an experimentally-optimized, solvothermal method. A variety of characterization techniques, including Synchrotron pXRD experiments, subsequent Rietveld refinements, IR spectroscopy, ^1H MAS SSNMR, and ultra-wideline SSNMR were used to elucidate the crystal structures of Ga-fumarate-H_2O with a high degree of accuracy. The comprehensive investigations have revealed that Ga- and In-fumarate are indeed porous materials and structural analog of Al-fumarate. The relatively high BET surface area and large, rigid pores of Ga- and In-fumarate point towards potential applications in fields such as gas storage, gas separation, and drug delivery. The hydrophobic In-fumarate-M has been successfully investigated by introducing bridging –OCH_3 groups into the In-fumarate, which provided a novel method to generated hydrophobic MOFs.

CO_2 adsorption isotherms have been measured for these materials and reveal that both fumarate MOFs are well-suited for potential applications in CO_2 adsorption. The affinity for CO_2 follows the trend: Al-fumarate > Ga-fumarate > In-fumarate-E > In-fumarate-M. Static ^{1}H-^{13}C CP SSNMR confirm the CO_2 adsorption site in Al-fumarate is indeed the bridging hydroxyl group connecting the AlO_6 SBUs, while the adsorption sites in Ga-fumarate appear to be the hydrogen atoms of the fumarate linkers lining the MOF channels. ^{13}C SSNMR experiments yield information on CO_2 adsorption and the complex CO_2 dynamics present in Al- and Ga-fumarate MOFs; in both MOFs, CO_2 locally rotates about the adsorption site, while in Ga-fumarate, CO_2 additionally hops between adjacent symmetry-equivalent adsorption sites. In both Al- and Ga-fumarate MOFs, the wobbling angle decreases with temperature, and in Ga-fumarate, the hopping angle also falls as temperature drops.

These fumarate MOFs are fascinating materials with very promising applications. More detailed studies in the future regarding gas adsorption, gas separation, and catalysis will surely reveal more intriguing features and properties in these unique MOFs. Future work on pXRD refinement of In-fumarate structures and molecular dynamic simulations of CO_2 motion and binding within fumarate MOFs are in progress.

5.5 References

1. Zhou, H.-C.; Kitagawa, S., *Chem. Soc. Rev.* **2014,** *43* (16), 5415-5418.

2. Zhou, H.-C.; Long, J. R.; Yaghi, O. M., *Chem. Rev.* **2012,** *112* (2), 673-674.

3. Mason, J. A.; Veenstra, M.; Long, J. R., *Chem. Sci.* **2014,** *5* (1), 32-51.

4. Li, B.; Wen, H.-M.; Zhou, W.; Chen, B., *J. Phys. Chem. Lett.* **2014,** *5* (20), 3468-3479.

5. Sumida, K.; Rogow, D. L.; Mason, J. A.; McDonald, T. M.; Bloch, E. D.; Herm, Z. R.; Bae, T.-H.; Long, J. R., *Chem. Rev.* **2012,** *112* (2), 724-781.

6. Qiu, S.; Xue, M.; Zhu, G., *Chem. Soc. Rev.* **2014,** *43* (16), 6116-6140.

7. Li, J.-R.; Kuppler, R. J.; Zhou, H.-C., *Chem. Soc. Rev.* **2009,** *38* (5), 1477-1504.

8. Chughtai, A. H.; Ahmad, N.; Younus, H. A.; Laypkov, A.; Verpoort, F., *Chem. Soc. Rev.* **2015,** *44* (19), 6804-6849.

9. Liu, J.; Chen, L.; Cui, H.; Zhang, J.; Zhang, L.; Su, C.-Y., *Chem. Soc. Rev.* **2014,** *43* (16), 6011-6061.

10. Horcajada, P.; Chalati, T.; Serre, C.; Gillet, B.; Sebrie, C.; Baati, T.; Eubank, J. F.; Heurtaux, D.; Clayette, P.; Kreuz, C.; Chang, J.-S.; Hwang, Y. K.; Marsaud, V.; Bories, P.-N.; Cynober, L.; Gil, S.; Ferey, G.; Couvreur, P.; Gref, R., *Nat. Mater.* **2010,** *9* (2), 172-178.

11. Vallet-Regí, M.; Balas, F.; Arcos, D., *Angew. Chem. Int. Ed.* **2007,** *46* (40), 7548-7558.

12. Furukawa, H.; Cordova, K. E.; O'Keeffe, M.; Yaghi, O. M., *Science* **2013,** *341* (6149), 974.

13. James, S. L., *Chem. Soc. Rev.* **2003,** *32* (5), 276-288.

14. Müller, U.; Luinstra G.; Yaghi O. M., *US Pat.* **2004,** *6617467*.

15. Gaab, M.; Trukhan, N.; Maurer, S.; Gummaraju, R.; Müller, U., *Microporous Mesoporous Mater.* **2012,** *157*, 131-136.

16. Kiener C.; Müller, U.; Maurer S., *Germany Pat.* **2007,** *WO2007/118841 A2*.

17. Alvarez, E.; Guillou, N.; Martineau, C.; Bueken, B.; Van de Voorde, B.; Le Guillouzer, C.; Fabry, P.; Nouar, F.; Taulelle, F.; de Vos, D.; Chang, J.-S.; Cho, K. H.; Ramsahye, N.; Devic, T.; Daturi, M.; Maurin, G.; Serre, C., *Angew. Chem. Int. Ed.* **2015,** *54* (12), 3664-3668.

18. Loiseau, T.; Serre, C.; Huguenard, C.; Fink, G.; Taulelle, F.; Henry, M.; Bataille, T.; Férey, G., *Chem. -Eur. J.* **2004,** *10* (6), 1373-1382.

19. Serre, C.; Millange, F.; Thouvenot, C.; Noguès, M.; Marsolier, G.; Louër, D.; Férey, G., *J. Am. Chem. Soc.* **2002,** *124* (45), 13519-13526.

20. Kiener C., Müller, U., Schubert, M., *US Pat.* **2009,** *US 12/297,666*.

21. Karmakar, S.; Dechnik, J.; Janiak, C.; De, S., *J. Hazard. Mater.* **2016,** *303*, 10-20.

22. Jeremias, F.; Frohlich, D.; Janiak, C.; Henninger, S. K., *RSC Adv.* **2014,** *4* (46), 24073-24082.

23. Yot, P. G.; Vanduyfhuys, L.; Alvarez, E.; Rodriguez, J.; Itie, J.-P.; Fabry, P.; Guillou, N.; Devic, T.; Beurroies, I.; Llewellyn, P. L.; Van Speybroeck, V.; Serre, C.; Maurin, G., *Chem. Sci.* **2016,** *7* (1), 446-450.

24. Ruano, D.; Díaz-García, M.; Alfayate, A.; Sánchez-Sánchez, M., *ChemCatChem* **2015,** *7* (4), 674-681.

25. Ravon, U.; Chaplais, G.; Chizallet, C.; Seyyedi, B.; Bonino, F.; Bordiga, S.; Bats, N.; Farrusseng, D., *ChemCatChem* **2010,** *2* (10), 1235-1238.

26. Ramaswamy, P.; Wieme, J.; Alvarez, E.; Vanduyfhuys, L.; Itie, J.-P.; Fabry, P.; Van Speybroeck, V.; Serre, C.; Yot, P. G.; Maurin, G., *J. Mater. Chem. A* **2017,** *5* (22), 11047-11054.

27. Zhang, Y.; Lucier, B. E. G.; Huang, Y., *Phys. Chem. Chem. Phys.* **2016,** *18*, 8327-8341.

28. Fulmer, G. R.; Miller, A. J. M.; Sherden, N. H.; Gottlieb, H. E.; Nudelman, A.; Stoltz, B. M.; Bercaw, J. E.; Goldberg, K. I., *Organometallics* **2010,** *29* (9), 2176-2179.

29. Harris, R. K.; Becker, E. D.; de Menezes, S. M. C.; Goodfellow, R.; Granger, P., *Solid State Nucl. Magn. Reson.* **2002,** *22* (4), 458-483.

30. Massiot, D.; Farnan, I.; Gautier, N.; Trumeau, D.; Florian, P.; Grandinetti, P. J., *J. Chim. Phys. Phys.-Chim. Biol.* **1995,** *92* (10), 1847-1850.

31. Bonhomme, C.; Gervais, C.; Babonneau, F.; Coelho, C.; Pourpoint, F.; Azaïs, T.; Ashbrook, S. E.; Griffin, J. M.; Yates, J. R.; Mauri, F.; Pickard, C. J., *Chem. Rev.* **2012,** *112* (11), 5733-5779.

32. Clark, S. J.; Segall, M. D.; Pickard, C. J.; Hasnip, P. J.; Probert, M. J.; Refson, K.; Payne, M. C., *Z. Kristall.* **2005,** *220* (5-6), 567-570.

33. Segall, M. D.; Lindan, P. J. D.; Probert, M. J.; Pickard, C. J.; Hasnip, P. J.; Clark, S. J.; Payne, M. C., *J. Phys. Condens. Matter* **2002,** *14* (11), 2717-2744.

34. Yates, J. R.; Pickard, C. J.; Mauri, F., *Phys. Rev. B* **2007,** *76* (2), 024401.

35. Pickard, C. J.; Mauri, F., *Phys. Rev. B* **2001,** *63* (24), 245101.

36. Perdew, J. P.; Burke, K.; Ernzerhof, M., *Phys. Rev. Lett.* **1996,** *77* (18), 3865-3868.

37. Eichele K.; Wasylishen R. E., *WSolids1* University of Tübingen, Tübingen, Germany, **2009**.

38. Perras, F. A.; Widdifield, C. M.; Bryce, D. L., *Solid State Nucl. Magn. Reson.* **2012,** *45–46*, 36-44.

39. Vold, R. L.; Hoatson, G. L., *J. Magn. Reson.* **2009,** *198* (1), 57-72.

40. Volkringer, C.; Loiseau, T.; Guillou, N.; Ferey, G.; Elkaim, E.; Vimont, A., *Dalton Trans.* **2009,** *12*, 2241-2249.

41. Chaplais, G.; Simon-Masseron, A.; Porcher, F.; Lecomte, C.; Bazer-Bachi, D.; Bats, N.; Patarin, J., *Phys. Chem. Chem. Phys.* **2009,** *11* (26), 5241-5245.

42. Stavitski, E.; Pidko, E. A.; Couck, S.; Remy, T.; Hensen, E. J. M.; Weckhuysen, B. M.; Denayer, J.; Gascon, J.; Kapteijn, F., *Langmuir* **2011,** *27* (7), 3970-3976.

43. Ramsahye, N. A.; Maurin, G.; Bourrelly, S.; Llewellyn, P. L.; Serre, C.; Loiseau, T.; Devic, T.; Férey, G., *J. Phys. Chem. C* **2008,** *112* (2), 514-520.

44. Pyykkö, P., *Mol. Phys.* **2008,** *106* (16-18), 1965-1974.

45. Volkringer, C.; Loiseau, T.; Férey, G.; Morais, C. M.; Taulelle, F.; Montouillout, V.; Massiot, D., *Microporous Mesoporous Mater.* **2007,** *105* (1–2), 111-117.

46. Hajjar, R.; Volkringer, C.; Loiseau, T.; Guillou, N.; Marrot, J.; Férey, G.; Margiolaki, I.; Fink, G.; Morais, C.; Taulelle, F., *Chem. Mater.* **2011,** *23* (1), 39-47.

47. Zhang, Y.; Lucier, B. E. G.; Terskikh, V. V.; Zheng, R.; Huang, Y., *Solid State Nucl. Magn. Reson.* **2017,** *84,* 118-131.

48. Johnston, K. E.; O'Keefe, C. A.; Gauvin, R. M.; Trebosc, J.; Delevoye, L.; Amoureux, J. P.; Popoff, N.; Taoufik, M.; Oudatchin, K.; Schurko, R. W., *Chem. -Eur. J.* **2013,** *19* (37), 12396-12414.

49. Lucier, B. E. G.; Reidel, A. R.; Schurko, R. W., *Can. J. Chem.* **2011,** *89* (7), 919-937.

50. Hamaed, H.; Johnston, K. E.; Cooper, B. F. T.; Terskikh, V. V.; Ye, E.; Macdonald, C. L. B.; Arnold, D. C.; Schurko, R. W., *Chem. Sci.* **2014,** *5* (3), 982-995.

51. Lo, A. Y. H.; Jurca, T.; Richeson, D. S.; Bryce, D. L., *J. Phys. Chem. Lett.* **2010,** *1* (20), 3078-3084.

52. Chen, F.; Ma, G.; Bernard, G. M.; Cavell, R. G.; McDonald, R.; Ferguson, M. J.; Wasylishen, R. E., *J. Am. Chem. Soc.* **2010,** *132* (15), 5479-5493.

53. Chen, F.; Ma, G.; Cavell, R. G.; Terskikh, V. V.; Wasylishen, R. E., *Chem. Commun.* **2008,** (45), 5933-5935.

54. He, P.; Lucier, B. E. G.; Terskikh, V. V.; Shi, Q.; Dong, J.; Chu, Y.; Zheng, A.; Sutrisno, A.; Huang, Y., *J. Phys. Chem. C* **2014,** *118* (41), 23728-23744.

55. Huang, Y.; Xu, J.; Gul-E-Noor, F.; He, P., Metal-organic frameworks: NMR studies of quadrupolar nuclei. In *Encyclopedia of Inorganic and Bioinorganic Chemistry*, John Wiley & Sons, Ltd: 2011.

56. Fernandez, C. A.; Nune, S. K.; Annapureddy, H. V.; Dang, L. X.; McGrail, B. P.; Zheng, F.; Polikarpov, E.; King, D. L.; Freeman, C.; Brooks, K. P., *Dalton Trans.* **2015,** *44* (30), 13490-13497.

57. Keskin, S.; van Heest, T. M.; Sholl, D. S., *ChemSusChem* **2010,** *3* (8), 879-891.

58. Coates, J., Interpretation of Infrared Spectra, A Practical Approach. In *Encyclopedia of Analytical Chemistry*, John Wiley & Sons, Ltd: 2006.

59. Boutin, A.; Bousquet, D.; Ortiz, A. U.; Coudert, F.-X.; Fuchs, A. H.; Ballandras, A.; Weber, G.; Bezverkhyy, I.; Bellat, J.-P.; Ortiz, G.; Chaplais, G.; Paillaud, J.-L.; Marichal, C.; Nouali, H.; Patarin, J., *J. Phys. Chem. C* **2013,** *117* (16), 8180-8188.

60. Liu, L.; Wang, X.; Jacobson, A. J., *Dalton Trans.* **2010,** *39* (7), 1722-1725.

61. Barthelet, K.; Marrot, J.; Riou, D.; Férey, G., *Angew. Chem. Int. Ed.* **2002,** *41* (2), 281-284.

62. Peksa, M.; Burrekaew, S.; Schmid, R.; Lang, J.; Stallmach, F., *Microporous Mesoporous Mater.* **2015,** *216*, 75-81.

63. Lin, L.-C.; Kim, J.; Kong, X.; Scott, E.; McDonald, T. M.; Long, J. R.; Reimer, J. A.; Smit, B., *Angew. Chem. Int. Ed.* **2013,** *52* (16), 4410-4413.

64. Gul-E-Noor, F.; Mendt, M.; Michel, D.; Pöppl, A.; Krautscheid, H.; Haase, J.; Bertmer, M., *J. Phys. Chem. C* **2013,** *117* (15), 7703-7712.

65. Kong, X.; Scott, E.; Ding, W.; Mason, J. A.; Long, J. R.; Reimer, J. A., *J. Am. Chem. Soc.* **2012,** *134* (35), 14341-14344.

66. Hoffmann, H.; Debowski, M.; Müller, P.; Paasch, S.; Senkovska, I.; Kaskel, S.; Brunner, E., *Materials* **2012,** *5* (12), 2537.

67. Wang, W. D.; Lucier, B. E. G.; Terskikh, V. V.; Wang, W.; Huang, Y., *J. Phys. Chem. Lett.* **2014,** *5* (19), 3360-3365.

68. Beeler, A. J.; Orendt, A. M.; Grant, D. M.; Cutts, P. W.; Michl, J.; Zilm, K. W.; Downing, J. W.; Facelli, J. C.; Schindler, M. S.; Kutzelnigg, W., *J. Am. Chem. Soc.* **1984,** *106* (25), 7672-7676.

5.6 Appendix

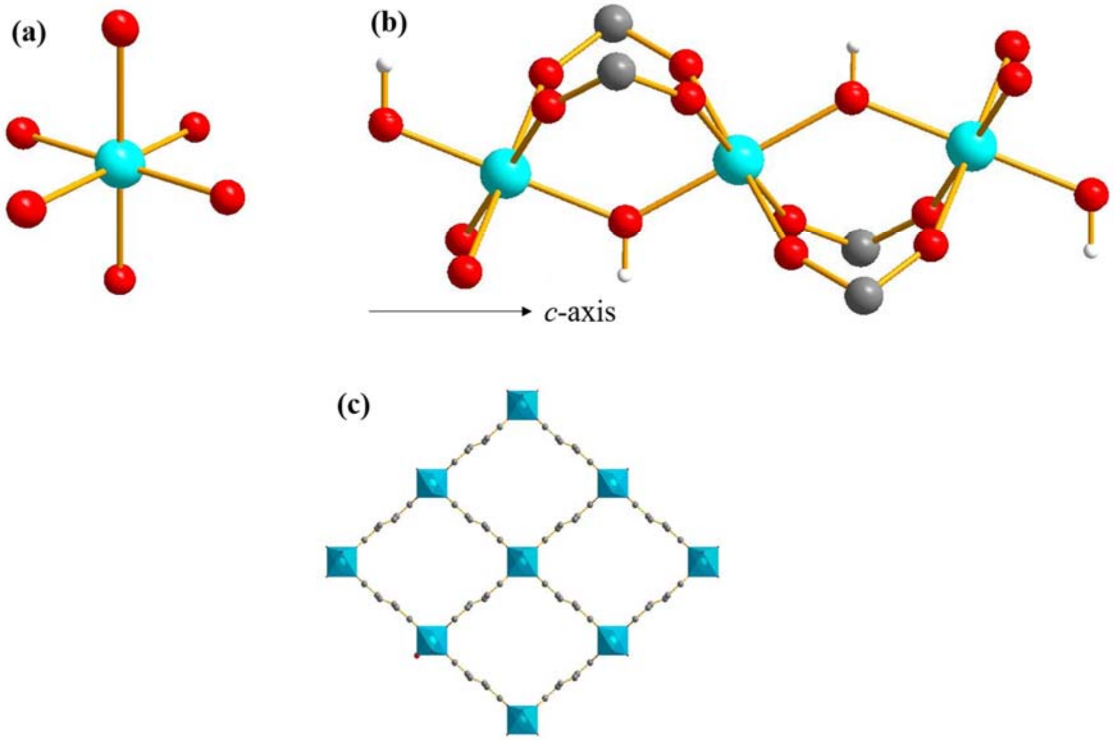

Figure 5-A1. The octahedral $MO_4(OH)_2$ secondary building unit (SBU) of the MIL-53 MOF is shown in (a). The chain formed by the SBUs along the crystallographic *c* axis is shown in (b); these chains are interconnected by benzenedicarboxylate (BDC) linkers to create the one-dimensional rhombic channels, as shown in (c). The colors red, grey, white and blue correspond to oxygen, carbon, hydrogen and the metal centre, respectively

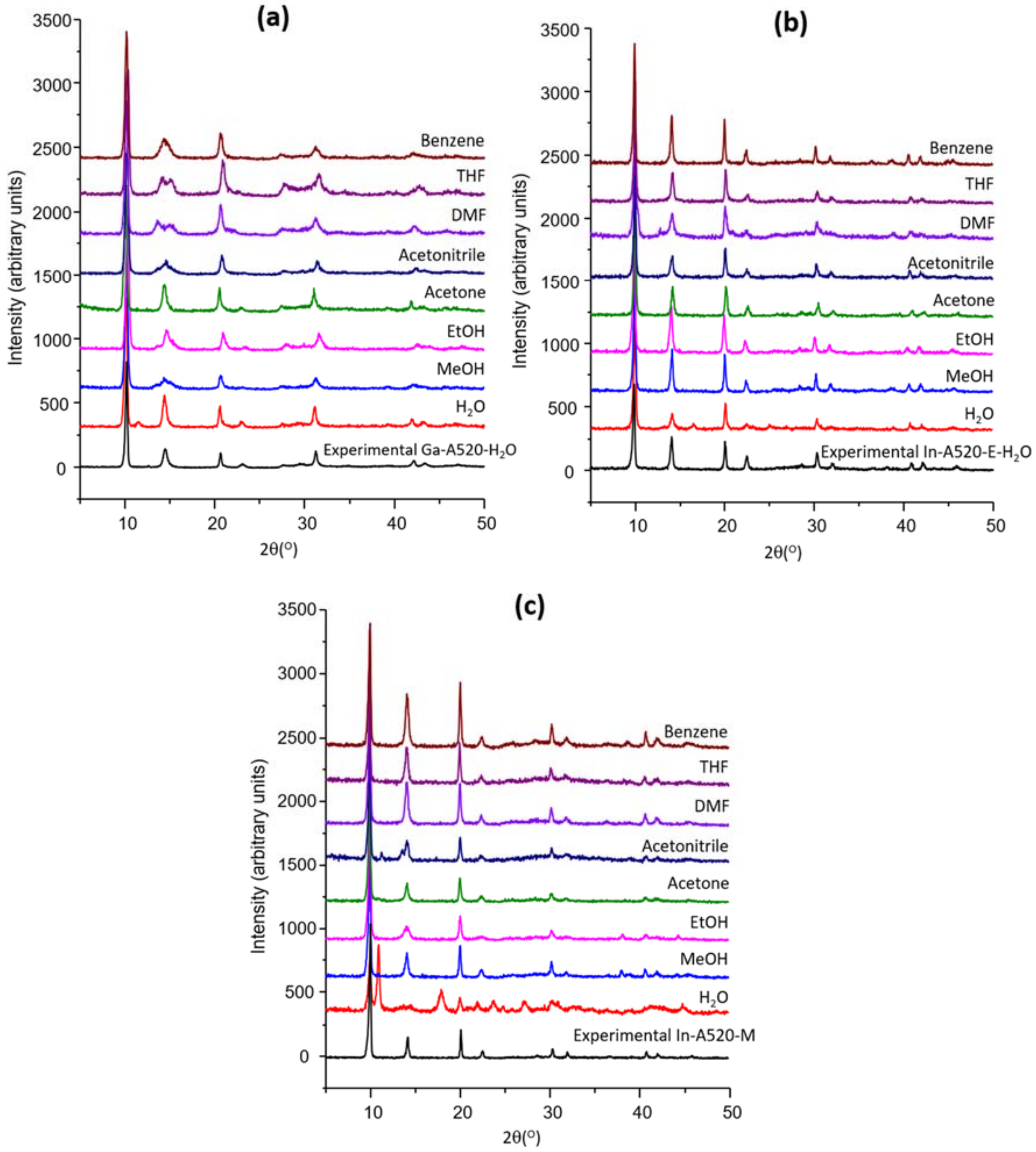

Figure 5-A2. The pXRD patterns of Ga-fumarate, In-fumarate-E, and In-fumarate-M MOF samples obtained after immersion in various solvents for 7 days are illustrated in (a), (b), and (c), respectively. The In-fumarate-M decomposed after H_2O treatment, while the rest of MOFs retain both their structures and their high degree of crystallinity after solvent treatment. Note the x-axis is truncated to exclude very low angles.

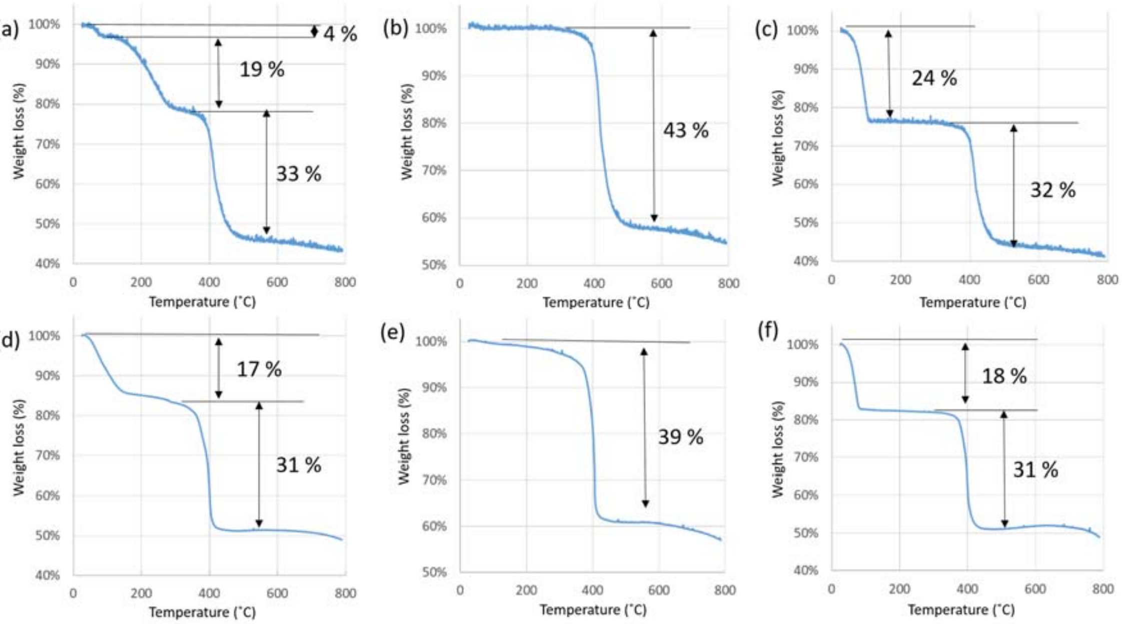

Figure 5-A3. Thermogravimetric analysis (TGA) plots of (a) Ga-fumarate(*as*) synthesized at 80 °C; (b) Ga-fumarate after activation under dynamic vacuum at 150 °C for 8 h; and (c) Ga-fumarate after activation followed by exposure to air (20 % r.h.) for 3 days to adsorb water (*i.e.*, Ga-fumarate-H_2O); (d) In-fumarate-E(*as*) synthesized at 40 °C; (e) In-fumarate-E after activation under dynamic vacuum at 150 °C for 8 h; and (f) In-fumarate-E after activation followed by exposure to air (20 % r.h.) for 3 days to adsorb water (*i.e.*, In-fumarate-E-H_2O).

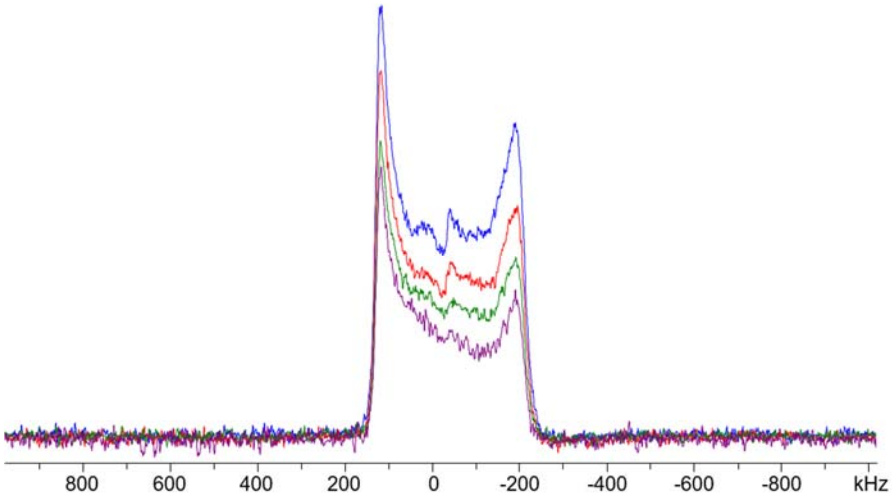

Figure 5-A4. An illustration of ^{71}Ga T_2 relaxation anisotropy in the ^{71}Ga SSNMR spectra of Ga-fumarate-H_2O at 21.1 T. Using a standard solids echo pulse sequence of the form ($\pi/2$-τ_1-$\pi/2$-τ_2-acq), these spectra were acquired using τ_1 values of 10 μs (blue trace), 70 μs (red), 120 μs (green) and 200 μs (purple). Note the pronounced reduced intensity of the low-frequency discontinuity or "horn" when longer τ_1 values are employed.

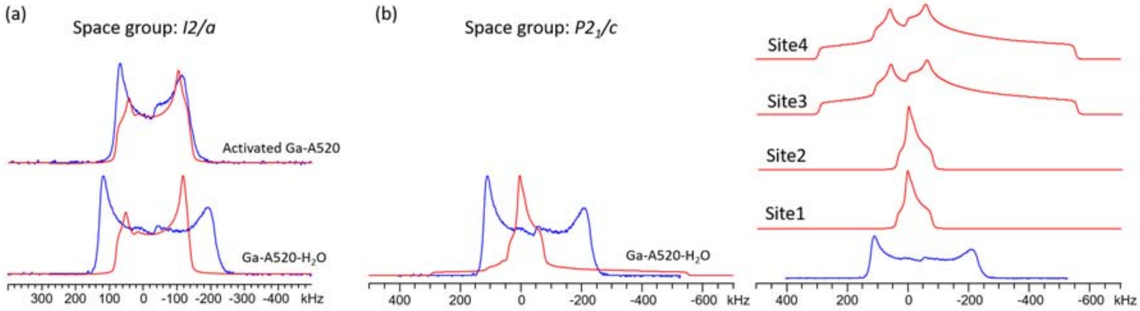

Figure 5-A5. The comparison of experimental (blue) and plane-wave DFT calculated (red) spectra are shown. In (a), the calculated spectra are obtained from the refined Ga-fumarate-H_2O structure with a space group of *I2/a*, while in (b), the calculated spectrum is generated from the reported Ga-fumarate-H_2O structure with a space group of $P2_1/c$. The overall calculated spectrum is illustrated in the left of (b), while the calculated spectra of distinct Ga sites are shown in the right of (b)

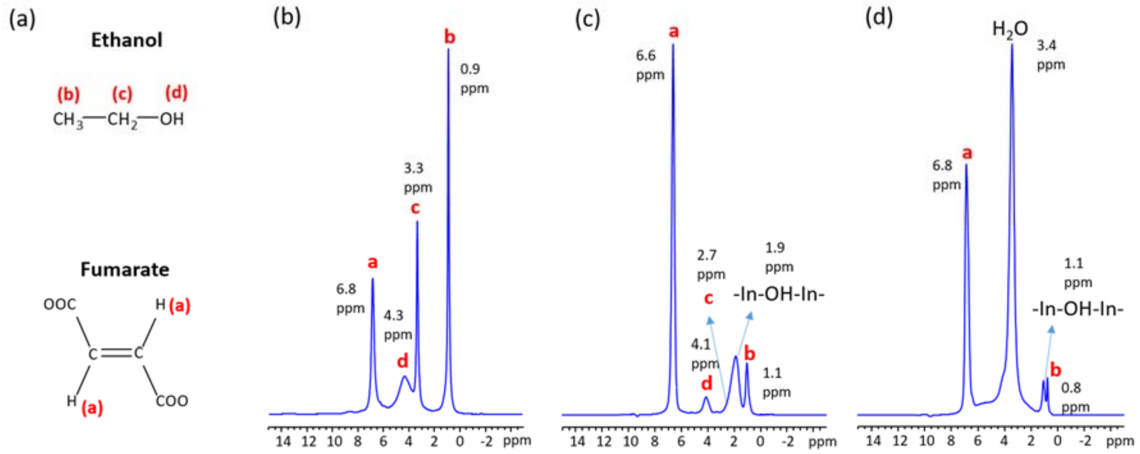

Figure 5-A6. ^{1}H MAS SSNMR spectra of various forms of In-fumarate-E are pictured, which were acquired at 21.1 T and a spinning frequency of 31.25 kHz. The chemical structural formulas of the ethanol guest and fumarate linker are illustrated in (a), with H atoms residing in distinct environments labeled with letters. It should be noted that the ^{1}H resonance of H atoms of guest water molecules overlaps with ^{1}H resonance of H atoms of -OH groups in ethanol, giving rise to the broad resonance at 4.3 ppm in (a). The ^{1}H SSNMR spectrum in (b) originates from as-made In-fumarate-E; the fumarate ^{1}H resonance is located at 6.8 ppm and the ethanol ^{1}H resonances are found at 0.9 ppm, 3.3 ppm, and 4.3 ppm. In (c), the ^{1}H MAS SSNMR spectrum of activated In-fumarate-E is shown, where the fumarate linker ^{1}H resonance is now at 6.6 ppm and the bridging –OH resonance is found at 1.9 ppm due to the change in chemical environments after evacuating guest ethanol molecules. The ^{1}H MAS SSNMR spectrum of activated In-fumarate-E also indicates the guest ethanol molecules are difficult to fully removed. The ^{1}H MAS SSNMR spectrum of In-fumarate-E-H_2O is shown in (d), featuring a large resonance at 3.4 ppm arising from adsorbed water, along with the fumarate resonance at 6.8 ppm. The bridging –OH resonance in (d) is observed at 1.1 ppm due to the change in chemical environments after water adsorption.

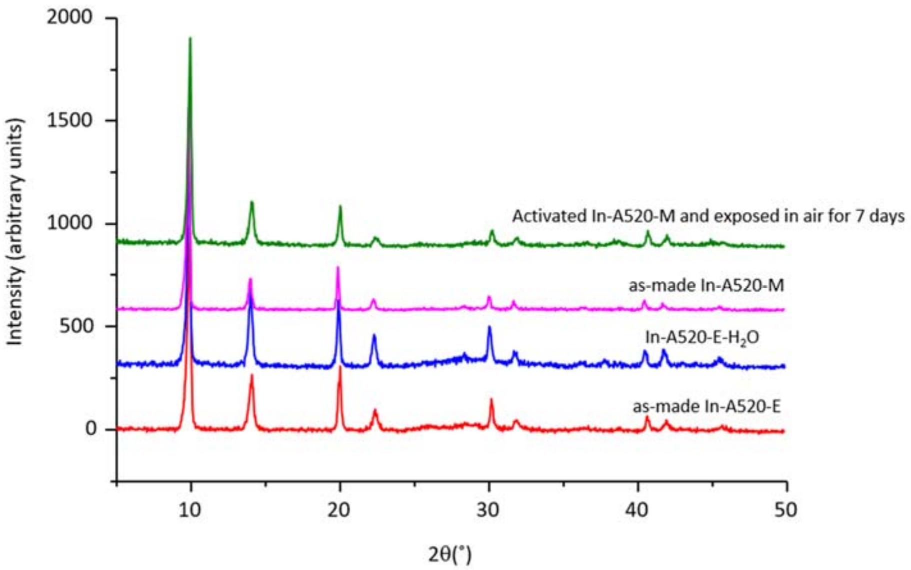

Figure 5-A7. The comparison of pXRD patterns of various form of In-fumarate MOFs.

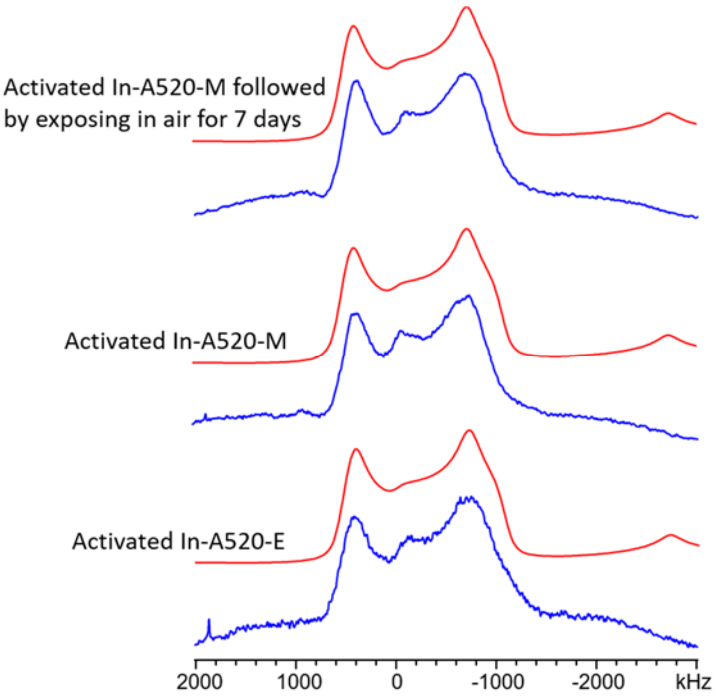

Figure 5-A8. Static ^{115}In SSNMR spectra of various form of In-fumarate MOFs acquired at 21.1 T are depicted. All the spectra show similar lineshapes, which suggest the In metal centres within these three MOFs have similar local environments.

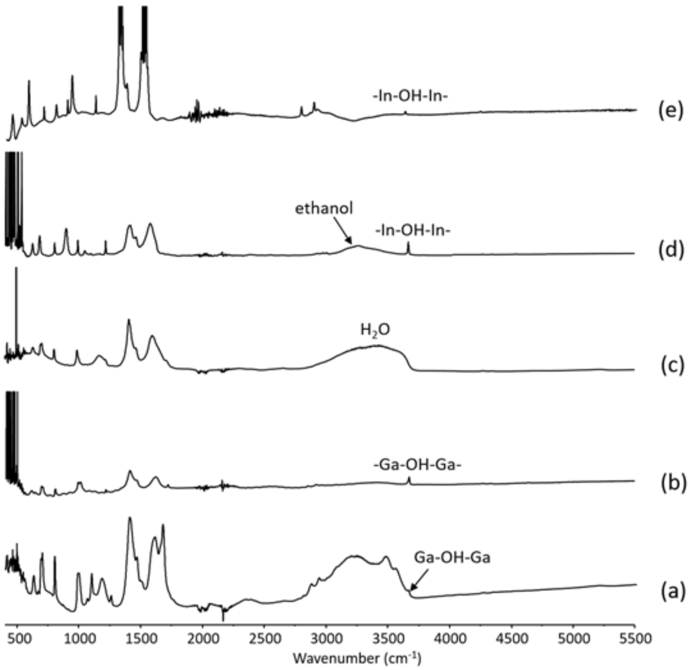

Figure 5-A9. The as-made Ga-fumarate IR spectrum is shown in (a). The broad adsorption in (a) from 2800-3700 cm^{-1} arises from water; the small secondary features on this broad peak are caused by C-H vibrations in the trapped residual solvent, while vibration of bridging hydroxyl groups gives rise to the small feature at 3657 cm^{-1}. In (b), the IR spectrum of activated Ga-fumarate is shown, which lacks the broad adsorption from 2800-3700 cm^{-1} due to the removal of guest H_2O molecules and residual solvent from the MOF channels. It is important to note that the O-H vibration of bridging hydroxyl groups persists at 3670 cm^{-1} in the activated sample. The IR spectrum in (c) corresponds to hydrated Ga-fumarate-H_2O, and the broad adsorption ranging from 2700 to 3700 cm^{-1} is again visible due to the presence of adsorbed water in the MOF channels. The IR spectrum of activated In-fumarate-E is shown in (d), the O-H vibration of bridging hydroxyl groups gives rise to the small feature at 3666 cm^{-1}; the broad adsorption from 3050 to 3570 cm^{-1} arises from unremoved ethanol. The activated In-fumarate-M IR spectrum is illustrated in (e), the O-H vibration of bridging hydroxyl groups at 3666 cm^{-1} presents a reduced S/N ratio, which suggests the replacement of bridging –OH groups.

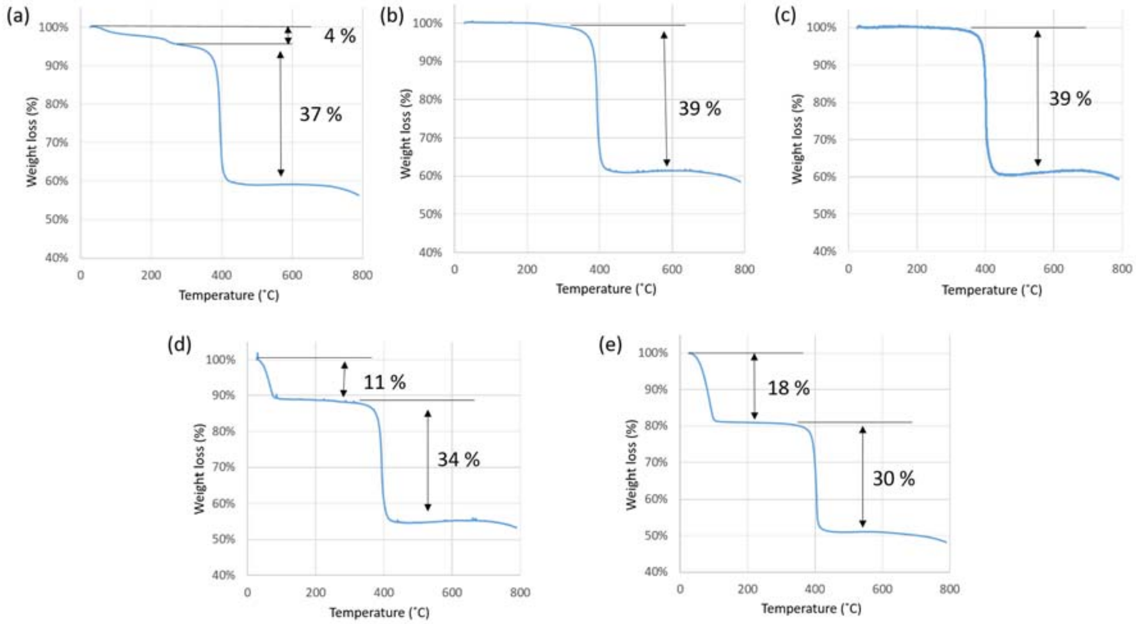

Figure 5-A10. Thermogravimetric analysis (TGA) plots of (a) In-fumarate-M(*as*) synthesized at 20 °C; (b) In-fumarate-M after activation under dynamic vacuum at 150 °C for 8 h; and (c) In-fumarate-M after activation followed by exposure to air (20 % r.h.) for 7 days; (d) In-fumarate-M(*as*) after activation followed by exposure to 80 % r.h. for 2 hours; (e) In-fumarate-M after activation followed by exposure to 80 % r.h. for 24 hours. The calculated chemical formula of In-fumarate-M(*as*) based on TGA plot is $In(OH)_{0.2}(OCH_3)_{0.8}(C_4H_2O_4){\cdot}0.33CH_3OH$, with a carbon percentage of 22.99 % and H percentage of 2.21 %, which is comparable to the elemental analysis results (C: 21.75 %, H: 1.70 %, N: 0.54 %). The difference should be caused by the presence of N containing impurity.

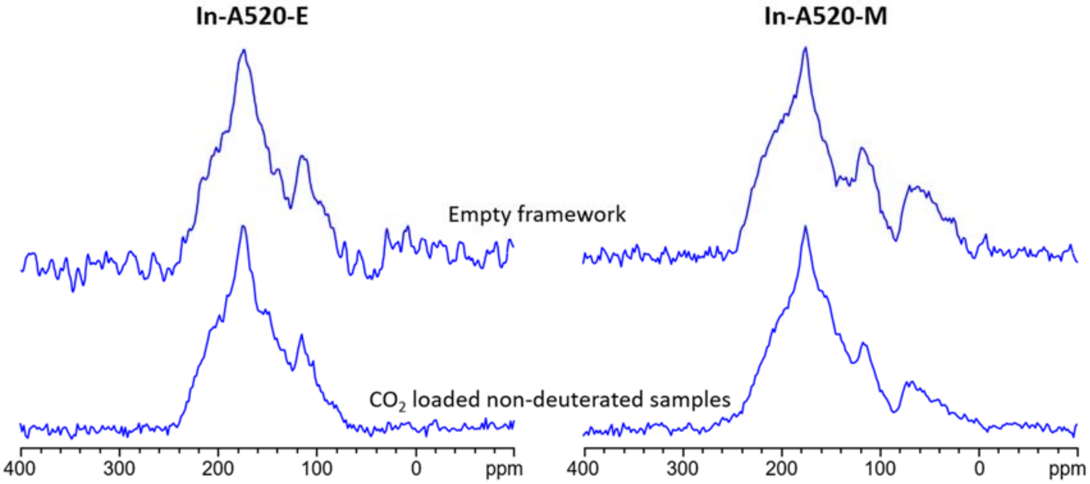

Figure 5-A11. Static ^{1}H-^{13}C CP SSNMR spectra of In-fumarate-E and In-fumarate-M MOFs in various states at a temperature of 133 K are shown. Due to the weak CO_2 binding strength, the adsorbed CO_2 resonance cannot be observed in CO_2 loaded non-deuterated samples.

Table 5-A1. Calculated $^{69/71}$Ga SSNMR parameters of activated Ga-fumarate and Ga-fumarate-H_2O.

	Sample	C_Q (^{71}Ga) (MHz)	C_Q (^{69}Ga) (MHz)	η_Q	Ω (ppm)	κ	α (°)	β (°)	γ (°)
Calculated Ga-fumarate-H_2O from JMCA paper (space group: $P2_1/c$)[a]	**Ga1**	11.499	18.376	0.896	62.293	-0.249	203.995	41.733	174.393
	Ga2	11.548	18.455	0.908	62.292	-0.268	155.610	41.766	186.213
	Ga3	30.688	49.044	0.892	315.986	0.781	183.230	2.165	280.639
	Ga4	30.720	49.094	0.891	316.141	0.783	356.694	3.141	79.411

[a] The calculated SSNMR parameters of Ga-fumarate-H_2O are based on the crystal structure obtained after geometry optimization using the CASTEP software package, which employs plane-wave DFT methods and was also used to calculate all NMR parameters; see Experimental section for further details.

Table 5-A2. Experimentally determined ^{115}In SSNMR parameters of activated In-fumarate-E, activated In-fumarate-M, and activated In-fumarate-M followed by exposed in air (20 % r.h.) for 7 days. All experimental ^{115}In SSNMR spectra were acquired at a magnetic field of 21.1 T.

Sample	C_Q (^{115}In) (MHz)	η_Q
Activated In-fumarate-M	188 (2)	0.20 (2)
Activated In-fumarate-M and exposed in air (20 % r.h.) for 7 days	189 (3)	0.20 (2)
Activated In-fumarate-E	192 (2)	0.21 (2)

Table 5-A3. The measured BET surface areas (in units of m^2/g) of Ga-fumarate samples synthesized at different temperatures using different molar ratios of $Ga(NO_3)_3$ and fumaric acid. The $Ga(NO_3)_3$: fumaric acid ratio is denoted as Ga: FA in the table.

Temperature (℃)		60	80	100	120	140	160	180
Ga: FA	**1： 1**	723	851	790	715	716	525	159
	1： 2	748	833	720	696	666	481	116

Table 5-A4. The measured BET surface areas (in units of m^2/g) of In-fumarate-E and In-fumarate-M samples synthesized at different temperatures using different molar ratios of $In(NO_3)_3$ and fumaric acid. The $In(NO_3)_3$: fumaric acid ratio is denoted as In: FA in the table.

Temperature (˚C)			20	40	60	80	100	120
In-fumarate-E	**In : FA**	1 : 1	596	695	691	503	490	383
		1 : 2	632	708	692	595	515	410
In-fumarate-M	**In : FA**	1 : 1	599	478	464	332	340	317
		1 : 2	237	478	551	385	373	351

Crystal Information File

```
data_
_chemical_name_mineral ??
_cell_length_a 6.8837(11)
_cell_length_b 12.129(2)
_cell_length_c 12.302(2)
_cell_angle_alpha 90
_cell_angle_beta 86.75(2)
_cell_angle_gamma 90
_cell_volume 1025.5(3)
_symmetry_space_group_name_H-M I2/a
loop_
        _symmetry_equiv_pos_as_xyz
        'x, y, z '
        '-x+1/2, y, -z '
        '-x, -y, -z '
        'x+1/2, -y, z '
        'x+1/2, y+1/2, z+1/2 '
        '-x, y+1/2, -z+1/2 '
        '-x+1/2, -y+1/2, -z+1/2 '
        'x, -y+1/2, z+1/2 '
loop_
_atom_site_label
_atom_site_type_symbol
_atom_site_symmetry_multiplicity
_atom_site_fract_x
_atom_site_fract_y
_atom_site_fract_z
_atom_site_occupancy
_atom_site_B_iso_or_equiv
H1 H   4 0.75 0.17(2) 0.5 1 0
H2 H   8 0.95(2) -0.281(8) 0.271(3) 1 0
C1 C   8 0.827(3) -0.1456(11) 0.3581(6) 1 0
C2 C   8 0.838(16) -0.2376(19) 0.2792(19) 1 0
O1 O   4 0.75 0.080(2) 0.5 1 0
O2 O   8 0.978(7) -0.108(9) 0.3992(14) 1 0
O3 O   8 0.651(6) -0.116(11) 0.3789(16) 1 0
Ga1 Ga   4 0.5 0 0.5 1 0
```

```
O4 O   8 0.059(2) 0.839(2) 0.0478(14) 1 0
O5 O   8 0.232(3) 0.519(3) 0.6513(14) 1 0
```

Chapter 6

6 Tracking the Evolution and Differences Between Guest-Induced Phases of Ga-MIL-53 *via* Ultra-wideline $^{69/71}$Ga Solid-State NMR Spectroscopy

Ga-MIL-53 is a metal-organic framework (MOF) that exhibits a "breathing effect," in which the pore size and overall MOF topology can be influenced by temperature, pressure, and host-guest interactions. The phase control afforded by this flexible framework renders Ga-MIL-53 a promising material for guest storage and sensing applications. In this work, the structure and behavior of four Ga-MIL-53 phases (*as*, *ht*, *enp* and *lt*), along with CO_2 adsorbed within Ga-MIL-53 at various loading levels, has been investigated using $^{69/71}$Ga solid-state NMR (SSNMR) experiments at 21.1 T and 9.4 T. $^{69/71}$Ga SSNMR spectra are observed to be very sensitive to distortions in the octahedral GaO_6 secondary building units within Ga-MIL-53; by extension, Ga NMR parameters are indicative of the particular crystallographic phase of Ga-MIL-53. The evolution of Ga NMR parameters with CO_2 loading levels in Ga-MIL-53 reveals that the specific CO_2 loading level offers a profound degree of control over the MOF phase, and the data also suggests that a re-entrant phase transition is present. Adsorption of various organic compounds within Ga-MIL-53 has been investigated using a combination of thermal gravimetric analysis (TGA), powder X-ray diffraction (pXRD) and $^{69/71}$Ga SSNMR experiments. Notably, pXRD experiments reveal that guest adsorption and host-guest interactions trigger unambiguous changes in the long-range structure of Ga-MIL-53, while $^{69/71}$Ga SSNMR parameters yield valuable information regarding the effect of the organic adsorbates on the local GaO_6 environments. This approach shows promise for the investigation of other quadrupolar metal nuclei in MIL-53 (*e.g.*, In-MIL-53) and MOFs in general, particularly in regards to adsorption-related applications.

6.1 Introduction

Metal-organic frameworks (MOFs) are a class of crystalline materials consisting of metal centres or metal-inorganic clusters linked by organic ligands to generate porous, three-dimensional frameworks on the molecular level.[1-3] MOFs exhibit useful properties, such as permanent porosities, large surface areas, and high thermal stabilities. These unique attributes have spurred research in potential MOF applications within fields such as gas storage, gas separation, catalysis, and drug delivery.[4-6]

Among the enormous variety of reported MOFs, a select number of flexible MOFs exhibit the phenomenon known as the "breathing effect," where the framework and pore dimensions expand or contract when influenced by external stimulus (*e.g.*, adsorption or desorption of guest molecules, changes in temperature and/or pressure).[7-8] Flexible MOFs have shown promise for applications such as gas storage and separation, sensing, and reversible guest adsorption.[7-9]

The MIL-53 series is a family of flexible MOFs that exhibit the breathing effect.[10-15] In general, M-MIL-53 (M: Cr^{3+}, Al^{3+}, Ga^{3+}, Fe^{3+}, Sc^{3+}, In^{3+}) incorporates corner-sharing octahedral MO_6 secondary building units (SBUs) (Figure 6-1(a)), which are linked by 1,4–benzenedicarboxylate (BDC) ligands. Each metal atom at the centre of the MO_6 octahedron is equatorially coordinated to four carboxylate oxygen atoms from four separate BDC linkers, while the two axially-coordinated oxygen atoms belong to μ_2-hydroxyl groups (*i.e.,* bridging hydroxyl groups) that interconnect MO_6 octahedra.[10-15]

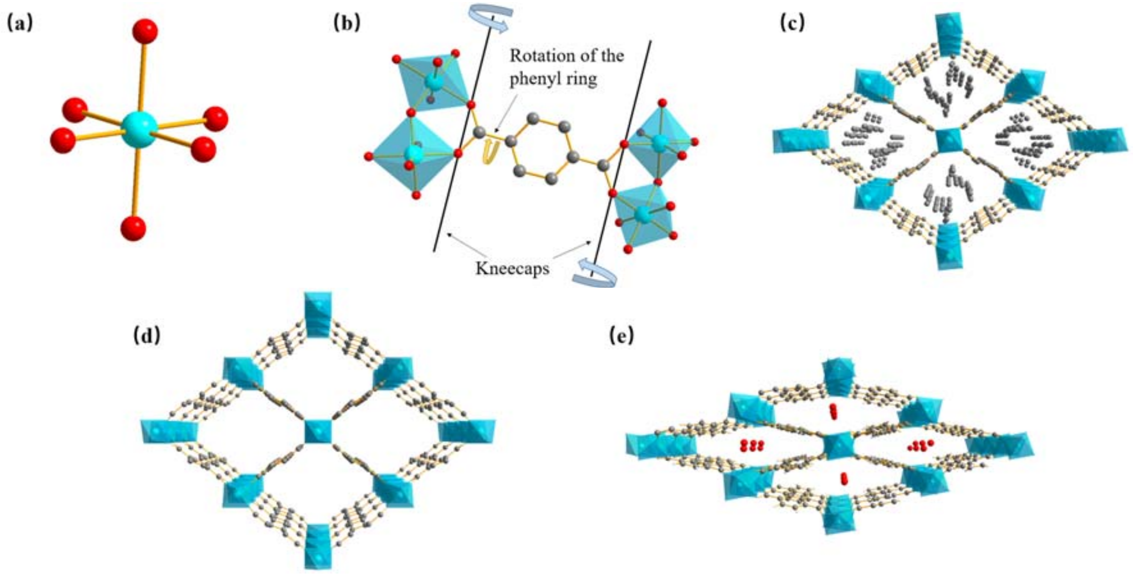

Figure 6-1. The octahedral secondary building unit of MIL-53 is shown in (a). Pictured in (b) is the schematic diagram of the "kneecap-like" linker rotation, which is responsible for the flexibility of MIL-53. The framework structures of MIL-53(*as*), MIL-53(*ht*) and MIL-53(*lt*) are shown in (c), (d) and (e), respectively. The colors light blue, grey, red and white represent the metal centre, carbon, oxygen and hydrogen, respectively.

MIL-53 exhibits permanent porosity and features one-dimensional channels. The documented "breathing effect"[10-11] significantly modifies the specific pore dimensions and geometry as MIL-53 "breathes" upon adsorption or desorption of guest molecules in certain temperature ranges, thus changing the crystallographic phase of MIL-53. The flexibility of MIL-53 originates from the BDC linker, where the O-O axis of each carboxylate group acts as a kneecap (Figure 6-1(b)) that permits alteration of the framework geometry and pore size.[16-17] The metal centre incorporated within MIL-53 has a clear influence on MOF flexibility and phase transitions,[18-19] while the relationship between the type of metal centre and guest adsorption at a molecular level is still being explored. MIL-53 is also a potential material for CO_2 storage but the CO_2 capacity differs depending on the metal centre incorporated.[20] Understanding how the local short-range structure about the metal centre changes during the CO_2 adsorption process may shed new light on the CO_2 adsorption process and associated phases in MIL-53.

The three most common forms of MIL-53, regardless of the metal centre incorporated, are the as-made (MIL-53(*as*)), high temperature (MIL-53(*ht*)), and low temperature (MIL-53(*lt*)) phases (Figure 6-1). In MIL-53(*as*) (Figure 6-1(c)), excess unreacted BDC ligands remaining from the MOF synthesis remain trapped inside the pores, resulting in a pore size of ca. 17 × 12 Å.[10-12, 14] By exposing most metal variants of MIL-53(*as*) to elevated temperatures (*e.g.,* > 330 °C for Al-MIL-53(*as*) and Cr-MIL-53(*as*)), the trapped excess BDC linkers can be evacuated from the pores, yielding the MIL-53(*ht*) phase (Figure 6-1(d)) which feature large ca. 17 × 13 Å pores that can then adsorb many different types of guest species.[10-11, 14] At room temperature, MIL-53(*ht*) rapidly adsorbs guest water molecules from atmospheric water vapor to generate MIL-53(*lt*) (Figure 6-1(e)), which features a much narrower pore size of ca. 19 × 7 Å due to the significant host-guest interactions between water and the framework.[10-11, 13-15]

Incorporating gallium into MIL-53 presents a unique challenge because unlike Al-MIL-53 and Cr-MIL-53, Ga-MIL-53(*ht*) cannot be directly generated by simply heating Ga-MIL-53(*as*). There are two known methods to obtaining Ga-MIL-53(*ht*): heating a DMF-exchanged sample of Ga-MIL-53(*as*) (known as Ga-MIL-53(*dmf*)) above 150 °C, or heating Ga-MIL-53(*lt*) above 250 °C.[21] Heating Ga-MIL-53(*lt*) at temperatures ranging from 60 – 220 °C only generates a Ga-MIL-53 sample with empty narrow pores (19.3 x 6.8 Å), known as Ga-MIL-53(*enp*).[21] Although Ga-MIL-53 is less flexible than analogues such as Cr-MIL-53 and Al-MIL-53,[10-11] Ga-MIL-53 also has high catalytic activities for Bronsted-type catalysis.[22] There are also many additional different phases of MIL-53 with varying pore sizes that can be generated upon organic guest molecule adsorption, depending on the specific nature of the guest species as well as the amount of adsorbed guest molecules.[19, 23-27]

Solid-state NMR (SSNMR) is a powerful tool for investigating the short-range structure in various materials, including MOFs.[28-30] ^{27}Al and ^{45}Sc SSNMR experiments targeting Al-MIL-53 and Sc-MIL-53 have been used to study the changes between their respective hydrated and dehydrated phases,[11, 15, 27, 31-34] while ^{27}Al SSNMR has shed light on changes in the local aluminum environment within Al-MIL-53 loaded with different organic guest species.[27, 32] Central transition (CT, spin $-1/2 \leftrightarrow +1/2$) ^{27}Al and ^{45}Sc SSNMR spectra of MOFs are relatively narrow and can typically be obtained within reasonable experimental times using magic-angle spinning (MAS) techniques, yielding a wealth of knowledge regarding the local metal environment along with information pertaining to the influence of the metal centre on MOF topology and phase transitions.[30, 35] In this sense, it would be of great interest to use SSNMR in order to survey the other metal centres that can be incorporated within MIL-53.

Studying diamagnetic NMR-active nuclei in the same periodic groups as ^{27}Al or ^{45}Sc would present an excellent opportunity for understanding the influence of the specific metal centre on the number and nature of MIL-53 phases associated with processes such as guest adsorption. Of the candidate nuclei, none are very appealing: ^{11}B, ^{89}Y, and $^{203/205}$Tl have no documented incorporation in MIL-53, while ^{89}Y also has a very low Larmor frequency and $^{203/205}$Tl is associated with severe toxicity hazards. The two indium isotopes ^{113}In and ^{115}In have extremely large electric quadrupole moments[36] that renders acquisition of $^{113/115}$In SSNMR spectra very challenging in MOFs.[37-38] This leaves gallium, which has the NMR-active spin-3/2 ^{69}Ga and ^{71}Ga isotopes with natural abundances of 60.4 % and 39.6 %, respectively;[39] however, these nuclei are not commonly studied by SSNMR spectroscopy in MOFs.[30, 40-42] Both Ga isotopes are quadrupolar (spin > 1/2), and their significant electric quadrupole moments (^{69}Ga: 171(2) mb; ^{71}Ga: 107(1) mb)[36] couple to the electric field gradients (EFGs) arising from the immediate nuclear surroundings, severely broadening $^{69/71}$Ga SSNMR resonances across hundreds to thousands of kHz. The very broad $^{69/71}$Ga powder patterns in MOFs present a challenging situation that cannot be adequately mitigated by MAS techniques in many circumstances, despite significant advances in MAS SSNMR spectroscopy in recent years.[43] When considering the weight dilution of both Ga isotopes in the large unit cell of Ga-MIL-53, spectral acquisition becomes even more difficult, as shown by Massiot et al.[40] If $^{69/71}$Ga SSNMR could be successfully performed on various forms of Ga-MIL-53 using ultra-wideline SSNMR acquisition strategies,[44] the resulting spectra would be quite useful for understanding how guest adsorption and phase changes affect the local metal environment, much like in the cases of ^{27}Al and ^{45}Sc.[15, 27]

Herein, we use static $^{69/71}$Ga SSNMR spectroscopy at 9.4 and 21.1 T to investigate the four basic phases of Ga-MIL-53, in addition to the various phases and metal environments associated with the adsorption of CO_2 and different organic molecules at various loading levels. Understanding the changes in the short-range structure between the basic phases and during guest adsorption in Ga-MIL-53 is important for the future rational design of flexible MOFs with enhanced guest uptake affinities and capacities.

6.2 Experimental Section

All chemicals were obtained from Sigma-Aldrich and were used without further purification.

6.2.1 Sample preparation

As-made Ga-MIL-53(*as*). Ga-MIL-53(*as*) was synthesized using a previously described method,[14] which is briefly summarized here. $Ga(NO_3)_3 \cdot xH_2O$ (0.26 g, 1 mmol), 1,4–benzenedicarboxylic acid (BDC, 0.33 g, 2 mmol) and 10 mL of deionized H_2O were mixed into a 23 mL Teflon-lined stainless steel autoclave, sealed, and heated at 200 °C for 3 days. The product was obtained as colorless crystals, which were then washed three times with deionized water and dried using vacuum filtration to obtain Ga-MIL-53(*as*).

Sample activation to obtain Ga-MIL-53(*lt*). The activation process of Ga-MIL-53(*as*) began by exchanging the trapped BDC organic linker with *N,N*-dimethylformamide (DMF), which was accomplished by sealing 0.50 g of Ga-MIL-53(*as*) along with 10 mL of DMF in an autoclave at a temperature of 473 K overnight (*i.e.*, ≥ 12 h). The resulting DMF-exchanged Ga-MIL-53 sample, Ga-MIL-53(*dmf*), was then heated at 473 K under dynamic vacuum (≤ 1 mbar) for 8 h in order to remove DMF molecules from the MOF pores. The sample was then exposed to air at room temperature; the empty channels rapidly adsorb water from air to form the water-adsorbed variant of this MOF, Ga-MIL-53(*lt*).

Preparation of the large pore Ga-MIL-53(*ht*) phase and the empty narrow pore Ga-MIL-53(*enp*) phase. To obtain Ga-MIL-53(*ht*), Ga-MIL-53(*dmf*) was heated at 603 K for 8 h under dynamic vacuum (≤ 1 mbar) in a homemade 5 mm o.d. L-shaped glass tube attached to a Schlenk line. The glass tube was then flame-sealed off from the Schlenk line to prevent the introduction of water vapor to the MOF channels. In order to produce Ga-MIL-53(*enp*), Ga-MIL-53(*lt*) was activated at a temperature of 473 K under dynamic vacuum using the same instrumentation and procedure described above.

CO_2 adsorption. A Schlenk line was also used to facilitate CO_2 adsorption within Ga-MIL-53. After producing Ga-MIL-53(*enp*), a known amount of pressurized CO_2 was then introduced to the empty vacuum line, and the CO_2 was allowed to occupy both the vacuum line and the glass tube containing the sample; the volume of this combined space is known to be 82.7 cm^3. The bottom of the CO_2-filled glass tube was then immersed in liquid nitrogen to load and freeze CO_2 within the sample, and the glass tube was flame-sealed off from the Schlenk line. In this work, the overall CO_2 loading amount is expressed by the molar ratio between CO_2 and the metal. In this study, 0.05, 0.1, 0.2, 0.3, 0.4, and 0.45 CO_2/metal samples were prepared and characterized by SSNMR.

Organic guest molecule adsorption. The Ga-MIL-53 samples loaded with low levels of organic adsorbates were obtained using the same method as was used for CO_2 loading; a known amount of organic adsorbate vapor was used instead of CO_2 in the empty vacuum line to achieve the loading level of 0.1 organic adsorbate/Ga.

The samples of Ga-MIL-53 fully loaded with organic guest adsorbates were prepared using a solvent exchange method to achieve full adsorption. 0.20 g of Ga-MIL-53(*lt*) and 10 mL of different organic solvents (*para*-xylene (PX), *ortho*-xylene (OX), benzene, ethylbenzene (EB), *N, N*-dimethylformamide (DMF), *N, N*-diethylformamide (DEF)) were mixed into a 23 mL Teflon-lined stainless steel autoclave, which was then sealed and heated at 150 °C for 16 hours. The resulting product was dried using vacuum filtration.

6.2.2 Characterization techniques

Powder X-ray diffraction (pXRD). All pXRD patterns were acquired using an Inel CPS powder diffractometer operating with Cu Kα radiation (λ = 1.5406 Å). Reflections were collected at 2θ values between 5 and 120 ° with a step size of 0.02 °.

Thermogravimetric analysis (TGA). The TGA curves for samples studied in this work were measured under dry N_2 flow using a Mettler Toledo TGA/SDTA851e instrument. For each TGA experiment, ca. 5-10 mg of the sample was placed within a ceramic crucible. A temperature range between 25 °C and 800 °C and a heating rate of 10 °C /min were utilized.

^{71}Ga SSNMR experiments at 9.4 T. All experiments at a magnetic field of 9.4 T were performed using a Varian InfinityPlus wide-bore NMR spectrometer (ν_0(^{1}H) = 399.5 MHz, ν_0(^{71}Ga) = 122.0 MHz) equipped with a Varian/Chemagnetics 5 mm HX static probe. The combination of wideband uniform-rate smooth-truncation (WURST)[45] and the Carr-Purcell-Meiboom-Gill (CPMG)[46] pulse sequences (WURST-CPMG)[45, 47-50] was employed with ^{1}H decoupling to enhance the signal-to-noise (S/N) ratio of the second order quadrupolar interaction (SOQI)-dominated powder patterns.[47] ^{71}Ga chemical shifts were referenced using an aqueous solution of 1 M $Ga_2(NO_3)_3$ (δ_{iso} = 0 ppm). An experimentally optimized radio frequency (rf) power of 15.6 kHz was used for all ^{71}Ga WURST-CPMG experiments, along with a spectral width of 2000 kHz and a WURST pulse length of 50 μs.

$^{69/71}$Ga SSNMR experiments at 21.1 T. Experiments at a magnetic field of 21.1 T were carried out using a Bruker Avance II NMR spectrometer located at the National Ultrahigh-Field NMR Facility for Solids in Ottawa, ON, Canada. A home-built 5 mm HX static probe was used to acquire all $^{69/71}$Ga spectra (ν_0(^{71}Ga) = 274.4 MHz, ν_0(^{69}Ga) = 216.0 MHz). All spectra were acquired using a modified 90 ° - 90 ° quadrupolar echo pulse sequence of the form ($\pi/2$ - τ_1 - $\pi/2$ - τ_2 – acq) with a full spectral width of 2000 kHz. The ^{71}Ga spectra were acquired using τ_1 and τ_2 values of 49 μs and 5.5 μs, respectively, while the ^{69}Ga spectra were acquired using τ_1 = 48.5 μs and τ_2 = 9.25 μs. 90 ° central-transition (CT, spin -1/2 ↔ +1/2) selective pulse lengths of 1.0 and 1.5 μs were used to acquire ^{71}Ga and ^{69}Ga spectra, respectively. A pulse delay of 1 s was used to obtain $^{69/71}$Ga SSNMR spectra at 21.1 T, with a typical number of scans of 4096, requiring just over one hour of total acquisition time. Due to the relatively large quadrupole moment of ^{69}Ga, the breadth of ^{69}Ga powder patterns was too large to properly excite and acquire in a single experiment with the quadrupolar echo pulse sequence. The overall ^{69}Ga powder pattern was constructed by co-adding two or more frequency-stepped individual sub-spectra; this technique is known as piecewise acquisition or variable-offset cumulative spectrum (VOCS) acquisition.[51]

Simulations of SSNMR spectra. Simulations of all static solid-state NMR spectra were performed using the WSolids software package.[52] For each $^{69/71}$Ga powder pattern, in addition to the isotropic chemical shielding (δ_{iso}), there are three parameters to be fit: C_Q, η_Q, and the relative intensity of the powder pattern to any other powder patterns present. The (^{71}Ga) and (^{69}Ga) values are related based on their respective nuclear quadrupole moments; $C_Q(^{69}\text{Ga}) = 1.6\ C_Q(^{71}\text{Ga})$.

Theoretical Calculations. All calculations were performed using the CASTEP software package[53-54] and the Materials Studio 4.4 environment. The $^{69/71}$Ga CS and EFG tensors were calculated using the NMR module[55-56] incorporated in CASTEP, which employed the gauge-including projector-augmented wave (GIPAW) method,[54] pseudopotentials, and plane-wave basis sets.[54] These calculations also employed the generalized gradient approximation (GGA) along with the Perdew− Burke−Ernzerhof (PBE) functional.[57] In all instances, a plane-wave cut off energy of 500 eV was used. All unit cell parameters and atomic coordinates originated from the reported structures of Ga-MIL-53(*lt*).[18]

6.3 Results and Discussion

6.3.1 SSNMR studies of the four standard Ga-MIL-53 phases: *as*, *ht*, *enp* and *lt*

In all four of the basic Ga-MIL-53 phases, the core GaO_6 octahedral SBU should be preserved, although MOF-guest interactions and subsequent alterations in pore size are expected to influence the O-Ga-O bond angles and Ga-O bond lengths. Accordingly, any changes in the short-range structure and electronic environment about Ga centres should be readily reflected in the $^{69/71}$Ga SSNMR spectra. In all instances, the ^{69}Ga SSNMR spectra will be broader than that of the corresponding ^{71}Ga spectra, owing to the larger quadrupole moment of ^{69}Ga.[36]

The experimental and simulated $^{69/71}$Ga SSNMR echo spectra acquired for the four standard phases of Ga-MIL-53 at a magnetic field of 21.1 T are illustrated in Figure 6-2, with the corresponding experimental and simulated ^{71}Ga WURST-CPMG SSNMR spectra at 9.4 T shown in Figure 6-3. In general, the 21.1 T results are of higher resolution and signal-to-noise ratio (S/N). At both fields, $^{69/71}$Ga SSNMR spectra are significantly broadened by the QI, with ^{71}Ga and ^{69}Ga powder patterns at 21.1 T exceeding widths of 200 kHz and 500 kHz respectively. These spectra are also quite sensitive to the phase of Ga-MIL-53, and it is evident that each phase gives rise to a unique SSNMR lineshape.

In almost all $^{69/71}$Ga SSNMR spectra, a narrow, nearly identical central resonance is present (Figure 6-2, denoted by asterisks), which is indicative of some residual Ga-containing impurity from the initial MOF synthesis. Upon examination of the reagents, the most likely impurity source is some mixture of Ga-OH and Ga-H_2O crystalline phases formed as a side product during the synthesis of Ga-MIL-53. A recrystallization of the $Ga(NO_3)_3{\cdot}xH_2O$ reagent with NaOH in H_2O yielded a crystalline compound; the $^{69/71}$Ga

SSNMR spectrum of this compound is very similar to that of the impurity in Ga-MIL-53 spectra and resembles literature accounts of a Ga hydroxo-aquo cluster (Figure 6-A1),[58] hence it is likely that the impurity in our spectra is a crystalline Ga-hydroxyl/hydroxide compound. The presence of this narrow central resonance in the $^{69/71}$Ga SSNMR spectra of all Ga-MIL-53 variants is reflective of a small amount of this impurity within the MOF samples.

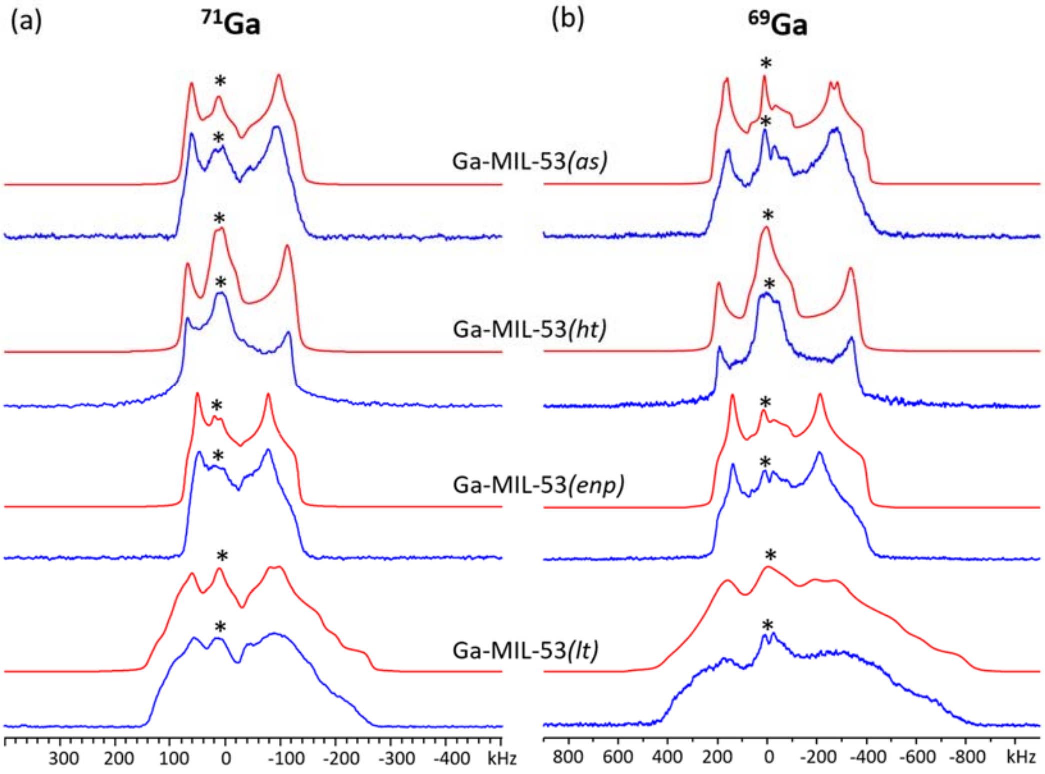

Figure 6-2. ^{71}Ga SSNMR echo spectra of Ga-MIL-53(*as*), Ga-MIL-53(*ht*), Ga-MIL-53(*enp*) and Ga-MIL-53(*lt*) acquired at 21.1 T are shown in (a), along with the corresponding ^{69}Ga SSNMR echo spectra at 21.1 T in (b). All experimental spectra are shown in blue, while simulated spectra are depicted in red. The narrow central powder pattern assigned to Ga hydroxyl/hydroxide impurities has been labeled with an asterisk (*), and this impurity is further described both in the main text and Figure 6-A1.

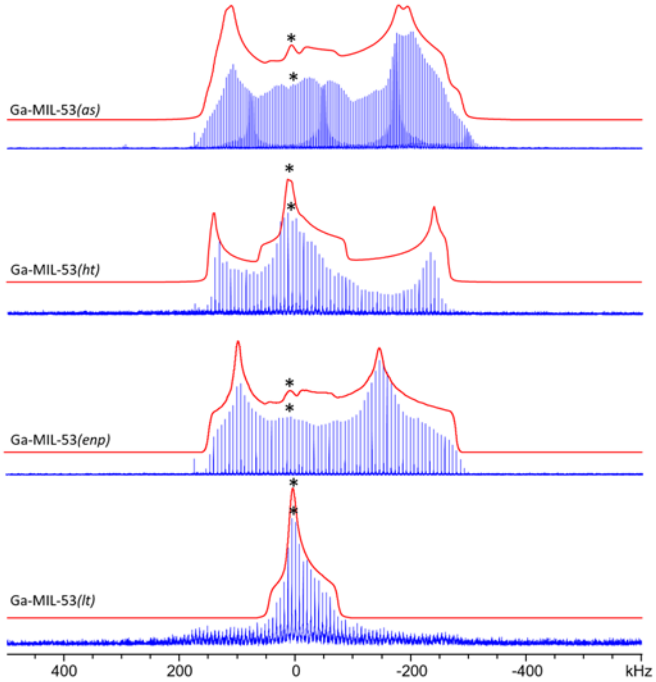

Figure 6-3. The ^{71}Ga WURST-CPMG SSNMR spectra of four Ga-MIL-53 phases (*as*, *ht*, *enp*, *lt*) are shown, as acquired at a magnetic field of 9.4 T. All experimental spectra are shown in blue, while simulated spectra are colored red. The narrow central powder patterns originating from Ga hydroxyl/hydroxide impurities are labeled with asterisks (*). The broad underlying feature in the Ga-MIL-53(*lt*) spectrum originates from the framework of Ga-MIL-53(*lt*); the low intensity of the broad Ga-MIL-53(*lt*) powder pattern in this instance is due to rapid T_2 relaxation. In contrast, the relatively long T_2 relaxation time of the impurity phase is preferentially enhanced by the WURST-CPMG pulse sequence, and this impurity phase dominates the spectral appearance. The short T_2 relaxation time of Ga-MIL-53(*lt*) is likely due to the rapid dynamics of water molecules adsorbed within the MOF channels and proximate to Ga centres. Accordingly, the broad powder pattern was not simulated at 9.4 T due to the lack of well-defined spectral features. Higher S/N ^{71}Ga SSNMR spectra with respect to Ga-MIL-53(*lt*) can be acquired by using solid quadrupolar-echo experiments (Figure 6-2), which are influenced to a far lesser degree by differences in T_2 values between powder patterns.

Table 6-1. $^{69/71}$Ga NMR parameters of Ga-MIL-53(*as*), Ga-MIL-53(*ht*), Ga-MIL-53(*enp*), and Ga-MIL-53(*lt*), as obtained from analytical simulations of static $^{69/71}$Ga SSNMR echo spectra at 21.1 T. The simulation results also fit the experimental ^{71}Ga WURST-CPMG spectra at 9.4 T (Figure 6-3).[a]

Sample	Site (relative intensity)	C_Q (^{71}Ga) (MHz)^b	C_Q (^{69}Ga) (MHz)^b	η_Q	Ω (ppm)	κ	δ_{iso} (ppm)
Ga-MIL-53(*as*)	Site 1 (1.00)	18.5 (1)	29.5 (1)	0.19 (1)	160 (20)	1.0 (1)	-15 (5)
	Site 2 (1.00)	17.7 (1)	28.3 (1)	0.22 (1)	200 (30)	1.0 (1)	-15 (5)
	Impurity (0.25)	7.5 (1)	12.0 (1)	1.00 (10)	50 (10)	0.0(2)	50 (10)
Ga-MIL-53(*ht*)	Site 1 (1.00)	19.1 (1)	30.2 (1)	0.05 (1)	130 (20)	1.0 (1)	0(15)
	Impurity (0.55)	8.3 (1)	13.3 (1)	0.80 (10)	60 (10)	0.0(2)	60 (10)
Ga-MIL-53(*enp*)	Site 1 (1.00)	17.4 (1)	27.8 (1)	0.32 (1)	150 (20)	1.0 (1)	-10 (5)
	Impurity (0.10)	7.5 (1)	12.0 (1)	1.00 (10)	100 (20)	0.0(2)	70 (10)
Ga-MIL-53(*lt*)	Site 1 (1.00)	22.0 (3)	35.2 (3)	0.65 (3)	250 (30)	1.0 (3)	-20 (10)
	Site 2 (0.50)	21.7 (3)	34.7 (3)	0.37 (3)	250 (30)	1.0 (3)	15 (5)
	Site 3 (0.50)	20.0 (3)	32.0 (3)	0.34 (3)	230 (30)	1.0 (3)	5 (5)
	Impurity (0.15)	7.5 (1)	12.0 (1)	1.00 (10)	50 (10)	0.0(2)	50 (10)

[a] The QI dominates spectral appearance, and the Euler angles that describe the relative orientations of the EFG and CS tensors (α, β, and γ) were set to 0 ° in all simulations. Euler angles other than 0 ° caused the simulations to diverge in appearance from the experimental spectra. [b] C_Q(^{71}Ga) and C_Q(^{69}Ga) values are related by C_Q(^{69}Ga) = 1.6 C_Q(^{71}Ga).

The ^{69}Ga SSNMR spectrum of Ga-MIL-53(*as*) reveals the presence of two similar yet distinct Ga powder patterns (Figure 6-2(b)) in a 1: 1 ratio, which corresponds to two crystallographically distinct Ga sites of equal occupancy in similar local environments. Interestingly, these two similar Ga powder patterns cannot be readily resolved in the 21.1 T ^{71}Ga SSNMR spectrum (Figure 6-2(a)), since the two relatively narrow ^{71}Ga lineshapes overlap due to the relatively smaller ^{71}Ga QI. Careful examination of the ^{71}Ga WURST-CPMG SSNMR spectrum at 9.4 T confirms the presence of two Ga powder patterns (Figure 6-3 and Figure 6-A2). The EFG parameters associated with these two powder patterns and corresponding two crystallographic sites are remarkably alike: for site 1, C_Q(^{71}Ga) = 18.5

(1) MHz and $C_Q(^{69}Ga)$ = 29.5 (1) MHz with η_Q = 0.19 (1), while for site 2, $C_Q(^{71}Ga)$ = 17.7 (1) MHz and $C_Q(^{69}Ga)$ = 28.3 (1) MHz with η_Q = 0.22 (1). The similar powder patterns (Figure 6-A2) and NMR parameters (Table 6-1) of these two Ga metal centres indicate that they reside in quite similar local electric environments in Ga-MIL-53(*as*). A previous XRD study[21], however, indicated that only a single Ga site was present in Ga-MIL-53(*as*). It appears that in this particular case, $^{69/71}$Ga SSNMR is more sensitive to local structure and can distinguish between these two very similar Ga centres. It should also be noted that the corresponding CS parameters of both Ga powder patterns are quite similar, again indicating the Ga centres reside in magnetically similar local environments; however, the QI dominates the appearance of these ultra-wideline spectra, so comparing CS parameters is quite difficult and associated with significant uncertainty.

The $^{69/71}$Ga spectra of Ga-MIL-53(*ht*) (Figure 6-2), while broad, are well-defined, and are somewhat dissimilar versus those of Ga-MIL-53(*as*), suggesting differences exist in the local Ga environment between these phases. Both the ^{69}Ga and ^{71}Ga SSNMR spectra of Ga-MIL-53(*ht*) feature a single powder pattern, corresponding to a single crystallographically unique Ga site. Although the crystal structure of Ga-MIL-53(*ht*) has not yet been solved due to the difficulties involved in obtaining highly crystalline samples for XRD,[18] previous studies on the analogous Cr-MIL-53(*ht*) and Al-MIL-53(*ht*) MOFs have indicated that a single unique metal site should be present;[10-11] these observations are in good agreement with our $^{69/71}$Ga SSNMR spectra of Ga-MIL-53(*ht*). The $^{69/71}$Ga NMR parameters of Ga-MIL-53(*ht*) (Table 1) are generally similar to those of Ga-MIL-53(*as*), but the C_Q values are slightly larger and the η_Q value is lower in Ga-MIL-53(*ht*). The ca. 3 % increase in C_Q values from the (*as*) to (*ht*) versions hints that the local environment about Ga (i.e., the GaO_6 SBU) is slightly more distorted in Ga-MIL-53(*ht*) versus Ga-MIL-53(*as*). The observation of a near-zero η_Q value in Ga-MIL-53(*ht*) indicates that the EFG tensor is nearly axially symmetric, unlike the slightly asymmetric EFG tensor in Ga-MIL-53(*as*).

The CS parameters are relatively unchanged between the (*as*) and (*ht*) phases of Ga-MIL-53, but it must again be noted that comparisons of CS data are unreliable due to the dominance of the EFG tensor on spectral appearance. There is an increased percentage of the impurity phase in Ga-MIL-53(*ht*) along with slight differences in the corresponding NMR parameters, which can be attributed to the relatively high activation temperature of 603 K that could have partially decomposed the MOF and perhaps converted some Ga hydroxyl impurities to alternate phases of similar composition. Judging from the $^{69/71}$Ga SSNMR spectra and associated NMR parameters, there are only slight alterations in the local Ga environments between Ga-MIL-53(*ht*) and Ga-MIL-53(*as*), with the most notable being the observation of two Ga sites in the (*as*) version versus one site in the (*ht*) sample. It is likely that host-guest interactions between the MOF and excess linker remaining in the pores are responsible for the existence of two crystallographically unique Ga sites in Ga-MIL-53(*as*); activation to the empty Ga-MIL-53(*ht*) form removes the possibility of host-guest interactions, and leaves only a single Ga site in the Ga-MIL-53(*ht*) crystal structure.

The distinct $^{69/71}$Ga SSNMR spectra of Ga-MIL-53(*enp*) (Figure 6-2) confirm that the significant changes in the phase and pore size from Ga-MIL-53(*ht*) to Ga-MIL-53(*enp*) also involves alterations to the local GaO_6 environment. There is a single Ga powder pattern and thus a single crystallographically unique Ga site in this phase, which agrees with prior XRD studies.[18] The Ga centre in Ga-MIL-53(*enp*) corresponds to $C_Q(^{71}Ga)$ = 17.4(1) MHz, $C_Q(^{69}Ga)$ = 27.8 (1) MHz, and η_Q = 0.32 (1). The ca. 9% drop in C_Q values from the (*ht*) to (*enp*) phases indicates that the smaller pore size and unique pore geometry in Ga-MIL-53(*enp*) is linked to a higher degree of spherical symmetry about Ga in the GaO_6 SBUs (i.e., more uniform Ga-O bond distances and more ideal O-Ga-O bond angles).

The movement of η_Q away from a near-zero value is also notable; the pore contraction in Ga-MIL-53(*enp*) eliminates the rotational axes of symmetry that were present in Ga-MIL-53(*ht*) and presumably disrupts the octahedral symmetry of the GaO_6 SBUs. The change in $^{69/71}$Ga NMR parameters reflects differences within the GaO_6 short-range structures, which are known from XRD studies.[18, 21] The GaO_6 SBUs in the Ga-MIL-53(*enp*) phase have a smaller Ga-O bond length distribution versus the GaO_6 SBUs within Ga-MIL-53(*as*), (Table 6-A1), which is likely the driving factor behind the smaller C_Q value in Ga-MIL-53(*enp*), while the relatively larger O-Ga-O bond angle distribution (Table 6-A1) could be responsible for changes in the observed η_Q values. The CS tensor parameters are similar between the (*ht*) and (*enp*) phases and, in general, do not seem particularly sensitive to phase changes in Ga-MIL-53. An intriguing observation is that aside from the number of Ga sites, the $^{69/71}$Ga SSNMR spectra and associated NMR parameters are similar between Ga-MIL-53(*enp*) and site 2 of Ga-MIL-53(*as*); this is unexpected given the different pore sizes and geometries between these phases along with the presence of adsorbed guests in (*as*) versus the empty channels of (*enp*).

The $^{69/71}$Ga SSNMR spectra of Ga-MIL-53(*lt*) are broader than those of all three other basic forms of Ga-MIL-53 and exhibit a lineshape that is the superposition of several individual powder patterns (Figure 6-2). The observed broad features in Ga-MIL-53(*lt*) spectra indicate the presence of short-range disorder about Ga, implying that the GaO_6 SBUs are not uniform in this (*lt*) phase and some variance exists in Ga-O bond lengths as well as O-Ga-O bond angles. Although pXRD results indicate that Ga-MIL-53(*lt*) has a long-range structure of high crystallinity (Figure 6-A3), SSNMR results suggest that a distribution of local environments exists about Ga in the (*lt*) phase. This short-range disorder can be attributed to the presence of H_2O molecules within the channels of Ga-MIL-53(*lt*); the location and specific orientation of guest H_2O molecules is likely not well-defined, and the ensuing distribution of host-guest interactions could slightly influence the channel dimensions of Ga-MIL-53(*lt*) and the local short-range structure of GaO_6 SBUs. The presence, or absence, of H_2O proximate to GaO_6 coupled with fast H_2O dynamics would also contribute to a distribution of local Ga environments. In support of this hypothesis, rapid T_2 relaxation has been observed in the ^{71}Ga WURST-CPMG SSNMR spectrum of Ga-MIL-53(*lt*) (Figure 6-3), in which only the spectrum of the impurity phase with a longer T_2 value can be acquired.

Nonetheless, the spectra of Ga-MIL-53(*lt*) can be simulated using three different Ga sites in a ratio of 2: 1: 1 based on the reported crystal structure,[18] these $^{69/71}$Ga SSNMR spectra are shown in Figure 6-2 and Figure 6-A4, and the NMR parameters are listed in Table 6-1. The EFG parameters corresponding to these three powder patterns and three crystallographic sites are obviously different: for site 1, $C_Q(^{71}Ga)$ = 22.0 (3) MHz and $C_Q(^{69}Ga)$ = 35.2 (3) MHz with η_Q = 0.65 (3), for site 2, $C_Q(^{71}Ga)$ = 21.7 (3) MHz and $C_Q(^{69}Ga)$ = 34.7 (3) MHz with η_Q = 0.37 (3), while for site 3, $C_Q(^{71}Ga)$ = 20.0 (3) MHz and $C_Q(^{69}Ga)$ = 32.0 (3) MHz with η_Q = 0.34 (3).

The calculated results based on the reported Ga-MIL-53(*lt*)[18] crystal structure are shown in Table 6-A2. Calculations based on the reported crystal structure generate C_Q values which come closest to experimental results, but one of these three calculated C_Q values is not in good agreement with experimental observations, and there is also a large spread in the corresponding calculated η_Q values for all three sites. After geometry optimization of the reported Ga-MIL-53(*lt*) crystal structure, the calculated and experimental NMR parameters diverge significantly. The difference between calculated and experimental results in both the unoptimized and optimized structures likely arise from the inability of XRD to properly place the hydrogen atoms of water, as well as the ensuing challenges associated with computationally modeling the guest H_2O molecules. All

CASTEP calculations were thus performed with empty Ga-MIL-53 channels, which is another contributing factor to the disagreement between experimental and calculated values. A pair of charts comparing experimental versus simulated $C_Q(^{71}Ga)$ and η_Q values are provided in Figure 6-A5; in most instances, calculations underestimate experimental $C_Q(^{71}Ga)$ values but overestimate η_Q values.

The C_Q and η_Q values in Ga-MIL-53(*lt*) are significantly larger than those of Ga-MIL-53(*enp*), despite the similar pore dimensions in these materials. All three Ga powder patterns in Ga-MIL-53(*lt*) correspond to C_Q values larger than those observed in the (*as*), (*ht*), or (*enp*) phases, pointing towards a relative lack of spherical symmetry in GaO_6 SBUs in this MOF phase. In addition, the small differences in C_Q values between the three powder patterns indicates that some minor variance exists between Ga-O bond lengths and O-Ga-O bond angles at each of the three crystallographically unique Ga site. The η_Q value of site 1 is the largest among these three powder patterns and all forms of Ga-MIL-53, representing a much more axially asymmetric EFG tensor and a geometrically distinct GaO_6 environment. The larger C_Q and η_Q values agree well with the XRD crystal structure,[18] in which the Ga sites in Ga-MIL-53(*lt*) have a larger Ga-O bond length and O-Ga-O bond angle distributions (Table 6-A1) versus the (*as*) and (*enp*) phases. The CS tensor parameters are similar among these three powder patterns, however, comparing CS parameters is again wrought with uncertainty due to the dominance of the EFG tensor on spectral appearance.

6.3.2 SSNMR studies of CO_2 adsorption in Ga-MIL-53

Previous reports have indicated that different metal variants of MIL-53 have distinct CO_2 adsorption abilities.[19, 59-60] Ga-MIL-53 exhibits a two-step adsorption of CO_2 at low pressures,[61] hinting a possible MOF phase transition or pore size change during the

CO_2 adsorption process. Unfortunately, detailed pXRD studies of this system during CO_2 adsorption are exceedingly difficult due to the complicated experimental setup and associated challenges such as anisotropic reflection broadening.[19] In this case, $^{69/71}$Ga SSNMR spectra should be sensitive to any CO_2-induced structural changes in Ga-MIL-53, and can act as a valuable probe of local structure to investigate what occurs in this MOF as CO_2 is introduced. Recent ^{13}C SSNMR experiments targeting CO_2 in ordinary and amine-functionalized Al-MIL-53 and Ga-MIL-53 have shown that CO_2 is adsorbed through a hydrogen-bonding interaction with the bridging hydroxyl group that connects the GaO_6 SBUs;[61] this adsorptive interaction should also influence the GaO_6 SBU geometry and have a measurable impact on $^{69/71}$Ga SSNMR spectra.

$^{69/71}$Ga SSNMR experiments have been performed on Ga-MIL-53(*enp*) at a variety of CO_2 loading levels of 0.05, 0.10, 0.20, 0.30, 0.40, and 0.45 CO_2/Ga (by mol) in order to examine the effect of CO_2 adsorption in this system, with ^{71}Ga SSNMR echo spectra at 21.1 T shown in Figure 6-4, ^{69}Ga SSNMR echo spectra at 21.1 T shown in Figure 6-A6, and simulations depicted in Figures 6-A7 and 6-A8, ^{71}Ga WURST-CPMG SSNMR spectra at 9.4 T detailed in Figure 6-5, and all $^{69/71}$Ga NMR parameters from 9.4 and 21.1 T summarized in Table 6-2. While the $^{69/71}$Ga SSNMR echo spectra at 21.1 T are of relatively high resolution and S/N, the spectra at the CO_2 loading levels of 0.10 CO_2/Ga, 0.30 CO_2/Ga and 0.40 CO_2/Ga lack well-defined features in key spectral regions such as the characteristic "horns," thus complicating spectral analysis. In these instances, ^{71}Ga WURST-CPMG experiments at a magnetic field of 9.4 T are quite useful; the increased spectral effects of the QI at this lower magnetic field results in relatively broader ^{71}Ga spectra, the increased spectral dispersion permits easy separation and simulation of the multiple overlapping powder patterns in CO_2-loaded samples of Ga-MIL-53. It should be noted that there is some disagreement between experimental and simulated intensities in

WURST-CPMG spectra at 9.4 T; this is due to anisotropic T_2($^{69/71}$Ga) relaxation across the large frequency range of these powder patterns, which has been noted in the ultra-wideline SSNMR spectra of other nuclei such as ^{195}Pt and ^{35}Cl.[62-63]

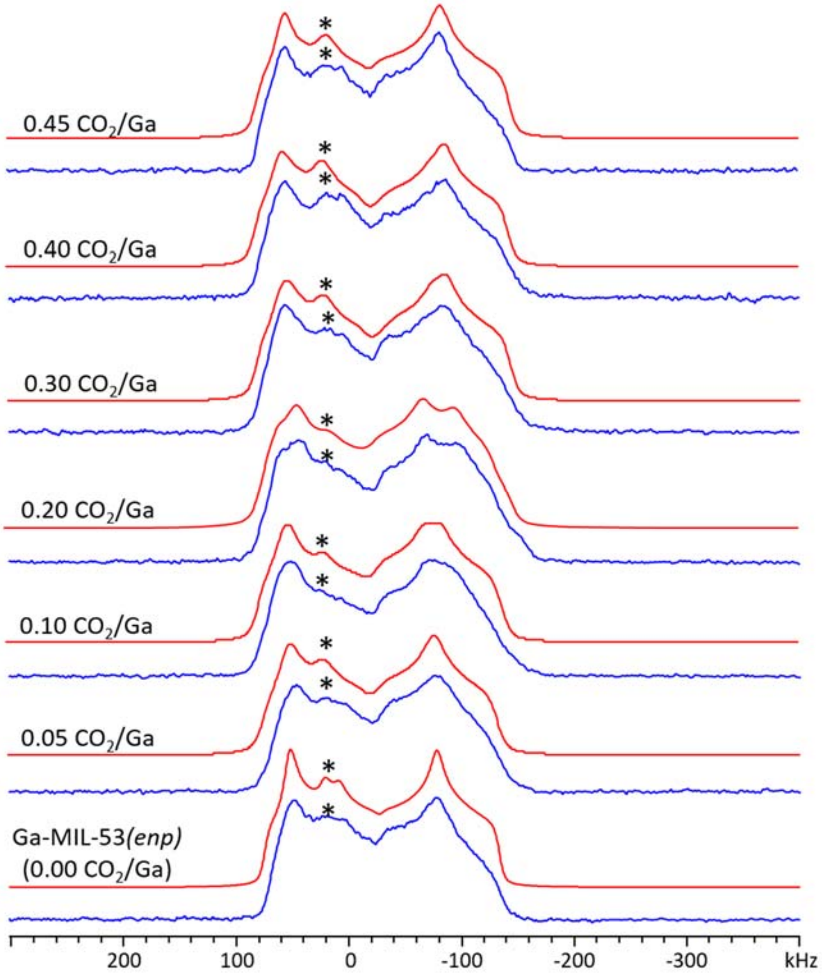

Figure 6-4. Experimental (blue) and simulated (red) ^{71}Ga SSNMR echo spectra of Ga-MIL-53(*enp*) and CO$_2$-loaded Ga-MIL-53 acquired at 21.1 T are shown. The CO$_2$ loading level is listed on the far left of each spectral pair. The central Ga hydroxyl/hydroxide impurity resonance is labeled with an asterisk (*). The corresponding simulations and lineshape deconvolutions of these powder patterns are shown in Figures 6-A7.

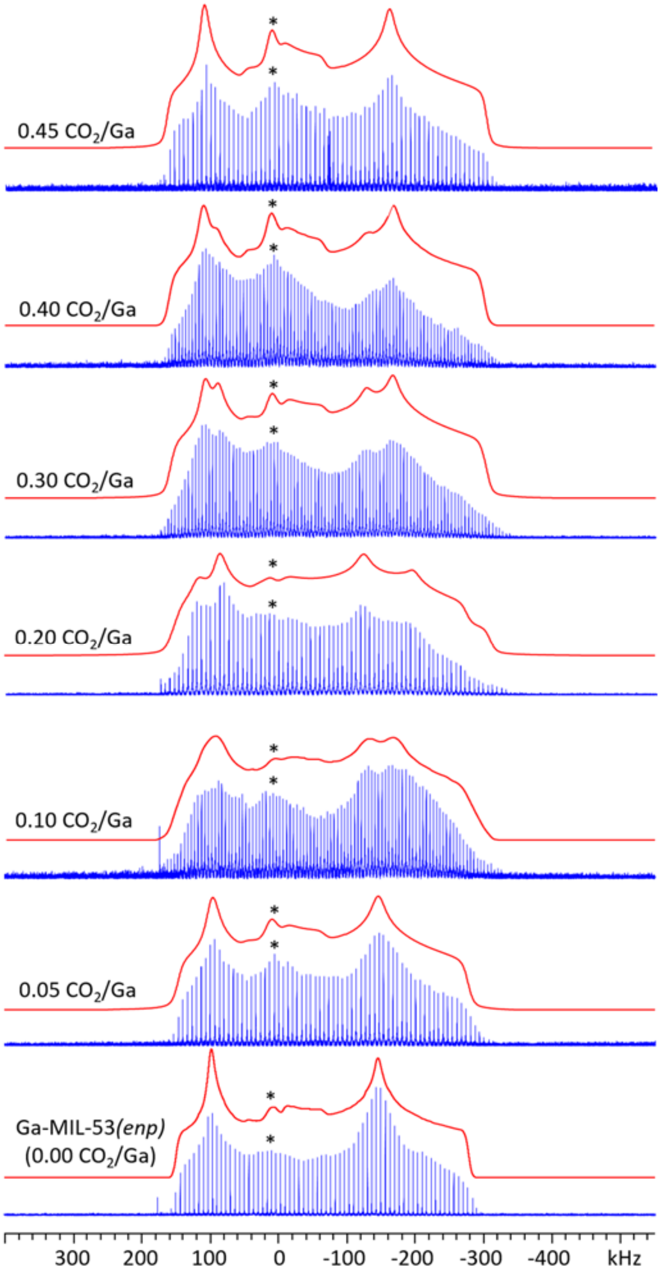

Figure 6-5. ^{71}Ga WURST-CPMG SSNMR spectra of empty Ga-MIL-53(*enp*) and CO$_2$-loaded Ga-MIL-53 at 9.4 T are shown at various CO$_2$ loading levels. The experimental and simulated spectra are shown in blue and red, respectively, with the CO$_2$ loading level indicated on the left of each spectrum. The spectral contribution from the Ga hydroxyl/hydroxide impurities is labeled with an asterisk (*).

Table 6-2. $^{69/71}$Ga NMR parameters of Ga-MIL-53 samples loaded with different amount of CO_2, as obtained from analytical simulations of static $^{69/71}$Ga SSNMR echo spectra at 21.1 T and ^{71}Ga WURST-CPMG spectra at 9.4 T.

Sample	Site (relative intensity)	$C_Q(^{71}Ga)$ (MHz)^a	$C_Q(^{69}Ga)$ (MHz)^a	η_Q	Ω (ppm)	κ	δ_{iso} (ppm)
0.05 CO_2/Ga	Site 1 (1.00)	17.5 (1)	27.8 (2)	0.33 (1)	150 (20)	0.9 (1)	-10 (5)
	Impurity (0.08)	7.5 (1)	12.0 (1)	1.00 (10)	50 (30)	0.0(2)	80 (10)
0.10 CO_2/Ga	Site 1 (1.00)	17.5 (1)	27.8 (2)	0.41 (2)	150 (20)	0.9 (1)	-10 (5)
	Site 2 (1.00)	17.9 (1)	28.5 (1)	0.27 (1)	150 (20)	1.0 (1)	-10 (5)
	Impurity (0.10)	7.5 (1)	12.0 (1)	1.00 (10)	50 (30)	0.0(2)	80 (10)
0.20 CO_2/Ga	Site 1 (1.00)	17.6 (1)	28.4 (2)	0.46 (2)	130 (20)	0.9 (1)	-15 (5)
	Site 2 (0.55)	18.4 (1)	29.2 (2)	0.17 (1)	120 (20)	1.0 (1)	-10 (5)
	Impurity (0.05)	7.5 (1)	12.0 (1)	1.00 (10)	50 (30)	0.0(2)	60 (10)
0.30 CO_2/Ga	Site 1 (0.55)	17.4 (1)	27.8 (2)	0.43 (2)	200 (30)	0.9 (1)	-15 (5)
	Site 2 (1.00)	18.4 (1)	29.2 (1)	0.28 (1)	150 (20)	1.0 (1)	-10 (5)
	Impurity (0.13)	7.5 (1)	12.0 (1)	1.00 (10)	50 (30)	0.0(2)	80 (10)
0.40 CO_2/Ga	Site 1 (0.25)]	17.4 (1)	27.8 (2)	0.42 (2)	200 (30)	0.9 (1)	-15 (5)
	Site 2 (1.00)	18.4 (1)	29.2 (1)	0.29 (1)	150 (20)	1.0 (1)	-10 (5)
	Impurity (0.15)	7.5 (1)	12.0 (1)	1.00 (10)	50 (30)	0.0(2)	80 (10)
0.45 CO_2/Ga	Site 1 (1.00)	18.4 (1)	29.2 (2)	0.31 (1)	130 (20)	1.0 (1)	-10 (5)
	Impurity (0.10)	7.5 (1)	12.0 (1)	1.00 (10)	50 (30)	0.0(2)	70 (10)

^{a} $C_Q(^{71}Ga)$ and $C_Q(^{69}Ga)$ values are related by $C_Q(^{69}Ga) = 1.6\ C_Q(^{71}Ga)$.

The NMR spectra of CO_2-loaded Ga-MIL-53 are profoundly influenced by the CO_2 loading level. At the lowest CO_2 loading level of 0.05 CO_2/Ga, the $^{69/71}$Ga echo spectra at 21.1 T and the ^{71}Ga WURST-CPMG spectrum at 9.4 T appear quite similar to the corresponding spectra of Ga-MIL-53(*enp*). The powder pattern in the $^{69/71}$Ga SSNMR spectra of 0.05 CO_2/Ga Ga-MIL-53 corresponds to $C_Q(^{71}Ga) = 17.5$ (1) MHz, $C_Q(^{69}Ga) = 27.8$ (2) MHz, and $\eta_Q = 0.33$ (1), which are almost identical to the $^{69/71}$Ga NMR parameters in Ga-MIL-53(*enp*) of $C_Q(^{71}Ga) = 17.4$ (1) MHz, $C_Q(^{69}Ga) = 27.8$ (1) MHz, and $\eta_Q = 0.32$

(1), strongly suggesting that the local Ga environment in 0.05 CO_2/Ga loaded Ga-MIL-53(*enp*) is similar to that of empty Ga-MIL-53(*enp*). The CS tensor parameters are also similar between Ga-MIL-53 loaded with 0.05 CO2/Ga and Ga-MIL-53(*enp*), however, the comparisons of CS data are unreliable due to the dominance of the EFG tensor on spectral appearance.

When loading level is increased to 0.1 CO_2/Ga in Ga-MIL-53, there are now two $^{69/71}$Ga powder patterns present, corresponding to the presence of two crystallographically unique Ga sites; for site 1, $C_Q(^{71}Ga)$ = 17.5(1) MHz, $C_Q(^{69}Ga)$ = 27.8(2) MHz, and η_Q = 0.41(2), while for site 2, $C_Q(^{71}Ga)$ = 17.9(1) MHz, $C_Q(^{69}Ga)$ = 28.5(1) MHz, and η_Q = 0.27(1). The C_Q value of site 1 is similar to that of the only Ga site in Ga-MIL-53(*enp*), indicating their respective GaO_6 SBUs are of a similar geometry, however, the η_Q values between site 1 and Ga-MIL-53(*enp*) are slightly different, which indicates differences in local structure between these two species. In contrast, the C_Q value of site 2 is larger than that of Ga-MIL-53(*enp*) and exhibits a relatively lower η_Q value, suggesting the corresponding GaO_6 SBUs are dissimilar to those of site 1 and Ga-MIL-53(*enp*). Phases which have larger pore dimensions, such as Ga-MIL-53(*as*), Ga-MIL-53(*ht*), and Ga-MIL-53(*lt*), are linked to elevated $C_Q(^{69/71}Ga)$ values (Table 6-1); with this in mind, we suggest that Ga site 2 in in 0.1 CO_2/Ga loaded Ga-MIL-53 corresponds to GaO_6 SBUs in pores with relatively larger dimensions than those of Ga-MIL-53(*enp*), while Ga site 1 is linked to GaO_6 SBUs in pores of similar dimensions to Ga-MIL-53(*enp*).

At a CO_2 loading level of 0.20 CO_2/Ga, two separate powder patterns are clearly visible in $^{69/71}$Ga SSNMR spectra at 21.1 T and ^{71}Ga SSNMR spectra at 9.4 T, which again indicates the presence of two crystallographically unique Ga sites and two distinct kinds of GaO_6 SBUs with different Ga-O bond lengths and O-Ga-O bond angles; this remains consistent with our hypothesis of a Ga-MIL-53(*int*) phase featuring two different pore sizes. Ga site 1, which corresponds to GaO_6 SBUs making up the smaller empty pores in Ga-MIL-53(*int*), is associated with $C_Q(^{71}Ga)$ = 17.6(1) MHz, $C_Q(^{69}Ga)$ = 28.4(2) MHz, and η_Q = 0.46. These values are quite similar to those of Ga site 1 in the 0.05 and 0.10 CO_2/Ga loaded samples, and suggests that no significant alteration to the empty closed pore geometry has occurred. In contrast, there has been a change in C_Q values for powder pattern 2: $C_Q(^{71}Ga)$ and $C_Q(^{69}Ga)$ values have increased from 17.9(1) and 28.5(1) MHz at a loading level of 0.10 CO_2/Ga to 18.4(1) and 29.2(2) MHz, respectively, at a loading level of 0.20 CO_2/Ga. Since increases in C_Q values are generally linked to larger pore dimensions in Ga-MIL-53 (*vide supra*, Table 6-1), the increase in $C_Q(^{69/71}Ga)$ of Ga site 2 suggests that the open, CO_2-occupied pores of Ga-MIL-53(*int*) are larger at a loading level of 0.20 CO_2/Ga.

A comprehensive XRD and computational study of CO_2 loading in the analogous Sc-MIL-53 and Fe-MIL-53 MOF has indicated the existence of an intermediate, or (*int*), phase of MIL-53 at low CO_2 loading levels.[19, 64] In Sc-MIL-53(*int*) and Fe-MIL-53(*int*), there are two types of pores that exist simultaneously in the same phase: very narrow unoccupied or “closed” pores, as well as CO_2-occupied “open” pores of relatively larger dimensions.[19, 64] The presence of a Ga-MIL-53(*int*) phase strongly agrees with our $^{69/71}Ga$ SSNMR data and permits assignment of experimental powder patterns to crystallographic sites. Ga site 1 denoted in the NMR data corresponds to GaO_6 SBUs constituting the empty and very narrow pores in Ga-MIL-53(*int*) which are of a similar dimension to Ga-MIL-53(*enp*), while Ga site 2 arises from GaO_6 SBUs which make up the relatively larger, open pores in Ga-MIL-53(*int*) that are occupied by CO_2 guests. The existence of two different pore sizes in the same material also agrees well with the reported observation of a two-step CO_2 adsorption isotherm at low pressure in Ga-MIL-53.[61]

The $^{69/71}Ga$ SSNMR spectra of CO_2-loaded Ga-MIL-53 continue to evolve as the loading level is increased to 0.30 CO_2/Ga. There are again two powder patterns evident, which confirms the presence of two distinct types of GaO_6 SBUs and two different pore structures in Ga-MIL-53(*int*). Notably, there are no significant changes in C_Q values when the CO_2 loading level is increased from 0.20 to 0.30 CO_2/Ga; in contrast, the η_Q value of Ga site 2 increases from 0.17 to 0.28 with the change in loading levels. It should be noted that 0.28 remains a relatively low η_Q value. The change in η_Q values is indicative of some very minor alteration in Ga local environment when more CO_2 molecules have been introduced into the channels of Ga-MIL-53, however, the very similar C_Q values and mutually low η_Q values at both loading levels suggest that the physical pore dimensions are not drastically altered between these two samples. In this instance, the most significant development is the change in relative intensities between the powder patterns corresponding to the two Ga sites. The powder pattern of Ga site 1, which corresponds to Ga near the empty small pores, now accounts for only ca. 50 % the relative intensity of the Ga site 2 resonance, which represents Ga proximate to the larger CO_2-occupied pores in Ga-MIL-53(*int*). The interpretation of this data is straightforward; as more CO_2 is introduced to the Ga-MIL-53 and this flexible MOF "inhales," an increasing fraction of the empty pores are filled and enlarged by CO_2, shifting spectral intensity from the site 1 resonance to that of site 2. With this in mind, it must be noted that there is an unexpected increase of spectral intensity corresponding to site 2, along with a decrease in site 1 intensity, at the CO_2 loading level of 0.10 CO_2/Ga; this does not follow the overall trends in intensity evolution with CO_2 loading and is denoted by the aberration in Figure 6-6. At this time, we cannot identify a source for this intensity anomaly, although experimental error and uncertainty in simulations may certainly play some part.

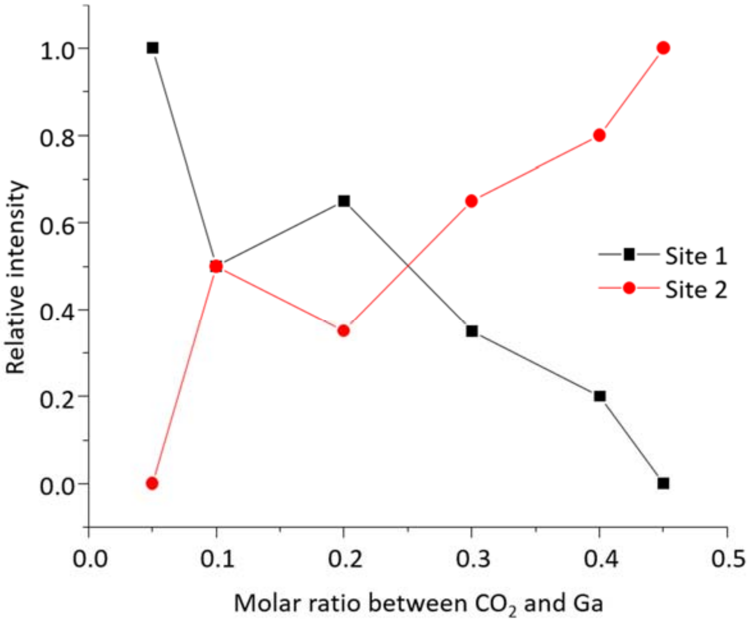

Figure 6-6. The evolution of the relative intensity between the two distinct Ga powder patterns and corresponding Ga site populations in Ga-MIL-53 during CO_2 adsorption.

When the CO_2 loading level rises from 0.30 to 0.40 CO_2/Ga in Ga-MIL-53, there is no significant change in observed $^{69/71}$Ga NMR parameters, however, there is again a reallocation of spectral intensity. The Ga powder pattern assigned to site 1 is now only 25 % intense as that assigned to site 2, which continues the trend observed from the 0.20 to 0.30 CO_2/Ga loading levels (Figure 6-6). As Ga-MIL-53(*int*) "inhales" additional CO_2 guests, more of the small, closed pores become occupied by CO_2 and exhibit expanded dimensions. This change is reflected by the migration of spectral intensity to the site 2 resonance representing GaO_6 SBUs next to the larger open, occupied pores in Ga-MIL-53(*int*) (Figure 6-6).

At the loading level of 0.45 CO_2/Ga, there is only a single Ga powder pattern evident in the well-defined $^{69/71}$Ga SSNMR spectra, which indicates that all GaO_6 SBUs share nearly identical short-range structures, and a single homogenous pore system with a well-defined dimension is present in the Ga-MIL-53 structure. Simulations of the $^{69/71}$Ga SSNMR spectra yield $C_Q(^{71}Ga)$ = 18.4 (1) MHz, $C_Q(^{69}Ga)$ = 29.2 (2) MHz, and η_Q = 0.31 (1) which are very similar to the NMR parameters associated with the larger, open, CO_2-occupied channels in Ga-MIL-53(*int*) at lower CO_2 loading levels; the dimensions of the single pore type in Ga-MIL-53 at a loading level of 0.45 CO_2/Ga are likely the same as those of the open, CO_2-occupied pores in Ga-MIL-53(*int*) at intermediate CO_2 loading levels between 0.10 and 0.40 CO_2/Ga. Finally, since there only one type of MOF pore present (Figure 6-6), and these pores are of similar dimensions to those in other CO_2-loaded samples, it appears that all pores in 0.45 CO_2/Ga Ga-MIL-53 are equally and homogenously occupied by guest CO_2 molecules. Prior studies on the analogous Fe-MIL-53 have indicated that the channels of Fe-MIL-53 were partially occupied by CO_2 at a loading level of 0.22 CO_2/Fe, while the pores of Fe-MIL-53 were fully occupied by CO_2 at a loading level of 0.63 CO_2/Fe.[64]

It should be noted that the $^{69/71}$Ga SSNMR data in this series of CO_2-loaded Ga-MIL-53 samples suggests the presence of a re-entrant phase transition[65] that occurs as progressively more CO_2 is loaded into empty Ga-MIL-53. The phase of Fe-MIL-53(*enp*) is monoclinic,[15, 66] while the phase of in Fe-MIL-53(*int*) is known to be triclinic.[19, 64] Interestingly, CO_2 fully loaded into Fe-MIL-53 results in the return to a monoclinic phase;[19, 64] this MOF undergoes a re-entrant phase transition from the monoclinic to triclinic and back to monoclinic phases as CO_2 loading increases. The $^{69/71}$Ga SSNMR data suggests that such behavior also occurs in Ga-MIL-53: the (*enp*) phase is known to be monoclinic[18] and gives rise to a single Ga powder pattern, the (*int*) phase present at CO_2 loading levels between 0.10 and 0.40 CO_2/Ga gives rise to two Ga powder patterns with distinct NMR parameters, while CO_2 fully loaded into Ga-MIL-53 brings about the return to a single Ga powder pattern with a similar η_Q and slightly larger C_Q value compared to the (*enp*) phase. Based on this $^{69/71}$Ga SSNMR data and prior reports of phases in CO_2-loaded Fe-MIL-53,[19, 64] it appears that the monoclinic Ga-MIL-53(*enp*)[18] undergoes a phase change to Ga-MIL-53 (*int*), which is likely triclinic, and then changes back to a monoclinic phase in fully CO_2-loaded Ga-MIL-53, meaning that Ga-MIL-53 indeed undergoes a re-entrant phase transition. The existence of re-entrant transitions or behavior similar to re-entrant transitions as a result of different stimuli in the Al-MIL-53 analogue have also been investigated.[67-69]

6.3.3 Ga-MIL-53 loaded with organic guests

It is evident that the guest adsorption and the breathing effect in this flexible Ga-MIL-53 framework have a readily detectable influence on $^{69/71}$Ga SSNMR spectra. Previous studies have demonstrated that MIL-53 is a potential material for the storage and separation of organic molecules.[70-72] With this in mind, the adsorption of various organic molecules and their effect on the breathing effect, long-range structure, and local Ga environment in Ga-MIL-53 have been investigated using a combination of TGA, pXRD, and $^{69/71}$Ga SSNMR.

TGA of Ga-MIL-53 loaded with organic guests. For TGA studies, all Ga-MIL-53 samples were fully loaded (*i.e.,* saturated) with organic compounds using a solvent exchange method at high temperatures (see Experimental section). To probe the effects of molecular size, shape, and solvent polarity, four non-polar compounds (para-xylene (PX), meta-xylene (MX), benzene, and ethylbenzene) as well as two polar compounds (dimethylformamide (DMF) and diethylformamide (DEF)) were introduced as guests.

TGA experiments reveal different relative weight losses depending on the nature of the guest adsorbed in Ga-MIL-53 (Figure 6-7), with the results and calculated adsorbate loading amounts listed in Table 6-3. It appears that Ga-MIL-53 can adsorb 4.2 MX molecules/unit cell, which is the most of all adsorbates examined. Interestingly, Ga-MIL-53 has a reduced capacity for loading the isomeric PX, and adsorbs 3.5 PX molecules/unit cell. The different loading levels of PX and MX adsorbates hint that these xylene isomers may engage in distinct host-guest and guest-guest (i.e., π-stacking) interactions within Ga-MIL-53, much like in the case of Fe-MIL-53.[26] Another sign of distinct behavior between MX and PX guests can be found in the shape of the TGA plots for Ga-MIL-53. The TGA curve of PX-loaded Ga-MIL-53 (Figure 6-7) is very similar to that of PX loaded Fe-MIL-53, which has a four-step desorption procedure.[26] However, the TGA curve of MX-loaded Ga-MIL-53 is similar to that of ortho-xylene (OX)-loaded Fe-MIL-53, which has a three-step desorption procedure.[26] The different number of segments in these stepwise desorption procedures again suggests that the PX and MX isomers engage in different host-guest and guest-guest interactions within the framework, which gives rise to different long-range packing geometries and specific adsorption capacities in Ga-MIL-53.

Table 6-3. TGA results for Ga-MIL-53 loaded with select organic adsorbates. All TGA curves are illustrated in Figure 6-7.

Adsorbate	**TGA weight loss (%)**	**Ga : adsorbate ratio**	**Adsorbate molecules/unit cell**
DEF	23	1 : 0.75	3.0
DMF	21	1 : 0.91	3.6
Ethylbenzene	20	1 : 0.59	2.4
Benzene	20	1 : 0.81	3.2
***m*-Xylene**	31	1 : 1.06	4.2
***p*-Xylene**	27	1 : 0.88	3.5

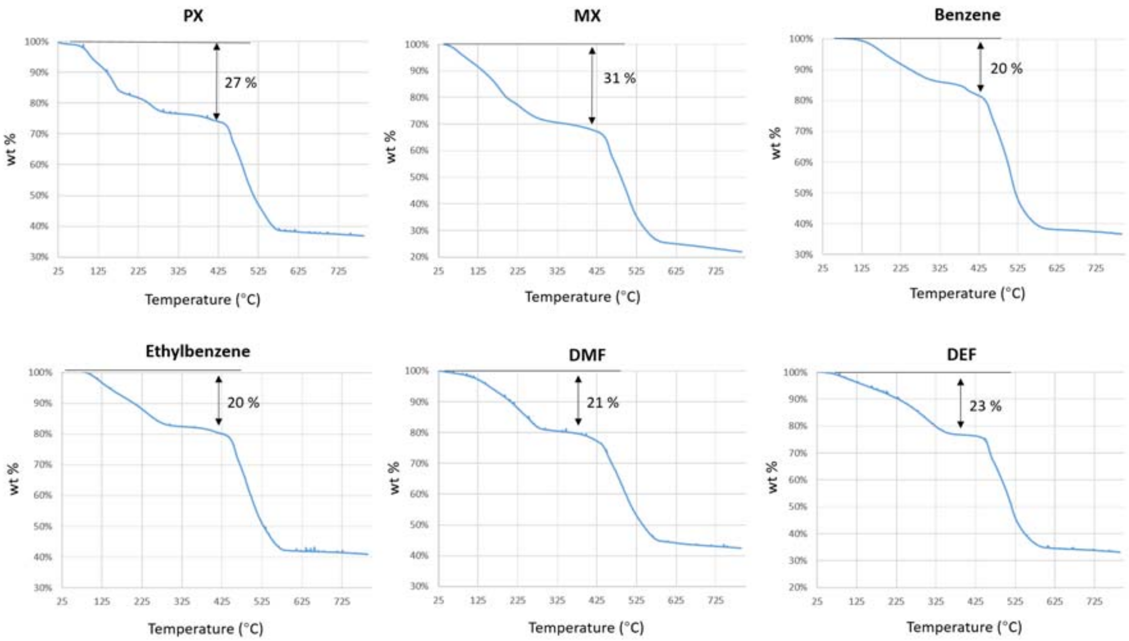

Figure 6-7. The experimental TGA curves for Ga-MIL-53 saturated with different organic adsorbates are shown, with the title above each graph denoting the specific adsorbate. Abbreviations are as follows: PX = para-xylene, MX = meta-xylene, DMF = dimethylformamide, and DEF = diethylformamide.

Ga-MIL-53 exhibits relatively lower capacities for adsorption of the other two non-polar adsorbates, benzene and ethylbenzene, with maximum loading levels of 3.2 benzene molecules per unit cell and 2.5 ethylbenzene molecules per unit cell; much like the case of PX and MX, the different adsorption capacities of benzene and ethylbenzene hints that these two adsorbates engage in different host-guest and guest-guest interactions inside the Ga-MIL-53 channels, which gives rise to unique packing densities and the observed differences in TGA weight losses.[73-74] A disfavored uptake of ethylbenzene was also observed in Al-MIL-53 and MIL-47.[70-71]

TGA indicates that the polar organic adsorbate DMF is adsorbed at a level of 3.6

DMF molecules per unit cell, which is the second highest adsorption amount of all guests tested in this study. This results, coupled with the highly polar nature of DMF, suggests the DMF molecules engage in host-guest and guest-guest interactions of significant strength within Ga-MIL-53. In contrast, the loading capacity of DEF in Ga-MIL-53 is only 3.0 DEF molecules per unit cell, despite the minor structural differences between DMF and DEF. The larger molecular size of DEF and its less polar nature prohibit host-guest and guest-guest interactions (*i.e.*, hydrogen bonding) on the magnitude of those for DMF, reducing the overall packing density of DEF in MIL-53-Ga. In order to understand the guest-induced differences in the long-range structure and phase of Ga-MIL-53, a detailed set of pXRD experiments were performed.

pXRD of organic guest-loaded Ga-MIL-53. The pXRD patterns of adsorbate-loaded (*i.e.*, saturated) Ga-MIL-53 samples are illustrated in Figure 6-8. Significant differences in the 2θ positions of the various characteristic reflections can be observed for all samples, which denotes significant differences in pore size, pore dimensions, and the packing of guest molecules.

Ga-MIL-53 samples loaded with PX and MX give rise to similar pXRD patterns, but close inspection reveals that the reflections in the 2θ angle regions of 11 – 14 ° and 18 – 20 ° have different positions and relative intensities for PX versus MX. The pXRD patterns suggest that PX and MX loaded Ga-MIL-53 have similar structures, however, the slight differences in pXRD patterns suggests some minor change in pore dimensions between these two phases. Comparing these two pXRD patterns with previous pXRD studies involving xylene loaded Fe-MIL-53, the pXRD pattern of PX-loaded Ga-MIL-53 is similar to that reported for PX-loaded Fe-MIL-53, while the pXRD pattern of MX-loaded Ga-MIL-53 is also similar to that of MX-loaded Fe-MIL-53,[26] implying that Fe-MIL-53 and Ga-MIL-53 have closely related long-range structures. PX and MX molecules were found to exhibit different packing structures inside Fe-MIL-53, owing to differences in host-guest and guest-guest interactions, and resulting in the observation of two similar but at the same time different phases.[26] By extension, it is reasonable to assume that the PX molecules inside Ga-MIL-53 have a similar packing motif as PX molecules within Fe-MIL-53, while the MX molecules adsorbed in Ga-MIL-53 should be arranged much like MX within Fe-MIL-53.

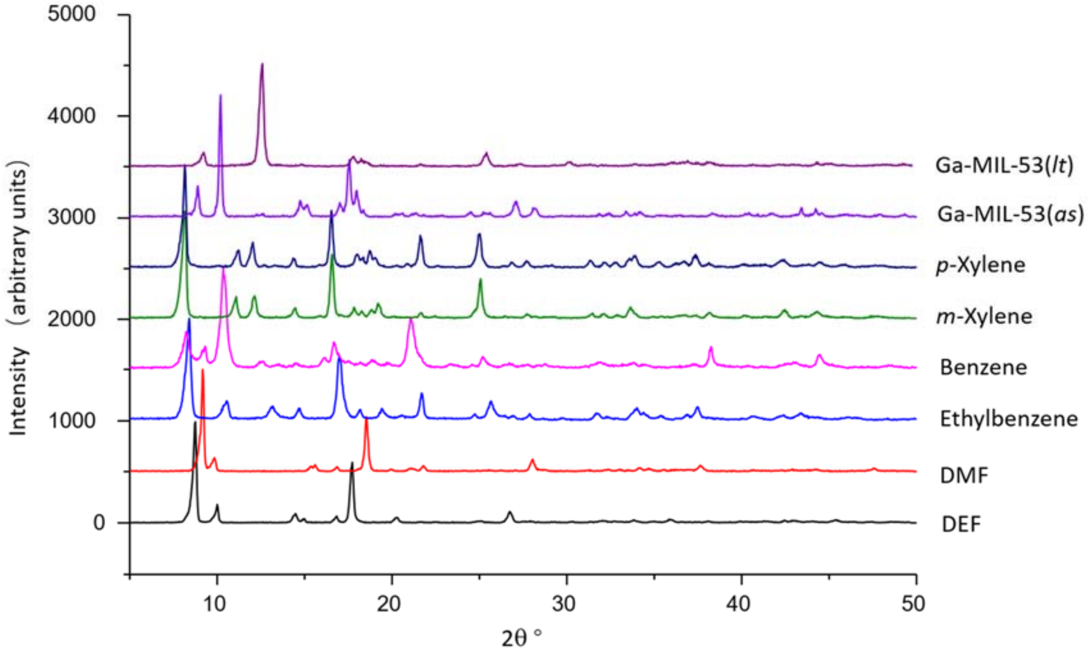

Figure 6-8. The pXRD patterns of Ga-MIL-53(*lt*), Ga-MIL-53(*as*), and Ga-MIL-53 loaded with selected adsorbates are shown. The distinct pXRD patterns indicate that adsorption of different guests gives rise to unique Ga-MIL-53 phases.

The lowest-angle reflections in the pXRD patterns of Ga-MIL-53 loaded with benzene and ethylbenzene are shifted to higher 2θ angles versus those of PX and MX loaded samples, indicating that the *d*-spacing (*i.e.,* pore size) is smaller when benzene and ethylbenzene guests are present. Since both benzene and ethylbenzene are non-polar adsorbates, the primary host-guest interaction in this case is likely a relatively weak π-π interaction of the adsorbate and framework benzene rings. In order to maximize π-π interactions with benzene and ethylbenzene guests, it appears the pore dimensions are reduced in Ga-MIL-53, as evidenced by (i) the reduced *d*-spacing in pXRD patterns, and (ii) the relatively low maximum loading levels of benzene and ethylbenzene (Table 6-3). The pXRD pattern of ethylbenzene loaded Ga-MIL-53 is very similar to the pXRD pattern of ethylbenzene loaded MIL-47,[70] but distinct from that of Al-MIL-53,[27, 75] suggesting that ethylbenzene loaded Ga-MIL-53 has a similar long-range structure as MIL-47. Interestingly, the differences between the pXRD patterns of Ga-MIL-53 and Al-MIL-53 loaded with ethylbenzene show that ethylbenzene guests pack differently in these two structurally similar MOFs.

The pXRD pattern of DMF and DEF loaded Ga-MIL-53 exhibit low-angle reflections at higher values of 2θ versus all four non-polar guests, indicating a relatively small *d*-spacing and reduced pore size in this MOF when polar solvents are present. Considering the relatively high loading levels of DMF and DEF in Ga-MIL-53 indicated from TGA (Table 6-3), this MOF likely “exhales” and reduces pore size in the presence of these solvents to maximize the strong host-guest interactions between the polar adsorbates and the polar components of the MOF framework (*i.e.*, bridging –OH groups between GaO_6 SBUs). In this sense, pXRD results indicate that polar organic compounds have stronger host-guest interactions with Ga-MIL-53 and induce a smaller pore size versus non-polar organic adsorbates.

pXRD and TGA experiments have both indicated that substantial host-guest interactions exist between guest organic molecules and the Ga-MIL-53 MOF. SSNMR of metal centres has proven valuable for investigating host-guest interactions in MIL-53; for example, ^{27}Al MAS SSNMR experiments have indicated that organic adsorbates within

Al-MIL-53 can interact with the framework, modify the short-range structure of the AlO_6 octahedral SBUs, and influence local electronic environments.[27] With this in mind, $^{69/71}Ga$ SSNMR experiments at 21.1 T and 9.4 T have been employed to investigate local structure in Ga-MIL-53 samples loaded with guest organic molecules.

^{71}Ga SSNMR at 9.4 T of Ga-MIL-53 loaded with organic guests at low levels. Ga-MIL-53 samples with organic adsorbates loaded at a low level of 0.1 adsorbates/Ga were examined by acquiring ^{71}Ga WURST-CPMG spectra at 9.4 T, with the resulting spectra shown in Figure 6-A9 and corresponding NMR parameters listed in Table 6-A3. ^{71}Ga WURST-CPMG spectra of Ga-MIL-53 loaded with the non-polar organic adsorbates PX, MX, benzene, and ethylbenzene feature a single powder pattern resembling that of empty Ga-MIL-53(*enp*), along with a second narrow powder pattern originating from the Ga-H_2O impurity species (vide supra). The similarities in appearance and NMR parameters between the spectra of empty Ga-MIL-53(*enp*) and the spectra of Ga-MIL-53 loaded with non-polar guests suggests that these adsorbates have very little effect on the geometry of GaO_6 SBUs at this low loading level. An interesting note is that in these spectra, the impurity phase appears especially intense versus other forms of Ga-MIL-53; these non-polar adsorbates are linked to accelerated $T_2(^{71}Ga)$ relaxation in the GaO_6 SBUs of the MOF, which is likely due to rapidly modulating Ga-guest dipolar couplings as a result of guest dynamics, resulting in preferential enhancement of the impurity powder pattern. The observed intensity of the central resonance is even higher when the polar organic DMF and DEF are loaded within Ga-MIL-53 at the same 0.1 adsorbate/Ga loading level (Figure 6-A9), indicating that adsorption of polar organic molecules is linked to even more rapid $T_2(^{71}Ga)$ relaxation. The extremely broad underlying powder pattern originating from the GaO_6 SBUs in the ^{71}Ga SSNMR spectrum of 0.1 DMF/Ga loaded Ga-MIL-53 also suggests DMF can greatly influence the geometry of the GaO_6 SBUs, perhaps through binding to the bridging –OH groups that connect GaO_6 octahedra.

In order to more fully investigate the influence of organic adsorbates on the local Ga environment, ^{71}Ga WURST-CPMG SSNMR experiments at 9.4 T were performed on Ga-MIL-53 samples that were fully loaded (*i.e.*, saturated) by organic adsorbates. Due to the strong influence of adsorbates on T_2(^{71}Ga) and the sheer volume of adsorbates present, the resulting spectra are dominated by the central impurity resonance (Figure 6-A10). In order to bypass the problems associated with short T_2($^{69/71}$Ga) times in adsorbate-loaded Ga-MIL-53, SSNMR spectra were acquired at 21.1 T using a solid-echo pulse sequence.

$^{69/71}$Ga SSNMR at 21.1 T of Ga-MIL-53 loaded with organic guests at high levels. The experimental and simulated ^{71}Ga SSNMR spectra at 21.1 T are illustrated in Figure 6-9, while, the experimental and simulated ^{69}Ga NMR spectra at the same field are exhibited in Figure 6-A11, with simulations of the individual $^{69/71}$Ga powder patterns shown in Figure 6-A12 and A13, and NMR parameters summarized in Table 6-4. All NMR spectra indicate the presence of a single unique Ga site in Ga-MIL-53, along with the usual Ga oxide/hydroxide impurity. EFG tensor parameters readily distinguish the individual samples of Ga-MIL-53, but the CS parameters are very similar, and it must again be noted that comparisons of CS data are unreliable due to the dominance of the EFG tensor on spectral appearance in this instance.

The $^{69/71}$Ga SSNMR echo spectra of PX and MX saturated Ga-MIL-53 exhibit a similar lineshape and are associated with nearly identical NMR parameters, suggesting their GaO_6 SBUs and short-range structures are quite alike. In PX saturated Ga-MIL-53, C_Q(^{71}Ga) = 20.2 (1) MHz, C_Q(^{69}Ga) = 32.1 (2) MHz, and η_Q = 0.13 (1), while for MX saturated Ga-MIL-53, C_Q(^{71}Ga) = 20.5 (1) MHz, C_Q(^{69}Ga) = 32.7 (3) MHz, and η_Q = 0.15 (1). The very similar short-range structure about Ga in these two samples is linked to the similar pore dimensions of PX and MX saturated Ga-MIL-53 indicated from pXRD; as seen in the prior SSNMR results regarding the four basic forms of Ga-MIL-53 and of CO_2-loaded Ga-MIL-53, $^{69/71}$Ga NMR parameters in this system are extremely sensitive to the pore dimensions. The increase in C_Q($^{69/71}$Ga) in MX and PX saturated Ga-MIL-53 versus empty Ga-MIL-53(*enp*) is due to the larger pore size in the guest-saturated MOF.

Table 6-4. $^{69/71}$Ga NMR tensor parameters of Ga-MIL-53 samples loaded with different adsorbates, which were obtained from analytical simulations of static $^{69/71}$Ga SSNMR echo spectra at 21.1 T.

Guest	Site (relative intensity)	C_Q (^{71}Ga) (MHz)[a]	C_Q (^{69}Ga) (MHz)[a]	η_Q	Ω (ppm)	κ	δ_{iso} (ppm)
DEF	Site 1 (1.00)	22.4 (1)	35.7 (2)	0.13 (1)	200 (30)	1.0 (1)	-5 (5)
	Impurity (0.07)	7.5 (1)	12.0 (1)	1.00 (10)	50 (20)	0.0(2)	50 (10)
DMF	Site 1 (1.00)	23.4 (1)	37.3 (2)	0.20 (2)	200 (30)	1.0 (1)	-10 (5)
	Impurity (0.55)	7.5 (1)	12.0 (1)	1.00 (10)	60 (20)	0.0(2)	55 (10)
Ethylbenzene	Site 1 (1.00)	19.9 (1)	31.6 (2)	0.06 (1)	160 (30)	1.0 (1)	-5 (5)
	Impurity (0.50)	7.5 (1)	12.0 (1)	1.00 (10)	50 (30)	0.0(2)	45 (10)
Benzene	Site 1 (1.00)	18.9 (1)	30.1 (2)	0.34 (1)	160 (30)	1.0 (1)	-5 (5)
	Impurity (0.15)	7.5 (1)	12.0 (1)	1.00 (10)	50 (30)	0.0(2)	50 (10)
***m*-Xylene**	Site 1 (1.00)	20.5 (1)	32.7 (3)	0.15 (1)	160 (30)	1.0 (1)	-5 (5)
	Impurity (0.20)	7.5 (1)	12.0 (1)	1.00 (10)	50 (30)	0.0(2)	55 (10)
***p*-Xylene**	Site 1 (1.00)	20.2 (1)	32.1 (2)	0.13 (1)	160 (30)	1.0 (1)	-5 (5)
	Impurity (0.55)	7.5 (1)	12.0 (1)	1.00 (10)	50 (30)	0.0(2)	50 (10)

[a] C_Q(^{71}Ga) and C_Q(^{69}Ga) values are related by C_Q(^{69}Ga) = 1.6 C_Q(^{71}Ga).

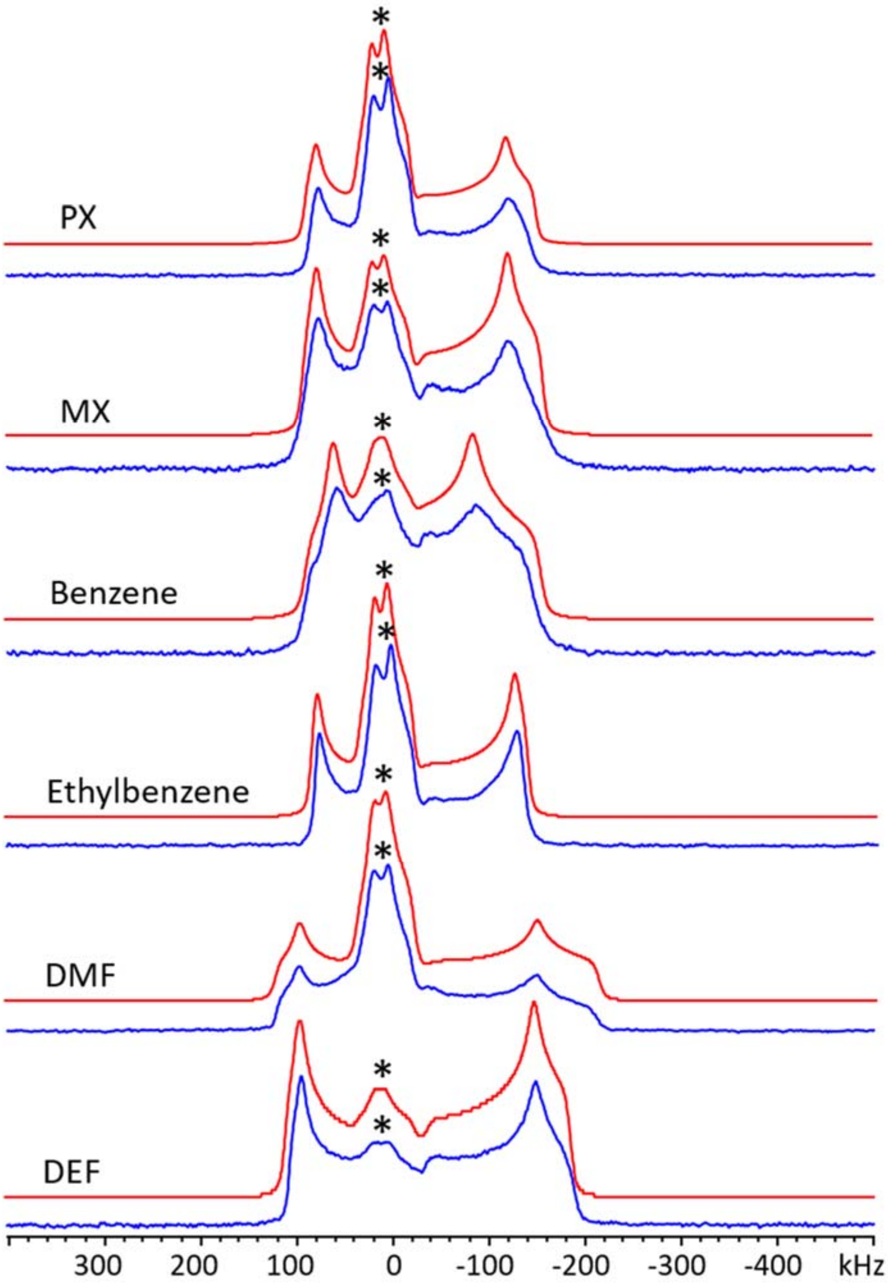

Figure 6-9. ^{71}Ga SSNMR echo spectra of guest-loaded Ga-MIL-53 samples at 21.1 T. Simulated spectra are shown in red and experimental spectra are depicted in blue. The Ga hydroxyl/hydroxide impurity is labeled with an asterisk (*).

The $^{69/71}$Ga powder patterns of benzene and ethylbenzene saturated Ga-MIL-53 exhibit smaller C_Q values than the MX and PX saturated samples. Benzene saturated Ga-MIL-53 is associated with $C_Q(^{71}Ga) = 18.9$ (1) MHz and $C_Q(^{69}Ga) = 30.1$ (2) MHz, while ethylbenzene saturation gives rise to $C_Q(^{71}Ga) = 19.9$ (1) MHz and $C_Q(^{69}Ga) = 31.6$ (2) MHz. These low C_Q values can again be linked to the pore size of Ga-MIL-53; pXRD revealed that the pore sizes associated with these guests were smaller than those linked to MX and PX in Ga-MIL-53, which should give rise to a lower C_Q value in this system. Interestingly, the η_Q value of ethylbenzene saturated Ga-MIL-53 is only 0.06(1), while the η_Q value of benzene saturated Ga-MIL-53 is a sizeable 0.34(1). The higher η_Q value in benzene saturated Ga-MIL-53 indicates a generally lower level of rotational symmetry in the GaO_6 SBUs; this could be due to the specific packing geometry of benzene within the Ga-MIL-53 channels, along with the resulting presence of benzene proximate to Ga and the associated effects on the $^{69/71}$Ga EFG tensor. In general, these distinct $^{69/71}$Ga echo SSNMR spectra indicate that different non-polar organic adsorbates loaded Ga-MIL-53 are associated with unique short-range Ga local structures, and by extension, different phases of Ga-MIL-53. The specific nature of the non-polar organic adsorbate within Ga-MIL-53 gives rise to distinct host-guest and guest-guest interactions, which could influence the local GaO_6 structures by altering the associated Ga-O bond lengths and O-Ga-O bond angles.

The $^{69/71}$Ga SSNMR echo spectra of the polar DMF and DEF guest saturated within Ga-MIL-53 are quite interesting. Unlike when non-polar adsorbates were saturated within Ga-MIL-53, where the small pore size gives rise to relatively smaller $C_Q(^{69/71}Ga)$ values, very large $C_Q(^{69/71}Ga)$ values are observed in DMF and DEF saturated Ga-MIL-53, despite the small pore size indicated from pXRD. In DMF saturated Ga-MIL-53, $C_Q(^{71}Ga) = 23.4$ (1) MHz, $C_Q(^{69}Ga) = 37.3$ (2) MHz, and $\eta_Q = 0.20$ (2), while for DEF saturated Ga-MIL-

53, $C_Q(^{71}Ga)$ = 22.4 (1) MHz, $C_Q(^{69}Ga)$ = 35.7 (2) MHz, and η_Q = 0.13 (1). These elevated $C_Q(^{69/71}Ga)$ values reflect decreased spherical symmetry in the GaO_6 SBUs, perhaps due to a non-uniform distribution of Ga-O bond lengths and O-Ga-O bond angles. The distortions away from octahedral symmetry in these SBUs could be caused by the strong host-guest interactions between the polar DMF or DEF molecules and the Ga-MIL-53 framework, which likely target the bridging –OH groups connecting GaO_6 SBUs. The very strong host-guest interactions likely also shrink the channels, which results in narrower pore dimensions versus non-polar organic adsorbates loaded within Ga-MIL-53.

In summary, the combination of TGA, XRD, and SSNMR has shown that the short-range structure of GaO_6 is strongly influenced by the presence and nature of adsorbed guests, the guest loading amount, and the strength of host-guest interactions. Paired with the difference in C_Q and η_Q values between the different organic adsorbates observed in this study, this data suggests that $^{69/71}$Ga SSNMR can also serve as valuable probe of the guest identity and loading level within Ga-MIL-53.

6.4 Conclusions

$^{69/71}$Ga SSNMR experiments are a powerful tool to probe the number of crystallographically distinct Ga sites, their respective local structures, the presence of host-guest interactions, and the phase of the Ga-MIL-53 metal-organic framework. By extension, this approach can also be applied to many other Ga-containing MOFs where ultra-wideline NMR powder patterns reign and MAS techniques are typically ineffective. The $^{69/71}$Ga EFG tensor parameters are very sensitive to the particular crystallographic phases and distortions of octahedral GaO_6 SBUs within the *as*, *ht*, *enp* and *lt* phases of Ga-MIL-53.

$^{69/71}$Ga SSNMR parameters are also very sensitive to the subtle differences in local structure and MOF phase that gradually occur with CO_2 adsorption at various loading levels. Our experiments confirm that host-guest interactions between CO_2 molecules and the bridging –OH groups that serve as adsorption sites in Ga-MIL-53, paired with changes in the pore size and geometry, significantly influence the GaO_6 SBU geometry. $^{69/71}$Ga SSNMR experiments, along with *a priori* knowledge,[15, 19] strongly suggests that CO_2 guests first occupy only some of the available empty pores in Ga-MIL-53 at lower loading levels, and then proceed to populate all of the empty channels as the CO_2 loading level increases to ca. 0.45 CO_2/Ga. The $^{69/71}$Ga SSNMR experiments accurately monitor the CO_2 adsorption process and the resulting distortions in GaO_6 SBUs; our data suggests that a re-entrant phase transition occurs in the system as empty Ga-MIL-53 is progressively occupied by increasingly higher amounts of CO_2. These results are very encouraging and should prove useful for further studies of CO_2 adsorption in similar flexible MOFs, the use of MOFs as CO_2 sensors, and in the design of new MOFs with higher CO_2 adsorption capacities.

The combination of TGA, pXRD and SSNMR experiments have clearly demonstrated that specific organic adsorbates are connected to distinct phases in the Ga-MIL-53 MOF. The interactions between organic adsorbates and the Ga-MIL-53 framework, paired with alterations of the pore size and shape, distinctly influence the geometry of local octahedral GaO_6 SBUs and give rise to unique pXRD patterns and $^{69/71}$Ga SSNMR parameters. SSNMR is a powerful tool that has the ability to identify the adsorbed guest molecules as well as the short-range structure and phase of Ga-MIL-53 when paired with complementary characterization techniques. $^{69/71}$Ga SSNMR holds potential for use as a powerful sensor for identifying the identity and loading level of various organic adsorbates in Ga-MIL-53 after a database of $^{69/71}$Ga NMR parameters for different adsorbed organic guests in Ga-MIL-53 has been established. In order to shed further light on the specific structures and phase transitions in various forms of Ga-MIL-53, and to obtain key crystallographic data, Rietveld refinements of high-quality pXRD patterns are currently underway in our laboratory.

6.5 References

1. James, S. L., *Chem. Soc. Rev.* **2003,** *32* (5), 276-288.

2. Zhou, H.-C.; Kitagawa, S., *Chem. Soc. Rev.* **2014,** *43* (16), 5415-5418.

3. Zhou, H.-C.; Long, J. R.; Yaghi, O. M., *Chem. Rev.* **2012,** *112* (2), 673-674.

4. Chughtai, A. H.; Ahmad, N.; Younus, H. A.; Laypkov, A.; Verpoort, F., *Chem. Soc. Rev.* **2015,** *44* (19), 6804-6849.

5. Horcajada, P.; Chalati, T.; Serre, C.; Gillet, B.; Sebrie, C.; Baati, T.; Eubank, J. F.; Heurtaux, D.; Clayette, P.; Kreuz, C.; Chang, J.-S.; Hwang, Y. K.; Marsaud, V.; Bories, P.-N.; Cynober, L.; Gil, S.; Ferey, G.; Couvreur, P.; Gref, R., *Nature Mater.* **2010,** *9* (2), 172-178.

6. Ma, S.; Zhou, H.-C., *Chem. Commun.* **2010,** *46* (1), 44-53.

7. Chang, Z.; Yang, D.-H.; Xu, J.; Hu, T.-L.; Bu, X.-H., *Adv. Mater.* **2015,** *27* (36), 5432-5441.

8. Schneemann, A.; Bon, V.; Schwedler, I.; Senkovska, I.; Kaskel, S.; Fischer, R. A., *Chem. Soc. Rev.* **2014,** *43* (16), 6062-6096.

9. Fletcher, A. J.; Thomas, K. M.; Rosseinsky, M. J., *J. Solid State Chem.* **2005,** *178* (8), 2491-2510.

10. Serre, C.; Millange, F.; Thouvenot, C.; Noguès, M.; Marsolier, G.; Louër, D.; Férey, G., *J. Am. Chem. Soc.* **2002,** *124* (45), 13519-13526.

11. Loiseau, T.; Serre, C.; Huguenard, C.; Fink, G.; Taulelle, F.; Henry, M.; Bataille, T.; Férey, G., *Chem. -Eur. J.* **2004,** *10* (6), 1373-1382.

12. Anokhina, E. V.; Vougo-Zanda, M.; Wang, X.; Jacobson, A. J., *J. Am. Chem. Soc.* **2005,** *127* (43), 15000-15001.

13. Whitfield, T. R.; Wang, X.; Liu, L.; Jacobson, A. J., *Solid State Sci.* **2005,** *7* (9), 1096-1103.

14. Vougo-Zanda, M.; Huang, J.; Anokhina, E.; Wang, X.; Jacobson, A. J., *Inorg. Chem.* **2008,** *47* (24), 11535-11542.

15. Mowat, J. P. S.; Seymour, V. R.; Griffin, J. M.; Thompson, S. P.; Slawin, A. M. Z.; Fairen-Jimenez, D.; Duren, T.; Ashbrook, S. E.; Wright, P. A., *Dalton Trans.* **2012,** *41* (14), 3937-3941.

16. Serre, C.; Bourrelly, S.; Vimont, A.; Ramsahye, N. A.; Maurin, G.; Llewellyn, P. L.; Daturi, M.; Filinchuk, Y.; Leynaud, O.; Barnes, P.; Férey, G., *Adv. Mater.* **2007,** *19* (17), 2246-2251.

17. Serre, C.; Mellot-Draznieks, C.; Surblé, S.; Audebrand, N.; Filinchuk, Y.; Férey, G., *Science* **2007,** *315* (5820), 1828-1831.

18. Volkringer, C.; Loiseau, T.; Guillou, N.; Ferey, G.; Elkaim, E.; Vimont, A., *Dalton Trans.* **2009,** (12), 2241-2249.

19. Chen, L.; Mowat, J. P. S.; Fairen-Jimenez, D.; Morrison, C. A.; Thompson, S. P.; Wright, P. A.; Düren, T., *J. Am. Chem. Soc.* **2013,** *135* (42), 15763-15773.

20. Alhamami, M.; Doan, H.; Cheng, C.-H., *Materials* **2014,** *7* (4), 3198.

21. Chaplais, G.; Simon-Masseron, A.; Porcher, F.; Lecomte, C.; Bazer-Bachi, D.; Bats, N.; Patarin, J., *Phys. Chem. Chem. Phys.* **2009,** *11* (26), 5241-5245.

22. Ravon, U.; Chaplais, G.; Chizallet, C.; Seyyedi , B.; Bonino , F.; Bordiga , S.; Bats, N.; Farrusseng, D., *ChemCatChem* **2010,** *2* (10), 1235-1238.

23. Millange, F.; Guillou, N.; Walton, R. I.; Greneche, J.-M.; Margiolaki, I.; Ferey, G., *Chem. Commun.* **2008,** (39), 4732-4734.

24. Finsy, V.; Kirschhock, C. E. A.; Vedts, G.; Maes, M.; Alaerts, L.; De Vos, D. E.; Baron, G. V.; Denayer, J. F. M., *Chem. -Eur. J.* **2009,** *15* (31), 7724-7731.

25. Guillou, N.; Walton, R. I.; Millange, F., *Z. Kristall.* **2010,** *225* (12), 552-556.

26. El Osta, R.; Carlin-Sinclair, A.; Guillou, N.; Walton, R. I.; Vermoortele, F.; Maes, M.; de Vos, D.; Millange, F., *Chem. Mater.* **2012,** *24* (14), 2781-2791.

27. Ibrahim, B.; Lucier, B. E. G.; Xu, J.; He, P.; Huang, Y., *Can. J. Chem.* **2015,** *93* (9), 960-969.

28. Hoffmann, H. C.; Debowski, M.; Muller, P.; Paasch, S.; Senkovska, I.; Kaskel, S.; Brunner, E., *Materials* **2012,** *5* (12), 2537-2572.

29. Sutrisno, A.; Huang, Y., *Solid State Nucl. Magn. Reson.* **2013,** *49–50*, 1-11.

30. Ashbrook, S. E.; Dawson, D. M.; Seymour, V. R., *Phys. Chem. Chem. Phys.* **2014,** *16* (18), 8223-8242.

31. Jiang, Y.; Huang, J.; Marx, S.; Kleist, W.; Hunger, M.; Baiker, A., *J. Phys. Chem. Lett.* **2010,** *1* (19), 2886-2890.

32. Lieder, C.; Opelt, S.; Dyballa, M.; Henning, H.; Klemm, E.; Hunger, M., *J. Phys. Chem. C* **2010,** *114* (39), 16596-16602.

33. Goesten, M. G.; Juan-Alcañiz, J.; Ramos-Fernandez, E. V.; Sai Sankar Gupta, K. B.; Stavitski, E.; van Bekkum, H.; Gascon, J.; Kapteijn, F., *J. Catal.* **2011,** *281* (1), 177-187.

34. Liu, J.; Zhang, F.; Zou, X.; Yu, G.; Zhao, N.; Fan, S.; Zhu, G., *Chem. Commun.* **2013,** *49* (67), 7430-7432.

35. Haouas, M.; Taulelle, F.; Martineau, C., *Prog. Nucl. Magn. Reson. Spectrosc.* **2016,** *94–95*, 11-36.

36. Pyykkö, P., *Mol. Phys.* **2008,** *106* (16-18), 1965-1974.

37. Huang, Y.; Xu, J.; Gul-E-Noor, F.; He, P., Metal-organic frameworks: NMR studies of quadrupolar nuclei. In *Encyclopedia of Inorganic and Bioinorganic Chemistry*, John Wiley & Sons, Ltd: 2011.

38. He, P.; Lucier, B. E. G.; Terskikh, V. V.; Shi, Q.; Dong, J.; Chu, Y.; Zheng, A.; Sutrisno, A.; Huang, Y., *J. Phys. Chem. C* **2014,** *118* (41), 23728-23744.

39. Berglund, M.; Wieser, M. E., *Pure Appl. Chem.* **2011,** *83* (2), 397-410.

40. Volkringer, C.; Loiseau, T.; Férey, G.; Morais, C. M.; Taulelle, F.; Montouillout, V.; Massiot, D., *Microporous Mesoporous Mater.* **2007,** *105* (1–2), 111-117.

41. Hajjar, R.; Volkringer, C.; Loiseau, T.; Guillou, N.; Marrot, J.; Férey, G.; Margiolaki, I.; Fink, G.; Morais, C.; Taulelle, F., *Chem. Mater.* **2011,** *23* (1), 39-47.

42. Martineau, C.; Loiseau, T.; Beitone, L.; Ferey, G.; Bouchevreau, B.; Taulelle, F., *Dalton Trans.* **2013,** *42* (2), 422-431.

43. Polenova, T.; Gupta, R.; Goldbourt, A., *Anal. Chem.* **2015,** *87* (11), 5458-5469.

44. Schurko, R. W., *Acc. Chem. Res.* **2013,** *46* (9), 1985-1995.

45. Kupce, E.; Freeman, R., *J. Magn. Reson., Ser A* **1995,** *115* (2), 273-276.

46. Larsen, F. H.; Jakobsen, H. J.; Ellis, P. D.; Nielsen, N. C., *J. Phys. Chem. A* **1997,** *101* (46), 8597-8606.

47. O'Dell, L. A.; Schurko, R. W., *Chem. Phys. Lett.* **2008,** *464* (1–3), 97-102.

48. Bhattacharyya, R.; Frydman, L., *J. Chem. Phys.* **2007,** *127,* 194503.

49. Schurko, R. W., Acquisition of Wideline Solid-State NMR Spectra of Quadrupolar Nuclei. In *eMagRes*, John Wiley & Sons, Ltd: 2007.

50. O'Dell, L. A.; Rossini, A. J.; Schurko, R. W., *Chem. Phys. Lett.* **2009,** *468* (4-6), 330-335.

51. Massiot, D.; Farnan, I.; Gautier, N.; Trumeau, D.; Florian, P.; Grandinetti, P. J., *J. Chim. Phys. Phys.-Chim. Biol.* **1995,** *92* (10), 1847-1850.

52. Eichele K.; Wasylishen R. E., *Wsolids1* University of Tübingen, Tübingen, Germany, **2009**.

53. Segall, M. D.; Lindan, P. J. D.; Probert, M. J.; Pickard, C. J.; Hasnip, P. J.; Clark, S. J.; Payne, M. C., *J. Phys. Condens. Matter* **2002,** *14* (11), 2717-2744.

54. Clark, S. J.; Segall, M. D.; Pickard, C. J.; Hasnip, P. J.; Probert, M. J.; Refson, K.; Payne, M. C., *Z. Kristall.* **2005,** *220* (5-6), 567-570.

55. Pickard, C. J.; Mauri, F., *Phys. Rev. B* **2001,** *63,* 245101.

56. Yates, J. R.; Pickard, C. J.; Mauri, F., *Phys. Rev. B* **2007,** *76,* 024401.

57. Perdew, J. P.; Burke, K.; Ernzerhof, M., *Phys. Rev. Lett.* **1996,** *77* (18), 3865-3868.

58. Ma, Z. L.; Wentz, K. M.; Hammann, B. A.; Chang, I. Y.; Kamunde-Devonish, M. K.; Cheong, P. H.-Y.; Johnson, D. W.; Terskikh, V. V.; Hayes, S. E., *Chem. Mater.* **2014,** *26* (17), 4978-4983.

59. Llewellyn, P. L.; Bourrelly, S.; Serre, C.; Filinchuk, Y.; Férey, G., *Angew. Chem. Int. Ed.* **2006,** *45* (46), 7751-7754.

60. Arstad, B.; Fjellvåg, H.; Kongshaug, K. O.; Swang, O.; Blom, R., *Adsorption* **2008,** *14* (6), 755-762.

61. Zhang, Y.; Lucier, B. E. G.; Huang, Y., *Phys. Chem. Chem. Phys.* **2016,** *18* (12), 8327-8341.

62. Lucier, B. E. G.; Reidel, A. R.; Schurko, R. W., *Can. J. Chem.* **2011,** *89* (7), 919-937.

63. Johnston, K. E.; O'Keefe, C. A.; Gauvin, R. M.; Trébosc, J.; Delevoye, L.; Amoureux, J.-P.; Popoff, N.; Taoufik, M.; Oudatchin, K.; Schurko, R. W., *Chem. -Eur. J.* **2013,** *19* (37), 12396-12414.

64. Guillou, N.; Bourrelly, S.; Llewellyn, P. L.; Walton, R. I.; Millange, F., *CrystEngComm* **2015,** *17* (2), 422-429.

65. Fatila, E. M.; Mayo, R. A.; Rouzières, M.; Jennings, M. C.; Dechambenoit, P.; Soldatov, D. V.; Mathonière, C.; Clérac, R.; Coulon, C.; Preuss, K. E., *Chem. Mater.* **2015,** *27* (11), 4023-4032.

66. Devic, T.; Salles, F.; Bourrelly, S.; Moulin, B.; Maurin, G.; Horcajada, P.; Serre, C.; Vimont, A.; Lavalley, J.-C.; Leclerc, H.; Clet, G.; Daturi, M.; Llewellyn, P. L.; Filinchuk, Y.; Ferey, G., *J. Mater. Chem.* **2012,** *22* (20), 10266-10273.

67. Boutin, A.; Springuel-Huet, M.-A.; Nossov, A.; Gédéon, A.; Loiseau, T.; Volkringer, C.; Férey, G.; Coudert, F.-X.; Fuchs, A. H., *Angew. Chem. Int. Ed.* **2009,** *48* (44), 8314-8317.

68. Boutin, A.; Coudert, F.-X.; Springuel-Huet, M.-A.; Neimark, A. V.; Férey, G.; Fuchs, A. H., *J. Phys. Chem. C* **2010,** *114* (50), 22237-22244.

69. Coudert, F.-X.; Boutin, A.; Fuchs, A. H., *Mol. Phys.* **2014,** *112* (9-10), 1257-1261.

70. Alaerts, L.; Kirschhock, C. E. A.; Maes, M.; van der Veen, M. A.; Finsy, V.; Depla, A.; Martens, J. A.; Baron, G. V.; Jacobs, P. A.; Denayer, J. E. M.; De Vos, D. E., *Angew. Chem. Int. Ed.* **2007,** *46* (23), 4293-4297.

71. Alaerts, L.; Maes, M.; Giebeler, L.; Jacobs, P. A.; Martens, J. A.; Denayer, J. F. M.; Kirschhock, C. E. A.; De Vos, D. E., *J. Am. Chem. Soc.* **2008,** *130* (43), 14170-14178.

72. Trung, T. K.; Trens, P.; Tanchoux, N.; Bourrelly, S.; Llewellyn, P. L.; Loera-Serna, S.; Serre, C.; Loiseau, T.; Fajula, F.; Férey, G., *J. Am. Chem. Soc.* **2008,** *130* (50), 16926-16932.

73. Duan, L. H.; Dong, X. Y.; Wu, Y. Y.; Li, H. L.; Wang, L.; Song, L. J., *J. Porous Mat.* **2013,** *20* (2), 431-440.

74. Kolokolov, D. I.; Jobic, H.; Rives, S.; Yot, P. G.; Ollivier, J.; Trens, P.; Stepanov, A. G.; Maurin, G., *J. Phys. Chem. C* **2015,** *119* (15), 8217-8225.

75. Maes, M.; Vermoortele, F.; Alaerts, L.; Couck, S.; Kirschhock, C. E. A.; Denayer, J. F. M.; De Vos, D. E., *J. Am. Chem. Soc.* **2010,** *132* (43), 15277-15285.

6.6 Appendix

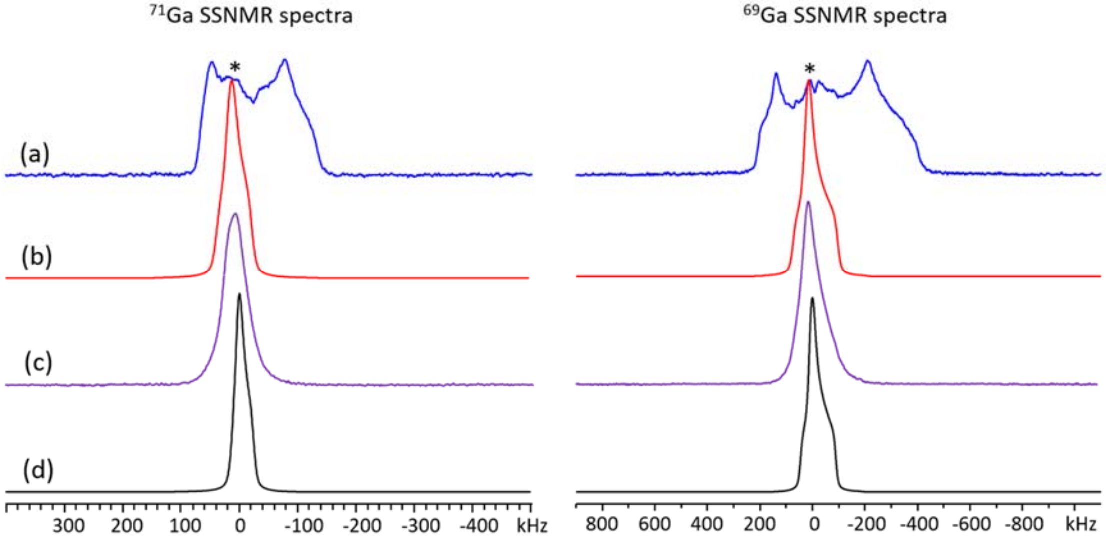

Figure 6-A1. Experimental $^{69/71}$Ga SSNMR echo spectra of Ga-MIL-53(*enp*) acquired at a magnetic field of 21.1 T are shown in (a), with the central Ga hydroxyl/hydroxide impurity resonance labeled by an asterisk (*). The simulated spectra of only the impurity phase is shown in (b). The experimental 21.1 T $^{69/71}$Ga SSNMR echo spectra of the Ga hydroxyl/hydroxide product generated by recrystallizing $Ga(NO_3)_3$ and NaOH from H_2O at room temperature are depicted in (c). The simulated spectra shown in (d) are of a reported Ga hydroxo-aquo cluster, simulated using the documented NMR parameters from reference 1. This comparison demonstrates that the impurity in Ga-MIL-53 samples is likely a Ga hydroxyl/hydroxide compound formed during the synthesis of Ga-MIL-53.

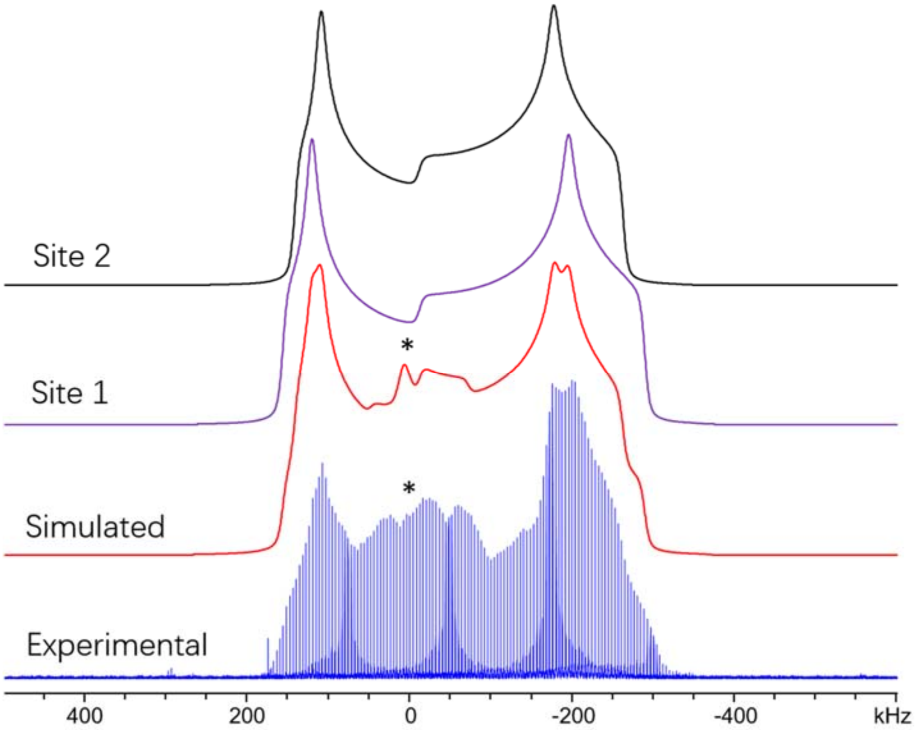

Figure 6-A2. Experimental and simulated ^{71}Ga WURST-CPMG SSNMR spectra of Ga-MIL-53(*as*) acquired at a magnetic field of 9.4 T. Two separate overlapping Ga powder patterns can be observed, which are indicative of two crystallographically unique Ga sites in the MOF. The different Ga powder patterns are colored in purple (C_Q: 18.5 (1) MHz, η_Q: 0.19 (1)) and black (C_Q: 17.7 (1) MHz, η_Q: 0.22 (1)). The central spectral contribution from Ga hydroxyl/hydroxide impurities is labeled by an asterisk (*).

Table 6-A1. The Ga-O bond length distribution and O-Ga-O bond angle distribution of GaO_6 SBUs in *as*, *enp*, and *lt* phases of Ga-MIL-53, which have been solved by previous XRD studies.[2, 3]

Phase		Ga-O bond length				O-Ga-O bond angle			
		max. bond length (Å)	min. bond length (Å)	avg. bond length (Å)	difference (Å)	max. bond angle (°)	min. bond angle (°)	avg. bond angle (°)	difference (°)
as		1.976	1.912	1.953	0.064	92.95	87.05	89.84	5.90
enp		2.006	1.953	1.972	0.053	94.62	85.38	90.00	9.24
lt	**site 1**	1.861	2.075	1.990	0.241	93.88	85.48	89.00	8.40
	site 2	1.908	2.036	1.978	0.128	94.52	85.48	90.21	9.04
	site 3	1.898	1.949	1.924	0.051	103.30	76.70	89.48	26.60

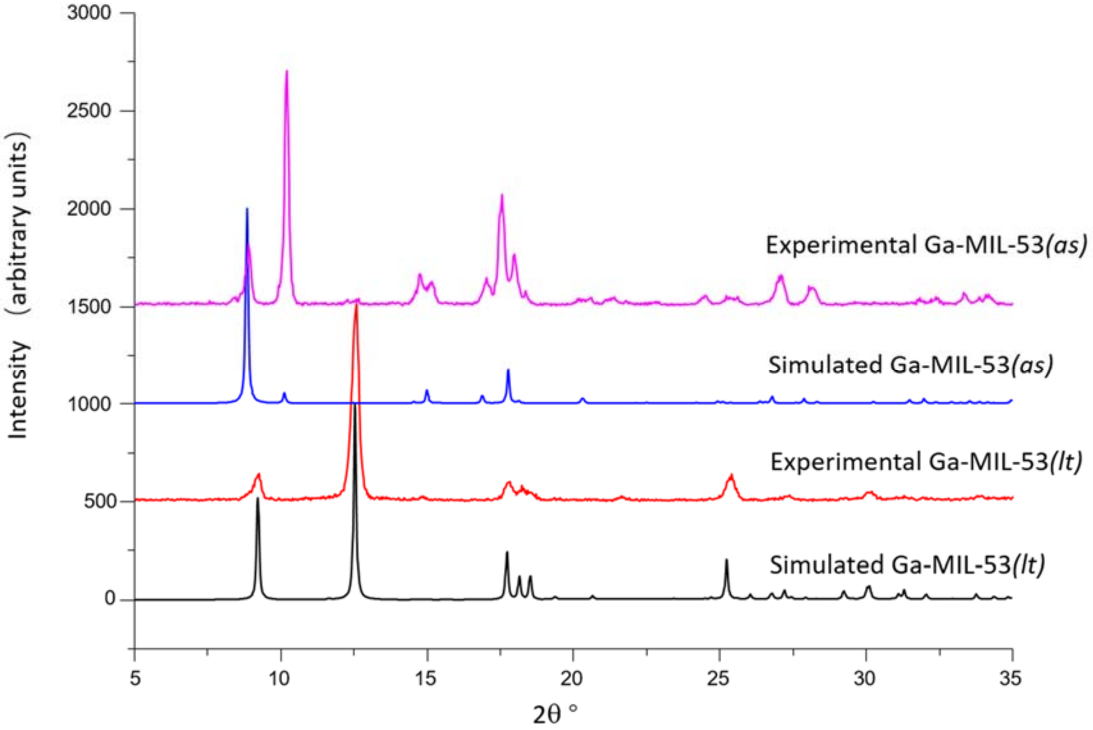

Figure 6-A3. Experimental and simulated pXRD patterns of Ga-MIL-53(*as*) and Ga-MIL-53(*lt*).

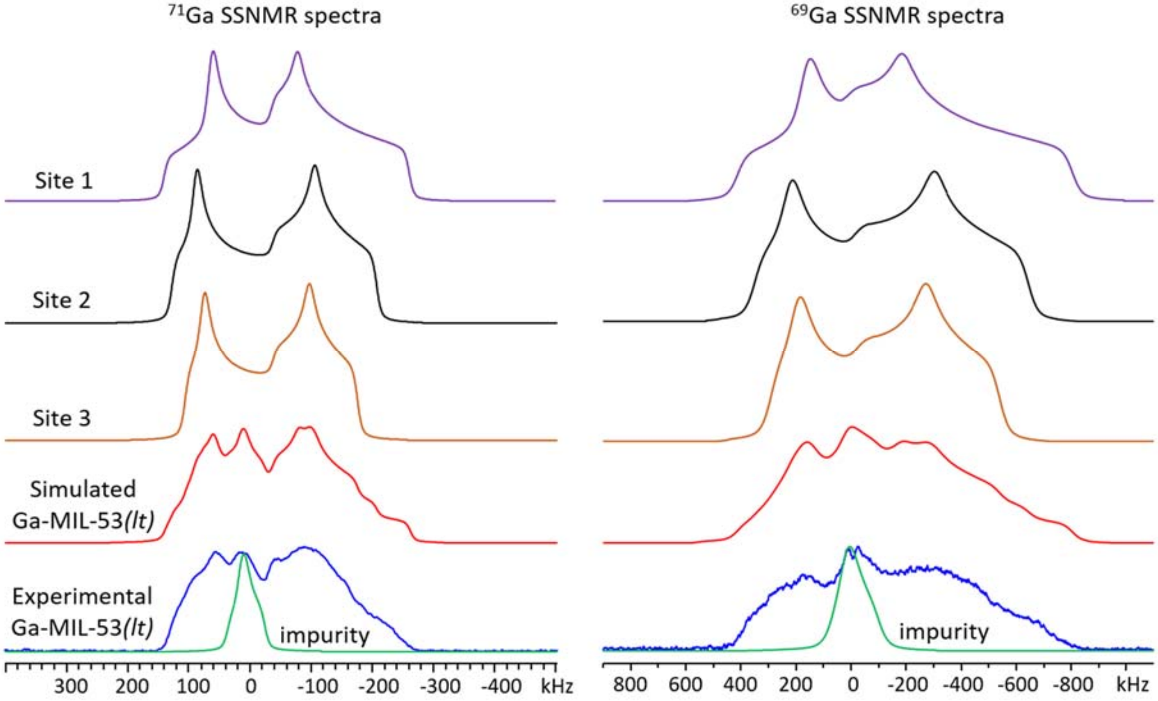

Figure 6-A4. A comparison and deconvolution of experimental and simulated $^{69/71}$Ga SSNMR echo spectra of Ga-MIL-53(*lt*) at 21.1 T. Three Ga powder patterns were simulated according to a prior XRD study on Ga-MIL-53(*lt*) that indicated three Ga sites were present.[3] The simulated spectra match quite well with experimental spectra, validating the presence of three crystallographically unique Ga sites. The $^{69/71}$Ga NMR tensor parameters extracted from simulations are listed in Table 6-A1.

Table 6-A2. The experimental and calculated $^{69/71}$Ga NMR tensor parameters of Ga-MIL-53(*lt*) from $^{69/71}$Ga SSNMR echo experiments at 21.1 T.[a]

Sample	Site	C_Q ((^{71}Ga)MHz)	C_Q ((^{69}Ga)MHz)	η_Q	Ω (ppm)	κ	δ_{iso} (ppm)	α (°)	β (°)	γ (°)
Experimental Ga-MIL-53(*lt*)	Site1 (1.00)	22.0 (3)	35.2 (3)	0.65 (3)	250 (30)	1.0 (3)	-20 (10)	0	0	0
	Site2 (0.50)	21.7 (3)	34.7 (3)	0.37 (3)	250 (30)	1.0 (3)	15 (5)	0	0	0
	Site3 (0.50)	20.0 (3)	32.0 (3)	0.34 (3)	230 (30)	1.0 (3)	5 (5)	0	0	0
Calculated Ga-MIL-53(*lt*)[b]	Site1 (1.00)	25.1	40.1	0.03	187	0.46		79.4	1.3	221.5
	Site2 (0.50)	22.5	36.0	0.66	111	-0.52		71.6	6.4	213.4
	Site3 (0.50)	14.2	22.8	0.23	145	-0.32		23.1	88.4	348.2
Calculated Ga-MIL-53(*lt*)[c]	Site1 (1.00)	13.6	21.7	0.74	179	0.47		124.2	4.7	191.0
	Site2 (0.50)	16.3	26.9	0.60	186	0.25		80.5	84.5	24.9
	Site3 (0.50)	10.3	16.5	0.70	114	-0.86		181.7	64.6	254.6
Calculated Ga-MIL-53(*lt*)[d]	Site1 (1.00)	15.6	25.0	0.31	201	0.38		64.1	6.0	230.6
	Site2 (0.50)	23.2	37.0	0.54	208	0.23		91.8	84.0	19.0
	Site3 (0.50)	12.0	19.1	0.82	171	0.24		114.0	9.0	302.1
Impurity phase		7.5 (1)	12.0 (1)	1.0 (1)	50 (10)		50 (10)			

[a] All CASTEP calculations were performed with empty Ga-MIL-53 channels, due to the various difficulties the incorporated H_2O molecules pose for geometry optimization and NMR calculations. [b] These calculations employed the reported crystal structure[3] without geometry optimization. [c] These calculations involved geometry optimization of the H atoms of the MOF, and the oxygen atomic positions were not optimized. [d] This geometry optimization was of the H atoms and the O atoms of the MOF.

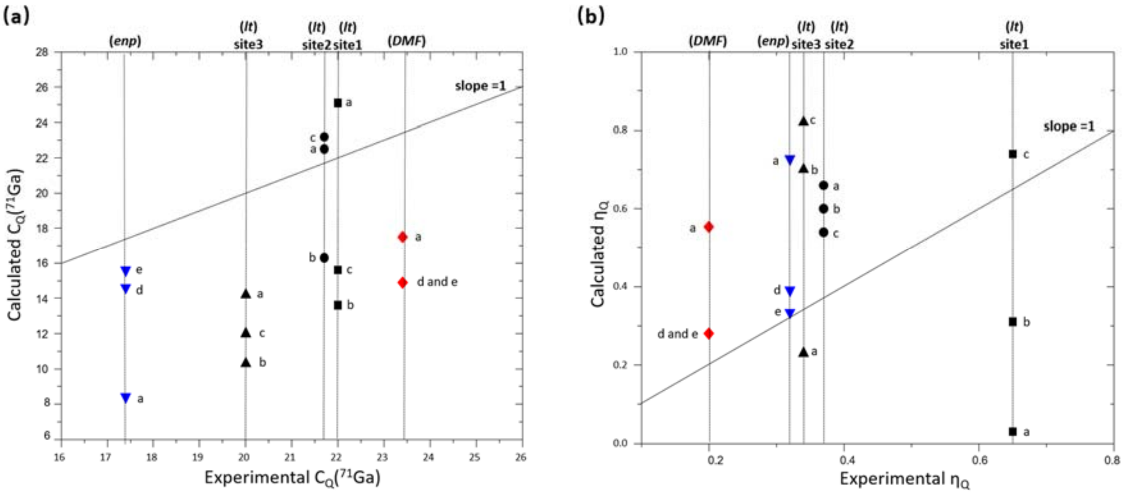

Figure 6-A5. Plots of experimental versus calculated $C_Q(^{71}Ga)$ and η_Q values in the various form of Ga-MIL-53 are shown in (a) and (b), respectively. The lowercase a, b, c, d, and e labels denote different calculation conditions. For calculations labeled a, calculations were performed on the reported crystal structure without carrying out any geometry optimization calculations. The label b denotes the calculation condition for the *lt* phase which involved geometry optimization of only the H atoms of the MOF, while c represents calculations on the *lt* phase which included geometry optimization of both H atoms and O atoms of the MOF. In the *enp* and *DMF* phases, d is used to label calculated results obtained after geometry optimization of all the atoms of the MOFs, while e represents calculations performed after geometry optimization of all atoms except Ga.

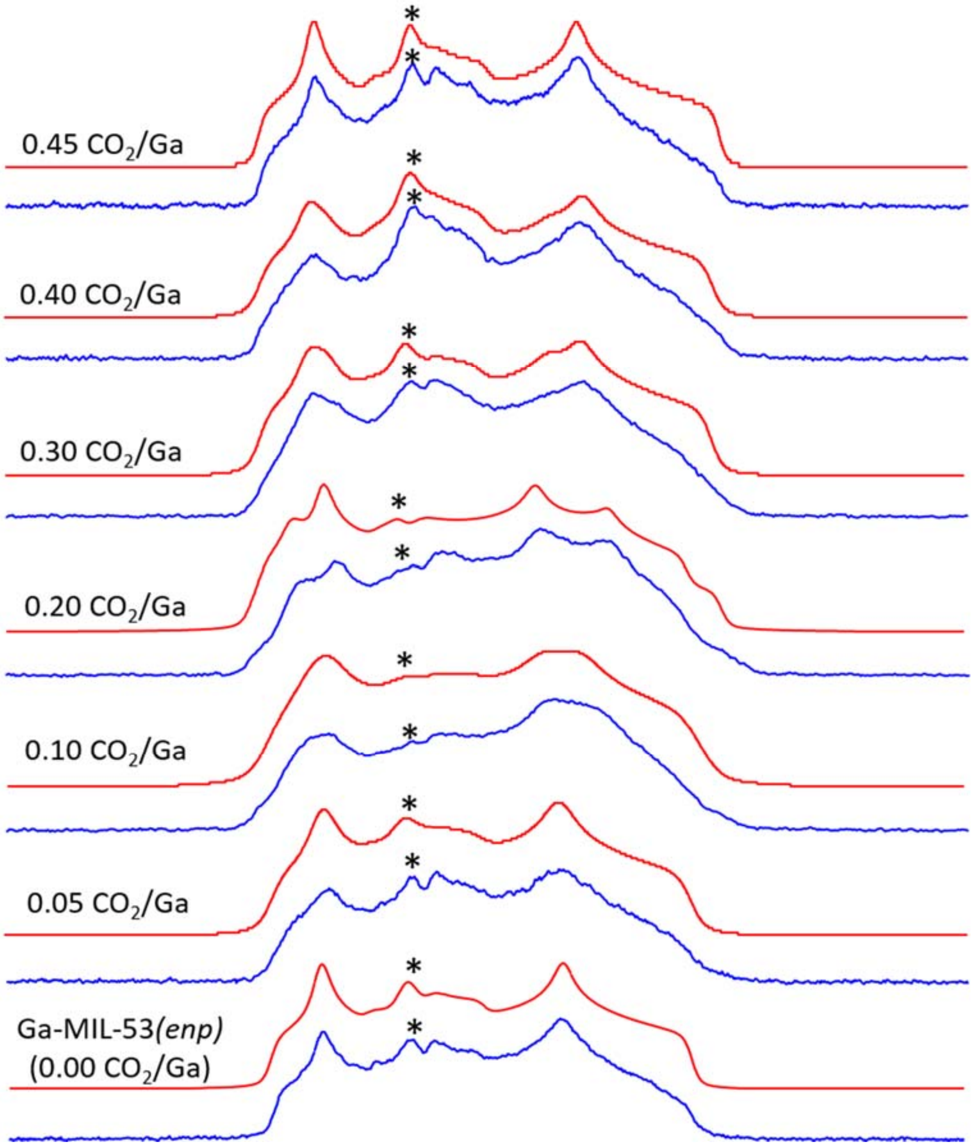

Figure 6-A6. Experimental (blue) and simulated (red) ^{69}Ga SSNMR echo spectra of CO_2-loaded Ga-MIL-53 acquired at 21.1 T are shown. The CO_2 loading level is listed on the far left of each spectral pair. The central Ga hydroxyl/hydroxide impurity resonance is labeled with an asterisk (*). The corresponding simulations and lineshape deconvolutions of these powder patterns are shown in Figures 6-A7.

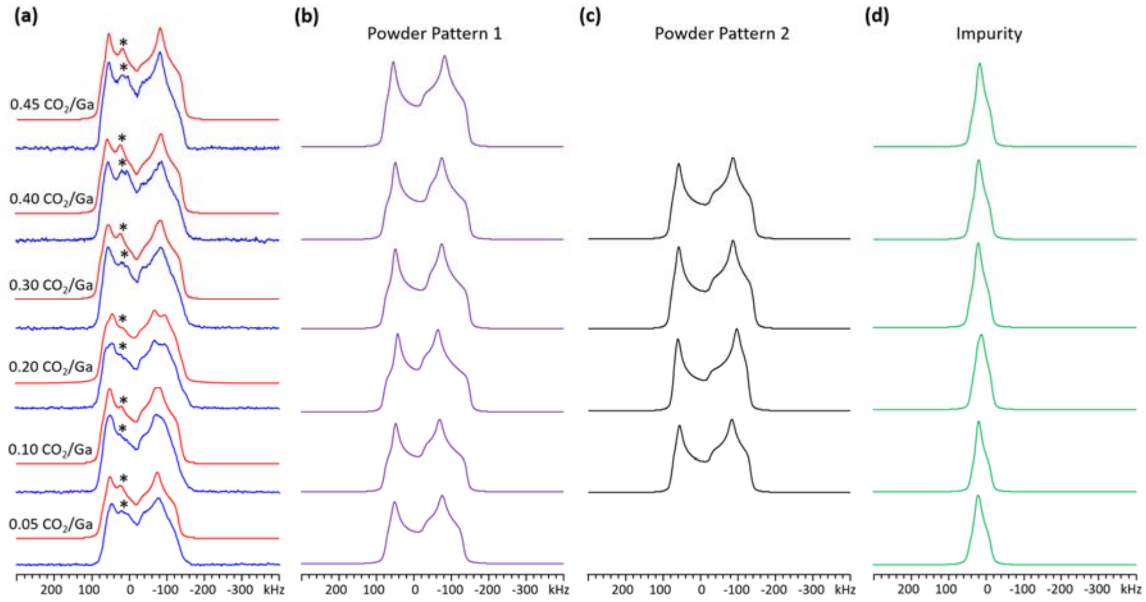

Figure 6-A7. The experimental (blue) and simulated (red) static ^{71}Ga SSNMR echo spectra of CO_2-loaded Ga-MIL-53 at 21.1 T are shown in (a). The individual simulated spectra for both powder patterns and the Ga hydroxyl/hydroxide impurity are illustrated in (b), (c) and (d), respectively. The presence of a second powder pattern indicates that two crystallographically distinct Ga sites are present in Ga-MIL-53 when CO_2 loading levels range from 0.10 to 0.40 CO_2/Ga. In (a), the powder pattern corresponding to the Ga hydroxyl/hydroxide impurity is labeled by an asterisk (*).

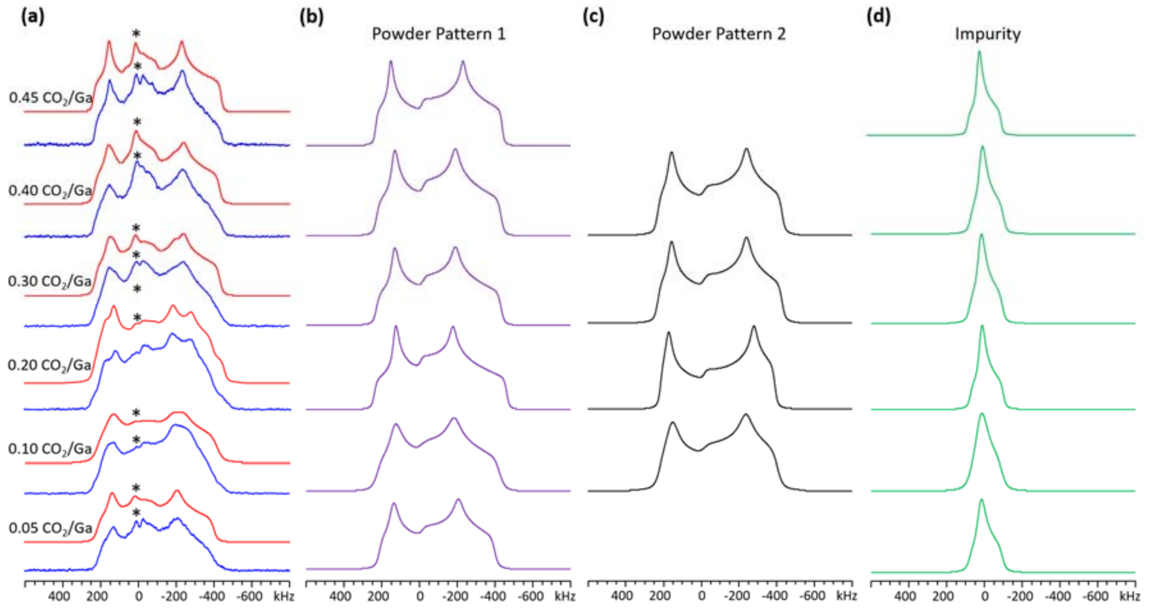

Figure 6-A8. A deconvolution of the static ^{69}Ga SSNMR echo spectra of CO_2 loaded Ga-MIL-53 at 21.1 T are shown in this Figure. A comparison of experimental (blue) and simulated (red) ^{69}Ga spectra is shown in (a). The individual simulated spectra for each powder pattern as well as the Ga hydroxyl/hydroxide impurity are illustrated in (b), (c) and (d), respectively. In a similar manner to the corresponding ^{71}Ga SSNMR spectra, the presence of two separate ^{69}Ga powder patterns between the CO_2 loading levels of 0.10 to 0.40 CO_2/Ga indicates that two crystallographically distinct Ga sites are present. In (a), the spectral contribution from the Ga hydroxyl/hydroxide impurity is labeled by an asterisk (*).

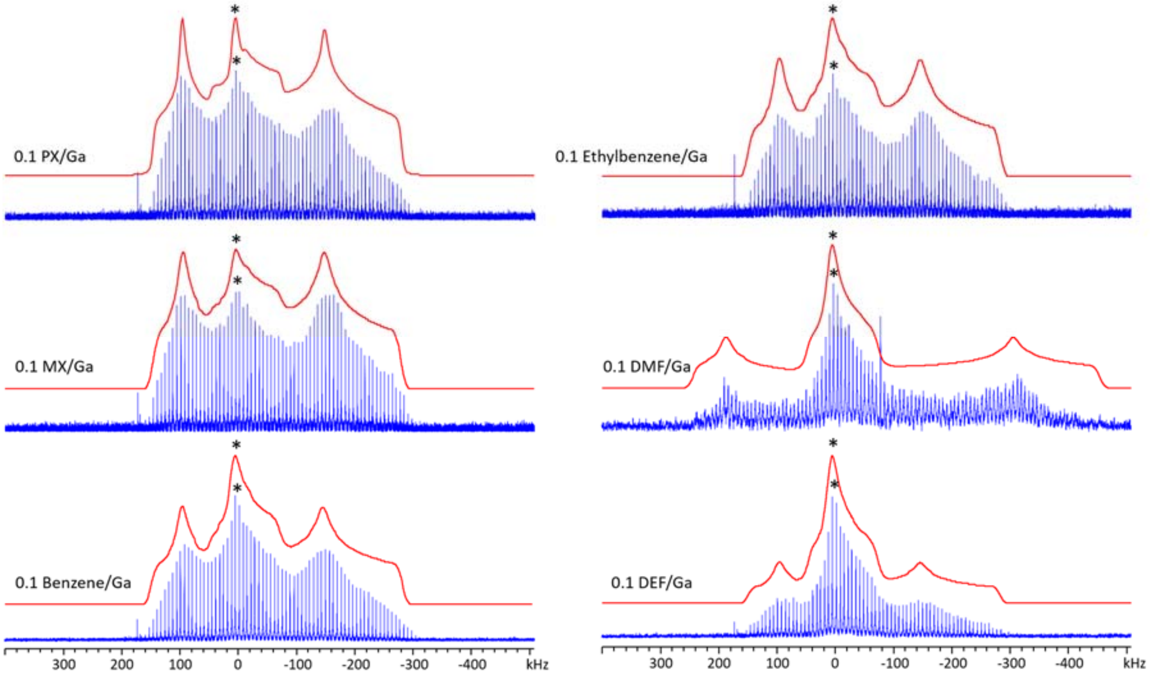

Figure 6-A9. The experimental (blue) and simulated (red) ^{71}Ga WURST-CPMG SSNMR spectra at 9.4 T of Ga-MIL-53 loaded with adsorbates at the relatively low level of 0.1 adsorbate/Ga. The central Ga hydroxyl/hydroxide impurity powder pattern is labeled by an asterisk (*).

Table 6-A3. $^{69/71}$Ga NMR tensor parameters of Ga-MIL-53 samples at a loading level of 0.1 adsorbate/Ga, which were obtained from analytical simulations of static ^{71}Ga WURST-CPMG spectra at 9.4 T.

Guest	Site (relative intensity)	C_Q ((^{71}Ga)MHz)	C_Q ((^{69}Ga)MHz)	η_Q	Ω (ppm)	κ	δ_{iso} (ppm)
DEF	Site 1 (1.00)	17.5 (1)	27.8 (2)	0.33 (1)	150 (20)	1.0 (1)	-5 (5)
	Impurity (0.70)	7.5 (1)	12.0 (1)	1.00 (10)	50 (30)	0.0(2)	50 (10)
DMF	Site 1 (1.00)	23.4 (1)	37.3 (2)	0.20 (2)	150 (20)	1.0 (1)	-10 (5)
	Impurity (0.40)	7.5 (1)	12.0 (1)	1.00 (10)	50 (20)	0.0(2)	50 (10)
0.1 Ethylbenzene/Ga	Site 1 (1.00)	17.5 (1)	27.8 (2)	0.33 (1)	150 (20)	1.0 (1)	-5 (5)
	Impurity (0.21)	7.5 (1)	12.0 (1)	1.00 (10)	50 (30)	0.0(2)	50 (10)
0.1 Benzene/Ga	Site 1 (1.00)	17.5 (1)	27.8 (2)	0.33 (1)	150 (20)	1.0 (1)	-5 (5)
	Impurity (0.25)	7.5 (1)	12.0 (1)	1.00 (10)	50 (30)	0.0(2)	50 (10)
0.1 MX/Ga	Site 1 (1.00)	17.4 (1)	27.8 (2)	0.32 (1)	150 (20)	1.0 (1)	-5 (5)
	Impurity (0.14)	7.5 (1)	12.0 (1)	1.00 (10)	50 (30)	0.0(2)	50 (10)
0.1 PX/Ga	Site 1 (1.00)	17.4 (1)	27.8 (2)	0.32 (1)	150 (20)	1.0 (1)	-5 (5)
	Impurity (0.15)	7.5 (1)	12.0 (1)	1.00 (10)	50 (30)	0.0(2)	50 (10)

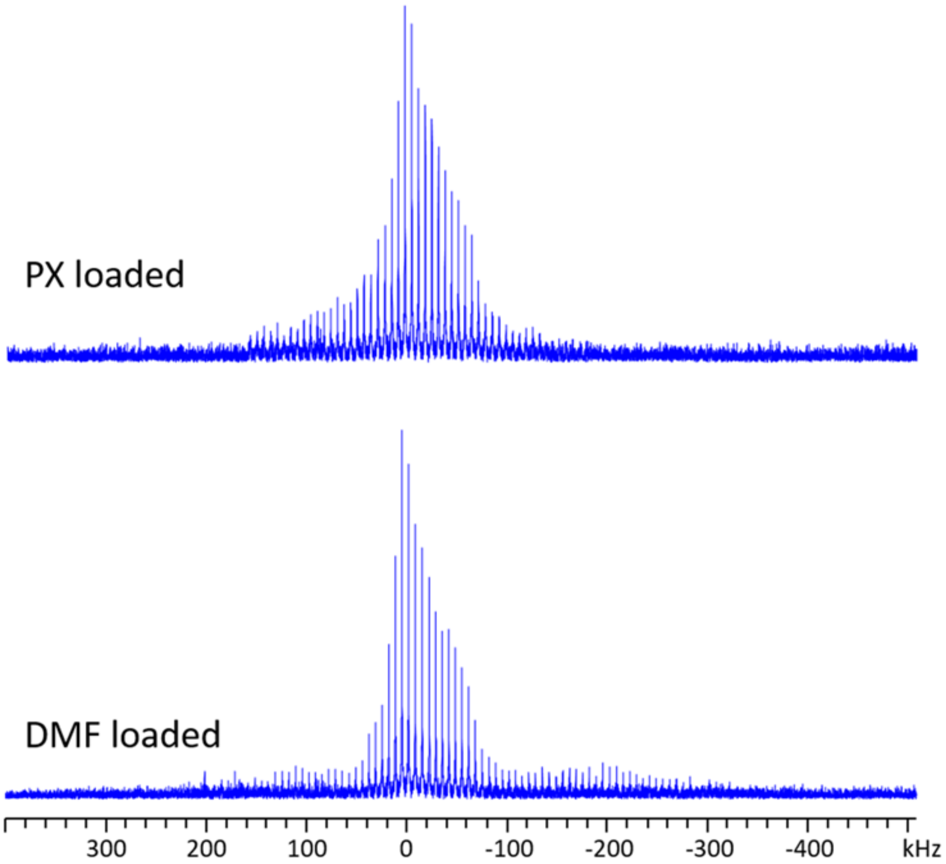

Figure 6-A10. Experimental ^{71}Ga WURST-CPMG spectra at 9.4 T of selected fully loaded non-polar and polar adsorbates (PX and DMF) in Ga-MIL-53 are shown. The observed spectra are dominated by the Ga-containing impurity powder patterns; this is because the impurity has a much longer T_2 value than Ga-MIL-53, which undergoes fast T_2 relaxation due to the dynamics of adsorbed guest molecules and fluctuating Ga-guest dipolar couplings. The $^{69/71}$Ga SSNMR echo spectra obtained at 21.1 T (Figures S11 and S12) are of higher resolution and S/N with respect to the underlying Ga-MIL-53 powder pattern.

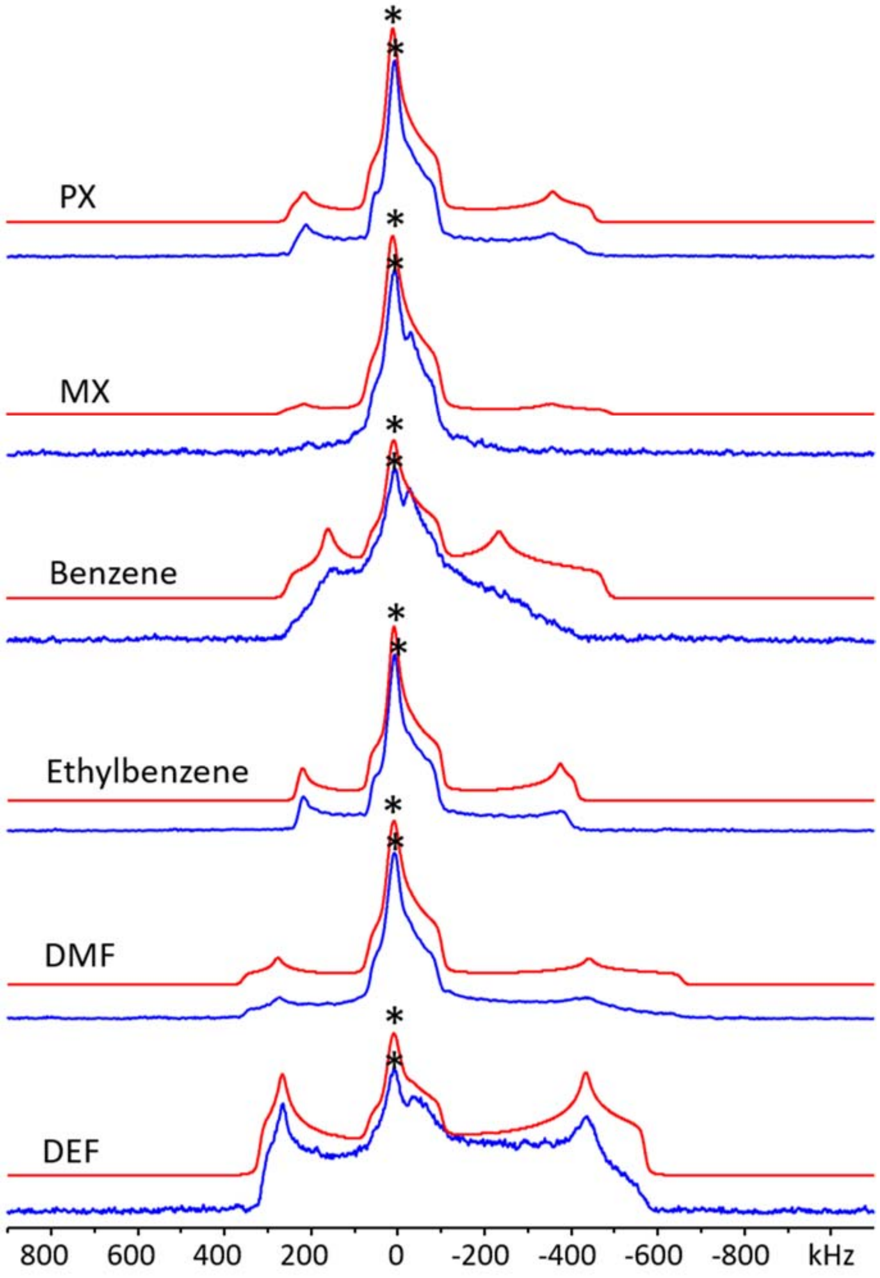

Figure 6-A11. ^{69}Ga SSNMR echo spectra of guest-saturated Ga-MIL-53 samples at 21.1 T. Simulated spectra are shown in red and experimental spectra are depicted in blue. The Ga hydroxyl/hydroxide impurity is labeled with an asterisk (*).

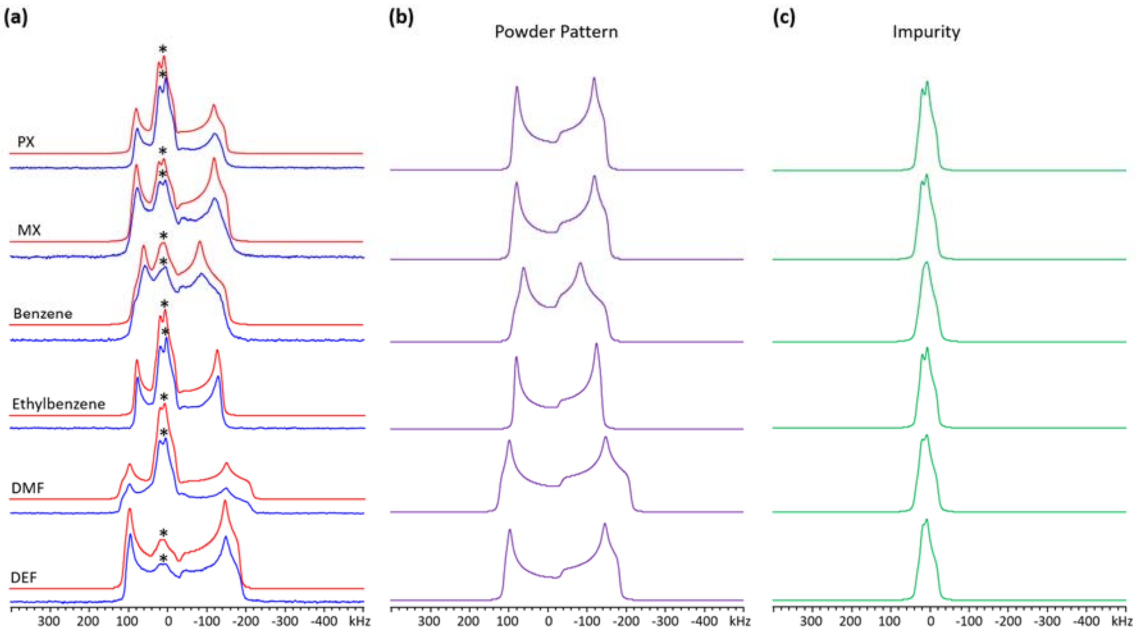

Figure 6-A12. The experimental (blue) and simulated (red) static ^{71}Ga SSNMR echo spectra at 21.1 T of Ga-MIL-53 fully loaded (*i.e.*, saturated) with organic adsorbates are shown in (a). The individual simulated spectra for both the broad Ga-MIL-53 powder pattern and the narrow Ga powder pattern corresponding to the Ga hydroxyl/hydroxide impurity are illustrated in (b) and (c), respectively. The differences in the Ga-MIL-53 powder patterns depicted in (b) are reflective of some guest-induced distortions of the Ga-MIL-53 framework (*i.e.*, phase changes). The Ga hydroxyl/hydroxide impurity resonance is labeled by an asterisk (*) in (a).

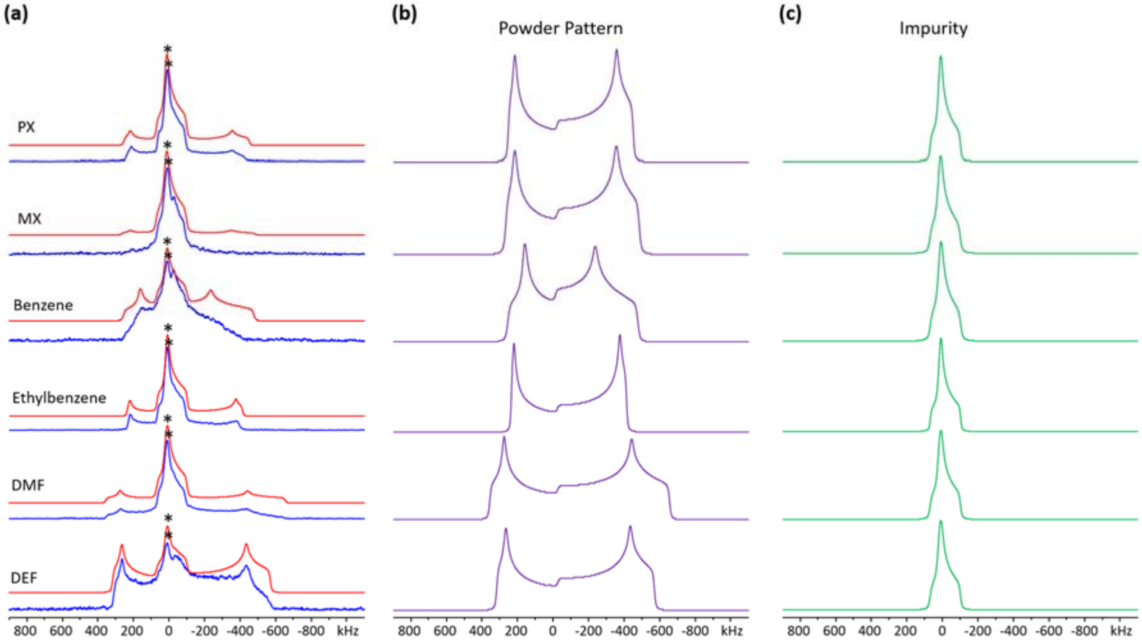

Figure 6-A13. A deconvolution of the static ^{69}Ga echo SSNMR spectra at 21.1 T of Ga-MIL-53 fully loaded with organic adsorbates are illustrated in this Figure; the experimental (blue) and simulated (red) spectra are shown in (a). The individual simulated spectra of the Ga-MIL-53 and the Ga hydroxyl/hydroxide impurity powder patterns are illustrated in (b) and (c), respectively. The differences between the ^{69}Ga SSNMR spectra shown in (b) are indicative of a change in the Ga local environment, and by extension, the Ga-MIL-53 crystal structure (*i.e.*, different phases) when Ga-MIL-53 is loaded with different adsorbates. The Ga hydroxyl/hydroxide impurity resonance is labeled with an asterisk (*) in (a).

References

(1) Ma, Z. L.; Wentz, K. M.; Hammann, B. A.; Chang, I. Y.; Kamunde-Devonish, M. K.; Cheong, P. H.-Y.; Johnson, D. W.; Terskikh, V. V.; Hayes, S. E., *Chem. Mater.* **2014**, 26, 4978-4983.

(2) Chaplais, G.; Simon-Masseron, A.; Porcher, F.; Lecomte, C.; Bazer-Bachi, D.; Bats, N.; Patarin, J., *Phys. Chem. Chem. Phys.* **2009**, 11, 5241-5245.

(3) Volkringer, C.; Loiseau, T.; Guillou, N.; Ferey, G.; Elkaim, E.; Vimont, A. *Dalton Trans.* **2009**, 12, 2241-2249.

Chapter 7

7 Conclusions and Future Works

7.1 Conclusions

Metal-organic frameworks are promising porous materials for industrial applications due to their outstanding properties such as large surface areas, selective guest adsorption, catalysis activities, and many others. Among all the applications, gas storage is the most promising one to be achieved, therefore, it is critical to understand the relationships between the porous framework and adsorbed guests. This thesis demonstrates the utility of SSNMR for studying gas dynamics, host-guest interactions, and short-range environments of target nuclei, which provides detailed information on rational design of MOFs with higher guest capacities.

In Chapter 2, CO_2 dynamics in MIL-53 series MOFs have been probed by investigating ^{13}C SSNMR experiments. CO_2 molecules adsorbed within MIL-53 (Al, Ga) and NH_2-MIL-53 (Al, Ga) undergo same motions, which present a localized wobbling and a non-localized hopping between two separate adsorption sites. Dynamic simulations also reveal the motional rates and angles of CO_2. All CO_2 molecules adsorbed within MIL-53 MOFs have motional rates greater than 10^9 s^{-1}. The motional angles are related to the experimental temperatures, where the values of motional angles decrease as temperatures reduce from 393 K to 153 K. The CO_2 binding strength in MIL-53 also has been revealed by these static ^{13}C SSNMR spectra, which follows the order NH_2-MIL-53 (Al) > NH_2-MIL-53 (Ga) > MIL-53 (Al) > MIL-53 (Ga). The CO_2 adsorption site within MIL-53 has been experimentally confirmed by acquiring ^{1}H-^{13}C CP SSNMR experiments. ^{1}H-^{13}C CP SSNMR spectra of deuterated MIL-53 suggest that the bridging -OH groups between SBUs act as the CO_2 adsorption sites. Our work advances the understanding of gas adsorption in MOFs without open metal sites, which may unlock avenues for designing MOFs with better CO_2 capacities.

The work in Chapter 3 focuses on studying the H_2 adsorption within various MOFs. The H_2 dynamics and the number of adsorption site within serval MOFs have been successfully revealed by investigating ^2H SSNMR experiments. Such information is very difficult to obtain by using adsorption isotherms or X-ray diffraction. The ^2H powder patterns of D_2 adsorbed within Mg-MOF-74 (loading level: 0.1 D_2/Mg) indicate that there are two similar, but non-equivalent D_2 molecules adsorbed on two different OMSs. The adsorbed D_2 molecules at these two adsorption sites have similar dynamics, which present a localized wobbling and a non-localized six-site hopping between six nearly coplanar OMSs along the pore edge. D_2 molecules adsorbed within α-$Mg_3(HCO_2)_6$ and α-$Zn_3(HCO_2)_6$ also locate on two distinct adsorption sites. Dynamic simulations indicated that the D_2 molecules adsorbed within formate MOFs have a combined motion of localized wobbling and non-localized two-site hopping. The ^2H SSNMR experiments also demonstrate the variation of the MOF topology, metal centre, and linker gives rise to different D_2 dynamic and adsorption strength. MOFs with OMSs or small pore size usually have stronger hydrogen binding strength.

In Chapter 4, methane adsorption within MOFs have been studied using various techniques including SCXRD, computational calculations, and SSNMR. SCXRD was used to determine the methane adsorption locations within α-$Mg_3(HCO_2)_6$, α-$Zn_3(HCO_2)_6$ and SIFSIX-3-Zn. The SCXRD studies are relative difficult due to the low electron density of methane molecules, however, quality SCXRD data has been acquired at 110 K, which clearly reveals the methane adsorption locations within α-$Mg_3(HCO_2)_6$, α-$Zn_3(HCO_2)_6$ and SIFSIX-3-Zn. DFT calculations have been investigated to optimize methane-loaded MOF structures and calculate methane adsorption energy. The calculated methane adsorption locations fit well with our SCXRD results. The calculated energy of adsorption also indicate pore size plays an important role in methane adsorption: MOFs with small pore size have stronger methane binding strength due to the dispersive contributions. ^2H SSNMR experiments have been investigated to study the host-guest interactions between frameworks and adsorbed deuterated-methane molecules. ^2H SSNMR spectra also indicate that MOFs with small pore size have stronger methane binding strength, reflected by broader spectral width. The lineshapes of ^2H SSNMR spectra also have been effected by nucleus independent chemical shifts (NICSs). To the best of our knowledge, such effect is first experimentally observed in MOF systems. Overall, this work is an excellent illustration of how much high-quality data regarding methane adsorption sites and host-guest interactions can be obtained when using a combination of SCXRD, computational, and SSNMR methods.

Chapter 5 describes studies of newly synthesized fumarate MOFs. Three fumarate MOFs including Ga-A520, hydrophilic In-A520-E, and hydrophobic In-A520-M have been successfully synthesised using solvothermal method. All three MOFs have same topology as Basolite A520 (Al-A520). The structure of Ga-A520 has been successfully determined using combined techniques including synchrotron pXRD, pXRD Rietveld refinements, SSNMR experiments, DFT calculations, TGA, and IR. The hydrophobic In-A520-M has been successfully investigated by introducing bridging –OCH_3 groups into the In-A520, which provided a novel method to generated hydrophobic MOFs. CO_2 adsorption in A520 MOFs has been studied by investigating CO_2 adsorption isotherms and SSNMR experiments. A520 MOFs with different metal centres have different CO_2 capacities, which follow the order: Al-A520 > Ga-A520 > In-A520-E > In-A520-M. CO_2 dynamics within A520 MOFs have been revealed by acquiring static ^{13}C SSNMR spectra. CO_2 within Al-A520, In-A520-E and In-A520-M only presents a localized wobbling upon CO_2 adsorption sites (bridging -OH groups), while in Ga-A520, CO_2 additionally hops between adjacent symmetry-equivalent adsorption sites, which are hydrogen atoms on the fumarate linkers.

$^{69/71}Ga$ SSNMR experiments were employed in Chapter 6 to study guest-induced phases of Ga-MIL-53. Experimental results indicate $^{69/71}Ga$ SSNMR is a powerful characterization method to probe the number of crystallographically Ga sites, their short-range structures, the presence of host guest interactions, and the phase of the Ga-MIL-53. Four phases (*as, ht, enp, lt*) of Ga-MIL-53 were studied first in this Chapter, $^{69/71}Ga$ EFG tensor parameters are very sensitive to the particular crystallographic phases and distortions of octahedral GaO_6 SBUs within these four phases. $^{69/71}Ga$ SSNMR experiments on CO_2-loaded Ga-MIL-53 monitor the CO_2 adsorption process and the resulting distortions in GaO_6 SBUs; and also strongly suggest that CO_2 guests first occupy only some of the available empty pores in Ga-MIL-53 at lower loading levels, and then proceed to populate all of the empty channels as the CO_2 loading level increases to ca. 0.45 CO_2/Ga. The Ga-MIL-53 samples loaded with organic guests also have been studied using TGA, pXRD and

$^{69/71}$Ga SSNMR experiments. The interactions between organic adsorbates and the Ga-MIL-53 framework, paired with alterations of the pore size and shape, distinctly influence the geometry of local octahedral GaO_6 SBUs and give rise to unique pXRD patterns and $^{69/71}$Ga SSNMR parameters. Therefore, SSNMR is a powerful tool that has the ability to identify the adsorbed guest molecules as well as the short-range structure and phase of Ga-MIL-53 when paired with complementary characterization techniques.

7.2 Future works

1. In a broad sense, Chapter 2, 3, and 4 in this thesis demonstrate the power of SSNMR spectroscopy in the study of gas dynamics, gas binding strength, number of adsorption sites, and adsorption locations within MOFs. In the future, it is hoped that other gases such as acetylene, ethylene, carbon monoxide and other toxic gases can be studied *via* SSNMR experiments to reveal the adsorption behaviours of other gases within MOFs.

Another important studying direction in the future is to study the competing adsorption of different guests within MOFs. By studying the dynamics and the host-guest or guest-guest interactions of these adsorbed guests, it would help us to understand the selectivity of MOFs.

In recent years, the chemisorption of gases, especially CO_2, by using functionalized MOFs has attracted a lot of attentions, since the chemisorption could avoid adsorbing other guests, such as water molecules. In the future, by investigating NMR experiments on target nuclei, a better understanding on chemisorption, including reaction sites, type of reactions, and chemisorption process can be established.

Gas conversion for fine chemicals by using MOFs as catalysts is another hot research topic in recent years, however, the mechanisms are barely studied. It is hoped that in the future, by investigating NMR experiments, the catalytic mechanisms could be revealed.

What's more, by combining SSNMR with other techniques such as SCXRD, neutron diffraction, and computational calculations, a well-understanding of MOFs in gas adsorption could be established in the future, and a rational design of MOFs with higher gas capacity and selectivity must be achieved eventually.

2. Chapter 4 describes the synthesis of analogous MOFs with different metal centres. The power of combined techniques including pXRD refinement, SSNMR, DFT calculations, IR, and TGA in determining the structure of powder crystals also has been predicted. This work provides a significant guiding function for the following exploration of structures of other powder crystals.

As one of the most promising MOF for practical use, the applications of A520 MOFs have been barely studied before due to the lack knowledge of their structures, therefore, exploring applications of A520 MOFs becomes very important in the future. Other applications such as methane adsorption, hydrogen adsorption, drug delivery, and catalysis need to be well studied.

Chapter 4 also describes the synthesis of a hydrophobic In-A520 MOF, which the hydrophobicity is achieved by replacing bridging -OH groups to bridging $-OCH_3$ groups. This method to enhance the MOF hydrophobicity also can be introduced to other MOFs, which contain bridging -OH groups. It is also hoped that A520 MOFs can be functionalized by other functional groups, thus, improving the framework properties and expanding their applications.

Another important direction in future study is introducing other metal centres into fumarate MOFs such as Fe, Cr, along with the study of their framework properties and applications. Different ligands such as oxalic acid, adipic acid, and sebacic acid also can be used to synthesize fumarate like MOFs, which may help us to control the pore size and the flexibility of the framework, thus extending the applications of fumarate MOFs into different areas.

3. Ultra-wideline SSNMR experiments on $^{69/71}$Ga and ^{115}In at 21.1 T have been investigated in Chapter 4 and Chapter 5. It is hoped that the quality spectra acquired in this thesis will stimulate SSNMR studies of other quadrupolar nuclei in MOFs. Two directions can be attempted in the future: i) acquiring quadrupolar SSNMR powder pattern at higher

magnetic field to narrow the spectral width, enhance the signal-to-noise ratio and shorten the acquisition time; ii) investigating comparison experiments between SSNMR experiments and computational calculations, thus assisting the study of the structure of a compound.

Copyright Permission

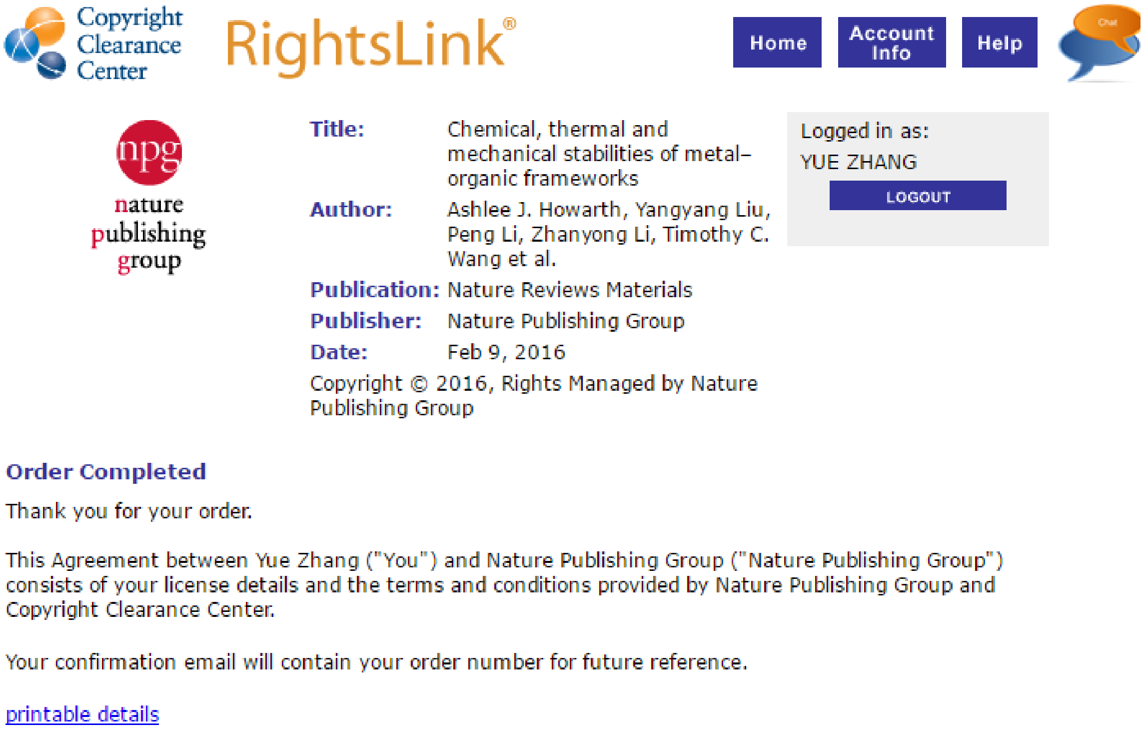

Title: Chemical, thermal and mechanical stabilities of metal–organic frameworks

Author: Ashlee J. Howarth, Yangyang Liu, Peng Li, Zhanyong Li, Timothy C. Wang et al.

Publication: Nature Reviews Materials

Publisher: Nature Publishing Group

Date: Feb 9, 2016

Copyright © 2016, Rights Managed by Nature Publishing Group

Logged in as:
YUE ZHANG

Order Completed

Thank you for your order.

This Agreement between Yue Zhang ("You") and Nature Publishing Group ("Nature Publishing Group") consists of your license details and the terms and conditions provided by Nature Publishing Group and Copyright Clearance Center.

Your confirmation email will contain your order number for future reference.

printable details

Title: Systematic Design of Pore Size and Functionality in Isoreticular MOFs and Their Application in Methane Storage

Author: Mohamed Eddaoudi,Jaheon Kim,Nathaniel Rosi,David Vodak,Joseph Wachter,Michael O'Keeffe,Omar M. Yaghi

Publication: Science

Publisher: The American Association for the Advancement of Science

Date: Jan 18, 2002

Copyright © 2002, The American Association for the Advancement of Science

Logged in as:
YUE ZHANG

Permissions Request

AAAS does not permit republication of its full text articles in unsecure electronic formats.

Title: Carbon Dioxide Capture in Metal–Organic Frameworks

Author: Kenji Sumida, David L. Rogow, Jarad A. Mason, et al

Publication: Chemical Reviews

Publisher: American Chemical Society

Date: Feb 1, 2012

Copyright © 2012, American Chemical Society

Logged in as:
YUE ZHANG

PERMISSION/LICENSE IS GRANTED FOR YOUR ORDER AT NO CHARGE

This type of permission/license, instead of the standard Terms & Conditions, is sent to you because no fee is being charged for your order. Please note the following:

- Permission is granted for your request in both print and electronic formats, and translations.
- If figures and/or tables were requested, they may be adapted or used in part.
- Please print this page for your records and send a copy of it to your publisher/graduate school.
- Appropriate credit for the requested material should be given as follows: "Reprinted (adapted) with permission from (COMPLETE REFERENCE CITATION). Copyright (YEAR) American Chemical Society." Insert appropriate information in place of the capitalized words.
- One-time permission is granted only for the use specified in your request. No additional uses are granted (such as derivative works or other editions). For any other uses, please submit a new request.

If credit is given to another source for the material you requested, permission must be obtained from that source.

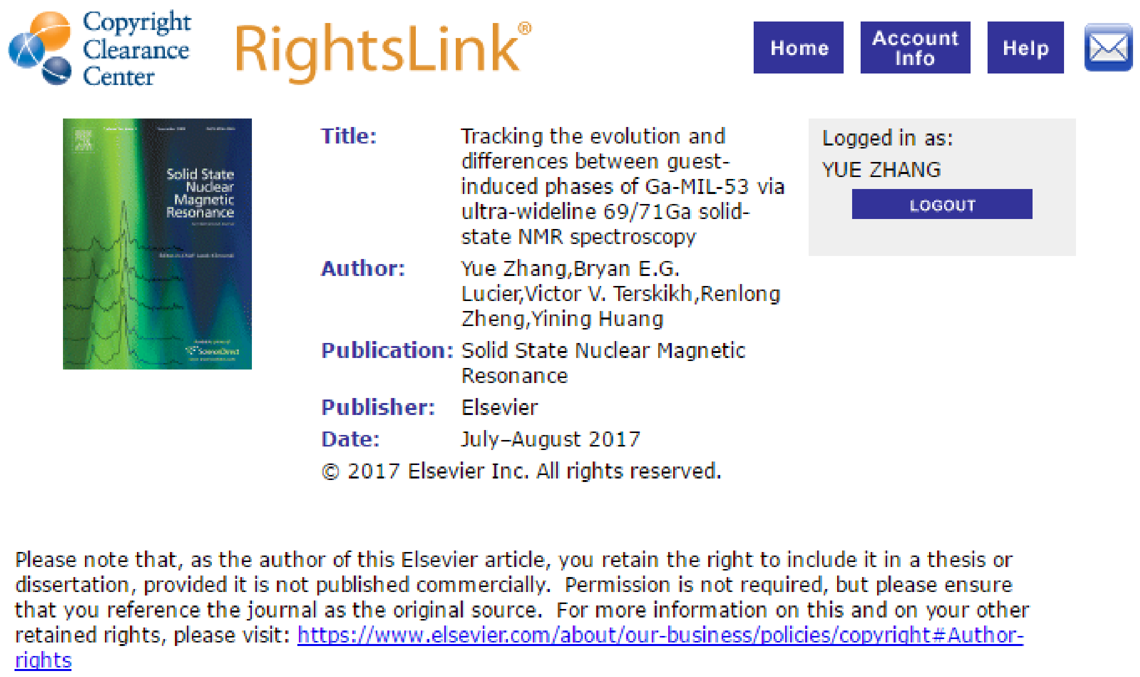

Title: Tracking the evolution and differences between guest-induced phases of Ga-MIL-53 via ultra-wideline 69/71Ga solid-state NMR spectroscopy

Author: Yue Zhang,Bryan E.G. Lucier,Victor V. Terskikh,Renlong Zheng,Yining Huang

Publication: Solid State Nuclear Magnetic Resonance

Publisher: Elsevier

Date: July–August 2017

© 2017 Elsevier Inc. All rights reserved.

Logged in as:
YUE ZHANG

Please note that, as the author of this Elsevier article, you retain the right to include it in a thesis or dissertation, provided it is not published commercially. Permission is not required, but please ensure that you reference the journal as the original source. For more information on this and on your other retained rights, please visit: https://www.elsevier.com/about/our-business/policies/copyright#Author-rights

---

Title: Methane storage in flexible metal–organic frameworks with intrinsic thermal management

Author: Jarad A. Mason, Julia Oktawiec, Mercedes K. Taylor, Matthew R. Hudson, Julien Rodriguez, Jonathan E. Bachman

Publication: Nature

Publisher: Nature Publishing Group

Date: Oct 26, 2015

Copyright © 2015, Rights Managed by Nature Publishing Group

Logged in as:
YUE ZHANG
Account #:
3001207189

Order Completed

Thank you for your order.

This Agreement between Yue Zhang ("You") and Nature Publishing Group ("Nature Publishing Group") consists of your license details and the terms and conditions provided by Nature Publishing Group and Copyright Clearance Center.

Your confirmation email will contain your order number for future reference.

Curriculum Vitae

Name: Yue Zhang

Post-secondary Education and Degrees:
East China University of Science and Technology
Shanghai, China
2008-2012 B.A.

Queen's University Belfast
Belfast, Northern Ireland, UK
2012-2013 M.A.

The University of Western Ontario
London, Ontario, Canada
2014-present Ph.D. candidate

Honours and Awards:
Western Graduate Research Scholarship
2014-2017

International Graduate Student Scholarship
2014-2017

Related Work Experience
Teaching Assistant
The University of Western Ontario
2014-2017

Research Assistant
The University of Western Ontario
2014-2017

Publications:

1. Bryan E. G. Lucier, **Yue Zhang**, Yining Huang, Complete Multinuclear Solid-State NMR of Metal-Organic Frameworks: The Case of α-Mg Formate, *Concepts Magn. Reson. Part A*, **2017**. (submitted)

2. **Yue Zhang**, Bryan E. G. Lucier, Victor V. Terskikh, Renlong Zheng, Yining Huang, Tracking the Evolution and Differences Between Guest-Induced Phases of Ga-MIL-53 *via* Ultra-Wideline $^{69/71}$Ga Solid-State NMR Spectroscopy, *Solid State Nucl. Magn. Reson.*, **2017**, 84, 118-131. **(Invited Article)**

3. Yuanjun Lu, Bryan E. G. Lucier, **Yue Zhang**, Pengju Ren, Anmin Zheng, Yining Huang, Sizable Dynamics in Small Pores: CO_2 Location and Motion in the α-Mg Formate Metal-Organic Framework, *Phys. Chem. Chem. Phys.*, **2017**, 19, 6130—6141.

4. Bryan E. G. Lucier,* **Yue Zhang**,* Kelly J. Lee, Yuanjun Lu and Yining Huang, Grasping Hydrogen Adsorption and Dynamics in Metal–Organic Frameworks using ^{2}H Solid-State NMR, *Chem. Commun.*, **2016**, 52, 7541—7544. **(Front Cover)**

5. **Yue Zhang**, Bryan E.G. Lucier, and Yining Huang, Deducing CO2 Motion, Adsorption Locations and Binding Strengths in a Flexible Metal–Organic Framework Without Open Metal Sites, *Phys. Chem. Chem. Phys.*, **2016**, 18, 8327—8341. **(Front Cover)**

6. Bryan E.G. Lucier, Hendrick Chan, **Yue Zhang,** and Yining Huang, Multiple Modes of Motion: Realizing the Dynamics of CO Adsorbed in M-MOF-74 (M = Mg, Zn) by Using Solid-State NMR Spectroscopy, *Eur. J. Inorg. Chem.,* **2016**, 13-14, 2017–2024.

Presentations

Sept/2017 **30th MOOT NMR Symposium, 2017, London**

Oral presentation: Studying metal-organic frameworks *via* solid-state NMR: structure determination, host-guest interactions, and gas dynamics

Jul/2017 **8th International Symposium Nanoporous Materials, 2017, Ottawa**

Poster presentation: Welcoming gallium and indium to the A520 MOF family: synthesis, comprehensive characterization, porous hydrophobicity, and CO_2 dynamics

Nov/2016 **49th Inorganic Discussion Weekend, 2016, Hamilton**

Oral presentation: Welcoming gallium and indium to the A520 MOF family: synthesis, comprehensive characterization, porous hydrophobicity, and CO_2 dynamics

Jun/2015 **98th Canadian Chemistry Conference and Exhibition, 2015, Ottawa**

Poster presentation: Inhaling and exhaling: using $^{69/71}$Ga solid-state NMR to study the breathing effect in the Ga-MIL-53 metal-organic framework

Oct/2014 **27th MOOT NMR Symposium, 2014, Montreal**

Poster presentation: Deducing CO2 motion, adsorption locations and binding strengths in flexible MIL-53 series MOFs using ^{13}C solid-state NMR